

# nature

THE INTERNATIONAL WEEKLY JOURNAL OF SCIENCE

## SCIENCE. FICTION.

An intimate relationship,  
from H.G. Wells to *Star Trek*  
and beyond **PAGE 162**



### EDUCATION

#### HOW TO BUILD A GENIUS

The maths prodigies who go  
on to change the world

**PAGE 152**

### ANTIMICROBIALS

#### A PRECIOUS RESOURCE

Respect and care required to  
combat resistance

**PAGE 158**

### DRUG DEVELOPMENT

#### THE PERFECT PAIN KILLER?

Opioid-like pain relief  
without the side effects

**PAGES 170 & 185**

NATURE.COM/NATURE

8 September 2016 £10

Vol. 537, No. 7619





# THIS WEEK

## EDITORIALS

**ANNOUNCEMENT** New Nature policy on data-sharing access **p.138**

**WORLD VIEW** How the GM-crop debate is making history **p.139**



**FOSSIL** Small pterosaur rewrites rules for ancient reptiles **p.141**

## Lessons from a scandal

*The Karolinska Institute has rightly tightened procedures in response to the controversy surrounding surgeon Paolo Macchiarini — but it should not do so to the detriment of its science.*

The Nobel Foundation next month will announce who has won the 2016 Nobel Prize in Physiology or Medicine. The Karolinska Institute (KI) in Stockholm, one of Europe's most highly ranked research institutions, will have selected those winners, as it has each year since 1901. The KI's reputation for intellectual quality and integrity has been a beacon in the world of biomedicine. But this year, that reputation has been rocked by a scandal.

In 2010, the KI recruited Paolo Macchiarini, a charismatic thoracic surgeon who had performed the world's first tracheal transplant using a donated windpipe seeded with the patient's stem cells. At the KI, he wanted to pioneer similar transplants using synthetic windpipes. Things didn't go so well. In the next few years, various allegations of clinical and scientific misconduct were brought against him. Yet the KI continued to clear him and to extend his employment.

Outside the sober scientific environment, other sides of Macchiarini's character were coming to light. In January, *Vanity Fair* magazine published a story about a US television news producer who said that Macchiarini had promised to marry her in a ceremony overseen by the Pope. Yet the surgeon seemed to be married already. The story included claims, since verified, that he had embellished his CV. The controversy hit the headlines when Swedish Television aired a moving three-part documentary following Macchiarini's work at the Karolinska University Hospital and — when he was stopped from doing further transplants there in 2013 — at a university hospital in Russia. The images of a young Russian woman who had the operation, and subsequently died, burnt into the Swedish psyche. Her life had not been in immediate danger, which would have been the only justification for such experimental surgery.

Things finally happened. The KI declined to renew Macchiarini's contract, and Swedish police are investigating a possible case of involuntary manslaughter and grievous bodily harm. Key figures in the affair, including the KI vice-chancellor and the dean of research, resigned their posts. Another resigned from his post as secretary-general of the KI Nobel Committee. The KI and its hospital both commissioned reports from independent experts, who have now published their results. They paint a damning picture, saying that the KI recruited Macchiarini despite negative professional references. In the rush to recruit, and hold on to, a bold clinician who promised a groundbreaking therapy using fashionable techniques, the upper echelons of the KI blinded themselves to warning signs, cutting regulatory corners to make sure that nothing would block the appointment. The KI seemed similarly blind when it renewed Macchiarini's contracts in 2013 and 2015, and it failed to follow regulations on handling allegations of scientific misconduct. Both the KI and the hospital have accepted the findings in the reports. Macchiarini has declined to comment to *Nature*.

Some KI scientists put the behaviour of their senior management down to increased government pressure to translate research from the lab to the clinic as fast as possible. But as noted by Sten Heckscher, a

former president of Sweden's Supreme Administrative Court who led the investigation into the KI, most institutions don't respond to such pressures in this way.

Public trust in the KI has plummeted, according to the latest national opinion poll on Swedish universities, in which it fell from fourth in 2015

**"The KI's wider reputation might be saved by how it has handled the affair."**

to twelfth this year. Outside Sweden, at least in scientific circles, its wider reputation might well be saved by how it has handled the affair since February. It has adopted a tactic of complete openness: a timeline of relevant events is available in English and Swedish on the KI homepage, and is regularly updated. The KI's

earlier weak — now discredited — responses to allegations of misconduct are collected on the same dedicated page ([go.nature.com/2cjunzr](http://go.nature.com/2cjunzr)).

The KI and its university hospital have learnt from the affair and have already fine-tuned many of their procedures, including those for recruitment and handling whistle-blowers. Still, the KI should not tighten its procedures so much that it no longer feels comfortable taking justifiable scientific risks. The institute has gained its standing in large part through its willingness to be adventurous in research. Observing its exemplary approach to the scandal, the world of biomedicine might yet forgive the KI this one major slip. It will not forgive a slip into mediocrity. ■

## Time machine

*Science fiction fights the past as much as it faces the future.*

Back in 1969, you could buy a stake in the future, even if it was only a plastic model kit of the Apollo Lunar Module. But the price was stuck in the past. The UK kit cost 5 shillings and 11 pence, in a pre-decimal system that dated back to the Middle Ages, with abbreviations that recalled the Roman occupation of Britain — the penny was abbreviated to 'd', standing for 'denarius'.

Such archaisms angered and frustrated Herbert George Wells (1866–1946), whose raillery against such relics is documented in Simon James's retrospective on page 162 as part of this week's science-fiction special issue. It is followed, on page 165, by Sidney Perkowitz's appreciation of *Star Trek*, the space-opera TV and movie franchise that has been visiting strange new worlds since 1966.

Britain changed to decimal coinage in 1971, but even countries that are long used to money in multiples of ten can't escape the history of their currency. The word 'dollar', for example, derives from 'thaler', a



coin that can be traced back to early sixteenth-century Bohemia; and the abiding fondness of one of the planet's most technically advanced nations for non-SI units is a source of some embarrassment or hilarity (depending on your point of view). The past is a loam of inertia through which the shoots of futurity struggle to emerge. As cyberpunk author William Gibson once said, the future is already here — it's just not very evenly distributed.

Wells had every reason to fight for the future. Fate saw him born into the smokes and stinks of Victorian Britain as the son of servants in 1866. Like all years, it was a potpourri of past and future: it was the year of the long-forgotten Austro-Prussian War between two ageing empires that have long since crumbled, but also the year that the Royal Aeronautical Society was founded, and that Alfred Nobel invented dynamite.

Wells nimbly avoided his fate of becoming a haberdasher and ended as one of the visionaries of his age, regularly published in these pages. Pulling himself upwards to the light became a personal as well as a professional preoccupation.

Living as we do in a much gentler age (for all that it occasionally seems otherwise), we are inclined to dissect Wells's achievement into discrete anticipations of such technological gewgaws as tanks and atomic bombs, without appreciating his drive and ambition to better not just himself, but the rest of humanity. We are likewise inclined to forget that his first full-length novel, *The Time Machine*, is not just a fantasy of the far future but an excoriating damnation of the class system, in which the classes evolve into two separate but interdependent species: the leisured, effete and mindless Eloi, preyed on by the ugly and industrious Morlocks. This is no hidden allegory: as a character says in *The Soul Of A Bishop* (1917), one of Wells's non-science-fictional novels, "we are the Morlocks, coming up!"

One could be flippant and say that the importance of Wells's work now lies in its intriguing mix of old and new — Wells was steam-punk when steam was still punk, his futuristic machines tricked out in hand-tooled leather and knurled brass. But Wells earns his place, in the words of Brian Aldiss (in *Trillion Year Spree*), as the 'Shakespeare' of sci-fi because he takes ordinary people and tests their reactions to technology and its consequences — shaven monkeys from Woking pitted against the intellects of Martians, vast and cool and unsympathetic.

**"The future is already here — it's just not very evenly distributed."**

*Star Trek* first aired in the centenary year of the US Civil Rights Act of 1866 — an appropriate date, seeing as the show's prime aim was to depict a harmoniously integrated future society rather than anticipate technological marvels such as the tricorder and the cloaking device. Arthur C. Clarke, another titan of sci-fi, dismissed (in *The Songs of Distant Earth*) one such technological trinket, the warp drive, as simply a McGuffin that allowed the crew to get from one locale to the next "in time for next week's exciting episode". *Star Trek* creator Gene Roddenberry, like Wells, drew his passion from a need to rise above the inequities of the present and forge a more equitable future.

Why are we celebrating Wells and *Star Trek* now, in this sci-fi special (which includes on page 259 our long-running Futures sci-fi series presented as a graphic novel for the first time)? It happens to be 150 years since Wells's birth, 70 years since his death and 50 years since *Star Trek* was first aired. All satisfying multiples of ten, but measured in units based on the revolution of a small planet round an unremarkable star in the suburbs of an ordinary galaxy. As Wells lamented, we are shackled to our past. It might be a while before we run such commemorations based on binary representations of elapsed numbers of Planck time units. ■

## ANNOUNCEMENT

## Where are the data?

As the research community embraces data sharing, academic journals can do their bit to help. Starting this month, all research papers accepted for publication in *Nature* and an initial 12 other Nature titles will be required to include information on whether and how others can access the underlying data.

These statements will report the availability of the 'minimal data set' necessary to interpret, replicate and build on the findings reported in the paper. Where applicable, they will include details about publicly archived data sets that have been analysed or generated during the study. Where restrictions on access are in place — for example, in the case of privacy limitations or third-party control — authors will be expected to make this clear.

The new policy (full details of which are available at [go.nature.com/2bf4vqn](http://go.nature.com/2bf4vqn)) builds on our long-standing support for data availability as a condition of publication. It also extends our support for data citation, the practice of citing data sets in reference lists in a similar way to citing papers. Authors are encouraged to cite data sets that have digital object identifiers (DOIs) assigned to them.

The introduction of data-availability statements follows a trial at five Nature journals — *Nature Cell Biology*, *Nature Communications*, *Nature Geoscience*, *Nature Neuroscience* and *Nature Physics* — that began in March 2016. The pilot confirmed differences in the culture of data sharing and access between different disciplines, and that the lack of obvious, public, community repositories can pose a significant barrier to public data deposition. Nevertheless,

even in disciplines that are not yet so able to embrace openness and sharing, there is increasing awareness and appreciation that data deposition can enhance the visibility and reuse of published research, and that data citation can increase the recognition of those who create and share data.

This new policy will be implemented across the diverse range of Nature journals by early 2017. We expect that its implementation will shed more light on the reasons for disciplinary differences in data sharing, identify challenges and help to promote the practice more widely.

It's not just journals. A broad drive across the research, funding and publishing communities is under way to make the availability of research data more transparent. Funders, for example, are also introducing data-availability statements. The seven UK research councils require their grant holders to include them. And the US National Institutes of Health is asking researchers to provide management plans for their research data.

We expect that offering consistent information on data availability in our papers will promote data reuse by future researchers. And where public data archiving is a mandatory requirement of journals, there is some evidence that including data-availability statements with persistent links to data in published articles is an effective approach to ensuring public data availability and policy compliance (T. H. Vines *et al.* *FASEB J.* 27, 1304–1308; 2013).

This new policy follows the launch, in July 2016, by our publisher Springer Nature of an ambitious project to introduce and standardize research data policies across all of its journals (see [go.nature.com/2by6l6x](http://go.nature.com/2by6l6x)). The project sets out a defined common framework for data policy — which Nature policies align with — that enables different journals to encourage data sharing in a way that reflects the circumstances of respective specialist communities. ■





## The debate over GM crops is making history

*An archive of material from all sides of the UK genetic-modification controversy is up and running and welcomes contributions, says Vivian Moses.*

When does history begin? Can we anticipate which of our contemporary events the historians of the future will find most interesting? A century from now, will there be universal acceptance of genetically modified (GM) crops, with little sign of the protest and controversy that has surrounded them until now? Or will those objections have killed off the development of what was once seen as a promising new technology?

Either way, events of the past two decades will be of great interest. Future historians could view this period either as signalling the birth of opposition to GM crops or as offering a case study of how and why that opposition was once significant — and how it was overcome.

Hoping to help those future historians, I and others have gathered a historical archive of material relevant to the debate over GM crops and the food derived from them.

It became clear more than ten years ago, quite early in the debate, that an interesting phenomenon was unfolding. A new set of scientific technologies had provoked widespread reactions, many of them antipathetic for a wide variety of reasons (including health risks), which themselves became topics for fierce argument and discussion.

The science underpinning the deployment of the technology and the safety of GM products was attested by most of the scientific community and essentially all of the official agencies internationally responsible for food and environmental safety. Opposition, it seemed to most scientists, was clearly not based primarily on the validity of scientific findings, although many opponents claimed that it was. Those counter-arguments were rejected by most scientists, who perceived them as motivated by political, commercial and other interests for which scientific validity was, at best, of secondary importance.

This was not the first vigorous public reaction to new technologies. Innovation is often accepted with alacrity — think of the Sony Walkman and the iPhone — but sometimes causes trouble. Riots in nineteenth-century London against compulsory smallpox vaccination of children (many parents then, as now, felt they should have the choice) were followed by objections in Oklahoma to the electric telegraph connection with New Orleans, which would bring bad news and encourage gambling. There were (and remain) objections to milk pasteurization and to mobile-phone transmitters, not to mention nuclear power.

The effort to prepare an archive of the GM debate began in 2008, when it became clear that the GM crop and food phenomenon would be a useful way to study societal reactions to new technologies.

Whatever the eventual outcome of the debate, we realized that there would be many lessons to learn about how (and how not) to introduce a new technology, as well as whether (or not) it might be wise to do so. Genetic modification would be an important subject for future, as

well as contemporary, study — but much would be lost if records and ephemera of all sorts were not retained under safe conditions.

We cannot know in advance what aspects of GM crops will be of interest to future scholars, so it is best to keep as much material as possible. Although archives are usually established in retrospect, as and when historical subjects attract interest, we set out to do so in prospect, knowing from the outset that we have an interesting and pertinent phenomenon to record. It would be presumptuous to estimate the archive's future value, but we did predict that, without it, a time would come when its absence would be regretted.

With collaboration from the British Library, we began a project with the Science Museum in London to find and preserve eligible papers, films, tapes, disks, websites, equipment and more. (We have no facilities for storing biological material.)

Much of the vulnerable material held by individuals needed to be secured before it was thrown away. By 2008 it was already late: filing cabinets are periodically cleaned out. Nevertheless, much interesting material was still held by scientists and other academics, industry, farming interests, government, campaigners, the media and others.

We planned a global archive, but talking to colleagues in the United States and elsewhere quickly showed that this was overambitious. Moreover, the Science Museum's remit is to collect material mainly from UK sources. So the archive focuses on the debate in Britain, which has been particularly strong and for which a large amount of material is available. The archive contains important records, including correspondence, from researchers, campaigners and the public-relations firms used

by the biotech companies to try to counter opposition.

Space and facilities had to be organized before the archive became public, but it is now finally open for use, housed at the Science Museum's Wroughton site, near Swindon (see [go.nature.com/2btqdk1](http://go.nature.com/2btqdk1)). It includes dozens of box files across 23 metres of shelf space and includes correspondence on the controversial publication of research that claimed to show health impacts of GM potatoes. Pending funding to prepare a full catalogue, a broad listing of contents is available at [go.nature.com/2cjtjq](http://go.nature.com/2cjtjq). (Click to search Science Museum, London; enter 'genetic' in the search box; select 'Title' in 'Sort By' and finally click on 'Search'.)

We continue to seek relevant material, and hope that UK colleagues will contribute more to the Wroughton collection and that others around the world will be inspired to establish GM archives in their own countries. We live in interesting times. Let's preserve them. ■

**Vivian Moses** is visiting professor of biotechnology at King's College London.

e-mail: [v.moses@qmul.ac.uk](mailto:v.moses@qmul.ac.uk)

A NEW SET OF  
**SCIENTIFIC**  
TECHNOLOGIES HAD  
**PROVOKED**  
WIDESPREAD  
**REACTIONS,**  
MANY OF THEM  
ANTIPATHETIC.



## ASTRONOMY

### Carbon monoxide in large-star disks

Stars twice as massive as the Sun can feature carbon-monoxide-rich gas disks around them, contrary to the expectation that ultraviolet radiation would have stripped away the gas.

Meredith Hughes at Wesleyan University in Middletown, Connecticut, and her colleagues used the Atacama Large Millimeter/submillimeter Array in northern Chile to probe the regions around 24 young star systems, only about 5 million to 10 million years old. They chose stars surrounded by a disk of dust debris — resembling a scaled-up version of the Solar System's Kuiper belt. This leftover material could form new planets, including gas giants. Surprisingly, three of the larger stars in the sample had strong carbon monoxide emissions. *Astrophys. J.* 828, 25 (2016)

## CANCER

### 'Perfect storm' of cancer risk

The ability of an organ's stem cells to generate new tissue over time — the cells' generative capacity — determines how prone that organ is to cancer.

Scientists have debated the relative importance of factors that contribute to an organ's cancer risk, including 'intrinsic' factors such as the number of stem-cell divisions and 'extrinsic' factors that cause tissue and DNA damage. To compare these factors, Richard Gilbertson at the CRUK Cambridge Institute, UK, Arzu Onar-Thomas at St Jude Children's Research Hospital in Memphis, Tennessee, and their colleagues studied stem

cells called Prom1<sup>+</sup> cells with varying levels of generative capacity in different organs in mice of various ages. The authors introduced key cancer-causing mutations into the cells, then looked for tumour growth in the organs.

The team found that cancer risk correlated closely with the generative capacity of the Prom1<sup>+</sup> cells. In liver tissue, cancer mutations alone did not cause cancer — tissue injury significantly increased cancer susceptibility. The authors propose that several factors contribute to a 'perfect storm' of tumour growth: mutated

stem cells and extrinsic factors that trigger cell proliferation. *Cell* <http://doi.org/bp73> (2016)

## CLIMATE-CHANGE ECOLOGY

### Trees flourish on the happy edge

As the climate warms, sugar maples expanding their populations uphill could outrun their insect predators and flourish on the 'happy edge' of their range.

Morgane Urli and her colleagues at the University of Sherbrooke in Quebec, Canada, transplanted

two-year-old sugar maples (*Acer saccharum*) uphill to sites just at, and beyond, their current elevation range limit. Some were given protection from herbivores. Of seedlings without protection, more than 75% at the range edge and beyond survived, compared with just 30% at the centre of the current range. The difference narrowed markedly in protected plants, suggesting that the increased survival was largely due to 'enemy release' at and beyond the current range.

Previously, the team showed that seed predation beyond elevation range limits is very



## DISEASE ECOLOGY

### Rapid evolution of cancer resistance

Tasmanian devils have developed a degree of genetic resistance to a virulent contagious facial cancer in just four to six generations.

Andrew Storfer at Washington State University in Pullman and his colleagues sequenced about one-sixth of the genome for 294 devils (*Sarcophilus harrisii*) from 3 wild populations. The authors used samples collected both before and after the groups first

encountered the facial cancer.

The team found five genes spread across two regions of the genome that showed strong signs of selection, including a large number of single-DNA-base changes, throughout the devil populations. Two of the genes, *CD146* and *THY1*, are known to help the immune system to recognize foreign cells in other animals. *Nature Commun.* 7, 12684 (2016)



high. However, those few seeds that do escape can look forward to a healthy future.  
*Ecology* <http://doi.org/bp5t> (2016)

## CONSERVATION BIOLOGY

## Lazy bustards live longer

Migration in great bustards seems to be on the decline because many of those that do migrate die in collisions with power lines.

Carlos Palacín at the National Museum of Natural Sciences in Madrid and his colleagues captured and radio-tagged 180 male great bustards (*Otis tarda*) across 29 breeding groups, covering most of the species' range in Iberia. Only some birds migrated north in summer. Of those that did, 21.3% died in crashes with power lines, whereas just 6.3% in the sedentary group died in this way.

The authors found a steady increase in the proportion of non-migratory males over the study period, from 17% in 1997 to 45% in 2012. They propose that males decide whether to migrate by observing other males. Thus, as the number of migrators declines, the behaviour may die out.  
*Conserv. Biol.* <http://doi.org/bp53> (2016)

## PALAEOONTOLOGY

## Tiny pterosaurs' tenure extended

The discovery of a surprisingly small fossilized pterosaur (pictured with domestic cat for scale) in rock some 77 million years old challenges the accepted history of the winged reptiles. Scientists had thought that, by around 100 million years ago, small pterosaurs had been replaced by larger species.

Elizabeth Martin-Silverstone at the University of Southampton, UK, and her colleagues uncovered a wing bone and vertebrae from a pterosaur in 80-million- to 72-million-year-old rock formations in British

Columbia, Canada. Although the creature's 1.5-metre wingspan was tiny compared with that of the 10-metre giants known from this period, bone analysis revealed that it was almost fully grown.

Fossilized juveniles of larger pterosaur species from this period are also rare, suggesting that the record may be biased against small pterosaurs.  
*R. Soc. Open Sci.* 3, 160333 (2016)

## STEM CELLS

## Bone cells on demand

Researchers have come up with a simple recipe for making bone from stem cells.

Embryonic stem cells can form every type of tissue in the body, but methods for forcing these and other pluripotent stem cells to differentiate into a specific type can be inefficient and costly. A team led by Shyni Varghese at the University of California, San Diego, added a chemical called adenosine — which occurs naturally in the body — to human stem-cell cultures and produced bone-making cells called osteoblasts in under three weeks. The cultured osteoblasts generated calcified bone, and scaffolds that had been coated with the osteoblasts and implanted into mice repaired skull defects.  
*Sci. Adv.* 2, e1600691 (2016)

## GENETICS

## Synthetic DNA overreacts to light

Synthetic DNA bases created in 2014 to expand the genetic code are light-sensitive and produce reactive oxygen species (ROS) when exposed to certain wavelengths.

Ultraviolet light can



damage natural DNA bases, but cells have in-built repair mechanisms to fix this. Carlos Crespo-Hernández of Case Western Reserve University in Cleveland, Ohio, and his co-workers found that two lab-made DNA bases — d5SICS and dNaM, which have been used to design semi-synthetic bacteria — generate up to 100 times more reactive species than the most reactive natural base, thymidine, when exposed to near-visible wavelengths of light. In response to light exposure, a carcinoma cell line grown with d5SICS had higher levels of ROS, and cell proliferation was reduced.

Synthetic DNA bases may accelerate photochemical damage to cells, the authors say.  
*J. Am. Chem. Soc.* <http://doi.org/bp55> (2016)

## CLIMATE CHANGE

## Melting ice opens Arctic to shipping

Thanks to melting Arctic sea ice, ships with moderate ice strengthening (lighter than currently required, pictured) may be able to travel northern waters all year round by the century's end.

Nathanael Melia and his colleagues at the University of Reading, UK, used several global climate models to simulate the fastest shipping routes through the Arctic, depending on future greenhouse-gas emissions. In their most extreme scenario, the route from Yokohama in Japan to Rotterdam in the Netherlands becomes 13 days shorter than

alternative routes by 2100.

Even ordinary vessels could see the period during which they can navigate Arctic waters double by mid-century.  
*Geophys. Res. Lett.* <http://doi.org/bp5x> (2016)

## STAR FORMATION

## Star-rich early galaxy clusters

Galaxy clusters in the early Universe produced more stars than their more modern counterparts.

When a galaxy becomes part of a cluster — a group of galaxies bound together by gravity — its crowded surroundings often cause it to stop producing stars, an effect called environmental quenching. Using the Keck Observatory in Hawaii and the Very Large Telescope in Chile, a team led by Julie Nantais at the Andres Bello University in Santiago observed four galaxy clusters nearly 10 billion years old. They found that, in these early clusters, only about 30% more of the galaxies had stopped producing stars than had the surrounding galaxies, compared with a difference of about 50% in newer clusters.

Knowing how quenching changes over the history of the Universe may help scientists to determine why the cluster environment causes the phenomenon.

*Astron. Astrophys.* 592, A161 (2016)

## NATURE.COM

For the latest research published by Nature visit:

[www.nature.com/latestresearch](http://www.nature.com/latestresearch)



# SEVEN DAYS

The news in brief

## FACILITIES

### UK chief of chiefs

The UK government opened applications on 30 August for the post of chief executive of UK Research and Innovation (UKRI), the body that will unite the country's nine existing research-funding bodies. The job comes with a salary package of around £300,000 (US\$400,000). The salary — about twice that of existing research-council chiefs — should be enough to lure university heads, say observers. The head of UKRI, which is yet to be created by parliamentary legislation, will oversee an annual budget of more than £6 billion.

## PEOPLE

### Macchiarini inquiry

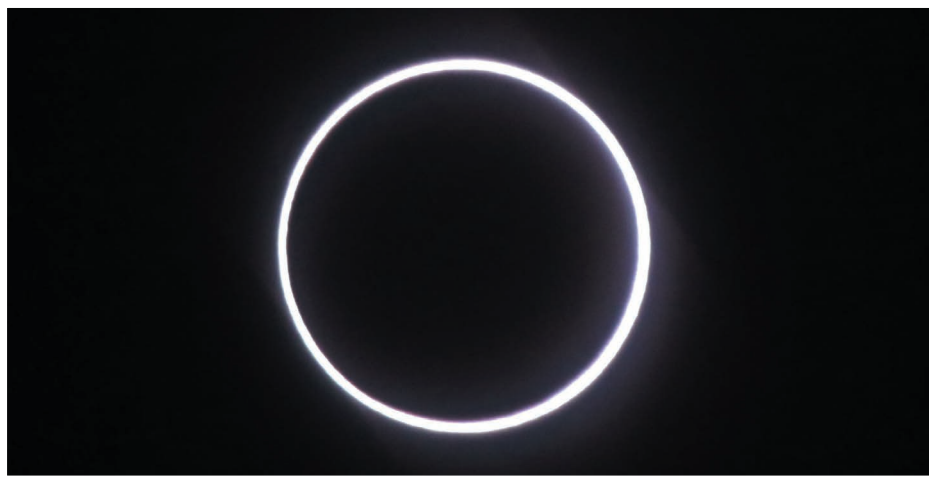
Paolo Macchiarini, a disgraced surgeon who was formerly a visiting professor at the Karolinska Institute (KI) in Stockholm, worked in an environment that fostered a “culture of silence” and a “nonchalant attitude towards regulations”. Those are the conclusions of two independent inquiries initiated by the KI and its affiliated university hospital, where Macchiarini carried out three artificial-trachea operations, including the

## NUMBER CRUNCH

# 30%

The decline in Africa's savannah elephant population from 2007 to 2014, equal to about 144,000 elephants. The current rate of decline is 8% per year, with poaching mainly to blame.

Source: Great Elephant Census



RICHARD BOUGET/AFP/GETTY

## ‘Ring of fire’ eclipse glows in African sky

A spectacular ‘ring of fire’ annular solar eclipse passed over southern parts of Africa and the Indian Ocean on 1 September. Astrophotographers captured the glowing ring of the Sun (pictured, as seen from Réunion) for the roughly three minutes of the eclipse. Annular eclipses happen when the Moon and Earth are

slightly farther away from one another in their orbits than they are during a total eclipse, so the Moon appears smaller when it passes across the face of the Sun. The resulting ring is known as an annulus. The next annular eclipse will be fleetingly visible, for 44 seconds, over the south Atlantic Ocean on 26 February 2017.

world's first, between 2011 and 2013. Two of the patients died. Allegations of misconduct against Macchiarini emerged in 2014, but the KI cleared him. A Swedish documentary about his work, aired in January, reopened the issue. The KI dismissed him in March. Macchiarini said this week in a statement to Swedish broadcaster SVT that he is not guilty of research mismanagement, and has always done the best for his patients. Two members of the KI's Nobel Assembly, which awards the medicine prize, have been asked to resign as a result of their links to the affair. See page 137 for more.

### Roger Tsien dies

Nobel-prizewinning chemist Roger Tsien, who used a jellyfish protein to illuminate molecular biology,

died on 24 August, aged 64. Tsien's work with green fluorescent protein turned it into a laboratory staple as researchers around the world used it to label molecules to track their expression and movements in living cells. Tsien worked at the University of California, San Diego, and shared the chemistry Nobel with two other researchers in 2008. See [go.nature.com/2clfomy](http://go.nature.com/2clfomy) for more.

## POLICY

### Gene-drive vote

Members of the International Union for Conservation of Nature (IUCN) have voted for a moratorium on research into the use of gene drives for conservation. Gene drives allow genetic modifications to be rapidly spread through wild populations, and some people

have proposed that they could be used to wipe out invasive species and restore natural ecosystems. But the approach raises concerns about possible unintended consequences of releasing gene drives into the environment.

### Animal research

In a policy turnaround, the Alliance of Science Organisations in Germany has launched an Internet platform for education and discussion on research with animals ([tierversuche-verstehen.de](http://tierversuche-verstehen.de)). Germany has been criticized for bucking the European trend towards openness on animal research. The website, launched on 6 September, allows interactive discussion and provides a service to journalists seeking scientific expertise. It includes extensive information — also through



a YouTube channel — on the legal environment for such research, as well as personal stories from scientists who work with animals, including non-human primates.

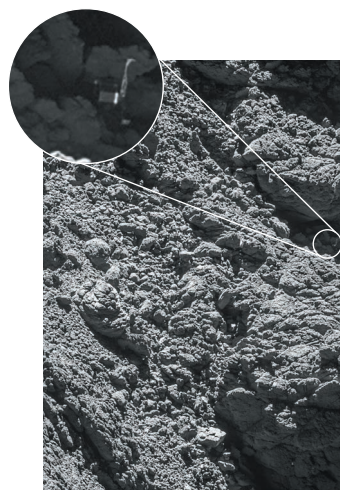
## RESEARCH

## Free Neanderthal

A newly sequenced Neanderthal genome is available to download for free, before formal publication, researchers have announced. A team led by Svante Pääbo at the Max Planck Institute for Evolutionary Anthropology in Leipzig, Germany, has released the genome sequence of a roughly 45,000-year-old Neanderthal bone from Vindija Cave in Croatia before publishing its own analysis of the data (see [go.nature.com/2bv1shu](http://go.nature.com/2bv1shu)). The researchers say that they want to allow other teams to start their own analyses.

## Lost Philae found

Photos taken by the mothership of Philae, the European Space Agency's comet lander, have revealed the craft's location definitively for the first time. Philae landed on comet 67P/Churyumov–Gerasimenko in November 2014, but it failed to grip the comet's surface and bounced into a shady spot. The lander's tilted position meant that its antenna was partially blocked,



making communication difficult, and it was unable to use its solar panels to charge its batteries. The pictures, taken by the Rosetta spacecraft's OSIRIS camera on 2 September, confirm that Philae is lying on its side in the shadow of a cliff, lodged in a crack, with one of its legs in the air (pictured). See [go.nature.com/2c90rwu](http://go.nature.com/2c90rwu) for more.

## EVENTS

## Rocket failure

A Falcon 9 rocket made by commercial-spaceflight company SpaceX exploded on the launch pad at Cape Canaveral in Florida on 1 September. The event occurred two days before the craft was set to carry an Israeli communications satellite into orbit. The cause of the explosion, which happened

in the minutes leading up to a planned engine test, is under investigation. The rocket's payload, the AMOS-6 communications satellite, was also destroyed. It had been intended to provide Internet connectivity across sub-Saharan Africa.

## Brexit warning

Japan's government has issued a 15-page warning over the United Kingdom's pending exit from the European Union. A memo posted online by Japan's foreign ministry lists requests from Japanese businesses operating in Britain, including continued access to EU research funding and the ability to take part in EU research projects. The document also warns that if the European Medicines Agency moves from its present location in London, money and researchers could be shifted to continental Europe.

## Academics sacked

Under state-of-emergency provisions, Turkey's government issued a decree on 1 September that sacked 2,346 university staff for alleged ties to an attempted military coup in July. The move is part of a wider purge of 40,000 civil servants who will be excluded from holding any government positions in the future. Academic organizations in Turkey have

protested that some of those fired are not part of the Gülen religious movement, which the government says was behind the coup, but opponents of certain government policies. More than 40 had been signatories of the 'academics for peace' petition released in January that called for an end to violence between government forces and Kurdish separatists, and which led to the immediate arrests of some signatories.

## Gorilla on the brink

The latest update of the IUCN Red List of Threatened Species, which tracks the health of animal and plant populations, has moved the eastern gorilla (*Gorilla beringei*) from the endangered to the critically endangered category, after a 70% crash in the primate's numbers in two decades. However, the giant panda (*Ailuropoda melanoleuca*) shifted from endangered to vulnerable as a result of increased protection helping its numbers. Two plants endemic to Hawaii, *Cyanea marksii* and *Wikstroemia villosa*, were listed as critically endangered, having previously been thought to be extinct.

## Boon for Paris deal

In a milestone step, the world's two biggest greenhouse-gas emitters, the United States and China, have ratified the Paris climate agreement. Last December, nearly 200 nations made a deal to cut emissions and keep global temperature increases to "well below" 2 °C. For the agreement to enter into force, 55 nations accounting for at least 55% of global emissions need to ratify the deal. Together, China and the United States generate some 38% of global carbon emissions. Before 3 September, only 24 signatories had ratified the deal, representing around 1% of global emissions. The move is expected to prompt a surge in ratifications.

► [NATURE.COM](http://NATURE.COM)

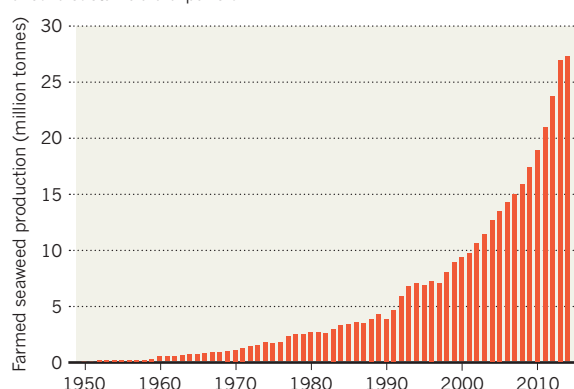
For daily news updates see:  
[www.nature.com/news](http://www.nature.com/news)

## TREND WATCH

Seaweed farming has undergone astonishing growth over the past 50 years, says a report from the United Nations University released on 4 September. In 2014, the industry produced more than 25 million tonnes of seaweed, mostly for food, with a value of US\$6.4 million. Widening uses for the crop, including in fertilizers and drugs, are driving growth. But seaweed can spread diseases, and few regulations exist to safeguard against this, the report says. The industry should learn from other agricultural sectors, it adds.

## BEWARE THE SEAWEED BOOM

Seaweed farming has grown exponentially over the past few decades — but experts warn that regulation is needed to ensure sustainable expansion.



# NEWS IN FOCUS

**EUROPE** Brexit looms over opening of giant London biomedical lab **p.147**

**BIOMEDICINE** US guidelines attempt to rein in rogue stem-cell clinics **p.148**

**POLITICS** Upcoming election creates budget uncertainty for US researchers **p.149**



**EDUCATION** The 45-year study that shows how best to nurture talented kids **p.152**

NASA



View from the Mars rover Curiosity at the foot of Aeolis Mons, before the rover starts to climb the mountain.

## PLANETARY SCIENCE

# Mars contamination fear could divert Curiosity rover

*NASA must keep Earth microbes from getting into hillside streaks suspected to hold water.*

BY ALEXANDRA WITZE

Four years into its travels across Mars, NASA's Curiosity rover faces an unexpected challenge: wending its way safely among dozens of dark streaks that could indicate water seeping from the red planet's hillsides.

Although scientists might love to investigate the streaks at close range, strict international

rules prohibit Curiosity from touching any part of Mars that could host liquid water, to prevent contamination. But as the rover begins climbing the mountain Aeolis Mons next month, it will probably pass within a few kilometres of a dark streak that grew and shifted between February and July 2012 in ways suggestive of flowing water.

NASA officials are trying to determine whether Earth microbes aboard Curiosity

could contaminate the potential Martian seeps from a distance. If the risk is too high, NASA could shift the rover's course — but that would present a daunting geographical challenge. There is only one obvious path to the ancient geological formations that Curiosity scientists have been yearning to sample for years (see 'All wet?').

"We're very excited to get up to these layers and find the 3-billion-year-old water," says ▶



Ashwin Vasavada, Curiosity's project scientist at NASA's Jet Propulsion Laboratory (JPL) in Pasadena, California. "Not the ten-day-old water."

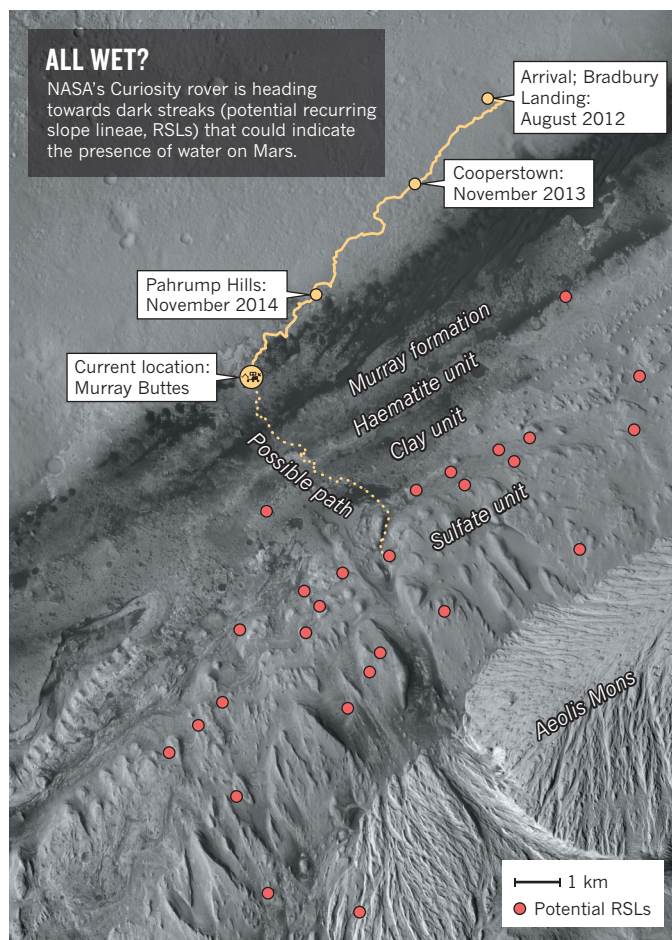
The streaks — dubbed recurring slope lineae (RSLs) because they appear, fade away and reappear seasonally on steep slopes — were first reported<sup>1</sup> on Mars five years ago in a handful of places. The total count is now up to 452 possible RSLs. More than half of those are in the enormous equatorial canyon of Valles Marineris, but they also appear at other latitudes and longitudes. "We're just finding them all over the place," says David Stillman, a planetary scientist at the Southwest Research Institute in Boulder, Colorado, who leads the cataloguing.

### DARK MARKS

RSLs typically measure a few metres across and hundreds of metres long. One leading idea is that they form when the chilly Martian surface warms just enough to thaw an ice dam in the soil, allowing water to begin seeping downhill. When temperatures drop, the water freezes and the hillside lightens again until next season. But the picture is complicated by factors such as potential salt in the water; brines may seep at lower temperatures than fresher water<sup>2</sup>.

Other possible explanations for the streaks include water condensing from the atmosphere, or the flow of bone-dry debris. "They have a lot of behaviours that resemble liquid water," says Colin Dundas, a planetary geologist at the US Geological Survey in Flagstaff, Arizona. "But Mars is a strange place, and it's worth considering the possibility there are dry processes that could surprise us."

A study published last month used orbital infrared data to suggest that typical RSLs contain no more than 3% water<sup>3</sup>. And other streaky-slope Martian features, known as gullies, were initially thought to be caused by liquid water but are now thought to be formed mostly by carbon dioxide frost.



Dundas and his colleagues have counted 58 possible RSLs near Curiosity's landing site in Gale Crater<sup>4</sup>. Many of them appeared after a planet-wide dust storm in 2007 — possibly because the dust acted as a greenhouse and temporarily warmed the surface, Stillman says.

Since January, mission scientists have used the ChemCam instrument aboard the rover — which includes a small telescope — to photograph nearby streaks whenever possible.

So far, the rover has taken pictures of 8 of the 58 locations and seen no changes. The features are lines on slopes, but they have not yet recurred. "We've got two of the three letters in the acronym," says Ryan Anderson, a geologist at the US Geological Survey who leads the imaging campaign.

Curiosity is currently about 5 kilometres

away from the potential RSLs; on its current projected path, it would never get any closer than about 2 kilometres, Vasavada says. The rover could not physically drive up and touch the streaks if it wanted to, because it cannot navigate the slopes of 25 degrees or greater on which they appear.

But the rover's sheer unexpected proximity to potential RSLs has NASA re-evaluating its planetary-protection protocols. Curiosity was only partly sterilized before going to Mars, and experts at JPL and NASA headquarters in Washington DC are calculating how long the remaining microbes could survive in Mars's harsh atmosphere — as well as what weather conditions could transport them several kilometres away and possibly contaminate a water seep. "That hasn't been well quantified for any mission," says Vasavada.

The work is an early test for the NASA Mars rover slated to launch in 2020, which will look for life and collect and stash samples for possible return to Earth. RSLs exist at several of the rover's eight possible landing sites.

For now, Curiosity is finishing exploring the Murray formation. This area is made of sediments from the bottom of ancient lakes — the sort of potentially life-supporting environment the rover was sent to find. Curiosity's second extended mission begins on 1 October.

Barring disaster, the rover's lifespan will be set by its nuclear-power source, which will continue to dwindle in coming years through radioactive decay. Curiosity still has kilometres to scale on Aeolis Mons as it moves towards its final destination, a sulfate-rich group of rocks. ■

1. McEwen, A. S. *et al. Science* **333**, 740–743 (2011).
2. Ojha, L. *et al. Nature Geosci.* **8**, 829–832 (2015).
3. Edwards, C. S. & Piqueux, S. *Geophys. Res. Lett.* <http://dx.doi.org/10.1002/2016GL070179> (2016).
4. Dundas, C. M. & McEwen, A. S. *Icarus* **254**, 213–218 (2015).

SOURCE: ROUTE: NASA; TERRAIN: ASU; RSLs: REF 4



#### TOP NEWS



Osiris-Rex spacecraft blazes trail for asteroid miners  
[go.nature.com/2c9cw4c](http://go.nature.com/2c9cw4c)

#### MORE NEWS

- Claim laid for Earth's oldest fossils [go.nature.com/2cgkdqp](http://go.nature.com/2cgkdqp)
- Culture of silence protected disgraced trachea surgeon [go.nature.com/2busbxs](http://go.nature.com/2busbxs)
- Giant ice volcano spotted on dwarf planet Ceres [go.nature.com/2cd8qxs](http://go.nature.com/2cd8qxs)

#### NATURE PODCAST



Solving ethical dilemmas Star Trek style, and three scientists on their sci-fi inspirations  
[nature.com/nature/podcast](http://nature.com/nature/podcast)

**CORRECTION**

The News story ‘Mars contamination fear could divert Curiosity rover’ (*Nature* **537**, 145–146; 2016) should have made it clear that the dark streaks near Curiosity are only ‘potential’ recurring slope lineae. And it should have said that the Murray formation — not the Murray Buttes — was formed from ancient lake sediments.



## BIOMEDICINE

# London super-lab opens under cloud of Brexit

*Research begins at the unabashedly international Francis Crick Institute.*

BY EWEN CALLAWAY

**I**t is amazing, isn't it," says Paul Nurse, as he stands on a bridge overlooking the grand atrium of the new Francis Crick Institute in London. Light floods in from the building's cathedral-like entrance. "I can't quite believe it's here."

Nurse, the institute's founding director, and his ten lab members are among the first researchers to begin working at the Crick, which opened to the media on 1 September.

The UK government and the Crick's other funders have gambled £700 million (US\$927 million) on the institute, in the hope that it will attract some of world's brightest young biomedical researchers and catalyse a boom in the UK life-sciences economy.

The building will eventually house 1,500 scientists and support staff, making it Europe's largest single-site biomedical institute. They will study a broad portfolio of biomedical research, from immunology to cancer genetics.

The 93,000-square-metre glass and steel temple looms over the neighbouring British Library, the largest public structure built in Britain in the twentieth century. But looming over the Crick is the prospect of Brexit.

## WORLD STAGE

The UK vote on 23 June to leave the European Union poses a range of uncertainties for UK researchers, from access to European funding to the ease of moving between EU countries. "Our vision is to be a major research institute of great significance on the world stage," says Nurse. "Internationalism is absolutely in our DNA."

The Crick's first researchers, who began arriving in mid-August, come mostly from two institutes in London: the National Institute of Medical Research, run by the Medical Research Council, and the London Research Institute, run by Cancer Research UK.

The plan is for the Crick to house a growing and ever-changing roster of young group leaders, who will spend up to 12 years there.

More than half of the Crick's current post-docs are from EU countries other than the United Kingdom, Nurse notes, and limits to freedom of movement for EU workers could make it harder to recruit. If Britain does not secure access to EU research-funding



Paul Nurse says that internationalism is in the DNA of London's Francis Crick Institute.

programmes, that could also limit funding for the Crick's scientists.

Jernej Ule, a molecular biologist at University College London who will spend three years at the Crick, is emblematic of Nurse's international vision. Ule is a native of Slovenia

***"It portrays the exact opposite sentiment that some people feel Brexit represents."***

and did his PhD and postdoctoral work in the United States. His lab, which studies how changes in gene expression influence motor neuron disease and other neural conditions, includes scientists from Spain, Italy, France, Germany and the United Kingdom. "For me to recruit the best people, I need to have a capacity to throw a net very broadly," he says.

Ule also receives EU funding. After he arrived in the United Kingdom, he won a grant from the European Research Council (ERC) in 2007 to study RNA regulatory networks in neurons, then a nascent area of research.

"Having the chance to apply for European funding at this top level is crucial to give us this independence of thinking in very new directions," he says. "Without the ERC I wouldn't be where I am right now."

He and several other scientists who have

begun working at the Crick say that the institute's mission is even more essential in the wake of the Brexit vote.

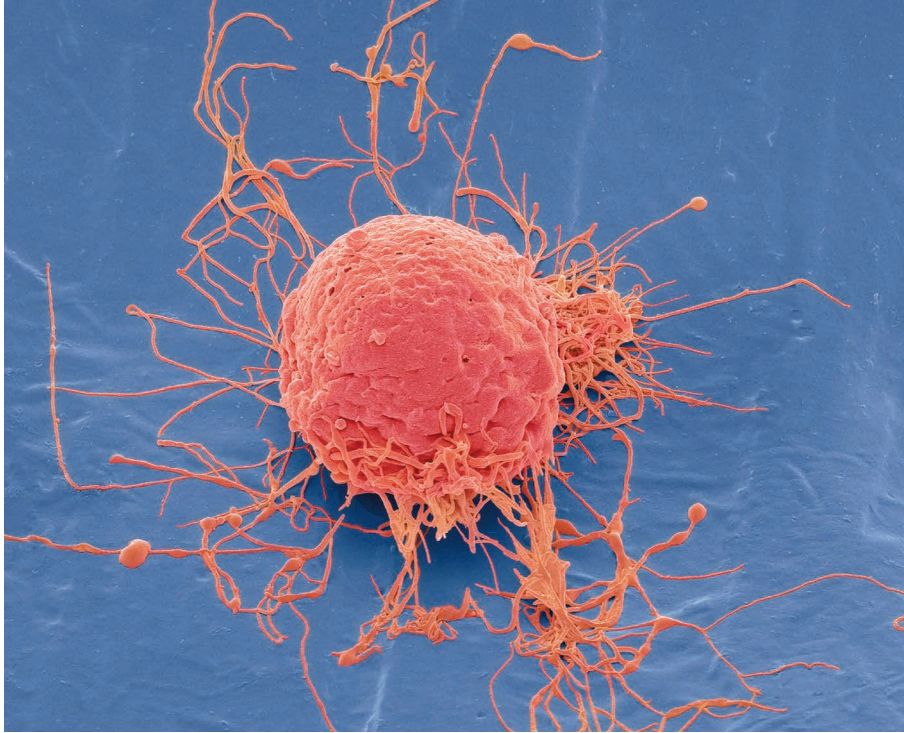
"It's almost like we have the Crick in spite of Brexit," says Matthew Swaffer, a postdoc in Nurse's lab. "I feel like it portrays the exact opposite sentiment that some people feel Brexit represents."

Swaffer's colleague Tiffany Mak, a first-year PhD student, joined the Crick in part because of its allure as a mecca for researchers from a wide variety of disciplines — and that has not diminished. "This project puts so much emphasis on bringing people from all sorts of backgrounds together. Hopefully it will act as a hub and not let politics get in the way of science and collaboration."

The Crick is likely to experience many of the same anxieties over Brexit as other UK research institutions, says Kieron Flanagan, a science-policy researcher at the University of Manchester.

But the institute's high profile — some have described it as "too big to fail" — could even buffer it from some Brexit worries, such as the ability to continue to recruit top scientists from Europe, he says. "They may have fewer problems than the university in the middle of nowhere in attracting people, but there will still be that concern there." ■

ALEX LENTATI/EVENING STANDARD/EVINE



STEVE GOSCHMEISSNER/SPL

Stem cells are increasingly being used in unproven therapies at clinics in the United States.

## BIOMEDICINE

# Cell-therapy rules stir debate

*Controversial US guidelines attempt to rein in rogue stem-cell clinics.*

BY HEIDI LEDFORD

Thomas Albini met his first patient blinded by a stem-cell ‘treatment’ last year. The elderly woman, who had macular degeneration, thought she was paying to participate in a clinical trial that would save her sight by injecting stem cells into both eyes. Instead, it left her legally blind.

By the time Albini, an ophthalmologist at the University of Miami in Florida, had treated two more women who had been blinded by the same procedure, he knew that there was a systemic problem. Two of the women had been lured by a posting in a clinical-trial registry — even though there was no real trial to speak of — and none of the injections had been administered by a physician. The clinic offering the injections claimed that its procedure did not require approval from the US Food and Drug Administration (FDA), in part because it used the patient’s own cells. Altogether, Albini found the cases shocking. “Any sort of review would have been helpful.”

The debate over whether the FDA should review such treatments is growing more intense as purported stem-cell clinics proliferate across the United States. Current FDA

regulations are poorly enforced and leave room for various interpretations. On 8 September, Albini will present his experiences at an FDA workshop. The following week, dozens of researchers, companies and patient advocates will flock to Bethesda, Maryland, for an FDA public hearing. Many of them will tout the virtues of unproven stem-cell therapies and insist that people should have the right to such treatments. The FDA has expanded the one-day hearing to two — and moved it to a larger auditorium — in response to overwhelming public interest.

The discussion will focus on FDA proposals that aim to better define which cell therapies deserve strict regulation. If adopted, these controversial guidelines could encompass a large chunk of the cell-therapy clinics that claim to fall largely outside the agency’s purview.

A burgeoning industry has sprung up in the absence of definitive oversight. A recent study of stem-cell clinics that advertise online uncovered 570 such centres operating in the United States (L. Turner and P. Knoepfler *Cell Stem Cell* **19**, 154–157; 2016).

Under FDA regulations, these clinics must prepare and store their therapies safely, and their facilities are subject to sporadic

inspections. But many clinics also operate under the assumption that they do not need the agency’s approval to carry out their procedures and do not have to conduct the clinical trials that the FDA normally demands to prove that a therapy works. Agency regulations state that clinics do not need regulatory approval if therapies involve “minimal manipulation” of cells that do not fundamentally alter their properties, and if those cells fulfil a “homologous” function similar to their original role in the body. But the precise definitions of “minimal manipulation” and “homologous use” are controversial.

A series of four FDA draft guidelines released in 2014 and 2015 addressed that ambiguity by providing concrete examples of what would trigger greater FDA oversight. After soliciting public comment, the FDA will decide whether to amend and finalize the proposals.

Not everyone is happy with the results up to now. Arnold Caplan, who studies regenerative medicine at Case Western Reserve University in Cleveland, Ohio, worries that the FDA will start seeking approvals for treatments that are now considered standard, including the use of abdominal fat in breast reconstruction following a mastectomy.

Others are concerned that tighter guidelines will make it harder to bring discoveries to market. “It will potentially slow down translation in many instances,” says Keith March, a cardiologist at Indiana University in Indianapolis, who will also present at the public hearing. “We need to be cognizant of that.”

## TOO LATE?

Some researchers are glad that the FDA is tackling the issue, however. Stem-cell researcher Jeanne Loring at the Scripps Research Institute in La Jolla, California, and her lab are talking to the FDA about starting clinical tests of a stem-cell treatment for Parkinson’s disease. “They’re making sure we know what we’re doing,” she says.

But even if the FDA finalizes the proposals, it is unclear what effect the rules will have, says bioethicist Leigh Turner at the University of Minnesota in Minneapolis. The stem-cell clinics are too entrenched to be chased away by FDA guidance, he says. “The real question is if the FDA is going to send inspectors and issue warning letters.”

For Albini, the proposed FDA guidance is not a perfect solution, but it is at least a step in the right direction. He may never know for sure why the treatments blinded his patients. And he acknowledges that clearer guidelines — and stricter enforcement — will not prevent every such tragedy in the future. Neither will they keep some clinics from recruiting patients under the guise of conducting clinical trials. But every step counts. “The more regulatory hurdles you put in the way of somebody who wants to use the term ‘research’ as marketing, the better off we’d be,” Albini says. ■



## FUNDING

# US science faces budget limbo

*Likelihood of stopgap spending measure grows in light of upcoming election.*

BY SARA REARDON

Another year, another round of budget roulette for US science agencies. When Congress returns from its summer break on 6 September, it will have just three weeks to pass a new government funding bill before the 2017 budget year begins on 1 October.

Policy analysts predict that lawmakers will pass a stopgap funding measure that will keep agencies' budgets flat until the presidential election in November — and perhaps into next year.

That would leave the US National Institutes of Health (NIH), the National Science Foundation and other science agencies in a familiar, if uncomfortable, position: unable to start new programmes or to end old ones without permission from Congress, and unsure about their total funding for the year.

More uncertainty will come early next year, when the next US president takes office and replaces most agency directors. "It will be a transition year, and will be difficult enough", even without the budget limbo, says Matt Hourihan, director of the research and development budget and policy programme at the American Association for the Advancement of Science in Washington DC.

One major question for agencies is how a budget deal between the House of Representatives and the Senate would reconcile the two bodies' very different 2017 spending plans.

The House has proposed increasing the NIH's budget by US\$1.3 billion over the 2016 level; the Senate has suggested a \$2-billion boost. The House spending bill for NASA includes an extra \$200 million for the agency's planetary-science programme compared with the current level, whereas the Senate has proposed cutting the programme's budget by about \$300 million.

Then there is the beleaguered international nuclear-fusion project ITER, which is funded by a consortium that includes the Department of Energy (DOE). The Senate has proposed cutting all US support for ITER in 2017 and redistributing the money saved to other energy programmes. But the House's plan would have the United States continue to contribute roughly \$115 million per year to ITER, with flat funding for most other DOE programmes.

The House and Senate do agree on some things, however. Neither included money for the White House's proposed \$680-million Cancer Moonshot Initiative. Ben Krinsky, legislative-affairs officer at the Federation of American Societies for Experimental Biology in Washington DC, says that Congress might be more willing to provide funding once it sees the NIH's final road map for the project, which

the agency is due to release later this month.

Meanwhile, the Senate is expected to vote this week on legislation that would create a \$1.1-billion emergency fund for response to the Zika virus and research towards a vaccine. The US Department of Health and Human Services says that its budget for fighting the virus has almost run out — even though in August it took back \$81 million from the budgets of the NIH and other agencies to pay for Zika response efforts.

But perhaps the most immediate question for Congress and the science agencies is how long a temporary spending measure would last. The timing will be influenced by the 8 November general election, in which the White House, all 435 House seats and one-third of the Senate are up for grabs. December is often mentioned as a probable end date, but that would require Congress to return for a 'lame duck' session after the election. And some conservative lawmakers have proposed that any temporary funding plan should be extended until after the next president takes office.

This would be a problem for the science agencies, says Jason Callahan, space-policy adviser at the Planetary Society in Alexandria, Virginia.

"Everything will increase in cost if there's uncertainty in the budget," he says. "It's bad policy to run the federal government on continuing resolutions, but it's an election year." ■

**"Everything will increase in cost if there's uncertainty in the budget."**

## BIOLOGY

## Mystery surrounds cells

*Samples of popular brain-cancer cell line do not match its 50-year-old source, puzzling researchers.*

BY ELIE DOLGIN

Biomedical scientists are often urged to check that their cell lines are not contaminated or mislabelled. But as a recent study shows, any effort to authenticate a cell line is only as good as the reference standard against which the cells are compared.

A cell line that is widely used to study brain cancer does not match the cells used to create the line nearly 50 years ago, or the tumour purported to be its source, researchers

reported on 31 August (M. Allen *et al. Sci. Transl. Med.* **8**, 354re3; 2016). In fact, no one is quite sure of the true provenance of the cell line distributed by most cell repositories.

Because few cell lines are ever verified against their primary-source material, "this paper is probably just the tip of the iceberg", says Christopher Korch, a geneticist at the University of Colorado Denver.

Many groups are trying to tackle the problem of misidentified cell lines to improve the reproducibility of research findings. This

year, the US National Institutes of Health started requiring grant applicants to describe how they will authenticate their cell lines. And journals such as *Nature* have begun to ask authors to check their cells against a database of 475 lines (and counting) that are known to be mixed up.

But no organizations have called for the kind of archival sleuthing that produced the new study. "It's hard enough to get people to do the standard authentication," says Leonard Freedman, president of the Global Biological Standards Institute, a non-profit organization in Washington DC that has found that most life scientists never authenticate their cells (L. P. Freedman *et al. BioTechniques* **59**, 189–192; 2015). "This is much more elaborate."

The cell line in question, U87, was established in 1966 at Uppsala University in Sweden, using tissue from a 44-year-old woman with an aggressive brain cancer known as glioblastoma. U87 has since been ▶

► used in countless investigations that have yielded around 2,000 scientific papers.

The enthusiasm for U87 initially puzzled Bengt Westermark, a tumour biologist at Uppsala. As a graduate student in the 1970s, he studied eight different brain-cancer cell lines. U87 was “hopeless to work with,” he says, because it grew much more slowly than the others.

Years later, Westermark got his hands on the version of U87 that is distributed by the American Type Culture Collection (ATCC), a cell repository in Manassas, Virginia. He could see from the cells’ growth properties that this U87 was clearly different from the cells that gave him so much grief in graduate school. Westermark decided to do a formal comparison.

Fortunately, Uppsala had preserved the tumour tissue that spawned the original cell line. This enabled Westermark’s team to verify the identity of the archival U87 sample in their freezer. The researchers then used DNA-fingerprinting techniques to show that the ATCC’s U87 was different — and that it didn’t match any other cell lines created at Uppsala.

Mindy Goldsborough, ATCC’s chief science and technology officer, says the repository acquired its U87 line in 1982 from the Memorial Sloan Kettering Cancer Center in New York City, which itself received the cell line



**The cell line U87 came from a glioma similar to this tumour, but beyond that its origin is unknown.**

from Uppsala in 1973. By the time it arrived at the ATCC, U87 had a Y chromosome — even though it was said to have come from a woman. This suggests that the mix-up probably happened at Sloan Kettering or during one of the hand-overs.

In light of these revelations, the ATCC plans to update the background details in its listing for U87, which it describes as male. But the origin of the U87 line remains a mystery.

Westermark’s team has conducted a comparison of gene-expression profiles that suggests that the ATCC cell line came from a brain tumour. “It’s bad news that it’s not what it should be,” he says, “but it’s good news that it’s probably a glioblastoma.” This means that studies of U87 still reflect brain-cancer biology and don’t need to be tossed out, he adds.

Still, many cancer researchers think that it is time to move beyond U87 and other ‘classical’ cell lines — regardless of their origins — because the culture conditions historically used to grow the cells change their biological nature. Westermark and others now favour newer cell lines that have been propagated on the types of growth medium that ensure genetic and epigenetic stability. Through its Human Glioma Cell Culture biobank, Uppsala provides these sorts of cell to other researchers for a small processing fee.

“What we’ve historically used is so poorly representative of the human disease,” says Howard Fine, a neuro-oncologist at the Weill Cornell Brain Tumor Center in New York City. “So, any time someone can shoot down the [U87] cell line, I’m happy.” ■

#### CORRECTIONS

The News story ‘Who will build the next LHC?’ (*Nature* **536**, 383–384; 2016) should have said that souping up the current LHC would take it to an energy of 28 TeV, not 20 TeV. And the News Feature ‘Digital DNA’ (*Nature* **537**, 22–24; 2016) gave an incorrect size for the 2013 EBI files. The correct figure is 739 kilobytes, not 739 kilobases.



# How to raise a genius

A long-running study of exceptional children reveals what it takes to produce the scientists who will lead the twenty-first century.

BY TOM CLYNES



**O**n a summer day in 1968, professor Julian Stanley met a brilliant but bored 12-year-old named Joseph Bates. The Baltimore student was so far ahead of his classmates in mathematics that his parents had arranged for him to take a computer-science course at Johns Hopkins University, where Stanley taught. Even that wasn't enough. Having leapfrogged ahead of the adults in the class, the child kept himself busy by teaching the FORTRAN programming language to graduate students.

Unsure of what to do with Bates, his computer instructor introduced him to Stanley, a researcher well known for his work in psychometrics — the study of cognitive performance. To discover more about the young prodigy's talent, Stanley gave Bates a battery of tests that included the SAT college-admissions exam, normally taken by university-bound 16- to 18-year-olds in the United States.

Bates's score was well above the threshold for admission to Johns Hopkins, and prompted Stanley to search for a local high school that would let the child take advanced mathematics and science classes. When that plan failed, Stanley convinced a dean at Johns Hopkins to let Bates, then 13, enrol as an undergraduate.

Stanley would affectionately refer to Bates as “student zero” of his Study of Mathematically Precocious Youth (SMPY), which would transform how gifted children are identified and supported by the US education system. As the longest-running current longitudinal survey of intellectually talented children, SMPY has for 45 years tracked the careers and accomplishments of some 5,000 individuals, many of whom have gone on to become high-achieving scientists. The study's ever-growing data set has generated more than 400 papers and several books, and provided key insights into how to spot and develop talent in science, technology, engineering, mathematics (STEM) and beyond.

“What Julian wanted to know was, how do you find the kids with the highest potential for excellence in what we now call STEM, and how do you boost the chance that they'll reach that potential,” says Camilla Benbow, a protégé of Stanley's who is now dean of education and human development at Vanderbilt University in Nashville, Tennessee. But Stanley wasn't interested in just studying bright children; he wanted to nurture their intellect and enhance the odds that they would change the world. His motto, he told his graduate students, was “no more dry bones methodology”.

With the first SMPY recruits now at the peak of their careers<sup>1</sup>, what has become clear is how much the precociously gifted outweigh the rest of society in their influence. Many of the innovators who are advancing science, technology and culture are those whose unique cognitive abilities were identified and supported in their early years through enrichment programmes such as Johns Hopkins University's Center for Talented Youth — which Stanley began in the 1980s as an adjunct to SMPY. At the start, both the study and the centre were open to young adolescents who scored in the top 1% on university entrance exams. Pioneering mathematicians Terence Tao and Lenhard Ng were one-percenters, as were Facebook's Mark Zuckerberg, Google co-founder Sergey Brin and musician Stefani Germanotta (Lady Gaga), who all passed through the Hopkins centre.

“Whether we like it or not, these people really do control our society,” says Jonathan Wai, a psychologist at the Duke University Talent Identification Program in Durham, North Carolina, which collaborates with the Hopkins centre. Wai combined data from 11 prospective and retrospective longitudinal studies<sup>2</sup>, including SMPY, to demonstrate the correlation between early cognitive ability and adult achievement. “The kids who test in the top 1% tend to become our eminent scientists

and academics, our Fortune 500 CEOs and federal judges, senators and billionaires,” he says.

Such results contradict long-established ideas suggesting that expert performance is built mainly through practice — that anyone can get to the top with enough focused effort of the right kind. SMPY, by contrast, suggests that early cognitive ability has more effect on achievement than either deliberate practice or environmental factors such as socioeconomic status. The research emphasizes the importance of nurturing precocious children, at a time when the prevailing focus in the United States and other countries is on improving the performance of struggling students (see ‘Nurturing a talented child’). At the same time, the work to identify and support academically talented students has raised troubling questions about the risks of labelling children, and the shortfalls of talent searches and standardized tests as a means of identifying high-potential students, especially in poor and rural districts.

“With so much emphasis on predicting who will rise to the top, we run the risk of selling short the many kids who are missed by these tests,”

says Dona Matthews, a developmental psychologist in Toronto, Canada, who co-founded the Center for Gifted Studies and Education at Hunter College in New York City. “For those children who are tested, it does them no favours to call them ‘gifted’ or ‘ungifted’. Either way, it can really undermine a child's motivation to learn.”

#### START OF A STUDY

On a muggy August day, Benbow and her husband, psychologist David Lubinski, describe the origins of SMPY as they walk across the quadrangle at Vanderbilt University. Benbow was a graduate student at Johns Hopkins when she met Stanley in a class he taught in 1976. Benbow and Lubinski, who have co-directed the study since Stanley's retirement, brought it to Vanderbilt in 1998.

“In a sense, that brought Julian's research full circle, since this is where he started his career as a professor,” Benbow says as she nears the university's psychology laboratory, the first US building dedicated to the study of the field. Built in 1915, it houses a small collection of antique calculators — the tools of quantitative psychology in the early 1950s, when Stanley began his academic work in psychometrics and statistics.

His interest in developing scientific talent had been piqued by one of the most famous longitudinal studies in psychology, Lewis Terman's Genetic Studies of Genius<sup>3,4</sup>. Beginning in 1921, Terman selected teenage subjects on the basis of high IQ scores, then tracked and encouraged their careers. But to Terman's chagrin, his cohort produced only a few esteemed scientists. Among those rejected because their IQ of 129 was too low to make the cut was William Shockley, the Nobel-prizewinning co-inventor of the transistor. Physicist Luis Alvarez, another Nobel winner, was also rejected.

Stanley suspected that Terman wouldn't have missed Shockley and Alvarez if he'd had a reliable way to test them specifically on quantitative reasoning ability. So Stanley decided to try the Scholastic Aptitude Test (now simply the SAT). Although the test is intended for older students, Stanley hypothesized that it would be well suited to measuring the analytical reasoning abilities of elite younger students.

In March 1972, Stanley rounded up 450 bright 12- to 14-year-olds from the Baltimore area and gave them the mathematics portion of the SAT. It was the first standardized academic ‘talent search’. (Later, researchers included the verbal portion and other assessments.)

“The first big surprise was how many adolescents could figure out math problems that they hadn't encountered in their course work,” says developmental psychologist Daniel Keating, then a PhD student at Johns Hopkins University. “The second surprise was how many of these young

**“Whether we like it or not, these people really do control our society.”**



kids scored well above the admissions cut-off for many elite universities.”

Stanley hadn't envisioned SMPY as a multi-decade longitudinal study. But after the first follow-up survey, five years later, Benbow proposed extending the study to track subjects through their lives, adding cohorts and including assessments of interests, preferences, and occupational and other life accomplishments. The study's first four cohorts range from the top 3% to the top 0.01% in their SAT scores. The SMPY team added a fifth cohort of the leading mathematics and science graduate students in 1992 to test the generalizability of the talent-search model for identifying scientific potential.

“I don't know of any other study in the world that has given us such a comprehensive look at exactly how and why STEM talent develops,” says Christoph Perleth, a psychologist at the University of Rostock in Germany who studies intelligence and talent development.

### SPATIAL SKILLS

As the data flowed in, it quickly became apparent that a one-size-fits-all approach to gifted education, and education in general, was inadequate.

“SMPY gave us the first large-sample basis for the field to move away from general intelligence toward assessments of specific cognitive abilities, interests and other factors,” says Rena Subotnik, who directs the Center for Gifted Education Policy at the American Psychological Association in Washington DC.

In 1976, Stanley started to test his second cohort (a sample of 563 13-year-olds who scored in the top 0.5% on the SAT) on spatial ability — the capacity to understand and remember spatial relationships between objects<sup>5</sup>. Tests for spatial ability might include matching objects that are seen from different perspectives, determining which cross-section will result when an object is cut in certain ways, or estimating water levels on tilted bottles of various shapes. Stanley was curious about whether spatial ability might better predict educational and occupational outcomes than could measures of quantitative and verbal reasoning on their own.

Follow-up surveys — at ages 18, 23, 33 and 48 — backed up his hunch. A 2013 analysis<sup>5</sup> found a correlation between the number of patents and peer-refereed publications that people had produced and their earlier scores on SATs and spatial-ability tests. The SAT tests jointly accounted for about 11% of the variance; spatial ability accounted for an additional 7.6%.

The findings, which dovetail with those of other recent studies, suggest that spatial ability plays a major part in creativity and technical innovation. “I think it may be the largest known untapped source of human potential,” says Lubinski, who adds that students who are only marginally impressive in mathematics or verbal ability but high in spatial ability often make exceptional engineers, architects and surgeons. “And yet, no admissions directors I know of are looking at this, and it's generally overlooked in school-based assessments.”

Although studies such as SMPY have given educators the ability to identify and support gifted youngsters, worldwide interest in this population is uneven. In the Middle East and east Asia, high-performing STEM students have received significant attention over the past decade. South Korea, Hong Kong and Singapore screen children for giftedness and steer high performers into innovative programmes.

## BRIGHT START

### *Nurturing a talented child*

“Setting out to raise a genius is the last thing we'd advise any parent to do,” says Camilla Benbow, dean of education and human development at Vanderbilt University in Nashville, Tennessee. That goal, she says, “can lead to all sorts of social and emotional problems”.

Benbow and other talent-development researchers offer the following tips to encourage both achievement and happiness for smart children.

- Expose children to diverse experiences.
- When a child exhibits strong interests or talents, provide opportunities to develop them.
- Support both intellectual and emotional needs.
- Help children to develop a ‘growth mindset’ by praising effort, not ability.
- Encourage children to take intellectual risks and to be open to failures that help them learn.
- Beware of labels: being identified as gifted can be an emotional burden.
- Work with teachers to meet your child's needs. Smart students often need more-challenging material, extra support or the freedom to learn at their own pace.
- Have your child's abilities tested. This can support a parent's arguments for more-advanced work, and can reveal issues such as dyslexia, attention-deficit/hyperactivity disorder, or social and emotional challenges. **T.C.**

In 2010, China launched a ten-year National Talent Development Plan to support and guide top students into science, technology and other high-demand fields.

In Europe, support for research and educational programmes for gifted children has ebbed, as the focus has moved more towards inclusion. England decided in 2010 to scrap the National Academy for Gifted and Talented Youth, and redirected funds towards an effort to get more poor students into leading universities.

### ON THE FAST TRACK

When Stanley began his work, the choices for bright children in the United States were limited, so he sought out environments in which early talent could blossom. “It was clear to Julian that it's not enough to identify potential; it has to be developed in appropriate ways if you're going to keep that flame well lit,” says Linda Brody, who studied with Stanley and now runs a programme at Johns Hopkins focused on counselling profoundly gifted children.

At first, the efforts were on a case-by-case basis. Parents of other bright children began to approach Stanley after hearing about his work with Bates, who thrived after entering university. By 17, he had earned bachelor's and master's degrees in computer science and was pursuing a doctorate at Cornell University in Ithaca, New York. Later, as a professor at Carnegie Mellon University in Pittsburgh, Pennsylvania, he would become a pioneer in artificial intelligence.

“I was shy and the social pressures of high school wouldn't have made it a good fit for me,” says Bates, now 60. “But at college, with the other science and math nerds, I fit right in, even though I was much younger. I could grow up on the social side at my own rate and

also on the intellectual side, because the faster pace kept me interested in the content.”

The SMPY data supported the idea of accelerating fast learners by allowing them to skip school grades. In a comparison of children who bypassed a grade with a control group of similarly smart children who didn't, the grade-skippers were 60% more likely to earn doctorates or patents and more than twice as likely to get a PhD in a STEM field<sup>6</sup>. Acceleration is common in SMPY's elite 1-in-10,000 cohort, whose intellectual diversity and rapid pace of learning make them among the most challenging to educate. Advancing these students costs little or nothing, and in some cases may save schools money, says Lubinski. “These kids often don't need anything innovative or novel,” he says, “they just need earlier access to what's already available to older kids.”

Many educators and parents continue to believe that acceleration is bad for children — that it will hurt them socially, push them out of childhood or create knowledge gaps. But education researchers generally agree that acceleration benefits the vast majority of gifted children socially and emotionally, as well as academically and professionally<sup>7</sup>.

Skipping grades is not the only option. SMPY researchers say that even modest interventions — for example, access to challenging material such as college-level Advanced Placement courses — have a demonstrable effect. Among students with high ability, those who were given a richer density of advanced precollegiate educational opportunities in STEM went on to publish more academic papers, earn more patents and

pursue higher-level careers than their equally smart peers who didn't have these opportunities<sup>8</sup>.

Despite SMPY's many insights, researchers still have an incomplete picture of giftedness and achievement. "We don't know why, even at the high end, some people will do well and others won't," says Douglas Detterman, a psychologist who studies cognitive ability at Case Western Reserve University in Cleveland, Ohio. "Intelligence won't account for all the differences between people; motivation, personality factors, how hard you work and other things are important."

Some insights have come from German studies<sup>9–11</sup> that have a methodology similar to SMPY's. The Munich Longitudinal Study of Giftedness, which started tracking 26,000 gifted students in the mid-1980s, found that cognitive factors were the most predictive, but that some personal traits — such as motivation, curiosity and ability to cope with stress — had a limited influence on performance. Environmental factors, such as family, school and peers, also had an impact.

The data from such intellectual-talent searches also contribute to knowledge of how people develop expertise in subjects. Some researchers and writers, notably psychologist Anders Ericsson at Florida State University in Tallahassee and author Malcolm Gladwell, have popularized the idea of an ability threshold. This holds that for individuals beyond a certain IQ barrier (120 is often cited), concentrated practice time is much more important than additional intellectual abilities in acquiring expertise. But data from SMPY and the Duke talent programme dispute that hypothesis (see 'Top of the charts'). A study published this year<sup>12</sup> compared the outcomes of students in the top 1% of childhood intellectual ability with those in the top 0.01%. Whereas the first group gain advanced degrees at about 25 times the rate of the general population, the more elite students earn PhDs at about 50 times the base rate.

But some of the work is controversial. In North America and Europe, some child-development experts lament that much of the research on talent development is driven by the urge to predict who will rise to the top, and educators have expressed considerable unease about the concept of identifying and labelling a group of pupils as gifted or talented<sup>13</sup>.

"A high test score tells you only that a person has high ability and is a good match for that particular test at that point in time," says Matthews. "A low test score tells you practically nothing," she says, because many factors can depress students' performance, including their cultural backgrounds and how comfortable they are with taking high-stakes tests. Matthews contends that when children who are near the high and low extremes of early achievement feel assessed in terms of future success, it can damage their motivation to learn and can contribute to what Stanford University psychologist Carol Dweck calls a fixed mindset. It's far better, Dweck says, to encourage a growth mindset, in which children believe that brains and talent are merely a starting point, and that abilities can be developed through hard work and continued intellectual risk-taking.

"Students focus on improvement instead of worrying about how smart they are and hungering for approval," says Dweck. "They work hard to learn more and get smarter." Research by Dweck and her colleagues shows that students who learn with this mindset show greater motivation at school, get better marks and have higher test scores<sup>14</sup>.

Benbow agrees that standardized tests should not be used to limit

students' options, but rather to develop learning and teaching strategies appropriate to children's abilities, which allow students at every level to reach their potential.

Next year, Benbow and Lubinski plan to launch a mid-life survey of the profoundly gifted cohort (the 1 in 10,000), with an emphasis on career achievements and life satisfaction, and to re-survey their 1992 sample of graduate students at leading US universities. The forthcoming studies may further erode the enduring misperception that gifted children are bright enough to succeed on their own, without much help.

"The education community is still resistant to this message," says David Geary, a cognitive developmental psychologist at the University of Missouri in Columbia, who specializes in mathematical learning. "There's a general belief that kids who have advantages, cognitive or otherwise, shouldn't be given extra encouragement; that we should focus more on lower-performing kids."

Although gifted-education specialists herald the expansion of talent-development options in the United States, the benefits have mostly been limited so far to students who are at the top of both the talent and socioeconomic curves.

"We know how to identify these kids, and we know how to help them," says Lubinski. "And yet we're missing a lot of the smartest kids in the country."

As Lubinski and Benbow walk through the quadrangle, the clock strikes noon, releasing packs of enthusiastic adolescents racing towards the dining hall. Many are participants in the Vanderbilt Programs for Talented Youth, summer enrichment courses in which gifted students spend three weeks gorging themselves on a year's worth of mathematics,

science or literature. Others are participants in Vanderbilt's sports camps.

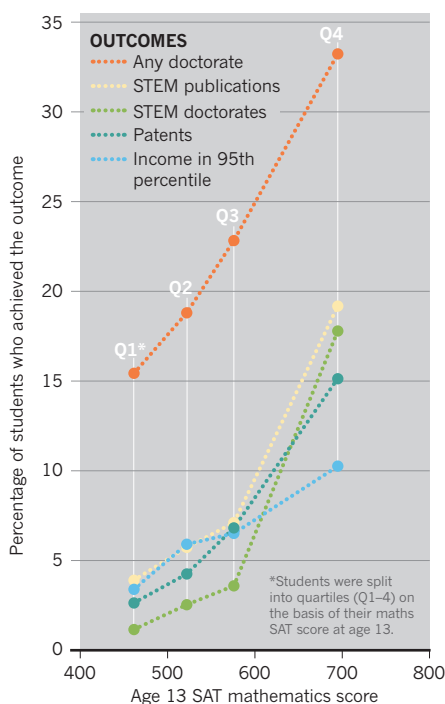
"They're just developing different talents," says Lubinski, a former high-school and college wrestler. "But our society has been much more encouraging of athletic talents than we are of intellectual talents."

And yet these gifted students, the 'mathletes' of the world, can shape the future. "When you look at the issues facing society now — whether it's health care, climate change, terrorism, energy — these are the kids who have the most potential to solve these problems," says Lubinski. "These are the kids we'd do well to bet on." ■

**Tom Clynes** is a journalist and the author of *The Boy Who Played With Fusion: Extreme Science, Extreme Parenting and How to Make a Star*.

## Top of the charts

Long-term studies of gifted students — those who scored in the top 1% as adolescents on the mathematics section of the SAT — reveal that people at the very top of the range went on to outperform the others.



1. Lubinski, D., Benbow, C. P. & Kell, H. J. *Psychol. Sci.* **25**, 2217–2232 (2014).

2. Wai, J. *Intelligence* **45**, 74–80 (2014).

3. Oden, M. H. *Genet. Psychol. Monogr.* **77**, 3–93 (1968).

4. Terman, L. M. *Am. Psychol.* **9**, 221–230 (1954).

5. Kell, H. J., Lubinski, D., Benbow, C. P. & Steiger, J. H. *Psychol. Sci.* **24**, 1831–1836 (2013).

6. Park, G., Lubinski, D. & Benbow, C. P. *J. Educ. Psychol.* **105**, 176–198 (2013).

7. Steenbergen-Hu, S. & Moon, S. M. *Gift. Child Q.* **55**, 39–53 (2011).

8. Wai, J., Lubinski, D., Benbow, C. P. & Steiger, J. H. *J. Educ. Psychol.* **102**, 860–871 (2010).

9. Heller, K. A., von Bistrum, A. & Collier, A. in *Munich Studies of Giftedness* (ed. Heller, K. A.) 433–454 (LIT, 2010).

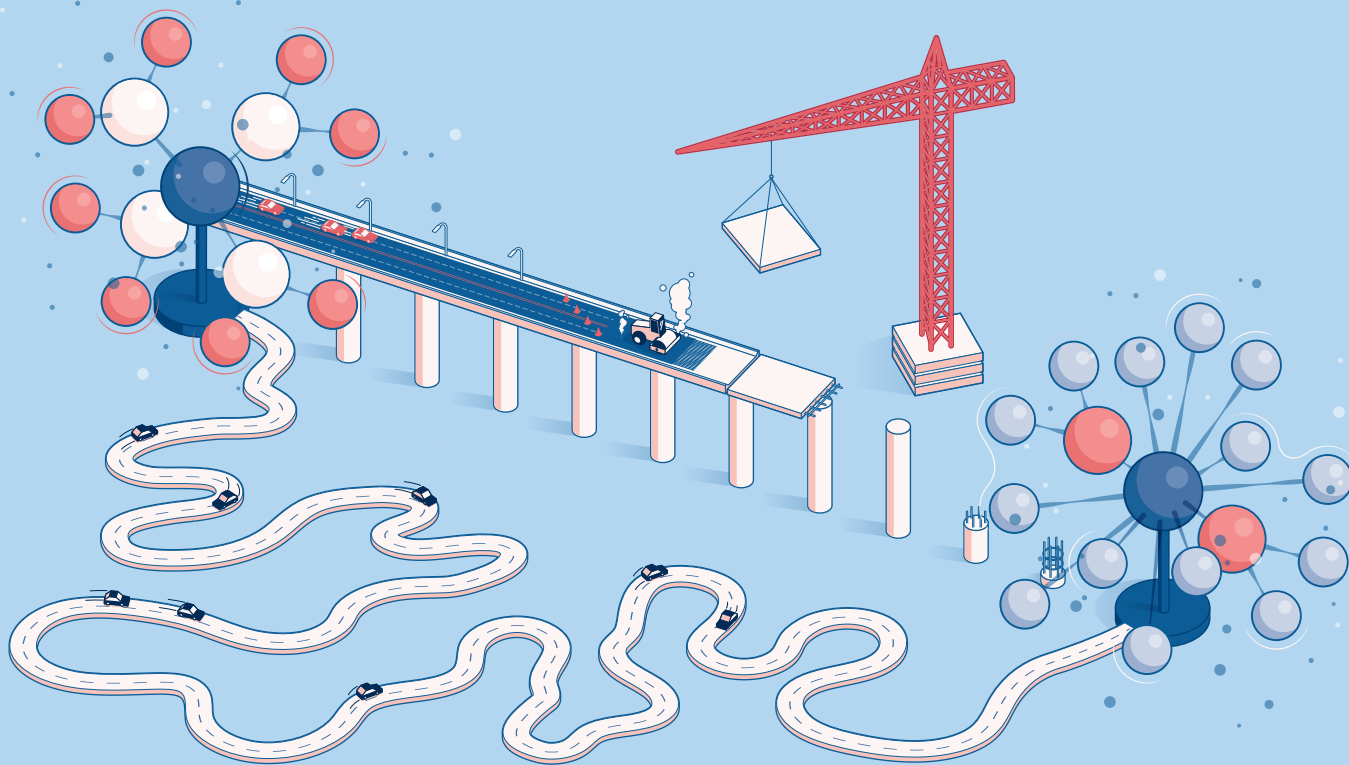
10. Heller, K. A. *Talent Dev. Excell.* **5**, 51–64 (2013).

11. Heller, K. A. in *Munich Studies of Giftedness* (ed. Heller, K. A.) 3–12 (LIT, 2010).

12. Makel, M. C. et al. *Psychol. Sci.* **27**, 1004–1018 (2016).

13. Koshy, V. & Pinheiro-Torres, C. *Br. Educ. Res. J.* **39**, 953–978 (2013).

14. Dweck, C. *Mindset: The New Psychology of Success* (Random House, 2006).



# CHEMISTRY ON THE FAST TRACK

ADVANCES IN CATALYST RESEARCH COULD CREATE A SUPERHIGHWAY TO CLEAN ENERGY SOURCES AND A MORE-SUSTAINABLE CHEMICAL INDUSTRY.

BY XIAOZHI LIM

In her 1794 book, *An Essay on Combustion*, Scottish chemist Elizabeth Fulhame noted a peculiar fact: substances such as coal and charcoal burned better when they were damp. After many experiments to understand why, she concluded that the water briefly split into hydrogen and oxygen, which interacted with the other compounds in a way that made the combustion go faster. Yet at the end, Fulhame wrote, the process “forms a new quantity of water equal to that decomposed”.

Many historians consider this to be the first scientific account of a catalyst: a material that speeds reactions by making or breaking chemical bonds, without being consumed. It was hardly the last: modern chemistry would be almost inconceivable without catalysts. “They not only make transformations accessible, but also direct them in new ways,” says Susannah Scott, a chemist at the University of California, Santa Barbara. “That’s very powerful.”

Catalysts are used in some 90% of processes in the chemical industry, and are essential for the production of fuels, plastics, drugs and fertilizers. At least 15 Nobel prizes have been awarded for work on catalysis. And thousands of chemists around the world are continually improving the catalysts they have and striving to invent new ones.

That work is partly driven by an interest in sustainability. The aim of

catalysis is to direct reactions along precisely defined pathways so that chemists can skip reaction steps, reduce waste, minimize energy use and do more with less. And with growing concerns about climate change and the environment, sustainability has become increasingly important. Catalysis is a key principle of ‘green chemistry’: an industry-wide effort to prevent pollution before it happens.

Catalysts are also seen as the key to unlocking energy sources that are much more inert and difficult to use than coal, oil or gas, but much cleaner. Catalysis can make it more economically feasible to split water into oxygen and hydrogen fuel, or can open up new ways to use raw materials such as biomass or carbon dioxide. “These are feedstocks that are ripe for advances in catalysis,” says Melanie Sanford, a chemist at the University of Michigan in Ann Arbor.

These challenges have led to an explosion in catalyst innovation, with the annual number of publications on the subject tripling in the past decade. Many groups are coming up with new small-molecule complexes or are chemically tailoring biological enzymes in search of radically new catalytic activity. Others are pursuing advances in nanotechnology, which allow them to engineer the action of solid catalysts at the atomic scale. Still others are experimenting with catalysts that

JASIEK KRZYSZTOFIAK/NATURE



are activated by light, or that incorporate the DNA double helix. And everyone in the field is trying to streamline the search for better catalysts with modern computational modelling tools.

The pace of innovation is such that even the experts are struggling to keep up, says Scott, who leads the US Department of Energy's efforts to develop benchmarks for the new catalysts' performance'. "We need to make sure we are advancing the science that's most efficient," she says.

And the scope of catalysis is increasing rapidly. "Twenty years ago," says John Hartwig, a chemist at the University of California, Berkeley, "catalysis to make molecules that were complex did not exist." Anyone who wanted to modify a large complicated structure would have to tear it down and build it back up, says Sanford. But now, chemists can often edit parts of a molecule precisely. "It's incredibly enabling," she says.

### CUT-PRICE CATALYSTS

Using a catalyst is like bulldozing a shortcut between reactants A and product B, bypassing convoluted chemical pathways that might otherwise take forever. Using a really good catalyst is like building a multilane superhighway. And some of the best are the 'homogeneous' catalysts: free-floating molecules that are mixed in with the reactants.

Industrial catalysts in this category most often consist of a metal ion that does the hard work of making or breaking chemical bonds, surrounded by 'ligands': connected groups, often carbon-based, that control the reactants' access to the ion. Much of the research in this field comes down to tailoring these ligands to produce a catalyst that performs only a desired reaction.

Unfortunately, many of the successes so far have come through the use of scarce and expensive metals such as palladium, platinum, ruthenium and iridium. Today, chemists are increasingly striving to build catalysts around cheaper, 'Earth-abundant' elements such as iron, nickel or copper — or to do without metals altogether.

Nickel is a particularly attractive candidate for mimicking the chemistry of palladium and platinum because it sits directly above them in the periodic table, and therefore has similar properties. At the Swiss Federal Institute of Technology in Lausanne, for example, synthetic chemist Xile Hu and his group are working with a remarkably versatile nickel complex<sup>2</sup> that they first reported in 2008. The complex consists of a nickel ion surrounded by a single, large ligand that binds to it in three places, leaving a fourth binding spot available for catalysing reactions. A similar ligand is already used in certain palladium catalysts. But the radius of a nickel ion is almost 20% smaller than that of a palladium ion, so Hu had to shrink the ligand to fit it more closely around the nickel. To do so, he replaced phosphorus atoms in the ligand with smaller nitrogen ones.

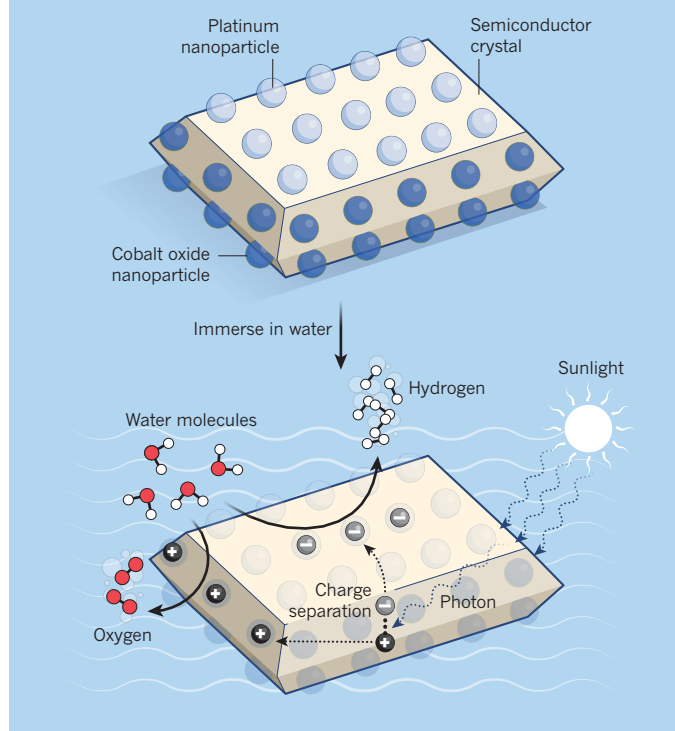
The result is a rigid ligand that stabilizes the nickel ion as it performs a wide array of reactions<sup>3–5</sup>. The original nickel catalyst is already available commercially, and Hu is systematically modifying the ligand to make a whole family of catalysts.

In 2008, chemists discovered that certain standard catalysts could be made more powerful by combining them with a technique known as photoredox catalysis. When photoredox catalysts absorb light, an electron leaps from the metal ion to the ligand and becomes stuck there, leaving the molecule in an unstable state. "The catalyst becomes desperate to fill the hole in the metal and get rid of the electron in the ligand," explains David MacMillan, a chemist at Princeton University in New Jersey who first reported<sup>6</sup> the idea in collaboration with chemist David Nicewicz from the University of North Carolina at Chapel Hill. But the only way the photoredox system can accomplish this is to trade electrons with the standard catalyst, supercharging it and triggering chemical transformations that were previously impossible. As a bonus, the photoredox catalysis drives the process with energy that it absorbed from light, reducing the heat required to keep the reaction going.

Nicewicz and MacMillan have independently used photoredox catalysis to make major improvements to the Buchwald–Hartwig reaction, which is frequently used to bond carbon with nitrogen when making drugs. Typically, the reaction requires the use of palladium salts,

## LIGHT SPLITTER

Attaching catalyst nanoparticles to different faces of a semiconductor crystal allows light to split water, but keeps the explosive products — hydrogen and oxygen — separate.



expensive, phosphorus-based ligands and difficult-to-make reactants. But in 2015, Nicewicz's group announced<sup>7</sup> that it had not only made a carbon–nitrogen bond using a completely metal-free catalyst, but had done so starting from cheaper and more accessible reactants; it is already being used by pharmaceutical companies, says Nicewicz. In June, MacMillan's group and its collaborators at Merck Research Laboratories in Rahway, New Jersey, reported<sup>8</sup> making the Buchwald–Hartwig reaction work with minute amounts of an iridium light absorber and a nickel salt, eliminating the need for ligands.

A specific challenge for many researchers is to find better ways of creating the carbon–fluorine bonds at the heart of fluorinated compounds that are widely used in pharmaceuticals, agrochemicals and medical imaging. Currently, the bonds are made using expensive specialized reagents or the highly corrosive gas hydrogen fluoride. In 2013, a team of researchers led by Sanford showed<sup>9</sup> how to make such bonds with a safer potassium fluoride salt using a copper catalyst. First, the catalyst is exposed to a compound that strips away three of its electrons. This leaves the catalyst so hungry for electrons that it can pull some from a nearby fluoride ion, which holds them in a notoriously tight grip. The fluoride is then so desperate for a replacement electron that it will readily bind with a carbon atom to get it.

### PEBBLES IN A STREAM

Despite their versatility, many homogeneous catalysts are fragile. Their internal bonds weaken after prolonged exposure to heat and collisions with reactant molecules, and their ligands start disintegrating. "They die after a while," says Sanford.

That is a big reason why large-scale industry tends to use 'heterogeneous' catalysts: solid materials that are fixed in place while the reactants stream past. A classic example is the mix of powdered platinum and other metals found in the catalytic converters that clean vehicle exhaust gases. In the past, chemists had a tough time designing heterogeneous catalysts with atomic precision because it was difficult

to make and study the active sites, where catalysis occurs, in a solid material. Mostly they had to optimize the catalysts through trial and error. But what's changing, says Scott, "is the synthetic control that we can exert over the materials". In particular, rapid advances in nanotechnology are allowing chemists to work towards systems with the robustness of solid catalysts and the high performance of homogeneous ones.

At the Chinese Academy of Sciences' State Key Laboratory of Catalysis in Dalian, director Can Li has used platinum and cobalt oxide nanoparticles to create a catalyst for splitting water with sunlight<sup>10</sup> (see 'Light splitter'). He starts by sticking the nanoparticles to crystals of a semiconductor called bismuth vanadium oxide, with each type of particle carefully isolated on a specific face of each crystal. Then, when he immerses the crystals in water and exposes them to light, photons strike the semiconductor and loosen electrons. The result is a flow of current that the nanoparticles use to break water molecules into hydrogen and oxygen. Oxygen gas comes bubbling off the cobalt oxide sites, while positively charged hydrogen ions migrate to the platinum particles. "We separated the active sites to block the reverse reaction," says Li — that is, a dangerously explosive conversion of hydrogen and oxygen back into water. (To simplify the experimental set-up, the hydrogen ions are currently captured by a separate compound rather than turned into gas.) The process is not yet efficient enough to be economically viable, says Li. But his team is testing combinations of semiconductors and metal catalysts to refine the design.

Audrey Moores, a chemist at McGill University in Montreal, Canada, is tackling a bothersome issue in the pharmaceutical, cosmetics and food industries, which often use heavy-metal-ion catalysts. Ions of palladium, ruthenium and platinum are toxic, so products made with them cannot be sold until they have been through a series of meticulous and expensive cleansing steps. Moores is working on alternative catalysts based on iron, which is much safer.

In 2014, her research group prepared a series of hollow, magnetic iron oxide nanoparticles for making benzaldehyde<sup>11</sup>: a molecule that smells like almonds and is widely used in flavourings. It is typically manufactured by reacting certain electron-hungry compounds with styrene: a sweet-smelling but hazardous liquid that is better known as a raw material for plastics. The process tends to generate a relatively small amount of benzaldehyde mixed with other molecules. But Moores' iron nanoparticles catalyse a more controllable reaction between styrene and oxygen, yielding almost pure benzaldehyde. And as an added advantage, iron is magnetic, so at the end of the reaction the iron nanoparticles can be extracted for reuse with a magnet.

## EVEN-HANDEDNESS

When making large, complex molecules such as steroids, antibiotics or hormones, a major challenge involves chirality, or the 'handedness' of a carbon atom. Such an atom carrying four different groups can have two configurations that are mirror images of each other, like human hands. A complex molecule may contain many such carbon atoms — and if even one of them has the wrong configuration, the compound can end up interacting badly with the human body. One notorious example is thalidomide, a drug developed in the 1950s for treating morning sickness in pregnant women. One chiral configuration was effective and safe for that purpose. But its mirror image, which was present in the over-the-counter drug, caused babies to be born with severe limb deformations.

Molecules from biomass feedstocks contain a wide variety of chiral carbon atoms in a chain, and it is almost impossible to distinguish one from another. "A small-molecule catalyst wouldn't recognize it," says Hartwig. Instead, chemists are turning to biological enzymes, which can be large enough to recognize the overall shape of the target molecule and home in on the bond where the reaction should occur. Enzymes also have the advantage of using water as a solvent and working at body

temperatures, which makes them more environmentally friendly than processes that require toxic solvents and large amounts of heat.

Naturally occurring enzymes don't always catalyse the reactions that chemists want, however — which is why one frontier of catalysis research is to rework these proteins so that they do. Hartwig has been looking at the haem enzyme, which is similar to the compounds that carry oxygen in red blood cells, and has developed<sup>12</sup> an artificial enzyme that substitutes an iridium complex for the haem's iron centre. Although this runs contrary to the goal of replacing precious metals with Earth-abundant ones, says Hartwig, iridium can work with strong bonds such as those between carbon and hydrogen, which iron cannot. His team is using crystallographic data to study the enzyme's structures near the iridium site and is systematically modifying them so that they can precisely transform a carbon–hydrogen bond into a carbon–carbon bond with the desired chiral configuration — a formidable challenge. The chemists can prepare hundreds or even thousands of new enzymes in this way, limited only by the time it takes to test them and analyse their activity.

Still, enzymes are very specific to their target, and although they yield a product with a single chiral configuration, it is often the configuration that isn't wanted. "If you're interested in the other, you're in trouble," says Stellos Arseniyadis, a synthetic chemist at Queen Mary University of London. To address that problem, Arseniyadis is collaborating with Michael Smietana of the University of Montpellier in France to make catalysts from DNA. Although most natural DNA spirals in only one direction, it is possible to make an artificial version that twists in the opposite direction. The two researchers and their teams make their catalysts by choosing a natural or non-natural helix of DNA and then attaching a metal ion inside it. The spiral grooves align the reactants so that they fuse with the desired chiral configuration. In 2015, Arseniyadis and Smietana reported a recyclable DNA–copper catalyst<sup>13</sup> that created the correct chiral products as reactants flowed past. With endless combinations of base pairs and metal ions, "there's a plethora of parameters that you can fine-tune", says Arseniyadis.

Chemists are continuing to push the boundaries of catalysis research. Li, for example, is experimenting with housing enzymes inside nanoparticles<sup>14</sup> to help them last longer. Others are synthesizing completely artificial enzymes<sup>15</sup> using techniques from synthetic biology. And earlier this year, an international team of researchers reported<sup>16</sup> using an electric field to catalyse the formation of ring-shaped carbon compounds. These ideas are starting to constitute entire new research fields in which conventionally distinct disciplines overlap — for example, combining chemical synthesis and DNA. That, says Arseniyadis, leaves "a lot of room for serendipity". ■

Chemists are continuing to push the boundaries of catalysis research. Li, for example, is experimenting with housing enzymes inside nanoparticles<sup>14</sup> to help them last longer. Others are synthesizing completely artificial enzymes<sup>15</sup> using techniques from synthetic biology. And earlier this year, an international team of researchers reported<sup>16</sup> using an electric field to catalyse the formation of ring-shaped carbon compounds. These ideas are starting to constitute entire new research fields in which conventionally distinct disciplines overlap — for example, combining chemical synthesis and DNA. That, says Arseniyadis, leaves "a lot of room for serendipity". ■

**XiaoZhi Lim** is a freelance writer based in Singapore.

1. Bligaard, T. *et al.* *ACS Catal.* **6**, 2590–2602 (2016).
2. Csok, Z., Vechorkin, O., Harkins, S. B., Scopelliti, R. & Hu, X. *J. Am. Chem. Soc.* **130**, 8156–8157 (2008).
3. Breitenfeld, J., Ruiz, J., Wodrich, M. D. & Hu, X. *J. Am. Chem. Soc.* **135**, 12004–12012 (2013).
4. Vechorkin, O., Proust, V. & Hu, X. *Angew. Chem. Int. Edn* **49**, 3061–3064 (2010).
5. Vechorkin, O., Barnaz, D., Proust, V. & Hu, X. *J. Am. Chem. Soc.* **131**, 12078–12079 (2009).
6. Nicewicz, D. A. & MacMillan, D. W. C. *Science* **322**, 77–80 (2008).
7. Romero, N. A., Margrey, K. A., Tay, N. E. & Nicewicz, D. A. *Science* **349**, 1326–1330 (2015).
8. Corcoran, E. B. *et al.* *Science* **353**, 279–283 (2016).
9. Ichiishi, N., Canty, A. J., Yates, B. F. & Sanford, M. S. *Org. Lett.* **15**, 5134–5137 (2013).
10. Li, R., Han, H., Zhang, F., Wang, D. & Li, C. *Energy Environ. Sci.* **7**, 1369–1376 (2014).
11. Rak, M. J., Lerro, M. & Moores, A. *Chem. Commun.* **50**, 12482–12485 (2014).
12. Key, H. M., Dydio, P., Clark, D. S. & Hartwig, J. F. *Nature* **534**, 534–537 (2016).
13. Benedetti, E. *et al.* *Chem. Commun.* **51**, 6076–6079 (2015).
14. Liu, J., Yang, Q. & Li, C. *Chem. Commun.* **51**, 13731–13739 (2015).
15. Sauer, D. F. *et al.* *ACS Catal.* **5**, 7519–7522 (2015).
16. Aragonès, A. C. *et al.* *Nature* **531**, 88–91 (2016).



# COMMENT

**SCIENCE-FICTION** A look at H. G. Wells's contributions to science — and *Nature* **p.162**

**TELEVISION** *Star Trek*'s science legacy, 50 years after the first episode **p.165**



**TERMINOLOGY** Spiders don't sting; they bite. What's the difference? **p.167**

**OBITUARY** Ahmed Zewail, Nobel-winning chemist, remembered **p.168**

STR/AFP/GETTY



Antibiotic use in livestock has contributed to drug resistance around the world.

## Use antimicrobials wisely

The United Nations must reframe action on antimicrobial resistance as the defence of a common resource, argue **Peter S. Jørgensen, Didier Wernli** and colleagues.

**T**he effectiveness of antibiotics has been waning since they were introduced into modern medicine more than 70 years ago. Today, our inability to treat infections ranks alongside climate change as a global threat<sup>1,2</sup>. New classes of antimicrobial drugs are unlikely to become widely available any time soon<sup>1</sup>; if and when they do, bacteria, viruses and other microbes will again evolve resistance<sup>3</sup>. In

any case, waging war on microbes is not tenable<sup>3</sup> — our bodies and planet depend on them<sup>4</sup> (see Supplementary Information; [go.nature.com/2c03p6n](http://go.nature.com/2c03p6n)).

Addressing resistance requires global collective action. Like the ozone layer, a stable climate or biodiversity, the global population of susceptible microbes is a common pool resource — one shared by all. But no individual or country has a strong enough

incentive to conserve this 'commons'. It has been depleted by the massive use of antimicrobial compounds and the growing competitive advantage of resistant microbes. It is a classic 'tragedy of the commons'.

This intimate relationship with microorganisms predates modern humans. It is the result of many millions of years of co-evolution. Our bodies need particular kinds of microbes for digestion, immune ►



► function and general health. Equally, microbes support planetary health, for example, through nutrient cycles, including those that maintain soil and water quality<sup>4</sup>. In other words, microbes sustain human civilization. Yet our understanding of the complex interactions and uncertainties that govern the relationships between humans and microbes is limited.

The 2015 *Global Action Plan on Antimicrobial Resistance*, drafted by the World Health Organization (WHO) with support from the United Nations Food and Agricultural Organization (FAO) and the World Organisation for Animal Health (OIE), recognizes the need for multisectoral cooperation to address resistance (see [go.nature.com/2bbijap](http://go.nature.com/2bbijap)). But, in our view, it does not go far enough in recognizing the life support we receive from the global microbiome. Tackling resistance urgently requires the scaling back of the massive overuse of antibiotics to secure the liveability of Earth in the long term.

On 21 September, heads of state will meet to take further action at the United Nations high-level meeting on antimicrobial resistance in New York City. A UN declaration currently under discussion must set global targets, accelerate implementation of the global action plan, plug its gaps and ensure stronger accountability and interagency coordination. It must emphasize the many benefits of microbes.

Parties should aim to build the resilience of society and the microbiome. In our opinion, this is the way to maintain low levels of resistance amid the many surprises of a rapidly changing planet. Advances from studying resilience in other common pool resources such as fisheries and forests<sup>5</sup> suggest key steps for antimicrobial resistance, which we set out below. Achieving these will require changes to institutions, regulations, education, community norms and expectations, notably in medicine and agriculture.

### EDUCATE TO LEARN

Until now, political and financial investments have focused largely on creating incentives to fuel drug innovation and new or faster diagnostics. Currently, such technological fixes appeal to and benefit mainly rich nations in the 'global north'. Incentives must be targeted to benefit not only large pharmaceutical companies in the north, but also to enlist research and development efforts globally. One of the most important outcomes of the UN meeting should be national commitments to the broadest and most creative participatory education campaigns about resistance<sup>2</sup> and the importance of the microbial world.

Why? Because the level of ignorance about the calamity that is antimicrobial resistance is staggering. A 2015 WHO survey across 12 countries found that 64% of the



Limited access to quality antimicrobials in the developing world drives unregulated sales.

public think that antibiotics also work for, for instance, viral infections such as influenza and colds (see [go.nature.com/2c7zvfu](http://go.nature.com/2c7zvfu)). Such basic knowledge gaps lead patients and physicians to reach for antibiotics without appreciating the costs.

Instead, institutions and citizens must understand the central facts, context and risks in a way that allows them to learn more independently. This goal requires awareness campaigns to be revised and scaled up by orders of magnitude<sup>2</sup>, as well as investment in new communication tools. Initiated in 2007, Thailand's Antibiotics Smart Use project sets a direction for upscaling. It enables patients in pharmacies to self-diagnose on the basis of the appearance of their sore throat to verify whether they need antibiotic treatment<sup>6</sup>. For further learning, citizen-science programmes in which participants monitor their own microbiomes should be extended to cover, for example, self-testing for resistance in various parts of the body<sup>7</sup>.

Such campaigns could engage communities and change norms about how and when to use antibiotics. Campaigns will need to be coordinated internationally for quality and impact, and adapted to suit

regional perspectives. Engagement can be spread through schools, mass media and social media.

### JOIN UP

Resistance affects animal and environmental health as well as human health, and so requires coordinated action across economic sectors. No single concern exemplifies this better than the high rate of antibiotic use in agriculture (largely as growth promoters or disease prevention). In the United States, 70–80% of all antimicrobials consumed are given to livestock; agricultural use in the BRICS emerging economies (Brazil, Russia, India, China and South Africa) is expected to double by 2030, as compared to 2010 levels<sup>8</sup> (see 'Farm forecast'). As a result, antibiotics and resistance genes enter the food chain, soil and the water table, threatening human health.

The European Union has phased out the use of medically important antibiotics for growth promotion in agriculture. Other countries, including Mexico and Taiwan<sup>9</sup>, have sought to reduce it. In the United States, a directive discourages the use of antibiotics for growth promotion through voluntary measures and stronger veterinary oversight

of therapeutic use. However, the powerful industrial farming lobby and a lack of perceived urgency have so far stalled stronger mandates.

Stronger political action to change how we use antibiotics, whether by humans or animals, requires citizens to be better informed. For instance, the public should have online access to surveillance that tracks how human resistance increases in settlements near farms. In the meantime, consumer groups play a crucial part by calling on retail chains to switch where their meat is sourced. For example, US food chains Chipotle, McDonald's and Chick-fil-A have responded (to varying degrees) to public demands with stricter limits on antibiotic use in the meat they sell.

A particularly worrying issue that is not confined to the use of antimicrobials in food production is the international spread of resistance genes, especially those conferring resistance to many drugs of 'last resort'. Most recently, a mobile plasmid gene carrying resistance to the last-resort antibiotic colistin has been found in Asia, Europe and North America. Clearly, countries cannot act alone to deal with the problem without jeopardizing the benefits of globalization.

Much better surveillance and containment is needed of the most dangerous multiresistant strains in people and food<sup>2</sup>. A global routine-surveillance initiative could help to prevent the spread of resistance. It could screen medical tourists or patients returning from hospitals abroad to identify carriers of multiple resistant strains. Hospitals that are centres of international travel for medical treatment must lead the way; funding and learning mechanisms must be increased for other hospitals to follow suit.

The International Health Regulations, revised by WHO member states in 2005, are a legally binding instrument that aims to provide global surveillance and response. Properly financed, they could be effective<sup>10</sup>. Yet the resources needed to respond to emerging diseases do not flow commensurately to low- and middle-income countries as they do in the global north — a key lesson of the recent Ebola outbreak. All governments have a collective responsibility to improve capacities for rapid response to resistance. Greater support by donor countries to new and existing funding mechanisms such as the Global Fund to Fight AIDS, Tuberculosis and Malaria is needed in low- and middle-income countries.

## EXTEND COALITIONS

International and national coalitions must be broadened. The global action plan strengthens the established collaboration between the WHO, FAO and OIE. This should be extended to cover other relevant sectors, including trade, development and environment. The model set up by UNAIDS (the Joint

United Nations Programme on HIV/AIDS) in 1996 serves as an example of how to intensify collaboration, leverage resources, involve more parties and reduce barriers.

The UN meeting must commit to driving learning between institutions. Global platforms are needed for sharing best practices and the latest data about resistance levels and antibiotic consumption, for instance, among national agencies. Such exchange happens in Europe for resistant human bloodstream infections, and human and veterinary antimicrobial consumption. This must be scaled up to monitor resistance in communities, food industry and the environment. A relevant model for exchange at the global level is the WHO's Pandemic Influenza Preparedness Framework. To engage the public effectively, more-frequent updating, vivid visualizations and engaging communications are needed.

As in the Paris climate agreement, countries should submit to the UN voluntary but monitored targets on limiting resistance. Parties may go further by making shortfalls subject to potential sanctions. A key priority is to establish measurable indicators at the country level, such as the median yearly consumption of antibiotics per person.

As for the climate issue, non-state actors from business to civil society can be central to societal transformations. Such stakeholders were consulted during the development of the WHO global action plan. But their participation in the long run must become more integral to the global coalition responsible for tackling resistance.

Available governance instruments range from binding treaties to guidelines, with each approach having pros and cons. A first step to holding companies accountable would be an international code on

the promotion of antibiotics (promotional spending in the United States in 1998 amounted to US\$1.6 billion), akin to that adopted by the WHO in 1981 on the marketing of breast-milk substitutes.

## ACT NOW

The complexity and gravity of resistance call for the immediate mass mobilization of society. Maintaining the susceptibility of microbes to drugs for global health is a matter of sustainable development. Improving understanding about humankind's dependence on the global microbiome should lead to action on many other important issues

**"Building global resilience to resistance is a long game."**

involving micro-organisms. These issues include infectious diseases, food security, natural resources and

environmental conservation. Action here could, in turn, lead to more-equitable forms of national progress across the sustainable-development goals<sup>3</sup>.

Building global resilience to resistance is a long game. But changes can be surprisingly fast when the time is ripe and a plan is ready. This month's UN high-level meeting is a rare opportunity for global collective action on human interactions with microbes. It must protect both the lifesaving power of antibiotics and the ability to use them when necessary. ■

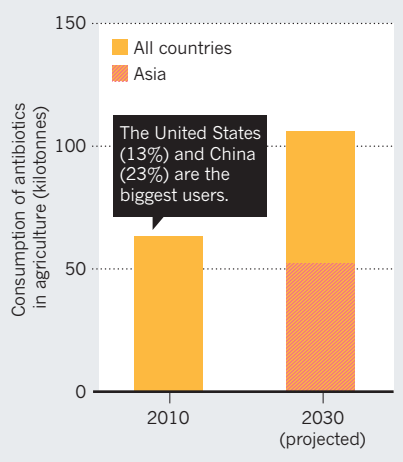
**Peter S. Jørgensen** is a researcher at the Global Economic Dynamics and the Biosphere, Royal Swedish Academy of Sciences, Stockholm, Sweden. **Didier Wernli** is a senior research associate at the Global Studies Institute, University of Geneva, Geneva, Switzerland. **Scott P. Carroll**, **Robert R. Dunn**, **Stephan Harbarth**, **Simon A. Levin**, **Anthony D. So**, **Maja Schlüter** and **Ramanan Laxminarayan**. e-mail: [psjorgensen@kva.se](mailto:psjorgensen@kva.se)

1. Laxminarayan, R. *et al.* *Lancet* **387**, 168–175, (2016).
2. *Review on Antimicrobial Resistance: Tackling Drug-Resistant Infections Globally — Final Report and Recommendations* (Wellcome Trust, UK Government, 2016).
3. Carroll, S. P. *et al.* *Science* **346**, 1245993 (2014).
4. Whitmee, S. *et al.* *Lancet* **386**, 1973–2028 (2015).
5. Biggs, R. *et al.* *Ann. Rev. Environ. Res.* **37**, 421–448 (2012).
6. Bigdeli, M., Peters, D. H., Wagner, A. K. (eds) *Medicines in Health Systems: Advancing Access, Affordability and Appropriate Use* (World Health Organization, 2014).
7. Hulcr, J. *et al.* *PLoS ONE* **7**, e47712 (2012).
8. Van Boeckel, T. P. *et al.* *Proc. Natl Acad. Sci. USA* **112**, 5649–5654 (2015).
9. Maron, D. F., Smith, T. J. & Nachman, K. E. *Glob. Health* **9**, 48 (2013).
10. Wernli, D. *et al.* *PLoS Med.* **8**, e1001022 (2011).

Full author affiliations and supplementary information accompany this article online: see [go.nature.com/2c03p6n](http://go.nature.com/2c03p6n).

## FARM FORECAST

By 2030, the use of antimicrobials in agriculture in Asia alone could equal 82% of global agricultural consumption in 2010. The drugs are largely given to promote growth or prevent infections, rather than to treat disease.







POPPER/GETTY

Wells in 1931, about to leave London for a tour of the United States.

## SCIENCE JOURNALS

# The worlds of H. G. Wells

**Simon J. James** looks back at the richly varied contribution of the science-fiction writer and science popularizer.

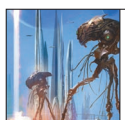
**H**erbert George Wells (1866–1946) occupies a singular place in science and culture. Practically reinventing science fiction in landmark books such as *The War of the Worlds*, he also wrote prolifically on science, education, history and politics: in a career spanning 6 decades, he penned more than 150 books and pamphlets, as well as numerous articles in, and letters to, the press. Living through the late-nineteenth-century burgeoning of the sciences, the societal and technological upheavals of the early twentieth century and two world wars, Wells both absorbed revelations and delivered some — foreseeing

powered flight, space travel, tanks and the atomic bomb, and becoming an enthusiastic and committed popularizer of science.

Behind Wells's enormous output was a desire to use writing to make the world better — by projecting either a utopian vision of a perfected future, or dystopias revealing how the lessons of his work went unheeded.

Among his extraordinary achievements, Wells was one of the earliest major English

writers to be a trained scientist. The word 'scientist' had been coined by historian William Whewell just 33 years before Wells's birth. Wells — the child of servants-turned-shopkeepers — escaped apprenticeships in drapers' shops to become a pupil-teacher at Midhurst Grammar School in the south of England. A scholarship propelled him to what is now Imperial College London, where he studied biology under champion of Darwinism T. H. Huxley, graduating in 1890. He never practised as a scientist; nor did he see himself as an 'artist', preferring 'journalist', particularly later in his career, when politics became more important in his writing.



**SCIENCE. FICTION.**  
A *Nature* special issue  
[nature.com/scifispecial](http://nature.com/scifispecial)



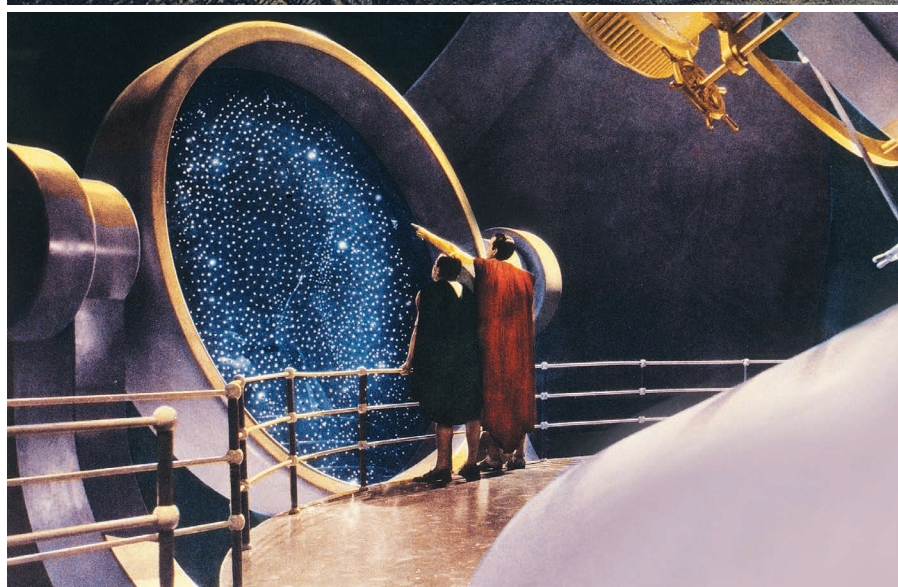
Wells's brilliance as a communicator of science drew him to many friendships with scientists — not least Richard Gregory. The astronomer, who was at university with Wells, was *Nature's* second editor. Wells was to publish 25 pieces in the journal over 50 years, inspiring and provoking scores of contemporary thinkers into contributing a rolling tide of correspondence, book reviews, notices and other commentary on his output.

Wells was also publishing inspired books at a furious pace. His first were the scientific textbooks *Honours Physiography* and *Text-book of Biology* (both 1893); the latter went into many editions. The topics rapidly ramified. The year 1895 alone saw a short-story collection (*The Stolen Bacillus and Other Incidents*), a fantastic romance in which an angel falls to Earth (*The Wonderful Visit*) and a volume of essays, as well as his first full-length work of fiction, *The Time Machine*. That book, with Wells's other late-1890s 'scientific romances' *The Island of Doctor Moreau*, *The War of the Worlds* and *The Invisible Man*, would set the bar for science fiction. They are also among a number of books by Wells that had an impact on science itself.

*The War of the Worlds* inspired Robert Goddard — inventor of the liquid-fuelled rocket, whose research led to NASA's Apollo programme — to devote his life to space travel. The book's "heat-rays" also presaged military lasers. The hero of *The Island of Doctor Moreau*, Edward Prendick, "had spent some years at the Royal College of Science, and had done some researches in biology under Huxley"; the book's animal-human hybrids are rough precursors to today's embryonic chimaeras. Wells's 1914 *The World Set Free* predicted the atomic bomb, drawing on and subsequently influencing chemist Frederick Soddy's work on radioactivity, and influencing physicist Leo Szilard in his work on the neutron chain reaction. *The Shape of Things to Come* (1933) foreshadows the Second World War, and its 1936 film adaptation *Things to Come* (produced by Alexander Korda and starring Raymond Massey) ends with humanity launching its first spacecraft.

Wells was irritated by comparisons to fellow science-fiction giant Jules Verne. The feeling was mutual. Verne complained that the antigravity metal cavorite in Wells's *The First Men in the Moon* (1901) was pure invention, compared to the gunpowder-fuelled rocket in his own 1865 *From the Earth to the Moon*. But Wells's main interest was never technology. After inventing the insectoid bodies of the Selenites in *The First Men in the Moon*, or the mind-reading aliens of 1937's *The* ▶

**"Wells was driven by the conviction that education was paramount to clear thinking and efficient, happy lives."**



An illustration for *The War of the Worlds* drawn by Henrique Alvim Corrêa (top) and a still from the 1936 film adaptation of *The Shape of Things to Come*.



► *Camford Visitation*, he went on to imagine the significance of these fantastic elements for human psychology and culture, setting a template that has since been followed by the most literary of science fiction (from the likes of Margaret Atwood and China Miéville).

Wells was also honing his journalistic skills. His first essay in *Nature*, 'Popularising Science' (*Nature* 50, 300–301; 1894), asks for standards to be set in popular scientific writing to promote accessibility. He would go on to publish *Nature* articles on a range of subjects (see John S. Partington's admirable and comprehensive *H. G. Wells in Nature, 1893–1946*; Peter Lang, 2008). But education, more than fiction, science or indeed science fiction, was to become the keynote of Wells's writing career.

Owing, in part, to his own escape from apprenticeship into an intellectual life, Wells was driven by the conviction that education was paramount to clear thinking and efficient, happy lives. Even his most fantastic, futuristic writings contained lessons for the present, intended to lead to a more utopian ordering of the world. A lecture to the Royal Institution of Great Britain, published as 'The Discovery of the Future' (*Nature* 65, 326–331; 1902), offers a window on the development of these ideas, arguing for the importance of conscious forward-thinking:

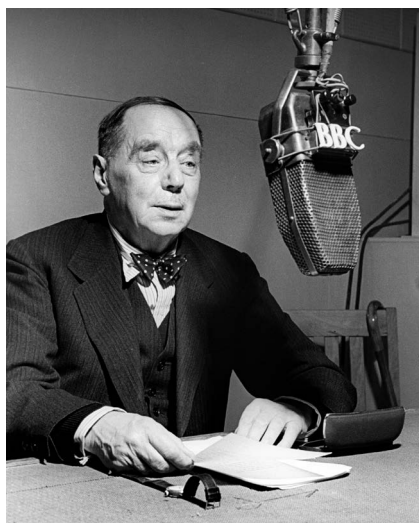
We travel on roads so narrow that they suffocate our traffic; we live in uncomfortable, inconvenient, life-wasting houses out of a love of familiar shapes and familiar customs and a dread of strangeness; all our public affairs are cramped by local boundaries impossibly restricted and small. Our clothing, our habits of speech, our spelling, our weights and measures, our coinage, our religious and political theories, all witness to the binding power of the past upon our minds.

For Wells, the scientific method conferred on its user the authority to rethink and challenge these stale ideas, and should underpin every area of human endeavour. (This positivistic idea of science was fairly short-lived, lasting only from Charles Darwin's dethroning of humanity as the summit of creation to the early-twentieth-century advent of quantum mechanics, which undermined claims of absolute scientific certainty.) But Britain's educational system failed to enshrine science properly, Wells felt; the privileged status of classics was a consistent target of his ire. The result was global woe: "to defective education was due the general neglect of science and 'muddling through,'" as he told the 11th

annual meeting of the British Science Guild (*Nature* 99, 186–187; 1917). His hope was that, if the intellectual enquirer were armed with the right kinds of knowledge, history might be predicted like the movements of planets and tides. Then, informed by the knowledge of humanity's shared evolutionary origins, the history of the future would see nation states dissolving in favour of a system of cooperative world government.

Wells's significance over most of his career rested on his status as a public intellectual, and he relished the international audience reached by his publications. His prescience was a vital element of his popularity, and not just in science fiction. For instance, he imagined something like a World State-sponsored Wikipedia. In an address to the Royal Institution in 1936 on the "World Encyclopaedia" or "World Brain", he described it as:

the mental background of every intelligent man in the world. It should be alive and growing and changing continually, under revision,



Wells recording for the BBC (top) and during his biology studies at university.

extension and replacement from the original thinkers in the world everywhere. Every university and research institution should feed it. Every fresh mind should be brought into contact with its standing editorial organization ... its contents would be the standard source of material for the instructional side of school and college work, for the verification of facts and the testing of statements — everywhere in the world.

*World Brain* (1938) amplified these ideas. This book, with the 1920 *The Outline of History* — a best-selling opus on the story of humanity from its evolutionary origins to his hoped-for utopia — was Wells's response to the catastrophe of the First World War.

Wells lived to see the catastrophe of the second. Having witnessed such a failure to act collectively, his final contribution to *Nature*, in 1944, was an attempt to understand the actions and motivations of the individual. 'The Illusion of Personality' suggests that the notion of a stable personality is an illusion, because consciousness constantly flits from one moment to the next (*Nature* 153, 395–397; 1944). Reading the piece now, it is fascinating to see a writer so long concerned with thinking on a global scale, and over hundreds to thousands of years, preoccupied at the end of his career with the micro-impressions of a single, impermanent sensibility.

Wells knew, and argued with, most of the significant writers and political leaders of the late nineteenth- and early twentieth-centuries. Two friendships were constant: one with fellow novelist Arnold Bennett, the other with Gregory. Before he became editor of *Nature*, Gregory had co-authored *Honours Physiology* with Wells; he was an assistant editor at the journal when Wells, a then-unknown teacher and jobbing science writer, published 'Popularising Science'. Gregory advised Wells on lunar gravity for *The First Men in the Moon*; and when Wells died in 1946, Gregory wrote the *Nature* obituary of the genius with whom he had first collaborated 50 years before (*Nature* 158, 399–402; 1946). Gregory's review of *The War of the Worlds* (*Nature* 57, 339–340; 1898) had ventured that "scientific romances are not without a value in furthering scientific interests; they attract attention to work that is being done in the realm of natural knowledge, and so create sympathy with the aims and observations of men of science". To attract attention and create such sympathy was Wells's steadfast aim. ■

**Simon J. James** is professor of Victorian literature and head of the Department of English Studies at Durham University, UK. He is the author of *Maps of Utopia: H. G. Wells and the End of Culture and the editor of a forthcoming edition of H. G. Wells's The First Men in the Moon*. e-mail: s.j.james@durham.ac.uk

TOP: BBC PHOTO LIBRARY; BOTTOM: ARCHIVO GBB/CONTRASTO/EVINE





The original crew of the USS *Enterprise*.

## SCIENCE FICTION

# Boldly going for 50 years

**Sidney Perkowitz** scans the impacts of *Star Trek* on science, technology and society.

**H**alf a century ago, in September 1966, the first episode of *Star Trek* aired on the US television network NBC. NASA was still three years short of landing people on the Moon, yet the innovative series was soon zipping viewers light years beyond the Solar System every week. After a few hiccups it gained cult status, along with the inimitable crew of the starship USS *Enterprise*, led by Captain James T. Kirk (William Shatner). It went into syndication and spawned 6 television series up to 2005; there are now also 13 feature films, with *Star Trek Beyond* debuting in July this year.

Part of *Star Trek*'s enduring magic is its winning mix of twenty-third-century technology and the recognizable diversity and complexity enshrined in the beings — human and otherwise — created by the show's originator Gene Roddenberry and his writers. As Roddenberry put it, “We stress humanity.” The series wore its ethics on its sleeve at a time when the Vietnam War was raging and anti-war protests were proliferating, along with racial tensions that culminated in major US urban riots in 1967–68. Roddenberry's United Federation of Planets, a kind

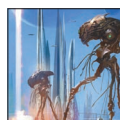
of galactic United Nations, is an advanced society wielding advanced technology, and the non-militaristic aims of the *Enterprise* are intoned at the beginning of every episode in the original series (TOS): “To explore strange new worlds; to seek out new life and new civilizations; to boldly go where no man [later, ‘no one’] has gone before.”

Over the decades, *Star Trek* technologies have fired the imaginations of physicists, engineers and roboticists. Perhaps the most intriguing innovation is the warp drive, the propulsion system that surrounds the *Enterprise* with a bubble of distorted space-time and moves the craft faster than light to traverse light years in days or weeks. In 1994, theoretical physicist Miguel Alcubierre showed that such a bubble is possible within Albert Einstein's general theory of relativity, but would demand massive amounts of negative energy, also known as exotic matter (M. Alcubierre *Class. Quantum Grav.* **11**,

L73; 1994). This is not known to exist except (possibly) in minuscule quantities; and some physicists speculate that the Alcubierre drive might annihilate the destined star system. The warp drive remains imaginary — for now.

However, another application of warped space-time in the series has been realized: a cloaking device that shields spacecraft from view by bending light around them. In 2006, electrical engineers David Smith and David Schurig built a ‘metamaterial’ electromagnetic cloak that hid an object from microwaves by refracting them to pass around it, much as water flows around an obstacle (D. Schurig *et al. Science* **314**, 977–980; 2006). Now, similar diversionary tactics are being used to hide small objects under visible light, for instance by electrical engineer Xingjie Ni and his colleagues, who devised a “skin cloak” 80 nanometres thick to do the job (X. Ni *et al. Science* **349**, 1310–1314; 2015).

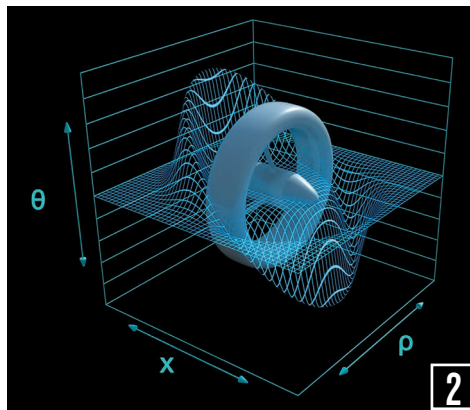
The exotic *Enterprise* transporter, which instantaneously dematerializes and teleports people and things (inspiring the catchphrase “Beam me up”), was supposedly conceived to save the costs of staging repeated spaceship landings. It has a real analogue in quantum



## SCIENCE. FICTION.

A *Nature* special issue  
[nature.com/scifispecial](http://nature.com/scifispecial)

CBS VIA GETTY



## TREK TECHNOLOGIES

The series' futuristic technologies have inspired real-life innovations — some further advanced than others. A version of the warp drive that propelled the USS *Enterprise* faster than light (1) was proposed by physicist Miguel Alcubierre in 1994 (2), but remains conceptual. The diagnostic tricorder (3) has been realized in Scanadu's SCOUT (4) and app, which measure vital signs such as blood pressure.

to delight in difference, even in alien life-forms, and ready itself to “meet the diversity that is almost certainly out there”.

Star Trek's portrayal of human diversity and refusal to engage in national exceptionalism remain landmark achievements. Emerging at a time of racial exclusion in US television, TOS crew included Lieutenant Nyota Uhura (Nichelle Nichols), the first prominent African American female role in a US television series, as well as the ‘pan-Asian’ helmsman Hikaru Sulu (George Takei), Russian navigator Pavel Chekov (Walter Koenig) — and, of course, Leonard Nimoy's star turn as half-Vulcan Commander Spock. Native American first officer Chakotay (Robert Beltran) emerged in the series *Voyager* (1995–2001). The gender balance tended to the heavily male until the advent of *Voyager* Captain Kathryn Janeway (Kate Mulgrew), with half-Klingon chief engineer B'Elanna Torres (Hispanic actress Roxann Dawson). Real-world impacts abound. Nichols, for instance, has related how US civil-rights leader Martin Luther King urged her to remain in the series when she was considering other professional options. Her character, in turn, inspired astronaut Mae Jemison, the first African American woman to be sent into space by NASA.

Fifty years later, how does our world compare with Roddenberry's universe? The changes in technology are transformational; and although interstellar travel has yet to become reality, NASA's projected 2030s human mission to Mars follows the dream “to boldly go”. The progressive social values that Star Trek pioneered on television are now much more widely held. But new conflicts and geopolitical stand-offs have erupted, despite efforts by our own federation, the United Nations. Amid these shifts and tensions, this vastly influential franchise continues to carry a subtle but clear message — we can be better than we are. ■

**Sidney Perkowitz** (<http://sidneyperkowitz.net>) is Charles Howard Candler Emeritus Professor of Physics at Emory University in Atlanta, Georgia. He writes frequently about science, technology and culture; his latest books are *Universal Foam 2.0* and *Frankenstein 2018* (in progress). e-mail: [phyp@emory.edu](mailto:phyp@emory.edu)

teleportation. In 2015, for instance, quantum optics researcher Hiroki Takesue and his colleagues harnessed entanglement to send the properties of one photon to another over 100 kilometres of optical fibre (H. Takesue *et al. Optica* 2, 832–835; 2015). Above the atomic level, however, we're a long way from teleporting entire organisms or objects.

Other Star Trek technologies anticipated modern trends. The tricorder that TOS medic Leonard ‘Bones’ McCoy (DeForest Kelley) uses for diagnosis has spawned real devices, such as SCOUT from medical-technology company Scanadu in Moffett Field, California. Meanwhile, activity trackers already perform basic health monitoring, recording pulse rate, calorie intake and quality of sleep.

Artificial intelligence has begun to emerge in technologies such as speech recognition by Apple's personal-assistant program Siri, Google's self-driving car and the ‘all-terrain’ Atlas robot created for the US Defense Advanced Research Projects Agency. All are significant developments that could pave the way to an eventual approximation of Lieutenant Commander Data (Brent Spiner), the sentient android who debuted on television series *The Next Generation* in the late 1980s.

Star Trek's holodeck — the immersive virtual-reality environment in which the *Enterprise* crew visits simulated locales — is also years away, but huge advances in the technology are afoot. The Oculus Rift headset, for instance, provides a visual and auditory virtual-reality experience, but must be

tethered to a computer, thus falling short of delivering the seamless holodeck experience.

Three-dimensional printers, which lay down successive layers of material to form intricate shapes, are now being adapted to handle food, perhaps a step towards *Enterprise* meal replicators. The Creative Machines Lab, then at Cornell University in Ithaca, New York, designed one model as part of its open-

access Fab@Home project, and Natural Machines in Barcelona, Spain, touts its Foodini printer as simplifying the making of textured or layered foods such as ravioli.

More generally, and arguably with greater long-term significance, Star Trek raised enthusiasm for space exploration and science. In 1975, fans convinced NASA to name its first test space shuttle orbiter *Enterprise* (the craft was unpowered and never reached space). And many young would-be scientists have found the series inspirational.

Its social message has been no less important. The federation ethic ensured that Kirk, *Next Generation* Captain Jean-Luc Picard (Patrick Stewart) and their successors ‘waged peace’ even when confronted by aliens such as the Klingons, a people genetically predisposed to hostility. The February 1968 episode ‘A Private Little War’, an allegory about Vietnam, was a pointed example. Roddenberry believed that humanity must learn

**“Many young would-be scientists have found the series inspirational.”**



# Correspondence

## Report released on antibiotic resistance

The Wellcome Trust today releases a report to inform the United Nations General Assembly's High-level Meeting on Antimicrobial Resistance later this month (see [www.wellcome.ac.uk/drugresistantinfections](http://www.wellcome.ac.uk/drugresistantinfections)). The report distils the findings of an international summit of researchers, policymakers and multilateral institutions that met in London in April 2016.

It identifies three areas for immediate action to alleviate the current and future impact of drug-resistant infections on the number of deaths and on national economies. The summit and report build on the independent review on antimicrobial resistance led by economist Jim O'Neill and commissioned by the UK government, in partnership with the Wellcome Trust, which was published in May 2016 (see [go.nature.com/2bsxoyi](http://go.nature.com/2bsxoyi)). Together, these reports should help to focus attention and galvanize support from national governments, the G7 and G20 countries, international agencies and non-governmental organizations.

The UN resolution on antimicrobial resistance should commit governments and international organizations to concerted and verifiable action, adapted locally as necessary. Continued support for scientific research and innovation is essential to shape future responses, but the need for further research must not be an excuse for delaying urgent interventions.

**Jeremy Farrar** *Wellcome Trust, London.*

**Sally Davies** *Department of Health, London.*  
[j.farrar@wellcome.ac.uk](mailto:j.farrar@wellcome.ac.uk)

## Antibiotic partners promote discovery

As president of the Infectious Diseases Society of America and a physician of infectious

diseases, I am greatly encouraged by the launch of the Combating Antibiotic Resistant Bacteria Biopharmaceutical Accelerator (CARB-X; see *Nature* <http://doi.org/bp7x>; 2016). Contrary to your implication, this public-private partnership is designed to foster antibiotic discovery as well as preclinical antibiotic development (see [www.carb-x.org](http://www.carb-x.org)). Physicians who treat the increasing numbers of people with infections caused by multidrug-resistant organisms know at first hand the urgent need for novel antibiotics.

Most pharmaceutical companies have been retreating from antibiotic research and development (R&D) over the past few decades because of economic, regulatory and scientific hurdles. Fresh incentives are needed to stimulate and support all stages of antibiotic R&D if new drugs are to be discovered and brought to market in a timely fashion. CARB-X can play an important part in this broader effort, which must also include other economic and regulatory incentives that are currently under consideration in the US Congress.

**Johan S. Bakken** *St. Luke's Medical Center, Duluth, Minnesota, USA.*  
[jbakken1@d.umn.edu](mailto:jbakken1@d.umn.edu)

## Brexit threatens China collaboration

Brexit — Britain's exit from the European Union — threatens to undermine the country's scientific relationships with nations outside the EU (see E. Masood *Nature* 535, 467; 2016). The country will need to invest more to maintain its valuable collaboration with China, for example, once EU funding is withdrawn.

The United Kingdom could be excluded from exchanges under the EU's Marie Skłodowska-Curie fellowship programme, which have benefited thousands

of talented Chinese and British scientists since 2007. For the country to retain its current exchange level of international research talent, it would need to invest more in its Newton Fund to make up the shortfall (see [go.nature.com/2bfgzq3](http://go.nature.com/2bfgzq3)).

Also under threat will be British scientists' participation in China's projects with the EU, such as its Five-hundred-meter Aperture Spherical Telescope, due to be completed this year (see W. Yang *Nature* 534, 467–469; 2016).

Despite such uncertainties, Brexit could still provide opportunities to strengthen scientific collaboration between the world's second and fifth largest economies — for example, through the collaboration between Research Councils UK and the National Natural Science Foundation of China (see [go.nature.com/2bflysi](http://go.nature.com/2bflysi)).

**Hong Yang** *Norwegian Institute of Bioeconomy Research; and University of Oslo, Norway.*

**Roger J. Flower** *University College London, UK.*

**Xianjin Huang** *Nanjing University, China.*  
[hongyanghy@gmail.com](mailto:hongyanghy@gmail.com)

## Gap widens for honorary PhDs

The changing nature of the standard PhD degree (*Nature* 535, 26–28; 2016) could make the honorary PhD seem increasingly hollow by comparison.

Universities confer honorary doctorates on those who have attained national or international prominence in the arts, sciences or sporting fields. Scholarly skills are rarely considered, although most recipients have sufficient expert knowledge to potentially write a thesis. Recipients often have links with the awarding institute, which benefits from the associated publicity.

By contrast, the standard PhD is awarded in recognition of research expertise. Now

that more PhD graduates pursue careers outside academia, programmes are placing greater emphasis on transferable scholarly skills and on developing management, entrepreneurship and teamwork skills. These additional training requirements threaten to stoke academic tensions over the existing gap in scholarship between standard and honorary PhDs.

**Steven Watterson** *University of Ulster, Londonderry, UK.*  
[s.watterson@ulster.ac.uk](mailto:s.watterson@ulster.ac.uk)

## Bite like a spider, sting like a scorpion

The image of a togo starburst tarantula (*Heteroscodra maculata*) on your Contents page in the print issue (*Nature* 534, 433; 2016) is incorrectly titled 'Sting like a spider'. Spiders do not sting, they bite.

Arthropod bites and stings are differentiated by the nature and purpose of the stinging or biting apparatus, and by their clinical effects (see J. Goddard *Physician's Guide to Arthropods of Medical Importance*; CRC Press, 2012). Bees and scorpions, for example, inject their stings mainly for defence; spiders bite usually to immobilize or kill their prey, by injecting venom from their fangs. These insults typically result in one or two puncture marks, respectively, in the victim's skin, serving as useful indicators for diagnosis and treatment.

**Reza Afshari** *BC Centre for Disease Control, Vancouver, Canada.*  
[reza.afshari@bccdc.ca](mailto:reza.afshari@bccdc.ca)

### CONTRIBUTIONS

Correspondence may be submitted to [correspondence@nature.com](mailto:correspondence@nature.com) after consulting the author guidelines at <http://go.nature.com/cmchno>.



# Ahmed Hassan Zewail

## (1946–2016)

Nobel-winning inventor of femtochemistry and statesman.

That the first science Nobel prizewinner from the Arabic-speaking world, Ahmed Hassan Zewail, pioneer of ultrafast chemistry, was also a diplomat is apparent in his unique list of distinctions. Few scientists can have been garlanded by foundations in both Israel and Saudi Arabia, served in the Pontifical Academy of Sciences — and had their face on several postage stamps while living. He died on 2 August 2016, aged 70.

The eldest child of a middle-class family, Zewail was born on 26 February 1946. He grew up in Desouk, Egypt, a small town 80 kilometres from Alexandria. After a state-school education, he took undergraduate and masters degrees in chemistry at the University of Alexandria. He then decided to further his studies in the United States, despite a fairly weak command of English (a fact which shocks those of us who knew this eloquent speaker later on).

He did his graduate work on novel spectroscopies, including optically detected magnetic resonance, with Robin Hochstrasser at the University of Pennsylvania in Philadelphia. His postdoctoral work was on coherence in multidimensional systems and energy transfer in solids, with Charles B. Harris at the University of California, Berkeley. In 1976 he joined the California Institute of Technology in Pasadena, where he remained for the rest of his career, rising to become the Linus Pauling professor of chemistry in 1995. Like Pauling, his reputation and impact would truly transcend science.

Throughout the 1980s and most of the 1990s he led his group to do experiments on ‘femtochemistry’ — his coinage for causing and watching reactions using light pulses lasting much less than a picosecond (a millionth of a millionth of a second). This is the timescale of chemical reactions at the molecular level — the timescale of vibrations and nuclear motions. For this work he became the sole recipient of the 1999 Nobel Prize in Chemistry. Before the advent of such ultrafast lasers in the 1970s, chemists’ ideas of the dynamics of molecules in excited states were very different from today’s. They believed



that the dominant force was intramolecular relaxation, and that this was largely incoherent.

Zewail’s work shattered this picture. Through elegant experiments, his group unravelled reaction dynamics, clarified molecular pathways and illuminated the quantum-mechanical evolution of atoms in molecules. The classic tool for him was the pump–probe experiment. Here the first pulse (the pump) started a chemical reaction, and the second (the probe) monitored what happened next. In this way he and his team took snapshots of vibrational flow, state rearrangement and reaction products. These revealed a much deeper role for coherence than anyone had anticipated.

After his Nobel Prize, Zewail’s focus shifted towards a new form of microscopy that used ultrafast pulses of electrons to track reactions in space and time at the atomic scale. It was no secret that he hoped (like Pauling) to win a second Nobel Prize: Zewail was not one to rest on his laurels. Once again, truly elegant science resulted.

Generations of talented students benefited greatly from his insight. He longed to boil down complex phenomena to the simplest underlying dynamics. He would urge his co-workers to avoid getting mired in detail. A very, very busy man, he still kept close tabs on his sub-basement labs. He would pop in during an experiment without warning, poke around, and start asking questions, saying he just wanted to “smell the cooking”.

His career and influence were shaped by

the view that science transcends political borders. One early incident illustrates this. In January 1983, he organized the International Conference on Photochemistry and Photobiology at his alma mater in Alexandria. He was clearly a rising star, but the work that would lead to the Nobel had barely started. The conference was a major milestone in his career, attracting a stunning collection of distinguished international scientists, with an obvious subtext of bootstrapping progress for Egyptian science in general.

Given the tumultuous politics of the region then, as now, it was no surprise that as soon as Israeli scientists arrived, most of the Arab representatives were ordered

by their governments to leave. Zewail surely would have expected this and could have taken the easy way out — asking his Israeli friends (who were numerous) to stay away. Instead he publicly denounced at the conference the destructive acts of the same governments he was trying to help guide to modernity.

Zewail never lost his drive to modernize science in the Arabic-speaking world. In speeches and articles he reminded his countrymen of the historical greatness of their science, and encouraged them to build to greatness again through investment in education and fundamental research. He was the driving force behind the Zewail City of Science and Technology in October City, Giza. After a troubled gestation due to political instability, this new university finally opened in 2013, with institutes intended to cover all the fields required for development of Egyptian society. Zewail was also on US president Barack Obama’s Council of Advisors on Science and Technology for four years and served as the US science envoy to the Middle East.

With his death, we have lost a talented scientist and true statesman of the world. ■

**Warren S. Warren** is the chair of the Physics Department at Duke University, and James B. Duke Professor of Chemistry, Physics, Radiology and Biomedical Engineering. He was a postdoctoral fellow with Zewail from 1981 to 1982.

e-mail: warren.warren@duke.edu

## DRUG DISCOVERY

## Designing the ideal opioid

The development of a drug that mimics the pain-relieving activity of opioid compounds, but has fewer side effects, points to an effective strategy for the discovery of many types of drug. [SEE ARTICLE P.185](#)

BRIGITTE L. KIEFFER

Opium has been used medicinally and recreationally for more than 4,000 years because of its remarkable pain-relieving and euphoria-inducing properties<sup>1</sup>. Today, abuse of prescription opioids — morphine and its derivatives — has escalated<sup>2</sup>, and heroin addiction represents a worldwide health and societal burden. An ideal opioid would kill pain potently without producing morphine's harmful respiratory effects, would show sustained efficacy in chronic treatments and would not be addictive. On page 185, Manglik *et al.*<sup>3</sup> describe a step towards this perfect drug.

It has been a long road. It was naively thought that identifying receptor proteins for morphine would rapidly deliver the ideal opioid. In the early 1990s, three opioid-receptor (OR) genes were isolated that encode the G-protein-coupled receptors (GPCRs)  $\mu$  (μOR), delta and kappa<sup>4</sup>. Genetic disruption of μOR in mice revealed that this protein mediates morphine-induced pain relief, reward and dependence all at once<sup>5</sup>. This discovery, coupled with the fact that thousands of morphine-related drugs had no better pharmacology than conventional opioids, dampened enthusiasm for developing μOR-targeting drugs.

The realization that distinct drugs acting at a given receptor can trigger diverse signalling responses<sup>6</sup> has since opened up the possibility of designing 'biased' opioids that activate signalling pathways relevant to therapy, but not those that produce unwanted effects. However, another breakthrough was required to move the field effectively to the next level — the development of a method to crystallize these rare, unstable membrane proteins. This technique has transformed GPCR research, leading to resolution of the structure of many proteins<sup>7</sup>, including μOR (ref. 8). Today, the availability of these crystal structures allows researchers to probe both the active and inactive conformations of GPCRs and the ways in which they bind their ligands, facilitating structure-based drug discovery<sup>9</sup>.

As part of this effort, Manglik *et al.* undertook a search for a molecule that would bind to μOR. Their goal was to use the power of computational docking to find new opioid

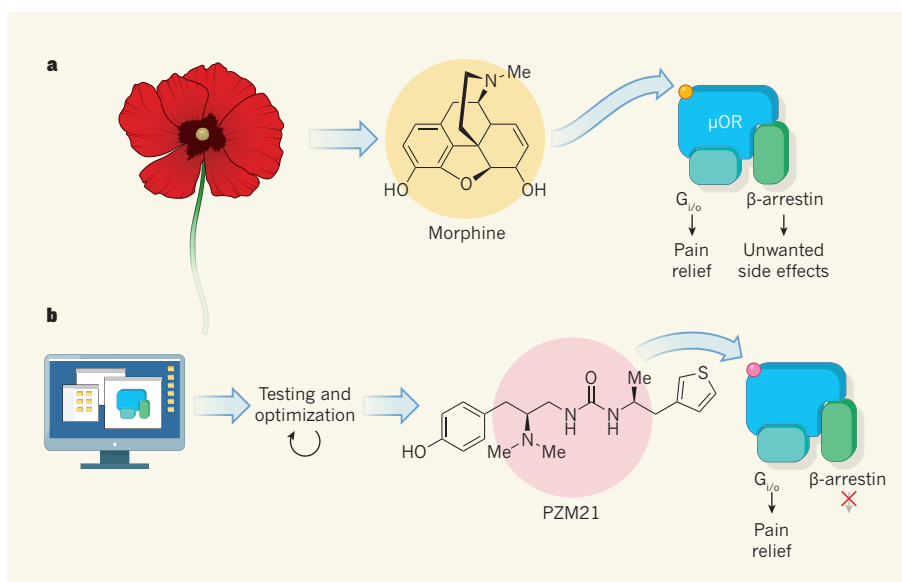


**Figure 1 | New biology for an old receptor.** **a**, The opioid molecule morphine is derived from poppies. Morphine binds to the  $\mu$  opioid receptor ( $\mu$ OR) protein in the mammalian brain to form an active complex with signalling proteins, including G<sub>i/o</sub> and  $\beta$ -arrestin. The G<sub>i/o</sub> signalling pathway is thought to mediate morphine's pain-relieving properties, whereas  $\beta$ -arrestin signalling results in unwanted side effects — euphoria, which can lead to addiction, as well as respiratory depression and gastrointestinal effects. **b**, Manglik *et al.*<sup>3</sup> used the crystal structure of  $\mu$ OR to develop a computational screening programme. The authors docked 3 million molecules to the  $\mu$ OR binding site, selected the most promising candidates and then tested and optimized these to produce the drug PZM21. This compound produces highly G<sub>i/o</sub>-biased signalling, and effectively reduces pain in mice without other detectable effects. (Me; methyl.)

structures (chemotypes), in the hope that some might stabilize μOR in as-yet-unexplored conformations, show unique, biased signalling profiles, and perhaps generate previously unseen biological effects.

The authors computationally docked 3 million commercially available molecules to the μOR binding pocket. For each compound, more than 1 million configurations were tested for complementarity to the binding site, and the 2,500 best-fitting molecules were examined by eye to identify those with chemotypes unrelated to known opioids. The authors selected 23 compounds for experimental testing, and further docking–testing rounds produced a set of molecules that had novel chemotypes, unusual docking poses in the receptor-binding site, and reasonable binding affinities and selectivity for μOR.

Activation of μOR triggers two major signalling cascades — those involving G<sub>i/o</sub> and

β-arrestin proteins. Manglik and colleagues found that, of their 23 molecules, compound 12 had strongly biased activity for G<sub>i/o</sub> signalling. This is interesting because μOR agonists (activators) that poorly engage β-arrestin signalling are thought<sup>10</sup> to confer more-efficient pain relief and cause fewer side effects than those that strongly activate this pathway. Indeed, a drug named TRV130 that is unrelated to either morphine-related drugs or compound 12 has been developed on this basis using conventional drug-screening methods and is currently in phase III clinical trials<sup>11</sup>. In their final optimization step, the authors used docking information from compound 12 to create a drug dubbed PZM21 (Fig. 1). They then compared PZM21 with morphine and TRV130.

In mice, the pain-relieving efficacy of PZM21 was comparable to that of morphine and lasted longer. PZM21 reduced pain responses mediated by the central nervous



system, but not those mediated at spine level. This activity has not previously been reported for a  $\mu$ OR agonist, and potentially has therapeutic value for targeting components of pain mediated by the central nervous system. The compound induced less constipation than morphine and did not modify respiratory activity. Strikingly, mice did not show a preference for the testing chamber in which they received PZM21 over the one in which they received saline, and the compound did not induce hyperactivity — signs of addiction-like behaviour in mice.

TRV130 produced effective pain relief in all modalities, induced only subtle respiratory depression and caused no significant place preference. Thus, despite slightly differing effects *in vivo*, the pain-relieving properties of both PZM21 and TRV130 supersede the adverse effects classically observed for morphine. Manglik and co-workers' study therefore definitively establishes the promise of  $G_{i/o}$ -biased  $\mu$ OR agonists for pain control.

There is little doubt that structure-based computational screening will accelerate the pace of drug discovery<sup>12</sup>. The current work provides a compelling example of how this technology can efficiently generate chemotypes, enable rapid optimization of candidate molecules with minimal experimental testing, and lead to the discovery of molecules that have innovative biological activities. The open-access docking tools now available (such as <http://blaster.docking.org>) should expand the practice of this approach.

Many challenges lie ahead in ligand-docking research. In particular, predicting biased activity remains beyond reach, and was not a goal of the present study. However, Manglik *et al.* did find that PZM21 and TRV130 adopt distinct docking poses in the  $\mu$ OR binding pocket. Hence, molecular interactions common to the PZM21- $\mu$ OR and TRV130- $\mu$ OR complexes deserve further attention, because they may contribute to selective  $G_{i/o}$  activation.

Whether the *in vivo* effects of PZM21 reflect only  $G_{i/o}$ -biased activity remains uncertain. Similarities in the pharmacology of PZM21 and TRV130 argue in favour of common modes of action for the two compounds, probably stemming from  $G_{i/o}$  signalling. On the other hand, the authors' docking analyses suggest that the compounds engage  $\mu$ OR amino-acid residues in different ways. The drugs also show opposing activities when binding kappa opioid receptors in cells, and have different pharmacokinetics *in vivo*. The authors did not investigate whether animals develop tolerance to PZM21, and other *in vivo* activities of the drug may yet be discovered. The common and distinct actions of PZM21 and TRV130 should be investigated in the brains of living organisms, which might reveal activities at the level of brain networks.

In summary, Manglik and colleagues study is an impressive demonstration that new

chemotypes can offer unusual biological opportunities, particularly for the study of opioids. Are we getting closer to the ideal pain-reliever? PZM21 is a leading member of a nascent club of pain-effective  $\mu$ OR agonists that seem to have reduced risk for abuse. These are not exactly opioids, and structure-based discovery approaches should increase their number and enhance the chances of a successful drug reaching the market at last. ■

Brigitte L. Kieffer is at the Douglas Mental Health Institute, Department of Psychiatry, McGill University, Montreal, Quebec H4H 1R3, Canada.  
e-mail: [brigitte.kieffer@douglas.mcgill.ca](mailto:brigitte.kieffer@douglas.mcgill.ca)

1. Brownstein, M. J. *Proc. Natl Acad. Sci. USA* **90**, 5391–5393 (1993).
2. Trang, T. *et al. J. Neurosci.* **35**, 13879–13888 (2015).
3. Manglik, A. *et al. Nature* **537**, 185–190 (2016).
4. Kieffer, B. L. & Gavériaux-Ruff, C. *Prog. Neurobiol.* **66**, 285–306 (2002).
5. Matthes, H. W. *et al. Nature* **383**, 819–823 (1996).
6. Galandrin, S., Oligny-Longpré, G. & Bouvier, M. *Trends Pharmacol. Sci.* **28**, 423–430 (2007).
7. Kobilka, B. & Schertler, G. F. *Trends Pharmacol. Sci.* **29**, 79–83 (2008).
8. Manglik, A. *et al. Nature* **485**, 321–326 (2012).
9. Audet, M. & Bouvier, M. *Cell* **151**, 14–23 (2012).
10. Raehal, K. M., Schmid, C. L., Groer, C. E. & Bohn, L. M. *Pharmacol. Rev.* **63**, 1001–1019 (2011).
11. DeWire, S. M. *et al. J. Pharmacol. Exp. Ther.* **344**, 708–717 (2013).
12. Shoichet, B. K. & Kobilka, B. K. *Trends Pharmacol. Sci.* **33**, 268–272 (2012).

This article was published online on 17 August 2016.

## NANOSCIENCE

# Slippery when narrow

An experimental technique has been developed to measure water flow through carbon nanotubes. Measurements reveal that flow can be almost frictionless, posing challenges for computer simulations of nanofluidics. [SEE LETTER P.210](#)

ANGELOS MICHAELIDES

Carbon nanotubes are hollow cylinders formed from carbon atoms arranged in a hexagonal, graphite-like lattice and have nanometre-scale diameters. It has been suggested that water transport through carbon nanotubes is almost frictionless, and that the flow rate exceeds predictions made using classical theories by many orders of magnitude (see refs 1–3, for example). However, because of challenges in performing

reliable measurements and computer simulations, and given the huge differences in the reported results, claims of rapid water transport have at times been met with scepticism (see, for example, ref. 4). On page 210, Secchi *et al.*<sup>5</sup> help to resolve this issue by reporting unambiguous measurements of water flow through individual carbon nanotubes. The unprecedented sensitivity of the authors' measurements reveals a strong dependence of water friction on the radius of the carbon nanotube: the

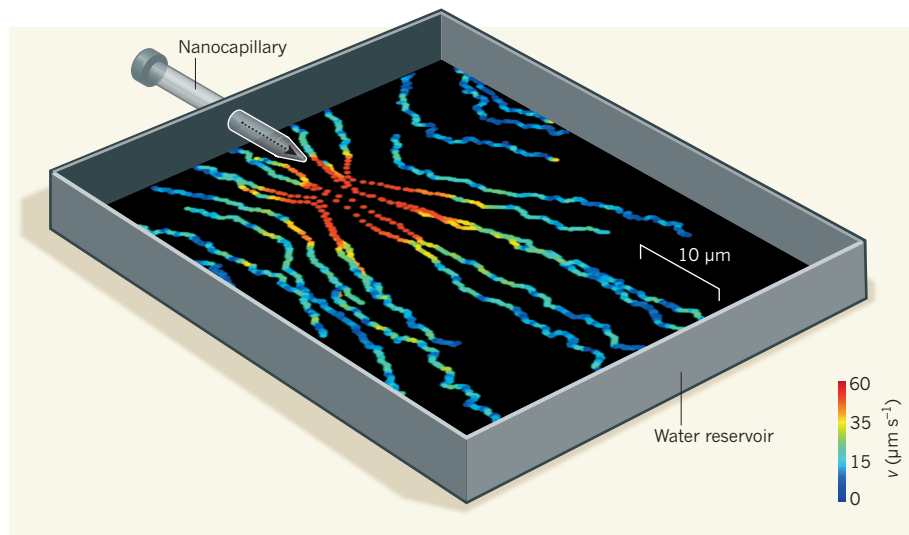


**Figure 1 | Tracking minuscule water flow.** Secchi *et al.*<sup>5</sup> measured the flow of water passing through a carbon nanotube (not visible) at the tip of a nanocapillary into a water reservoir by observing the motion of polystyrene nanoparticles suspended in the reservoir. The trajectories of different nanoparticles are indicated; colours correspond to the particle velocity,  $v$  (measured in micrometres per second).

narrower the tube, the less friction there is.

Why is water flow through carbon nanotubes of interest? One reason is that increasingly severe shortages of clean water are on the horizon, and so better water-purification and desalination technology is needed. Carbon nanotubes have generated excitement because measurements and computer simulations<sup>6</sup> have revealed that water can travel much more rapidly through these tiniest of pipes than, for example, salt ions can. Carbon nanotubes might therefore enable higher-performance filters that are more cost-effective than the conventional carbon-based filters currently ubiquitous in water-purification devices.

To explore water flow through nanotubes, the authors built nanoscale devices in which two reservoirs of water were separated by a water-tight membrane pierced by an individual nanotube. By raising the pressure on one reservoir, water flows through the nanotube to the other. The flow is incredibly small: about a femtolitre ( $10^{-15}$  litres) per second. To put this in perspective, 1 fl is less than the amount of water in a single human red blood cell.

Given the minuscule amounts of water involved, Secchi and colleagues could not track the motion of water itself. Instead, they built on previously reported work<sup>7</sup> by monitoring how the jets of water emerging from the nanotube displaced polystyrene nanoparticles suspended in the low-pressure water reservoir (Fig. 1). Ignoring the differences in relative size, this is like counting the number of children sliding into a ball pit by watching the motion of the balls. The polystyrene nanoparticles were large enough to be seen with an optical microscope, and, by tracking their motion, ultrasensitive measurements of water flow through the tubes were possible. This sensitivity is the key methodological advance of the study.

Using this technique, the authors measured flow through carbon nanotubes that had different radii, and through nanotubes built from boron nitride — a technologically promising material that forms nanotubes with a similar atomic structure to that of carbon nanotubes. The key metric commonly used to evaluate flow across surfaces and in confinement is known as slip length (see ref. 8, for example). Essentially, the larger the slip length, the more slippery the surface and the less friction is exerted on a fluid flowing across it. Slip lengths have been measured previously for water flow through aligned arrays of carbon nanotubes of different radii, but the values obtained differed by several orders of magnitude<sup>4</sup>.

Secchi and co-workers' measurements of flow through individual nanotubes help to reconcile some of the previous measurements by revealing a strong dependence of slip length on nanotube radius. In addition, the measurements confirm that carbon surfaces are indeed unusually slippery, allowing almost frictionless flow through the tubes with the smallest

radius (approximately 15 nanometres). The authors also observed that boron nitride nanotubes are rather sticky compared with carbon nanotubes — for the range of radii considered (about 10–30 nm), water does not flow anywhere near as freely through boron nitride nanotubes, and is almost at the detection limits of the experimental set-up.

By providing a deeper understanding of well-defined aqueous interfaces, these measurements might aid the design of improved membranes and nanofluidic devices. The results also create opportunities and challenges for computer simulations of fluid motion. For example, the quantitative measurements of slip length can serve as a benchmark against which computer simulations can be verified. This is important, because understanding how well computers simulate interfacial water is relevant not just to potential applications such as membranes and water desalination, but also to fields such as the atmospheric sciences, energy production and storage, and catalysis.

But an explanation is needed for the relative stickiness of nanotubes made of boron nitride compared with carbon. Only modest disparities in the behaviour of water at these two materials are expected on the basis of their similar structures and from previous simulation studies<sup>9</sup>, including reference-quality quantum-mechanical simulations<sup>10,11</sup>. The huge differences observed by Secchi *et al.* imply that factors such as water dissociation (the break-up of water molecules into their constituent parts), ion adsorption to the nanotubes, nanotube defects and defect-induced chemistry, or gating effects at the ends of the nanotubes might have a role

in determining water flow. Resolving which factors are involved will require further experiments and high-quality quantum-mechanical simulations.

To extend this work for desalination applications, it will be essential to understand the connection between water flow and (salt) ion motion. More broadly, the authors' experimental approach could readily be applied to nanofluidics in general, by examining the flow of different liquids through different materials. If the sensitivity of the technique can be improved, then studies of water flow through the pores in biological membranes — including the most efficient water filter of all, the aquaporin protein — should also be within reach. ■

Angelos Michaelides is at the Thomas Young Centre, Department of Physics and Astronomy, and at the London Centre for Nanotechnology, University College London, London WC1H 0AH, UK.  
e-mail: angelos.michaelides@ucl.ac.uk

1. Hummer, G., Rasaiah, J. C. & Noworyta, J. P. *Nature* **414**, 188–190 (2001).
2. Majumder, M. *et al.* *Nature* **438**, 44 (2005).
3. Holt, J. K. *et al.* *Science* **312**, 1034–1037 (2006).
4. Kannam, S. K., Todd, B. D., Hansen, J. S. & Davis, P. J. *J. Chem. Phys.* **138**, 094701 (2013).
5. Secchi, E. *et al.* *Nature* **537**, 210–213 (2016).
6. Park, H. G. & Jung, Y. *Chem. Soc. Rev.* **43**, 565–576 (2014).
7. Laohakunakorn, N. *et al.* *Nano Lett.* **13**, 5141–5146 (2013).
8. Whitby, M. & Quirke, N. *Nature Nanotechnol.* **2**, 87–94 (2007).
9. Tocci, G., Joly, L. & Michaelides, A. *Nano Lett.* **14**, 6872–6877 (2014).
10. Ma, J. *et al.* *Phys. Rev. B* **84**, 033402 (2011).
11. Al-Hamdani, Y. S., Alfè, D., von Lilienfeld, O. A. & Michaelides, A. *J. Chem. Phys.* **144**, 154706 (2016).

## CONSERVATION

# Mapping the terrestrial human footprint

**An analysis of direct human impacts across Earth's land surface using global satellite images and ground surveys reveals the scale of the 'human footprint' on the world and its changes between 1993 and 2009.**

PHILIP J. K. MCGOWAN

Humanity is causing unprecedented changes to Earth, such that we may be entering a human-dominated geological era termed the Anthropocene<sup>1,2</sup> and transgressing the environmental boundaries within which we can live safely<sup>3,4</sup>. The impact of the growing extent and intensity of human influences on our landscapes is reflected in changes, usually of loss and degradation, in natural habitats and in the species that they contain.

We need to understand not only where human pressures occur, but also where they are greatest and how they change over time. Taking advantage of the availability of global data sets on a range of human pressures across 16 years, papers by Venter *et al.* in *Nature Communications*<sup>5</sup> and *Scientific Data*<sup>6</sup> provide the first analysis of this changing 'human footprint' on the world's terrestrial landscape.

Humans exert pressures on the planet in a great many ways that may lead directly or indirectly to changes in natural systems (Fig. 1).



The first step in documenting where human pressures act across the world was taken in 2002 by Sanderson *et al.*<sup>7</sup> with the development of a framework to map the human footprint using eight global data sets of human activities. Constructing such a map presents profound challenges because of the complexity of our impacts on the planet. Therefore, some decisions had to be made about what to include when developing their map of the world's human footprint, and Venter and colleagues have followed the approach taken by Sanderson *et al.*<sup>7</sup>

Venter *et al.* confined their analysis to the terrestrial landscape because assessing the footprint in the marine environment would require a different approach and data sets. They concentrated on direct, rather than indirect, measures of human influence for which data were available. Only accessible data sets were used that had global coverage and that were easily available and of sufficient quality. Antarctica and many oceanic islands that were absent from these global data sets were excluded. These decisions sought to match current data availability with the ambition of developing a global framework for assessing human impacts on the terrestrial environment.

The authors have built substantially on the work of Sanderson and colleagues and have brought it up to date by analysing the most recently available comprehensive data sets, and by adding an assessment of human footprint changes over time. Furthermore, Venter and colleagues provide a service for the future by clearly describing all data sets<sup>6</sup> and how they were used. This allows easy access to the data and methods so that the approach can be developed, and it will enable changes in patterns of human influence to be assessed in the future using data available at the time.

The heart of Venter and colleagues' work lies in combining data sets on several pressures to produce an assessment of how human influences accumulate, an approach that the authors say is more indicative of the totality of direct human pressures than is producing maps of single pressures, some of which are easier to detect than others. The result is a 'cumulative threat map'<sup>5</sup> and a human footprint that represents an accumulation of a range of pressures. Venter *et al.* identified eight data sets representing human population density, land transformation, human transit routes and electrical power infrastructure to serve as proxies for this footprint. Some data were remotely sensed and others collected through ground surveys.

Three data sets (for pasturelands, roads and railways) were not available for the dates needed by the authors to make comparisons

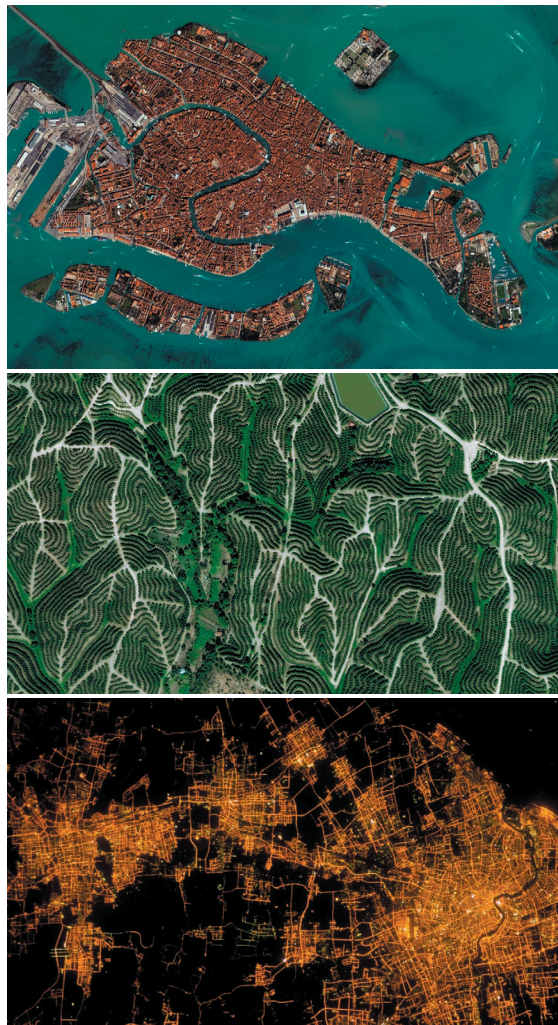


**Figure 1 | Human footprints across Earth.** Venter *et al.*<sup>5,6</sup> assessed the scale of change of human impacts across the globe between 1993 and 2009 by analysing satellite images or using ground-survey data. Five aspects of human activity were monitored: the presence of built environments; areas of population density; navigable waterways (top, satellite image of Venice, Italy); areas of crop growth (middle, vineyards near Huelva, Spain); and electrical infrastructure such as artificial lights (bottom, Shanghai, China).

over time and were therefore not used when assessing change. This exemplifies the challenge of addressing the fundamental question of how human influence on the planet's terrestrial landscapes has changed. If a study was commissioned to address this from scratch, it would not get off the ground because of the scale of data collection required. Together, the two studies by Venter and colleagues represent a pragmatic approach to these challenges.

The headline findings are that direct impacts of human development can be measured in 75% of the world's terrestrial systems, and that the human footprint increased by 9% between 1993 and 2009, during which time the human population increased by 23% and the global economy increased by 153%. The comparison of footprints reveals intriguing insights, all of which merit further analysis and, potentially,

should be brought to the attention of those who make policies and decisions, including governments. For example, 'pressure-free lands' are now restricted to high northern latitudes, some deserts and the most distant parts of the Amazon and Congo rainforests. The change in the footprint over that period varies with geography and habitat. Areas such as the North American tundra, most New Guinea forests and some forests in the Neotropics (the tropical part of the American continent) showed the biggest increases in human impact.

Although these findings provide food for thought, they will also trigger questions regarding caveats and qualifiers about the data that are available and how adequately they reflect human pressures on terrestrial ecosystems. This is inevitable when tackling an issue that is so complex in lots of different ways. Rather than diminishing such work, this should spur us on to improve both its conceptual basis and its technical execution, so that an even better map of human influence across the world's land masses can be developed in the future.

Earth is being changed substantially, and we need ways to both understand and communicate how human pressures on the planet combine. Venter *et al.* have created a framework that will allow researchers to track a range of direct pressures and, crucially, provide information that could be relevant to those who make high-level policy decisions.

However, we do need to add to this framework. For example, ecologists have no single metric yet for measuring the influence of hunting across terrestrial systems, and, given the huge pressures from over-exploitation of species<sup>8</sup> and escalating pressures from the illegal trade in wildlife<sup>9</sup>, this would be a key step forward. It would be fascinating, and probably alarming, to see how such a metric might change the human footprint map. ■

**Philip J. K. McGowan** is at the School of Biology, Newcastle University, Newcastle upon Tyne NE1 7RU, UK. e-mail: philip.mcgowan@newcastle.ac.uk

1. Crutzen, P. J. & Stoermer, E. F. *IGBP Global Change Newsl.* **41**, 17–18 (2000).
2. Corlett, R. T. *Trends Ecol. Evol.* **30**, 36–41 (2015).
3. Rockström, J. *et al. Nature* **461**, 472–475 (2009).
4. Steffen, W. *et al. Science* **347**, 1259855 (2015).
5. Venter, O. *et al. Nature Commun.* <http://dx.doi.org/10.1038/ncomms12558> (2016).
6. Venter, O. *et al. Sci. Data* <http://dx.doi.org/10.1038/sdata.2016.67> (2016).
7. Sanderson, E. W. *et al. BioScience* **52**, 891–904 (2002).
8. Maxwell, S. L. *Nature* **536**, 143–145 (2016).
9. United Nations Environment Assembly. Resolution 2/14 Illegal trade in wildlife and wildlife products. Available at [go.nature.com/2bzmsdv](http://go.nature.com/2bzmsdv)

## ASTROPHYSICS

# Violent emissions of newborn stars

**Interactions between young stars and their parent molecular clouds are poorly understood. High-resolution observations of the Orion nebula now reveal these interactions, which have implications for star formation. [SEE LETTER P.207](#)**

MARKUS RÖLLIG

Stars are not static objects — they form, evolve and are then destroyed. In galaxies such as the Milky Way, the gas and dust between stars, which comprise the interstellar medium, accumulate in giant molecular clouds. The densest parts of these clouds eventually collapse under their own weight to create stars. On page 207, Goicoechea *et al.*<sup>1</sup> report their latest observations of one of the closest stellar nurseries, the Orion molecular cloud. They find evidence of strong interactions between young massive stars and the cloud, shedding light on some unknown aspects of star formation.

The general process of star formation is fairly well understood, but many details remain a mystery. In particular, there is a lack of information on the formation of the most massive stars (those about 8–150 times more massive than the Sun). Such massive stars are rare, but they are the primary sources of light in the Milky Way — some are a few hundred thousand times more luminous than the Sun<sup>2</sup>.

When massive stars form, they start to emit energetic radiation, largely in the ultraviolet region of the electromagnetic spectrum. This UV radiation destroys the molecules in the surrounding cloud, creating a layer of atomic gas around young massive stars. In this layer, in the region closest to the star, the radiation is energetic enough to ionize the atoms, forming a bubble of ionized gas. At the edge of this bubble, the most energetic UV photons have already been absorbed, and the atomic gas can survive. The transition zone between the edge of the bubble and the molecular gas is called the photodissociation region (PDR)<sup>3</sup>. Just like human skin, the PDR protects molecules in the cloud from harmful UV radiation.

Goicoechea and colleagues show that it is possible to observe a PDR with sufficient resolution to directly study how the molecular cloud is pushed away and dispersed by the stellar radiation and winds of young massive stars. The authors use the

Atacama Large Millimeter/submillimeter Array (ALMA) in Chile to study a PDR of the Orion molecular cloud: the Orion Bar (Fig. 1). The data set presented by Goicoechea *et al.* and the level of detail revealed by the ALMA observations are unparalleled, allowing unknown aspects of star formation to be explored.

The Orion Bar is an archetypal PDR that makes an ideal study candidate for two reasons: it is close to Earth, and it is oriented edge-on, which allows astronomers a good look at how radiation is absorbed as it enters the molecular cloud. The local gas density in the PDR controls how quickly this absorption occurs. In low-density gas (a few hundred to a few thousand gas particles per cubic centimetre), the medium gradually becomes opaque to radiation, whereas denser gas (a few million particles per cubic centimetre) becomes opaque much more suddenly. In the Orion Bar, this gradual absorption happens on a scale of 15 arcseconds<sup>4</sup> (equivalent to less than 1% of the full Moon's angular diameter) before the UV radiation is sufficiently absorbed so that the molecules can survive.

The measurement of 15 arcseconds surprised astronomers because standard

models of PDRs<sup>5</sup> can explain this value only if the gas in the Orion Bar has a low density. However, radiation observed from the Orion Bar requires high-density gas (a few million particles per cubic centimetre) to explain its emission<sup>6,7</sup>. In theoretical models, such a high density would require a smaller distance than 15 arcseconds between the atomic and molecular gas layers. In other words, UV radiation is observed to penetrate deeply into the cloud, whereas it should be absorbed by high-density gas.

Earlier studies<sup>6–8</sup> tried to reconcile this discrepancy by suggesting that the Orion Bar consists of clumps of dense gas embedded in a thinner gas. Such a structure would allow for both high-density molecular emission and deeper penetration of UV radiation into the cloud. Goicoechea *et al.* are the first to directly observe such clumps of dense gas in the Orion Bar. Their results have strong implications for models of PDRs, because they demonstrate that even such an archetypal PDR does not have the stratified transition between atomic and molecular gas layers that was previously assumed<sup>9</sup>.

The authors' results also provide some explanation for the evolution of the Orion Bar. They find evidence of a high-pressure wave expanding into the molecular cloud, which is consistent with the picture of an expanding bubble of ionized gas created by the young massive star in its centre. The bubble pushes against the molecular cloud, compressing dense regions, while dispersing less-dense regions. However, because of the experimental limitations of ALMA, Goicoechea and colleagues only observe a small region of the Orion Bar, in a snapshot of time and at a limited wavelength. To rule out the possibility that the authors observed an atypical region with respect to PDRs in general, it will be necessary to consider a larger sample size, including PDRs with various local physical conditions.

An expanding bubble of ionized gas is one of the prime candidates proposed to explain how the interaction of young stars with their parent interstellar clouds controls the efficiency of star formation<sup>10</sup>. Without these interactions, star formation would be about 10 to 100 times more efficient than what is observed. The detailed nature and relative importance of these interactions with respect to other factors that influence star formation remain largely unknown. Therefore, any direct observation of these processes, as presented by Goicoechea and colleagues, provides a step towards a better understanding of star formation and, consequently, of how the Sun and the Solar System formed. ■

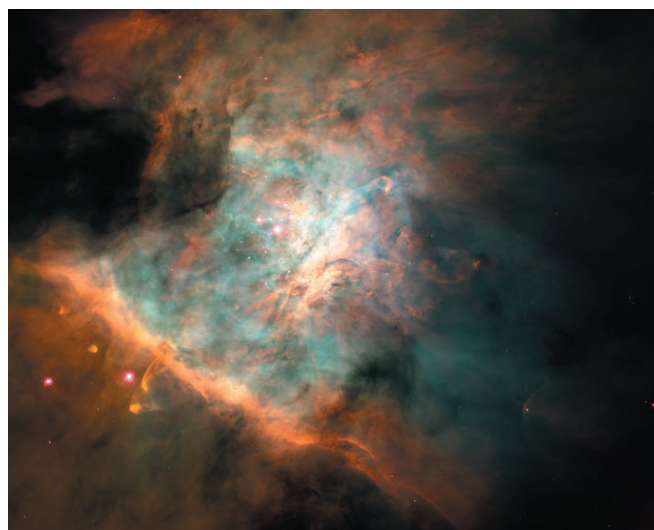


**Figure 1 | The Orion Bar.** In this image of the Orion nebula taken by the Hubble Space Telescope, the Orion Bar is the bright ridge at the bottom left. Goicoechea *et al.*<sup>1</sup> use high-resolution images of the Orion Bar to study the impact of young stars on their parent molecular clouds.

NASA/C. R. O'DELL & S. K. WONG (RICE UNIV.)



Markus Röllig is at *I. Physikalisches Institut, University of Cologne, 50937 Cologne, Germany.*  
e-mail: roellig@ph1.uni-koeln.de

1. Goicoechea, J. R. *et al.* *Nature* **537**, 207–209 (2016).
2. Martins, F., Schaerer, D. & Hillier, D. J. *Astron.*

- Astrophys.* **436**, 1049–1065 (2005).
3. Hollenbach, D. J. & Tielens, A. G. G. M. *Annu. Rev. Astron. Astrophys.* **35**, 179–215 (1997).
4. Walmsley, C. M., Natta, A., Oliva, E. & Testi, L. *Astron. Astrophys.* **364**, 301–317 (2000).
5. Röllig, M. *et al.* *Astron. Astrophys.* **467**, 187–206 (2007).
6. Parmar, P. S., Lacy, J. H. & Achtermann, J. M. *Astrophys. J.* **372**, L25–L28 (1991).
7. Hogerheijde, M. R., Jansen, D. J. & van Dishoeck, E. F.

- Astron. Astrophys.* **294**, 792–810 (1995).
8. Stutzki, J., Bensch, F., Heithausen, A., Ossenkopf, V. & Zielinsky, M. *Astron. Astrophys.* **336**, 697–720 (1998).
9. Andree-Labsch, S., Ossenkopf, V. & Röllig, M. Preprint at: <http://arxiv.org/abs/1405.5553> (2014).
10. Krumholz, M. R. *et al.* in *Protostars and Planets VI* (eds Beuther, H., Klessen, R. S., Dullemond, C. P. & Henning, T.) 243–266 (Univ. Arizona Press, 2014).

## STRUCTURAL BIOLOGY

# Catalytic spliceosome captured

**Spliceosome complexes remove non-coding sequences from RNA transcripts in two steps. A structure of a spliceosome after the first step reveals active-site interactions and evolutionary constraints on these non-coding regions. [SEE ARTICLE P.197](#)**

BRIAN KOSMYNA & CHARLES C. QUERY

The presence of non-coding sequences called introns in nascent RNA transcripts is a defining characteristic of the genomes of eukaryotic organisms, which include plants, animals and fungi. Intron removal by a spliceosome complex is an essential step in gene expression and regulation. Decades of biochemical and genetic studies have provided detailed insights into the composition of these complexes and the RNA structures within them. However, the dynamic nature of the complexes has hindered efforts at modelling and structure determination at atomic resolution. On page 197, Galej *et al.*<sup>1</sup> present a structure of the catalytic spliceosome at 3.8 ångströms resolution, obtained using single-particle cryo-electron microscopy (cryo-EM). This structure not only provides evidence in support of reported interactions<sup>2</sup> that bind and position catalytic metal ions, but also reveals previously unknown molecular features of splicing catalysis.

The spliceosome is a large, dynamic RNA–protein complex that catalyses intron removal in two sequential chemical reactions (Fig. 1). The chemical mechanism of intron removal, as well as the core spliceosomal RNAs and proteins, are highly evolutionarily conserved in most eukaryotes. The first reaction cleaves the nascent transcript at the 5' end of the intron (the 5' splice site; 5'SS), causing the intron to form a lasso-shaped, or 'lariat', structure. Compositional and structural changes in the spliceosome then occur, whereupon the second reaction joins together (ligates) the coding exon sequences that flank the intron, simultaneously generating the mature messenger RNA and excising the intron lariat.

Technological and computational advances<sup>3</sup> in cryo-EM have led to the structural determination of many spliceosomal complexes within the past year<sup>4–9</sup>. To obtain particles for their study, Galej and co-workers assembled spliceosomes *in vitro* on RNA substrates that can proceed through the first catalytic step, but not the second one. They then purified

the resulting complexes using proteins that interact with the spliceosome only after the first step has occurred. The reported structure (Fig. 2) therefore represents complexes that form immediately after the first catalytic step. This, along with another recently published structure<sup>9</sup>, is the most relevant structure to splicing catalysis available.

Spliceosomal complexes follow an intricate pathway during assembly, catalysis and recycling, characterized by compositional and structural changes (Fig. 1). Enzymes known as ATPases facilitate many of the transitions between spliceosome complexes. The ATPase Prp2 remodels the fully assembled but inactive complex (B<sup>act</sup>) to form the catalytically active complex (C). Another ATPase, Prp16, removes the intron lariat from the active site after the first reaction, and positions the 3'SS near to the 5'SS to allow exon ligation. Once the second reaction has excised the intron, the ATPase Prp22 binds the 3' exon and moves along the mRNA, thus releasing the mRNA from the spliceosome.

Shi and colleagues<sup>8</sup> recently reported a structure in which Prp2 is bound in the B<sup>act</sup> form of the spliceosome, whereas, in Galej and co-workers' structure, Prp2 has been replaced by Prp16 in the C complex. These structures are the first visualizations of these two ATPases bound to spliceosomes. Both enzymes are positioned similarly in the overall topology of the spliceosome near the 3' end of the intron. On the basis of the interactions between Prp16 and the spliceosome observed in their structure, Galej *et al.* suggest that splicing factors unique to each complex recruit the specific ATPase needed (see Fig. 6

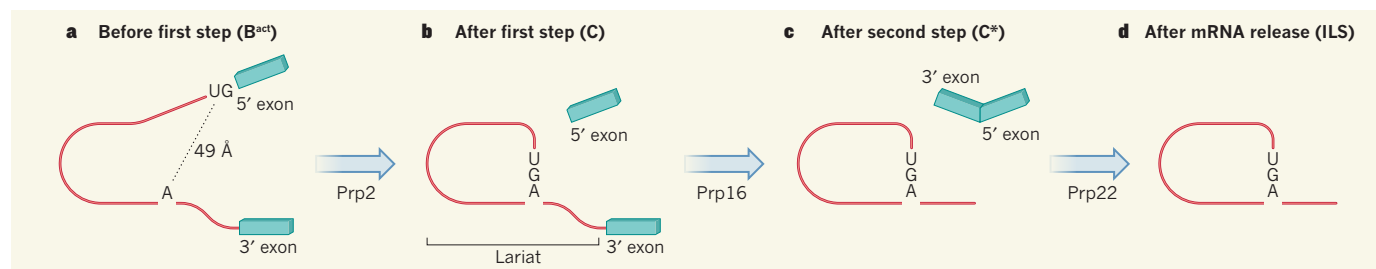


**Figure 1 | Spliceosomal processing of RNA transcripts.** The spliceosome complex catalyses splicing — the removal of non-coding intron sequences (red) from RNA transcripts and the joining together of coding exon sequences. **a**, The spliceosome (not shown) and transcript form the B<sup>act</sup> complex, a fully assembled but catalytically inactive complex. The adenosine nucleotide (A) at the intron's 'branch site' is far from the 5' splice site (5'SS) at one end of the intron<sup>8</sup>. G and U represent two nucleotides, guanosine and uridine, of the 5'SS. **b**, The Prp2 enzyme facilitates transition to

the C complex, which catalyses the first step of splicing: cleavage of the 5'SS from the adjacent exon and formation of a lariat structure, in which the branch-site A bonds covalently to the 5'SS-GU. **c**, The Prp16 enzyme drives formation of the C<sup>\*</sup> complex, which catalyses the second splicing step: cleavage of the 3' splice site and joining together of the two exons to form a mature messenger RNA. **d**, Finally, the Prp22 enzyme releases the mRNA from the spliceosome and generates a stable intron lariat spliceosome (ILS).

of the paper<sup>1</sup>). Hydrolysis of ATP molecules by the ATPases could subsequently destabilize the associated splicing factors, allowing the RNA structures in the catalytic core to be remodelled.

The two substrates for the first catalytic step are the 5'SS and an adenosine nucleotide, known as the branch site, within the intron. Although it has long been thought that these two substrates almost certainly interact with each other, to help bring them together as needed for the catalytic step, neither evidence nor models for such an interaction existed. Galej and co-workers' structure reveals intimate interactions between the 5'SS (specifically, its GU sequence, which consists of a guanosine nucleotide next to a uridine nucleotide) and the sequence flanking the branch site; these interactions help to explain the evolutionary conservation of the two sequences. For example, an RNA base triple (a structure analogous to a base pair, but involving three bases) was identified between the uridine of the 5'SS-GU and the helix created by base pairing between the intron sequence flanking the branch site and U2, one of the small nuclear RNAs that forms the spliceosome's active site. This base triple helps to position the 5'SS near the branch-site adenosine, as required for the first catalytic step.

By contrast, in Shi and colleagues' structure<sup>8</sup>, the 5'SS and branch site are separated by a large distance (approximately 49 Å). The guanosine of the 5'SS-GU is protected by a pocket formed by a protein subunit of the spliceosome and a first-step splicing factor. Analogously, the branch-site adenosine is positioned in a positively charged pocket of another protein subunit (SF3B1, which is highly mutated in human cancers<sup>10</sup>). These two pockets protect the reactive groups involved in the first catalytic step until the spliceosome has transitioned to a catalytically active conformation.

Galej and colleagues' structure also helps to explain the evolutionary sequence conservation of the branch site–U2 duplex by revealing another base triple interaction between the branch-site adenosine and the intron–U2 RNA helix two nucleotides away. This was presaged in part by interactions observed between the branch-site adenosine and the intron–U2 RNA helix in an RNA-only structure<sup>11</sup> previously determined by nuclear magnetic resonance spectroscopy. This base triple positions the reactive hydroxyl group of the branch-site adenosine outward towards the 5'SS.

The structural insights obtained through the identification of hundreds of RNA–protein and protein–protein interactions in the new structures<sup>1,8,9</sup> suggest innumerable biochemical and genetic experiments to ascertain which splicing step these interactions contribute most to, and for what intron features they are most important. The stage is now set for the exploration and discovery of many other spliceosome

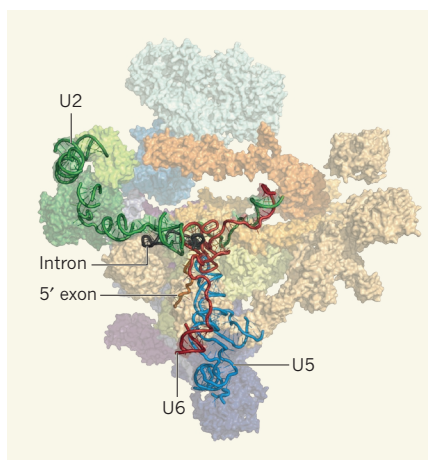


**Figure 2 | Model of the catalytically active spliceosome structure.** Galej *et al.*<sup>1</sup> report the structure of the spliceosome in complex with an RNA substrate immediately after the first catalytic step of splicing. Most of the spliceosome complex is shown as a fainter surface representation (different colours represent different components). The three small nuclear RNAs (U2, U5 and U6) that form the active site are shown in bold, as are the intron and 5' exon of the RNA substrate.

structures. Like the explosion of successes that followed the determination of the ribosome structure<sup>12</sup> (the protein-synthesis apparatus), we eagerly await structures not just for normal spliceosome complexes, but also for complexes that include mutations in pre-mRNA

substrates or in spliceosomal components, such as those found in many cancers<sup>10</sup>. The future will allow a more comprehensive picture of the basic mechanisms of splicing catalysis, and of how splice sites are recognized and catalysis is regulated. Other achievements may also include the determination of features vital to the alternative splicing regulation found in complex organisms. ■

**Brian Kosmyna and Charles C. Query** are in the Department of Cell Biology, Albert Einstein College of Medicine, New York, New York 10461-1975, USA.  
e-mails: [brian.kosmyna@phd.einstein.yu.edu](mailto:brian.kosmyna@phd.einstein.yu.edu); [charles.query@einstein.yu.edu](mailto:charles.query@einstein.yu.edu)

1. Galej, W. P. *et al.* *Nature* **537**, 197–201 (2016).
2. Fica, S. M. *et al.* *Nature* **503**, 229–234 (2013).
3. Nogales, E. *Nature Methods* **13**, 24–27 (2016).
4. Agafonov, D. E. *et al.* *Science* **351**, 1416–1420 (2016).
5. Nguyen, T. H. *et al.* *Nature* **530**, 298–302 (2016).
6. Wan, R. *et al.* *Science* **351**, 466–475 (2016).
7. Yan, C. *et al.* *Science* **349**, 1182–1191 (2015).
8. Yan, C., Wan, R., Bai, R., Huang, G. & Shi, Y. *Science* <http://dx.doi.org/10.1126/science.aag0291> (2016).
9. Wan, R., Yan, C., Bai, R., Huang, G. & Shi, Y. *Science* <http://dx.doi.org/10.1126/science.aag2235> (2016).
10. Yoshida, K. *et al.* *Nature* **478**, 64–69 (2011).
11. Newby, M. I. & Greenbaum, N. L. *Nature Struct. Mol. Biol.* **9**, 958–965 (2002).
12. Schmeing, T. M. & Ramakrishnan, V. *Nature* **461**, 1234–1242 (2009).

This article was published online on 10 August 2016.

#### EVOLUTIONARY BIOLOGY

## Fin to limb within our grasp

**There was thought to be little in common between fish fin bones and the finger bones of land-dwellers. But zebrafish studies reveal that *hox* genes have a surprisingly similar role in patterning the two structures. [SEE LETTER P.225](#)**

ADITYA SAXENA & KIMBERLY L. COOPER

The next time you gaze at fish in an aquarium, or order a whole trout at your favourite restaurant, you may wish to ponder how the dozens of thin, delicate bones in the fish pectoral fins that lie just behind the gills compare with your own fingers. Although scientists have long known that the human arm evolved from the pectoral fin of our fish ancestors, the relationship between the bones of the two strikingly different skeletons has remained mysterious. Nakamura *et al.*<sup>1</sup> address this issue on page 225 and provide evidence that fish fin-ray bones and human fingers have more in common than was previously thought.

There are two types of bone, and they form

in different ways. Most of the bones in our skeleton, including our limbs, start out in the embryo as rod-shaped pieces of cartilage that build a mineralized scaffold on which the bone grows, in a process known as ossification. Bone that develops using a cartilage template is called endochondral bone and includes the short, broad radial fin bones in fish.

The other type of bone is dermal bone, which is found in human shoulder blades and in the plate-like bones that form the roof of our skulls. Dermal-bone formation does not use a cartilage scaffold, but instead proceeds by depositing bone material directly on the innermost layer of skin, the dermis. Although the fin rays of fish and the bones of our fingers may seem superficially similar because they



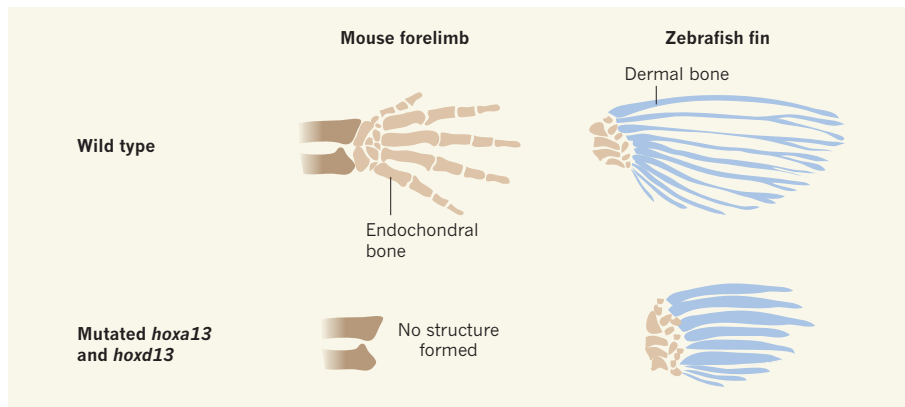


**Figure 1 | Fin and limb development.** Fin rays and mouse digits are formed from different types of bone — mouse digits are made of endochondral bone and fish fins are made of dermal bone. The genes *hoxa13* and *hoxd13* are expressed in cells that will become the mouse digits, and mice with mutations in these two genes do not form wrist or digit structures in their forelimb<sup>9</sup>. Nakamura *et al.*<sup>1</sup> assessed the effect of loss-of-function mutations of *hoxa13* and *hoxd13* in zebrafish, and found that the mutant fish fins had dermal-bone structures that were reduced in length and had extra endochondral-bone structures, indicating that these *hox13* genes are required for both tetrapod digits and fish fin rays.

are both rod-like structures oriented away from the body, fish fin rays are dermal bones, whereas our fingers are endochondral bones.

It has long been thought<sup>2</sup> that the digits of our earliest four-legged (tetrapod) vertebrate ancestors were a structural innovation when they first appeared in aquatic species, and that fin rays were lost. Digits form at the end of a limb skeleton that has three segments: the upper arm, the lower arm, and the wrist and finger area (also known as the autopod). Formation of these segments in the developing embryo depends on the function of a few key members of the large group of Hox-family transcription-factor proteins<sup>3</sup>.

In tetrapods, regions of *hox* gene expression shift in space and time from an early pattern of nested areas across the anterior–posterior axis of the developing limb to a late pattern that is characterized by restriction of *hoxa13* and *hoxd13* expression to the autopod region<sup>4,5</sup>. Zebrafish also express *hox* genes in the cells that will form the endochondral skeleton<sup>2,6</sup>. However, in transgenic mouse embryos, none of the identified regulatory DNA sequences of the zebrafish *hox* genes seem to be active in the region where digits will form<sup>7,8</sup>. This had led researchers to think that the wrist and digits were a tetrapod innovation that arose as a result of a newly acquired region of *hox* expression.

The zebrafish is the most commonly used model fish, for which well-established genetic approaches and laboratory techniques are available. However, among the fishes, zebrafish are said to be highly derived because they have evolved many traits that are not thought to have been present in ancestral species. The spotted gar fish and zebrafish share a common ancestor with tetrapods, but, in some ways, the spotted gar has changed less than the zebrafish in comparison with their ancestor. An enhancer DNA sequence for *hoxA* from the

spotted-gar genome can promote a late phase of gene expression both in the digit-forming region of developing mouse limbs and, surprisingly, in the distal fin of zebrafish<sup>8</sup>. Fish don't have fingers, so what do these cells become in the zebrafish that can respond to the same regulatory sequence that is active in developing mouse digits?

To answer this question, Nakamura and colleagues used the spotted-gar *hoxA* enhancer DNA sequences to develop a genetic marker system with which to trace the development of the population of cells near the tip of the zebrafish fin that respond to the enhancer. The authors found that these cells go on to contribute exclusively to the dermal skeleton of the fin rays. Although this is not evidence that fin rays and mouse digits are the same, or even that tetrapod digits evolved from the rays of fish, it does show that there is much more similarity between the structures than was previously thought. This further supports the hypothesis that autopod evolution may have occurred by the hijacking of some of the developmental processes that were already shaping the fins of our ancestors.

The *hoxa13* and *hoxd13* genes are more than mere identifiers of the developing tetrapod digits; they are also essential for autopod development, and mice that lack the two proteins encoded by these genes do not form autopods<sup>9</sup>. However, testing the role of these genes in zebrafish has been difficult because the species has undergone full-genome duplication, and so there are multiple copies of many genes. This can hinder loss-of-function studies using conventional mutation and breeding approaches, and the effect of loss of function of *hoxa13* and *hoxd13* on the zebrafish fin was not known.

To study loss of function of *hoxa13* and *hoxd13* in zebrafish, Nakamura and colleagues used CRISPR–Cas9 genome-editing

technology, which offers a fast and specific way to create mutations both in the *hoxa13* duplicate genes (*hoxa13a* and *hoxa13b*) and in the single copy of *hoxd13*. The resulting mutant fish have a dermal-fin-ray skeleton that is dramatically reduced in length, together with an increased number of distal endochondral radial bones (Fig. 1).

This result is interesting because it is a transformation of the fish fin that is in some ways similar to what is expected to have occurred in the earliest tetrapods that lost their dermal-fin-ray skeleton and elaborated an endochondral skeleton to include true digits. Tetrapod endochondral digits were previously thought<sup>10</sup> to be homologous with the distal row of fish endochondral radial bones that are adjacent to the dermal-fin rays. However, the loss of rays and gain of true digits are thought<sup>2</sup> to be the result of further elaboration, not loss, of the late phase of *hox13* expression in tetrapods.

Some caution should be taken in the interpretation of these data. Because zebrafish are highly derived compared with more-basal fishes, it is possible that the role of *hox13* transcription factors in the development of fin rays is a recent zebrafish acquisition. It will be important, where possible, to perform some of the same fate-mapping and gene loss-of-function experiments in fish species, such as the paddlefish and gar, that diverged closer to the shared ancestor with tetrapods and that have fin skeletons with more similarities to ancestral tetrapods. Fortunately, these exciting questions are emerging just as CRISPR–Cas9 genome-editing technologies are becoming options for a variety of unusual model species. The answers may soon be within our grasp. ■

**Aditya Saxena and Kimberly L. Cooper** are in the Division of Biological Sciences, University of California, San Diego, La Jolla, California 92093, USA. e-mails: adsaxena@ucsd.edu; kcooper@ucsd.edu

1. Nakamura, T., Gehrke, A. R., Lemberg, J., Szymaszek, J. & Shubin, N. H. *Nature* **537**, 225–228 (2016).
2. Sordino, P., van der Hoeven, F. & Duboule, D. *Nature* **375**, 678–681 (1995).
3. Zakany, J. & Duboule, D. *Curr. Opin. Genet. Dev.* **17**, 359–366 (2007).
4. Dollé, P., Izpisua-Belmonte, J. C., Falkenstein, H., Renucci, A. & Duboule, D. *Nature* **342**, 767–772 (1989).
5. Nelson, C. E. *et al. Development* **122**, 1449–1466 (1996).
6. Ahn, D. & Ho, R. K. *Dev. Biol.* **322**, 220–233 (2008).
7. Woltering, J. M., Noordermeer, D., Leleu, M. & Duboule, D. *PLoS Biol.* **12**, e1001773 (2014).
8. Gehrke, A. R. *et al. Proc. Natl Acad. Sci. USA* **112**, 803–808 (2015).
9. Fromental-Ramain, C. *et al. Development* **122**, 2997–3011 (1996).
10. Boisvert, C. A., Mark-Kurik & Ahlberg P. E. *Nature* **456**, 636–638 (2008).

This article was published online on 17 August 2016.

# Photocontrol of fluid slugs in liquid crystal polymer microactuators

Jiu-an Lv<sup>1</sup>, Yuyun Liu<sup>1</sup>, Jia Wei<sup>1</sup>, Erqiang Chen<sup>2</sup>, Lang Qin<sup>1</sup> & Yanlei Yu<sup>1</sup>

**The manipulation of small amounts of liquids has applications ranging from biomedical devices to liquid transfer. Direct light-driven manipulation of liquids, especially when triggered by light-induced capillary forces, is of particular interest because light can provide contactless spatial and temporal control. However, existing light-driven technologies suffer from an inherent limitation in that liquid motion is strongly resisted by the effect of contact-line pinning. Here we report a strategy to manipulate fluid slugs by photo-induced asymmetric deformation of tubular microactuators, which induces capillary forces for liquid propulsion. Microactuators with various shapes (straight, 'Y'-shaped, serpentine and helical) are fabricated from a mechanically robust linear liquid crystal polymer. These microactuators are able to exert photocontrol of a wide diversity of liquids over a long distance with controllable velocity and direction, and hence to mix multiphase liquids, to combine liquids and even to make liquids run uphill. We anticipate that this photodeformable microactuator will find use in micro-reactors, in laboratory-on-a-chip settings and in micro-optomechanical systems.**

Manipulating small amounts of liquids to perform reactions, analysis or fundamental investigations in biology, physics or chemistry is of great interest in both scientific research and practical applications<sup>1–5</sup>. Conversion of light energy to liquid motion is a new paradigm for the actuation of microfluidic systems by using optical forces (through radiation pressure and optical tweezers)<sup>6,7</sup>, light modulation of electrical actuation (optoelectrowetting and photocontrol of electro-osmotic flow)<sup>8–12</sup> or light-induced capillary forces<sup>13–19</sup>. The last of these actuation approaches has advantages over the first two in that it requires neither special optical set-ups nor complex microfabrication steps<sup>1</sup>: it uses capillary forces generated from a light-induced wettability gradient and Marangoni effects. However, the capillary force arising from a wettability gradient is too small to overcome the effect of contact-line pinning, so the motion is limited to specific liquids over a relatively short distance, in simple linear trajectories, and at low speed ( $10\text{--}50\text{ }\mu\text{m s}^{-1}$ )<sup>13–15</sup>. And use of the light-induced Marangoni effect requires either local heating or the addition of photosensitive surfactants to liquids, which is undesirable for biomedical applications and undoubtedly produces sample contamination<sup>1,16–19</sup>.

## Design of tubular microactuators

It is well known that a completely wetting liquid droplet confined in a conical capillary is self-propelled towards the narrower end because of the axial force arising from differing curvature pressures across its end caps<sup>20,21</sup>. If we were able to build tubular microactuators whose geometry could be dynamically adjusted by light, a simple and straightforward method to manipulate liquids would be achieved; therefore, a smart material capable of photodeformation is crucial to building such tubular microactuators. Photodeformable crosslinked liquid crystal polymers are ordered polymers that show large and reversible deformation through the orientation change of liquid crystals (LCs) and allow temporal, localized, remote and isothermal triggering and actuation<sup>22–37</sup>. Hence, crosslinked liquid crystal polymers are good candidates for actuators for precise and direct manipulation of liquids through photodeformation.

Unfortunately, to the best of our knowledge, tubular microactuators (TMAs) have not yet been fabricated from existing photodeformable

crosslinked liquid crystal polymers, since they show poor processability (incompatible with common solution and melt processing) owing to chemical crosslinking<sup>38,39</sup>. Here we report robust TMAs prepared from a newly designed linear liquid crystal polymer (LLCP) that show asymmetric geometry change upon irradiation by 470-nm light with an intensity gradient along the TMA (Fig. 1a); such irradiated TMAs can thus successfully manipulate liquid motion by light (Fig. 1b, Supplementary Video 1). (For brevity, we refer to light that has an intensity gradient as 'attenuated light', as this gradient is produced by varying attenuation.) The critical design premise of the LLCP includes ensuring enough mechanical robustness without chemical crosslinks, and the facile attainment of macroscopic LC orientation.

Arteries are natural robust soft actuators which are capable of withstanding impressive pressure stress, displaying rupture strengths up to 2,000 mm Hg (ref. 40). In the wall of an artery, the components of the tunica media, alternate muscle layers and elastic layers, are responsible for stimuli-responsive deformation and mechanical robustness<sup>41</sup>, respectively (Fig. 1c). Inspired by the lamellar structure of artery walls, we designed the novel LLCP, which has a long alkyl backbone containing double bonds and azobenzene moieties in side chains acting as both mesogens and photoresponsive groups (Fig. 1d). We expected the flexible backbones and the azobenzene mesogens to self-assemble into a nano-scaled lamellar structure due to the molecular cooperation effect of LCs. In addition, the long spacers provide enough free volume for the azobenzene mesogens to generate a highly ordered structure and undergo a fast photoresponse. The transmission electron microscope (TEM) image in Fig. 2a clearly demonstrates that the LLCP self-assembles into a lamellar structure; this is confirmed by the atomic force microscope (AFM) image of the LLCP film (Extended Data Fig. 1). Two-dimensional wide-angle X-ray diffraction (2D WAXD) indicates that the layer spacing of the lamellar structure is 4.6 nm (Fig. 2b), and the azobenzene mesogens are tilted at an angle of  $\varphi = 65^\circ$  in the lamellar layers (Fig. 2c).

In order to promote mechanical robustness, ring-opening metathesis polymerization—living polymerization that allows synthesis of a high-molecular-weight polyolefin with narrow polydispersity—was employed to prepare the LLCP<sup>42</sup>. The number-average molecular

<sup>1</sup>Department of Materials Science, State Key Laboratory of Molecular Engineering of Polymers, Fudan University, 220 Handan Road, Shanghai 200433, China. <sup>2</sup>Beijing National Laboratory for Molecular Sciences, Key Laboratory of Polymer Chemistry and Physics of Ministry of Education, Peking University, Beijing 100871, China.



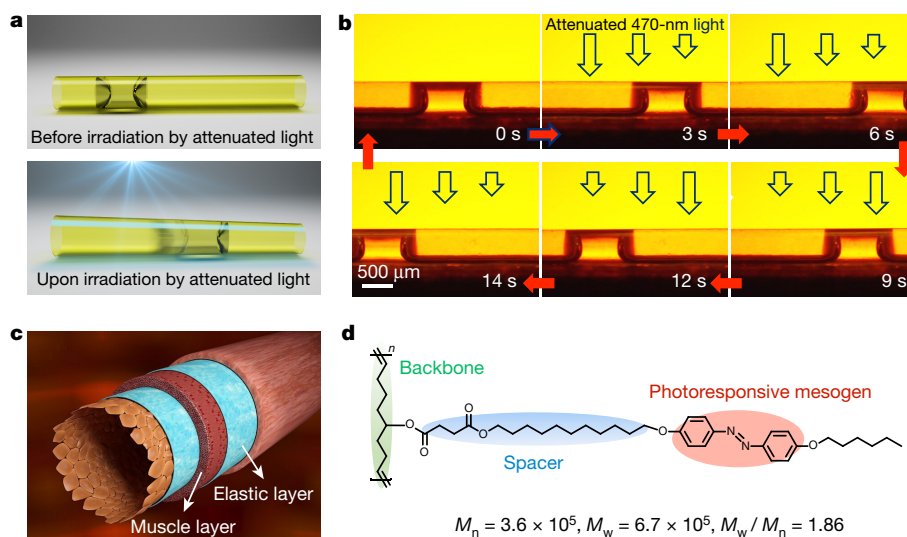


**Figure 1 | Design of tubular microactuators.** **a**, Schematics showing the motion of a slug of fully wetting liquid confined in a tubular microactuator (TMA) driven by photodeformation. The light is incident perpendicular to the long axis of the TMA and has a gradient of incident intensity (produced by attenuation), decreasing from left to right. Shape transformation of the TMA from cylindrical to conical is induced by this gradient of light intensity. As a result, the slug advances to the narrower end of the TMA. **b**, Lateral photographs of the light-induced motion of a silicone oil slug in a TMA fixed on a substrate that were taken through an optical filter to remove light with wavelengths below 530 nm. On irradiation by 470-nm light whose intensity (represented by

open arrows) is attenuated increasingly from left to right (top row), the silicone oil slug is self-propelled towards the right; when the direction of attenuation is reversed (bottom row), the direction of movement of the slug is also reversed (Supplementary Video 1). **c**, Schematic illustration of the structure of artery walls. The middle coat of an artery, called the tunica media, consists of alternating muscle layers and elastic layers, which are responsible for stimuli-responsive deformation and mechanical robustness, respectively. Image adapted from ref. 51, Elsevier. **d**, Molecular structure of a novel linear liquid crystal polymer (LLCP).  $M_n$ , number-average molecular weight;  $M_w$ , weight-average molecular weight.

weight of the LLCP reached  $3.6 \times 10^5 \text{ g mol}^{-1}$ , which is at least one order of magnitude larger than that of the generally used photoresponsive azobenzene LC polymers<sup>43,44</sup>. Tensile tests show that the LLCP fibre has a moderate elastic modulus ( $96 \pm 19 \text{ MPa}$ ), high toughness ( $319 \pm 41 \text{ MJ m}^{-3}$ ), high strength ( $\sim 20 \text{ MPa}$ ) and a large elongation at break (or fracture strain;  $2,089\% \pm 275\%$ ) (Supplementary Video 2). Thus the LLCP is a strong and tough material, which we ascribe to the

ordered lamellar structure and the high molecular weight. Moreover, the absence of a chemical network means that broken samples can be reshaped; a 'healed' fibre with a cross-sectional area of  $0.02 \text{ mm}^2$  can still sustain a large load, up to  $\sim 52 \text{ g}$  (Extended Data Fig. 2).

Thanks to rational structure design and the robust mechanical properties of the LLCP, we were able, for the first time, to fabricate structurally defined and robust TMAs via a solution processing

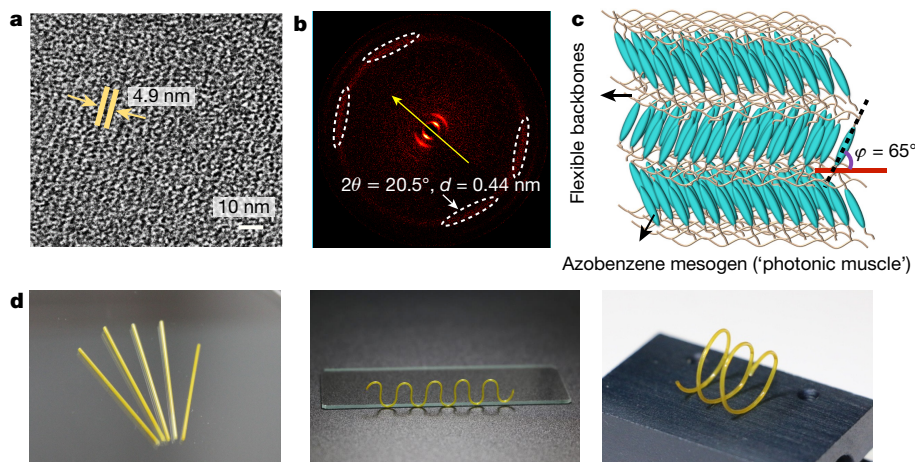


**Figure 2 | Structures of the LLCP and images of freestanding TMAs.** **a**, TEM image showing the lamellar structure of the LLCP film. **b**, Two-dimensional wide-angle X-ray diffraction pattern of the LLCP film exhibiting lamellar reflections on the meridian and LC diffraction arcs in the quadrants. The X-ray beam is applied to the side of the film and parallel to the plane of the film.  $2\theta$  denotes the diffraction angle,  $d$  represents the lateral distance between the LC mesogens. The yellow arrow indicates the film horizontal. The dashed ellipses display the outline of the diffraction spots in the wide angle area. The white arrow indicates the diffraction angle and the lateral distance values of the diffraction spots. **c**, Schematic representation of packing structure in the LLCP film. The LC

mesogens self-assemble into a smectic phase, and the zigzag tilting of LC mesogens takes place in smectic lamella.  $\varphi$  denotes the tilt angle between the long axis of the azobenzene mesogens and the plane of the lamella. The long axis of the azobenzene mesogen is along the black dashed line. The normal of smectic lamellar is perpendicular to the horizontal of the LLCP film. **d**, Photographs showing left to right a batch of free-standing straight, serpentine and helical TMAs. The serpentine TMA is leaning against the edge of a glass slide. The inner diameter of the straight TMAs is  $0.5 \text{ mm}$ , and that of both serpentine and helical TMAs is  $0.6 \text{ mm}$ . The wall thickness of all the TMAs is  $\sim 8 \mu\text{m}$ .

method. We filled a glass capillary with a solution of the LLCP in dichloromethane ( $\sim 3$  wt%). After evaporation of the dichloromethane at  $50^\circ\text{C}$ , the inner surface of the glass capillary was uniformly coated with the LLCP. The coated capillary was annealed at  $50^\circ\text{C}$  for 30 min and then immersed in hydrofluoric acid to remove the glass. The free-standing TMA that was produced is robust enough to resist large deformation for many cycles (Extended Data Fig. 3, Supplementary Video 3). TMAs with arbitrary geometries, such as 'Y'-shaped, serpentine and helical, were also prepared by the same method.

### Photocontrol of fluid slugs

Previously reported liquid manipulation based on light-induced capillary force is usually applicable only to specific liquids (oil and some LCs)<sup>1</sup>, and still faces great challenges in handling most commonly used liquids. We note that each type of our TMAs (straight, 'Y'-shaped, serpentine and helical) shows unique abilities to propel a wide range of liquids spanning nonpolar to polar liquids, such as silicone oil, hexane, ethyl acetate, acetone, ethanol and water (Part 1 of Supplementary Video 4). More surprisingly, our TMAs can also propel complex fluids efficiently, such as a train of slugs, emulsion, liquid–solid fluid mixtures and even petrol (Fig. 3a, b, Extended Data Fig. 4, and Parts 2–5 of Supplementary Video 4), which have not yet been handled using existing light manipulation principles<sup>1</sup>. We also successfully manipulated liquids widely used in biomedical engineering with the TMAs, such as bovine serum albumin solution, phosphate buffer solution, cell culture medium and cell suspension (Part 6 of Supplementary Video 4), which is of great significance for biomedical analysis and micro-engineering.

Furthermore, our TMA works as a micromixer, offering a versatile toolbox for microfluidic mixing. Extended Data Fig. 4 and Part 4 of Supplementary Video 4 demonstrate the mixing of polyethylene microspheres and ethyl acetate with the aid of vortex circulation in the moving liquid slug, which is ascribed to the viscous stresses caused by the shear between the slug and the inner surface<sup>45</sup>. This stirring behaviour takes advantage of the hydrodynamic effect and thus relies on neither stirrers nor special microfluidic designs. Figure 3c shows that the light-induced vortex circulation strongly promotes the dissolution of benzophenone in 75 vol% ethanol (Supplementary Video 5). Upon exposure to attenuated 470-nm light, benzophenone completely dissolves in ethanol within 45 s. However, a similar weight of benzophenone dissolves little

under the same conditions but without the light irradiation (Extended Data Fig. 5). The stirring behaviour in the photodeformable TMA is fully triggered by the external light, and allows repeatable and reversible switching between a non-mixing mode and an efficient mixing action. This approach could be easily adapted to diverse microfluidic configurations because it does not require the implementation of any specific element (such as a valve or an electrode)<sup>46</sup>. More interestingly, our TMA is able to drive a silicone oil slug to capture and convey a microsphere by spatially controlled irradiation (Fig. 3d, Supplementary Video 6), which implies great potential in applications of microscale reaction and micromechanical operation.

### Photodeformation mechanism of the TMAs

All these liquid handling abilities arise from asymmetric photo-deformation of the TMAs in response to attenuated 470-nm light, which is a novel principle for inducing capillary force. It has been reported that azobenzene mesogens can be realigned along the direction perpendicular to the polarized direction of actinic linearly polarized blue light after repetition of *trans*–*cis*–*trans* isomerization cycles (Extended Data Fig. 6), which is known as the Weigert effect<sup>47</sup>. In the case of unpolarized light, only the propagation direction is perpendicular to the polarized direction of the unpolarized light, thus the azobenzene mesogens orientate along the propagation direction of the actinic unpolarized light<sup>47,48</sup> (Fig. 4a). When the TMAs are exposed to unpolarized 470-nm light whose actinic direction is perpendicular to the long axis of the TMAs, the azobenzene mesogens are reorientated along the propagation direction (Fig. 4b), which has also been experimentally confirmed by 2D-WAXD patterns of the TMA wall cut and flattened out into a plane before and after irradiation (Extended Data Fig. 7). Therefore, the tilt angles  $\varphi$  of azobenzene mesogens in the different exposed areas are different because the lamellae of the LLCP are arranged coaxially in the TMA wall.

In order to facilitate understanding of this photo-reorientation, the wall of the TMA is flattened out into a plane, as shown in Fig. 4b. According to the tilt angle of azobenzene mesogens calculated from 2D WAXD (Fig. 2b), the azobenzene mesogens in  $\sim 70\%$  of the exposed area are reoriented to exhibit  $\varphi \leq 65^\circ$ , which means this area expands along the  $y$  axis. The rest of the azobenzene mesogens are tilted with  $65^\circ < \varphi \leq 90^\circ$ , leading to contraction along the  $y$  axis. In other words, the expansion of the light-exposed area is far larger than the contraction

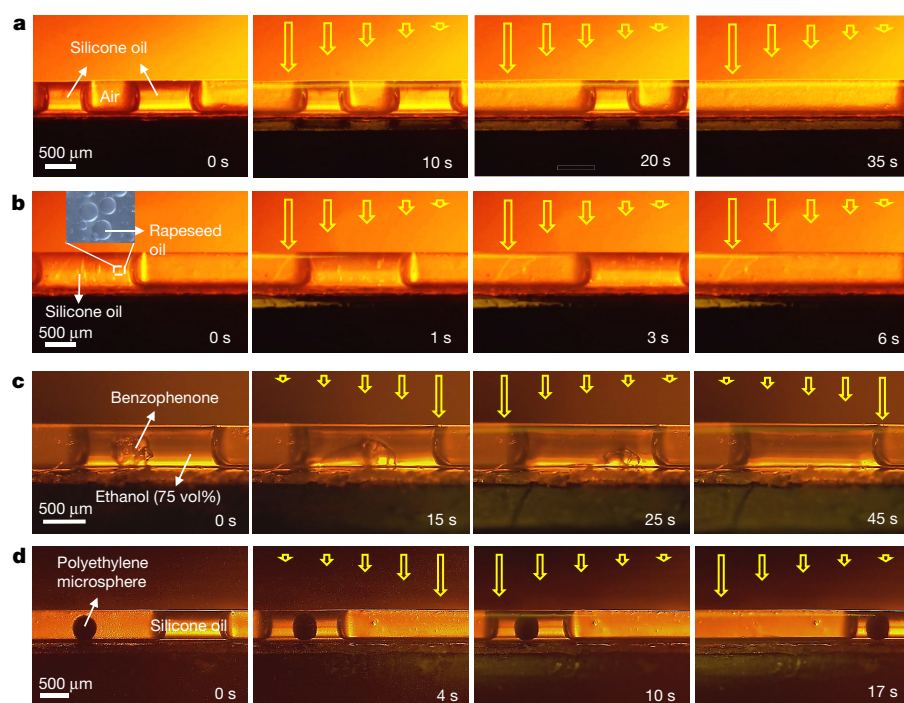


**Figure 3 | Photocontrol of fluid slugs.** **a**, Lateral photographs showing light-induced motion of a biphasic fluid, containing an air bubble sandwiched between two silicone oil slugs. In all rows, the open arrows denote the intensity of the incident light. **b**, Lateral photographs showing light-controlled transportation of an emulsion prepared by dispersing rapeseed oil slugs in silicone oil (see Part 3 of Supplementary Video 4). Inset, an enlarged photograph exhibiting the small droplets of rapeseed oil in the emulsion. The diameter of the arrowed small droplet is  $\sim 0.12$  mm. **c**, Lateral photographs showing that light-induced vortex circulation strongly promotes the dissolution of benzophenone ( $\sim 0.03$  mg) in ethanol ( $\sim 0.3$   $\mu\text{l}$ , 75 vol%). See Supplementary Video 5. **d**, Lateral photographs showing that a silicone oil slug captures and conveys a polyethylene microsphere (0.43 mm) through the light-induced deformation of the TMA (Supplementary Video 6). All photographs were taken through an optical filter that removed light with wavelengths below 530 nm; time is shown at lower right of each panel.



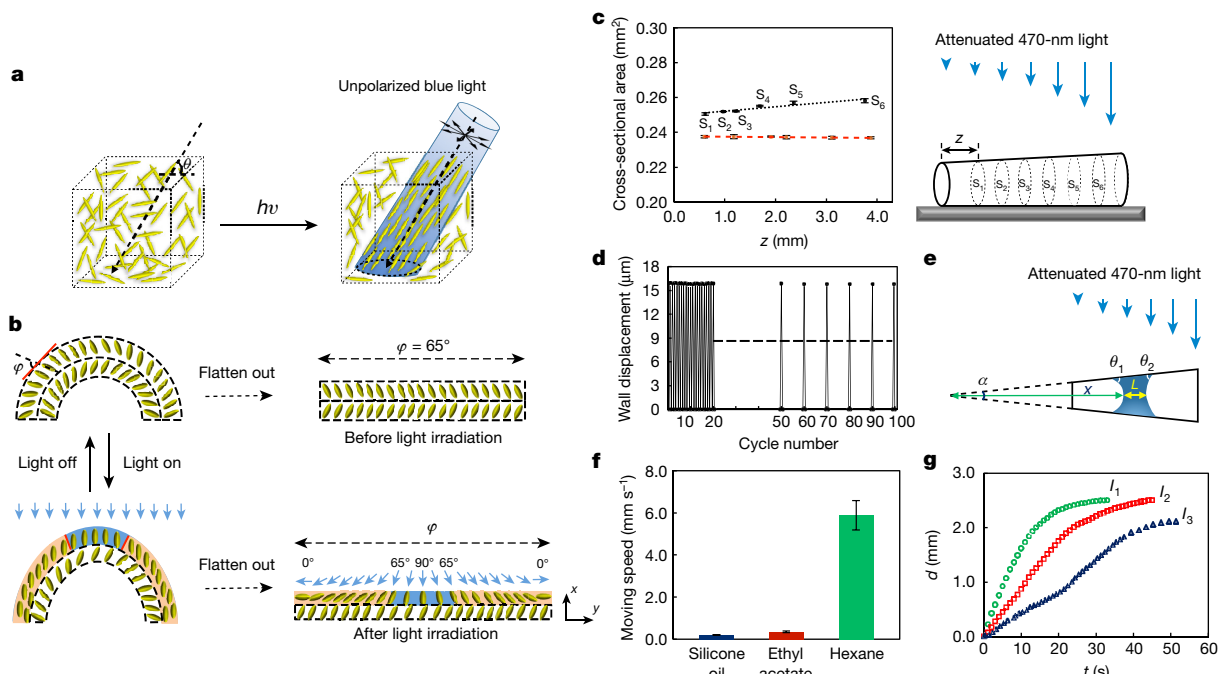


**Figure 4 | Mechanism of photodeformation of the TMA and velocity of light-induced liquid motion.** **a**, Schematics showing reorientation of mesogens in azobenzene-containing LC systems with non-polarized blue light that is incident at angle  $\theta$ . Double arrows show the polarization direction of the light. **b**, Schematics illustrating the reorientation of mesogens in the cross-sectional area of the TMA before and after irradiation by unpolarized 470-nm light. To facilitate understanding the photo-reorientation, the wall is flattened out into a plane. The normal direction of the lamellae is along the  $x$  direction in the scheme. Before irradiation by the light,  $\varphi$  of all the LC mesogens is  $65^\circ$  (top). On light irradiation, the LC mesogens in the exposed surface of the TMA are realigned to the direction of the actinic light, which results in the change of  $\varphi$  in the exposed area (bottom). The orange and blue parts of the cross-sectional area respectively expand and contract along the  $y$  axis on light irradiation. This photoinduced reorientation leads to the decrease in thickness of the TMA wall (along the  $x$  axis) and the elongation of the perimeter of the TMA (along the  $y$  axis), which contributes to the increase of cross-sectional area. **c**, Left, plot showing the area of six different cross-sections ( $S_1$ – $S_6$ , shown right) before (red line) and after (black line) irradiation by attenuated 470-nm light. Error bars, s.d. ( $n = 3$ ).  $z$  represents

of that area. This photoinduced reorientation results in a decrease of the thickness of the TMA wall (along the  $x$  axis in Fig. 4b) and an elongation of the perimeter of the TMA (along the  $y$  axis in Fig. 4b), which together cause an increase of the cross-sectional area of the TMA. Moreover, the higher the light intensity, the larger the increase in cross-sectional area. Figure 4c shows that the cross-sectional areas of the photodeformed TMA at different positions increase with the increase of the light intensity upon irradiation by attenuated 470-nm light, whereas the cross-sectional areas at different positions without irradiation are almost the same. Therefore, the TMA deforms to an asymmetric cone-like geometry, which generates adjustable capillary force to propel liquids in the direction of light attenuation (Fig. 1a, Supplementary Video 7).

## Discussion

We find that the direction of movement of the slug can easily be controlled by varying the direction in which the intensity of the actinic light decreases (Supplementary Video 1). To the best of our knowledge, this kind of directed motion of liquids in closed channels has not been reported before. Supplementary Video 8 demonstrates that the TMA undergoes an obvious wall displacement upon exposure to unpolarized 470-nm light. After turning off the light source, the TMA returns to its

initial size due to elastic recovery of unexposed regions and entropic restoring forces imparted by the exposed region<sup>49</sup>. Such reversible deformation on intermittent irradiation with 470-nm light can be repeated over 100 cycles without obvious fatigue (Fig. 4d), because the creep of the LLCP is minimized by the smectic organization of the side groups, which might act as physical crosslinks.

In the TMA, the slug of wetting liquid (Extended Data Table 1) is subjected to two forces: capillary driving force and viscous force, which oppose each other. The balance between these two forces yields a steady speed  $v \approx \alpha\gamma/(8\eta)$  that is independent of slug position  $x$  and slug length  $L$ , where  $\alpha$  is the opening angle schematically shown in Fig. 4e,  $\eta$  is the dynamic viscosity of the liquid and  $\gamma$  is its surface tension. Hence the moving speed of different wetting liquids varies because of their different ratio of  $\gamma/\eta$  (Fig. 4f), when  $\alpha$  is fixed. The speed at which hexane moves reaches  $5.9 \text{ mm s}^{-1}$ , which is the fastest speed of liquid motion driven by light-induced capillary force found so far.

For liquids that only partially wet the wall of the TMA (Extended Data Table 1), we coated the inner wall with a layer that the liquid could wet completely. This enables partially wetting liquids to move like wetting liquids in the TMA. For example, ethanol wets a polyacrylamide surface but only partially wets the inner wall of the TMA, so a TMA coated with polyacrylamide propels an ethanol slug

at a speed of  $\sim 0.3 \text{ mm s}^{-1}$ . As for water, which has relatively large surface tension, we succeeded in enhancing both the wettability and the roughness of the TMA inner wall by applying a composite gel layer; this made water fully spread out, that is, become fully wetting (see details in Supplementary Information). Consequently, the coated TMA is capable of handling various aqueous liquids, including those used in biomedical applications (Part 6 of Supplementary Video 4). Since any partially wetting liquid can be propelled as a wetting liquid by modifying the TMA with a suitable coating layer, the resistance generated by contact-line pinning is completely excluded from liquid being moved using our system; thus our TMAs are in theory able to propel any liquid.

The speed at which wetting liquids can be moved is also affected by the  $\alpha$  of the conical TMAs, which can be simply tuned through the intensity of actinic light (Fig. 4g). For example, the moving speed of a silicone oil slug changed from  $0.05$  to  $0.2 \text{ mm s}^{-1}$  when the intensity of light source changed from  $60$  to  $125 \text{ mW cm}^{-2}$ . We further calculated the uniform velocity of the liquid slug when the capillary driving force and the viscous resistance reached balance; for the silicone oil slug we calculate this velocity to be  $0.04$ – $0.15 \text{ mm s}^{-1}$ , which is close to the measured speed mentioned above (for details see Supplementary Information). Moreover, Part 1 of Supplementary Video 9 shows a silicone oil slug moving a distance of  $57 \text{ mm}$ , which is two orders of magnitude larger than its length ( $\sim 0.53 \text{ mm}$ ). As long as the slug is confined in the conical TMA, it keeps moving until the actinic light is switched off: that is, there is theoretically no limit to the moving distance. Additionally, the movement of the slug is synchronized to the switching of the light source, whereas the previous principles based on light-induced wettability gradient require a period of time to activate droplet movement<sup>13</sup>.

In the previous reports, droplet motions driven by light were usually limited to linear moving trajectories on a horizontal surface<sup>15</sup>, and there was only one work related to light-driven motion of a droplet on a slope, specifically a  $12^\circ$  incline, with a velocity of  $\sim 0.002 \text{ mm s}^{-1}$ . It is noteworthy that our TMAs can propel a silicone oil slug uphill on a  $17^\circ$  incline with a speed of  $\sim 0.1 \text{ mm s}^{-1}$  (Fig. 5a, Part 2 of Supplementary Video 9). More intriguingly, the versatile TMAs can not only enable light control of liquid motion on a horizontal 'S'-shaped trajectory, but also enable helical trajectories in three dimensions (Fig. 5b, c, and Parts 3 and 4 of Supplementary Video 9). To our knowledge, this is

the first time light-driven liquid motion has been achieved in curved closed microchannels. Compared with straight tubes, propelling liquids in curved tubes is more difficult because of remarkably larger flow resistance arising from secondary flow<sup>50</sup>. Moreover, liquid fusion, which is crucial in biomedical fluid processing and microscale reactor operation<sup>17,19</sup>, has been achieved by using a 'Y'-shaped TMA (Fig. 5d, Part 5 of Supplementary Video 9).

Our approach to handling liquids requires only a single, standard LED source: there is no need for special optical set-ups or high power laser sources. Moreover, the propelled liquids are confined in closed microchannels, and the irradiating light on the outer surface of the TMAs has no direct contact with the propelled liquids. Hence our light-driven liquid manipulation avoids photo-induced thermal effects and any resulting sample damage, which are especially undesirable for biology-oriented applications. In order to demonstrate the possibility of using  $470\text{-nm}$  blue light as an excitation source to induce the motion of liquids in biological systems, a piece of  $\sim 1\text{-mm}$ -thick lean pork was placed between the light source and the TMA (Extended Data Fig. 8). The intensity of the incident light was reduced from  $140$  to  $\sim 60 \text{ mW cm}^{-2}$  after passing through the pork; however, it was still able to drive the movement of a silicone oil slug at an average speed of  $0.048 \text{ mm s}^{-1}$  owing to the ability of  $470\text{-nm}$  blue light to penetrate into tissues (Part 6 of Supplementary Video 9). These experiments demonstrate that our TMAs have promise for application in microfluidic systems embedded in biological tissues.

## Conclusions

Our TMAs present a conceptually novel way to propel liquids by capillary force arising from photo-induced asymmetric deformation, which relies on neither wettability gradients nor the Marangoni effect. The TMAs can propel not only simple liquids spanning a broad range of polarity, but also complex fluids widely used in biomedical and chemical engineering; they thus have considerable potential application as micro-pumps in microsystems technology and architecture without any aid from additional components. Moreover, the demonstrated effective light-control of liquid mixing and the capture and movement of microspheres on the microscale could greatly simplify microfluidic devices. Therefore, our photodeformable TMAs are excellent candidates for application in the fields of micro-reactors, laboratory-on-a-chip contexts and micro-optomechanical systems.

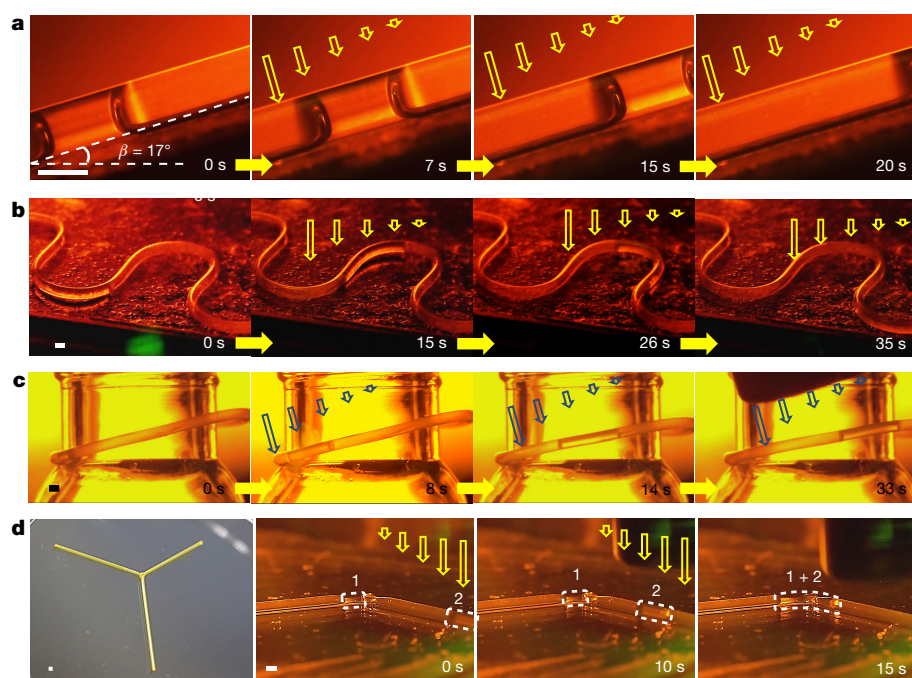


**Figure 5 | Light-driven manipulation of liquid in straight, serpentine, helical and 'Y'-shaped TMAs.** **a**, Lateral photographs showing light-driven motion of a silicone oil slug in a straight TMA tilted up at  $\beta = 17^\circ$  (Part 2 of Supplementary Video 9). The slug moved about  $2 \text{ mm}$  in  $20 \text{ s}$ . **b**, Lateral photographs showing light-driven motion of a silicone oil slug in a serpentine TMA (Part 3 of Supplementary Video 9). **c**, Lateral photographs showing the motion of a silicone oil slug in a helical TMA around the neck of a glass bottle (Part 4 in Supplementary Video 9). **d**, First image, photograph of a 'Y'-shaped TMA; other images, lateral photographs showing light-driven liquid fusion of two silicone oil slugs **1** and **2** at the junction of the 'Y'-shaped TMA (Part 5 of Supplementary Video 9). The white dashed frames indicate the outline of the slugs. The intensity of the  $470\text{-nm}$  light source is  $125$ – $140 \text{ mW cm}^{-2}$ , and the lengths of the open arrows indicate the varying intensity after attenuation. The actinic light direction is perpendicular to the long axis of the TMA. The photographs except the first image in **d** were taken through an optical filter to remove light with wavelengths below  $530 \text{ nm}$ . Scale bars,  $0.5 \text{ mm}$ .



**Online Content** Methods, along with any additional Extended Data display items and Source Data, are available in the online version of the paper; references unique to these sections appear only in the online paper.

**Received 7 December 2015; accepted 20 July 2016.**

- Baigl, D. Photo-actuation of liquids for light-driven microfluidics: state of the art and perspectives. *Lab Chip* **12**, 3637–3653 (2012).
- Sackmann, E. K., Fulton, A. L. & Beebe, D. J. The present and future role of microfluidics in biomedical research. *Nature* **507**, 181–189 (2014).
- Nge, P. N., Rogers, C. I. & Woolley, A. T. Advances in microfluidic materials, functions, integration, and applications. *Chem. Rev.* **113**, 2550–2583 (2013).
- Mark, D., Haeberle, S., Roth, G., Stetten, F. & Zengerle, R. Microfluidic lab-on-a-chip platforms: requirements, characteristics and applications. *Chem. Soc. Rev.* **39**, 1153–1182 (2010).
- Elvira, K. S., Solvas, X. C. i., Wootton, R. R. & deMello, A. J. The past, present and potential for microfluidic reactor technology in chemical synthesis. *Nat. Chem.* **5**, 905–915 (2013).
- Ashkin, A. & Dziedzic, J. M. Radiation pressure on a free liquid surface. *Phys. Rev. Lett.* **30**, 139–142 (1973).
- Ashkin, A., Dziedzic, J. M., Bjorkholm, J. E. & Chu, S. Observation of single beam gradient force optical trap for dielectric particles. *Opt. Lett.* **11**, 288–290 (1986).
- Chiou, P. Y., Moon, H., Toshiyoshi, H., Kim, C.-J. & Wu, M. C. Light actuation of liquid by optoelectrowetting. *Sens. Actuators A* **104**, 222–228 (2003).
- Chiou, P. Y., Park, S.-Y. & Wu, M. C. Continuous optoelectrowetting for picoliter droplet manipulation. *Appl. Phys. Lett.* **93**, 221110 (2008).
- Park, S.-Y., Teitell, M. A. & Chiou, E. P. Y. Single-sided continuous optoelectrowetting (SCOEW) for droplet manipulation with light patterns. *Lab Chip* **10**, 1655–1661 (2010).
- Moorthy, J., Khoury, C., Moore, J. S. & Beebe, D. J. Active control of electroosmotic flow in microchannels using light. *Sens. Actuators B* **75**, 223–229 (2001).
- Oroszi, L., Dér, A., Kerei, H., Ormos, P. & Rakovics, V. Control of electro-osmotic flow by light. *Appl. Phys. Lett.* **89**, 263508 (2006).
- Ichimura, K., Oh, S.-K. & Nakagawa, M. Light-driven motion of liquids on a photoresponsive surface. *Science* **288**, 1624–1626 (2000).
- Yang, D. et al. Photon control of liquid motion on reversibly photoresponsive surfaces. *Langmuir* **23**, 10864–10872 (2007).
- Berná, J. et al. Macroscopic transport by synthetic molecular machines. *Nat. Mater.* **4**, 704–710 (2005).
- Kotz, K. T., Noble, K. A. & Faris, G. W. Optical microfluidics. *Appl. Phys. Lett.* **85**, 2658–2660 (2004).
- Kotz, K. T., Gu, Y. & Faris, G. W. Optically addressed droplet-based protein assay. *J. Am. Chem. Soc.* **127**, 5736–5737 (2005).
- Diguet, A. et al. Photomanipulation of a droplet by the chromocapillary effect. *Angew. Chem. Int. Ed.* **48**, 9281–9284 (2009).
- Venancio-Marques, A. & Baigl, D. Digital optofluidics: LED-gated transport and fusion of microliter-sized organic droplets for chemical synthesis. *Langmuir* **30**, 4207–4212 (2014).
- Prakash, M., Quéré, D. & Bush, J. W. M. Surface tension transport of prey by feeding shorebirds: the capillary ratchet. *Science* **320**, 931–934 (2008).
- Rennois, P., Bush, J. W. M., Prakash, M. & Quéré, D. Drop propulsion in tapered tubes. *Europhys. Lett.* **86**, 64003 (2009).
- Finkelmann, H., Nishikawa, E., Pereira, G. G. & Warner, M. A new opto-mechanical effect in solids. *Phys. Rev. Lett.* **87**, 015501 (2001).
- Yu, Y., Nakano, M. & Ikeda, T. Directed bending of a polymer film by light. *Nature* **425**, 145 (2003).
- Wu, W. et al. NIR-light-induced deformation of cross-linked liquid-crystal polymers using upconversion nanophosphors. *J. Am. Chem. Soc.* **133**, 15810–15813 (2011).
- Wang, W., Sun, X., Wu, W., Peng, H. & Yu, Y. Photoinduced deformation of crosslinked liquid-crystalline polymer film oriented by a highly aligned carbon nanotube sheet. *Angew. Chem. Int. Ed.* **51**, 4644–4647 (2012).
- Li, M., Keller, P., Li, B., Wang, X. & Brunet, M. Light-driven side-on nematic elastomer actuators. *Adv. Mater.* **15**, 569–572 (2003).
- Ohm, C., Brehmer, M. & Zentel, R. Liquid crystalline elastomers as actuators and sensors. *Adv. Mater.* **22**, 3366–3387 (2010).
- Fleischmann, E.-K. & Zentel, R. Liquid-crystalline ordering as a concept in materials science: from semiconductors to stimuli-responsive devices. *Angew. Chem. Int. Ed.* **52**, 8810–8827 (2013).
- van Oosten, C. L., Bastiaansen, C. W. M. & Broer, D. J. Printed artificial cilia from liquid-crystal network actuators modularly driven by light. *Nat. Mater.* **8**, 677–682 (2009).
- Liu, D., Liu, L., Onck, P. R. & Broer, D. J. Reverse switching of surface roughness in a self-organized polydomain liquid crystal coating. *Proc. Natl Acad. Sci. USA* **112**, 3880–3885 (2015).
- Liu, D. & Broer, D. J. New insights into photoactivated volume generation boost surface morphing in liquid crystal coatings. *Nat. Commun.* **6**, 8334 (2015).
- Lee, K. M. et al. Photodrive, flexural-torsional oscillation of glassy azobenzene liquid crystal polymer networks. *Adv. Funct. Mater.* **21**, 2913–2918 (2011).
- McConney, M. E. et al. Topography from topology: photoinduced surface features generated in liquid crystal polymer networks. *Adv. Mater.* **25**, 5880–5885 (2013).
- Ube, T. & Ikeda, T. Photomobile polymer materials with crosslinked liquid-crystalline structures: molecular design, fabrication, and functions. *Angew. Chem. Int. Ed.* **53**, 10290–10299 (2014).
- White, T. J. & Broer, D. J. Programmable and adaptive mechanics with liquid crystal polymer networks and elastomers. *Nat. Mater.* **14**, 1087–1098 (2015).
- Iamsaard, S. et al. Conversion of light into macroscopic helical motion. *Nat. Chem.* **6**, 229–235 (2014).
- Zeng, H. et al. Light-fueled microscopic walkers. *Adv. Mater.* **27**, 3883–3887 (2015).
- Petr, M., Katzman, B., DiNatale, W. & Hammond, P. T. Synthesis of a new, low-*T<sub>g</sub>* siloxane thermoplastic elastomer with a functionalizable backbone and its use as a rapid, room temperature photoactuator. *Macromolecules* **46**, 2823–2832 (2013).
- Pei, Z. et al. Mouldable liquid-crystalline elastomer actuators with exchangeable covalent bonds. *Nat. Mater.* **13**, 36–41 (2014).
- Hasan, A. et al. Electrospun scaffolds for tissue engineering of vascular grafts. *Acta Biomater.* **10**, 11–25 (2014).
- Shadwick, R. E. Mechanical design in arteries. *J. Exp. Biol.* **202**, 3305–3313 (1999).
- Drouin, S. D., Zamanian, F. & Fogg, D. E. Multiple tandem catalysis: facile cycling between hydrogenation and metathesis chemistry. *Organometallics* **20**, 5495–5497 (2001).
- Li, X. et al. Photoresponsive side-chain liquid crystalline polymers with amide group-substituted azobenzene mesogens: effects of hydrogen bonding, flexible spacers, and terminal tails. *Soft Matter* **8**, 5532–5542 (2012).
- Li, C. et al. In situ fully light-driven switching of superhydrophobic adhesion. *Adv. Funct. Mater.* **22**, 760–763 (2012).
- Kinoshita, H., Kaneda, S., Fujii, T. & Oshima, M. Three-dimensional measurement and visualization of internal flow of a moving droplet using confocal micro-PIV. *Lab Chip* **7**, 338–346 (2007).
- Venancio-Marques, A., Barbaud, F. & Baigl, D. Microfluidic mixing triggered by an external LED illumination. *J. Am. Chem. Soc.* **135**, 3218–3223 (2013).
- Yu, Y. & Ikeda, T. Alignment modulation of azobenzene-containing liquid crystal systems by photochemical reactions. *J. Photochem. Photobiol. Chem.* **5**, 247–265 (2004).
- Wu, Y., Ikeda, T. & Zhang, Q. Three-dimensional manipulation of an azo polymer liquid crystal with unpolarized light. *Adv. Mater.* **11**, 300–302 (1999).
- White, T. J. A high frequency photodrive polymer oscillator. *Soft Matter* **4**, 1796–1798 (2008).
- Vashisth, S., Kumar, V. & Nigam, K. D. P. A review on the potential applications of curved geometries in process industry. *Ind. Eng. Chem. Res.* **47**, 3291–3337 (2008).
- Fortier, A., Gullapalli, V. & Mirshams, R. A. Review of biomechanical studies of arteries and their effect on stent performance. *J. Heart Vessels* **4**, 12–18 (2014).

**Supplementary Information** is available in the online version of the paper.

**Acknowledgements** This work was supported by the National Natural Science Foundation of China (51225304, 21134003 and 21273048) and by the Shanghai Outstanding Academic Leaders Plan (15XD1500600). We thank Y. Xu, X. Liu and E. Chen for assistance with 2D-WAXD measurements; G. Guan, S. Yan and L. Gao for help with TEM tests; H. Guo and X. Feng for assistance with the analytical model and the related calculation; Z. Dai and Q. Liu for assistance with the calculation of the moving speed of slugs; F. Guo and Y. Zhao for help with static CA tests; and Y. Gong for assistance with dynamic CA tests.

**Author Contributions** J.L., J.W. and Y.Y. designed the LLC. J.L. and Y.L. synthesized and characterized the LLC. J.L., Y.L. and Y.Y. designed the T.M.A.s. J.L. performed the related experiments and characterization of the T.M.A.s. J.L. and Y.Y. discussed the results and analysed the data. J.L., E.C. and Y.Y. analysed the 2D-WAXD results. J.L. drafted the manuscript. J.L., L.Q., E.C., Y.L. and Y.Y. revised the manuscript. Y.Y. supervised the research.

**Author Information** Reprints and permissions information is available at [www.nature.com/reprints](http://www.nature.com/reprints). The authors declare no competing financial interests. Readers are welcome to comment on the online version of the paper. Correspondence and requests for materials should be addressed to Y.Y. ([ylyu@fudan.edu.cn](mailto:ylyu@fudan.edu.cn)).

**Reviewer Information** Nature thanks D. Baigl, D. J. Broer and the other anonymous reviewer(s) for their contribution to the peer review of this work.

## METHODS

**Preparation of LLCP fibres.** A small amount of the LLCP (20 mg) was heated to 120 °C (isotropic phase) on a glass slide placed on a hot stage (Mettler, FP-90 and FP-82). LLCP fibres were prepared by dipping the tip of a toothpick into the melt and pulling away as quickly as possible.

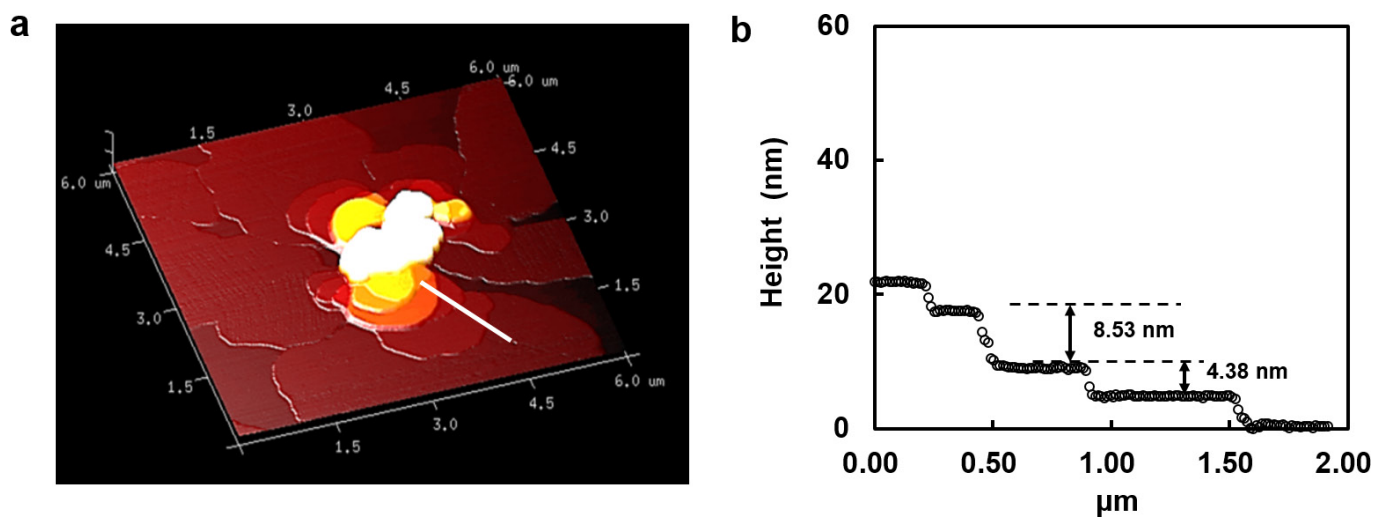
**LLCP films prepared by solution processing.** A solution of the LLCP in CH<sub>2</sub>Cl<sub>2</sub> (~1 wt%) was drop-coated on a glass slide. The LLCP films formed after the evaporation of the CH<sub>2</sub>Cl<sub>2</sub>, and were then annealed at 50 °C for 1 h and separated from the glass slide by immersion in water.

**Characterization.** <sup>1</sup>H NMR and <sup>13</sup>C NMR spectra of the azobenzene functional cyclooctene monomer C11AB6 and the LLCP were recorded on a Bruker DMX500 NMR spectrometer using tetramethylsilane as the internal standard and CDCl<sub>3</sub> as solvent. MALDI-TOF-MS spectra of C11AB6 were measured on an AB SCIEX 5800 spectrometer. Gel permeation chromatography of the LLCP was performed in THF with an eluent rate of 1.0 ml min<sup>-1</sup> on an Agilent 1100 with a G1310A pump, a G1362A refractive-index detector, and a G1314A variable-wavelength detector. AFM tapping mode images were acquired by using a Bruker Dimension FastScan AFM. The AFM samples of a thin LLCP film were prepared by spin-coating a flat glass substrate with the solution of the LLCP in CH<sub>2</sub>Cl<sub>2</sub> (~0.1 wt %) and annealed at 50 °C for 1 h. High-resolution TEM images were recorded on a JEM-2100 TEM at an accelerating voltage of 200 kV. The TEM samples of sheared LLCP film were cut at -100 °C using a cryomicrotome apparatus (Leica, FC7-UC7) with a liquid nitrogen cooling instrument, and were mounted on a copper grid and stained with OsO<sub>4</sub> for 30 min to increase the mass-thickness contrast for TEM. 2D-WAXD

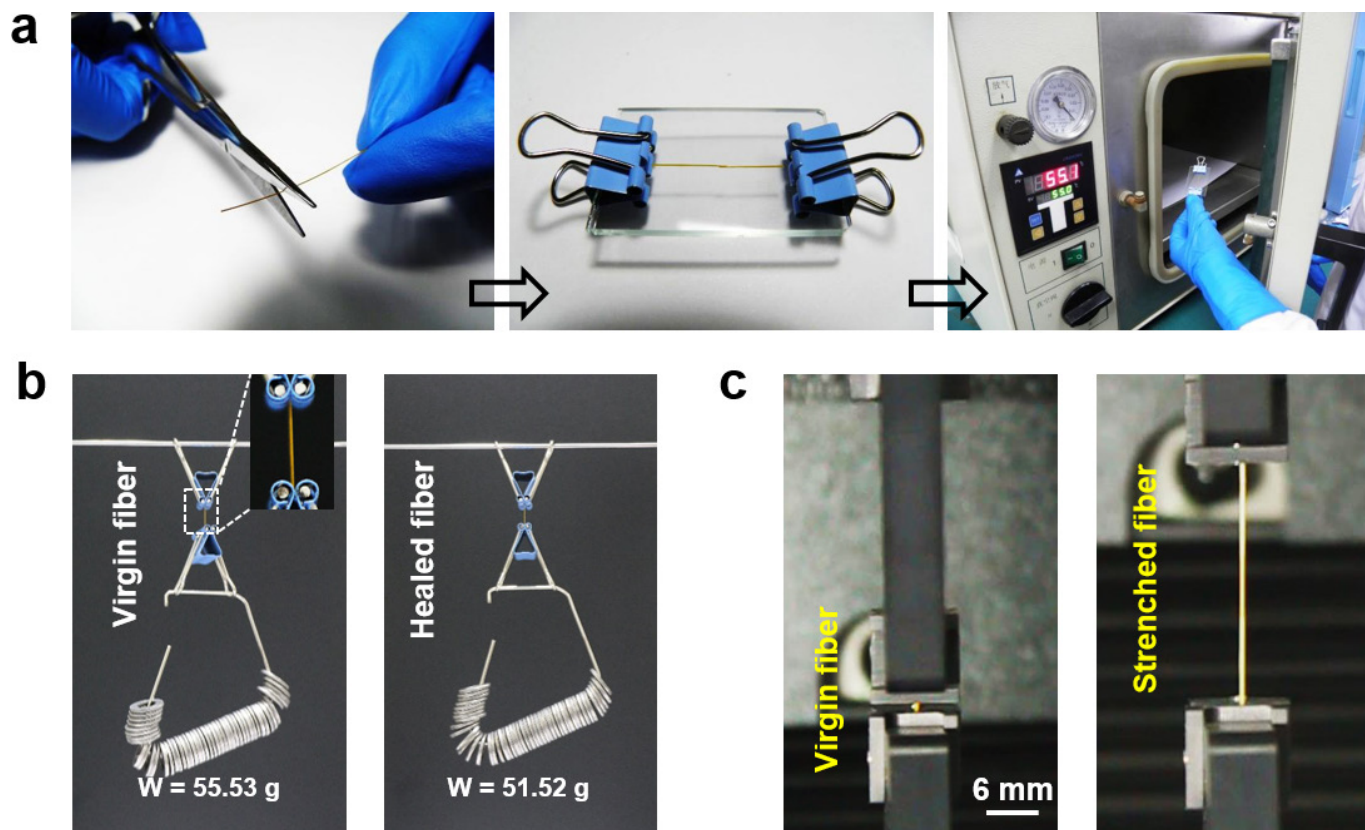
experiments on the LLCP films and the TMAs prepared by solution processing were conducted on a Bruker D8 Discover diffractometer with a 2D detector of GADDS in transmission mode. The X-ray sources (Cu K $\alpha$ ,  $\lambda$  = 0.154 nm) were provided by 3 kW ceramic tubes and the peak positions were calibrated with silicon powder ( $2\theta > 15^\circ$ ) and silver behenate ( $2\theta < 10^\circ$ ). The background scattering was recorded and subtracted from the sample patterns. High-resolution scanning electron microscopy (SEM) images were recorded on a field-emission scanning electron microscope (Zeiss, Ultra 55).

The tensile stress-strain measurements of the LLCP fibre were performed using an Instron Universal Testing Machine (Model 5943) at a deformation rate of 60 mm min<sup>-1</sup> in air. The toughness, a parameter that characterizes the work required to fracture the sample per unit volume, was calculated from the area below the tensile stress-strain curve until fracture. The wall thickness, cross-sectional area and photodeformation (photographs and displacement) of the TMAs as well as photographs and videos of the light-induced liquid motion were taken by a super-resolution digital microscope (Keyence, VHX-1000C). Visible light at 470 nm was obtained from an LED irradiator (CCS, HLV-24GR-3W). Attenuated 470-nm light was produced by placing a rectangular, continuously variable and metallic neutral density filter (Thorlabs, NDL-25C-4) in front of the 470-nm LED irradiator. The thermal effect of 470-nm light on the LLCP film was recorded by a thermal imaging camera (FLIR, E40). Contact angles (CAs) were measured on a contact angle analyser (Dataphysics OCA15) with 2  $\mu$ l measuring droplets. Dynamic contact angles were obtained with a DCAT 21 tensiometer (DataPhysics Instruments GmbH). In each case, a minimum of three samples were analysed to ensure reproducibility.





**Extended Data Figure 1 | Lamellar structure of the LLCP film.** **a**, AFM topographic image of the LLCP film. **b**, The line profile along the white line in **a**, showing that the thickness of one lamella and two lamellas is 4.38 nm and 8.53 nm, respectively.

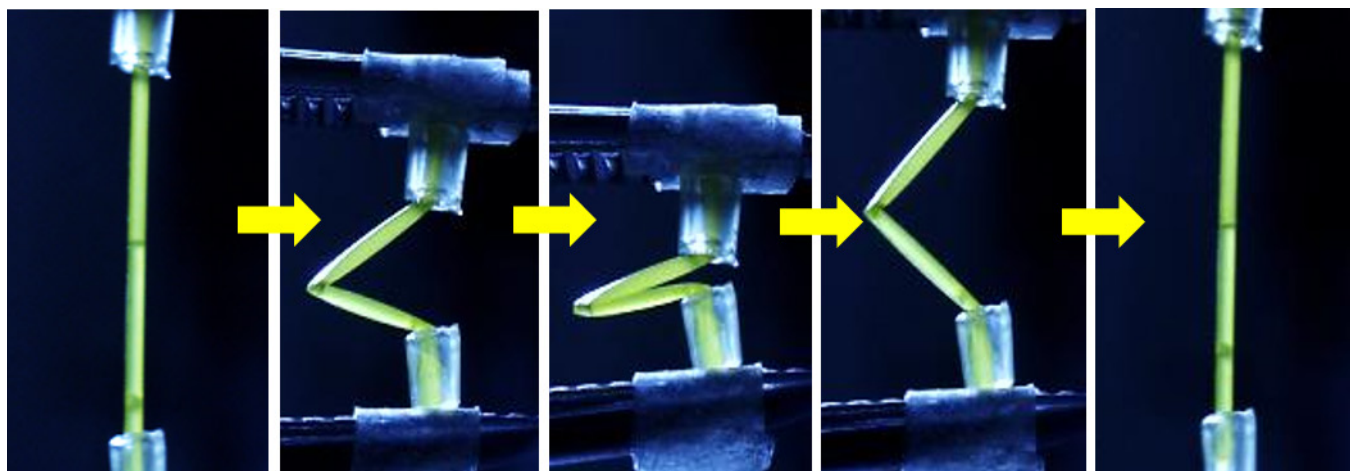


#### Extended Data Figure 2 | Mechanical properties of the LLCp.

**a**, Photographs showing preparation of the healed LLCp fibre. The two cut pieces of the fibre (left) were overlapped for a length of 5 mm and covered by two glass slides (middle). Then, the fixed fibres were put into an oven and heated for 1 h at 55 °C (right). **b**, Photographs demonstrating the strength of a virgin and healed LLCp fibre (left and right, respectively). The inset in the left photograph shows that the fibre has a clip at each end;

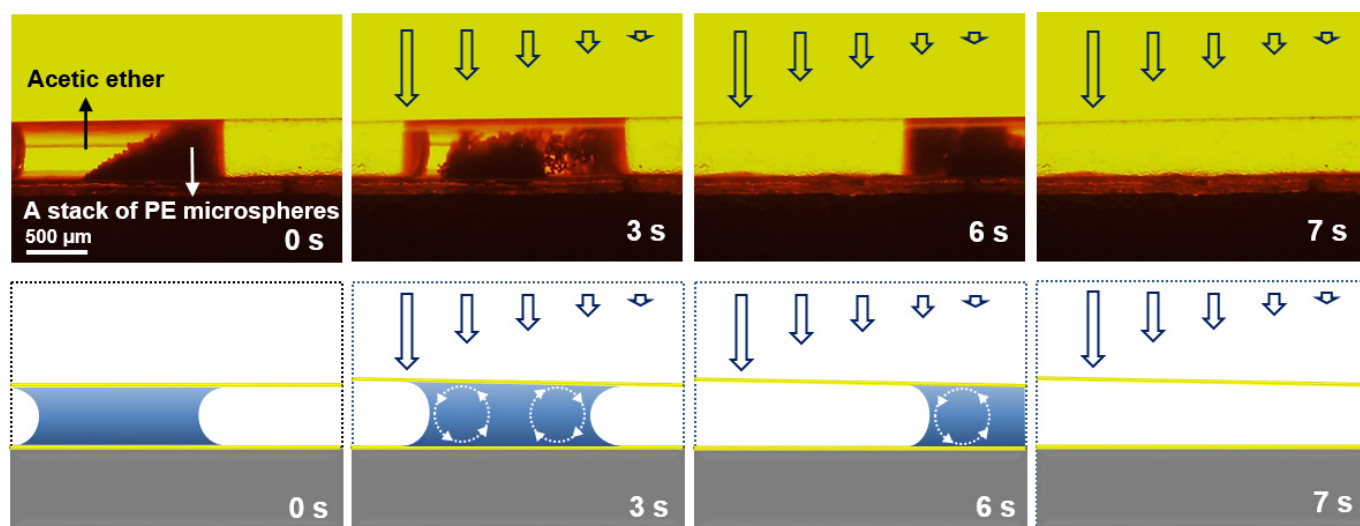
the upper clip is hung below an iron beam, and the bottom clip is loaded (weight  $w$ ) with many iron rings strung together by an iron wire. The healed fibre supports a load of 51.52 g, while the virgin fibre is loaded with 55.53 g. **c**, Photographs demonstrating the toughness of a LLCp fibre. The LLCp fibre was stretched to 22 times its initial length by a tensile machine (Instron model 5943) (Supplementary Video 2). Left, unstretched; right, stretched.





**Extended Data Figure 3 | Mechanical robustness of a tubular microactuator, TMA.** The sequence of photographs shows the unloaded TMA (left) buckling under an external force without damage. The buckled TMA (middle) spontaneously recovered its initial shape when the external

force was released (right). This buckling was repeated for 30 cycles without any damage to the TMA (Supplementary Video 3). The TMA was clipped between the tips of a pair of tweezers, and was buckled by the opening and closing of the tweezers. The diameter of the TMA is 0.5 mm.

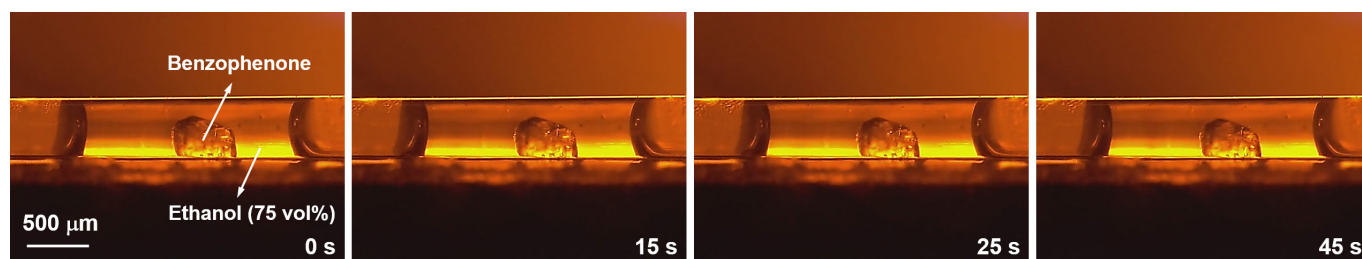


**Extended Data Figure 4 | Light-induced motion of a solid-liquid slug consisting of acetic ether and polyethylene microspheres.**

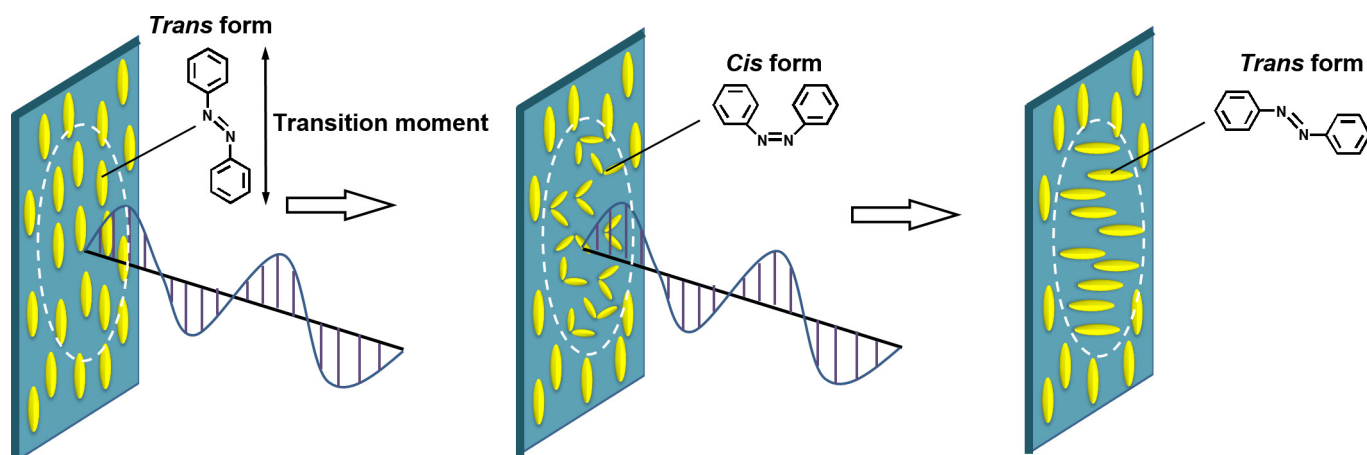
Top, a sequence of side-on photographs (at times of 0, 3, 6 and 7 s) showing the mixing of acetic ether (ethyl acetate) and PE (polyethylene) microspheres in the slug that occurs when the TMA photodeforms

(Part 4 in Supplementary Video 4). Bottom, schematic illustration of vortex circulation in the slug. The diameter of the polyethylene microspheres is  $\sim 35\ \mu\text{m}$ . The length of the open arrows denotes the intensity of 470-nm light.





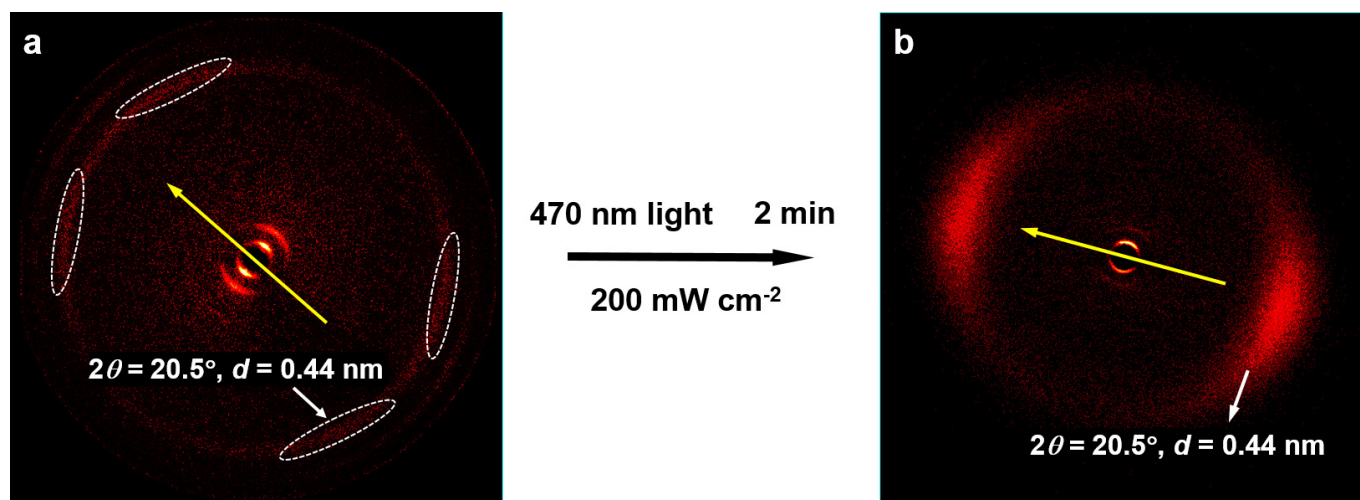
**Extended Data Figure 5 | Dissolution of benzophenone in ethanol through passive diffusion in the TMA.** This sequence of side-on photographs (at times 0, 15, 25 and 45 s) shows that benzophenone ( $\sim 0.03$  mg) within an ethanol ( $\sim 0.3$   $\mu$ l, 75 vol%) slug dissolves little over a period of 45 s without the light irradiation.



**Extended Data Figure 6 | Schematics demonstrating the mechanism of photoalignment of azobenzene mesogens under linear polarized blue light.** Left, *trans*-azobenzene molecules with their transition moments parallel to the polarization direction of the light are effectively activated to their excited states, which is followed by *trans*–*cis* isomerization (middle); but molecules with their transition moments perpendicular to the polarization direction of actinic light are inactive towards isomerization.

The *cis*–*trans* isomerization of azobenzene molecules is also induced by the light. After repetition of many *trans*–*cis*–*trans* isomerization cycles, *trans*-azobenzene molecules have reoriented to be perpendicular to the polarization direction of the actinic light, and hence inactive towards the incident radiation (right); this production of a net population of *trans*-azobenzene molecules aligned perpendicularly to the light polarization is known as the 'Weigert effect'.

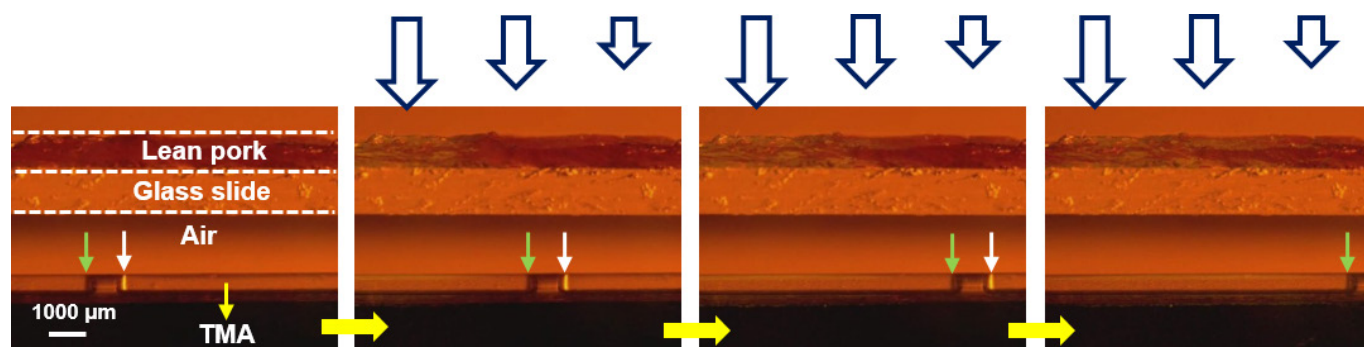




**Extended Data Figure 7 | Effect of irradiation on the 2D-WAXD patterns of the flat TMA wall cut and flattened out into a plane.**

**a, b**, Before (**a**) and after (**b**) irradiation. A higher intensity and a longer irradiation time of the 470-nm light are employed in this 2D-WAXD measurement compared with those in the experiments on light-induced liquid motion in the TMA, which ensures that most of the azobenzene

mesogens in the flat wall are reorientated along the light propagation direction. Thus, the 2D-WAXD signal of the flat wall is strong enough to be detected. The X-ray beam is applied from the lateral side of the wall and parallel to the plane of the wall.  $2\theta$  denotes the diffraction angle and  $d$  represents the lateral distance between the azobenzene mesogens. Yellow arrows denote the horizontal direction of the flat TMA wall.



**Extended Data Figure 8 | Light-driven liquid motion on irradiation by 470-nm light that has been attenuated by passing through lean pork.** The white and green arrows indicate the leading edge and the trailing edge of a silicone oil slug, respectively. The length of the open arrows denotes

the intensity of 470-nm light. The volume of the silicone oil slug is  $0.2\mu\text{l}$ ; the thickness of the lean pork and the glass slide is  $\sim 1\text{ mm}$  and  $1.2\text{ mm}$ , respectively. Part 6 of Supplementary Video 9 shows this process in full.



Extended Data Table 1 | Dynamic and static contact angles of different liquids on the LLCP film surface

Probe liquid	$\theta$ (°)	$\theta_a$ (°)	$\theta_r$ (°)	$\Delta\theta$ (°)
Silicone oil	0	0	0	0
Petroleum ether	0	0	0	0
Acetic ether	0	0	0	0
Hexane	0	0	0	0
Acetone	17.7±2.1	67.8±0.6	67.0±0.6	0.8±0.1
Isopropyl alcohol	14.6±3.8	69.2±1.0	69.2±1.1	0.1±0.1
Ethanol	17.5±3.6	69.8±1.2	68.3±1.0	1.5±0.2
Water	96.5±2.6	127.3±2.3	73.0±2.6	54.4±3.4

$\theta$ ,  $\theta_a$ ,  $\theta_r$ ,  $\Delta\theta$  represent static contact angle, advancing angle, receding angle and the difference between advancing angle and receding angle on flat LLCP films; data are from three individual measurements of each variable. Errors, s.d.

# Structure-based discovery of opioid analgesics with reduced side effects

Aashish Manglik<sup>1\*</sup>, Henry Lin<sup>2\*</sup>, Dipendra K. Aryal<sup>3\*</sup>, John D. McCorvy<sup>3</sup>, Daniela Dengler<sup>4</sup>, Gregory Corder<sup>5</sup>, Anat Levit<sup>2</sup>, Ralf C. Kling<sup>4,6</sup>, Viachaslau Bernat<sup>4</sup>, Harald Hübner<sup>4</sup>, Xi-Ping Huang<sup>3</sup>, Maria F. Sassano<sup>3</sup>, Patrick M. Giguère<sup>3</sup>, Stefan Löber<sup>4</sup>, Da Duan<sup>2</sup>, Grégory Scherrer<sup>1,5</sup>, Brian K. Kobilka<sup>1</sup>, Peter Gmeiner<sup>4</sup>, Bryan L. Roth<sup>3</sup> & Brian K. Shoichet<sup>2</sup>

**Morphine is an alkaloid from the opium poppy used to treat pain. The potentially lethal side effects of morphine and related opioids—which include fatal respiratory depression—are thought to be mediated by  $\mu$ -opioid-receptor ( $\mu$ OR) signalling through the  $\beta$ -arrestin pathway or by actions at other receptors. Conversely, G-protein  $\mu$ OR signalling is thought to confer analgesia. Here we computationally dock over 3 million molecules against the  $\mu$ OR structure and identify new scaffolds unrelated to known opioids. Structure-based optimization yields PZM21—a potent  $G_i$  activator with exceptional selectivity for  $\mu$ OR and minimal  $\beta$ -arrestin-2 recruitment. Unlike morphine, PZM21 is more efficacious for the affective component of analgesia versus the reflexive component and is devoid of both respiratory depression and morphine-like reinforcing activity in mice at equi-analgesic doses. PZM21 thus serves as both a probe to disentangle  $\mu$ OR signalling and a therapeutic lead that is devoid of many of the side effects of current opioids.**

Opiate addiction, compounded by the potentially lethal side effects of opiates such as respiratory depression, has driven optimization campaigns for safer and more effective analgesics since the 19th century. Although the natural products morphine and codeine, and the semi-synthetic drug heroin, are more reliably effective analgesics than raw opium, they retain its liabilities. The classification of opioid receptors into  $\mu$ ,  $\delta$ , and  $\kappa$  and nociception subtypes<sup>1,2</sup> raised hopes that subtype-specific molecules would lack the liabilities of morphinan-based opiates. Despite the introduction of potent synthetic opioid agonists like methadone and fentanyl, and the discovery of endogenous opioid peptides<sup>3</sup>, developing analgesics without the drawbacks of classic opioids has remained an elusive goal. Recent studies have suggested that opioid-induced analgesia results from

$\mu$ OR signalling through the G protein  $G_i$ , while many side effects, including respiratory depression and constipation, may be conferred via  $\beta$ -arrestin pathway signalling downstream of  $\mu$ OR activation (Fig. 1a)<sup>4–6</sup>. Agonists specific to the  $\mu$ OR and biased towards the  $G_i$  signalling pathway are therefore sought both as therapeutic leads and as molecular probes to understand  $\mu$ OR signalling. Recent progress has supported the feasibility and potential clinical utility of such biased  $\mu$ OR agonists<sup>7,8</sup>.

The determination of the crystal structures of the  $\mu$ ,  $\delta$ ,  $\kappa$  and nociceptin opioid receptors<sup>9–12</sup> (Fig. 1b, c) provided an opportunity to seek new  $\mu$ OR agonists via structure-based approaches. Recent discovery campaigns have used crystal structures of other Family A G-protein-coupled receptors (GPCRs) to computationally dock large libraries of

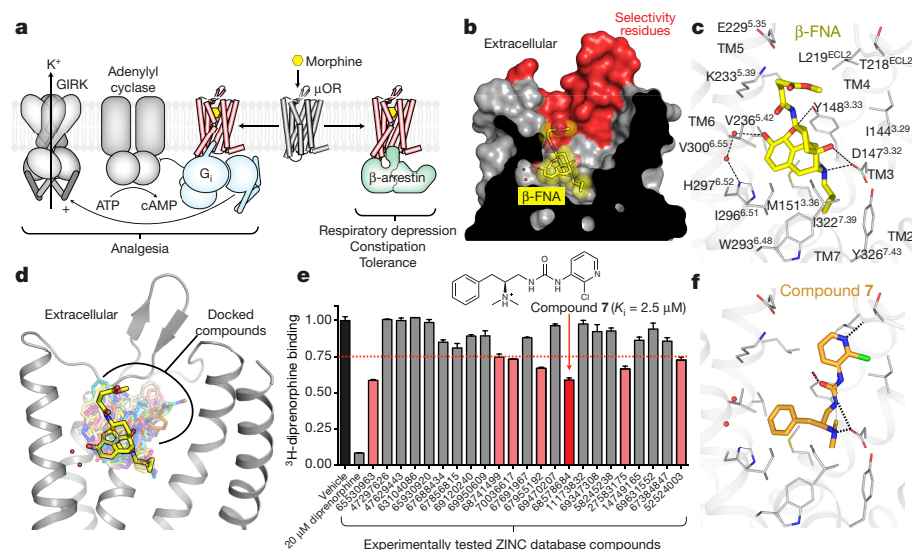


**Figure 1 | Structure based ligand discovery for the  $\mu$ OR.** **a**, Opiate-induced  $\mu$ OR signalling through  $G_i$  activates G-protein-gated inwardly rectifying potassium channels (GIRKs) and inhibits adenylyl cyclase, leading to analgesia. Conversely, recruitment of  $\beta$ -arrestin is implicated in tolerance, respiratory depression, and constipation. **b**, Cutaway of the  $\mu$ OR orthosteric site to which  $\beta$ -FNA binds. Highlighted regions on the extracellular side diverge between the opioid receptors. **c**, Conserved features of opioid ligand recognition in the  $\mu$ OR. **d**, Overlaid docking poses of 23 compounds selected for experimental testing. **e**, Single-point competition binding assay of 23 candidate molecules against the  $\mu$ OR antagonist  $^3$ H-diprenorphine. Each ligand was tested at 20  $\mu$ M and for those with  $>25\%$  inhibition affinity was calculated in full displacement curves; data represent mean  $\pm$  s.e.m. ( $n = 3$  measurements). One of these hits, compound 7, was subsequently optimized. **f**, Docking pose of compound 7.

<sup>1</sup>Department of Molecular and Cellular Physiology, Stanford University School of Medicine, Stanford, California 94305, USA. <sup>2</sup>Department of Pharmaceutical Chemistry, University of California, San Francisco, California 94158, USA. <sup>3</sup>Department of Pharmacology, UNC Chapel Hill Medical School, Chapel Hill, North Carolina 27514, USA. <sup>4</sup>Department of Chemistry and Pharmacy, Friedrich-Alexander-Universität Erlangen-Nürnberg, Schuhstraße 19, 91052 Erlangen, Germany. <sup>5</sup>Department of Anesthesiology, Perioperative and Pain Medicine, Neurosurgery, Stanford Neurosciences Institute, Stanford University School of Medicine, Stanford, California 94305, USA. <sup>6</sup>Institut für Physiologie und Pathophysiologie, Paracelsus Medical University, 90419 Nuremberg, Germany.

\*These authors contributed equally to this work.



molecules, identifying ligands with new scaffolds and with nanomolar-range potencies<sup>13–17</sup>. We thus targeted the  $\mu$ OR for structure-based docking, seeking ligands with new chemotypes. We reasoned that such new chemotypes might confer signalling properties with new biological effects, as has been true for other structure-based campaigns<sup>18,19</sup>.

### Structure-based docking to the $\mu$ OR

We docked over 3 million commercially available lead-like compounds<sup>20</sup> against the orthosteric pocket of inactive  $\mu$ OR<sup>9</sup>, prioritizing ligands that interact with known affinity-determining residues and with putative specificity residues that differ among the four opioid receptor subtypes (Fig. 1b, d). For each compound, an average of 1.3 million configurations was evaluated for complementarity to the receptor using the physics-based energy function<sup>21</sup> in DOCK3.6. As is common in docking<sup>22,23</sup> and screening, the top ranking molecules were inspected for features not explicitly captured in the scoring function. We manually examined the top 2,500 (0.08%) docked molecules for their novelty, their interactions with key polar residues such as Asp147<sup>3,32</sup> (superscripts indicate Ballesteros–Weinstein numbering<sup>24</sup>), and deprioritized those that showed conformational strain (a term occasionally poorly modelled by the scoring function). Ultimately, 23 high-scoring molecules with ranks ranging from 237 to 2,095 out of the over 3 million docked were selected for testing (Fig. 1e). Compared to the 5,215  $\mu$ OR ligands annotated in ChEMBL16<sup>25</sup>, these docking hits had Extended Connectivity Fingerprint 4 (ECFP4)-based Tanimoto coefficients ( $T_c$ ) ranging from 0.28 to 0.31, which is consistent with the exploration of novel scaffolds<sup>26</sup>. Of the 23 tested, seven had  $\mu$ OR binding affinities ( $K_i$ ) ranging from 2.3  $\mu$ M to 14  $\mu$ M (Extended Data Table 1, Extended Data Fig. 1).

The new ligands are predicted to engage the  $\mu$ OR in new ways (Fig. 1f and Extended Data Fig. 1). Most opioid ligands use a cationic amine to ion-pair with Asp147<sup>3,32</sup>, a canonical interaction<sup>27</sup> observed in structures of the  $\mu$ OR,  $\delta$ OR,  $\kappa$ OR and nociceptin receptor bound to

ligands of different scaffolds<sup>9–12,28</sup>. As anticipated, the docked ligands recapitulated this interaction. Much less precedence exists for the formation of an additional hydrogen bond with this anchor aspartate, often mediated in the docking poses by a urea amide. In several of the new ligands the urea carbonyl is modelled to hydrogen bond with Tyr148<sup>3,33</sup>, while the rest of the ligands often occupy sites unexplored by morphinans (Extended Data Fig. 1). To our knowledge, the double hydrogen bond coordination of Asp147<sup>3,32</sup> modelled in the docking poses has not been anticipated or observed previously for opioid ligands, and only 50 of the 5,215 annotated opioid ligands in ChEMBL16 contain a urea group.

Despite the structural novelty of the initial docking hits, their affinities were low. To enhance binding and selectivity, we docked 500 analogues of compounds 4, 5 and 7 that retained the key recognition groups but added packing substituents or extended further towards the extracellular side of the receptor, where the opioid receptors are more variable. Of the 15 top-scoring analogues that were tested, seven had  $K_i$  values between 42 nM and 4.7  $\mu$ M (Extended Data Table 2). Encouragingly, several were specific for the  $\mu$ OR over  $\kappa$ OR (compounds 12–15, Extended Data Table 2). We then investigated the more potent analogues for signalling potency and efficacy. Although the structure we docked against was the inactive state of the  $\mu$ OR, compounds 8 and 12–14 activated  $G_{i/o}$  (Extended Data Table 2). A similar enrichment for agonists was previously seen in a docking study against the inactive state of the  $\kappa$ OR<sup>23</sup>, perhaps reflecting the small changes in the orthosteric pocket associated with opioid receptor activation<sup>29</sup>. Encouragingly, the most potent compound, 12 (Fig. 2a, b), strongly activated  $G_{i/o}$  with low levels of  $\beta$ -arrestin-2 recruitment (Fig. 2c, d).

### Structure-guided synthetic optimization

To optimize compound 12, we synthesized stereochemically pure isomers and introduced a phenolic hydroxyl (Fig. 3a). The synthesis of the (S,S) stereoisomer of 12 improved affinity ( $K_i$ ) to 4.8 nM and had a signalling  $EC_{50}$  of 65 nM; it was the most potent and efficacious  $G_{i/o}$  signalling agonist among the four isomers (Fig. 3e). The phenolic hydroxyl, introduced to make compound (S,S)-21, was designed to exploit a water-mediated hydrogen bond with His297<sup>6,52</sup>, an interaction observed in the structure of  $\mu$ OR in complex with  $\beta$ -funaltrexamine ( $\beta$ -FNA) (Fig. 3b) and in other structures of the  $\delta$ OR<sup>28</sup> and  $\kappa$ OR<sup>11</sup>. This hydroxyl was readily accommodated in the docked  $\mu$ OR-12 complex, improving the predicted docking energy (Fig. 3c). Compound (S,S)-21 had an  $EC_{50}$  of 4.6 nM in a  $G_{i/o}$  activation assay, with 76% efficacy (Fig. 3f), and a  $K_i$  of 1.1 nM in radioligand binding assays (Extended Data Table 3), an improvement of 40-fold versus 12. The other three stereoisomers of (S,S)-21 were much less potent or efficacious (Extended Data Fig. 2a, b), suggesting a specific stereochemical requirement for both potency and efficacy in agreement with the docked poses of (S,S)-21 to the inactive and active structures<sup>29</sup> of  $\mu$ OR (Fig. 3c, Extended Data Fig. 2c, d). We refer to (S,S)-21 as compound PZM21 henceforth.

Because PZM21 was discovered against the inactive structure of  $\mu$ OR, its docked complex to active  $\mu$ OR retains ambiguities. To investigate its receptor-bound structure further, more detailed docking and molecular dynamics simulations were conducted. The resulting model was tested by synthesizing molecules that either perturbed or exploited specific modelled interactions (Fig. 3c, d, Extended Data Figs 2 and 3). Neutralization of charge by amidation (compound PZM28) decreases potency by 1,000-fold, supporting a key ionic interaction between the PZM21 tertiary amine and Asp147<sup>3,32</sup> (Fig. 3d and Extended Data Fig. 3). Compound PZM27, which adds steric bulk to the tertiary amine, was synthesized to disrupt putative hydrophobic interactions between the *N*-methyl group and Met151<sup>3,36</sup> and Trp293<sup>6,48</sup>, consistent with its 30-fold loss of potency and decreased efficacy (Fig. 3d and Extended Data Fig. 3). Compounds PZM23, PZM24 and PZM25, which were synthesized to disrupt hydrogen bonding interactions in the model between the urea and Asp147<sup>3,32</sup>, Tyr326<sup>7,43</sup> and Gln124<sup>2,60</sup>,

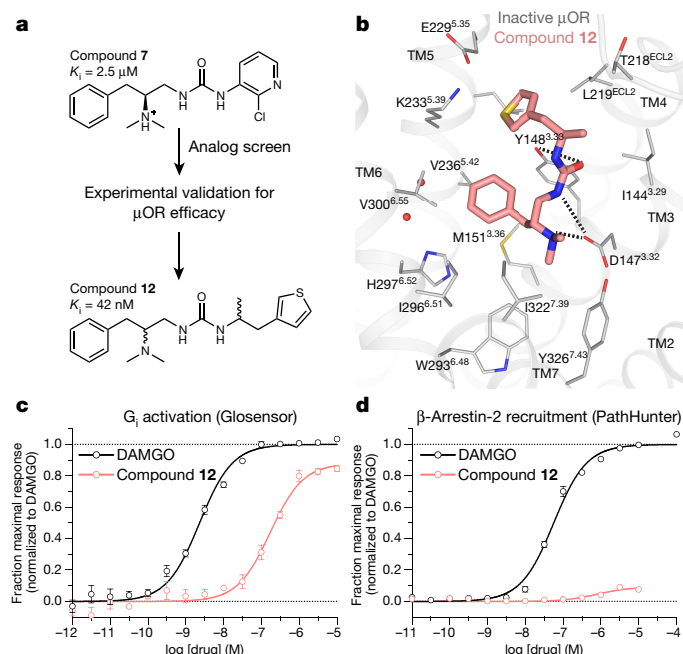
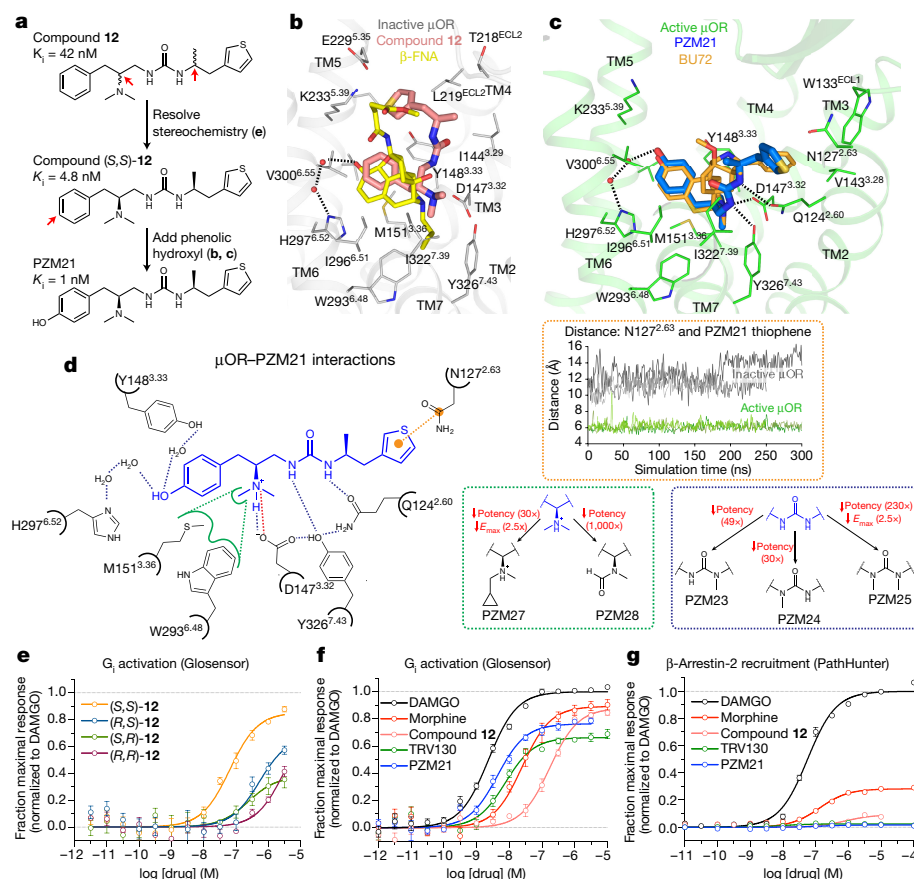


**Figure 2 | Discovery of a novel  $G_{i/o}$ -biased  $\mu$ OR agonist.** **a**, Compound 12 was identified among a series of analogues to compound 7 and further investigated due to its  $\mu$ OR specificity and efficacy as a  $\mu$ OR agonist. **b**, Docking pose of Compound 12. **c**, Compound 12 is a  $\mu$ OR agonist in a  $G_{i/o}$  signalling assay with an  $EC_{50}$  of 180 nM. DAMGO is a prototypical unbiased opioid agonist. **d**, Despite robust activation of  $G_{i/o}$ , compound 12 induces minimal arrestin recruitment as compared to DAMGO. For **c**, **d**, data are mean  $\pm$  s.e.m. of normalized results ( $n = 3$ –6 measurements).

**Figure 3 | Structure-guided optimization towards a potent biased  $\mu$ OR agonist.**

**a**, Structure guided optimization towards PZM21. **b**, Docking pose of **12** compared to  $\beta$ -FNA. The phenolic hydroxyl of  $\beta$ -FNA coordinates His297<sup>6.52</sup> with two water molecules, providing an optimization strategy for **12**. **c**, PZM21 docked to active  $\mu$ OR with a water-mediated network between the PZM21 phenol and His297<sup>6.52</sup>. The co-crystallized agonist BU72 is shown as orange sticks. **d**,  $\mu$ OR–PZM21 interactions include hydrogen bonds (blue dash), hydrophobic interactions (green dash), and an ionic bond (red dash). Insets show select data from structure–activity relationship and molecular dynamics studies presented in more detail in Extended Data. **e**, Stereoisomers of **12** in a  $G_{i/o}$  signalling assay. **f**,  $G_{i/o}$  signalling assay shows robust  $\mu$ OR agonist activity for PZM21. **g**, PZM21 shows undetectable  $\beta$ -arrestin-2 recruitment in the PathHunter assay. For **e–g**, data are mean  $\pm$  s.e.m. of normalized results ( $n = 3–6$  measurements).



lose between 30- and 230-fold potency despite their decreased solvation penalties (Fig. 3d and Extended Data Fig. 3). These key ionic and hydrogen-bonding interactions are maintained for 3  $\mu$ s of molecular dynamics simulations of PZM21 in complex with active  $\mu$ OR, as are interactions between the phenolic hydroxyl and the bridging waters to His297<sup>6.52</sup>, further supporting their relevance to the modelled pose (Extended Data Fig. 2g). The thiophene of PZM21, modelled to fit in the more open specificity region of the  $\mu$ OR, can be replaced with a larger benzothiophene without loss of potency (Extended Data Fig. 3). Interactions of this thiophene with residues that differ among the opioid receptor sub-types may contribute to PZM21 specificity (Extended Data Fig. 2e). More compellingly, the simulations and docking predict that the PZM21 thiophene comes within 6 Å of Asn127<sup>2.63</sup> in the active  $\mu$ OR (Extended Data Fig. 2g). Accordingly, we synthesized an irreversible version of PZM21 (compound PZM29) designed to form a covalent bond with  $\mu$ OR engineered with an N127C mutation. Compound PZM29 binds irreversibly to this mutant but not the wild-type receptor and retains its efficacy as an agonist (Extended Data Fig. 3), supporting the overall orientation of PZM21 as modelled and simulated in the orthosteric  $\mu$ OR site.

### PZM21 is a selective $G_i$ -biased $\mu$ OR agonist

PZM21 had no detectable  $\kappa$ OR or nociceptin receptor agonist activity—it is actually an 18 nM  $\kappa$ OR antagonist—while it is a 500-fold weaker  $\delta$ OR agonist (Extended Data Fig. 4 and Extended Data Table 3), making it a selective  $\mu$ OR agonist. To investigate specificity more broadly, PZM21 was counter-screened for agonism against 316 other GPCRs<sup>30</sup>. Activity at 10  $\mu$ M was observed at several peptide and protein receptors; however, no potent activity was confirmed with a full dose–response experiment at these receptors. PZM21 therefore has high agonist specificity among GPCRs (Extended Data Fig. 5a–c). PZM21 was also tested for inhibition of the hERG ion channel and the dopamine, norepinephrine and serotonin neurotransmitter transporters. At hERG, PZM21 had an  $IC_{50}$  of between 2 and 4  $\mu$ M,

500- to 1,000-fold weaker than its potency as a  $\mu$ OR agonist (Extended Data Fig. 5d). Its inhibition of the neurotransmitter transporters, which are also analgesia targets, was even weaker with  $IC_{50}$  values ranging from 7.8 to 34  $\mu$ M (Extended Data Fig. 5e). Thus, PZM21 is a potent, selective, and efficacious  $\mu$  opioid agonist.

A major goal of this study was to find new chemotypes that might display biased signalling and perhaps, unlike canonical opioid drugs, have more favourable *in vivo* profiles. Signalling by PZM21 and other  $\mu$ OR agonists appears to be mediated primarily by the heterotrimeric G protein  $G_{i/o}$ , as its effect on cAMP levels was eliminated by pertussis toxin and no activity was observed in a calcium release assay (Extended Data Fig. 6a–d). A maximal concentration of PZM21 led to no detectable  $\beta$ -arrestin-2 recruitment in the PathHunter assay (DiscoverRx) (Fig. 3g and Extended Data Fig. 6c) and a minimal level of  $\mu$ OR internalization compared to DAMGO and morphine (Extended Data Fig. 6e). Indeed,  $\beta$ -arrestin-2 recruitment was too low to even permit a formal calculation of bias<sup>31</sup>, which quantifies the preference for one signalling pathway over another. Since  $\beta$ -arrestin recruitment can depend on the expression level of G protein-coupled receptor kinase 2 (GRK2)<sup>32</sup>, we also investigated  $G_{i/o}$  signalling and arrestin recruitment in cells co-transfected with this kinase. Even in the presence of overexpressed GRK2, PZM21 still has weak arrestin recruitment efficacy compared to DAMGO and even to morphine (Extended Data Fig. 6g–i). In fact, the signalling bias of PZM21 was undistinguishable from TRV130, a  $G_i$ -biased opioid agonist now in Phase III clinical trials (Fig. 3f, g), whereas its G-protein-bias substantially exceeded that of herkinorin, which has also been purported to be a  $G_i$ -biased agonist<sup>33</sup> (Extended Data Fig. 6). An intriguing distinction in these signalling studies is the lack of agonist activity of PZM21 at  $\kappa$ OR. While PZM21 is an 18-nM antagonist of this receptor, the other biased agonist, TRV130, activates  $\kappa$ OR with similar potency to morphine (Extended Data Fig. 6f). Additionally, despite having similar levels of signalling bias, in modelling studies TRV130 and PZM21 appear to engage the  $\mu$ OR in distinct ways (Extended Data Fig. 2f).

## Analgesia with diminished side effects

Consistent with its  $\mu$ OR agonist activity, PZM21 displayed dose-dependent analgesia in a mouse hotplate assay, with a per cent maximal possible effect (% MPE) of 87% reached 15 min after administration of the highest dose of drug tested (Fig. 4a). The highest dose of morphine tested plateaued at 92% after 30 min. Intriguingly, we observed no analgesic effect for PZM21 in the tail-flick assay (Fig. 4b). Such a distinction is unprecedented among opioid analgesics. The hotplate experiment assesses analgesia at both higher-level central nervous system (CNS) brain and spinal nociceptive circuits, while the tail-flick experiment is more specific for spinal reflexive responses<sup>34</sup>. Subcategorizing the behavioural responses in the hotplate experiment as either affective (CNS mediated) or reflexive (spinally mediated) showed that, unlike morphine, PZM21 solely confers analgesia to the affective component of pain (Fig. 4c and Extended Data Fig. 7a, b). Though separation of these two analgesic pathways is unique to PZM21 among known opioid analgesics, it has been observed by selective chemogenetic activation<sup>35</sup> or toxin-induced inactivation of CNS neurons in rodents<sup>36</sup>. Indeed, PZM21 is also active in a formalin injection nociception assay, likely from supraspinal activation of descending inhibitory circuits<sup>37</sup> (Fig. 4d). Whether this circuit-specificity reflects the biased signalling of PZM21, its specificity for the  $\mu$ OR versus other opioid receptors and other GPCRs, an unusual CNS distribution phenomenon, or some other signalling property, is uncertain at this time.

More certain is that PZM21 analgesia results from  $\mu$ OR activation *in vivo* as genetic knockout of the  $\mu$ OR completely ablates the observed analgesic response in the hotplate assay (Fig. 4e). Meanwhile, PZM21 is metabolized relatively slowly by mouse liver microsomes, with only 8% metabolism over one hour. Signalling experiments with the resulting metabolite pool show no evidence of a metabolite with more potent activation of the  $\mu$ OR, confirming that the observed analgesic activity results primarily from the originally administered dose of PZM21 (Extended Data Fig. 7e, f).

Based on previous genetic studies with arrestin knockout mice and pharmacological studies with biased compounds<sup>4–7</sup>, we anticipated that PZM21 would confer longer-lasting analgesia with decreased respiratory depression and constipation—both key dose-limiting side-effects of classic opioid agonists. Analgesia induced by PZM21 lasts up to 180 min, substantially longer than that induced by a maximal dose of morphine (Extended Data Fig. 7a, b) and the biased agonist TRV130 (Fig. 4a). Whereas PZM21 does reduce defecation, its constipating effect is substantially less than morphine (Fig. 4f). Respiratory depression was investigated by dosing unrestrained mice with equi-analgesic doses of PZM21, TRV130 and morphine ( $40 \text{ mg kg}^{-1}$ ,  $1.2 \text{ mg kg}^{-1}$ , and  $10 \text{ mg kg}^{-1}$ , respectively), and measuring respiration by whole-body plethysmography. While morphine profoundly depressed respiration frequency, PZM21 was almost undistinguishable from vehicle (Fig. 4g). By comparison, TRV130 significantly depresses respiration

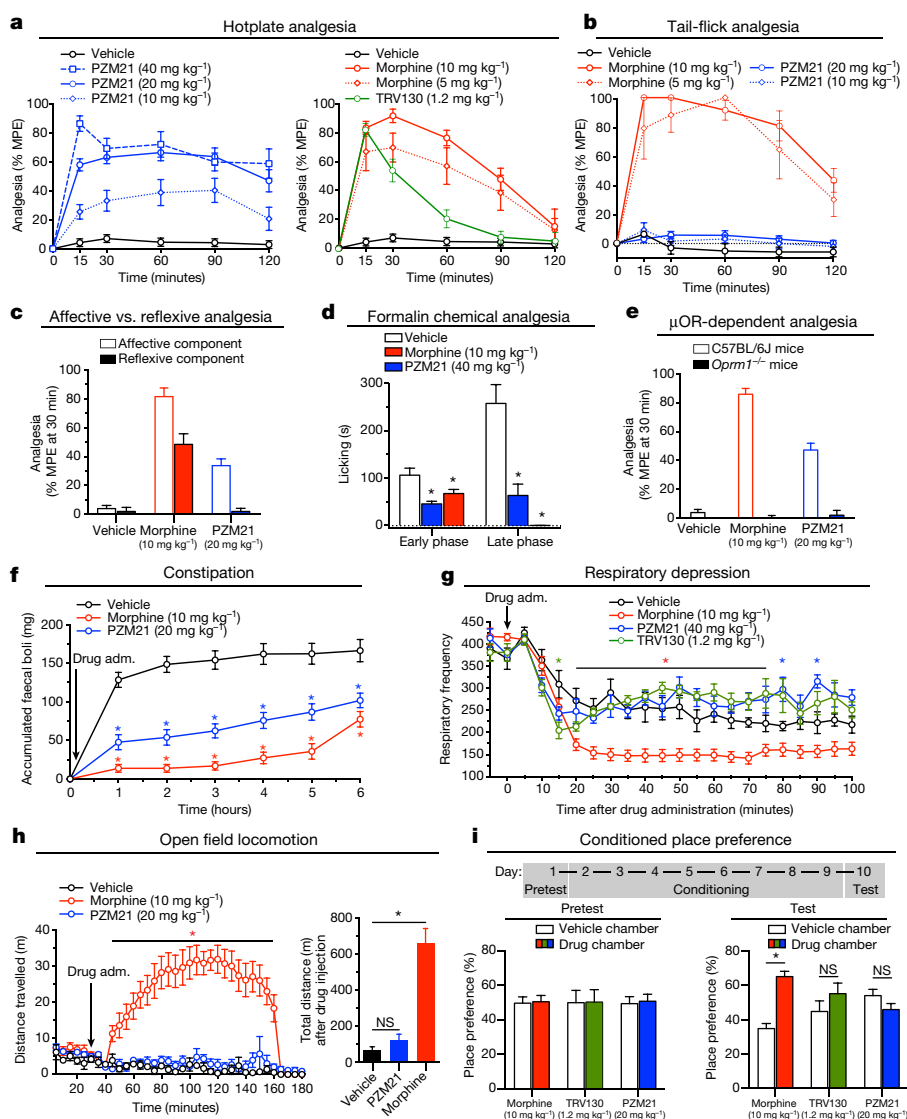


**Figure 4 | PZM21 is an analgesic with reduced on-target liabilities.**

**a**, Analgesia in the mouse hotplate assay. Latency of withdrawal to noxious stimuli is shown as percentage of the maximal possible effect (% MPE). The highest dose of PZM21 ( $40 \text{ mg kg}^{-1}$ ) yields an equi-analgesic response to  $10 \text{ mg kg}^{-1}$  morphine and  $1.2 \text{ mg kg}^{-1}$  TRV130 at 15 min. **b**, Compared to morphine, PZM21 shows no analgesia in the tail-flick assay. **c**, Unlike morphine, PZM21 decreases affective pain perception with minimal effect on reflexive pain. **d**, PZM21 and morphine produce sustained analgesia in a formalin injection nociception assay. **e**, PZM21 shows no analgesic effect in *Oprm1*<sup>-/-</sup> mice, supporting engagement of  $\mu$ OR *in vivo*. **f**, Constipatory effects of morphine and PZM21 compared to vehicle assessed by accumulated faecal boli. **g**, Whole-body mouse plethysmography shows decrease in respiratory frequency for morphine starting 20 min after administration of drug. An equi-analgesic dose of PZM21 has no effect on respiration versus vehicle, while TRV130 induces transient respiratory depression at 15 min. **h**, Open field locomotor assay. **i**, Place preference is induced by conditioning with  $10 \text{ mg kg}^{-1}$  morphine but not with  $20 \text{ mg kg}^{-1}$  PZM21 nor with  $1.2 \text{ mg kg}^{-1}$  TRV130. Per cent of time spent in either vehicle or drug chamber before (pretest) or after (test) conditioning regimen. All data are mean  $\pm$  s.e.m. and asterisks indicate statistically significant differences between drug and vehicle. The number of animals in each group and statistical tests are described in the Methods.



at 15 min, correlating with its peak analgesic response. Although respiratory depression by  $\mu$ OR may be partially mediated by activation of G-protein-coupled inwardly rectifying potassium channels (GIRKs), systemically infused opioids can decrease respiratory frequency even in GIRK-deficient mice<sup>38</sup>, consistent with the G-protein-independent signalling mechanisms first suggested by the arrestin knockout studies<sup>4–6</sup>. The rapid respiratory depression observed for morphine and TRV130 may reflect GIRK activation. At later time points, however, PZM21 induces minimal respiratory depression despite providing robust analgesia. Conversely, morphine induces a prolonged course of respiratory depression that does not subside with resolution of the analgesic response at 90 min. This dissociation in analgesia and respiratory depression at later time points may reflect differential recruitment of  $\beta$ -arrestin-2. Taken together, these studies support minimal  $\beta$ -arrestin-2 signalling *in vivo* by PZM21 (biased signalling, Fig. 1a).

A major liability of current opioid analgesics is reinforcement and addiction, which are both postulated to be mediated—at least in part—by activation of the dopaminergic reward circuits<sup>39</sup>. A biomarker for such activation in mice is an acute hyperlocomotive response, reflecting mesolimbic dopaminergic activation<sup>40</sup>. Whereas morphine induced mouse hyperlocomotion in an open-field assay (Fig. 4h), a nearly equi-analgesic dose of PZM21 had no apparent effect on locomotion versus vehicle. The decreased distance travelled does not reflect a cataleptic effect of PZM21 (Extended Data Fig. 7c). Consistent with decreased activation of reward circuits, administration of PZM21 also does not induce a conditioned place preference response (Fig. 4i), unlike morphine and other opioids<sup>41</sup>. Though TRV130 does trend more towards inducing place preference, its activity is also not significant relative to vehicle; this lack of conditioned place preference for both biased agonists may support a role for G-protein bias in the lack of opioid-induced reinforcing behaviour. The differences between morphine and PZM21 in conditioned place preference do not simply reflect dissimilarities in CNS penetration between the two drugs, as a substantial fraction of PZM21 crosses the blood–brain barrier (Extended Data Fig. 7d).

Several caveats deserve to be mentioned. Although structure-based discovery succeeded in finding novel scaffolds and supported facile optimization, some of the properties of PZM21 were likely fortuitous. Biased signalling through G protein and arrestin pathways reflects the stabilization of conformations over 30 Å from the orthosteric site where PZM21 binds. We did not select molecules that preferentially stabilize these conformations, but instead relied on chemical novelty to confer new biological properties. Receptor subtype selectivity was attained by simply selecting molecules that extended into variable regions of the receptor, a strategy that may not always work. Several aspects of the pharmacology presented here remain preliminary, including the metabolic stability studies and the pharmacokinetics, and it is not clear at this time whether the unprecedented *in vivo* activity of PZM21 reflects its biased and specific agonism, or some other feature conferred by its novel chemotype. Finally, identification of agonists from docking to an inactive state receptor structure cannot always be relied upon<sup>13,16,42,43</sup>, though there is precedence for doing so against opioid receptors<sup>23</sup>.

## Discussion

Notwithstanding these caveats, this study supports a structure-based approach for GPCR ligand discovery. Whereas this method cannot yet reliably find leads with tailored specificity and signalling efficacy, it can reliably identify entirely new scaffolds and chemotypes. These new chemotypes may stabilize receptor conformations not explored previously and so generate novel biological effects. With a novel chemotype in hand, the docked structure provides a straight-forward strategy for optimization. Here, we optimized an initial docking hit, compound 7, 1,000-fold to the final lead molecule, PZM21, by evaluating fewer than 50 molecules. Though this campaign was inspired by existing  $\mu$ OR-biased agonists like TRV130<sup>7</sup>, the structure-based approach led

to a compound with novel properties; it was structurally distinct compared to previously explored opioid ligands, with not only substantial signalling bias but also with unexpected opioid receptor selectivity. These features have contributed to favourable biological effects, with long-lasting analgesia coupled to apparent elimination of respiratory depression, specificity for central over reflex analgesia, lack of locomotor potentiation and conditioned place preference, and hence a reduced potential for opioid-induced reinforcement for PZM21 and molecules like it. The selectivity, potency, and biased signalling of PZM21 make it a tool molecule of a sort previously unavailable to interrogate  $\mu$ OR signalling. More broadly, the *in vitro* results of multiple GPCR campaigns, and the *in vivo* results reported here, portend a general approach to the problem of new tool and lead discovery for this pharmacologically important family of receptors.

**Online Content** Methods, along with any additional Extended Data display items and Source Data, are available in the online version of the paper; references unique to these sections appear only in the online paper.

**Received 25 November 2015; accepted 14 July 2016.**

**Published online 17 August 2016.**

1. Lord, J. A. H., Waterfield, A. A., Hughes, J. & Kosterlitz, H. W. Endogenous opioid peptides: multiple agonists and receptors. *Nature* **267**, 495–499 (1977).
2. Martin, W. R., Eades, C. G., Thompson, J. A., Huppler, R. E. & Gilbert, P. E. The effects of morphine- and nalorphine-like drugs in the nondependent and morphine-dependent chronic spinal dog. *J. Pharmacol. Exp. Ther.* **197**, 517–532 (1976).
3. Hughes, J. *et al.* Identification of two related pentapeptides from the brain with potent opiate agonist activity. *Nature* **258**, 577–580 (1975).
4. Bohn, L. M., Gainetdinov, R. R., Lin, F.-T., Lefkowitz, R. J. & Caron, M. G.  $\mu$ -opioid receptor desensitization by  $\beta$ -arrestin-2 determines morphine tolerance but not dependence. *Nature* **408**, 720–723 (2000).
5. Bohn, L. M. *et al.* Enhanced morphine analgesia in mice lacking  $\beta$ -arrestin 2. *Science* **286**, 2495–2498 (1999).
6. Raehal, K. M., Walker, J. K. & Bohn, L. M. Morphine side effects in  $\beta$ -arrestin 2 knockout mice. *J. Pharmacol. Exp. Ther.* **314**, 1195–1201 (2005).
7. DeWire, S. M. *et al.* A G protein-biased ligand at the  $\mu$ -opioid receptor is potently analgesic with reduced gastrointestinal and respiratory dysfunction compared with morphine. *J. Pharmacol. Exp. Ther.* **344**, 708–717 (2013).
8. Soergel, D. G. *et al.* Biased agonism of the  $\mu$ -opioid receptor by TRV130 increases analgesia and reduces on-target adverse effects versus morphine: a randomized, double-blind, placebo-controlled, crossover study in healthy volunteers. *Pain* **155**, 1829–1835 (2014).
9. Manglik, A. *et al.* Crystal structure of the  $\mu$ -opioid receptor bound to a morphinan antagonist. *Nature* **485**, 321–326 (2012).
10. Granier, S. *et al.* Structure of the  $\delta$ -opioid receptor bound to naltrindole. *Nature* **485**, 400–404 (2012).
11. Wu, H. *et al.* Structure of the human  $\kappa$ -opioid receptor in complex with JDTic. *Nature* **485**, 327–332 (2012).
12. Thompson, A. A. *et al.* Structure of the nociceptin/orphanin FQ receptor in complex with a peptide mimetic. *Nature* **485**, 395–399 (2012).
13. Carlsson, J. *et al.* Ligand discovery from a dopamine D3 receptor homology model and crystal structure. *Nat. Chem. Biol.* **7**, 769–778 (2011).
14. de Graaf, C. *et al.* Crystal structure-based virtual screening for fragment-like ligands of the human histamine H<sub>1</sub> receptor. *J. Med. Chem.* **54**, 8195–8206 (2011).
15. Katritch, V. *et al.* Structure-based discovery of novel chemotypes for adenosine A<sub>2A</sub> receptor antagonists. *J. Med. Chem.* **53**, 1799–1809 (2010).
16. Kolb, P. *et al.* Structure-based discovery of  $\beta_2$ -adrenergic receptor ligands. *Proc. Natl Acad. Sci. USA* **106**, 6843–6848 (2009).
17. Langmead, C. J. *et al.* Identification of novel adenosine A<sub>2A</sub> receptor antagonists by virtual screening. *J. Med. Chem.* **55**, 1904–1909 (2012).
18. Powers, R. A., Morandi, F. & Shoichet, B. K. Structure-based discovery of a novel, noncovalent inhibitor of AmpC  $\beta$ -lactamase. *Structure* **10**, 1013–1023 (2002).
19. Huang, X. P. *et al.* Allosteric ligands for the pharmacologically dark receptors GPR68 and GPR65. *Nature* **527**, 477–483 (2015).
20. Irwin, J. J., Sterling, T., Mysinger, M. M., Bolstad, E. S. & Coleman, R. G. ZINC: a free tool to discover chemistry for biology. *J. Chem. Inf. Model.* **52**, 1757–1768 (2012).
21. Mysinger, M. M. & Shoichet, B. K. Rapid context-dependent ligand desolvation in molecular docking. *J. Chem. Inf. Model.* **50**, 1561–1573 (2010).
22. Mysinger, M. M. *et al.* Structure-based ligand discovery for the protein–protein interface of chemokine receptor CXCR4. *Proc. Natl Acad. Sci. USA* **109**, 5517–5522 (2012).
23. Negri, A. *et al.* Discovery of a novel selective kappa-opioid receptor agonist using crystal structure-based virtual screening. *J. Chem. Inf. Model.* **53**, 521–526 (2013).

24. Ballesteros, J. A. & Weinstein, H. Integrated methods for the construction of three-dimensional models and computational probing of structure-function relations in G protein-coupled receptors. *Methods in Neurosciences* **25**, 366–428 (1995).
25. Gaulton, A. *et al.* ChEMBL: a large-scale bioactivity database for drug discovery. *Nucleic Acids Res.* **40**, D1100–D1107 (2012).
26. Muchmore, S. W. *et al.* Application of belief theory to similarity data fusion for use in analog searching and lead hopping. *J. Chem. Inf. Model.* **48**, 941–948 (2008).
27. Pasternak, G. W. & Pan, Y.-X.  $\mu$  opioids and their receptors: evolution of a concept. *Pharmacol. Rev.* **65**, 1257–1317 (2013).
28. Fenalti, G. *et al.* Structural basis for bifunctional peptide recognition at human  $\delta$ -opioid receptor. *Nat. Struct. Mol. Biol.* **22**, 265–268 (2015).
29. Huang, W. *et al.* Structural insights into  $\mu$ -opioid receptor activation. *Nature* **524**, 315–321 (2015).
30. Kroeze, W. K. *et al.* PRESTO-Tango as an open-source resource for interrogation of the druggable human GPCRome. *Nat. Struct. Mol. Biol.* **22**, 362–369 (2015).
31. Kenakin, T. & Christopoulos, A. Signalling bias in new drug discovery: detection, quantification and therapeutic impact. *Nat. Rev. Drug Discov.* **12**, 205–216 (2013).
32. Nickolls, S. A., Humphreys, S., Clark, M. & McMurray, G. Co-expression of GRK2 reveals a novel conformational state of the  $\mu$ -opioid receptor. *PLoS One* **8**, e83691 (2013).
33. Groer, C. E. *et al.* An opioid agonist that does not induce  $\mu$ -opioid receptor–arrestin interactions or receptor internalization. *Mol. Pharmacol.* **71**, 549–557 (2007).
34. Le Bars, D., Gozariu, M. & Cadden, S. W. Animal models of nociception. *Pharmacol. Rev.* **53**, 597–652 (2001).
35. Li, C. *et al.*  $\mu$  opioid receptor modulation of dopamine neurons in the periaqueductal gray/dorsal raphe: a role in regulation of pain. *Neuropsychopharmacology* **41**, 2122–2132 (2016).
36. Han, S., Soleiman, M. T., Soden, M. E., Zweifel, L. S. & Palmiter, R. D. Elucidating an affective pain circuit that creates a threat memory. *Cell* **162**, 363–374 (2015).
37. Gogas, K. R., Presley, R. W., Levine, J. D. & Basbaum, A. I. The antinociceptive action of supraspinal opioids results from an increase in descending inhibitory control: correlation of nociceptive behavior and c-fos expression. *Neuroscience* **42**, 617–628 (1991).
38. Montandon, G. *et al.* G-protein-gated inwardly rectifying potassium channels modulate respiratory depression by opioids. *Anesthesiology* **124**, 641–650 (2016).
39. Spanagel, R., Herz, A. & Shippenberg, T. S. Opposing tonically active endogenous opioid systems modulate the mesolimbic dopaminergic pathway. *Proc. Natl Acad. Sci. USA* **89**, 2046–2050 (1992).
40. Bohn, L. M. *et al.* Enhanced rewarding properties of morphine, but not cocaine, in  $\beta$ (arrestin)-2 knock-out mice. *J. Neurosci.* **23**, 10265–10273 (2003).
41. Tszschentke, T. M. Measuring reward with the conditioned place preference paradigm: a comprehensive review of drug effects, recent progress and new issues. *Prog. Neurobiol.* **56**, 613–672 (1998).
42. Weiss, D. R. *et al.* Conformation guides molecular efficacy in docking screens of activated  $\beta$ -2 adrenergic G protein coupled receptor. *ACS Chem. Biol.* **8**, 1018–1026 (2013).
43. Carlsson, J. *et al.* Structure-based discovery of A2A adenosine receptor ligands. *J. Med. Chem.* **53**, 3748–3755 (2010).

**Supplementary Information** is available in the online version of the paper.

**Acknowledgements** Supported by the US National Institutes of Health grants GM106990 (B.K.K., B.K.S. and P.G.), DA036246 (B.K.K.), GM59957 (B.K.S.), and the National Institutes of Mental Health Psychoactive Drug Screening Program (B.L.R.) and DA017204 (B.L.R., D.A.), DA035764 (B.L.R.) and the Michael Hooker Distinguished Professorship (B.L.R.) and the German Research Foundation Grants Gm 13/10 and GRK 1910 (P.G.). A.M. received support from the Stanford University Medical Scientist Training Program (T32GM007365) and the American Heart Association (12PRE8120001).

**Author Contributions** A.M. and H.L. initiated the project. H.L. performed docking and identified compounds to be tested in the initial and analogue screens. A.M. performed binding studies to identify initial hits and devised structure-guided optimization strategies for subsequent analogues. D.K.A. performed *in vivo* studies, including analgesia assays, mouse plethysmography, faecal boli accumulation studies, open field locomotor assay, and conditioned place preference. J.D.M., M.F.S. and P.M.G. performed radioligand binding and signalling studies. X.P.H. performed signalling studies and assessed compound activity against the GPCRome. D.De., V.B., S.L. and H.H. synthesized compounds and determined affinities by radioligand binding and performed signalling studies. A.L. and A.M. docked PZM21 and TRV130 and R.C.K. simulated PZM21 binding to  $\mu$ OR. G.C. performed reflexive and affective analgesia studies of  $\mu$ OR knockout mice and was supervised by G.S. D.Du. performed pharmacokinetic studies. The manuscript was written by A.M., H.L. and B.K.S. with editing and suggestions from B.L.R. and input from D.K.A., B.K.K. and P.G. P.G. supervised chemical synthesis of compounds and the separation and identification of diastereomers, B.K.K. supervised testing of initial docking hits, B.L.R. supervised radioligand binding, signalling and *in vivo* studies and B.K.S. supervised the compound discovery and design. The project was conceived by A.M., H.L., B.K.K., P.G., B.K.S. and B.L.R.

**Author Information** Reprints and permissions information is available at [www.nature.com/reprints](http://www.nature.com/reprints). The authors declare competing financial interests: details are available in the online version of the paper. Readers are welcome to comment on the online version of the paper. Correspondence and requests for materials should be addressed to B.K.K. ([kobilka@stanford.edu](mailto:kobilka@stanford.edu)), P.G. ([peter.gmeiner@fau.de](mailto:peter.gmeiner@fau.de)), B.L.R. ([bryan\\_roth@med.unc.edu](mailto:bryan_roth@med.unc.edu)) or B.K.S. ([shoichet@cgl.ucsf.edu](mailto:shoichet@cgl.ucsf.edu)).

**Reviewer Information** *Nature* thanks G. Henderson, E. Kelly, B. Kieffer and J. Meiler for their contribution to the peer review of this work.

## METHODS

No statistical methods were used to predetermine sample size.

**Chemicals, reagents, and cell lines.** Chemicals and reagents used in this study were purchased from commercial sources (Sigma, Tocris, Fisher scientific, ZINC database suppliers) or synthesized as outlined in the Supplementary Information. HEK293 (ATCC CRL-1573; 60113019; certified mycoplasma free and authentic by ATCC) and HEK293-T (HEK293T; ATCC CRL-11268; 59587035; certified mycoplasma free and authentic by ATCC) cells were from the ATCC and are well validated for signalling studies. Cells were also validated by analysis of short tandem repeat (STR) DNA profiles and these profiles showed 100% match at the STR database from ATCC. U2OS cells expressing human  $\mu$ OR were obtained as cryopreserved stocks from DiscoverX and were not further authenticated.

**Molecular docking and analogue selection.** The inactive-state  $\mu$ -opioid receptor structure (PDB: 4DKL) was used as input for receptor preparation with DOCK Blaster (<http://blaster.docking.org>)<sup>44</sup>. Forty-five matching spheres were used based on a truncated version of the crystallized ligand. The covalent bond and linker region of the antagonist  $\beta$ -funaltrexamine were removed for sphere generation. The ligand sampling parameters were set with bin size, bin size overlap, and distance tolerances of 0.4 Å, 0.1 Å, and 1.5 Å, respectively, for both the matching spheres and for the docked molecules. Ligand poses were scored by summing the receptor–ligand electrostatics and van der Waals interaction energy corrected for ligand desolvation. Receptor atom partial chargers were used from the united atom AMBER force field except for Lys233 and Tyr326, where the dipole moment was increased as previously described<sup>43</sup>. Over 3 million commercially available molecules from the ZINC<sup>20</sup> (<http://zinc.docking.org>) lead-like set were docked into the receptor using DOCK3.6<sup>21</sup> (<http://dock.compbio.ucsf.edu>). Among the top ranking 0.08% of molecules were inspected and 23 were selected for experimental testing in the primary screen. A resource to perform these docking studies is publicly available (<http://blaster.docking.org>).

For a secondary screen, analogues of the top three hits from the primary screen (compounds 4, 5 and 7) with a similarity of greater than 0.7 (as defined in the ZINC search facility) were identified in the ZINC database. Additionally, substructure searches were performed using the scaffolds of each of these three compounds. The searches yielded 500 purchasable compounds, which were then docked as in the primary screen. Analogues were manually inspected for interactions and selected for further experimental testing.

**Radioligand binding studies.** For a primary screen of selected molecules, binding to  $\mu$ OR was assessed by measuring competition against the radioligand <sup>3</sup>H-diprenorphine (<sup>3</sup>H-DPN). Each compound was initially tested at 20  $\mu$ M and was incubated with <sup>3</sup>H-DPN at a concentration equal to the  $K_d$  (0.4 nM) of the radioligand in  $\mu$ OR containing Sf9 insect cell membranes. The reaction contained 40 fmol of  $\mu$ OR and was incubated in a buffer of 20 mM HEPES pH 7.5, 100 mM sodium chloride, and 0.1% bovine serum albumin for 1 h at 25 °C. To separate free from bound radioligand, reactions were rapidly filtered over Whatman GF/B filters with the aid of a Brandel harvester and <sup>3</sup>H-DPN counts were measured by liquid scintillation. Compounds with more than 25% of <sup>3</sup>H-DPN radioactivity were further tested in full dose–response to determine the affinity ( $K_i$ ) in HEK293 membranes. Subsequently, the 15 analogues were tested in full dose–response for affinity at the  $\mu$ OR and the  $\kappa$ OR by the National Institutes of Mental Health Psychoactive Drug Screen Program (PDSP)<sup>45</sup>, as were the affinities of compounds 12, PZM21, and their stereoisomers at the  $\mu$ OR,  $\delta$ OR,  $\kappa$ OR and nociception receptor.

Radioligand depletion assays to test the irreversible binding of compound PZM29 were performed as described previously<sup>46</sup>. Human embryonic kidney 293 (HEK 293) cells were transiently transfected with  $\mu$ OR or the cysteine mutant  $\mu$ OR:N127C using the Mirus TransIT-293 transfection reagent (MolBioTec, Goettingen, Germany), grown for 48 h, harvested, and homogenates were prepared as described<sup>47</sup>. For radioligand depletion experiments, homogenates were preincubated in TRIS buffer (50 mM Tris at pH 7.4) at a protein concentration of 50–100  $\mu$ g/ml or 70–120  $\mu$ g/ml for  $\mu$ OR and  $\mu$ OR:N127C, respectively and the covalent ligand (at 5  $\mu$ M) for different time intervals. Incubation was stopped by centrifugation and reversibly bound ligand was washed three times (resuspension in buffer for 30 min and subsequent centrifugation). Membranes were then used for radioligand binding experiments with <sup>3</sup>H-diprenorphine (final concentration: 0.7 nM, specific activity: 30 Ci/mmol, purchased from Biotrend, Cologne, Germany) to determine specific binding at the  $\mu$ OR ( $B_{max}$  = 4,000–6,500 fmol/mg protein,  $K_D$  = 0.25–0.45 nM) and the  $\mu$ OR:N127C receptor ( $B_{max}$  = 1,300–6,000 fmol/mg protein,  $K_D$  = 0.18–0.25 nM), respectively as described<sup>48</sup>. Non-specific binding was determined in the presence of 10  $\mu$ M naloxone. For data analysis, the radioactivity counts were normalized to values where 100% represents effect of buffer and 0% represents non-specific binding. Five independent experiments, each done in quadruplicate, were performed and the resulting values were calculated and pooled to a mean curve which is displayed.

**GTP $\gamma$ S Binding Experiments.** The [<sup>35</sup>S]-GTP $\gamma$ S binding assay was performed with membrane preparations from HEK 293 cells coexpressing the human  $\mu$ OR and the PTX insensitive G-protein subunits  $G_{\alpha o1}$  or  $G_{\alpha i2}$ <sup>49</sup>. Cells were transiently transfected using the Mirus TransIT-293 transfection reagent (MolBioTec, Goettingen, Germany), grown for 48 h, harvested and homogenates were prepared as described<sup>47</sup>. The receptor expression level ( $B_{max}$ ) and  $K_D$  values were determined in saturation experiments with <sup>3</sup>H-diprenorphine (specific activity: 30 Ci/mmol, purchased from Biotrend, Cologne, Germany) ( $B_{max}$  = 3,700  $\pm$  980 fmol/mg protein,  $K_D$  = 0.30  $\pm$  0.093 nM for  $\mu$ OR+ $G_{\alpha o1}$  or  $B_{max}$  = 5,800  $\pm$  2,000 fmol/mg,  $K_D$  = 0.46  $\pm$  0.095 nM for  $\mu$ OR+ $G_{\alpha i2}$ , respectively). The assay was carried out in 96-well plates with a final volume of 200  $\mu$ l. In each well, 10  $\mu$ M GDP, the compounds (0.1 pM to 100  $\mu$ M final concentration) and the membranes (30  $\mu$ g/ml final protein concentration) were incubated for 30 min at 37 °C in incubation buffer containing 20 mM HEPES, 10 mM MgCl<sub>2</sub>  $\cdot$  6 H<sub>2</sub>O and 70 mg/l saponin. After the addition of 0.1 nM [<sup>35</sup>S]-GTP $\gamma$ S (specific activity 1,250 Ci/mmol, PerkinElmer, Rodgau, Germany) incubation was continued at 37 °C for further 30 min or 75 min for  $\mu$ OR+ $G_{\alpha o1}$  or  $\mu$ OR+ $G_{\alpha i2}$ , respectively. Incubation was stopped by filtration through Whatman GF/B filters soaked with ice cold PBS. Bound radioactivity was measured by scintillation measurement as described previously<sup>48</sup>.

Data analysis was performed by normalizing the radioactivity counts (cpms) to values when 0% represents the non-stimulated receptor and 100% the maximum effect of morphine or DAMGO. Dose–response curves were calculated by nonlinear regression in GraphPad Prism 6.0. Mean values  $\pm$  s.e.m. for EC<sub>50</sub> and  $E_{max}$  values were derived from 3–12 individual experiments each done in triplicate. **G<sub>i/o</sub> induced cAMP inhibition.** To measure  $\mu$ OR G<sub>i/o</sub>-mediated cAMP inhibition, HEK-293T cells were co-transfected using calcium phosphate in a 1:1 ratio with human  $\mu$ OR and a split-luciferase based cAMP biosensor (pGloSensor<sup>TM</sup>-22F; Promega). For experiments including GRK2 co-expression, cells were transfected with 1  $\mu$ g/15-cm dish of GRK2. After at least 24 h, transfected cells were washed with phosphate buffered saline (PBS) and trypsin was used to dissociate the cells. Cells were centrifuged, resuspended in plating media (1% dialysed FBS in DMEM), plated at a density of 15,000–20,000 cells per 40  $\mu$ l per well in poly-lysine coated 384-well white clear bottom cell culture plates, and incubated at 37 °C with 5% CO<sub>2</sub> overnight. For inactivation of pertussis-toxin (PTX) G<sub>o</sub> experiments, cells were plated with 100 ng/ml final concentration PTX. The next day, drug dilutions were prepared in fresh assay buffer (20 mM HEPES, 1  $\times$  HBSS, 0.1% bovine serum albumin (BSA), and 0.01% ascorbic acid, pH 7.4) at 3  $\times$  drug concentration. Plates were decanted and 20  $\mu$ l per well of drug buffer (20 mM HEPES, 1  $\times$  HBSS, pH 7.4) was added to each well. Drug addition to 384-well plates was performed by FLIPR adding 10  $\mu$ l of drug per well for a total volume of 30  $\mu$ l. Plates were allowed to incubate for exactly 15 min in the dark at room temperature. To stimulate endogenous cAMP via  $\beta$  adrenergic-G<sub>s</sub> activation, 10  $\mu$ l of 4  $\times$  isoproterenol (200 nM final concentration) diluted in drug buffer supplemented with GloSensor assay substrate was added per well. Cells were again incubated in the dark at room temperature for 15 min, and luminescence intensity was quantified using a Wallac TriLux microbeta (Perkin Elmer) luminescence counter. Data were normalized to DAMGO-induced cAMP inhibition and analysed using nonlinear regression in GraphPad Prism 6.0 (Graphpad Software Inc., San Diego, CA).

Determination of functional activity of PZM21-29 for SAR studies was performed using a BRET-based cAMP accumulation assay<sup>50</sup>. HEK-293T cells were transiently co-transfected with pcDNA3L-His-CAMYEL42 (purchased from ATCC via LCG Standards, Wesel, Germany) and human  $\mu$ OR, achieving a cDNA ratio of 2:2 using Mirus TransIT-293 transfection reagent. 24 h post-transfection, cells were seeded into white half-area 96-well plates at 20  $\times$  10<sup>4</sup> cells/well and grown overnight. On the following day, phenol-red-free medium was removed and replaced by PBS and cells were serum starved for 1 h before treatment. The assay was started by adding 10  $\mu$ l coelenterazine h (Promega, Mannheim, Germany) to each well to yield a final concentration of 5  $\mu$ M. After 5 min incubation, compounds were added in PBS containing forskolin (final concentration 10  $\mu$ M). Reads of the plates started 15 min after agonist addition. BRET readings were collected using a CLARIOstar plate reader (BMG LabTech, Ortenberg, Germany). Emission signals from Renilla Luciferase and YFP were measured simultaneously using a BRET1 filter set (475–30 nm/535–30 nm). BRET ratios (emission at 535–30 nm/emission at 475–30 nm) were calculated and dose–response curves were fitted by nonlinear regression using GraphPad Prism 6.0. Curves were normalized to basal BRET ratio obtained from dPBS and the maximum effect of morphine and DAMGO. Each curve is derived from three to five independent experiments each done in duplicate.

**Calcium release.** Calcium release was measured using a FLIPR<sup>TETRA</sup> fluorescence imaging plate reader (Molecular Devices). Calcium release experiments were run in parallel to G<sub>i/o</sub> GloSensor experiments with the same HEK-293T cells transfected with  $\mu$ OR, except cells for FLIPR were plated in poly-lysine coated 384-well black clear bottom cell culture plates. Cells were incubated at 37 °C with 5% CO<sub>2</sub> overnight and next day media was decanted and replaced with Fluo-4



direct calcium dye (Life Technologies) made up in HBSS with 20 mM HEPES, pH 7.4. Dye was incubated for 1 h at 37 °C. Afterwards, cells were equilibrated to room temperature, and fluorescence in each well was read for the initial 10 s to establish a baseline. Afterwards, 10  $\mu$ l of drug (3 $\times$ ) was added per well and the maximum-fold increase in fluorescence was determined as fold-over-baseline. Drug solutions used for the FLIPR assay were exactly the same as used for  $G_{i/o}$  Glosensor experiments. To activate endogenous  $G_q$ -coupled receptors as a positive control for calcium release, TFLR-NH<sub>2</sub> (10  $\mu$ M, PAR-1 selective agonist) was used.

**Receptor internalization.** Internalization was measured using the eXpress DiscoverX PathHunter GPCR internalization assay using split  $\beta$ -galactosidase complementation. In brief, cryopreserved U2OS cells expressing the human  $\mu$ OR were thawed rapidly and plated in supplied medium and 96-well culture plates. Next day, cells were stimulated with drugs (10 $\times$ ) and allowed to incubate for 90 min at 37 °C with 5% CO<sub>2</sub>. Afterwards, substrate was added to cells and chemiluminescence was measured on a TriLux (Perkin Elmer) plate counter. Data were normalized to DAMGO and analysed using Graphpad Prism 6.0.

**$\beta$ -Arrestin recruitment assays.**  $\beta$ -Arrestin recruitment was measured by either the PathHunter enzyme complementation assay (DiscoverX) or by previously described bioluminescence resonance energy transfer (BRET) methods<sup>51</sup>. Assays using DiscoverX PathHunter eXpress OPRM1 CHO-K1  $\beta$ -Arrestin GPCR Assays were conducted exactly as instructed by the manufacturer. Briefly, supplied cryopreserved cells were thawed and resuspended in the supplied medium, and plated in the furnished 96-well plates. Next day, 10 $\times$  dilutions of agonist (prepared in HBSS and 20 mM HEPES, pH 7.4) were added to the cells and incubated for 90 min. Next, the detection reagents were reconstituted, mixed at the appropriate ratio, and added to the cells. After 60 min, luminescence per well was measured on a TriLux (Perkin-Elmer) plate counter. Data were normalized to DAMGO and analysed using the sigmoidal dose-response function built into GraphPad Prism 6.0.

To measure  $\mu$ OR mediated  $\beta$ -arrestin recruitment by BRET in the presence or absence of GRK2 co-expression, HEK-293T cells were co-transfected in a 1:1:15 ratio with human  $\mu$ OR containing C-terminal *renilla* luciferase (RLuc8), GRK2, and venus-tagged N-terminal  $\beta$ -arrestin-2, respectively. In the case of experiments where GRK2 expression was varied, pcDNA3.1 was substituted for GRK2 to maintain the same concentration of DNA transfected. After at least 24 h, transfected cells were plated in poly-lysine coated 96-well white clear bottom cell culture plates in plating media at a density of 125,000–250,000 cells per 200  $\mu$ l per well and incubated overnight. The next day, media was decanted and cells were washed twice with 60  $\mu$ l of drug buffer and incubated at room temperature for at least 10 min before drug stimulation. 30  $\mu$ l of drug (3 $\times$ ) was added per well and incubated for at least 30 min in the dark. Then, 10  $\mu$ l of the RLuc substrate, coelenterazine H (Promega, 5  $\mu$ M final concentration) was added per well, and plates were read for both luminescence at 485 nm and fluorescent eYFP emission at 530 nm for 1 s per well using a Mithras LB940 microplate reader. The ratio of eYFP/RLuc was calculated per well and the net BRET ratio was calculated by subtracting the eYFP/RLuc per well from the eYFP/RLuc ratio without venus-arrestin present. Data were normalized to DAMGO-induced stimulation and analysed using nonlinear regression in GraphPad Prism 6.0.

**Ligand bias calculation.** Multiple approaches have been described to quantitate ligand bias, including operational models, intrinsic relative activity models, and allosteric models<sup>31,52</sup>. In the absence of GRK2, we observe no  $\beta$ -arrestin-2 recruitment for PZM21 and TRV130. This prevents a quantitative assessment of bias by the operational model. In the case where GRK2 is overexpressed, we observe arrestin recruitment for PZM21 and TRV130. In this case, we utilize the operational model to calculate ligand bias and display equiactive bias plots for comparison of ligand efficacy for distinct signalling pathways<sup>31,53</sup>. The Glosensor  $G_{i/o}$ , DiscoverX PathHunter  $\beta$ -arrestin, or net BRET concentration response curves were fit to the Black-Leff operational model to determine transduction coefficients ( $\tau/K_A$ ). Compound bias factors are expressed after normalization against the prototypical opioid agonist DAMGO used as a reference. Bias factors are expressed as the value of  $\Delta\Delta\log(\tau/K_A)$ .

**Assessment of off-target PZM21 activity.** To identify potential off-target activity of PZM21, we used the National Institutes of Mental Health Psychoactive Drug Screen Program. Compound PZM21 was first tested for activity against 320 non-olfactory GPCRs using the PRESTO-Tango GPCRome screening  $\beta$ -arrestin recruitment assay<sup>30</sup>. We used 10  $\mu$ M PZM21 and activity at each receptor was measured in quadruplicate. Potential positive receptor hits were defined as those that increase the relative luminescence value twofold. Positive hits were subsequently re-tested in full dose-response mode to determine whether the luminescence signal titrates with increasing concentrations of PZM21. A number of false-positive hits were discounted by this approach. PZM21 inhibition of hERG channel was performed as described previously<sup>54</sup> and neurotransmitter transporter assays were determined used the Molecular Devices Neurotransmitter Assay Kit (Molecular Devices).

**In vivo studies.** Adult male C57BL/6J (aged 3–5 months) obtained from Jackson Laboratories (Bar Harbour, Maine) were used to investigate behavioural responses, respiratory effects, and hyperlocomotion induced by PZM21 and compared with morphine or vehicle (0.9% sodium chloride). For  $\mu$ OR knockout animals, *Oprm1*<sup>−/−</sup> mice (B6.129S2-Oprm1tm1Kff/J) were obtained from Jackson Laboratories. All drugs were dissolved in vehicle and injected subcutaneously. Behavioural studies were conducted at the University of North Carolina and Stanford University following the National Institutes of Health's guidelines for care and use of animals and with approved mouse protocols from the institutional animal care and use committees. Sample sizes (number of animals) were not predetermined by a statistical method and animals were assigned to groups randomly. Drug treatment groups were only blinded for measurement of affective versus reflexive analgesia; other experiments were not blinded to investigators. Predefined exclusion criteria were set for analgesia and conditioned preference experiments. No animals were excluded from statistical analysis. Statistical analyses were performed after first assessing the normality of distributions of data sets and Leven's test was used to assess equality of variances.

**Measurement of analgesia.** Analgesia-like responses in were measured as previously described<sup>55</sup> using a hotplate analgesia meter with dimensions of 29.2  $\times$  26.7 cm with mice restricted to a cylinder 8.9 cm in diameter and 15.2 cm high (ITC Life Sciences, Woodland Hills, California). Response was measured by recording the latency to lick, flutter, or splay hind paw(s), or an attempt to jump out of the apparatus at 55 °C, with a maximum cut-off time of 30 s. Once a response was observed or the cut-off time had elapsed, the subject was immediately removed from the hotplate and placed back in its home cage. The animals were acclimated to the hotplate, while cool, and a baseline analgesic response time was acquired several hours before drug treatment and testing. Mice were injected with either vehicle ( $n$  = 8), morphine (5 mg/kg,  $n$  = 8 or 10 mg/kg,  $n$  = 8), TRV130 (1.2 mg/kg,  $n$  = 9) or PZM21 (10 mg/kg,  $n$  = 8; 20 mg/kg,  $n$  = 11; or 40 mg/kg,  $n$  = 8). After injection of drug, the analgesic effect expressed as percentage maximum possible effect (%MPE) was measured at 15, 30, 60, 90 and 120 min after drug treatment. If animals did not display hind paw lick, splay, or flutter, they were removed from the trial. Additionally, if animals attempted to jump out of the plate or urinated on the hotplate they were removed from the trial. To assess analgesia by the tail-flick assay, a tail-flick analgesia meter (Columbus Instruments, Columbus, Ohio). Mice were gently immobilized with a cotton towel and the tail base was placed on a radiant light source emitting a constant temperature of 56 °C. The tail withdrawal latency was measured at similar time points as the hotplate assay after administration of vehicle ( $n$  = 8), morphine (5 mg/kg,  $n$  = 4; 10 mg/kg,  $n$  = 8) or PZM21 (10 mg/kg,  $n$  = 8; 20 mg/kg,  $n$  = 14). The cut-off time for the heat source was set at 10 s to avoid tissue damage. Analgesic response times were measured similar to the hotplate assay.

**Analgesia in  $\mu$ OR knockout mice and subcategorization of affective/reflexive pain.** *Oprm1*<sup>−/−</sup> and wild-type C57BL/6J mice (male; 8–11 weeks) were acclimated to the testing environment and thermal-plate equipment for three non-consecutive days between 11:00 and 13:00 before any pharmacological studies. Acclimation was achieved by individually confining mice within an enclosed semi-transparent red plastic cylinder (10 cm depth  $\times$  15 cm height) on a raised metal-mesh rack (61 cm height) for 30 min, and then exposing each mouse to the thermal-plate equipment (non-heated; floor dimensions, 16.5  $\times$  16.5 cm; Bioseb), while confined within a clear plastic chamber (16 cm length  $\times$  16 cm width  $\times$  30 cm height). Acclimation exposure to the thermal plate lasted for 30 s, and exposure was repeated after 30 min to mimic the test day conditions. The testing environment had an average ambient temperature of 22.6 °C and illumination of 309 lx from overhead fluorescence lighting. The same male experimenter (G.C.) was present throughout the entire duration of habituation and testing to exclude possible olfaction-induced alterations in sensory thresholds<sup>56</sup>.

Cutaneous application of a noxious stimulus, or time spent on a hotplate apparatus can broadly elicit several distinct behavioural responses: 1) withdrawal reflexes: rapid reflexive retraction or digit splaying of the paw; 2) affective-motivational responses: directed licking and biting of the paw, and/or a motivational response characterized by jumping away from the heated floor plate. Paw withdrawal reflexes are classically measured in studies of hypersensitivity, and involve simple spinal cord and brainstem circuits<sup>57</sup>. In contrast, affective responses are complex, non-stereotyped behaviours requiring processing by limbic and cortical circuits in the brain, the appearance of which indicates the subject's motivation and arousal to make the unpleasant sensation cease by licking the affected tissue, or seeking an escape route<sup>36,57–64</sup>. To distinguish between potential differential analgesic effects of PZM21, mice were placed on the heated apparatus (52.5 °C), and the latency to exhibition of the first sign of a hindpaw reflexive withdraw, and the first sign of an affective response was recorded. A maximum exposure cut-off of 30 s was set to reduce tissue damage. Mice were injected with either vehicle ( $n$  = 6), morphine (10 mg/kg,  $n$  = 10), or PZM21 (20 mg/kg,  $n$  = 13). After injection of drug, the

analgesic effect on either reflex or attending responses was expressed as percentage maximum possible effect (%MPE), and was measured at –30 (baseline), 15, 30, 60, 90, 120, and 180 min relative to drug treatment. For studies comparing *Oprm1*<sup>–/–</sup> and wild-type C57Bl/6J mice, the analgesic response in the hotplate assay was measured 30 min after injection of vehicle ( $n = 5$  for both genotypes), morphine (10 mg/kg,  $n = 5$  for both genotypes) or PZM21 (20 mg/kg,  $n = 6$  for *Oprm1*<sup>–/–</sup> and  $n = 5$  for wild-type).

**Formalin injection assay.** Analgesia to formalin injection was carried out as described previously<sup>65</sup>. Mice were first habituated for 20 min to the testing environment which included a home cage without bedding, food, and water. After habituation, vehicle ( $n = 6$ ), morphine (10 mg/kg,  $n = 7$ ), or PZM21 (40 mg/kg,  $n = 7$ ) was injected subcutaneously. This was followed by injection of 20  $\mu$ l of 1% formalin in 0.9% saline under the skin of the dorsal surface of the right hindpaw. Animals were returned to their home cage and behavioural responses were recorded for one hour. Nociception was estimated by measuring the cumulative time spent by animals licking the formalin-injected paw. As opioids classically display two phases of analgesic action, nociceptive behaviour was measured during both the early phase (0 to 5 min) and the late phase (20 to 30 min). In Fig. 4, an asterisk indicates a significant difference between drug and vehicle ( $P < 0.05$  calculated using a one-way ANOVA with Bonferroni correction).

**Mouse plethysmography.** Respiration data was collected using a whole body plethysmography system (Buxco Electronics Inc., Wilmington, North Carolina) as described<sup>66</sup>. This method measures respiratory frequency, tidal volume, peak flows, inspiratory time, and expiratory time in conscious and unrestrained mice. Briefly, Buxco airflow transducers were attached to each plethysmography chamber and a constant flow rate was maintained for all chambers. Each chamber was calibrated to its attached transducer before the experiment. Animals were first habituated to the clear plexiglass chambers for 10 min. Respiratory parameters were recorded for 10 min to establish a baseline before injection of vehicle ( $n = 8$ ), morphine (10 mg/kg,  $n = 8$ ), TRV130 (1.2 mg/kg,  $n = 8$ ) or PZM21 (40 mg/kg,  $n = 8$ ). Respiratory parameters were then collected on unrestrained mice for 100 min post drug injection. To decrease respiratory variability induced by anxiety, mice were shielded from view of other animals and experimenter. In Fig. 4, an asterisk indicates a significant difference between drug and vehicle ( $P < 0.05$  calculated using a repeated measures ANOVA with Bonferroni correction).

**Accumulated faecal boli quantification.** To measure constipatory effects of morphine and PZM21, we assessed the total accumulated faecal boli as described<sup>6</sup>. Briefly, mice were injected with vehicle ( $n = 10$ ), morphine (10 mg/kg,  $n = 16$ ) or PZM21 (20 mg/kg,  $n = 16$ ) and placed within a plexiglass chamber (5 cm  $\times$  8 cm  $\times$  8 cm) positioned on a mesh screen. Mice were maintained without food or water for 6 h. Faecal boli were collected underneath the mesh on a paper towel and the cumulative mass was measured every hour for six hours. In Fig. 4, an asterisk indicates a significant difference between drug and vehicle ( $P < 0.05$  calculated using a repeated measures ANOVA with Bonferroni correction).

**Open field locomotor response.** A photocell-equipped automated open field chamber (40 cm  $\times$  40 cm  $\times$  30 cm; Versamax system, Accuscan Instruments) contained inside sound-attenuating boxes was used to assess locomotor activity. Baseline ambulation of freely moving mice was monitored over 30 min, followed by injection with vehicle ( $n = 7$ ), morphine (10 mg/kg,  $n = 5$ ) or PZM21 (20 mg/kg,  $n = 6$ ). Locomotor activity was monitored for another 150 min. In Fig. 4, an asterisk indicates a significant difference between drug and vehicle ( $P < 0.05$  calculated using a repeated measures ANOVA with Bonferroni correction).

**Conditioned place preference.** A three-chambered conditioned place preference apparatus (Med-Associates, St. Albans, Vermont) consisting of white or black chambers (16.8  $\times$  12.7  $\times$  12.7 cm each) with uniquely textured white mesh or black rod floors and separated by a neutral central chamber (7.2  $\times$  12.7  $\times$  12.7 cm) was used for conditioned place preference testing. On day 1 (preconditioning day), mice were placed in the central chamber and allowed to explore freely for 30 min. Time spent in each compartment was used to estimate baseline chamber preferences and mice showing specific chamber bias more than 70% were not studied further. On days 2–9 (conditioning days) mice were injected with either vehicle or drug and paired with either the white mesh or the black rod chambers. All mice received vehicle on days 2, 4, 6, 8 and drug on days 3, 5, 7, 9. On day 10 (test day), mice were again placed in the central chamber as on day 1 and allowed to explore freely for 30 min. Time spent in each chamber was expressed as percentage preference. Place preference was tested with morphine (10 mg/kg,  $n = 16$ ), PZM21 (20 mg/kg,  $n = 8$ ), or TRV130 (1.2 mg/kg,  $n = 7$ ). In Fig. 4, an asterisk indicates a significant difference between vehicle and drug chambers ( $P < 0.05$  by one-sample  $t$ -test with hypothetical value of 50) while NS indicates non-significance ( $P > 0.05$ ).

**Cataleptic effect.** Drug induced catalepsy was measured in mice using the bar test<sup>67</sup>, which includes a horizontally placed 3-mm diameter wooden bar fixed 4 cm above the floor. Mice were habituated with the bar and the environment for 20 min before subcutaneous injection of either haloperidol (2 mg/kg,  $n = 8$ ), morphine

(10 mg/kg,  $n = 8$ ), or PZM21 (20 mg/kg,  $n = 8$ ). To measure catalepsy, both forepaws were gently placed on the bar and the length of time during which each mouse remained in the initial position was measured. The effect was measured at 15, 30 and 90 min after drug injection. Maximum cut-off time for each challenge was 90 s.

**Pharmacokinetics of PZM21.** Studies were performed by the Preclinical Therapeutics Core and the Drug Studies Unit at the University of California San Francisco. Ten mice were injected subcutaneously with 20 mg/kg of PZM21. At each time point, 1 ml of blood was collected from three mice and the serum concentration of PZM21 determined by liquid chromatography–mass spectrometry (LC/MS). Mice were subsequently sacrificed and entire brains were homogenized for determination of PZM21 concentrations by LC/MS. All studies were performed with approved mouse protocols from the institutional animal care and use committees.

**Metabolism of PZM21.** Metabolism experiments were performed as described previously<sup>68</sup>. In brief, pooled microsomes from male mouse liver (CD-1) were purchased (Sigma Aldrich) and stored at –75 °C until required. NADPH was purchased (Carl Roth) and stored at –8 °C. The incubation reactions were carried out in polyethylene caps (Eppendorf, 1.5 ml) at 37 °C. The incubation mixture contained PZM21 (80  $\mu$ M) or positive controls (imipramine and rotigotine), pooled liver microsomes (0.5 mg of microsomal protein/ml of incubation mixture) and Tris–MgCl<sub>2</sub> buffer (48 mM Tris, 4.8 mM MgCl<sub>2</sub>, pH 7.4). The final incubation volume was 0.5 ml. Microsomal reactions were initiated by addition of 50  $\mu$ l of enzyme cofactor solution NADPH (final concentration of 1 mM). At 0, 15, 30 and 60 min the enzymatic reactions were terminated by addition of 500  $\mu$ l of ice-cold acetonitrile (containing 8  $\mu$ M internal standard), and precipitated protein was removed by centrifugation (15,000 rcf for 3 min). The supernatant was analysed by HPLC/MS (binary solvent system, eluent acetonitrile in 0.1% aqueous formic acid, 10–40% acetonitrile in 8 min, 40–95% acetonitrile in 1 min, 95% acetonitrile for 1 min, flow rate of 0.3 ml/min). The experiments were repeated in three independent experiments. Parallel control incubations were conducted in the absence of cofactor solution to determine unspecific binding to matrix. Substrate remaining and metabolite formation was calculated as a mean value  $\pm$  s.e.m. of three independent experiments by comparing AUC of metabolites and substrate after predetermined incubation time to AUC of substrate at time 0, estimating a similar ionization rate, corrected by a factor calculated from the AUC of internal standard at each time point.

**Chemical synthesis.** The stereochemically pure isomers of **12** and PZM21 were synthesized from corresponding (R)- and (S)-amino acid amides, which were either commercially available or readily prepared from the corresponding acid or ester (see Supplementary Information). The primary amino group was dimethylated using an excess of aqueous formaldehyde and sodium triacetoxyborohydride in aqueous acetonitrile. The carboxamides **16a,b** were converted to primary amines by treatment with borane–tetrahydrofuran complex under reflux yielding the diamines **17a,b**. Henry reaction of thiophene-3-carbaldehyde with nitroethane afforded the nitropropene derivative **18**, which was converted into the racemic alkylamine **19**. Activation with 4-nitrophenyl chloroformate yielded the carbamates **20**, which were coupled with the enantiopure primary amines **17a,b** to achieve diastereomeric mixtures of the corresponding ureas **12** and **21**. HPLC separation using a semi-preparative Chiralpak AS-H column gave the overall eight pure stereoisomers of **12** and **21** including PZM21.

To determine the absolute configuration of the final products and efficiently prepare PZM21, we synthesized enantiomerically enriched carbamate **20**, coupled it with the corresponding primary amines. For enantiomeric enrichment, we performed chiral resolution of the racemic primary amine **19** via repetitive crystallization with di-*p*-anisoyl-(S)-tartaric acid. After triple crystallization, we obtained **19** enriched in dextrorotatory enantiomer ( $[\alpha]_D^{25} = +20.5^\circ$ ). The corresponding (R)-acetamide has been previously characterized as dextrorotatory ( $[\alpha]_D^{20} = +49.8^\circ$ ), so enantiomerically enriched **19** was treated with acetic anhydride and triethylamine, and the specific rotation of the product was measured. Based on the value of specific rotation of the resulting acetamide ( $[\alpha]_D^{21} = -46.6^\circ$ ), we assigned the absolute configuration of the major isomer to be (S). (S)-enriched **20** was used for synthesis of the final urea derivatives and absolute configuration of diastereomers in pairs was assigned based on the equality of retention time in chiral HPLC. A full description of the synthetic routes and analytical data of the compounds **12**, PZM21 and its analogues PZM22–29 are presented in the Supplementary Information.

**Detailed modelling of PZM21 and TRV130 binding poses.** PZM21 was docked to the inactive state  $\mu$ OR structure using DOCK3.6 (ref. 21) as described for the primary screen, with the exception that the 45 matching spheres used were generated based on the docked pose of compound **12**. The resulting ligand–receptor complex was further optimized through minimization with the AMBER protein force field<sup>69</sup> and the GAFF ligand force field supplemented with AM1-BCC

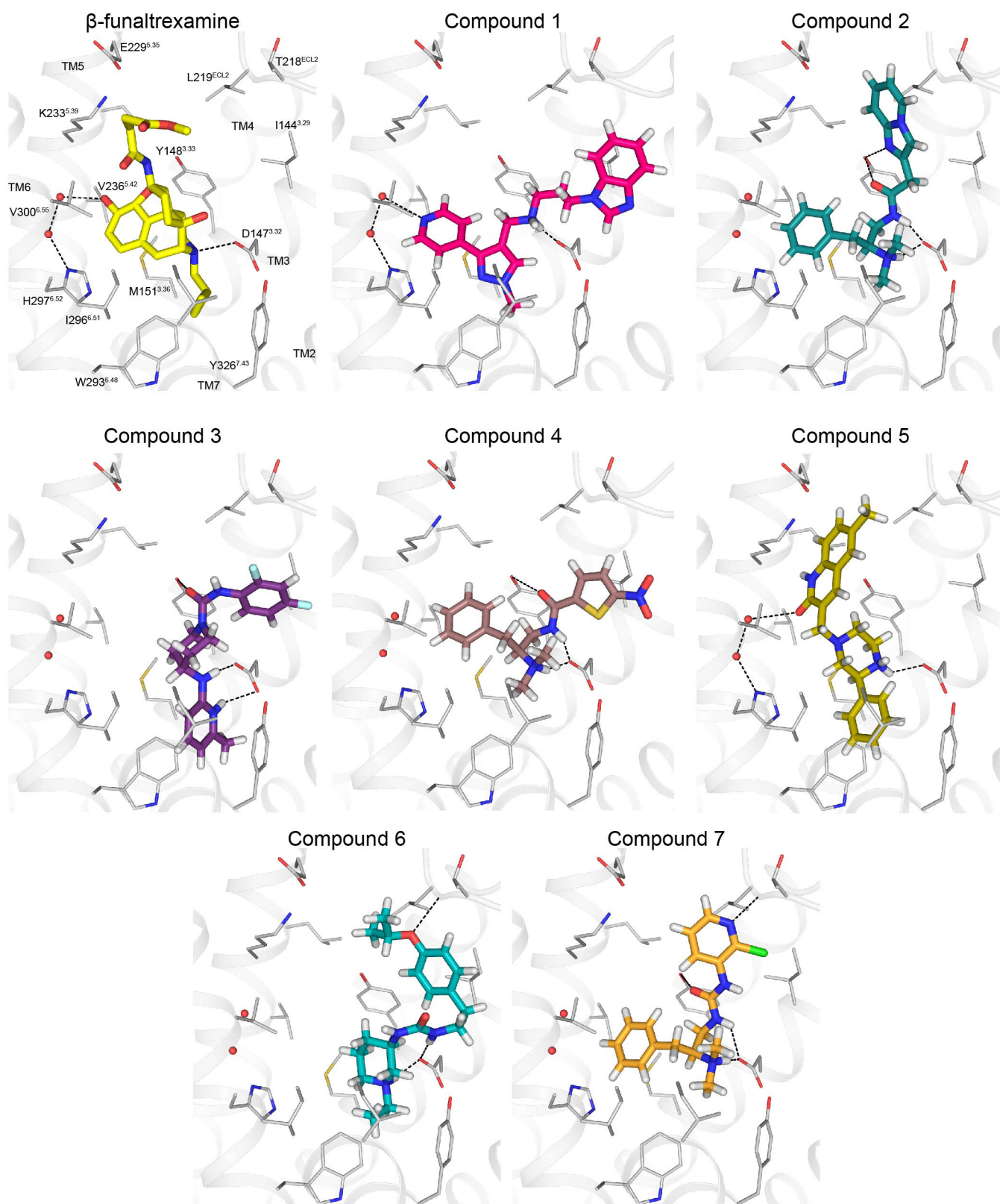
charges. Docking of PZM21 and TRV130 to the active state  $\mu$ OR structure (PDB: 5C1M) was also performed with DOCK3.6 with parameters as described above. The amino terminus of the active state  $\mu$ OR, which forms a lid over the orthosteric binding site (residues Gly52–Met65) was removed before receptor preparation. Matching spheres were generated based on the pose of PZM21 in the inactive state. The resulting complexes were then minimized with AMBER. The pose of PZM21 in the active state  $\mu$ OR structure was further refined using Glide (Schrödinger) in XP mode.

Molecular dynamics simulations were based on crystal structures of  $\mu$ OR in the inactive- and active-state conformation (PDB: 4DKL and 5C1M, respectively). In both cases, all non-receptor residues (T4 lysozyme in the inactive state and Nb39 in the active state) were removed. For the active state, amino-terminal residues were removed as in the docking studies. Initial coordinates of PZM21 were generated by molecular docking as described above. The receptor was simulated with two tautomers of His297<sup>6,52</sup>, either in the neutral N $\delta$  or the N $\epsilon$  state. The  $\mu$ OR-PZM21 complex was embedded in a lipid bilayer consisting of dioleoylphosphatidylcholine (DOPC) molecules as described previously<sup>47</sup>. The charges of the inactive- and active-state simulation systems were neutralized by adding 11 and 14 chloride ions, respectively. To carry out MD simulations, the GROMACS package was used as described previously<sup>70</sup>. Briefly, the general AMBER force field (GAFF)<sup>71</sup> was used for PZM21 and the lipids and the AMBER force field ff99SB<sup>72</sup> for the receptor. Parameters for PZM21 were assigned using antechamber, and charges were calculated using Gaussian09 (Gaussian, Inc.) at the HF/6-31(d,p) level and the RESP procedure according to the literature<sup>73</sup>. During the simulations, PZM21 was protonated at its tertiary amine and simulated as a cation. The SPC/E water model<sup>74</sup> was used, and the simulations were carried out at 310 K. Analysis of the trajectories was performed using GROMACS. Each simulation in a given condition was initiated from identical coordinates, but with initial atom velocities assigned independently and randomly. An overview of the simulation systems and their simulation times is shown in the Supplementary Information.

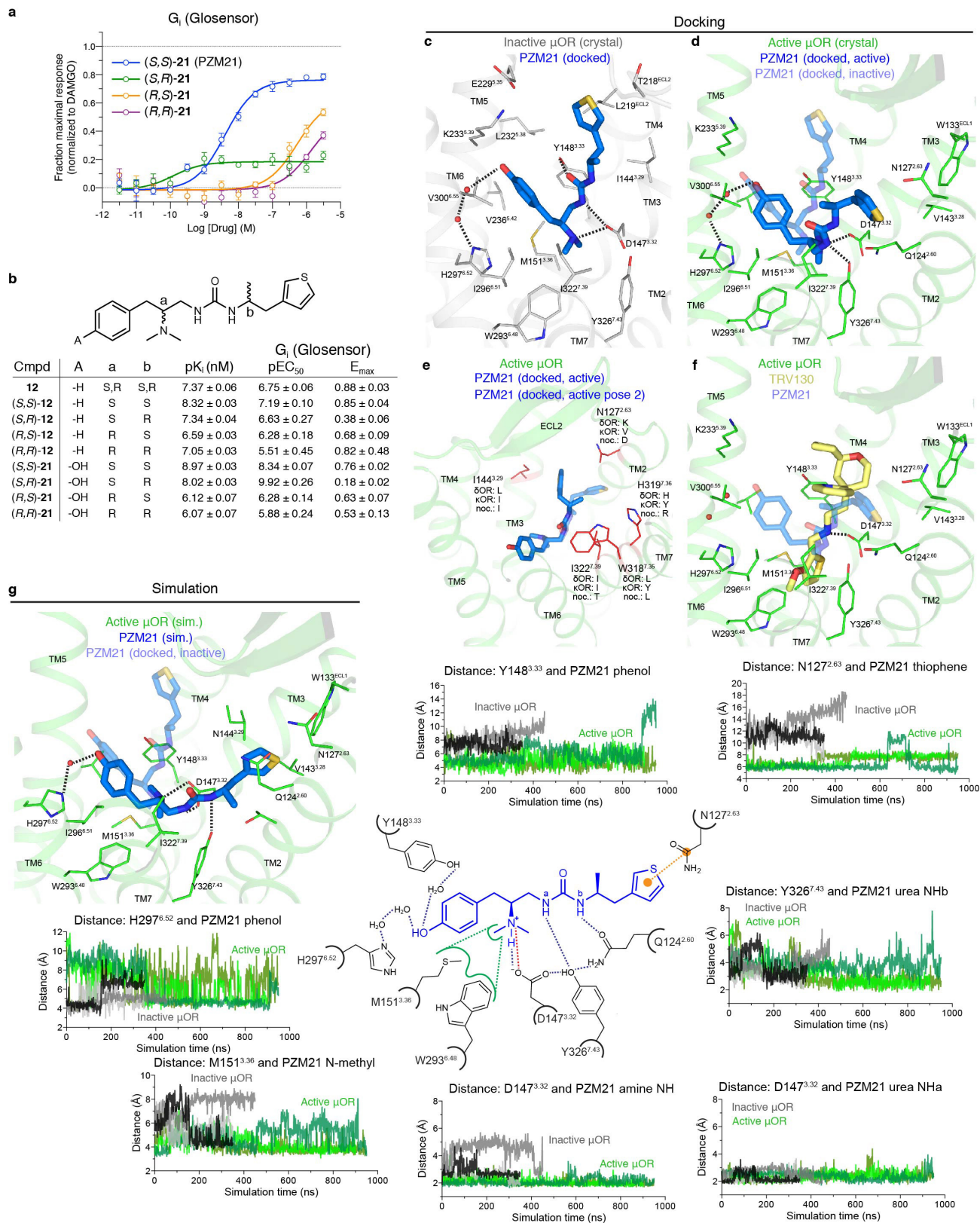
**Data analysis and reporting.** Other than the *in vivo* studies, no statistical analysis was applied to *in vitro* or cell-based signalling assays. Sample size (number of assays for each compound or receptor) was predetermined to be in triplicate or quadruplicate for primary screening assays at a single concentration. For concentration–response assays, the sample size (number of assays for each compound at selected receptors) was also predetermined to be tested for a minimum of three assays, each in triplicate or quadruplicate. None of the functional assays were blinded to investigators.

44. Irwin, J. J. *et al.* Automated docking screens: a feasibility study. *J. Med. Chem.* **52**, 5712–5720 (2009).
45. Besnard, J. *et al.* Automated design of ligands to polypharmacological profiles. *Nature* **492**, 215–220 (2012).
46. Weichert, D. *et al.* Covalent agonists for studying G protein-coupled receptor activation. *Proc. Natl Acad. Sci. USA* **111**, 10744–10748 (2014).
47. Möller, D. *et al.* Functionally selective dopamine D<sub>2</sub>, D<sub>3</sub> receptor partial agonists. *J. Med. Chem.* **57**, 4861–4875 (2014).
48. Hübner, H., Haubmann, C., Utz, W. & Gmeiner, P. Conjugated enynes as nonaromatic catechol bioisosteres: synthesis, binding experiments, and computational studies of novel dopamine receptor agonists recognizing preferentially the D<sub>3</sub> subtype. *J. Med. Chem.* **43**, 756–762 (2000).
49. Lane, J. R., Powney, B., Wise, A., Rees, S. & Milligan, G. G protein coupling and ligand selectivity of the D<sub>2L</sub> and D<sub>3</sub> dopamine receptors. *J. Pharmacol. Exp. Ther.* **325**, 319–330 (2008).
50. Jiang, L. *et al.* Use of a cAMP BRET sensor to characterize a novel regulation of cAMP by the sphingosine 1-phosphate/G13 pathway. *J. Biol. Chem.* **282**, 10576–10584 (2007).
51. Nakajima, K.-i., Gimenez, L. D., Gurevich, V. & Wess, J. in *Designer Receptors Exclusively Activated by Designer Drugs* Vol. 108 *Neuromethods* (ed Thiel, G.) Ch. 2, 29–48 (Springer New York, 2015).
52. Rajagopal, S. *et al.* Quantifying ligand bias at seven-transmembrane receptors. *Mol. Pharmacol.* **80**, 367–377 (2011).
53. Rajagopal, S. Quantifying biased agonism: understanding the links between affinity and efficacy. *Nat. Rev. Drug Discov.* **12**, 483 (2013).
54. Huang, X.-P., Mangano, T., Hufeisen, S., Setola, V. & Roth, B. L. Identification of human Ether-à-go-go related gene modulators by three screening platforms in an academic drug-discovery setting. *Assay Drug Dev. Technol.* **8**, 727–742 (2010).
55. Balter, R. E. & Dykstra, L. A. Thermal sensitivity as a measure of spontaneous morphine withdrawal in mice. *J. Pharmacol. Toxicol. Methods* **67**, 162–168 (2013).
56. Sorge, R. E. *et al.* Olfactory exposure to males, including men, causes stress and related analgesia in rodents. *Nat. Methods* **11**, 629–632 (2014).
57. Woolf, C. J. Long term alterations in the excitability of the flexion reflex produced by peripheral tissue injury in the chronic decerebrate rat. *Pain* **18**, 325–343 (1984).
58. Blanchard, R. J. & Blanchard, D. C. Passive and active reactions to fear-eliciting stimuli. *J. Comp. Physiol. Psychol.* **68**, 129–135 (1969).
59. Bolles, R. C. Species-specific defense reactions and avoidance learning. *Psychol. Rev.* **77**, 32 (1970).
60. Bolles, R. C. & Fanselow, M. S. A perceptual-defensive-recuperative model of fear and pain. *Behav. Brain Sci.* **3**, 291–301 (1980).
61. Estes, W. K. Discriminative conditioning; effects of a Pavlovian conditioned stimulus upon a subsequently established operant response. *J. Exp. Psychol.* **38**, 173–177 (1948).
62. Estes, W. K. & Skinner, B. F. Some quantitative properties of anxiety. *J. Exp. Psychol.* **29**, 390 (1941).
63. Rescorla, R. A. & Lolordo, V. M. Inhibition of avoidance behavior. *J. Comp. Physiol. Psychol.* **59**, 406–412 (1965).
64. Skinner, B. F. *The behavior of organisms; an experimental analysis.* (D. Appleton-Century Company, Incorporated, 1938).
65. Hunskaar, S. & Hole, K. The formalin test in mice: dissociation between inflammatory and non-inflammatory pain. *Pain* **30**, 103–114 (1987).
66. Clougherty, J. E. *et al.* Chronic social stress and susceptibility to concentrated ambient fine particles in rats. *Environ. Health Perspect.* **118**, 769–775 (2010).
67. Sanberg, P. R., Bunsey, M. D., Giordano, M. & Norman, A. B. The catalepsy test: its ups and downs. *Behav. Neurosci.* **102**, 748–759 (1988).
68. Hiller, C. *et al.* Functionally selective dopamine D<sub>2</sub>/D<sub>3</sub> receptor agonists comprising an enyne moiety. *J. Med. Chem.* **56**, 5130–5141 (2013).
69. Case, D. *et al.* AMBER 15. San Francisco, CA: University of California (2015).
70. Goetz, A., Lanig, H., Gmeiner, P. & Clark, T. Molecular dynamics simulations of the effect of the G-protein and diffusible ligands on the  $\beta$ 2-adrenergic receptor. *J. Mol. Biol.* **414**, 611–623 (2011).
71. Wang, J., Wolf, R. M., Caldwell, J. W., Kollman, P. A. & Case, D. A. Development and testing of a general amber force field. *J. Comput. Chem.* **25**, 1157–1174 (2004).
72. Hornak, V. *et al.* Comparison of multiple amber force fields and development of improved protein backbone parameters. *Proteins* **65**, 712–725 (2006).
73. Bayly, C. I., Cieplak, P., Cornell, W. & Kollman, P. A. A well-behaved electrostatic potential based method using charge restraints for deriving atomic charges: the RESP model. *J. Phys. Chem.* **97**, 10269–10280 (1993).
74. Berendsen, H., Grigera, J. & Straatsma, T. The missing term in effective pair potentials. *J. Phys. Chem.* **91**, 6269–6271 (1987).
75. Kissin, I., Brown, P. T., Robinson, C. A. & Bradley, E. L. Acute tolerance in morphine analgesia continuous infusion and single injection in rats. *Anesthesiology* **74**, 166–171 (1991).





**Extended Data Figure 1 | Docking poses of active compounds.** Seven of 23 experimentally tested compounds bound to the  $\mu$ OR with micromolar affinity. Their docked poses often occupy sites not exploited by the antagonist  $\beta$ -funaltrexamine. In each case, a canonical ionic interaction with D147<sup>3.32</sup> is observed.



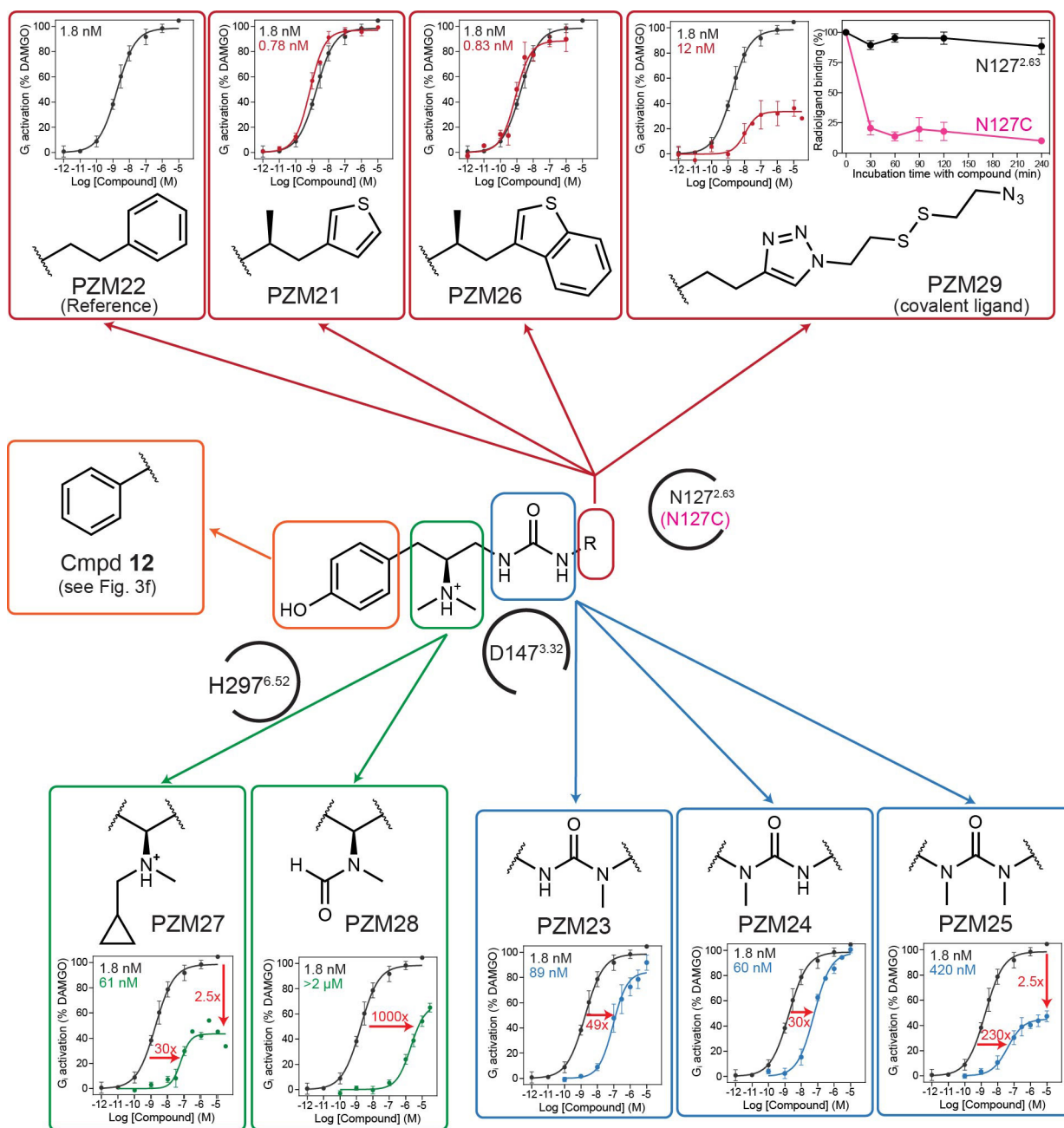
Extended Data Figure 2 | See next page for caption.

**Extended Data Figure 2 | Stereochemical structure-activity**

**relationship.** **a**, As with the different stereoisomers of **12**, variation of the chiral centres in compound PZM21 results in large changes in efficacy and potency. Data are mean  $\pm$  s.e.m. of normalized results ( $n = 3$  measurements). **b**, Structure-activity relationship of compound **12** and **21** stereoisomers with affinities displayed as pKi values and agonist potency and efficacy in a  $G_{i/o}$  Glosensor assay. **c**, **d**, PZM21 docked to active  $\mu$ OR shows a more extended conformation as compared to the inactive state. **e**, In the docked active state, the PZM21 thiophene extends into the specificity-determining region of opioid receptors. Key interacting residues here are highlighted as red lines and corresponding residues at

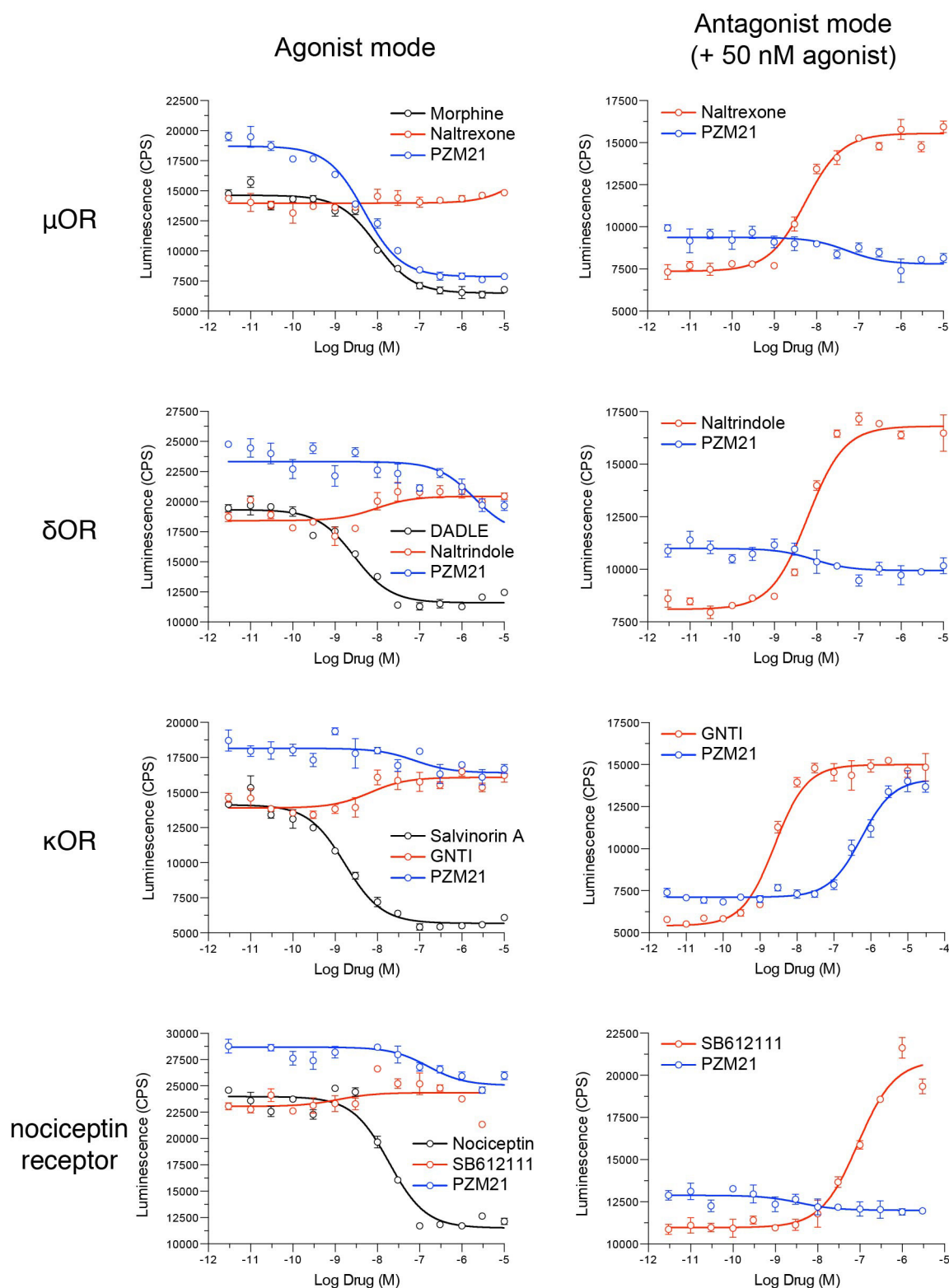
the other human opioid receptors are indicated. **f**, Docked pose of TRV130 within the  $\mu$ OR site, showing minimal overlap in key pharmacophores with PZM21 besides the ionic interaction between the cationic amine and D147<sup>3,32</sup>. **g**, Molecular dynamics simulations of PZM21 in the inactive  $\mu$ OR state (grey and black traces) leads to a stable conformation with the thiophene positioned  $>10 \text{ \AA}$  away from N127<sup>2,63</sup> (total of 2  $\mu$ s of simulation time over three independent trajectories). In contrast, PZM21 adopts a more extended pose when simulated with active  $\mu$ OR, with an average distance of 6  $\text{\AA}$  between the thiophene and N127<sup>2,63</sup>. Other key interactions between  $\mu$ OR and PZM21 are also highlighted.





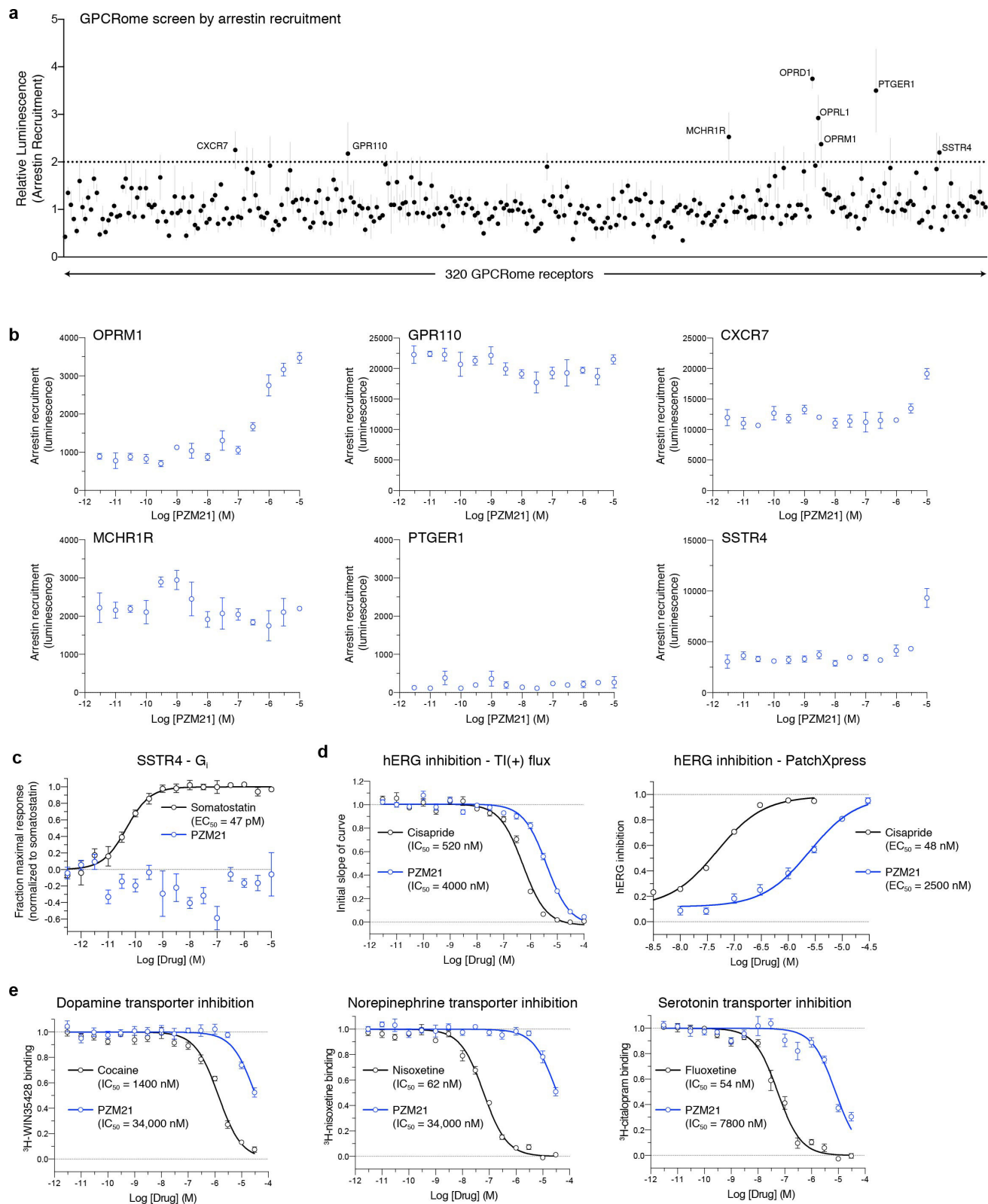
**Extended Data Figure 3 | Structure activity relationship defined by PZM21 analogues.** Eight analogues were synthesized to probe the binding orientation of PZM21 and their efficacy as agonists was tested in a CAMYEL-based  $G_{i/o}$  signalling assay. Analogues were compared to a parent reference compound (PZM22) with similar efficacy and potency to

PZM21. In each case, the EC<sub>50</sub> value for PZM22 is shown in black (1.8 nM) and the EC<sub>50</sub> for the analogue is coloured. The covalent compound PZM29 binds to the  $\mu$ OR:N127C variant irreversibly, as evidenced by wash-resistant inhibition of radioligand binding. Signalling data are mean  $\pm$  s.e.m. of normalized results ( $n = 3$  measurements).



**Extended Data Figure 4 | Signalling properties of PZM21 at the opioid receptors.** Displayed are raw luminescence data from a  $G_{i/o}$  Glosensor assay. In agonist mode, agonists decrease luminescence while inverse agonists increase it by diminishing basal signalling. For each opioid receptor, a prototypical well-characterized agonist (black curves) and antagonist (red curves) were used to validate the assay. In antagonist

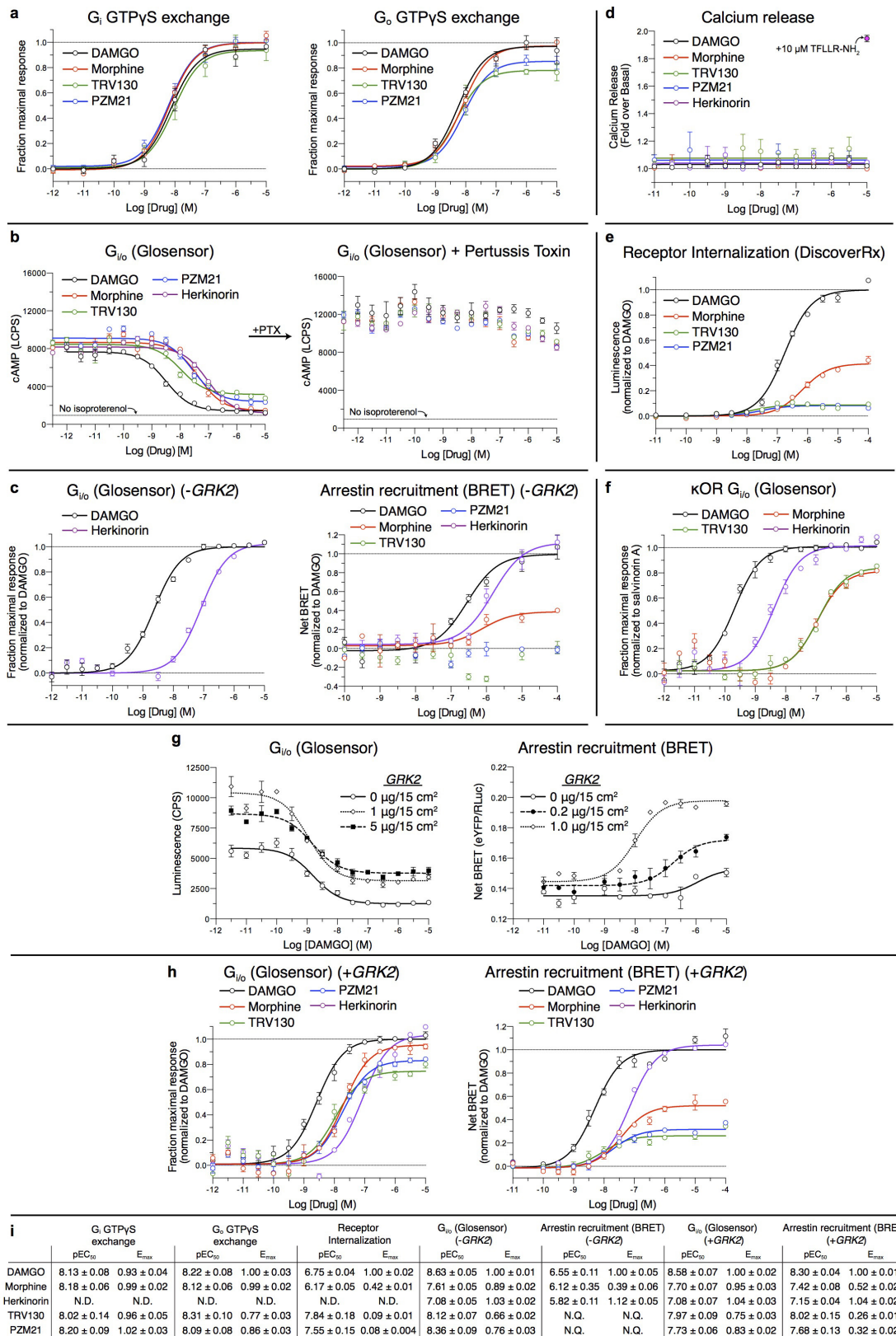
mode, a competition reaction is performed with 50 nM agonist and an escalating amount of tested drug. Here, true antagonists increase the observed signal, consistent with their ability to compete with the agonist but not induce  $G_i$  signalling. Data are mean  $\pm$  s.e.m. of non-normalized results ( $n = 3$  measurements).



**Extended Data Figure 5 | PZM21 is selective for  $\mu$ OR.** **a**, Compound PZM21 was screened against 320 non-olfactory GPCRs for agonism in the arrestin recruitment TANGO assay. Each point shows luminescence normalized to basal level at a given GPCR, with vertical lines indicating the standard error of the mean. **b**, GPCRs for which PZM21 induces an increase in signal twofold over background were further tested in full dose-response mode. Several potential targets (GPR110, MCHR1R, PTGER1) did not show dose-dependent increase in signal and probably represent screening false positives. CXCR7 and SSTR4 did show dose-dependent signals at high concentrations of PZM21, and were further

tested in non-arrestin signalling assays. **c**, PZM21 does not show a dose-dependent change in cAMP inhibition in a  $G_{i/o}$  Glosensor assay measuring SSTR4 activation, indicating that the single elevated point in **b** is probably a false positive result. **d**, **e**, Inhibition assays of hERG (**d**) and the dopamine transporter (DAT), norepinephrine transporter (NET), and serotonin transporter (SERT) (**e**) show that PZM21 has weak inhibitory activity ranging from 2–34  $\mu$ M at these targets. For **a**, data are mean  $\pm$  s.e.m. of non-normalized results ( $n = 4$  measurements). For **b–e**, data are mean  $\pm$  s.e.m. of normalized results ( $n = 3–6$  measurements).

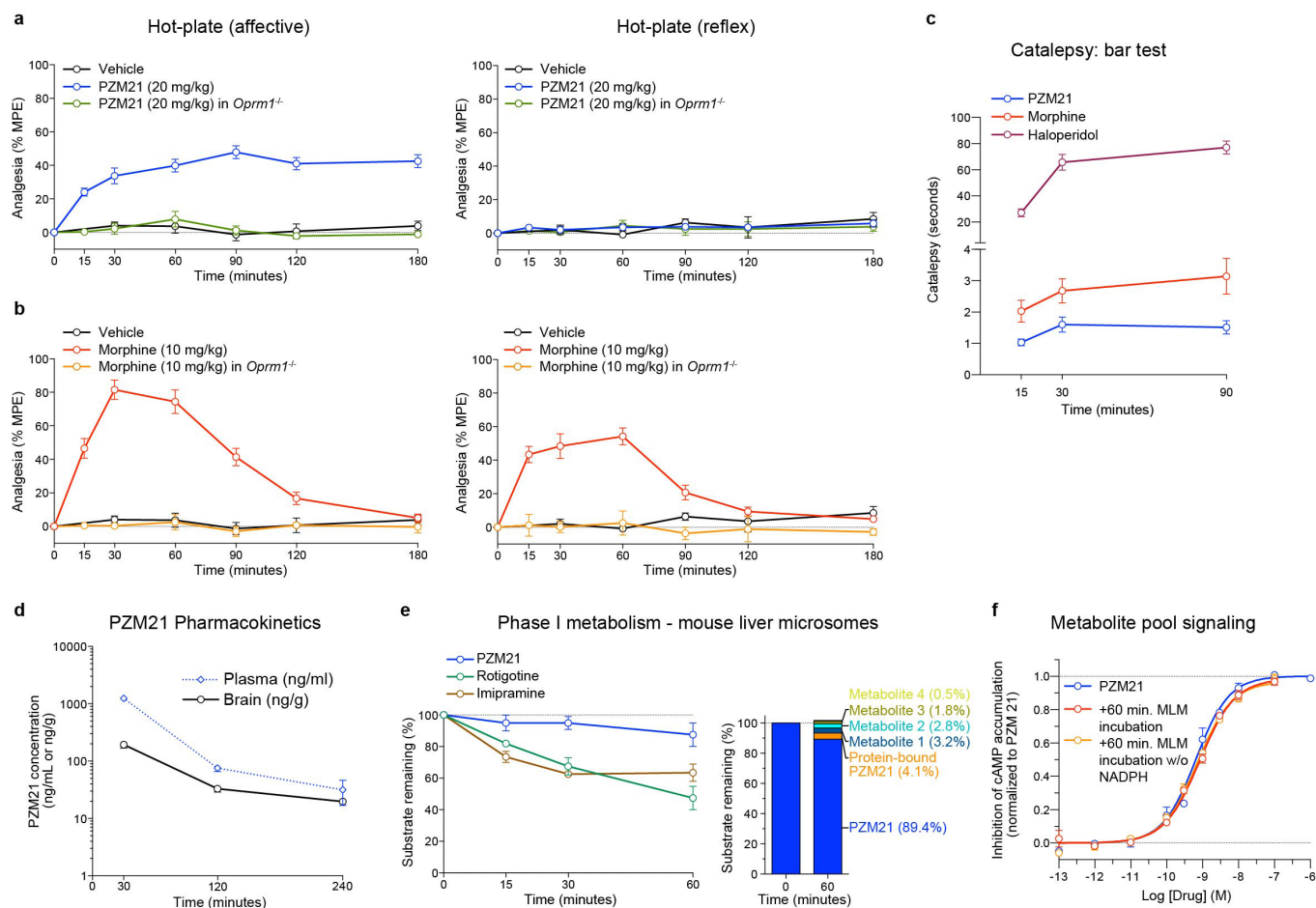




Extended Data Figure 6 | See next page for caption.

**Extended Data Figure 6 | Signalling profile of PZM21 and other  $\mu$ OR agonists.** **a**, PZM21 is an efficacious  $G_i$  and  $G_o$  agonist in a GTP $\gamma$ S assay. **b**, Like other  $\mu$ OR agonists, PZM21 induces a dose-dependent decrease in cAMP levels that is sensitive to pertussis toxin, confirming  $G_{i/o}$  mediated signalling. **c**, Herkinorin is a  $G_{i/o}$  agonist and robustly recruits arrestin in a BRET assay performed in the absence of GRK2 overexpression. TRV130 or PZM21 show undetectable levels of arrestin recruitment in the same experiment. **d**, PZM21 and other opioids show no activity in a calcium-release assay, indicating no  $G_q$ -mediated second messenger signalling. The positive control TFLR-NH<sub>2</sub> efficiently activates the  $G_q$  coupled receptor PAR-1. **e**, PZM21 and TRV130 induce much decreased receptor internalization versus DAMGO and even morphine. **f**, Herkinorin and TRV130 are potent agonists of the  $\kappa$ OR. PZM21 is a  $\kappa$ OR antagonist (see Extended Data Fig. 4). **g**, In HEK293 cells, GRK2 expression levels have minimal effect on the potency and efficacy of the unbiased agonist DAMGO in a  $G_{i/o}$  activation assay. Increased GRK2 levels change the basal

cAMP signal due to increased desensitization of  $\mu$ OR, which lowers receptor basal activity and leads to elevated isoproterenol-induced cAMP. In an arrestin-recruitment BRET assay, increased GRK2 expression increases both the potency and maximal efficacy of the unbiased agonist DAMGO. This is likely because GRK2 mediated phosphorylation is required for efficient  $\beta$ -arrestin recruitment. **h**,  $G_i$  activation and arrestin recruitment in cells co-expressing 1.0  $\mu$ g/15 cm<sup>2</sup> of GRK2. Notably, PZM21 induces a higher maximal level of arrestin recruitment as compared to U2OS cells, which express very low levels of GRK2, but this level is significantly lower than morphine. Despite the lower efficacy for arrestin recruitment observed for morphine, TRV130 and PZM21 compared to DAMGO, a formal calculation of bias by the operational models fails to show that this effect is significant. **i**, Table of pEC<sub>50</sub> values and  $E_{max}$  values for various signalling assays. All data are mean  $\pm$  s.e.m. of results ( $n = 2-6$  measurements).



### Extended Data Figure 7 | Additional *in vivo* studies of PZM21.

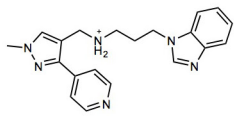
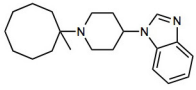
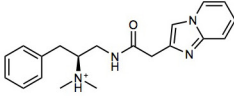
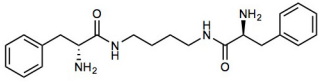
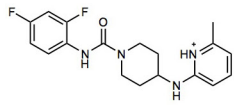
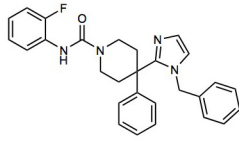
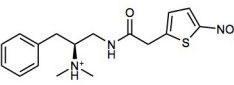
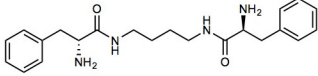
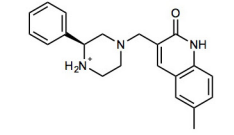
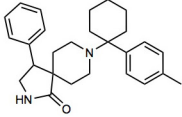
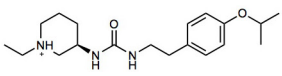
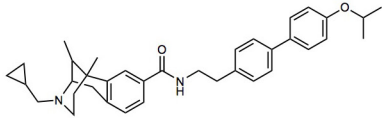
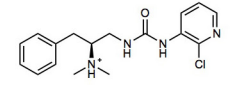
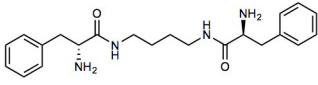
**a**, Analgesic responses measured in the hotplate assay were subcategorized into either affective or reflexive behaviours and scored separately. **b**, Morphine ( $n = 10$  animals) induces changes in both behaviours, while PZM21 ( $n = 13$  animals) only modulates the attending (affective) component. Knockout of the  $\mu$ OR ablates all analgesic responses by morphine and PZM21. **c**, PZM21 shows minimal cataleptic effect compared to morphine at different time points. The effect of haloperidol was included as a positive control. **d**, Pharmacokinetic studies of PZM21 ( $n = 3-4$  animals for each time point) show central nervous system penetration of the compound, with a peak level of 197 ng of PZM21 per g of brain tissue. With a concomitant serum concentration of 1,253 ng/ml, this represents a serum:brain concentration ratio of 6.4. These levels are similar to those achieved by morphine, which shows a

peak brain concentration of approximately 300 ng/g and a serum:brain concentration ratio of 3.7 30 min after subcutaneous injection<sup>75</sup>.

**e**, Metabolism of PZM21 over 60 min exposure to mouse liver microsomes. Rotigotine and imipramine serve as positive controls for extensive phase I metabolism. The total amount of PZM21 and metabolite pool is slightly greater than 100% (101.8%) reflecting cumulative error in LC/MS analysis. **f**, A  $G_{i/o}$  signalling assay shows that none of the metabolites are measurably more potent activators of the  $\mu$ OR versus PZM21 alone. The metabolite pool after the 60-min incubation was used directly in the signalling assay. As a negative control, the pooled material from a reaction carried out in the absence of the key cofactor NADPH was used in the signalling assay. All data are mean  $\pm$  s.e.m. For **e**, reactions were run in triplicate and the s.e.m. was calculated from individual measurements of each reaction.



Extended Data Table 1 | Molecules with  $\mu$ OR activity identified in the initial screen

Cmpd	Structure	Rank	$T_c^a$	$\mu$ OR $K_i$ ( $\mu$ M)	Nearest ChEMBL $\mu$ OR ligand
1		467	0.28	7.2	
2		358	0.28	5.8	
3		1281	0.30	13.8	
4		1465	0.30	2.3	
5		2418	0.31	4.7	
6		2211	0.30	10.0	
7		1140	0.30	2.5	

<sup>a</sup>The ECFP4 Tanimoto similarity ( $T_c$ ) to the most similar  $\mu$ OR ligand in ChEMBL16.

Extended Data Table 2 | Analogues tested at the  $\mu$ OR

Cmpd	Structure	Docking Score	$T_c^a$	$\mu$ OR $K_i$ ( $\mu$ M)	$\kappa$ OR $K_i$ ( $\mu$ M)	$\mu$ OR $G_i$ EC50 ( $\mu$ M)	Nearest ChEMBL $\mu$ OR ligand
8		-42.08	0.31	0.82	0.46	6.6	
9		-48.30	0.31	>10	1.36	N.A. <sup>b</sup>	
10		-51.73	0.31	4.75	>10	N.A. <sup>b</sup>	
11		-46.79	0.35	1.86	>10	N.A. <sup>b</sup>	
12		-51.88	0.35	0.042	0.46	0.18	
13		-51.22	0.35	0.550	1.02	3.1	
14		-50.42	0.37	0.087	0.51	0.44	
15		-43.17	0.37	0.130	>10	N.A. <sup>b</sup>	

<sup>a</sup>The ECFP4 Tanimoto similarity ( $T_c$ ) to the most similar  $\mu$ OR ligand in ChEMBL16.<sup>b</sup>No measurable activity.

Extended Data Table 3 | Binding and signalling properties of compounds 12 and PZM21

	12	PZM21
<b>K<sub>i</sub> (nM)</b>		
μOR	42	1.1
δOR	N.A.	506
κOR	464	18
nociceptin	N.D. <sup>a</sup>	N.D. <sup>a</sup>
<b>G<sub>i/o</sub> (Glosensor)</b>		
<b>EC<sub>50</sub> (nM)   E<sub>max</sub> (%)</b>		
μOR	180   88	4.6   77
δOR	N.A. <sup>b</sup>	1900   78
κOR	N.A. <sup>b</sup>	N.A. <sup>b</sup>
nociceptin	1400   43	N.A. <sup>b</sup>
<b>Arrestin recruitment (PathHunter)</b>		
<b>EC<sub>50</sub> (nM)   E<sub>max</sub> (%)</b>		
μOR	940   9.4	N.A. <sup>a</sup>

<sup>a</sup>Not determined.<sup>b</sup>No measurable activity.



# Structure of the voltage-gated calcium channel $\text{Ca}_v1.1$ at 3.6 Å resolution

Jianping Wu<sup>1,2,3\*</sup>, Zhen Yan<sup>1,2\*</sup>, Zhangqiang Li<sup>1,2,3\*</sup>, Xingyang Qian<sup>3</sup>, Shan Lu<sup>4</sup>, Mengqiu Dong<sup>4</sup>, Qiang Zhou<sup>1,2</sup> & Nieng Yan<sup>1,2,3</sup>

The voltage-gated calcium ( $\text{Ca}_v$ ) channels convert membrane electrical signals to intracellular  $\text{Ca}^{2+}$ -mediated events. Among the ten subtypes of  $\text{Ca}_v$  channel in mammals,  $\text{Ca}_v1.1$  is specified for the excitation-contraction coupling of skeletal muscles. Here we present the cryo-electron microscopy structure of the rabbit  $\text{Ca}_v1.1$  complex at a nominal resolution of 3.6 Å. The inner gate of the ion-conducting  $\alpha 1$ -subunit is closed and all four voltage-sensing domains adopt an 'up' conformation, suggesting a potentially inactivated state. The extended extracellular loops of the pore domain, which are stabilized by multiple disulfide bonds, form a windowed dome above the selectivity filter. One side of the dome provides the docking site for the  $\alpha 2\delta$ -subunit, while the other side may attract cations through its negative surface potential. The intracellular I–II and III–IV linker helices interact with the  $\beta_{1a}$ -subunit and the carboxy-terminal domain of  $\alpha 1$ , respectively. Classification of the particles yielded two additional reconstructions that reveal pronounced displacement of  $\beta_{1a}$  and adjacent elements in  $\alpha 1$ . The atomic model of the  $\text{Ca}_v1.1$  complex establishes a foundation for mechanistic understanding of excitation-contraction coupling and provides a three-dimensional template for molecular interpretations of the functions and disease mechanisms of  $\text{Ca}_v$  and  $\text{Na}_v$  channels.

Voltage-gated calcium ( $\text{Ca}_v$ ) channels activate upon changes in membrane potential and mediate  $\text{Ca}^{2+}$  entry, which triggers multitudes of  $\text{Ca}^{2+}$ -dependent cellular events. Malfunction or dysregulation of  $\text{Ca}_v$  channels are associated with various neurological, cardiovascular, and muscular disorders, making  $\text{Ca}_v$  channels major targets for drug development<sup>1–3</sup>.

In mammals, ten  $\text{Ca}_v$  subtypes have been identified and classified into three families,  $\text{Ca}_v1$ ,  $\text{Ca}_v2$ , and  $\text{Ca}_v3$ , on the basis of the ion-conducting  $\alpha 1$ -subunit<sup>4–6</sup>. Among these, the  $\text{Ca}_v1$  channels ( $\text{Ca}_v1.1$ – $1.4$ ) are L-type high-voltage-activated channels that co-assemble with auxiliary subunits including the extracellular  $\alpha 2\delta$ , the intracellular  $\beta$ , and the transmembrane  $\gamma$ . These auxiliary subunits modulate the activation and inactivation kinetics, gating properties, and membrane trafficking of the  $\alpha 1$ -subunit<sup>7–9</sup>.  $\text{Ca}_v1$  channels, known as DHP receptors, are responsive to dihydropyridine (DHP) drugs<sup>10,11</sup>.

$\text{Ca}_v1.1$ , being the first  $\text{Ca}_v\alpha 1$  to be cloned, has been a prototype in the functional, structural, and mechanistic investigations of  $\text{Ca}_v$  channels<sup>12,13</sup>.  $\text{Ca}_v1.1$  serves as the voltage sensor for excitation-contraction coupling of skeletal muscles<sup>14,15</sup>. The action-potential-induced conformational changes of  $\text{Ca}_v1.1$  activate the type 1 ryanodine receptor (RyR1), which is responsible for rapid release of  $\text{Ca}^{2+}$  from the sarcoplasmic reticulum to cytoplasm, an event that triggers subsequent muscle contraction<sup>16–18</sup>.

The cryo-electron microscopy (cryo-EM) structure of the rabbit  $\text{Ca}_v1.1$  complex containing  $\alpha 1$ -,  $\alpha 2\delta$ -,  $\beta_{1a}$ -, and  $\gamma$ -subunits was determined to 4.2 Å resolution<sup>19</sup>. The four homologous repeats (I–IV) of  $\alpha 1$ , each containing six transmembrane segments (S1–S6) organized into a canonical voltage-gated ion channel fold, are arranged clockwise in the extracellular view. The  $\gamma$ -subunit, which contains four transmembrane helices and shares identical structural fold with claudins<sup>20</sup>, contacts the voltage-sensing domain of the fourth repeat (VSD<sub>IV</sub>). The von Willebrand factor domain A (VWA) and two cache domains in  $\alpha 2\delta$

interact with the extended extracellular loops of  $\alpha 1$ . The cytoplasmic  $\beta_{1a}$ -subunit was placed in the vicinity of VSD<sub>II</sub>. However, owing to the moderate resolution, side chains were assigned to merely one-quarter of the molecular mass. Half of the EM map for the extracellular  $\alpha 2\delta$ -subunit could not be resolved. In particular, the VSDs in repeats II and III were nearly invisible and the molecular details of the pore domain are yet to be elucidated.

## Structural determination of the $\text{Ca}_v1.1$ complex

Carbon-film-coated grids were used to enrich particles for EM imaging that yielded the 4.2 Å reconstruction<sup>19</sup>. To increase contrast, we determined an optimal condition in which sufficient numbers of protein particles entered ice without carbon film. The new condition resulted in elimination of orientation preference and resolution of all four VSDs (Extended Data Fig. 1a–c). Out of 527,833 selected particles (class I), an EM map was calculated to 3.6 Å according to the gold-standard Fourier shell correlation 0.143 criterion (Extended Data Figs 1d and 2).

The resolution for the majority of the  $\alpha 2\delta$ - and  $\alpha 1$ -subunits was beyond 3.5 Å and allowed *de novo* model building. However, the density for the  $\beta$ -subunit was still largely missing. After further 3D classification, a 3.9 Å map was obtained from a subgroup of particles (class Ia) that showed a discernible  $\beta$ -subunit. Meanwhile, a separate group of particles (class II) yielded another 3.9 Å map. In addition to the  $\beta$ -subunit, several intracellular segments of the  $\alpha 1$ -subunit were well resolved in the class Ia and class II reconstructions (Extended Data Figs 1d–f and 2).

On the basis of the three EM maps, a structural model consisting of 2,661 residues, among which 2,595 had side groups assigned, was generated for the  $\text{Ca}_v1.1$  complex. In addition to the protein subunits, 14 lipids were built and 25 sugar moieties were assigned to 16 glycosylation sites, 15 on the  $\alpha 2\delta$ -subunit and 1 on the  $\alpha 1$ -subunit (Fig. 1 and Extended Data Table 1). The structural assignment was verified by

<sup>1</sup>State Key Laboratory of Membrane Biology, School of Life Sciences and School of Medicine, Tsinghua University, Beijing 100084, China. <sup>2</sup>Beijing Advanced Innovation Center for Structural Biology, School of Life Sciences and School of Medicine, Tsinghua University, Beijing 100084, China. <sup>3</sup>Tsinghua-Peking Joint Center for Life Sciences, School of Life Sciences, Tsinghua University, Beijing 100084, China. <sup>4</sup>National Institute of Biological Sciences, Beijing, Beijing, 102206, China.

\*These authors contributed equally to this work.

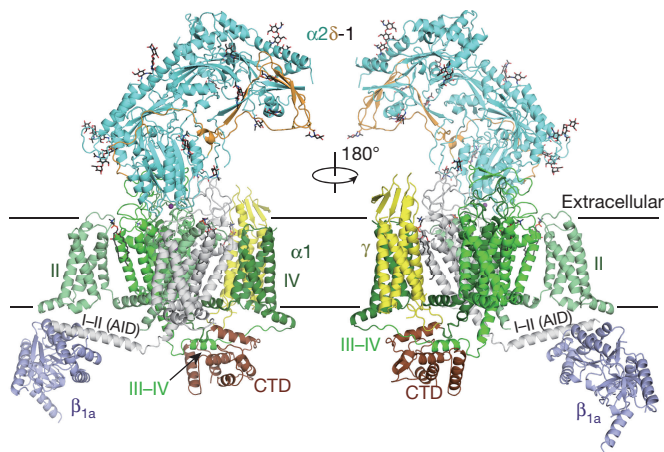


**Figure 1 | Overall structure of the rabbit  $\text{Ca}_v1.1$  complex.** The structure shown here was primarily modelled and refined with the 3.6 Å class I EM map. The intracellular segments were modelled on the basis of the class Ia map and VSD<sub>III</sub> was built on the class I and class II maps. See Extended Data Figs 1 and 2 for details of cryo-EM analysis. The structure is colour-coded for distinct subunits. The four homologous repeats (repeats I–IV) of the  $\alpha 1$ -subunit are coloured with increasingly darker green. The same colour scheme is used in Figs 2–6 unless otherwise indicated. The glycosyl moieties and lipids are shown as black sticks. All structure figures were prepared with PyMol<sup>48</sup>.

mass spectrometric (MS) analysis of crosslinked complex and disulfide bonds (Extended Data Table 2).

### Structure of the $\alpha 2\delta$ -subunit

In the new 3.6 Å map, two additional cache domains were resolved in the  $\alpha 2\delta$ -subunit (Fig. 2a and Extended Data Figs 3 and 4). Therefore, the  $\alpha 2\delta$ -subunit in total comprises four tandem cache domains and one VWA domain. Despite distinct domain organization in the three-dimensional space, the five domains are intertwined in the primary sequence (Extended Data Fig. 4a).

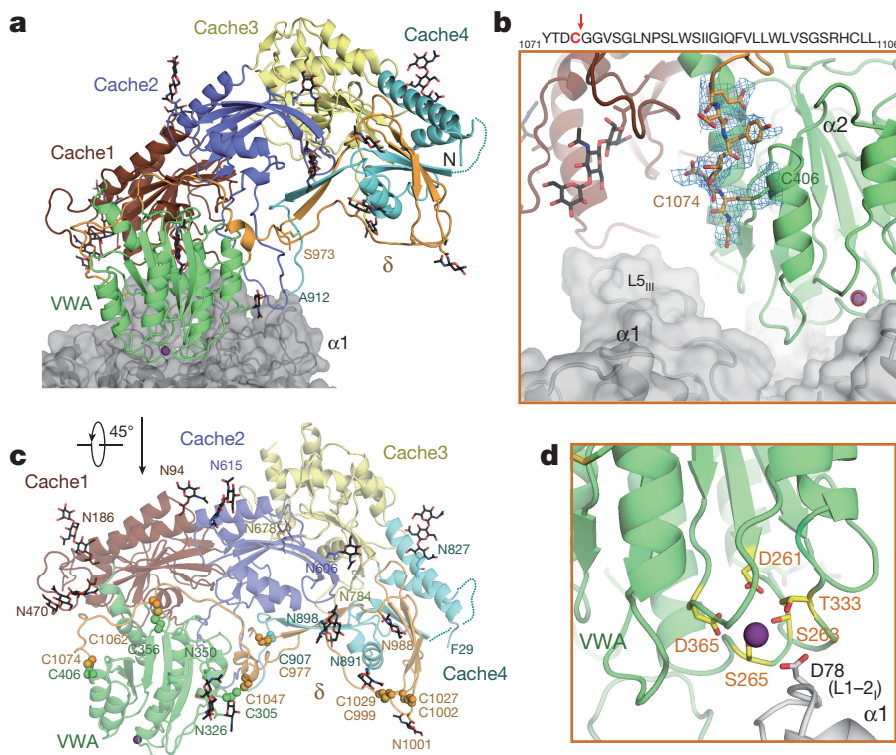


**Figure 2 | Structure of the extracellular  $\alpha 2\delta$ -1-subunit.** **a**, The  $\alpha 2\delta$ -1-subunit comprises one VWA domain and four tandem cache domains. The extracellular region of the  $\alpha 1$ -subunit is shown in semi-transparent surface view. The  $\delta$ -subunit is coloured orange and the  $\alpha 2$ -subunit is domain coloured. A topological cartoon of the  $\alpha 2\delta$ -1-subunit is presented in Extended Data Fig. 4a. **b**, The structure appears to support glycosylphosphatidylinositol modification of the cleavage-exposed C terminus (Cys1074) of the  $\delta$ -subunit<sup>21</sup>. The primary sequence of the C terminus of the  $\delta$  subunit is shown. The red arrow indicates the potential cleavage site. The 5σ EM map that extends beyond Cys1074 may correspond to the ethanolamine of the glycosylphosphatidylinositol. **c**, The glycosylation sites (black sticks) and disulfide bonds (spheres) identified in the cryo-EM structure of the  $\alpha 2\delta$ -1-subunit. Mass spectrometric analysis is summarized in Extended Data Table 2. **d**, A metal ion coordinated by the MIDAS motif in the VWA domain of  $\alpha 2$ . The bound ion is shown as purple sphere.

The  $\delta$ -subunit, which is separated from the  $\alpha 2$ -subunit in the primary structure through proteolytic cleavage, completes the fourth cache domain by contributing three  $\beta$ -strands (Fig. 2a and Extended Data Fig. 4a, b). The ensuing segment of the  $\delta$ -subunit displays an extended conformation, wrapping alongside the concave side of cache1 and cache2 and the top surface of the VWA domain before reaching the extracellular loops of the  $\alpha 1$ -subunit. The last unambiguously assigned residue of the  $\delta$ -subunit in the EM map is Cys1074, which forms a disulfide bond with Cys406 in the VWA domain (Fig. 2b and Extended Data Fig. 4b). The  $\delta$ -subunit was predicted to possess a single transmembrane helix formed by the carboxy (C)-terminal hydrophobic sequence (Fig. 2b). A recent characterization suggested that the  $\delta$ -subunit may be anchored to the membrane through a glycosylphosphatidylinositol modification<sup>21</sup>, which appears to be supported by the structure and MS characterizations. We modelled an ethanolamine to the density following Cys1074 (Fig. 2b). See the legend of Extended Data Fig. 4b for details.

The extended conformation of  $\delta$  is stabilized through multiple intra- and inter-subunit disulfide bonds. In total, four disulfide bonds were observed between the  $\alpha 2$ - and  $\delta$ -subunits and two within the  $\delta$ -subunit (Fig. 2c and Extended Data Table 2a). On the surface of the  $\alpha 2\delta$ -subunit, 15 out of 16 predicted glycosyl moieties were identified (Fig. 2c).

The VWA domain exhibited an ‘open’ conformation in the 4.2 Å structure despite the lack of density for a metal ion in the metal-ion-dependent adhesion site (MIDAS) motif<sup>49</sup>. In the current map, the MIDAS residues, Ser263, Ser265, Asp261, Thr333, and Asp365, coordinate a density that should correspond to a cation. As the protein was purified in the presence of 10 mM  $\text{Ca}^{2+}$ , we tentatively assigned a  $\text{Ca}^{2+}$  into the map (Fig. 2d and Extended Data Fig. 4e). In addition to the MIDAS residues, Asp78 of  $\alpha 1$ , which is located on the L1–2<sub>1</sub> loop, also contributes to ion coordination, providing a structural interpretation for the MIDAS-dependent augmentation of cell surface density of the  $\text{Ca}_v$  channels<sup>22</sup>.

### The closed channel

On the basis of the three maps, an atomic model of the  $\alpha 1$ -subunit was generated including the pore domain, the four VSDs, the intracellular  $\alpha 1$ -interacting domain (AID)-containing helix between repeats I and II



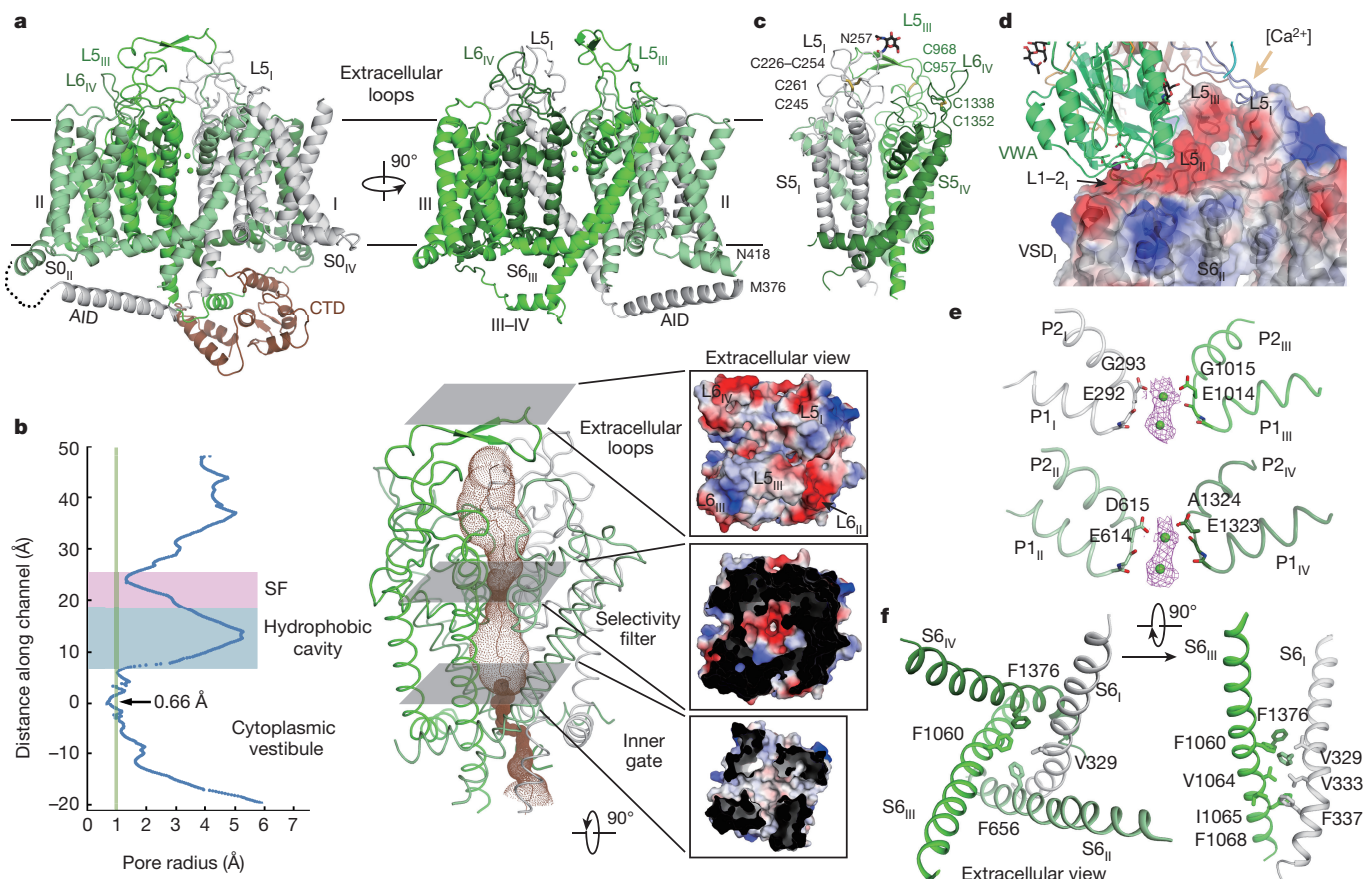


**Figure 3 | The ion permeation path of  $\text{Ca}_v1.1$ .** **a**, The overall structure of the  $\alpha 1$ -subunit. The CTD is omitted in the right panel to better illustrate the III–IV linker. The tentatively assigned  $\text{Ca}^{2+}$  ions in the selectivity filter vestibule are presented as green spheres. **b**, The permeation path of the pore domain. The ion conducting passage, calculated by HOLE<sup>49</sup>, is illustrated by brown dots in the middle panel. The pore radii along the pore are tabulated on the left. The cut-open extracellular views of the electrostatic potentials calculated in PyMol are shown for the indicated layers. **c**, The extracellular loops of the pore domain are stabilized by multiple disulfide bonds. **d**, The extracellular loops of the pore domain form a domed window above the selectivity filter. While the extended

loops between S5 and P1 helices in repeats II and III (designated the  $\text{L5}_{\text{II}}$  and  $\text{L5}_{\text{III}}$  loops, respectively) provide the primary docking site for the VWA domain in  $\alpha 2$ , a cavity enclosed by the negative charges on  $\text{L5}_{\text{I}}$ ,  $\text{L5}_{\text{II}}$ , and  $\text{L5}_{\text{III}}$  may represent the major extracellular entrance for  $\text{Ca}^{2+}$  ions. **e**, The selectivity filter of  $\text{Ca}_v1.1$ . A stretch of EM density alongside the selectivity filter vestibule can be deconvoluted to a sphere at the inner site and a flattened disc in the middle. Two  $\text{Ca}^{2+}$  ions are tentatively assigned. See Extended Data Figs 5d and 7 for detailed analysis. **f**, Closed inner gate. Four hydrophobic residues, Val329, Phe656, Phe1060, and Phe1376, on the S6 bundle seal the inner gate. The closure is buttressed by additional hydrophobic residues, particularly those on  $\text{S6}_{\text{I}}$  and  $\text{S6}_{\text{III}}$ .

(the I–II helix), and the intact III–IV linker. The invisible segments include 40 residues following the AID in linker I–II, 100 residues between repeats II and III, and the C-terminal residues after Asp1515 (Fig. 3a, Extended Data Fig. 5 and Supplementary Fig. 1). The assignment of all the side groups of the pore domain allows close examination of the channel permeation path (Fig. 3b).

The extended extracellular loops, which are stabilized by multiple intra-loop disulfide bonds, form a windowed dome above the selectivity filter (Fig. 3c and Extended Data Fig. 6a, b). The window formed by the  $\text{L5}$  loops from repeats I, II, and III is enriched in negatively charged residues, representing a potential main entrance in  $\text{Ca}^{2+}$  to the selectivity filter vestibule, while the one encircled by  $\text{L5}_{\text{III}}$  and  $\text{L6}_{\text{IV}}$  may also allow passage of  $\text{Ca}^{2+}$  ions (Fig. 3d and Extended Data Fig. 6c). On the other side, loops  $\text{L1}$ – $\text{L2}_{\text{I}}$ ,  $\text{L5}_{\text{II}}$  and  $\text{L5}_{\text{III}}$  together constitute the docking site for the  $\alpha 2\delta$ -subunit (Extended Data Fig. 6d).

Despite the fact that the carboxylate groups of Glu and Asp are invisible in the EM map owing to radiation damage, the high-quality map of the P1 and P2 helices allows accurate backbone assignment of the residues constituting the selectivity filter vestibule, including the critical EEEE residues (Glu292/614/1014/1323) that provide the side groups and the two preceding residues in each repeat that contribute the carbonyl oxygens (C=O) (Fig. 3e and Extended Data Fig. 5d). A consecutive stretch of density stands along the selectivity filter vestibule

that can be deconvoluted to a round disc in the centre of the four Glu residues and a sphere surrounded by the eight C=O groups. We tentatively assigned two  $\text{Ca}^{2+}$  ions to the middle disc and the inner sphere (Fig. 3e and Extended Data Fig. 7a). The structural assignment of the selectivity filter and  $\text{Ca}^{2+}$  ions supports previous characterizations of the residues critical for ion selectivity<sup>23–25</sup>.

We used 10 mM and 0.5 mM  $\text{Ca}^{2+}$  ions for protein purifications that yielded the present and previous EM reconstructions, respectively. The shape and position of the density in the selectivity filter vestibule in the current map, even when low-pass filtered to 4.2 Å, are distinct from those in the previous map<sup>19</sup> (Extended Data Fig. 7a–c). The heights of the two  $\text{Ca}^{2+}$  ions in the current structure are similar to those in  $\text{Ca}_v\text{Ab}^{26}$ , except that the inner one is slightly off the central axis and closer to repeats I and II (Extended Data Fig. 7d).

Below the selectivity filter vestibule is the typical hydrophobic cavity with side portals that are penetrated by transverse lipids, a feature observed in bacterial  $\text{Na}_v$  channels<sup>27,28</sup> (Fig. 3b and Extended Data Fig. 6a, b). The asymmetric S6 bundle of  $\text{Ca}_v1.1$  screws tightly at the inner gate. Three aromatic residues at the corresponding positions on S6 from repeats II–IV (Phe656/1060/1376) together with Val329 on  $\text{S6}_{\text{I}}$  completely seal the pore from the cytoplasm. Below the aromatic ring are hydrophobic residues on  $\text{S6}_{\text{I}}$  and  $\text{S6}_{\text{III}}$  that buttress the closure (Fig. 3f).





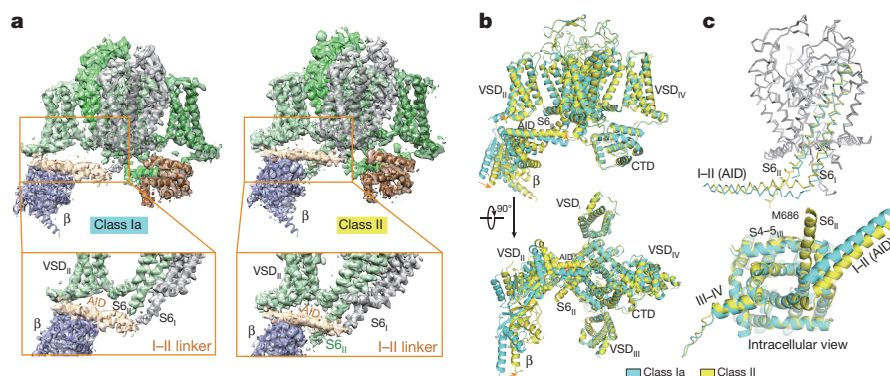


**Figure 6 | Conformational changes of the intracellular elements of  $\text{Ca}_v1.1$ .** **a**, The intracellular I–II linker of  $\alpha 1$ - and the  $\beta$ -subunits resolved in class Ia and class II maps. The maps were generated in Chimera<sup>50</sup>. **b**, The pronounced shifts of  $\beta$  and the intracellular segments of  $\alpha 1$  between the two 3.9 Å structures. The orange arrows indicate the movements of the intracellular domains from class Ia to class II. **c**, Conformational changes

### Distinct conformations of the intracellular domains

The secondary structural elements of the  $\beta$ -subunit are resolved in the class Ia and II maps, supporting reliable docking of the crystal structure of AID-bound  $\beta$ -subunit<sup>34</sup>. The AID motif is part of a seemingly rigid helix that represents the intracellular extension of  $\text{S6}_I$  bent by approximately 60° and lies along one diagonal axis of the  $\alpha 1$ -subunit on the intracellular surface (Fig. 6a and Extended Data Fig. 8a). Residues 670–686 constituting the extension of the  $\text{S6}_{II}$  helix are resolved in the class II, but not class Ia, map (Fig. 6b, c and Extended Data Fig. 8b). The  $\text{S6}_{II}$  extension is adjacent to the  $\beta$ -subunit, consistent with the MS analysis of crosslinked  $\text{Ca}_v1.1$  complex (Fig. 6b and Extended Data Table 2b).

The AID motif is sandwiched between  $\alpha 1$ -VSD<sub>II</sub> and  $\beta$ . This structural feature predicts that conformational changes of  $\text{S6}_I$  or VSD<sub>II</sub> would be translated to the motion of  $\beta$ -subunit through the I–II linker helix. Supporting this notion, comparison of the class Ia and II reconstructions reveals shifts of the C terminus of  $\text{S6}_I$  and the ensuing I–II helix. Meanwhile, the  $\beta$ -subunit undergoes a pronounced displacement between the two reconstructions (Fig. 6b, c, Extended Data Fig. 8b and Supplementary Video).

The intact III–IV linker, which is the shortest among the three inter-repeat linkers of  $\alpha 1$ , is resolved in all three maps. Residues 1,083–1,094, which connect to the  $\text{S6}_{III}$  segment through a turn, form a helix that together with the helices in carboxy-terminal domain (CTD) completes a globular domain (Figs 3a, 6a and Extended Data Fig. 8c). The succeeding linker residues 1,095–1,105 interact with the C terminus of the  $\gamma$ -subunit (Fig. 5d).

### Perspective

$\text{Ca}_v1.1$  and RyR1 are the principal membrane components for excitation–contraction coupling. Structural determination of the two  $\text{Ca}^{2+}$  channels illuminates the avenue towards mechanistic understanding of this fundamental physiological process<sup>19,35–37</sup>. However, the complex formation between  $\text{Ca}_v1.1$  and RyR1 has not been recapitulated biochemically *in vitro*, probably owing to weak affinities between individual proteins or dissociation of bridging components during protein isolation. The concerted motions of the  $\alpha 1$ -segments and the  $\beta$ -subunit revealed in this study provide important clues to the molecular understanding for excitation–contraction coupling as the  $\beta$ -subunit is an indispensable component for the formation of the ultrastructure between  $\text{Ca}_v1.1$  and RyR1 (refs 38–40). The advent of atomic structures of the  $\text{Ca}_v1.1$  complex and RyR1 establishes a solid foundation for future investigations of excitation–contraction coupling using biophysical and biochemical approaches such as electron tomography and super-resolution imaging.

The structural elucidation of the proximity between the  $\beta_{1a}$ -subunit and the extended  $\text{S6}_{II}$  segment and VSD<sub>II</sub> of  $\alpha 1$ , as well as the observation

of the intracellular segments of  $\alpha 1$ . To highlight the differences between class Ia and class II structures, the  $\text{S6}_I$ , AID, and  $\text{S6}_{II}$  segments are coloured cyan and yellow, respectively, while other segments are coloured grey in the top panel. Additional residues up to Met686 were resolved in class II maps for  $\text{S6}_{II}$ . See the Supplementary Video for the morph illustrating the conformational changes.

that the  $\beta$ -subunit-interacting AID is part of the bent extension of  $\text{S6}_I$ , provide an important clue to understanding the coupling mechanism between the  $\beta$ -subunit and the  $\text{S6}$  segments in the voltage-dependent inactivation of  $\text{Ca}_v$  channels<sup>41</sup>. Despite the fact that the conformational states of the class Ia and II structures remain to be defined, the observed conformational changes of the intracellular segments in the  $\alpha 1$ -subunit and the concordant movement of the  $\beta$ -subunit lay out an important foundation for future investigations (Supplementary Video).

The  $\text{Ca}_v$  channels and closely related  $\text{Na}_v$  channels play a major role in multitudes of physiological and pathological processes. Hundreds of disease-associated mutations have been identified in these channels. The atomic model of the  $\text{Ca}_v1.1$  complex presented here provides the structural template for mechanistic interpretation of a large body of experimental and clinical observations concerning  $\text{Ca}_v$  and  $\text{Na}_v$  channels (Supplementary Figs 1 and 2).

One unexpected structural finding is the formation of a globular domain by the CTD and the III–IV linker helix of the  $\alpha 1$ -subunit. Consistent with the sequence similarities between  $\text{Ca}_v$  and  $\text{Na}_v$  channels, structural comparison of the  $\text{Ca}_v1.1$ -CTD with the CTDs of  $\text{Na}_v1.2$  and  $\text{Na}_v1.5$  reveals identical fold of the first four helices and intervening  $\beta$ -strands (Supplementary Fig. 2)<sup>42,43</sup>. However, marked conformational deviations occur to the last two helices. The  $\alpha 5$  and  $\alpha 6$  helices in  $\text{Ca}_v1.1$ -CTD form a hairpin that interacts with the III–IV helix. In contrast, the  $\alpha 5$  helix in the  $\text{Na}_v$ -CTDs is almost the equivalent of the III–IV helix in  $\text{Ca}_v1.1$ , and the IQ motif-containing  $\alpha 6$  helix, which is substantially longer than that in  $\text{Ca}_v1.1$ -CTD, adopts an extended conformation and interacts with  $\text{Ca}^{2+}$ -loaded calmodulin in the crystal structures (Supplementary Fig. 2, inset). The differences between the  $\text{Ca}_v1.1$ -CTD in the context of the full-length protein and the isolated  $\text{Na}_v$ -CTD in complex with calmodulin may suggest potential conformational changes of the  $\text{Ca}_v$ -CTDs upon binding to calmodulin in different  $\text{Ca}^{2+}$  loading states. Further investigation of this caveat may shed light on the mechanistic understanding of calcium-dependent inactivation of  $\text{Ca}_v$  channels<sup>44,45</sup>. Finally, the structural similarity between the III–IV linker in the intact  $\text{Ca}_v1.1$  channel and an isolated  $\text{Na}_v$  channel inactivation gate will facilitate mechanistic understanding of fast inactivation of  $\text{Na}_v$  channels (Supplementary Fig. 2)<sup>46,47</sup>.

In sum, the EM structure of the  $\text{Ca}_v1.1$  complex at near-atomic resolution presented here serves as the template for homologous modelling and structure-based engineering of related  $\text{Ca}_v$  and  $\text{Na}_v$  channels, establishes the framework for computational and experimental characterizations and interpretations of the function and disease mechanism of these channels, and provides the basis for structure-guided ligand design.



**Online Content** Methods, along with any additional Extended Data display items and Source Data, are available in the online version of the paper; references unique to these sections appear only in the online paper.

**Received 6 February; accepted 15 July 2016.**

**Published online 31 August 2016.**

- Clapham, D. E. Calcium signaling. *Cell* **131**, 1047–1058 (2007).
- Zamponi, G. W., Striessnig, J., Koschak, A. & Dolphin, A. C. The physiology, pathology, and pharmacology of voltage-gated calcium channels and their future therapeutic potential. *Pharmacol. Rev.* **67**, 821–870 (2015).
- Catterall, W. A. Voltage-gated calcium channels. *Cold Spring Harb. Perspect. Biol.* **3**, a003947 (2011).
- Nowycky, M. C., Fox, A. P. & Tsien, R. W. Three types of neuronal calcium channel with different calcium agonist sensitivity. *Nature* **316**, 440–443 (1985).
- Ertel, E. A. et al. Nomenclature of voltage-gated calcium channels. *Neuron* **25**, 533–535 (2000).
- Hille, B. *Ion Channels of Excitable Membranes*, 814 (Sinauer, 2001).
- Kang, M. G. & Campbell, K. P.  $\gamma$  Subunit of voltage-activated calcium channels. *J. Biol. Chem.* **278**, 21315–21318 (2003).
- Davies, A. et al. Functional biology of the  $\alpha_2\delta$  subunits of voltage-gated calcium channels. *Trends Pharmacol. Sci.* **28**, 220–228 (2007).
- Buraei, Z. & Yang, J. The  $\beta$ -subunit of voltage-gated  $\text{Ca}^{2+}$  channels. *Physiol. Rev.* **90**, 1461–1506 (2010).
- Kohlhardt, M. & Fleckenstein, A. Inhibition of the slow inward current by nifedipine in mammalian ventricular myocardium. *Naunyn Schmiedeberg's Arch. Pharmacol.* **298**, 267–272 (1977).
- Fleckenstein, A. History of calcium antagonists. *Circ. Res.* **52**, I3–I16 (1983).
- Tanabe, T. et al. Primary structure of the receptor for calcium channel blockers from skeletal muscle. *Nature* **328**, 313–318 (1987).
- Bannister, R. A. & Beam, K. G. Ca(V)1.1: The atypical prototypical voltage-gated  $\text{Ca}^{2+}$  channel. *Biochim. Biophys. Acta* **1828**, 1587–1597 (2013).
- Rios, E. & Brum, G. Involvement of dihydropyridine receptors in excitation–contraction coupling in skeletal muscle. *Nature* **325**, 717–720 (1987).
- Tanabe, T., Beam, K. G., Powell, J. A. & Numa, S. Restoration of excitation–contraction coupling and slow calcium current in dysgenic muscle by dihydropyridine receptor complementary DNA. *Nature* **336**, 134–139 (1988).
- Block, B. A., Imagawa, T., Campbell, K. P. & Franzini-Armstrong, C. Structural evidence for direct interaction between the molecular components of the transverse tubule/sarcoplasmic reticulum junction in skeletal muscle. *J. Cell Biol.* **107**, 2587–2600 (1988).
- Adams, B. A., Tanabe, T., Mikami, A., Numa, S. & Beam, K. G. Intramembrane charge movement restored in dysgenic skeletal muscle by injection of dihydropyridine receptor cDNAs. *Nature* **346**, 569–572 (1990).
- Takekura, H., Bennett, L., Tanabe, T., Beam, K. G. & Franzini-Armstrong, C. Restoration of junctional tetrads in dysgenic myotubes by dihydropyridine receptor cDNA. *Biophys. J.* **67**, 793–803 (1994).
- Wu, J. et al. Structure of the voltage-gated calcium channel Cav1.1 complex. *Science* **350**, aad2395 (2015).
- Simske, J. S. Claudins reign: the claudin/EMP/PMP22/ $\gamma$  channel protein family in *C. elegans*. *Tissue Barriers* **1**, e25502 (2013).
- Davies, A. et al. The  $\alpha_2\delta$ -subunits of voltage-gated calcium channels form GPI-anchored proteins, a posttranslational modification essential for function. *Proc. Natl Acad. Sci. USA* **107**, 1654–1659 (2010).
- Cantí, C. et al. The metal-ion-dependent adhesion site in the Von Willebrand factor-A domain of  $\alpha_2\delta$ -subunits is key to trafficking voltage-gated  $\text{Ca}^{2+}$  channels. *Proc. Natl Acad. Sci. USA* **102**, 11230–11235 (2005).
- Yang, J., Ellinor, P. T., Sather, W. A., Zhang, J. F. & Tsien, R. W. Molecular determinants of  $\text{Ca}^{2+}$  selectivity and ion permeation in L-type  $\text{Ca}^{2+}$  channels. *Nature* **366**, 158–161 (1993).
- Ellinor, P. T., Yang, J., Sather, W. A., Zhang, J. F. & Tsien, R. W.  $\text{Ca}^{2+}$  channel selectivity at a single locus for high-affinity  $\text{Ca}^{2+}$  interactions. *Neuron* **15**, 1121–1132 (1995).
- Cloues, R. K., Cibulsky, S. M. & Sather, W. A. Ion interactions in the high-affinity binding locus of a voltage-gated  $\text{Ca}^{2+}$  channel. *J. Gen. Physiol.* **116**, 569–586 (2000).
- Tang, L. et al. Structural basis for  $\text{Ca}^{2+}$  selectivity of a voltage-gated calcium channel. *Nature* **505**, 56–61 (2014).
- Payandeh, J., Scheuer, T., Zheng, N. & Catterall, W. A. The crystal structure of a voltage-gated sodium channel. *Nature* **475**, 353–358 (2011).
- Zhang, X. et al. Crystal structure of an orthologue of the NaChBac voltage-gated sodium channel. *Nature* **486**, 130–134 (2012).
- Ahuja, S. et al. Structural basis of Nav1.7 inhibition by an isoform-selective small-molecule antagonist. *Science* **350**, aac5464 (2015).
- Armstrong, C. M. & Bezanilla, F. Currents related to movement of the gating particles of the sodium channels. *Nature* **242**, 459–461 (1973).
- Noda, M. et al. Primary structure of *Electrophorus electricus* sodium channel deduced from cDNA sequence. *Nature* **312**, 121–127 (1984).
- Tao, X., Lee, A., Limapichat, W., Dougherty, D. A. & MacKinnon, R. A gating charge transfer center in voltage sensors. *Science* **328**, 67–73 (2010).
- Andronache, Z. et al. The auxiliary-subunit  $\gamma_1$  of the skeletal muscle L-type  $\text{Ca}^{2+}$  channel is an endogenous  $\text{Ca}^{2+}$  antagonist. *Proc. Natl Acad. Sci. USA* **104**, 17885–17890 (2007).
- Almagor, L. et al. The role of a voltage-dependent  $\text{Ca}^{2+}$  channel intracellular linker: a structure-function analysis. *J. Neurosci.* **32**, 7602–7613 (2012).
- Yan, Z. et al. Structure of the rabbit ryanodine receptor RyR1 at near-atomic resolution. *Nature* **517**, 50–55 (2015).
- Zalk, R. et al. Structure of a mammalian ryanodine receptor. *Nature* **517**, 44–49 (2015).
- Eftremov, R. G., Leitner, A., Aebersold, R. & Raunser, S. Architecture and conformational switch mechanism of the ryanodine receptor. *Nature* **517**, 39–43 (2015).
- Gregg, R. G. et al. Absence of the  $\beta$  subunit (*cchb1*) of the skeletal muscle dihydropyridine receptor alters expression of the  $\alpha_1$  subunit and eliminates excitation–contraction coupling. *Proc. Natl Acad. Sci. USA* **93**, 13961–13966 (1996).
- Cheng, W., Altafaj, X., Ronjat, M. & Coronado, R. Interaction between the dihydropyridine receptor  $\text{Ca}^{2+}$  channel  $\beta$ -subunit and ryanodine receptor type 1 strengthens excitation–contraction coupling. *Proc. Natl Acad. Sci. USA* **102**, 19225–19230 (2005).
- Schredelseker, J. et al. The  $\beta_{1a}$  subunit is essential for the assembly of dihydropyridine-receptor arrays in skeletal muscle. *Proc. Natl Acad. Sci. USA* **102**, 17219–17224 (2005).
- Stotz, S. C., Jarvis, S. E. & Zamponi, G. W. Functional roles of cytoplasmic loops and pore lining transmembrane helices in the voltage-dependent inactivation of HVA calcium channels. *J. Physiol. (Lond.)* **554**, 263–273 (2004).
- Wang, C., Chung, B. C., Yan, H., Lee, S. Y. & Pitt, G. S. Crystal structure of the ternary complex of a Nav C-terminal domain, a fibroblast growth factor homologous factor, and calmodulin. *Structure* **20**, 1167–1176 (2012).
- Wang, C. et al. Structural analyses of  $\text{Ca}^{2+}$ /CaM interaction with Nav channel C-termini reveal mechanisms of calcium-dependent regulation. *Nature Commun.* **5**, 4896 (2014).
- Lee, K. S., Marban, E. & Tsien, R. W. Inactivation of calcium channels in mammalian heart cells: joint dependence on membrane potential and intracellular calcium. *J. Physiol. (Lond.)* **364**, 395–411 (1985).
- Zühlke, R. D., Pitt, G. S., Deisseroth, K., Tsien, R. W. & Reuter, H. Calmodulin supports both inactivation and facilitation of L-type calcium channels. *Nature* **399**, 159–162 (1999).
- Armstrong, C. M. & Bezanilla, F. Inactivation of the sodium channel. II. Gating current experiments. *J. Gen. Physiol.* **70**, 567–90 (1977).
- Rohl, C. A. et al. Solution structure of the sodium channel inactivation gate. *Biochemistry* **38**, 855–61 (1999).
- DeLano, W. L. The PyMOL Molecular Graphics System (2002).
- Smart, O. S., Neduvellil, J. G., Wang, X., Wallace, B. A. & Sansom, M. S. HOLE: a program for the analysis of the pore dimensions of ion channel structural models. *J. Mol. Graph.* **14**, 354–360, 376 (1996).
- Pettersen, E. F. et al. UCSF Chimera—a visualization system for exploratory research and analysis. *J. Comput. Chem.* **25**, 1605–1612 (2004).

**Supplementary Information** is available in the online version of the paper.

**Acknowledgements** We thank J. Lei, Y. Xu, and X. Li for technical support. We thank the Tsinghua University Branch of the China National Center for Protein Sciences (Beijing) for providing the facility support. The computation was completed on the ‘Explorer 100’ cluster system of Tsinghua National Laboratory for Information Science and Technology. This work was supported by funds from the Ministry of Science and Technology of China (2015CB9101012014, 2016YFA0500402, ZX09507003006) and the National Natural Science Foundation of China (project 31321062). The research of N.Y. was supported in part by an International Early Career Scientist grant from the Howard Hughes Medical Institute and an endowed professorship from Bayer Healthcare.

**Author Contributions** N.Y. conceived the project. N.Y., J.W., Z.Y., and Z.L. designed all experiments. J.W., Z.Y., Z.L., X.Q., and S.L. performed experiments. J.W., Z.Y., Z.L., and Q.Z. conducted the cryo-EM analysis. All authors contributed to data analysis. J.W., M.D., and Q.Z. contributed to manuscript preparation. N.Y. wrote the paper.

**Author Information** The atomic coordinates of the overall structure of the rabbit  $\text{Ca}_v1.1$  complex shown in Fig. 1 have been deposited in the Protein Data Bank (PDB) under accession number 5GJV, and those of the structure built on the class II reconstruction have been deposited in the PDB under accession number 5GJW. The cryo-EM maps have been deposited in the Electron Microscopy Data Bank under accession numbers EMD-9513 (class I), EMD-9514 (class Ia), and EMD-9515 (class II). Reprints and permissions information is available at [www.nature.com/reprints](http://www.nature.com/reprints). The authors declare no competing financial interests. Readers are welcome to comment on the online version of the paper. Correspondence and requests for materials should be addressed to N.Y. ([nyan@tsinghua.edu.cn](mailto:nyan@tsinghua.edu.cn)).

**Reviewer Information** Nature thanks W. Sather, G. Zamponi and the other anonymous reviewer(s) for their contribution to the peer review of this work.



## METHODS

No statistical methods were used to predetermine sample size. The experiments were not randomized. The investigators were not blinded to allocation during experiments and outcome assessment.

**Purification of the rabbit  $\text{Ca}_v1.1$  complex.** Purification of the  $\text{Ca}_v1.1$  complex from rabbit skeletal muscle was performed essentially as described<sup>19</sup> except for two major variations. First, the calcium concentration was increased from 0.5 mM to 10 mM. Second, the protein solution was applied to grids without size-exclusion chromatography purification to achieve high concentration. The protein was first concentrated by Amicon Ultra-15 Centrifugal Filter Unit with Ultracel-100 membrane (Merck Millipore) after elution from Glutathione Sepharose 4B resin (GE Healthcare). When the volume reached approximately 2 ml, the solution was transferred to an Amicon Ultra-4 Centrifugal Filter Unit with Ultracel-100 membrane (Merck Millipore) for further concentration. The final protein volume was about 50  $\mu\text{L}$  at a concentration of approximately 2 mg/ml. The protein was mixed with 18 mM pregabalin (Adamas) for 30 min on ice before cryo-sample preparation.

**Mass spectrometric analysis.** Crosslinking of protein coupled with mass spectrometry analysis was performed as described<sup>19</sup>. For the disulfide bond analysis, purified  $\text{Ca}_v1.1$  complex was precipitated with 20% TCA, washed with cold acetone twice and then dissolved at 0.5  $\mu\text{g}/\mu\text{L}$  in 8 M urea, 2 mM *N*-ethylmaleimide, 0.1 M Tris, pH 6.5. Following Lys-C digestion at a 1:100 enzyme:substrate ratio for 4 h at 37°C, the sample was diluted to 2 M urea with 0.1 M Tris, pH 6.5 for further digestion with trypsin (1:20, 12 h, 37°C), elastase (1:40, 12 h, 37°C), or trypsin (1:20, 12 h, 37°C) followed by Glu-C (1:20, 10 h, 25°C). One aliquot of sample was directly diluted to 2 M urea and digested with proteinase K (1:20, 3 h, 37°C). PNGase F was added 2 h before the digestion was quenched with 5% formic acid to remove N-linked glycans off  $\text{Ca}_v1.1$  peptides.

LC-MS/MS analysis was performed using a Q-Exactive mass spectrometer equipped with an Easy Nano-LC 1000 liquid chromatography system. Digested peptides were loaded onto a 75  $\mu\text{m} \times 6$  cm pre-column that was packed with 10  $\mu\text{m}$ , 120 Å ODS-AQ C18 resin (YMC, Kyoto, Japan) and connected to a 75  $\mu\text{m} \times 10$  cm analytical column packed with 1.8  $\mu\text{m}$ , 120 Å UHPLC-XB-C18 resin (Welch Materials, Shanghai, China). The peptides were separated over a 77-min linear gradient from 3% buffer B (100% acetonitrile, 0.1% formic acid), 97% buffer A (0.1% formic acid) to 27% buffer B, followed by a 6-min gradient from 27% to 80% buffer B, then maintained at 80% buffer B for 10 min. The flow rate was 200 nl/min. The MS parameters were  $R = 140,000$  in full scan,  $R = 17,500$  in higher-energy collisional dissociation MS2 scan; the 30 most intense ions in each full scan were selected for higher-energy collisional dissociation; the AGC targets were  $10^6$  for Fourier transform mass spectrometry full scan and  $5 \times 10^4$  for MS2; minimal signal threshold for MS2 was  $4 \times 10^4$ ; precursors having a charge state of +1, higher than +6 or unassigned were excluded; normalized collision energy was set to 27; peptide match preferred.

The raw data were pre-processed using pParse<sup>51</sup>, and co-eluting precursor ions were excluded. To identify disulfide-linked peptides, the MS data were searched using pLink-SS<sup>52</sup> against a protein database containing the sequences of the five subunits of  $\text{Ca}_v1.1$  and all the proteases used. The pLink search parameters were as follows: three missed cleavage sites for trypsin; eight missed cleavage sites for Trypsin/Glu-C; for elastase and proteinase K, no specificity; peptide length 4–25 amino acids; fixed modification of  $-1.007285$  Da on cysteine and the disulfide mass was set to zero; deamidation on asparagine was set as variable modification. The search results were filtered by requiring  $\leq 10$  ppm mass deviation between an observed precursor mass and the monoisotopic mass of the matched candidate,  $E < 0.001$ , false discovery rate  $< 0.05$ . The spectra of the disulfide-bonded peptides thus obtained were labelled and verified manually.

**Sample preparation and cryo-EM data acquisition.** Aliquots of 4  $\mu\text{L}$  purified  $\text{Ca}_v1.1$  complex at a concentration of approximately 2 mg/ml were placed on glow-discharged holey carbon grids (Quantifoil Cu R1.2/1.3, 300 mesh). Grids were blotted for 2 s and flash-frozen in liquid ethane cooled by liquid nitrogen using Vitrobot Mark IV (FEI). Grids were transferred to a Titan Krios (FEI) electron microscope that was operating at 300 kV with a nominal magnification of 22,500 $\times$ . Images were recorded manually using a K2 Summit electron counting direct detection camera (Gatan) in super-resolution mode and binned to a pixel size of 1.32 Å. Defocus values varied from 1.3 to 2.9  $\mu\text{m}$ . Each image was acquired at an exposure time of 8 s and dose-fractionated to 32 frames with a dose rate of about 8.2 counts (or  $\sim 10.9$  electrons) per second per physical pixel. UCSFImage4 was used for all data collection<sup>53</sup>.

**Image processing.** A simplified diagram of the procedure for image processing is presented in Extended Data Fig. 2a. A total of 9,704 cryo-EM micrographs were collected. The images were aligned and summed using the whole-image motion correction<sup>54</sup>. The estimation of the contrast transfer function parameters were determined by CTFFIND3<sup>55</sup>. Templates for reference-based particle picking were

obtained from the 2D class average calculated from  $\sim 3,000$  manually picked particles. A total of 1,630,272 particles were picked by RELION 1.4 (ref. 56) using low-pass filtered templates to 20 Å to limit reference bias. Subsequent 2D and 3D classifications and refinements were performed using RELION 1.4.

Two rounds of reference-free 2D classification were performed to further remove ice spots, contaminants, and aggregates, yielding 1,222,388 particles. The particles were directly subjected to an auto-refine procedure, resulting in a 4.1 Å map. The initial model used during auto-refinement was from the 4.2 Å map (Electron Microscopy Data Bank accession number EMD-6475), which was adjusted to the same box size by e2proc3d.py application in EMAN<sup>57</sup> and low-pass filtered to 40 Å in RELION. The 4.1 Å map shows qualitatively improved density with amino-acid side chains clearly visualized in the central region compared with reported 4.2 Å map. With the refined particles as input, per-particle motion correction and radiation-damage weighing (particle polishing) was performed. The polished particles were subjected to auto-refine procedure and resulted in a reconstruction with an improved overall resolution of 3.9 Å.

A 3D classification into eight classes was performed using the polished particles. Local angular searches around the refined orientations were used with an angular sampling of 1.8°. Among the eight classes, two classes were suboptimal and discarded. Five classes showed similar overall features and were combined for auto-refinement, yielding a 3.8 Å map (class I). The remaining one class showed characteristic features: discernible density for the 'tail' region ( $\beta$ -subunit), intracellular loops including the AID, the extended S6<sub>III</sub>, and a much better resolved VSD<sub>III</sub>. This class was refined separately and resulted in a reconstruction with the overall resolution of 4.3 Å (class II). The particles from class I were subjected to one additional round of 3D classification. Auto-refinement for subgroups of the classes did not result in improvement of the overall resolution. Nevertheless, one class that showed both clear 'tail' and AID was selected for auto-refinement, which resulted in a map with an overall resolution of 4.3 Å (class Ia).

To further eliminate heterogeneous particles, we developed a method named 'random-phase 3D classification'<sup>58</sup>. Briefly, the particles were classified against two references, among which the second reference was the same as the first one but phase-randomized above a specified spatial frequency in each iteration. The data set was 3D classified for several cycles with sufficient iterations in each cycle. The spatial frequency above which the second reference was phase-randomized was  $1/40 \text{ \AA}^{-1}$ ,  $1/20 \text{ \AA}^{-1}$ ,  $1/15 \text{ \AA}^{-1}$ ,  $1/12 \text{ \AA}^{-1}$  and  $1/10 \text{ \AA}^{-1}$  for each cycle, respectively. After each cycle, the particles prone to be classified into the phase-randomized class were removed before the next cycle. The remaining particles after several cycles of random-phase 3D classification were considered as 'good' particles and subjected to routine 3D auto-refinement with RELION 1.4. The random-phase 3D classification method was implemented with home-modified RELION 1.4. Eventually, the resolutions of the three classes (I, Ia, and II) were improved to 3.57 Å, 3.94 Å, and 3.94 Å, respectively.

Reported resolutions are based on the gold-standard Fourier shell correlation 0.143 criterion. All density maps were corrected for the modulation transfer function of the detector and sharpened by applying a negative B-factor that was estimated using automated procedures<sup>59</sup>. Local resolution variations were estimated using ResMap<sup>60</sup>.

**Model building and refinement.** The 3.6 Å map (class I) was used for the majority of model building, while the two 3.9 Å maps (class Ia and class II) were used for model building of VSD<sub>III</sub> and the intracellular domains, as well as analysis of conformational changes.

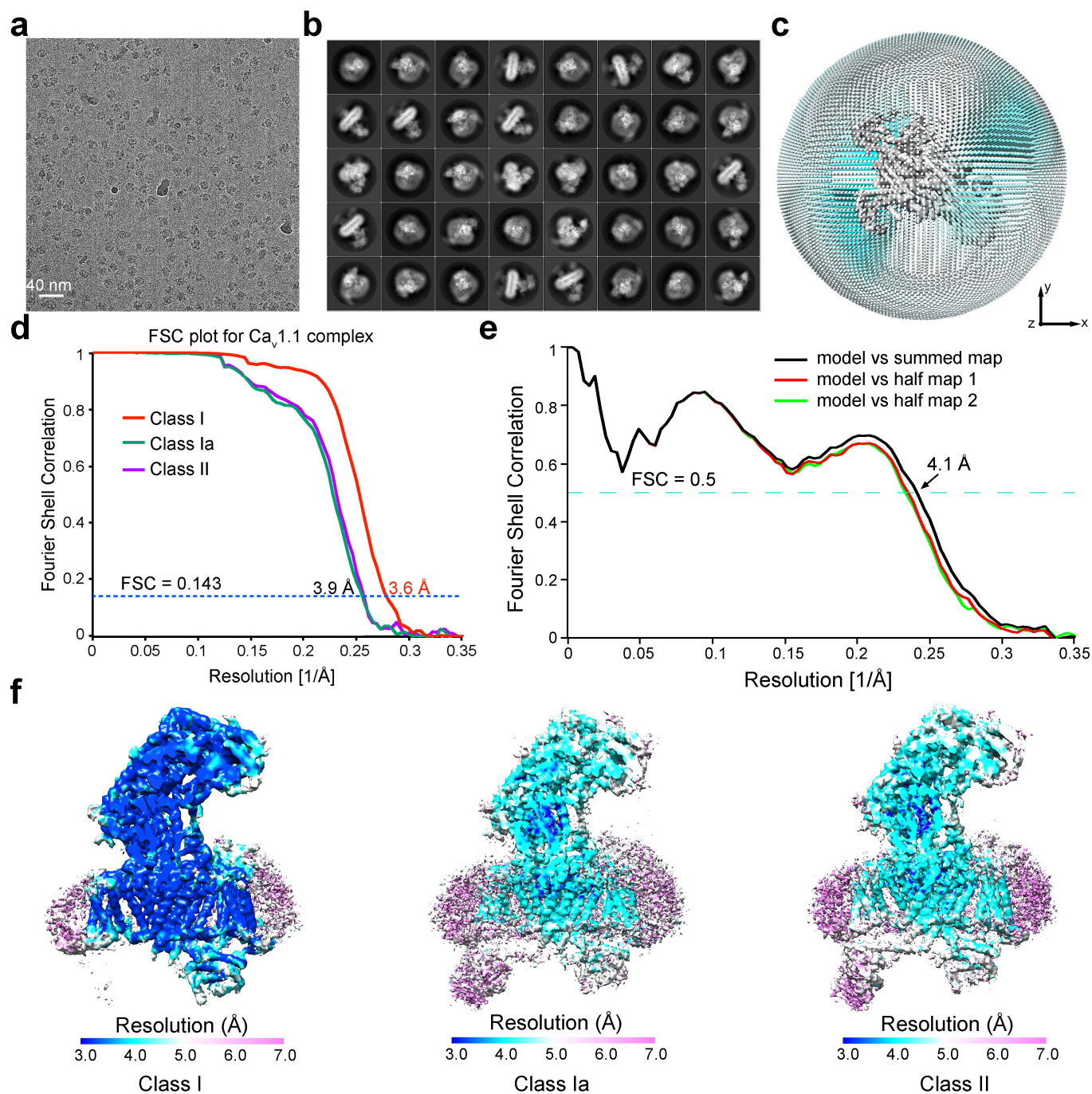
The previously reported structure (PDB accession number 3JBR)<sup>19</sup> was used as the starting model. *De novo* building was performed for  $\alpha 1$ -,  $\alpha 2\delta$ - and  $\gamma$ -subunits in COOT<sup>61</sup>. Sequence assignment was guided mainly by bulky residues such as Phe, Tyr, Trp, and Arg. The chemical properties of amino acids were considered to facilitate model building. The densities for glycosylation sites and mass spectrometric analysis of the crosslinking results and disulfide bonds were used for model confirmation. Then the modelling of each subunit was separately performed with RosettaCM using the manually built model as template and the experimental cryo-EM maps as guide<sup>62–64</sup>. This process helped to optimize the model and to build some missing parts in the structure. For this step, ten models were generated in Rosetta for each subunit and the best one was selected by comparison of the models with the map. The selected models for each-subunit were then merged together and further manually adjusted in COOT. As the density for 'tail' region is weak in the class I map, we used the class Ia map for identification and docking of  $\beta$ -subunit. The structure of  $\beta 2$ -subunit in complex with  $\text{Ca}_v1.2$  I–II linker (PDB accession number 4DEY<sup>34</sup>) was docked into the class Ia map by COOT, and fitted into the density by CHIMERA<sup>50</sup>. The distinguishable secondary structures in the map of 'tail' and the discernible AID ensured reliable docking. We also generated model of the  $\alpha 1$ -subunit and docked the  $\beta$ -subunit into class II map. The model building procedure was similar to the afore-mentioned process. For VSD<sub>III</sub>, the backbones were first built in class II

map, and subsequently transferred to class I map for side-chain assignment of S1–2<sub>III</sub> and S4<sub>III</sub> segments.

In total, we built 2,661 residues with 2,595 assigned side chains for the overall complex. The CTD and S<sub>III</sub> segment of the  $\alpha$ I-subunit were built as poly Ala. The intracellular II–III linker and the C-terminal sequences following CTD in  $\alpha$ I and a small fragment of  $\gamma$ -subunit were not modelled owing to the lack of corresponding densities in the maps.

Structure refinement was performed using phenix.real\_space\_refine application in PHENIX<sup>65</sup> in real space with secondary structure and geometry restraints to prevent structure over-fitting. The final model was refined against the overall 3.6 Å map cryo-EM map using REFMAC<sup>66</sup> in reciprocal space, using secondary structure restraints that were generated by ProSMART<sup>67</sup>. Overfitting of the overall model was monitored by refining the model in one of the two independent maps from the gold-standard refinement approach and testing the refined model against the other map<sup>68</sup> (Extended Data Fig. 1b). Statistics of 3D reconstruction and model refinement can be found in Extended Data Table 1.

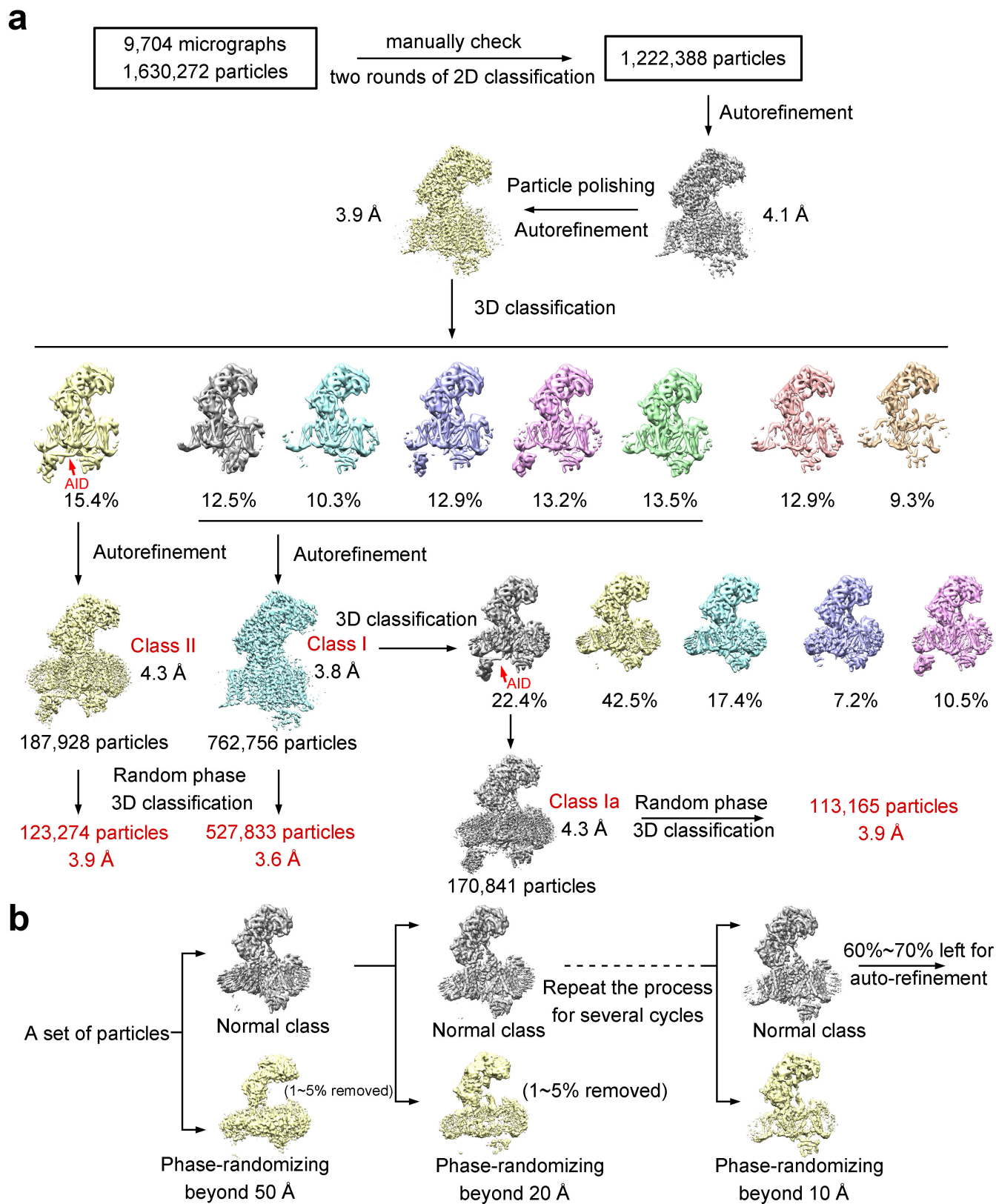
51. Yuan, Z. F. *et al.* pParse: a method for accurate determination of monoisotopic peaks in high-resolution mass spectra. *Proteomics* **12**, 226–235 (2012).
52. Lu, S. *et al.* Mapping native disulfide bonds at a proteome scale. *Nature Methods* **12**, 329–331 (2015).
53. Li, X., Zheng, S., Agard, D. A. & Cheng, Y. Asynchronous data acquisition and on-the-fly analysis of dose fractionated cryoEM images by UCSFImage. *J. Struct. Biol.* **192**, 174–178 (2015).
54. Li, X. *et al.* Electron counting and beam-induced motion correction enable near-atomic-resolution single-particle cryo-EM. *Nature Methods* **10**, 584–590 (2013).
55. Mindell, J. A. & Grigorieff, N. Accurate determination of local defocus and specimen tilt in electron microscopy. *J. Struct. Biol.* **142**, 334–347 (2003).
56. Scheres, S. H. W. RELION: implementation of a Bayesian approach to cryo-EM structure determination. *J. Struct. Biol.* **180**, 519–530 (2012).
57. Tang, G. *et al.* EMAN2: an extensible image processing suite for electron microscopy. *J. Struct. Biol.* **157**, 38–46 (2007).
58. Gong, X. *et al.* Structural insights into the Niemann-Pick C1 (NPC1)-mediated cholesterol transfer and Ebola infection. *Cell* **165**, 1467–1478 (2016).
59. Rosenthal, P. B. & Henderson, R. Optimal determination of particle orientation, absolute hand, and contrast loss in single-particle electron cryomicroscopy. *J. Mol. Biol.* **333**, 721–745 (2003).
60. Kucukelbir, A., Sigworth, F. J. & Tagare, H. D. Quantifying the local resolution of cryo-EM density maps. *Nature Methods* **11**, 63–65 (2014).
61. Emsley, P., Lohkamp, B., Scott, W. G. & Cowtan, K. Features and development of Coot. *Acta Crystallogr. D* **66**, 486–501 (2010).
62. DiMaio, F., Tyka, M. D., Baker, M. L., Chiu, W. & Baker, D. Refinement of protein structures into low-resolution density maps using Rosetta. *J. Mol. Biol.* **392**, 181–190 (2009).
63. Song, Y. *et al.* High-resolution comparative modeling with RosettaCM. *Structure* **21**, 1735–1742 (2013).
64. DiMaio, F. *et al.* Atomic-accuracy models from 4.5-Å cryo-electron microscopy data with density-guided iterative local refinement. *Nature Methods* **12**, 361–365 (2015).
65. Adams, P. D. *et al.* PHENIX: a comprehensive Python-based system for macromolecular structure solution. *Acta Crystallogr. D* **66**, 213–221 (2010).
66. Murshudov, G. N., Vagin, A. A. & Dodson, E. J. Refinement of macromolecular structures by the maximum-likelihood method. *Acta Crystallogr. D* **53**, 240–255 (1997).
67. Nicholls, R. A., Fischer, M., McNicholas, S. & Murshudov, G. N. Conformation-independent structural comparison of macromolecules with ProSMART. *Acta Crystallogr. D* **70**, 2487–2499 (2014).
68. Amunts, A. *et al.* Structure of the yeast mitochondrial large ribosomal-subunit. *Science* **343**, 1485–1489 (2014).
69. Guo, J. *et al.* Structure of the voltage-gated two-pore channel TPC1 from *Arabidopsis thaliana*. *Nature* **531**, 196–201 (2016).
70. Kintzer, A. F. & Stroud, R. M. Structure, inhibition and regulation of two-pore channel TPC1 from *Arabidopsis thaliana*. *Nature* **531**, 258–264 (2016).



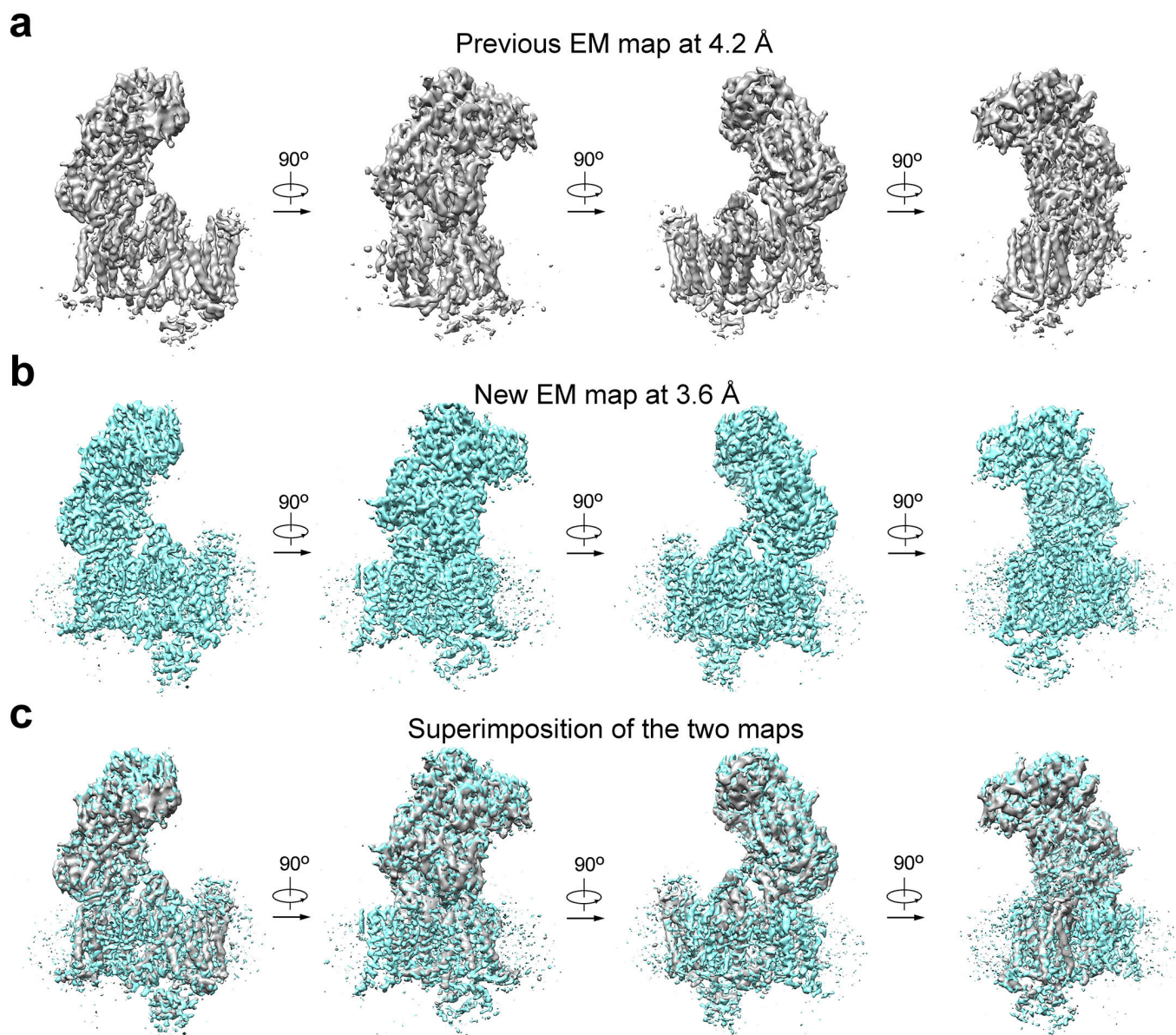
**Extended Data Figure 1 | Cryo-EM analysis of the rabbit  $\text{Ca}_v1.1$  complex.** **a**, A representative electron micrograph of the  $\text{Ca}_v1.1$  complex. Scale bar, 400 Å. **b**, Two-dimensional class averages of the electron micrographs. The box size and circle diameter are 264 Å and 220 Å, respectively. **c**, Angular distribution for the final reconstruction of the  $\text{Ca}_v1.1$  complex. Each cylinder represents one view and the height of the cylinder is proportional to the number of particles for that view. **d**, The gold-standard Fourier shell correlation curves for the EM maps. See Extended Data Fig. 2 and Methods for details of the three classes. **e**, Fourier shell correlation curves of the refined model versus the overall

3.6 Å map that it was refined against (black); of the model refined in the first of the two independent maps used for the gold-standard Fourier shell correlation curves versus that same map (red); and of the model refined in the first of the two independent maps versus the second independent map (green). The small difference between the red and green curves indicates that the refinement of the atomic coordinates did not suffer from overfitting. **f**, The overall EM maps of the  $\text{Ca}_v1.1$  complex are colour-coded to indicate the range of resolutions. See Extended Data Fig. 2 for the definition of classes I, Ia, and II. The resolution maps are calculated with ResMap<sup>60</sup>.

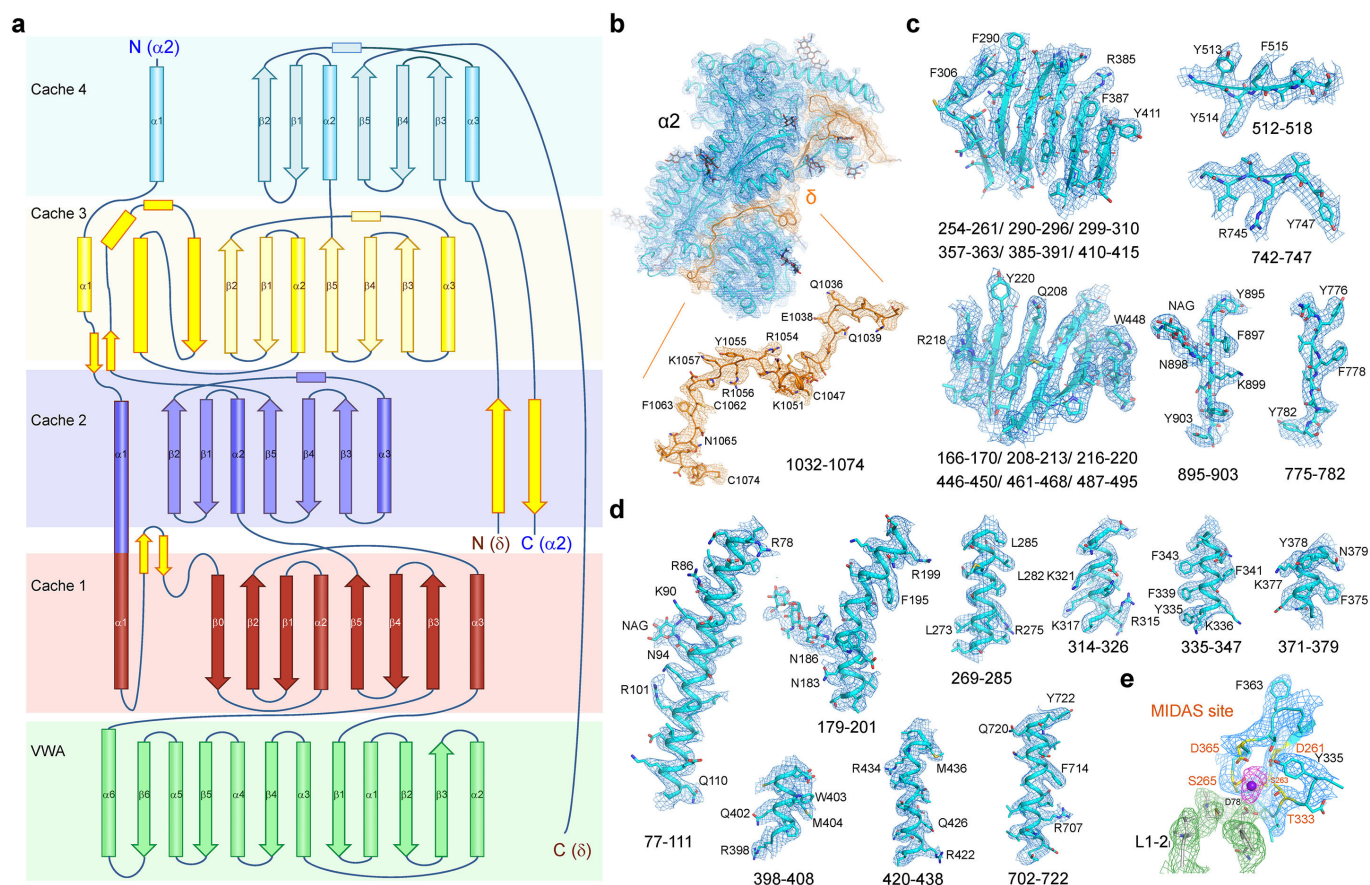




**Extended Data Figure 2 | Flowchart for cryo-EM data processing of the  $\text{Ca}_v1.1$  complex.** See 'Image processing' in Methods for details of (a) the flowchart and (b) the random-phase 3D classification method<sup>58</sup>.



**Extended Data Figure 3 | The new map reconstructed at 3.6 Å exhibits qualitative improvement over the reported 4.2 Å map.** The same four perpendicular side views are shown for the published 4.2 Å map (a), the new 3.6 Å map presented here (b), and their superimposition (c). The EM maps were generated in Chimera.

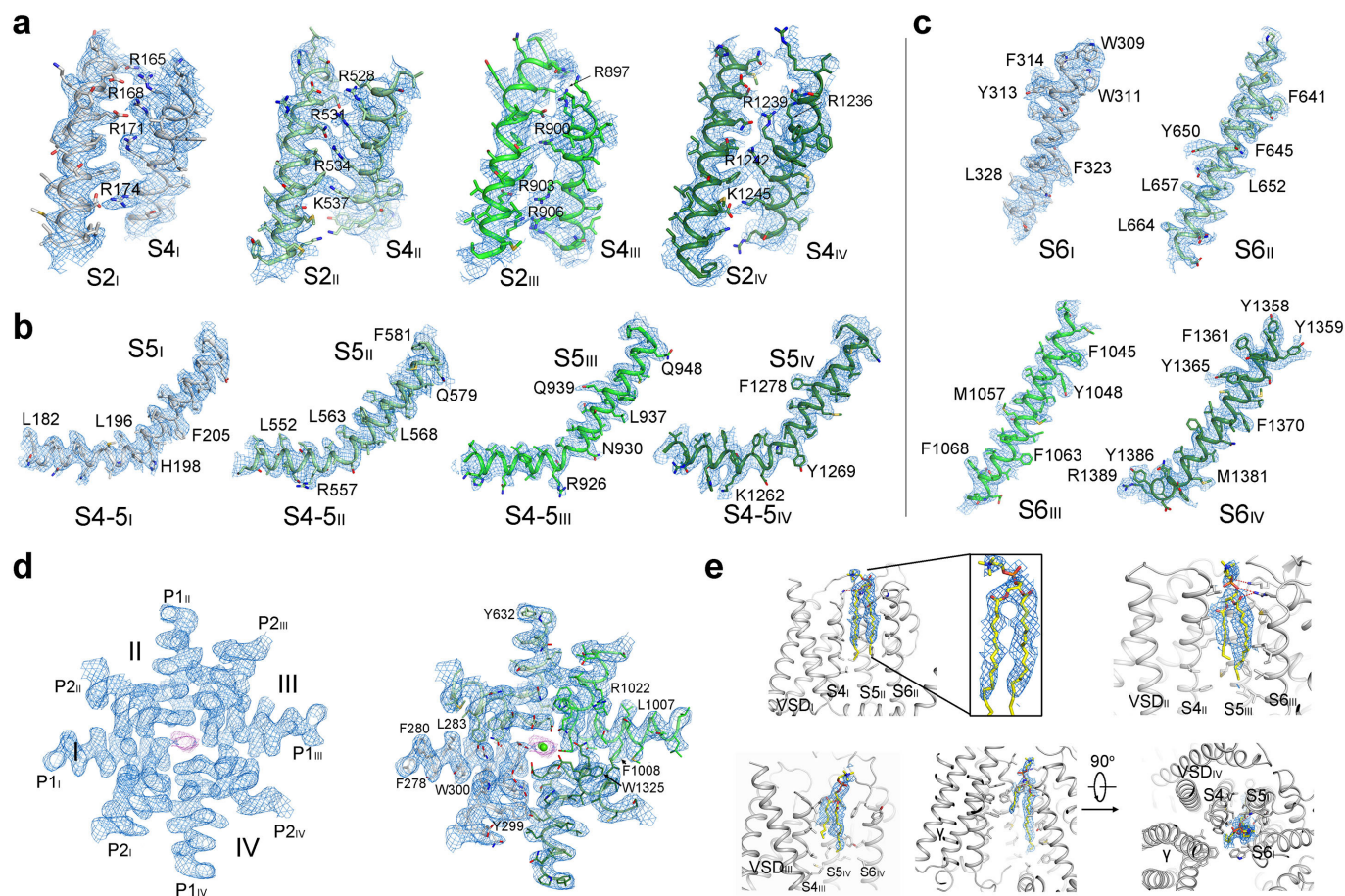


#### Extended Data Figure 4 | Topology and EM maps of the $\alpha 2\delta$ -1-subunit.

**a**, Topology of the  $\alpha 2\delta$ -subunit. The domains are coloured the same as the domain structures shown in Fig. 2. **b**, EM map for the overall  $\alpha 2\delta$ -1-subunit. The EM map for the C-terminal stretch of the  $\delta$ -subunit is shown at the bottom and coloured orange. As seen in the EM map, the consecutive density of the  $\delta$ -subunit extends slightly beyond Cys1074. The additional density would correspond to Gly1075 if the C terminus were not cleaved during maturation, or alternatively, the ethanolamine of glycosphosphatidylinositol (GPI) that modifies Cys1074. No peptide was detected for sequences after Cys1074 in the MS analysis of the purified  $\text{Ca}_v1.1$  complex, and no additional density was found that may

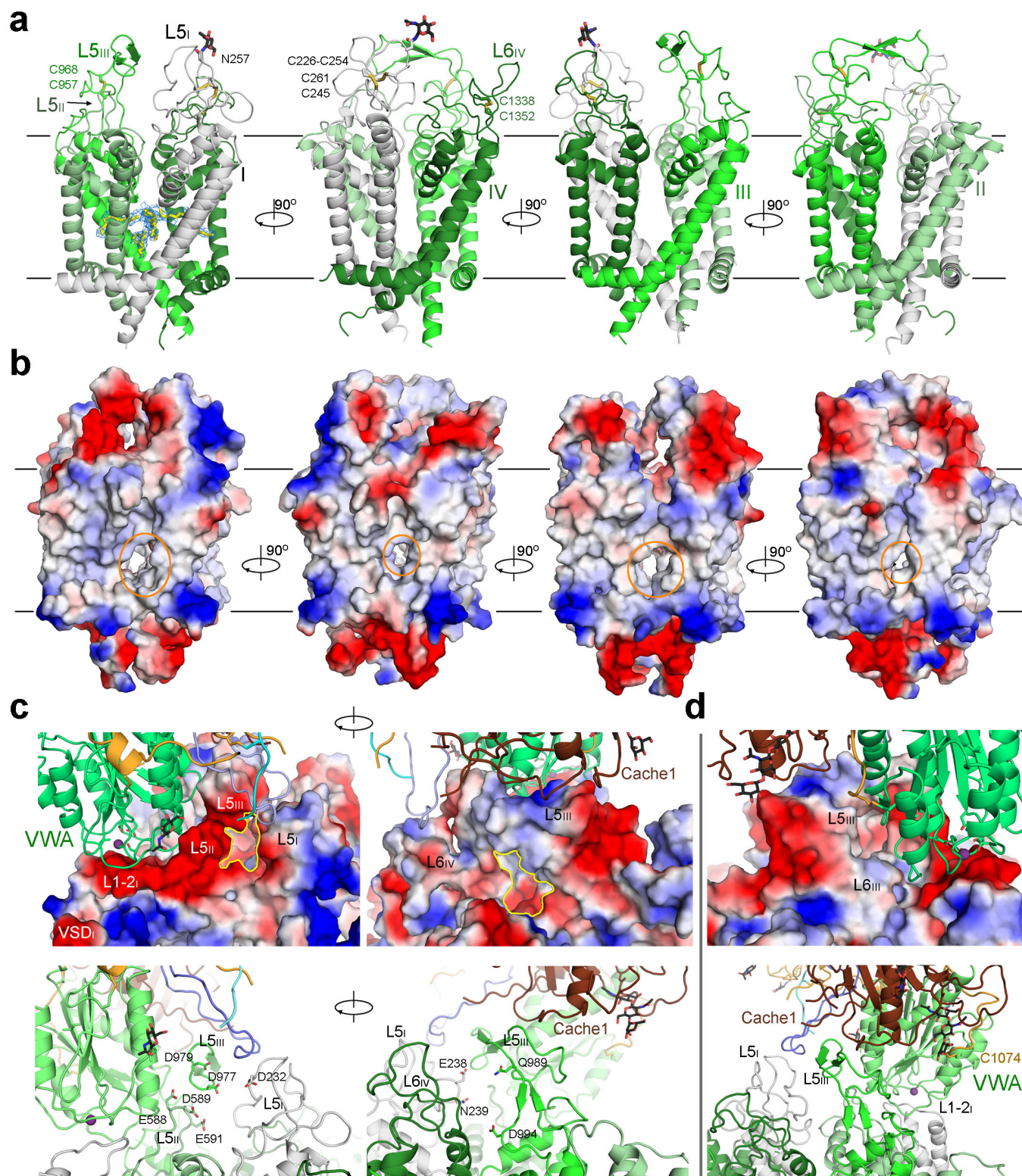
correspond to the C-terminal sequences of the  $\delta$ -subunit. We thereby assigned an ethanolamine to the density following Cys1074. **c**, EM maps of representative  $\beta$ -strands in the  $\alpha 2$ -subunit. Left: the EM maps for the  $\beta$ -sheets in the VWA (upper) and cache1 (bottom) domains. Right: the EM maps for representative  $\beta$ -strands in the  $\alpha 2$ -subunit. NAG, N-acetylglucosamine. **d**, EM maps of representative  $\alpha$ -helices in the  $\alpha 2$ -subunit. **e**, The EM maps for the MIDAS motif in the VWA domain and the loop between S1 and S2 in the first VSD of  $\alpha 1$  (designated the L1-2<sub>1</sub> loop). The density corresponding to the cation is coloured magenta. The maps were generated using class I reconstruction and contoured at 6–8 $\sigma$  in PyMol.





**Extended Data Figure 5 | Representative EM maps for segments in the  $\alpha 1$ -subunit.** The EM maps for the S2 and S4 segments in the four VSDs (**a**), the S5 (**b**), and S6 (**c**) segments in the pore domain are shown. **d**, The EM map of the selectivity filter and the supporting P1 and P2 helices. Side-chain assignment was assisted by bulky residues in P1 and P2 helices

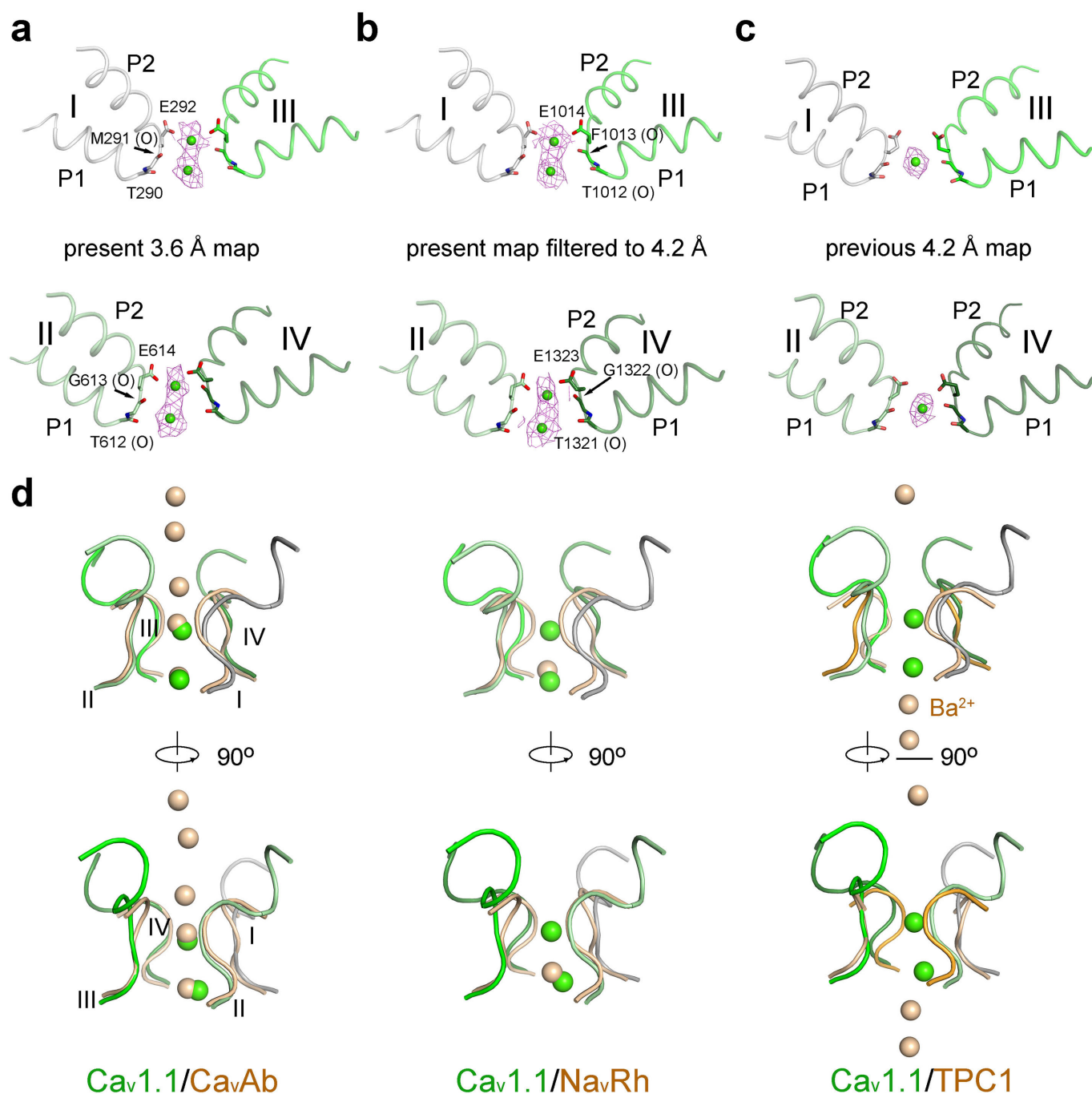
as exemplified in the right panel. A consecutive stretch of density was observed along the selectivity filter vestibule. **e**, The densities that may correspond to lipid molecules bound to the  $\alpha 1$ -subunit. The maps were made using class I reconstruction and contoured at 4–6 $\sigma$  in PyMol.



**Extended Data Figure 6 | Structural features of the pore domain of the  $\alpha 1$ -subunit.** **a**, The structure of the pore domain in four perpendicular side views. The disulfide bonds and glycosyl moieties are shown as sticks. Left: the densities below selectivity filter that may correspond to lipid tails are shown at  $5\sigma$ . The modelled lipids are shown as yellow sticks. Similar densities that penetrate the side portals of the central cavity of the pore domain were previously observed in the structures of Na<sub>v</sub>Ab<sup>27</sup> and Na<sub>v</sub>Rh<sup>28</sup>. **b**, The negative surface potential of the extracellular loops and the fenestrations of the pore domain. The surface electrostatic potential

was calculated in PyMol. The fenestrations in the transmembrane region are highlighted by orange circles. **c**, The potential extracellular Ca<sup>2+</sup> entrances through the windowed dome of the  $\alpha 1$ -subunit. Two potential entrances for Ca<sup>2+</sup> are contoured with yellow lines in the top panels. The residues that underlie the negative surface potentials are shown in the bottom panels. **d**, The interface between the  $\alpha 2\delta$ -1- and  $\alpha 1$ -subunits. The L1-2<sub>I</sub>, L5<sub>II</sub>, and L5<sub>III</sub> loops form the docking site for the VWA and cache1 domains of the  $\alpha 2\delta$ -1-subunit.

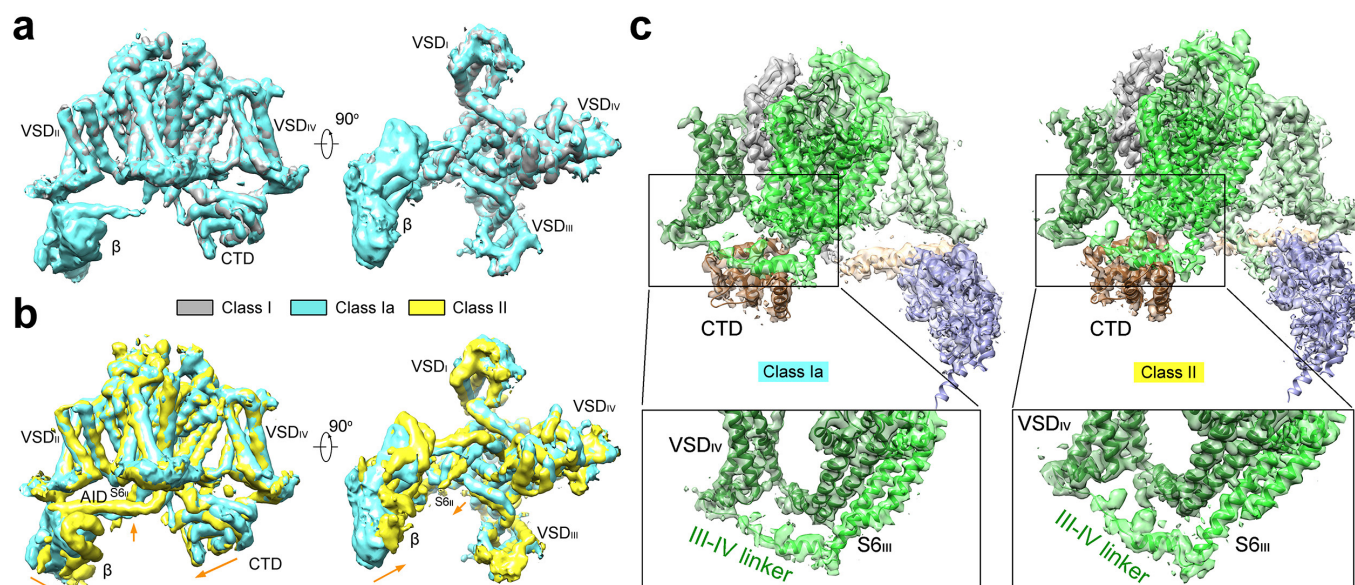




**Extended Data Figure 7 | Putative  $\text{Ca}^{2+}$  coordination in the selectivity filter vestibule.** **a–c**, The densities that may correspond to bound  $\text{Ca}^{2+}$  ions in the selectivity filter vestibule exhibit distinct features in the present and previously published maps<sup>19</sup>. The  $\text{Ca}^{2+}$  concentrations for the samples that yielded the new 3.6 Å and previous 4.2 Å maps are 10 and 0.5 mM, respectively. The maps were contoured at  $5\sigma$ . Even when low-pass filtered to 4.2 Å, the density in the selectivity filter vestibule remains a stretch instead of a sphere. Nevertheless, it remains to be investigated whether

the stretch of the density observed in the selectivity filter vestibule indeed corresponds to two  $\text{Ca}^{2+}$  ions. **d**, Comparison of  $\text{Ca}^{2+}$  coordination by different  $\text{Ca}_v$  and  $\text{Na}_v$  channels. The structure of  $\text{Ca}_v1.1$  is superimposed with  $\text{Ca}_v\text{Ab}$ <sup>26</sup>,  $\text{Na}_v\text{Rh}$ <sup>28</sup>, and  $\text{TPC1}$ <sup>69,70</sup> relative to their respective selectivity filters. The PDB accession numbers for  $\text{Ca}_v\text{Ab}$ ,  $\text{Na}_v\text{Rh}$ , and  $\text{TPC1}$  are 4MS2, 4DXW, and 5E1J, respectively. The tentatively assigned  $\text{Ca}^{2+}$  ions in  $\text{Ca}_v1.1$  are coloured green and those in the other three indicated channels are coloured wheat.





**Extended Data Figure 8 | Conformational changes of the intracellular domains.** **a**, The 3.9 Å map calculated from class Ia particles is almost identical to the 3.6 Å map (class I) except for the better resolution of the β-subunit and the AID motif of α1. **b**, Distinct conformations of the intracellular domains in class Ia and II reconstructions. The shifts of the β-subunit and the AID motif from class Ia to class II maps are indicated by orange arrows. The adjacent segments in the pore domain

also drift to different degrees. For visual clarity, the maps are low-pass filtered to 6 Å. See the Supplementary Video for the morph illustrating the conformational changes of the intracellular elements of the Ca<sub>v</sub>1.1 complex. **c**, The intracellular III–IV linker of α1 is well resolved. Shown here are class Ia and class II EM maps generated in Chimera. The III–IV linker of α1 forms a short helix that interacts with the carboxyl terminal domain (CTD) of the α1-subunit.

Extended Data Table 1 | Statistics of 3D reconstructions and model refinement

Data collection			
EM equipment	FEI Titan Krios		
Voltage (kV)	300		
Detector	Gatan K2		
Pixel size (Å)	1.32		
Electron dose (e <sup>-</sup> /Å <sup>2</sup> )	50		
Defocus range (μm)	1.3~2.9		
Reconstruction			
Software	RELION 1.4		
Maps	Class I	Class Ia	Class II
Number of used Particles	527,833	113,165	123,274
Symmetry	C1		
Final Resolution (Å)	3.57	3.94	3.94
Map sharpening B-factor (Å <sup>2</sup> )	-157.5	-146.7	-142.3
Accuracy of rotation (°)	1.444	1.638	1.531
Accuracy of translation (pixels)	0.704	0.779	0.760
Model building			
Software	Coot & Rosetta		
Refinement			
Software	Phenix & Refmac		
Average Fourier shell correlation	0.859		
R-factor	0.306		
Model composition			
Protein residues	2,661		
Side chains	2,595		
Ion (Ca <sup>2+</sup> )	3		
Sugar	25		
Lipid	14		
Validation			
R.m.s deviations			
Bonds length (Å)	0.013		
Bonds Angle (°)	1.360		
Ramachandran plot statistics (%)			
Preferred	86.7		
Allowed	11.0		
Outlier	2.3		

Extended Data Table 2 | Disulfide bonds and chemically crosslinked lysine pairs identified from the Ca<sub>v</sub>1.1 complex

**a**

Site1- Site2	Proteinase K	Lys-C/Elastase	Lys-C/Trypsin	Lys-C/Trypsin/Glu-C
<u>α2 (907)- δ (977)</u>	3.23E-04 (4,7)	1.21E-16 (5,34)	3.66E-23 (1,77)	4.78E-20 (2,32)
<u>α1 (957)- α1 (968)</u>		7.40E-10 (1,3)	9.30E-14 (3,14)	9.34E-14 (1,6)
<u>α2 (356)- δ (1062)</u>				4.31E-06 (1,3)
<u>α2 (305)- δ (1047)</u>	6.84E-08 (3,5)	3.35E-19 (20,156)	9.39E-18 (1,10)	8.34E-18 (4,20)
<u>α2 (305)- δ (1027,1029,1047)*</u>		7.09E-08 (2,6)		
<u>δ (999,1002)</u>	1.67E-05 (3,4)	7.76E-05 (1,2)	5.47E-18 (1,13)	9.06E-12 (1,4)
<u>δ (1027,1029)</u>	1.43E-06 (2,3)	2.38E-14 (1,2)	1.64E-08 (1,5)	7.56E-07 (1,4)
<u>δ (999,1002)- δ (1027,1029)</u>	4.69E-09 (19,37)		3.19E-07 (1,15)	5.75E-09 (1,9)
<u>α2 (670)- α2 (700)</u>	6.13E-10 (25,65)		1.30E-18 (3,57)	
<u>α2 (837,842,844,853)</u>	3.52E-06 (4,8)			
<u>α2 (837,842,844)- α2 (853)*</u>		6.14E-09 (4,30)	1.02E-09 (2,10)	4.81E-08 (4,17)
<u>α2 (844,853)</u>	7.64E-12 (2,3)			
<u>α1 (1214,1219)</u>	6.00E-13 (2,2)			
<u>γ (57)-γ (80)</u>			1.99E-07 (2,13)	

**b**

Site1- Site2	#Spec-Total	Best E-value
<u>α2 (234)- α1 (976)</u>	8	2.37E-14
<u>α1 (356)- β (395)</u>	47	3.39E-11
<u>β (151)- α1 (693)</u>	19	6.57E-11
<u>α1 (352)- β (402)</u>	15	1.02E-09
<u>α1 (352)- β (395)</u>	18	3.42E-09
<u>γ (1)- α1 (1094)</u>	8	2.96E-07
<u>β (395)- α1 (693)</u>	4	2.46E-06
<u>β (83)- α1 (352)</u>	3	2.48E-06
<u>β (83)- α1 (356)</u>	4	3.94E-06
<u>β (151)- α1 (685)</u>	4	1.34E-05
<u>β (139)- α1 (1535)</u>	3	1.80E-05
<u>β (402)- α1 (1414)</u>	3	3.67E-05
<u>α1 (162)- β (402)</u>	3	5.07E-05
<u>α1 (356)- β (402)</u>	11	8.13E-05
<u>β (402)- α1 (677)</u>	8	1.27E-04
<u>γ (1)- α1 (1414)</u>	3	2.66E-04

Site1- Site2	#Spec-Total	Best E-value
<u>α2 (90)- α2 (97)</u>	25	6.50E-11
<u>α2 (148)- α2 (693)</u>	3	7.31E-11
<u>β (95)- β (99)</u>	17	1.15E-10
<u>α1 (356)- α1 (677)</u>	31	4.67E-10
<u>β (322)- β (331)</u>	18	5.08E-10
<u>α1 (704)- α1 (719)</u>	9	2.12E-09
<u>α1 (698)- α1 (704)</u>	11	4.28E-09
<u>α1 (1414)- α1 (1418)</u>	19	6.79E-09
<u>α1 (693)- α1 (708)</u>	13	6.98E-09
<u>α1 (356)- α1 (685)</u>	3	1.39E-08
<u>α1 (677)- α1 (693)</u>	13	1.47E-08
<u>α1 (685)- α1 (693)</u>	14	1.71E-08
<u>β (83)- β (322)</u>	6	1.74E-08
<u>α1 (1478)- α1 (1550)</u>	2	1.81E-08
<u>β (83)- β (99)</u>	19	2.19E-08
<u>β (395)- β (402)</u>	27	2.26E-08
<u>α1 (677)- α1 (719)</u>	4	2.61E-08
<u>α2 (97)- α2 (108)</u>	35	4.65E-08
<u>α1 (704)- α1 (710)</u>	4	5.37E-08
<u>β (83)- β (97)</u>	11	6.25E-08
<u>α1 (352)- α1 (677)</u>	19	7.29E-08
<u>α1 (703)- α1 (719)</u>	5	1.77E-07
<u>α1 (677)- α1 (704)</u>	3	2.60E-07
<u>α1 (708)- α1 (719)</u>	4	3.09E-07
<u>α1 (693)- α1 (703)</u>	6	3.14E-07
<u>α1 (1496)- α1 (1504)</u>	9	3.88E-07
<u>α2 (97)- α2 (197)</u>	8	4.10E-07
<u>α1 (693)- α1 (710)</u>	8	4.62E-07
<u>α1 (677)- α1 (685)</u>	10	5.31E-07
<u>α1 (703)- α1 (710)</u>	10	5.54E-07

Site1- Site2	#Spec-Total	Best E-value
<u>α1 (1094)- α1 (1504)</u>	14	6.66E-07
<u>α1 (1446)- α1 (1476)</u>	6	6.95E-07
<u>α1 (1245)- α1 (1478)</u>	4	1.19E-06
<u>α2 (336)- α2 (377)</u>	13	2.21E-06
<u>α1 (1446)- α1 (1538)</u>	4	2.89E-06
<u>α1 (1535)- α1 (1550)</u>	10	3.89E-06
<u>α1 (677)- α1 (698)</u>	3	5.12E-06
<u>α1 (1496)- α1 (1550)</u>	4	7.60E-06
<u>β (83)- β (139)</u>	3	8.93E-06
<u>α1 (703)- α1 (708)</u>	3	1.27E-05
<u>α1 (1478)- α1 (1496)</u>	20	1.69E-05
<u>α1 (693)- α1 (719)</u>	7	1.86E-05
<u>α1 (352)- α1 (719)</u>	2	1.94E-05
<u>α1 (14)- α1 (18)</u>	3	1.98E-05
<u>α1 (1538)- α1 (1549)</u>	5	2.56E-05
<u>β (402)- β (406)</u>	8	3.12E-05
<u>α1 (698)- α1 (708)</u>	6	3.34E-05
<u>α1 (698)- α1 (719)</u>	4	3.59E-05
<u>α1 (1538)- α1 (1550)</u>	2	4.63E-05
<u>α1 (1418)- α1 (1535)</u>	2	5.92E-05
<u>α2 (727)- α2 (733)</u>	3	7.29E-05
<u>α2 (336)- α2 (380)</u>	2	1.14E-04
<u>α1 (162)- α1 (1478)</u>	2	1.44E-04
<u>α1 (1094)- α1 (1499)</u>	4	2.02E-04
<u>α1 (1535)- α1 (1549)</u>	4	2.11E-04
<u>α2 (108)- α2 (442)</u>	2	2.76E-04
<u>α2 (148)- α2 (579)</u>	6	2.84E-04
<u>α1 (352)- α1 (693)</u>	2	3.01E-04
<u>α1 (356)- α1 (1414)</u>	2	3.46E-04
<u>α1 (345)- α1 (352)</u>	7	7.12E-04

**c**

Site1- Site2	#Spec-Total	Best E-value
<u>α2 (652)- α2 (693)</u>	11	2.21E-28
<u>α2 (637)- α2 (693)</u>	10	2.86E-18
<u>β (99)- β (139)</u>	59	1.06E-15
<u>α2 (137)- α2 (148)</u>	12	1.08E-15
<u>β (139)- β (331)</u>	76	5.53E-15
<u>α2 (234)- α2 (554)</u>	6	1.53E-13
<u>α2 (137)- α2 (234)</u>	7	2.85E-13
<u>α1 (693)- α1 (704)</u>	48	4.50E-13
<u>α1 (1083)- α1 (1094)</u>	11	6.40E-13
<u>β (99)- β (331)</u>	25	2.10E-12
<u>β (83)- β (95)</u>	25	2.13E-12
<u>α2 (97)- α2 (442)</u>	4	4.64E-11

**a**, Disulfide bonds of Ca<sub>v</sub>1.1 were identified using pLink-SS after the complex was digested with different proteases and subjected to LC-MS/MS analysis. In the structure, four disulfide bonds are observed between α2- and δ-subunits (Cys305–Cys1047, Cys356–Cys1062, Cys406–Cys1074, Cys907–Cys977), and two adjacent disulfide bonds are found within the δ-subunit (Cys999–Cys1029, Cys1002–Cys1027). Shown in the table are the best E values (number of peptide pairs, number of spectra). The underlined Cys residues form a loop-linked disulfide bond. **b**, **c**, The Ca<sub>v</sub>1.1 complex was crosslinked with DSS (disuccinimidyl suberate) and digested with trypsin. Following LC-MS/MS analysis of the peptides, crosslinked lysine pairs between (**b**) or within (**c**) subunits were identified using pLink. The filtering criteria were the same for **a–c**: identified spectra passing a false discovery rate cutoff of 0.05 were further filtered by requiring E value <0.001 and spectral counts ≥2. The disulfide bonds and crosslinked lysine pairs that match the cryo-EM structure are highlighted in red.



# Cryo-EM structure of the spliceosome immediately after branching

Wojciech P. Galej<sup>1</sup>, Max E. Wilkinson<sup>1</sup>, Sebastian M. Fica<sup>1</sup>, Chris Oubridge<sup>1</sup>, Andrew J. Newman<sup>1</sup> & Kiyoshi Nagai<sup>1</sup>

**Precursor mRNA (pre-mRNA) splicing proceeds by two consecutive transesterification reactions via a lariat-intron intermediate. Here we present the 3.8 Å cryo-electron microscopy structure of the spliceosome immediately after lariat formation. The 5'-splice site is cleaved but remains close to the catalytic Mg<sup>2+</sup> site in the U2/U6 small nuclear RNA (snRNA) triplex, and the 5'-phosphate of the intron nucleotide G(+1) is linked to the branch adenosine 2'OH. The 5'-exon is held between the Prp8 amino-terminal and linker domains, and base-pairs with U5 snRNA loop 1. Non-Watson-Crick interactions between the branch helix and 5'-splice site dock the branch adenosine into the active site, while intron nucleotides +3 to +6 base-pair with the U6 snRNA ACAGAGA sequence. Isy1 and the step-one factors Yju2 and Cwc25 stabilize docking of the branch helix. The intron downstream of the branch site emerges between the Prp8 reverse transcriptase and linker domains and extends towards the Prp16 helicase, suggesting a plausible mechanism of remodelling before exon ligation.**

The spliceosome is a dynamic molecular machine<sup>1,2</sup> that catalyses pre-mRNA splicing in two sequential transesterifications analogous to group II intron self-splicing<sup>3</sup>. The major spliceosomal components—U1, U2, U4/U6, and U5 small nuclear ribonucleoprotein particles (snRNPs), and the two large NineTeen and NineTeen Related (NTC and NTR) protein complexes—assemble *de novo* on pre-mRNA substrates in an ordered manner<sup>4–6</sup>. Initially U1 and U2 snRNPs recognize the 5'-splice site (5'SS) and branch point sequences of pre-mRNA; subsequently the pre-assembled U4/U6.U5 tri-snRNP is recruited to form the fully assembled spliceosome (complex B). During catalytic activation Prp28 helicase displaces the 5'SS from U1 snRNP and allows it to base-pair with the U6 snRNA ACAGAGA sequence<sup>7,8</sup>. Brr2 helicase unwinds the U4/U6 snRNA duplex to release U4 snRNA and its associated proteins<sup>9,10</sup>, allowing recruitment of the NTC and NTR complexes. The resulting complex B<sup>act</sup> is then remodelled to complex B\*, which recruits step-one-specific factors Yju2 and Cwc25. These factors stabilize a network of RNA interactions comprising U2, U5 and U6 snRNAs, which position the pre-mRNA 5'SS and branch point sequences for catalysis of the first transesterification (branching) producing 5'-exon and lariat intron-3'-exon intermediates. The resulting complex C is further remodelled to complex C\* in which the 5'- and 3'-exons are aligned on U5 snRNA loop 1 to produce spliced mRNA and lariat intron products via the second transesterification (exon ligation)<sup>11,12</sup>. The spliced mRNA is released and the remaining intron lariat spliceosome (ILS) is disassembled, recycling the snRNPs for new rounds of splicing.

During this splicing cycle DExD/H-box helicases are recruited to the spliceosome at specific steps to remodel RNA–RNA interactions and induce binding or release of auxiliary factors<sup>13,14</sup>. Specifically, after branching, the step-one factors Yju2 and Cwc25 are released by Prp16 helicase and Prp18–Slu7 and Prp22 are recruited to produce catalytically active complex C\* (ref. 13). Following exon ligation, the spliced mRNA is released by Prp22 helicase<sup>15</sup> and the residual ILS is disassembled by Prp43 helicase<sup>16,17</sup>.

Here we describe the cryo-electron microscopy (cryo-EM) structure of the spliceosome captured immediately after branching. This structure provides insight into recognition and positioning of the 5'SS and branch point at the active site, elucidates how proteins stabilize the architecture of the catalytic RNA core, and provides a molecular basis

to understand the functions of RNA helicases and auxiliary factors in remodelling the spliceosome.

## Overview of the structure

Spliceosomes from the yeast *Saccharomyces cerevisiae* were assembled on *UBC4* pre-mRNA substrate<sup>18</sup> with a mutation of the 3'-splice site (3'SS) sequence UAGAG to UACAC, and purified via an affinity-tag on Slu7 or Prp18 (Methods). The purified spliceosomes contained predominantly lariat intron-3'-exon intermediates (Extended Data Fig. 1), indicating that the purified spliceosomes represent complex C. We obtained a cryo-EM reconstruction at 3.8 Å overall resolution

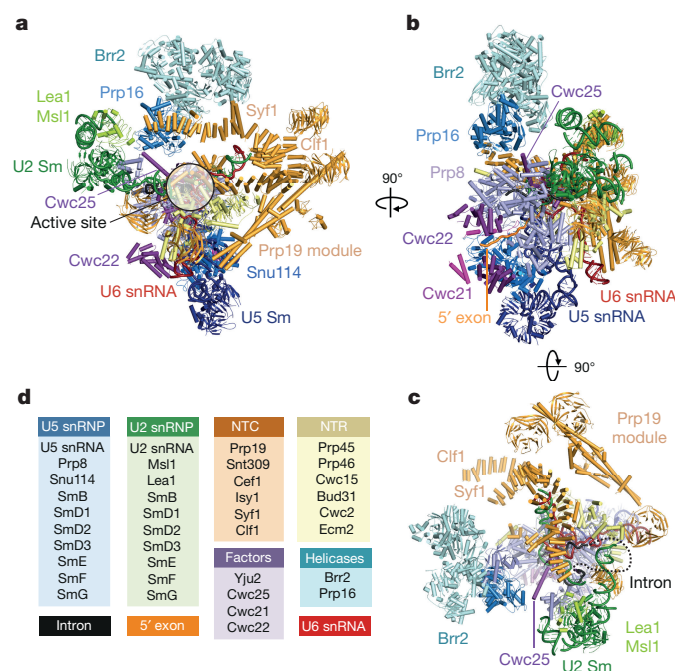


**Figure 1 | Subunit architecture of the spliceosomal complex C.** a–c, Three orthogonal views of the complex coloured according to the subunit identity. d, A list of all 44 modelled subunits of the complex grouped into functional sub-complexes.

<sup>1</sup>MRC Laboratory of Molecular Biology, Francis Crick Avenue, Cambridge CB2 0QH, UK.

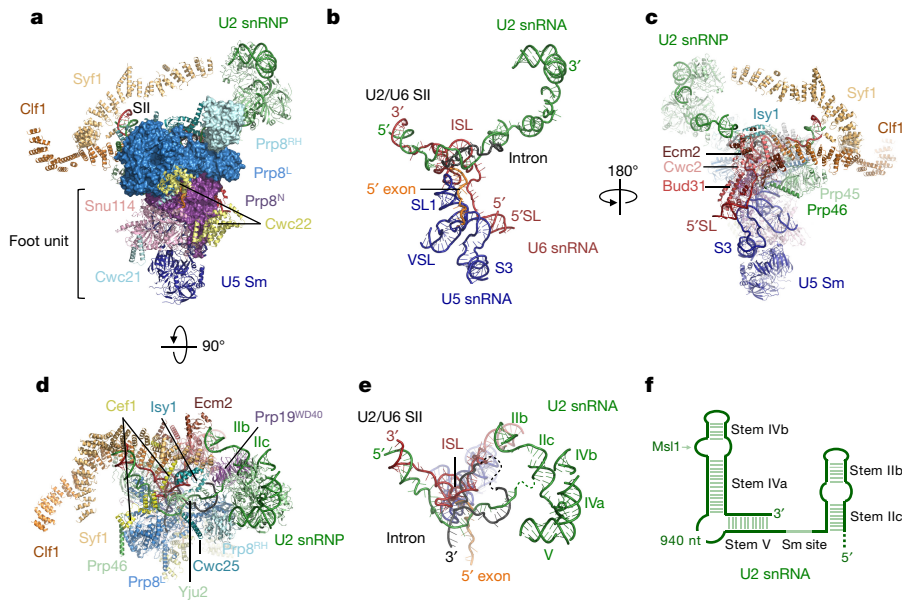


**Figure 2 | Overview of the core structure.** **a**, Prp8 and its central role in organizing the entire assembly (SII denotes U2/U6 stem II). **b**, RNA only in the same orientation as in **a** (ISL, U6 snRNA internal stem-loop; 5'SL, U6 snRNA 5' stem-loop; SL1, U5 snRNA stem-loop 1; VSL, U5 snRNA variable stem-loop; S3, U5 snRNA Stem III). **c**, Ecm2, Cwc2 and Bud31 binding to the 5' end of the U6 snRNA. **d**, Top view of the complex. **e**, RNA only in the same orientation as in **d**. **f**, Secondary structure diagram for the 3' end of U2 snRNA. Prp8<sup>N</sup>, Prp8<sup>L</sup> and Prp8<sup>RH</sup> denote N-terminal, Large and RNaseH-like domains of Prp8.

(Methods; Extended Data Figs 1–6; Extended Data Table 1) into which 44 components have been modelled (Fig. 1; Extended Data Table 2; Supplementary Information). The U5 snRNP forms the core of the complex, which cradles the active site (Fig. 1a). Assembling onto this core, the NTC and NTR act as a multipronged clamp that stabilizes binding of the U2 snRNP core, the substrate, and auxiliary splicing factors to the U5 snRNP (Fig. 1a–c). The helicase module containing Brr2 and Prp16 protrudes from the U5 snRNP core (Fig. 1a, b).

As in U4/U6.U5 tri-snRNP<sup>19,20</sup>, the Large domain of Prp8 (ref. 21) forms the foundation of the assembly together with the stable foot unit, comprising GTP-bound Snu114 and the N-terminal domain of Prp8, firmly gripping the U5 snRNA (Fig. 2a, b). Prp8 has undergone a large structural change including a 30° rotation of the foot with respect to the Large domain when compared to U4/U6.U5 tri-snRNP<sup>19</sup> (Extended Data Fig. 7). U4 snRNA and its associated proteins have been released upon unwinding of the U4/U6 duplex by Brr2 (ref. 6). The 3'-domain of U2 snRNP comprising Msl1 (U2B''), Lea1 (U2A') and the Sm core domain bridges the Prp8 RNaseH-like domain and the N-terminal HAT (Half-a-TPR)-repeat domain of Syf1 (Fig. 2a). Isy1 and Cef1 dock with the N-terminal and reverse transcriptase (RT)-like domains of Prp8 (ref. 21), respectively, and anchor the N-terminal end of Cfl1 together with Prp45/Prp46 (Fig. 2c, d). These interactions support the HAT-repeat arches of Syf1 and Cfl1 suspended over the Large domain of Prp8. The 5' part of U2 snRNA and the 3' part of U6 snRNA run side-by-side from the active site forming nine consecutive base-pairs extending towards the centre of the Syf1 HAT-repeat arch (Fig. 2a–e). Bud31 anchors the 5'-stem of U6 snRNA to the N-terminal domain of Prp8 (Fig. 2c). Cwc2 is wedged between Bud31, Ecm2 and Prp45 and guides the path of U6 snRNA<sup>22</sup> (Fig. 2c). U2 snRNA downstream of the branch helix extends from the active site towards the 3'-domain of U2 snRNP, forming two stems bridging the U2 Sm ring with Ecm2/Cwc2 and the main body of the complex (Fig. 2d, e). Density for two RNA helices emanating from the U2 Sm ring is consistent with a stem-loop IIB/stem IIC arrangement and the catalytically competent conformation of the active site<sup>23,24</sup> (Fig. 2f). The C-terminal region of Cwc21 forms a coiled-coil that interacts with Snu114 (ref. 25) (Fig. 2a) while the N-terminal half of Cwc21 extends towards Prp8 and points into the U5 snRNA stem minor groove.

Two large regions of weak density extend from the well-ordered core of the complex (Extended Data Fig. 1e). Focused classification allowed us to select subsets of particles (core + helicase, core + Prp19) (Extended Data Fig. 2), in which less well-ordered components can be more clearly visualized. The weak density observed in the latter class is readily attributable to Prp19, Cef1 and Snt309 based on its distinct

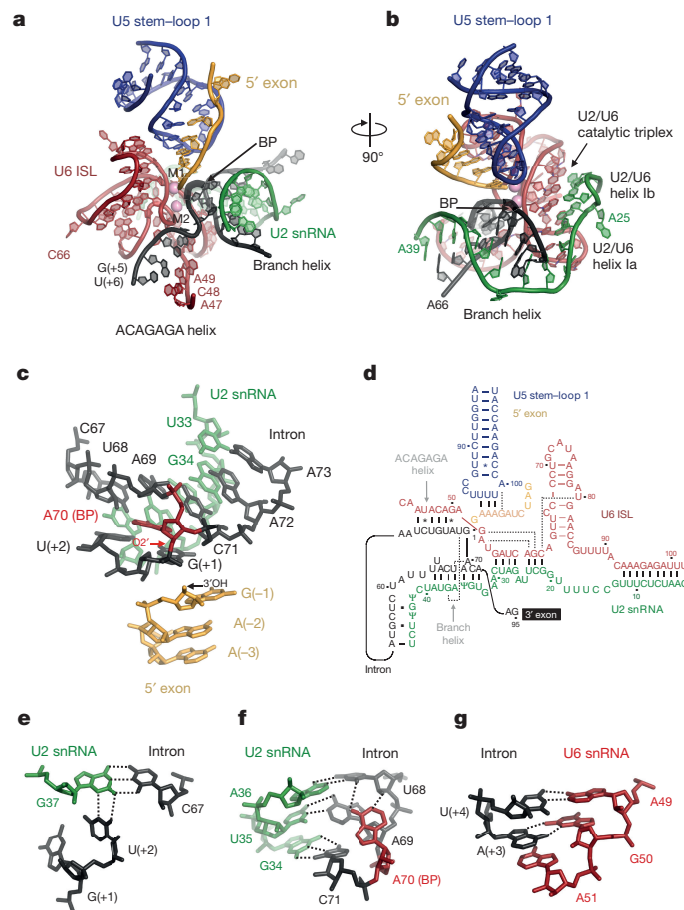


**Figure 3 | Structure of the RNA catalytic core.** **a**, Key RNA elements at the active site. BP, branch point; ISL, internal stem-loop; M1 and M2, catalytic metal ion one and two. **b**, Orthogonal view illustrating the branch helix and helices Ia and Ib of U2/U6 snRNA duplex. **c**, The branch helix and 5'-exon with the 2'-5' phosphodiester linkage (red arrow). **d**, Intricate RNA interactions at the active site (dotted lines indicate base triples; dot and star indicate G-U wobble and other non-canonical base-pairs). **e**, Base triple interaction between the branch helix and 5'-splice site. **f**, A network of interactions in the branch helix. **g**, Hoogsteen base-pair between intron A(+3) and G50 of U6 snRNA.



shape first observed in ILS<sup>26</sup>, but the weaker density in complex C suggests these proteins are more loosely attached to the core than in ILS. A large lobe corresponding to a DEAH helicase in contact with Cwc25 is observed near the intron exit channel, downstream of the branch point. Although its limited resolution does not allow us to build a model *de novo*, the density is of sufficient quality to fit a DEAH box helicase model unambiguously (Extended Data Fig. 6; Extended Data Table 2) and it has been interpreted as Prp16 as it contacts Cwc25. An even larger domain is observed in contact with the DEAH helicase domain. The structure of Brr2 helicase coupled to the Jab1/MPN domain of Prp8 (ref. 27) can be docked into this density, consistent with an interaction between Prp16 and Brr2 (ref. 28).

### Active site

The map shows that the phosphodiester bond at the 5'SS is cleaved and the 5'-phosphate of the first intron nucleotide G(+1) forms a 2'-5' phosphodiester linkage with the branch point adenosine (A70), in agreement with the RNA analysis (Extended Data Figs 1b and 4b). The key RNA elements assemble around the active site harbouring the magnesium ion binding sites (Fig. 3). The 3'OH of the 5'-exon remains close to the 5'-phosphate of G(+1) such that the normal 5'-3' phosphodiester linkage at the 5'SS could be restored with minimal structural alteration (Fig. 3c). The adenine base of branch point A70 is bulged out from the branch helix and its N1 and 6-amino group are hydrogen-bonded to the 2'OH and O2 of U68 creating a unique backbone conformation which enables the 2'OH of A70 to project towards the 5'-phosphate of intron G(+1) (Fig. 3f). In yeast the intron sequence following the 5'SS is stringently conserved as GUAUGU<sup>2</sup>. The G(+1) base is partially packed against the A70 base while the U(+2) base is within hydrogen-bonding distance of U2 snRNA G37 suggesting a possible base-triple interaction with intron C67 (Fig. 3e). Mutation of G(+1) to C, or of the branch A70 to C, would disrupt these interactions, consistent with the strong branching defects observed for these mutations<sup>29</sup>. Four conserved intron nucleotides A(+3)U(+4)G(+5)U(+6) form sequence-specific base-pairs with part of the ACAGAGA sequence of U6 snRNA<sup>7,8,30,31</sup>. The three 5'-exon nucleotides A(-2)A(-3)A(-4) form Watson-Crick base-pairs with loop 1 of U5 snRNA<sup>11</sup> (Figs 3b, 4). Notably, the 5'-exon winds through a narrow channel between the Large and N-terminal domains of Prp8 formed during spliceosome activation (via 30° foot rotation) (Extended Data

Fig. 7c) and stabilized by Cwc21 and the C-terminal domain of Cwc22 (Fig. 4a, b). Cwc22 consists of two HEAT repeat-containing domains that straddle the 5'-exon tunnel, providing insight into exon-junction complex deposition in higher eukaryotes<sup>32</sup> (Extended Data Fig. 8).

U6 snRNA following the ACAGAGA sequence forms helices Ia and Ib by base-pairing with U2 snRNA and folds back to form an intramolecular stem loop (ISL), in agreement with the structure inferred from genetics<sup>33</sup> (Fig. 3b, d). Helices Ia and Ib show continuous base-stacking and the bulged U2 snRNA nucleotides U24 and A25 protrude from helix I and bind to the Prp8 RT domain (Figs 3d, 4d, e and 5a). The Watson-Crick faces of U6 snRNA nucleotides G52 and A53 interact with the Hoogsteen faces of G60 and A59, respectively, forming two consecutive base triples as inferred from genetics<sup>34</sup> (Fig. 4e, f). C66 and A79 bulge out from the ISL (Fig. 3a, b), allowing continuous base-stacking of the bulged U80 with G52 and A53 and stabilizing the catalytic triplex. It has been proposed that pre-mRNA splicing reactions are catalysed by a two-metal-ion mechanism<sup>35</sup>. Indeed ligands for the two divalent metal ions have been identified by stereo-specific phosphorothioate substitutions and metal rescue experiments<sup>36</sup> and density attributable to Mg<sup>2+</sup> ions is observed adjacent to these ligands (Extended Data Fig. 5). The 5'-exon 3'OH and the 5' phosphate of G(+1) remain close to M1, while U6 snRNA metal ligands have repositioned slightly, in agreement with the previously observed repositioning of the branch in structures of a branched group II intron<sup>37</sup>. Nonetheless, the branch helix remains 'docked' at the catalytic Mg<sup>2+</sup> site, in contrast to its 'undocked' configuration observed in the ILS structure, where it swings away from the ACAGAGA helix by 90° (ref. 26; Extended Data Fig. 5).

The intron downstream of the 5'SS GUAUGU sequence exits the active site near Cwc2, Ecm2, Clf1, Cef1 and Isy1 (Fig. 2), re-enters the spliceosome and runs side-by-side with U2 snRNA in the opposite direction through a channel between the Prp8 Endonuclease and RNaseH-like domains (Extended Data Fig. 7). The intron then forms the branch helix with the GΨAGUA sequence of U2 snRNA in proximity to the catalytic Mg<sup>2+</sup> site (Fig. 3b, d) and exits the active site through a channel made by the linker and RT-like domains of Prp8 (Fig. 2).

### Roles of proteins around the active site

The RNA network at the active centre, comprising U2, U5 and U6 snRNAs and RNA substrate, is stabilized by a number of proteins (Figs 1, 2 and 4). The catalytic RNA core is surrounded by the linker

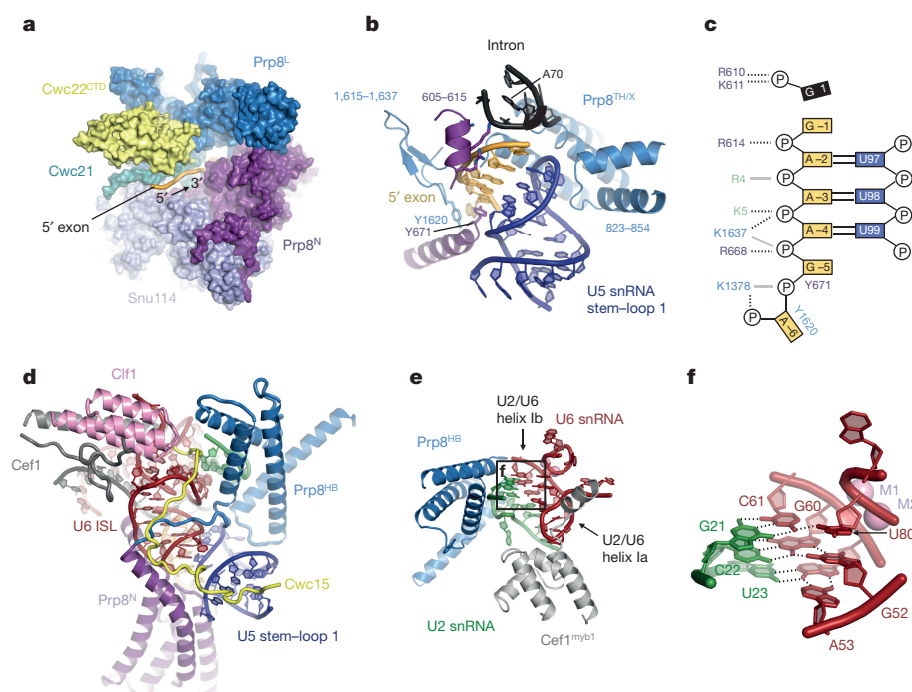


**Figure 4 | Proteins at the active site.**

**a**, 5'-exon channel formed between the Large and N-terminal domains of Prp8, Cwc21 and Cwc22. **b**, 5'-exon-U5 loop 1 interaction surrounded by Prp8. Th/X denotes thumb/domain X of Prp8 (residues 1,300–1,375). **c**, Interactions between the 5'-exon, the N-terminal (purple) and Large (blue) domains of Prp8, and Yju2 (green). Interactions involving protein main and side chains are shown by solid and dotted lines. **d**, Components surrounding U6 internal stem-loop. **e**, Prp8 and Cef1 (Myb1 domain) stabilize the catalytic triplex. HB denotes helix bundle of the RT-like domain (residues 750–870). **f**, Structure of the catalytic triplex.



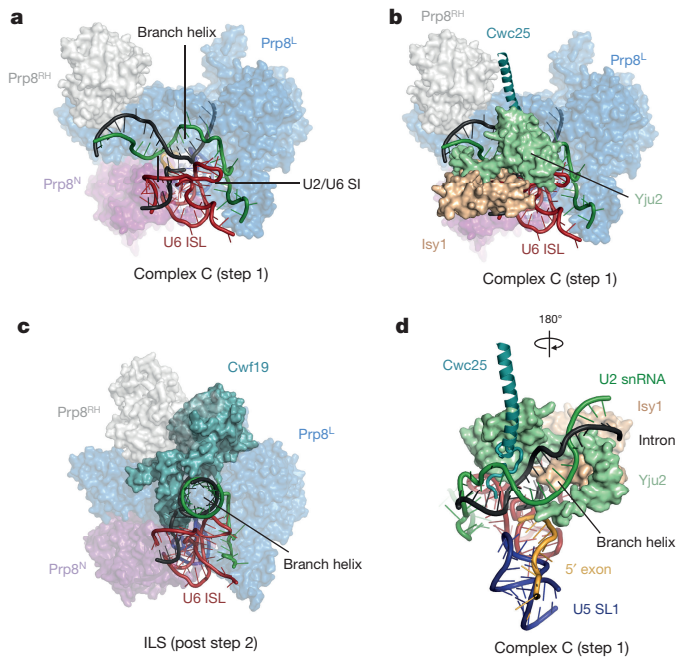


**Figure 5 | Step-one factors and branch-site positioning.** **a**, Interaction between the RNA catalytic core and Prp8. **b**, Positioning of the branch helix by step-one factors. **c**, Corresponding view in *S. pombe* post splicing ILS complex<sup>26</sup>, showing marked repositioning of the branch helix and its further stabilization by debranching co-factor Cwf19. **d**, A close-up view of step-one factors interacting with the branch helix.

and the helix bundle domains of Prp8 (refs 19,21) on one side and by NTC proteins (Prp45, Prp46, Isy1 and Cef1) and step-one factors (Yju2 and Cwc25) on the other side, which together stabilize the catalytic RNA core for branching. Remarkable stacking of Prp8 Tyr671 and Tyr1620 against bases at positions G(−5) and A(−6) stabilizes the 5'-exon:U5 snRNA loop 1 pairing (Fig. 4b, c). The linker between the N-terminal and Large domains of Prp8 runs across the major groove of U6 ISL, which is positioned in a pocket formed by Prp8 and Clf1, and the interactions are sealed by the extended N terminus of Cwc15 (Fig. 4d). Cef1 stabilizes the U2/U6 catalytic triplex<sup>34</sup> (Fig. 4e, f).

Step-one-specific factors probe the branch helix and stabilize its docking at the catalytic core (Fig. 5). A long  $\alpha$ -helix of Cwc25 contacts the RNaseH-like domain and  $\alpha$ -finger of Prp8 and its N terminus is inserted into the widened major groove of the bulged branch helix (Fig. 5b, d). The N terminus of Yju2 wraps around the branch helix (Fig. 5d) and its Arg4 makes a base-specific contact with the intron U(+2) while its main chain amide group contacts the backbone phosphate of the 5'-exon A(−2) (Fig. 4c). Isy1 projects its N terminus deep into the active site forming contacts with the phosphate backbone of intron U68. Ser2 of Isy1 forms a hydrogen-bond with the O2 carbonyl group of U(+2) of the intron. One of the Isy1 helices inserts into the minor groove of the ACAGAGA/5'SS helix. Cwc25 forms multiple contacts with the branch site, consistent with cross-linking experiments<sup>38</sup> and its role in juxtaposition of the 5'SS and branch

point for branching<sup>39–41</sup>. These spliceosomal factors are reminiscent of ribosomal proteins L27 and L16, which penetrate into the peptidyl transferase active site and stabilize tRNA binding<sup>42</sup>.

### Remodelling of the spliceosome

The intron downstream of the branch point emerges from the exit channel formed by the Prp8 RT-like and linker domains and the  $\alpha$ -finger, and projects towards Prp16 (Fig. 6a). Twelve nucleotides could span the distance between the last ordered intron nucleotide (branch point + 6) and the substrate RNA entry site of Prp16, consistent with Prp16 crosslinking to 4-thiouridine introduced 18 nucleotides downstream of the branch point<sup>43</sup>. Prp16 translocates 3'→5' towards the branch point along the intron upon ATP hydrolysis<sup>43–45</sup>. Prp16 would thus pull the branch helix out of its pocket and hence destabilize the binding of Yju2 and Cwc25 (Fig. 6b). The undocked branch helix would allow the 3'-exon to enter the active site<sup>31,45</sup> and bind to U5 snRNA loop 1 (refs 11,12). Consistent with this, destabilization of the branch helix by Isy1 deletion suppresses splicing defects caused by Prp16 mutations<sup>46</sup>. The step-two factors Prp18 and Slu7 are likely to dock into the space vacated by the branch helix/Yju2/Cwc25 to stabilize the 3'SS into the active site as Slu7 and Prp18 are in direct contact with the 3'SS bound to U5 snRNA loop 1 before exon ligation<sup>47</sup> (Fig. 6b). Prp22 binds the 3'-exon at position +17 (ref. 15). Translocation of Prp22 on the 3'-exon in the 3'→5' direction towards the active centre<sup>15,43</sup> would displace Prp18–Slu7, releasing the mRNA. In our structure, the density assigned to Prp16 is in direct contact with Cwc25 (Fig. 6a), consistent with Cwc25 stabilizing Prp16 binding to the spliceosome before branching<sup>44</sup>. We propose that the branch helix and 3'-exon confer specificity for auxiliary factors such as Cwc25–Yju2, Slu7–Prp18, which may act as adaptors that determine the identity of the next DEAH box helicase to remodel the active site.

The structure of the *Schizosaccharomyces pombe* spliceosomal complex<sup>26,48</sup> contains a lariat intron but not 5'-exon or the spliced mRNA. The catalytic RNA core is surrounded by a similar set of NTC and NTR proteins but the structure lacks step-one or step-two factors<sup>26,48</sup>, suggesting this corresponds to a post-splicing ILS<sup>49</sup>. Instead Cwf19, a homologue of the debranching enzyme co-factor Drn1 (ref. 50), intrudes between the Large and RNaseH-like domains of Prp8, occupying the binding sites for Isy1, Cwc25, and Yju2 found in our complex C. Cwf19 marks the ILS complex for disassembly by displacing the branch helix, which rotates by 90° in ILS with respect to complex C (Fig. 5c, Extended Data Fig. 7).

A pronounced conformational change between ILS and complex C is a large rotation of the NTC (Extended Data Fig. 7d). In ILS the N terminus of Syf1 moves away from the core, promoting undocking of U2 snRNP. In complex C, the position of U2 snRNP is stabilized by the formation of stem IIc and binding of Prp19. U2 snRNP is in direct contact with the RNaseH-like domain of Prp8, which holds Cwc25 in place. This network of interactions suggests that binding of Prp19 and formation of stem IIc in U2 snRNA may have an allosteric effect on the positioning of the branch helix via step-one factors. Extended arches of Syf1 and Clf1 may have a role in communicating the signal over long distance.

Our spliceosomal complex C structure reveals the active configuration of the catalytic core, elucidating the arrangement of the RNA

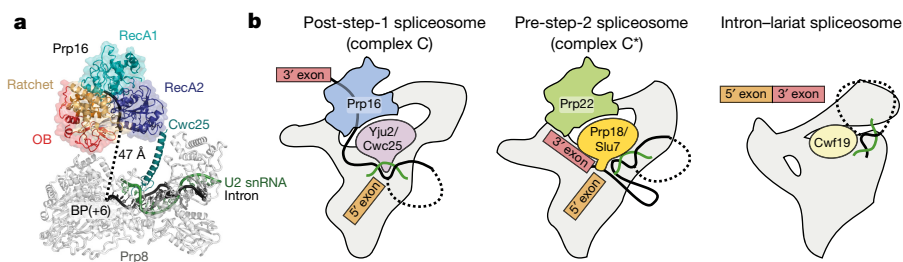


**Figure 6 | The role of helicases in active site remodelling.** **a**, The intron sequence downstream from the branch site exits the spliceosome via a channel in Prp8 and extends towards Prp16. Translocation of Prp16 towards the branch helix would destabilize step-one factors and displace the branch helix from its pocket. BP, branch point; OB, oligonucleotide/ oligosaccharide binding domain. **b**, Schematic illustrating how step-one- or step-two-specific factors can determine the specificity of the helicase recruited to the spliceosome at particular stages of splicing.

substrate and its interaction with proteins. The structure accounts for a large body of biochemical and genetic data and provides crucial insights into substrate docking and catalysis and the role of DEAH helicases and auxiliary factors in spliceosome remodelling.

**Online Content** Methods, along with any additional Extended Data display items and Source Data, are available in the online version of the paper; references unique to these sections appear only in the online paper.

**Received 9 June; accepted 19 July 2016.**

**Published online 26 July 2016.**

- Will, C. L. & Lührmann, R. Spliceosome structure and function. *Cold Spring Harb. Perspect. Biol.* **3**, a003707 (2011).
- Burge, C. B., Tuschl, T. & Sharp, P. A. in *The RNA World II* (eds Gesteland, R. F., Cech, T. R. & Atkins, J. F.) 525–560 (Cold Spring Harbor Laboratory Press, 1999).
- Lambowitz, A. M. & Zimmerly, S. Group II introns: mobile ribozymes that invade DNA. *Cold Spring Harb. Perspect. Biol.* **3**, a003616 (2011).
- Chan, S.-P., Kao, D.-I., Tsai, W.-Y. & Cheng, S.-C. The Prp19p-associated complex in spliceosome activation. *Science* **302**, 279–282 (2003).
- Oh, M. D. & Gould, K. L. Characterization of interactions among the Cef1p-Prp19p-associated splicing complex. *RNA* **8**, 798–815 (2002).
- Fabrizio, P. *et al.* The evolutionarily conserved core design of the catalytic activation step of the yeast spliceosome. *Mol. Cell* **36**, 593–608 (2009).
- Lesser, C. F. & Guthrie, C. Mutations in U6 snRNA that alter splice site specificity: implications for the active site. *Science* **262**, 1982–1988 (1993).
- Kandels-Lewis, S. & Séraphin, B. Involvement of U6 snRNA in 5' splice site selection. *Science* **262**, 2035–2039 (1993).
- Raghuathan, P. L. & Guthrie, C. RNA unwinding in U4/U6 snRNPs requires ATP hydrolysis and the DEH-box splicing factor Brr2. *Curr. Biol.* **8**, 847–855 (1998).
- Laggerbauer, B., Achsel, T. & Lührmann, R. The human U5-200kD DEXH-box protein unwinds U4/U6 RNA duplexes *in vitro*. *Proc. Natl Acad. Sci. USA* **95**, 4188–4192 (1998).
- Newman, A. J. & Norman, C. U5 snRNA interacts with exon sequences at 5' and 3' splice sites. *Cell* **68**, 743–754 (1992).
- Sontheimer, E. J. & Steitz, J. A. The U5 and U6 small nuclear RNAs as active site components of the spliceosome. *Science* **262**, 1989–1996 (1993).
- Ohrt, T. *et al.* Molecular dissection of step 2 catalysis of yeast pre-mRNA splicing investigated in a purified system. *RNA* **19**, 902–915 (2013).
- Cordin, O., Hahn, D. & Beggs, J. D. Structure, function and regulation of spliceosomal RNA helicases. *Curr. Opin. Cell Biol.* **24**, 431–438 (2012).
- Schwer, B. A conformational rearrangement in the spliceosome sets the stage for Prp22-dependent mRNA release. *Mol. Cell* **30**, 743–754 (2008).
- Company, M., Arenas, J. & Abelson, J. Requirement of the RNA helicase-like protein PRP22 for release of messenger RNA from spliceosomes. *Nature* **349**, 487–493 (1991).
- Tsai, R.-T. *et al.* Spliceosome disassembly catalyzed by Prp43 and its associated components Ntr1 and Ntr2. *Genes Dev.* **19**, 2991–3003 (2005).
- Abelson, J. *et al.* Conformational dynamics of single pre-mRNA molecules during *in vitro* splicing. *Nat. Struct. Mol. Biol.* **17**, 504–512 (2010).
- Nguyen, T. H. D. *et al.* Cryo-EM structure of the yeast U4/U6.U5 tri-snRNP at 3.7 Å resolution. *Nature* **530**, 298–302 (2016).
- Wan, R. *et al.* The 3.8 Å structure of the U4/U6.U5 tri-snRNP: Insights into spliceosome assembly and catalysis. *Science* **351**, 466–475 (2016).
- Gale, J. P., Oubridge, C., Newman, A. J. & Nagai, K. Crystal structure of Prp8 reveals active site cavity of the spliceosome. *Nature* **493**, 638–643 (2013).
- Rasche, N. *et al.* Cwc2 and its human homologue RBM22 promote an active conformation of the spliceosome catalytic centre. *EMBO J.* **31**, 1591–1604 (2012).
- Hilliker, A. K., Mefford, M. A. & Staley, J. P. U2 toggles iteratively between the stem IIa and stem IIc conformations to promote pre-mRNA splicing. *Genes Dev.* **21**, 821–834 (2007).
- Perriman, R. J. & Ares, M., Jr. Rearrangement of competing U2 RNA helices within the spliceosome promotes multiple steps in splicing. *Genes Dev.* **21**, 811–820 (2007).
- Grainger, R. J., Barras, J. D., Jacquier, A., Rain, J.-C. & Beggs, J. D. Physical and genetic interactions of yeast Cwc21p, an ortholog of human Srm300/SRRM2, suggest a role at the catalytic center of the spliceosome. *RNA* **15**, 2161–2173 (2009).
- Yan, C. *et al.* Structure of a yeast spliceosome at 3.6-angstrom resolution. *Science* **349**, 1182–1191 (2015).
- Nguyen, T. H. D. *et al.* Structural basis of Brr2-Prp8 interactions and implications for U5 snRNP biogenesis and the spliceosome active site. *Structure* **21**, 910–919 (2013).
- van Nues, R. W. & Beggs, J. D. Functional contacts with a range of splicing proteins suggest a central role for Brr2p in the dynamic control of the order of events in spliceosomes of *Saccharomyces cerevisiae*. *Genetics* **157**, 1451–1467 (2001).
- Smith, D. J., Query, C. C. & Konarska, M. M. "Nought may endure but mutability": spliceosome dynamics and the regulation of splicing. *Mol. Cell* **30**, 657–666 (2008).
- Konarska, M. M., Vilardell, J. & Query, C. C. Repositioning of the reaction intermediate within the catalytic center of the spliceosome. *Mol. Cell* **21**, 543–553 (2006).
- Kim, C. H. & Abelson, J. Site-specific crosslinks of yeast U6 snRNA to the pre-mRNA near the 5' splice site. *RNA* **2**, 995–1010 (1996).
- Buchwald, G., Schüssler, S., Basquin, C., Le Hir, H. & Conti, E. Crystal structure of the human eIF4AIII-CWC22 complex shows how a DEAD-box protein is inhibited by a MIF4G domain. *Proc. Natl Acad. Sci. USA* **110**, E4611–E4618 (2013).
- Madhani, H. D. & Guthrie, C. A novel base-pairing interaction between U2 and U6 snRNAs suggests a mechanism for the catalytic activation of the spliceosome. *Cell* **71**, 803–817 (1992).
- Fica, S. M., Mefford, M. A., Piccirilli, J. A. & Staley, J. P. Evidence for a group II intron-like catalytic triplex in the spliceosome. *Nat. Struct. Mol. Biol.* **21**, 464–471 (2014).
- Steitz, T. A. & Steitz, J. A. A general two-metal-ion mechanism for catalytic RNA. *Proc. Natl Acad. Sci. USA* **90**, 6498–6502 (1993).
- Fica, S. M. *et al.* RNA catalyses nuclear pre-mRNA splicing. *Nature* **503**, 229–234 (2013).
- Robart, A. R., Chan, R. T., Peters, J. K., Rajashankar, K. R. & Toor, N. Crystal structure of a eukaryotic group II intron lariat. *Nature* **514**, 193–197 (2014).
- Chen, H.-C., Tseng, C.-K., Tsai, R.-T., Chung, C.-S. & Cheng, S.-C. Link of NTR-mediated spliceosome disassembly with DEAH-box ATPases Prp2, Prp16, and Prp22. *Mol. Cell. Biol.* **33**, 514–525 (2013).
- Warkocki, Z. *et al.* Reconstitution of both steps of *Saccharomyces cerevisiae* splicing with purified spliceosomal components. *Nat. Struct. Mol. Biol.* **16**, 1237–1243 (2009).
- Chiu, Y.-F. *et al.* Cwc25 is a novel splicing factor required after Prp2 and Yju2 to facilitate the first catalytic reaction. *Mol. Cell. Biol.* **29**, 5671–5678 (2009).
- Krishnan, R. *et al.* Biased Brownian ratcheting leads to pre-mRNA remodeling and capture prior to first-step splicing. *Nat. Struct. Mol. Biol.* **20**, 1450–1457 (2013).
- Voorhees, R. M., Weixlbaumer, A., Loakes, D., Kelley, A. C. & Ramakrishnan, V. Insights into substrate stabilization from snapshots of the peptidyl transferase center of the intact 70S ribosome. *Nat. Struct. Mol. Biol.* **16**, 528–533 (2009).
- Semlow, D. R., Blanco, M. R., Walter, N. G. & Staley, J. P. Spliceosomal DEAH-Box ATPases remodel pre-mRNA to activate alternative splice sites. *Cell* **164**, 985–998 (2016).
- Tseng, C.-K., Liu, H.-L. & Cheng, S.-C. DEAH-box ATPase Prp16 has dual roles in remodeling of the spliceosome in catalytic steps. *RNA* **17**, 145–154 (2011).
- Schwer, B. & Guthrie, C. A conformational rearrangement in the spliceosome is dependent on PRP16 and ATP hydrolysis. *EMBO J.* **11**, 5033–5039 (1992).
- Villa, T. & Guthrie, C. The Isy1p component of the NineTeen complex interacts with the ATPase Prp16p to regulate the fidelity of pre-mRNA splicing. *Genes Dev.* **19**, 1894–1904 (2005).
- Umen, J. G. & Guthrie, C. Prp16p, Slu7p, and Prp8p interact with the 3' splice site in two distinct stages during the second catalytic step of pre-mRNA splicing. *RNA* **1**, 584–597 (1995).
- Chen, W. *et al.* Endogenous U2-U5-U6 snRNA complexes in *S. pombe* are intron lariat spliceosomes. *RNA* **20**, 308–320 (2014).
- Nguyen, T. H. D. *et al.* CryoEM structures of two spliceosomal complexes: starter and dessert at the spliceosome feast. *Curr. Opin. Struct. Biol.* **36**, 48–57 (2016).
- Garrey, S. M. *et al.* A homolog of lariat-debranching enzyme modulates turnover of branched RNA. *RNA* **20**, 1337–1348 (2014).

**Supplementary Information** is available in the online version of the paper.

**Acknowledgements** We thank K. Nguyen, X.-C. Bai and S. Scheres for their help and advice on data collection and processing; C. Sava, S. Chen, K. R. Vinothkumar, G. McMullan, J. Grimmett and T. Darling for smooth running of the EM and computing facilities; the mass spectrometry facility for help with protein identification, A. Brown, P. Emsley, G. Murshudov and J. Llaser for help and advice with model building and refinement; L. Langer and the members of the spliceosome group for help and advice throughout the project. We thank J. Löwe, V. Ramakrishnan, D. Barford and R. Henderson for their continuing support, S. Scheres, C. Plaschka and L. Strittmatter for critical reading of the manuscript and J. Vilardell for a generous gift of reagent. The project was supported by the Medical Research Council (MC\_U105184330). M.E.W. was supported by a Rutherford Memorial Cambridge Scholarship, S.M.F. by EMBO and Marie Skłodowska-Curie fellowships.

**Author Contributions** W.P.G., M.E.W. and S.M.F. established experimental procedures; W.P.G. and M.E.W. prepared the sample and grids, and processed EM data. W.P.G., M.E.W. and S.M.F. collected EM data. W.P.G., M.E.W. and C.O. carried out model building and refinement. W.P.G., M.E.W., S.M.F., C.O. and K.N. analysed the structure. A.J.N. contributed to the project through his knowledge and experience on yeast splicing. Manuscript was written by W.P.G., M.E.W. and K.N. and finalized with input from all authors. K.N. initiated and orchestrated the spliceosome project.

**Author Information** The cryo-EM maps have been deposited in the Electron Microscopy Data Bank with accession codes EMD-4055, EMD-4056, EMD-4057, EMD-4058 and EMD-4059. The coordinates of the atomic models have been deposited in the Protein Data Bank under accession code 5LJ3 (core of the complex) and 5LJ5 (overall structure). Reprints and permissions information is available at [www.nature.com/reprints](http://www.nature.com/reprints). The authors declare no competing financial interests. Readers are welcome to comment on the online version of the paper. Correspondence and requests for materials should be addressed to W.P.G. ([wgalej@mrc-lmb.cam.ac.uk](mailto:wgalej@mrc-lmb.cam.ac.uk)) or K.N. ([kn@mrc-lmb.cam.ac.uk](mailto:kn@mrc-lmb.cam.ac.uk)).



## METHODS

No statistical methods were used to predetermine sample size. The experiments were not randomized and the investigators were not blinded to allocation during experiments and outcome assessment.

**Prp18-HA and Slu7-TAPS tagging.** *SLU7*-TAPS homology recombination cassettes were generated by PCR from pFA6a-TAPS-kanMX6, a modified version of pFA6a-TAP-kanMX6 in which the Calmodulin-binding peptide tag is replaced by two tandem copies of the StrepII tag<sup>51</sup>. The PCR product was used to transform yeast strain YSCC1 (*MATa prc1 prb1 pep4 leu2 trp1 ura3 PRP19-HA*)<sup>4</sup> selecting for G418-resistance. *PRP18*-3xHA kanMX6 cassette was transformed into BY4741 strain (*MATa his3Δ1 leu2Δ0 met15Δ0 ura3Δ0*) and selected as above. Integration of the cassettes was confirmed by PCR and western blotting.

**Sample preparation.** The Prp18-HA or Slu7-TAPS yeast strains were grown in a 120 l fermenter, and splicing extract was prepared using liquid nitrogen method<sup>36</sup> essentially as previously described<sup>52</sup>. A DNA template for *in vitro* transcription was generated by addition of  $2 \times$  MS2 stem loops<sup>53</sup> to the 5'-end of the *UBC4* pre-mRNA sequence<sup>18</sup>, in which the 3'-splice site sequence UAGAG was mutated to UACAC. Pre-mRNA substrate was generated by run-off transcription from a plasmid DNA template and labelled at the 3'-end with fluorescein-5-thiosemicarbazide<sup>54</sup>. *In vitro* splicing reactions were assembled using pre-mRNA substrate pre-bound to MS2-MBP fusion protein as previously described<sup>6,53</sup>. The resulting spliceosomes were bound by amylose resin in HE-75 (20 mM HEPES KOH pH 7.8, 75 mM KCl, 0.25 mM EDTA, 5% glycerol, 0.01% NP-40) and eluted with 12 mM maltose. The sample was subsequently immobilised on either anti-HA-agarose (for Prp18-HA yeast extract) or Streptactin resin (for Slu7-TAPS yeast extract) in HE-100 (20 mM HEPES KOH pH 7.8, 100 mM KCl, 0.25 mM EDTA, 5% glycerol, 0.01% NP-40) and eluted with either HA peptide (for anti-HA-agarose) or desthiobiotin (for Streptactin resin), essentially as described<sup>55</sup>. The eluate was finally dialysed against HE-75 buffer (without glycerol and NP-40) for EM sample preparation. Analysis of fluorescently labelled RNA showed that pre-mRNA is converted to the lariat intron-3'-exon intermediate in our sample and hence it is referred to as complex C (Extended Data Fig. 1b). Our experimental set-up was designed to purify step-two complexes after Prp16 action, however the presence of step-one factors in the structure and configuration of the active site clearly indicate that the complex has not undergone Prp16-mediated remodelling. It has been shown previously<sup>13</sup> that in low salt conditions Prp18, Slu7 and Prp16 associate with complex B\* and C. Analysis of protein components by gel electrophoresis and subsequent mass spectrometry shows that Prp16 as well as Prp22 are present, in agreement with the previous results (Extended Data Fig. 1a; Extended Data Table 2)<sup>6,13,43</sup>.

**Electron microscopy.** For cryo-EM analysis, Quantifoil R2/2 Cu 400 mesh grids were coated with a 5–7 nm-thick layer of homemade carbon film and glow discharged. After applying 3  $\mu$ l of the sample, the grids were blotted for 2.5–3 s and vitrified in liquid ethane in FEI Vitrobot MKIII, at 100% humidity at 4°C. Grids were loaded into an FEI Titan Krios transmission electron microscope operated at 300 kV and imaged using a Gatan K2 summit direct electron detector and a GIF Quantum energy filter (slit width 20 eV). Images were collected in super-resolution counting mode at 1.25 frames s<sup>-1</sup> and a calibrated pixel size of 1.43 Å. A total dose of 40 e Å<sup>-2</sup> over 16 s and a defocus range of 0.5–4  $\mu$ m were used.

**Image processing.** A total of 2213 micrographs were subjected to whole-frame drift correction in MOTIONCORR<sup>56</sup> followed by contrast transfer function (CTF) parameter estimation in CTFFIND4 (ref. 57). All subsequent processing steps were done using RELION<sup>58</sup> unless otherwise stated. An initial subset of 5,000 particles was selected manually and subjected to reference-free 2D classification. Resulting 2D class averages were low-pass filtered to 20 Å and used as templates for subsequent automated particle picking within RELION<sup>59</sup>. A total of 247,603 particles were selected after initial reference-free 2D classification and subjected to 3D classification (Extended Data Fig. 2). An initial 3D reference was prepared by scaling and low-pass filtering (60 Å) the reconstruction of the intron-lariat complex (EMD-6413). A subset of 93,106 particles was selected after 3D classification. Particle-based beam-induced motion correction and radiation-damage weighting (particle polishing) followed by 3D refinement resulted in a final reconstruction at 3.8 Å overall resolution and estimated accuracies of rotations of 1.1° (Extended Data Fig. 3).

Very weak density observed at two peripheral regions of the map corresponds to Brr2/Prp16 (helicase module) and Prp19/Cef1/Snt309 (Prp19 module). We used focused classification with signal subtraction to improve the resolution of these regions<sup>60</sup>. The region of interest was masked out and the projection of the remaining map was subtracted from the experimental particles using angular assignment from the last iteration of the 3D auto-refine run. Subtracted particles were 3D classified without image alignment and the best classes were selected for further refinement of the original (not subtracted) particles. This resulted in a smaller subset of the original particles, in which Brr2/Prp16 and Prp19/Cef1/

Snt309 are more homogeneous and consequently the density is improved in those regions (Extended Data Figs 2 and 3). 3D refinement of the selected 29,210 Prp19-selected particles resulted in a map at overall 5.1 Å resolution, while 15,872 of the helicase-containing particles yielded a map at 10 Å resolution. For the global classification approach we generated a soft mask around the core of the complex and classified polished particles with finer angular sampling of 1.8° and local searches of 10°. The resulting two major classes of 37K and 47K particles were refined to 4.1 Å and 3.9 Å respectively. They revealed a subtle conformational change of the U2 snRNP and Syf1 HAT arch correlated with the presence of WD40 domain near the stem IIC and IIB region of U2 snRNA. This WD40 domain belongs to Prp17 or Prp19, but the local resolution did not allow us to make an unambiguous assignment. All reported resolutions are based on the gold-standard Fourier shell correlation (FSC) = 0.143 criterion<sup>61</sup>. FSC curves were calculated using soft spherical masks and high-resolution noise substitution was used to correct for convolution effects of the masks on the FSC curves<sup>62</sup>. Prior to visualization, all maps were corrected for the modulation transfer function of the detector. Local resolution was estimated using RESMAP<sup>63</sup>.

**Model building.** A list of protein and RNA components included in the model is given in Extended Data Table 2. Building started by docking known structures of *S. cerevisiae* Prp8, Snu114, U5 Sm ring, U5 snRNA<sup>19</sup>, Cwc2 (ref. 64) and Bud31 (ref. 65) into the map. Homology models for Cef1, Prp45, Prp46, Ecm2 and Cwc15 were built with SWISS-MODEL<sup>66</sup>, using structures from the *S. pombe* intron-lariat spliceosome<sup>26</sup> as templates, and were docked into the map. This accounted for the majority of the protein density in the core, allowing building of the intron, U6 snRNA and U2 snRNA. RNA extending from the loop 1 of U5 snRNA was assigned to nucleotides –1 to –16 of the 5'-exon as previously predicted<sup>11</sup>. A model for the NTD of Cwc22 was built using SWISS-MODEL based on the structure of the human Cwc22:eIF4AIII complex<sup>32</sup> and docked near Snu114. Clear density near the NTD of Cwc22 was interpreted as the MA3 domain at the C terminus of Cwc22; this domain was built *de novo*. A coiled-coil was found contacting domain IV of Snu114. Based on an unpublished NMR structure from *Arabidopsis thaliana* (PDB ID: 2E62) and biochemical data<sup>25</sup> we assigned this density to the CTD of Cwc21. Weak density was observed connecting this coiled-coil to a peptide contacting the 5'-exon. We therefore assigned this peptide as the N terminus of Cwc21. Unassigned density remained near the branch-point helix. Based on secondary structure prediction<sup>67</sup> we assigned a portion of this density to Yju2 and were able to build its NTD *de novo*; our assignment was supported by clear density for a zinc atom coordinated by four conserved cysteines. The remainder of the density could then be assigned to the N termini of Cwc25 and Isy1.

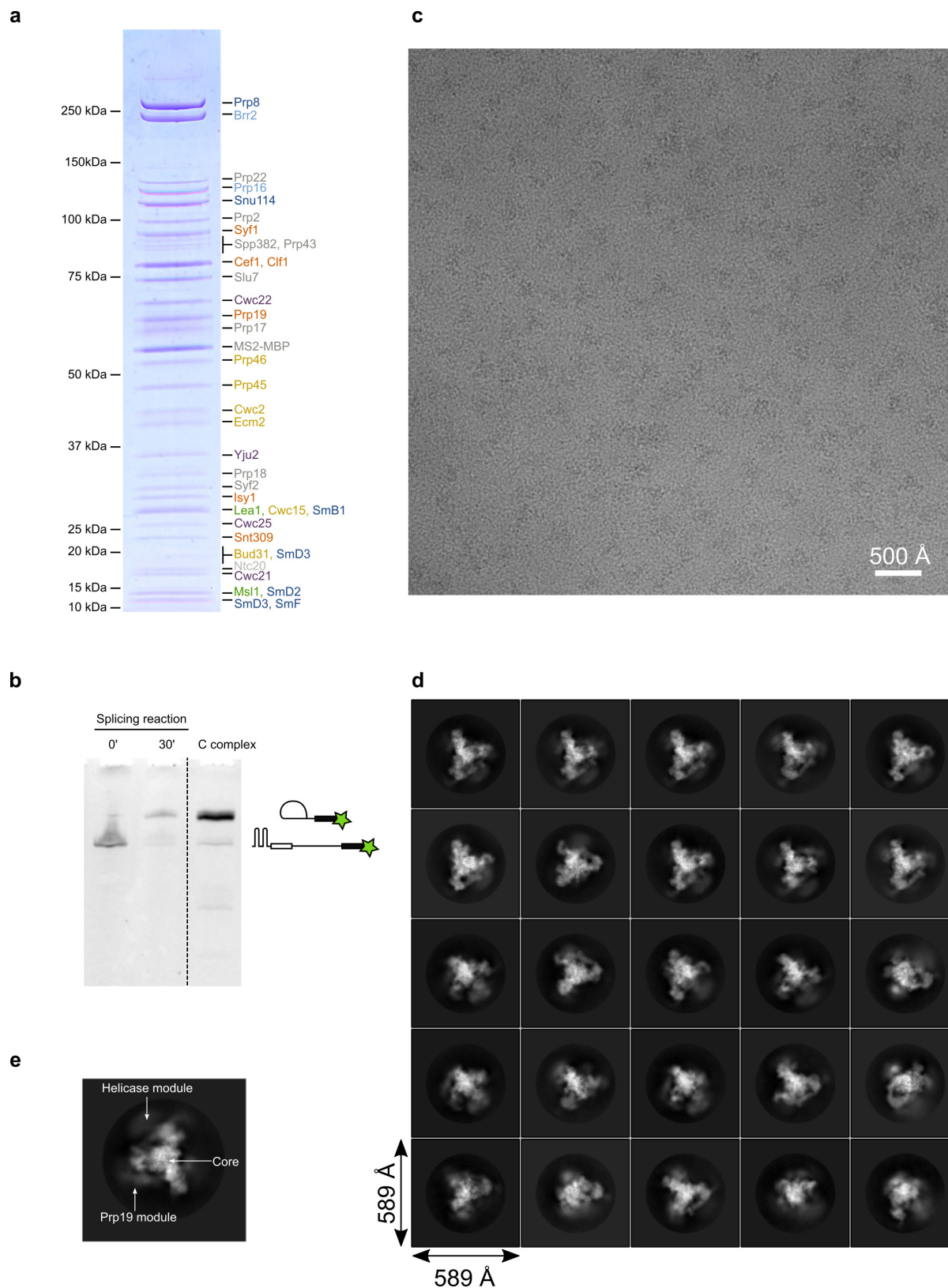
The majority of the model building described above was for the core of the spliceosome where the resolution was uniformly between 3.5–4.5 Å (Extended Data Fig. 4). For the periphery of the complex, the resolution was more heterogeneous, ranging from 4 to 20 Å. Clear features of the periphery were two large proteins with extended architectures. One of these proteins started in the core and projected outwards to the periphery. At the core, side-chains were easily visible for this protein and allowed assignment as the N terminus of Clf1. Towards the C terminus of Clf1 the resolution only allowed building of idealised poly-alanine helices, which were then assigned sequence based on secondary structure predictions<sup>67</sup>. For the other extended protein, few side-chains were visible but helices could be distinguished. This protein was generally built as poly-alanine helices, and based on secondary structure predictions<sup>67</sup> was assigned as Syf1. A second Sm ring at medium-resolution was found in the map and was assigned as the U2 snRNA Sm ring. Homology models for the U2 snRNP proteins Lea1 and Msl1 were generated using SWISS-MODEL<sup>66</sup> based on the structure of the human U2B'-U2A'-U2 snRNA complex<sup>68</sup> and were docked into the adjacent density. The portion of the U2 snRNA in contact with Msl1 was most consistent with the previously proposed stem IV + stem V architecture and was built based on the secondary structure prediction<sup>69</sup>. Two RNA double helices were observed bridging the U2 Sm ring to Ecm2 and were assigned as stems IIB and IIC of the U2 snRNA. Using 3D classification, we found that some of the particles contained a large lobe of extra density connected to the RT-like and RNaseH-like domains of Prp8 (see above). Although we could not resolve secondary structure in this region, we could perfectly dock the crystal structure of Brr2 and the Jab1/MPN domain of Prp8 (ref. 27). The remainder of the density could then well accommodate an I-TASSER<sup>70</sup> homology model of Prp16 based on the crystal structure of Prp43 (ref. 71). Weak density connected to Clf1 and Syf1 had the characteristic shape of Prp19–Snt309–Cef1 (ref. 26). Focused classification in this region could improve the density enough to resolve the U-box dimers and thus dock a homology model of these proteins. Finally, three copies of the Prp19 WD40 domain crystal structure could be docked into very weak density adjacent to the Prp19 coiled-coils. With the exception of the helicase and Prp19 modules all models were manually rebuilt in order to obtain the best fit to the cryo-EM density. The model was refined using REFMAC 5.8 (ref. 72)



with secondary structure restraints generated in PROSMART<sup>73</sup> and RNA base-pair and stacking restraints generated in LIBG<sup>74</sup>. Extended Data Table 1 summarizes refinement statistics and PBD and EMDDB accession codes.

**Map visualization.** Maps were visualized in Chimera<sup>75</sup> and figures were prepared using PyMOL (<http://www.pymol.org>).

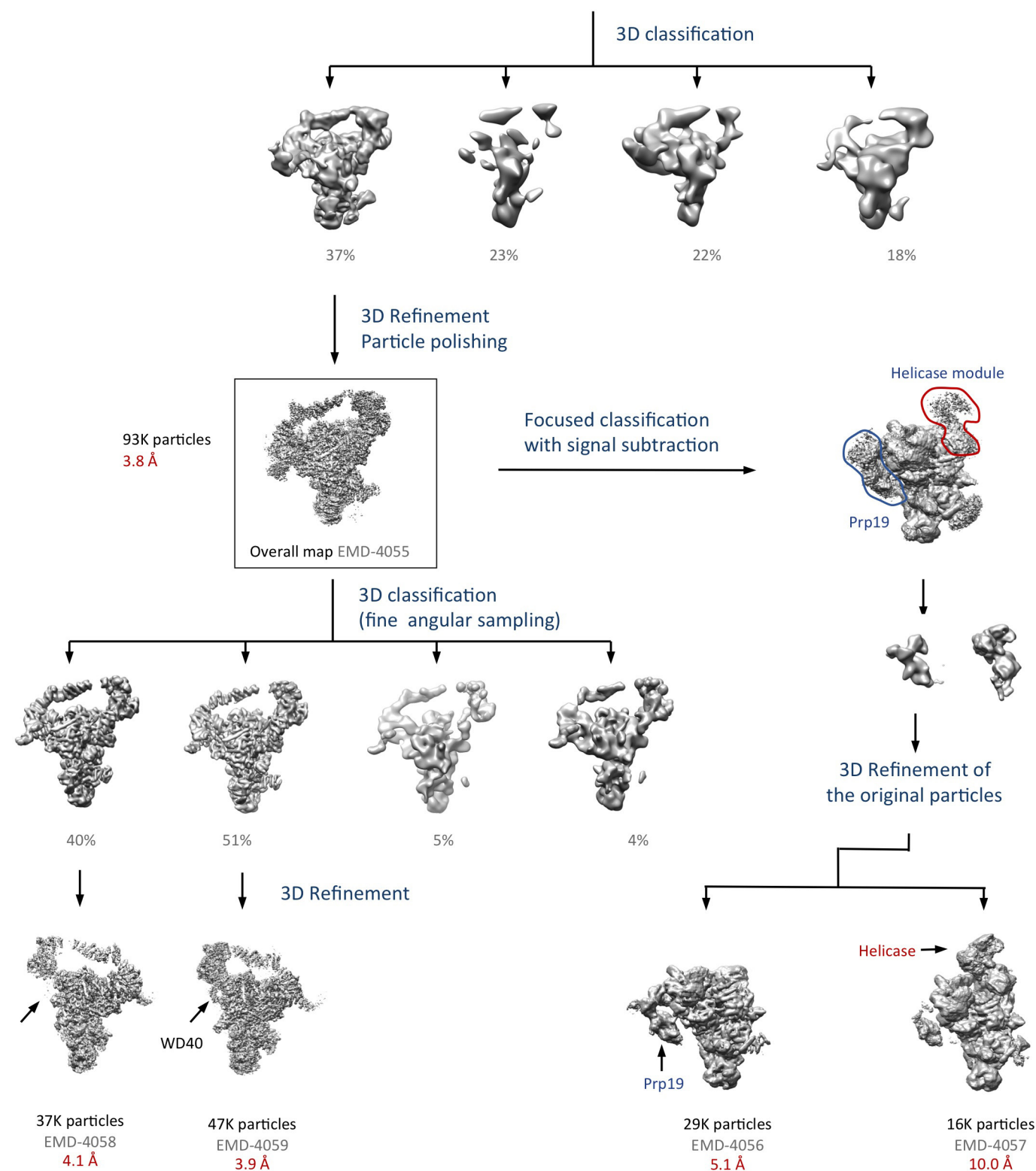
51. Schreieck, A. *et al.* RNA polymerase II termination involves C-terminal-domain tyrosine dephosphorylation by CPF subunit Glc7. *Nat. Struct. Mol. Biol.* **21**, 175–179 (2014).
52. Lin, R. J., Newman, A. J., Cheng, S. C. & Abelson, J. Yeast mRNA splicing in vitro. *J. Biol. Chem.* **260**, 14780–14792 (1985).
53. Zhou, Z., Licklider, L. J., Gygi, S. P. & Reed, R. Comprehensive proteomic analysis of the human spliceosome. *Nature* **419**, 182–185 (2002).
54. Hardin, J. W., Warnasooriya, C., Kondo, Y., Nagai, K. & Rueda, D. Assembly and dynamics of the U4/U6 di-snRNP by single-molecule FRET. *Nucleic Acids Res.* **43**, 10963–10974 (2015).
55. Nguyen, T. H. D. *et al.* The architecture of the spliceosomal U4/U6.U5 tri-snRNP. *Nature* **523**, 47–52 (2015).
56. Li, X. *et al.* Electron counting and beam-induced motion correction enable near-atomic-resolution single-particle cryo-EM. *Nat. Methods* **10**, 584–590 (2013).
57. Rohou, A. & Grigorieff, N. CTFFIND4: Fast and accurate defocus estimation from electron micrographs. *J. Struct. Biol.* **192**, 216–221 (2015).
58. Scheres, S. H. W. RELION: implementation of a Bayesian approach to cryo-EM structure determination. *J. Struct. Biol.* **180**, 519–530 (2012).
59. Scheres, S. H. W. Semi-automated selection of cryo-EM particles in RELION-1.3. *J. Struct. Biol.* **189**, 114–122 (2015).
60. Bai, X.-C., Rajendra, E., Yang, G., Shi, Y. & Scheres, S. H. W. Sampling the conformational space of the catalytic subunit of human  $\gamma$ -secretase. *eLife* **4**, 1485 (2015).
61. Scheres, S. H. W. & Chen, S. Prevention of overfitting in cryo-EM structure determination. *Nat. Methods* **9**, 853–854 (2012).
62. Chen, S. *et al.* High-resolution noise substitution to measure overfitting and validate resolution in 3D structure determination by single particle electron cryomicroscopy. *Ultramicroscopy* **135**, 24–35 (2013).
63. Kucukelbir, A., Sigworth, F. J. & Tagare, H. D. Quantifying the local resolution of cryo-EM density maps. *Nat. Methods* **11**, 63–65 (2014).
64. Lu, P. *et al.* Structure of the mRNA splicing complex component Cwc2: insights into RNA recognition. *Biochem. J.* **441**, 591–597 (2012).
65. van Roon, A.-M. M. *et al.* <sup>113</sup>Cd NMR experiments reveal an unusual metal cluster in the solution structure of the yeast splicing protein Bud31p. *Angew. Chem. Int. Edn Engl.* **54**, 4861–4864 (2015).
66. Biasini, M. *et al.* SWISS-MODEL: modelling protein tertiary and quaternary structure using evolutionary information. *Nucleic Acids Res.* **42**, W252–W258 (2014).
67. Kurowski, M. A. & Bujnicki, J. M. GeneSilico protein structure prediction meta-server. *Nucleic Acids Res.* **31**, 3305–3307 (2003).
68. Price, S. R., Evans, P. R. & Nagai, K. Crystal structure of the spliceosomal U2B''-U2A' protein complex bound to a fragment of U2 small nuclear RNA. *Nature* **394**, 645–650 (1998).
69. Kudla, G., Granneman, S., Hahn, D., Beggs, J. D. & Tollervy, D. Cross-linking, ligation, and sequencing of hybrids reveals RNA-RNA interactions in yeast. *Proc. Natl Acad. Sci. USA* **108**, 10010–10015 (2011).
70. Yang, J. *et al.* The I-TASSER Suite: protein structure and function prediction. *Nat. Methods* **12**, 7–8 (2015).
71. Walbott, H. *et al.* Prp43p contains a processive helicase structural architecture with a specific regulatory domain. *EMBO J.* **29**, 2194–2204 (2010).
72. Murshudov, G. N., Vagin, A. A. & Dodson, E. J. Refinement of macromolecular structures by the maximum-likelihood method. *Acta Crystallogr. D Biol. Crystallogr.* **53**, 240–255 (1997).
73. Nicholls, R. A., Fischer, M., McNicholas, S. & Murshudov, G. N. Conformation-independent structural comparison of macromolecules with ProSMART. *Acta Crystallogr. D Biol. Crystallogr.* **70**, 2487–2499 (2014).
74. Brown, A. *et al.* Tools for macromolecular model building and refinement into electron cryo-microscopy reconstructions. *Acta Crystallogr. D Biol. Crystallogr.* **71**, 136–153 (2015).
75. Goddard, T. D., Huang, C. C. & Ferrin, T. E. Visualizing density maps with UCSF Chimera. *J. Struct. Biol.* **157**, 281–287 (2007).
76. Marcia, M. & Pyle, A. M. Visualizing group II intron catalysis through the stages of splicing. *Cell* **151**, 497–507 (2012).
77. Le Hir, H., Saulière, J. & Wang, Z. The exon junction complex as a node of post-transcriptional networks. *Nat. Rev. Mol. Cell Biol.* **17**, 41–54 (2016).
78. Bessonov, S., Anokhina, M., Will, C. L., Urlaub, H. & Lührmann, R. Isolation of an active step I spliceosome and composition of its RNP core. *Nature* **452**, 846–850 (2008).
79. Alexandrov, A., Colognori, D., Shu, M.-D. & Steitz, J. A. Human spliceosomal protein CWC22 plays a role in coupling splicing to exon junction complex deposition and nonsense-mediated decay. *Proc. Natl Acad. Sci. USA* **109**, 21313–21318 (2012).
80. Steckelberg, A.-L., Boehm, V., Gromadzka, A. M. & Gehring, N. H. CWC22 connects pre-mRNA splicing and exon junction complex assembly. *Cell Reports* **2**, 454–461 (2012).
81. Barbosa, I. *et al.* Human CWC22 escorts the helicase eIF4AIII to spliceosomes and promotes exon junction complex assembly. *Nat. Struct. Mol. Biol.* **19**, 983–990 (2012).
82. Bono, F., Ebert, J., Lorentzen, E. & Conti, E. The crystal structure of the exon junction complex reveals how it maintains a stable grip on mRNA. *Cell* **126**, 713–725 (2006).
83. Andersen, C. B. F. *et al.* Structure of the exon junction core complex with a trapped DEAD-box ATPase bound to RNA. *Science* **313**, 1968–1972 (2006).
84. Davis, I. W., Murray, L. W., Richardson, J. S. & Richardson, D. C. MOLPROBITY: structure validation and all-atom contact analysis for nucleic acids and their complexes. *Nucleic Acids Res.* **32**, W615–W619 (2004).



**Extended Data Figure 1 | Biochemical characterization of the complex and initial cryo-EM analysis.** **a**, SDS-PAGE analysis of the purified sample. Protein identities were confirmed by mass spectrometry analysis. Protein labels are coloured according to sub-complex identity (dark blue, U5 snRNP; light blue, helicase module; orange, NTC; yellow, NTR; green, U2 snRNP; purple, splicing factors; grey, not found in density). **b**, Analysis of the fluorescently labelled substrate in the sample by denaturing PAGE, showing conversion of linear pre-mRNA (time point 0') into branched

lariat-intron intermediate (time point 30'), which is a predominant species in the purified sample (C complex). The two hairpins on the right depict the  $2 \times$  MS2 stem-loops attached to the 5' end of the *UBC4* pre-mRNA substrate for affinity purification. **c**, A typical cryo-EM micrograph collected on an FEI Titan Krios microscope operated at 300 kV and detected with a Gatan K2 Summit camera. **d**, Reference-free 2D classification results. **e**, Detail of a single class average with major domains labelled.

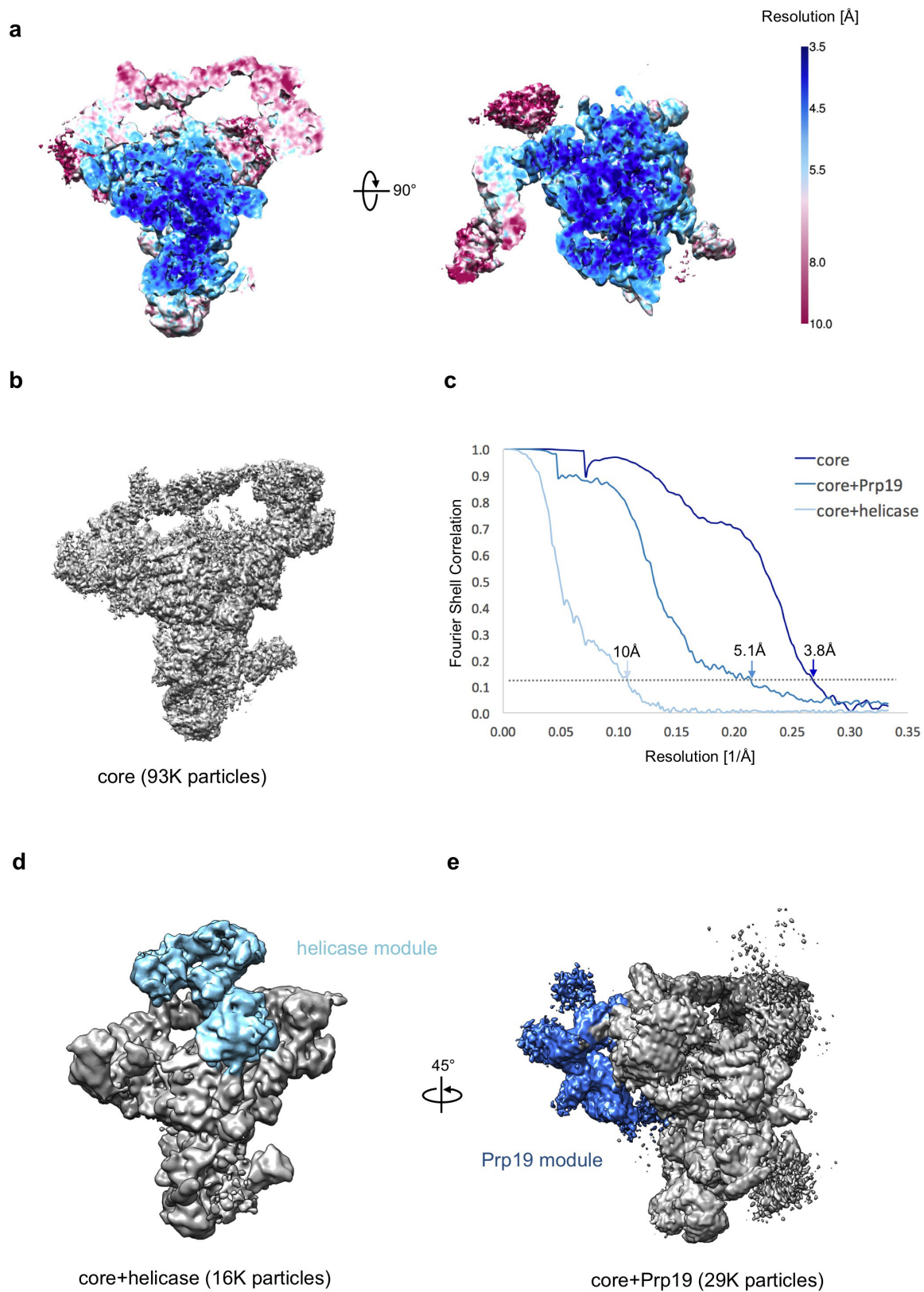
## Autopicking and initial reference-free 2D classification (248K particles)



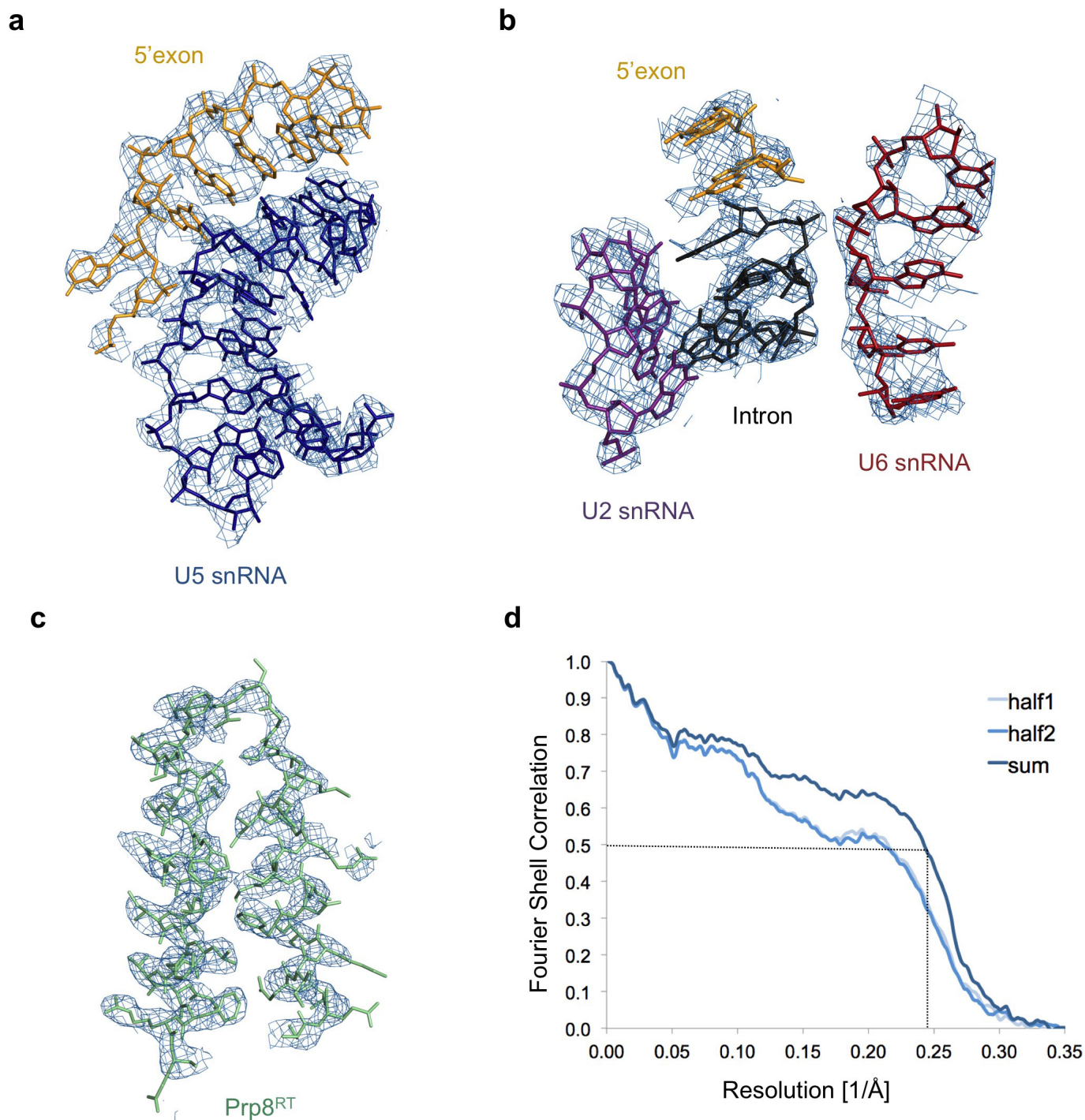
**Extended Data Figure 2 | Overview of the data processing scheme used in this study.** Iterative 2D classification, template selection and automated particle picking resulted in 248K particles which were classified in 3D with a scaled and low-pass-filtered model of ILS (EMDB-6413) as a reference. The best class was refined to 3.8 Å resolution overall. Focused classification allowed us to obtain two other maps with improved quality

of the peripheral regions (Prp19 and helicase modules, EMD-4056 and EMD-4057). Classification of the core complex with fine angular sampling and local searches revealed a subtle movement of the U2 snRNP which correlates with the appearance of the extra density, interpreted as a WD40 domain which belongs to Prp17 or Prp19.



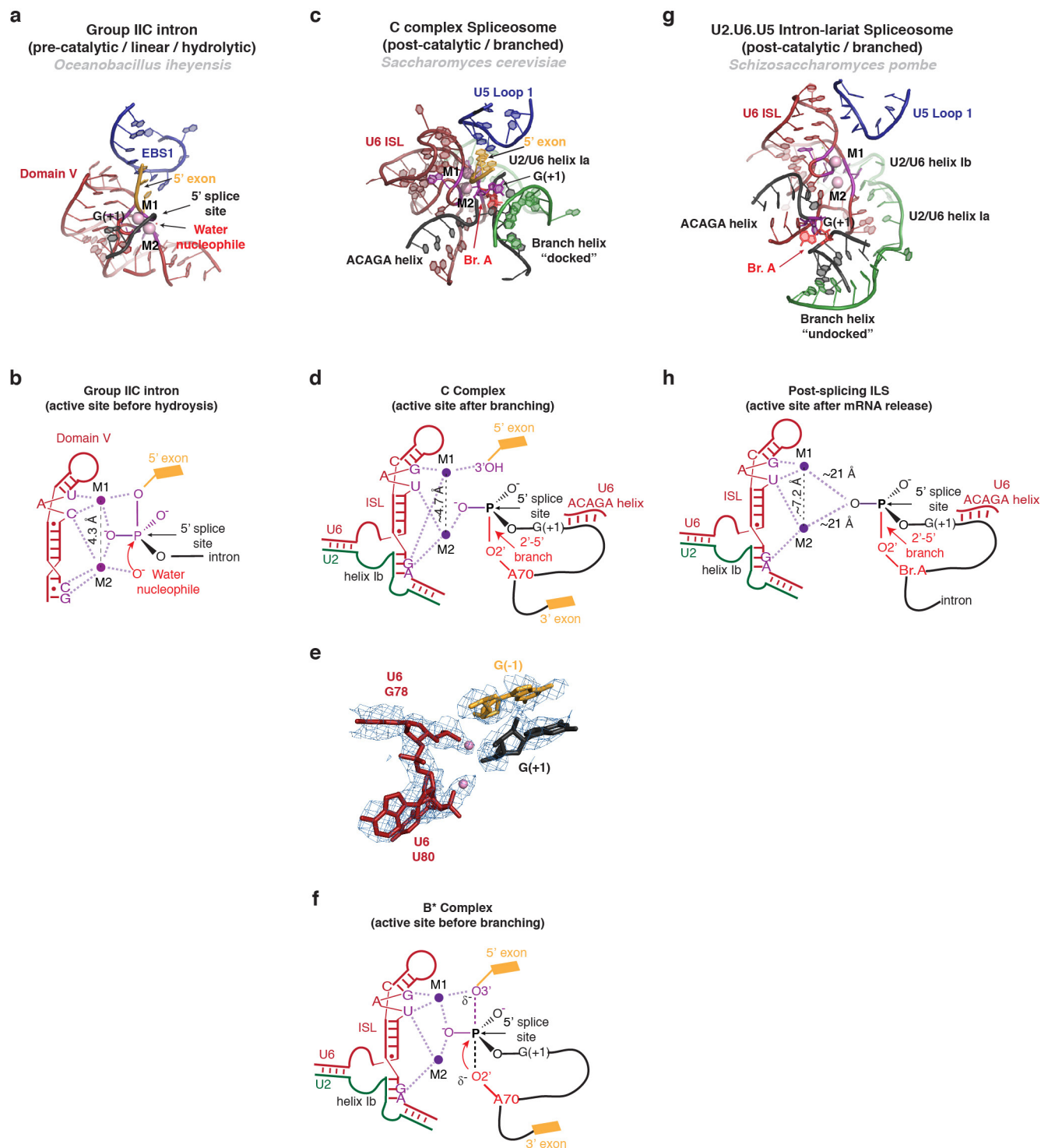


**Extended Data Figure 3 | Global and local resolution analysis.** **a**, Two orthogonal sections through the map showing variation in the local resolution as estimated by Resmap. **b**, An overall map of the core complex **c**, Gold-standard FSC plots for three maps used in this study. **d**, Map of the core complex with a helicase module. **e**, A map of the core complex with Prp19 module.



**Extended Data Figure 4 | Examples of cryo-EM density at the core of the complex with atomic models built in. a,** U5 snRNA loop 1 with 5'-exon bound. **b,** The active site with exon, intron, U2 and U6 snRNAs. **c,** Two helices of the Prp8 reverse transcriptase thumb/X domain, showing a clear helical pitch and excellent densities for the side chains. **d,** Fourier Shell Correlation between model and the map and cross-validation of the

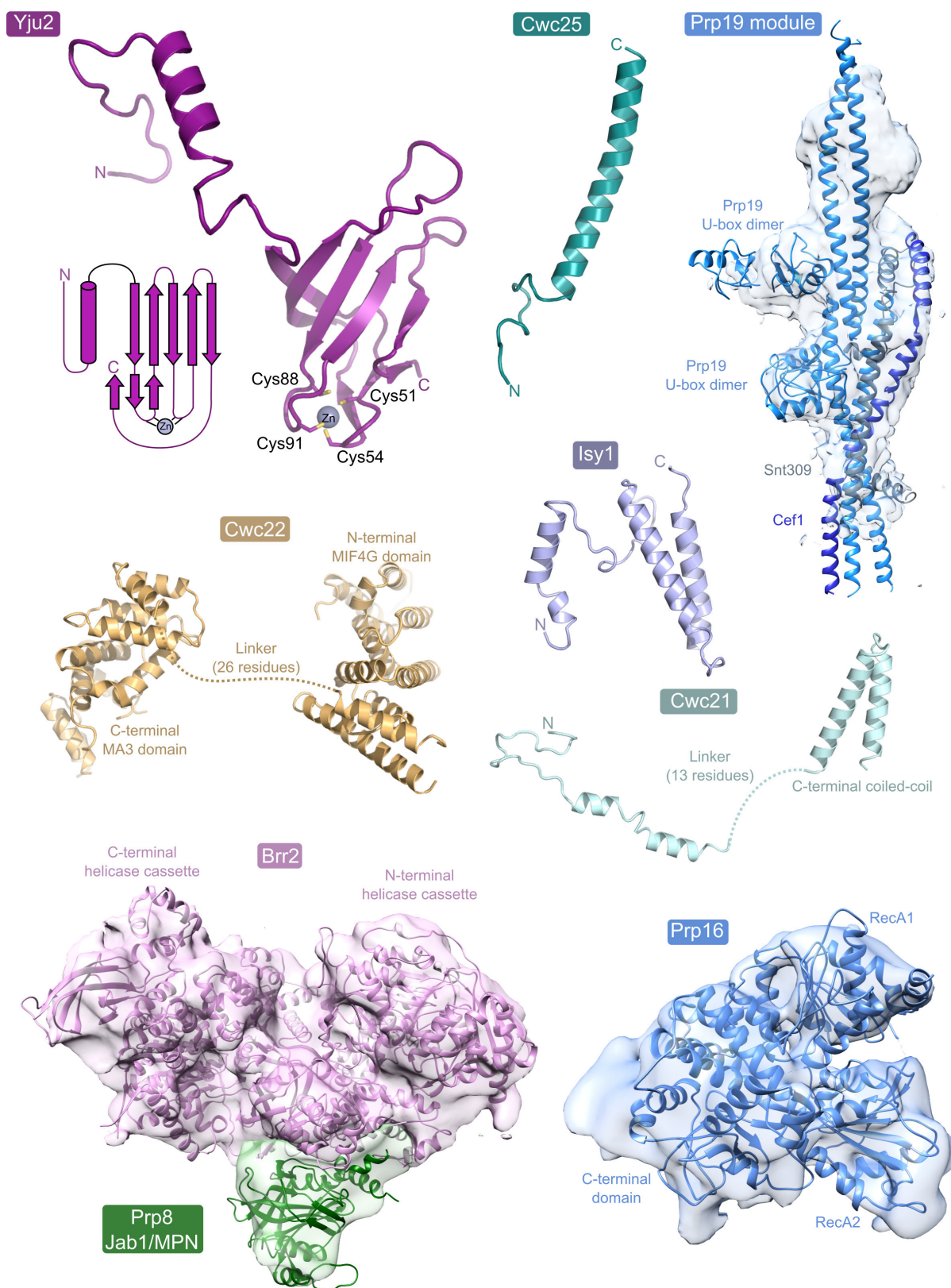
model fitting. (The original atom positions have been randomly displaced up to 0.5 Å and refined with restraints against the half1 map only. FSC was calculated for two half maps. Excellent correlation up to high resolution between the model and the half2 map (which was not used in refinement) cross-validates the model for overfitting.



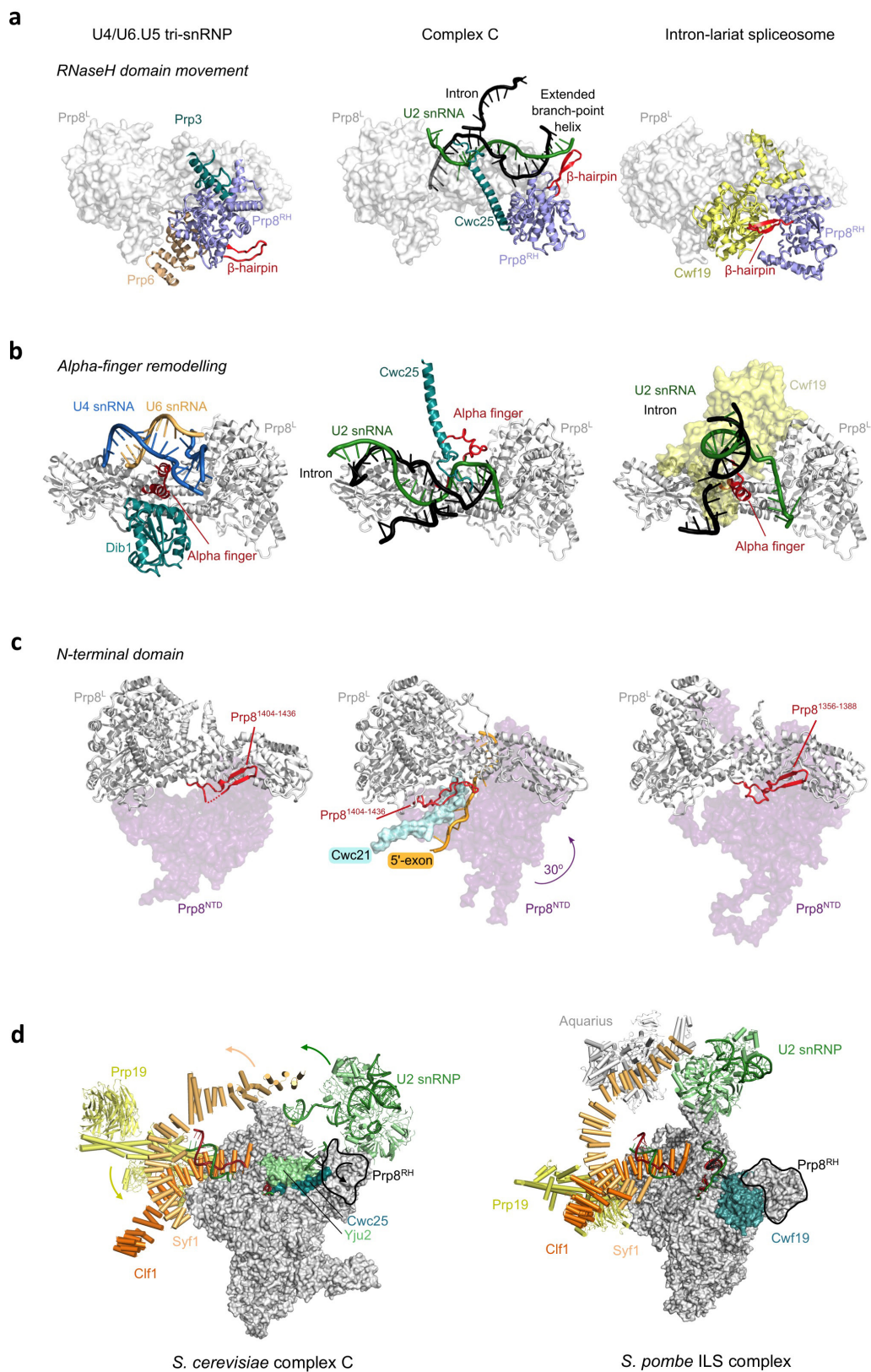
**Extended Data Figure 5 | Metal binding by the catalytic core of C complex.** **a, b**, Structure (**a**) and schematic representation (**b**) of the active site of a group IIC intron trapped in the pre-catalytic state in the presence of  $\text{Ca}^{2+}$  (PDB 4FAQ, ref. 76). The 5' splice site scissile phosphate is aligned with the two metals bound at the core in a catalytic configuration, as shown in **b**. Note that, in this pre-catalytic structure, the group II domain VI is not present and therefore the structure does not contain the bulged adenosine nucleophile required for the branching reaction. As a result, the nucleophile is a water molecule, rather than the 2'-OH of the branch site adenosine found in spliceosomal introns. **c, d, e**, Structure of the RNA at the active site of spliceosomal C complex, showing the overall architecture (**c**), schematic of metal binding (**d**), and comparison of the model with the EM density (**e**). Note conservation of the metal binding residues compared to the group II intron (compare with ref. 36) and proximity of the cleaved G(-1)-G(+1) bond to putative M1. **f**, Proposed interactions

between U6 snRNA and the two catalytic  $\text{Mg}^{2+}$  during the transition state for branching, as inferred from biochemistry<sup>36</sup>. **g, h**, Structure (**g**) and schematic (**h**) of the RNA core of the U2.U6.U5 ILS complex in a post-catalytic configuration (PDB 3JB9, ref. 26), probably following release of the mRNA. The two  $\text{Mg}^{2+}$  are shown as modelled in the coordinates deposited by the authors of the ILS structure (PDB 3JB9, ref. 26). In the ILS structure M1 and M2 are further apart (7.2 Å) than in most other structures of RNAs that coordinate catalytic metals (usually 3.9–5 Å); nonetheless, the ligands modelled for M1 and M2 are consistent with the ligands identified biochemically for the two catalytic  $\text{Mg}^{2+}$  necessary for splicing (compare PDB 3JB9 and 4R0D with the data in refs 34,36). Note that the branch helix is undocked from the U6 snRNA metal binding site and G(+1) is far away from the two  $\text{Mg}^{2+}$  at the core. The substrate and snRNAs are colour-coded while residues that position the catalytic metals are shown in magenta.





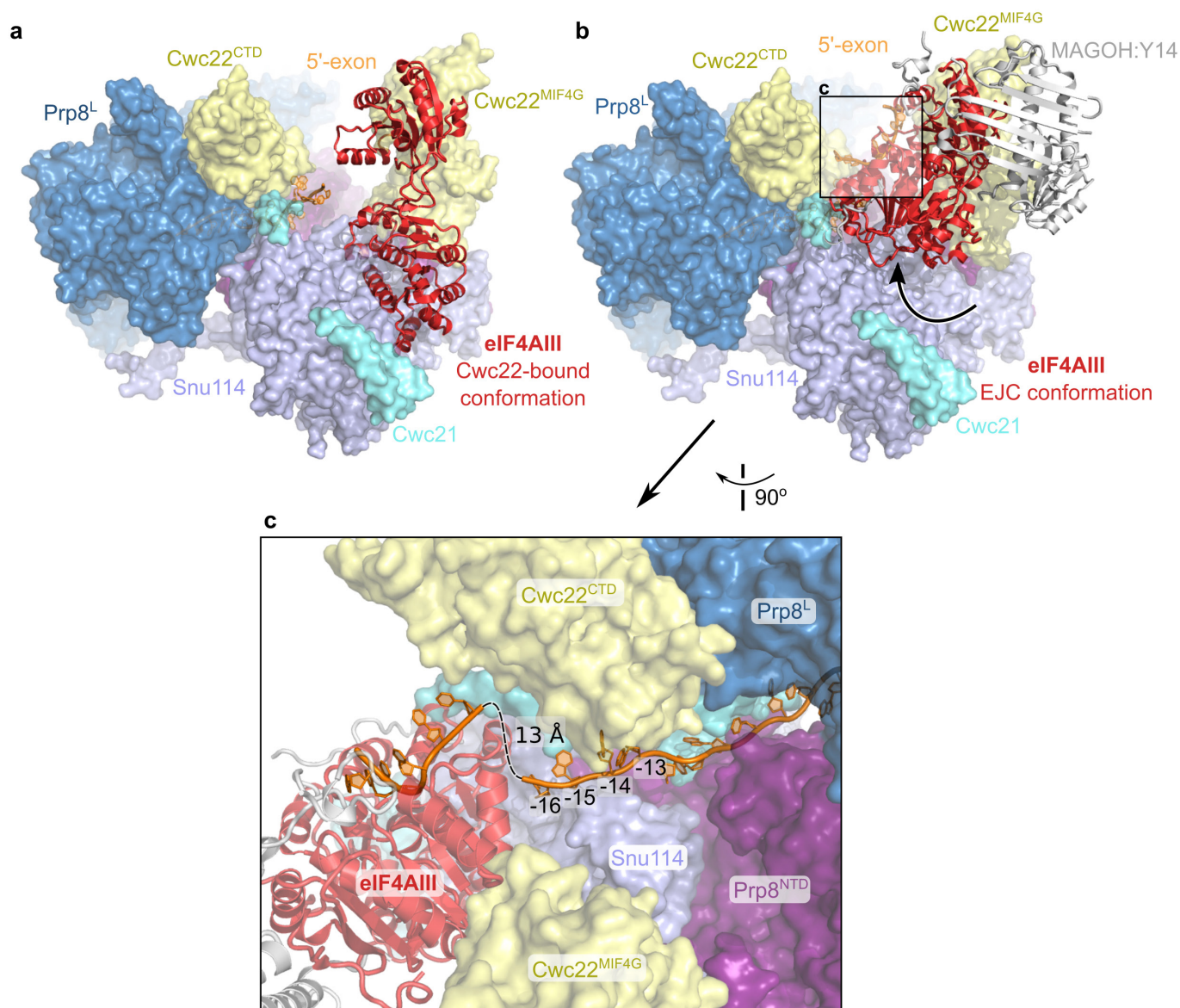
**Extended Data Figure 6 | Examples of the structures of isolated components.** *De novo*-built proteins are shown in cartoon form, along with a secondary structure diagram for the novel zinc-finger fold of Yju2. Proteins that were modelled into low-resolution regions by rigid-body docking of crystal structures or homology models (Prp19 module, Brr2, Prp16, Prp8<sup>Jab1/MPN</sup>) are shown in their cryo-EM densities.



**Extended Data Figure 7 | Conformational changes between U4/U6.U5 tri-snRNP, complex C and intron-lariat spliceosome. a,** Rearrangement of the RNaseH-like domain with respect to the main body of Prp8 in all three complexes. **b,**  $\alpha$ -Finger (1,575–1,598) contacting the key RNA and proteins in a context-dependent manner. **c,** Prp8 N-terminal domain

movements along with Prp8 residues 1,406–1,436 transiently docking on top of the 5'-exon and Cwc21 in complex C, stabilizing the 5'-exon and interdomain contacts in Prp8. **d,** Conformational rearrangements between complex C and *S. pombe* ILS<sup>26</sup> showing a coupled movement of the U2 snRNP, Syf1 and Prp19.





**Extended Data Figure 8 | Implications for deposition of the exon-junction complex.** In higher eukaryotes exon-junction complexes (EJCs) are deposited 20–24 nucleotides (nt) upstream of splice junctions, and form a binding platform for factors involved in nuclear export, translation, alternative splicing and nonsense-mediated mRNA decay<sup>77</sup>. The core EJC components eIF4AIII, MAGOH and Y14 are found in human B and C complexes<sup>78</sup>. Cwc22 is required for eIF4AIII recruitment to spliceosomes<sup>79–81</sup> and holds it in an open, inactive conformation<sup>32</sup>.

**a**, Crystal structure of the eIF4AIII-Cwc22 complex<sup>32</sup> docked onto the spliceosomal C complex via superposition on Cwc22. **b**, Crystal structure of the core EJC<sup>82,83</sup> superimposed on the previous model via the second RecA domain of eIF4AIII. **c**, The 5'-exon exiting the channel at the interface between the Prp8 Large and N-terminal domains is positioned perfectly for the deposition of the EJC, explaining how the Cwc22 MIF4G domain is involved in determining the distance of EJC deposition from the splice junction.



Extended Data Table 1 | Cryo-EM data collection and refinement statistics

	Core	Core+Prp19 <sup>*</sup>	Core+helicase <sup>*</sup>
<b>Data collection</b>			
Microscope	FEI Titan Krios	FEI Titan Krios	FEI Titan Krios
Voltage (kV)	300	300	300
Electron dose (e Å <sup>-2</sup> )	40	40	40
Detector	Gatan K2 Summit	Gatan K2 Summit	Gatan K2 Summit
Pixel size (Å)	1.43	1.43	1.43
Defocus Range (μm)	0.5-4.0	0.5-4.0	0.5-4.0
<b>Reconstruction (Relion)</b>			
Particles	93 106	29 210	15 872
Box size (pix)	412	412	412
Accuracy of rotations (°)	1.13	1.13	1.51
Accuracy of translations (pix)	0.64	0.96	1.30
Map sharpening B-factor (Å <sup>2</sup> )	-57	-17	-350
Final resolution (Å)	3.75	5.08	9.78
<b>Model composition</b>			
Protein residues	7447	11978 <sup>‡</sup>	
RNA bases	458	458	
Ligands	10	10	
<b>Refinement (Refmac)</b>			
Resolution (Å)	3.8		
FSC <sub>average</sub>	0.82		
R factor	0.32		
<b>R.m.s deviations</b>			
Bond lengths (Å)	0.007		
Bond angles (°)	1.25		
<b>Validation<sup>†</sup></b>			
Molprobity score	2.5 (98 <sup>th</sup> percentile)		
Clashscore, all atoms	5.3 (100 <sup>th</sup> percentile)		
Good rotamers (%)	80		
<b>Ramachandran plot</b>			
Favoured (%)	90.84		
Outliers (%)	1.16		
<b>RNA validation<sup>†</sup></b>			
Correct sugar puckers (%)	95		
Good backbone conformations (%)	60		
<b>Deposition</b>			
PDB ID	5LJ3	5LJ5 <sup>‡</sup>	5LJ5 <sup>‡</sup>
EMDB ID	EMDB-4055	EMDB-4056	EMDB-4057

\*Represents a sub-set of the whole data set (Core).

†Determined by Molprobity<sup>84</sup>.

‡Overall model including Prp19 and helicase modules.

Extended Data Table 2 | Summary of model building for spliceosomal complex C

Proteins and RNA included in the model										
Sub-complexes	Protein/RNA	Domains	Total residues	M.W. (Da)	Modelled	Modelling template (PDB ID)	Modelling	Resolution <sup>1</sup>	Chain ID	Human/ <i>S. pombe</i> names
U5 snRNP	Prp8	N-terminal	1-870	101,767	128-870	5GAN	Docked & rebuilt	3.4 - 5.8	A	220K/ <i>Spp42</i>
		Large	871-1827	111,525	871-1827	5GAN	Docked & rebuilt	3.6 - 6.2		
		RNaseH	1828-2085	29,453	1837-2085	5GAN	Docked & rebuilt	4.2 - 6.6		
		Jab1/MPN	2086-2413	36,812	2148-2396	4BGD	Rigid docking	~15 - 20		
	Snu114		1008	114,041	67-998	5GAN	Docked & rebuilt	3.8 - 7.2	C	116K/ <i>Cwf10</i>
	SmB		196	22,403	4-102	5GAN	Docked	4.6 - 7.2	b	SmB/ <i>SmB</i>
	SmD3		110	11,229	4-85	5GAN	Docked	4.4 - 7.8	d	SmD3/ <i>SmD3</i>
	SmD1		146	16,288	1-109	5GAN	Docked	4.8 - 7.8	h	SmD1/ <i>SmD1</i>
	SmD2		110	12,856	15-108	5GAN	Docked	5.2 - 8.0	j	SmD2/ <i>SmD2</i>
	SmF		94	10,373	12-83	5GAN	Docked	5.2 - 8.0	f	SmF/ <i>SmF</i>
U2 snRNP	SmE		96	9,659	10-92	5GAN	Docked	5.4 - 8.0	e	SmE/ <i>SmE</i>
	SmG		77	8,479	2-76	5GAN	Docked	5.0 - 7.8	g	SmG/ <i>SmG</i>
	U5 snRNA-L		214	68,847	4-144		De novo	3.8 - 7.6	U	
	Msl1		111	12,830	28-111	1A9N	Homology modelled	6.6 - 8.8	Y	U2-B"
	Lea1		238	27,193	1-167	1A9N	Homology modelled	5.6 - 8.6	W	U2-A'
	SmB		196	22,403	4-102	5GAN	Docked	5.4 - 8.2	k	SmB/ <i>SmB</i>
	SmD3		110	11,229	4-85	5GAN	Docked	6.0 - 8.2	n	SmD3/ <i>SmD3</i>
	SmD1		146	16,288	1-118	5GAN	Docked	5.0 - 8.0	l	SmD1/ <i>SmD1</i>
	SmD2		110	12,856	15-108	5GAN	Docked	5.0 - 7.6	m	SmD2/ <i>SmD2</i>
	SmF		94	10,373	12-83	5GAN	Docked	5.2 - 7.4	q	SmF/ <i>SmF</i>
U6	SmE		96	9,659	10-92	5GAN	Docked	5.4 - 8.0	p	SmE/ <i>SmE</i>
	SmG		77	8,479	2-76	5GAN	Docked	5.8 - 8.2	r	SmG/ <i>SmG</i>
	U2 snRNA		1175	363,824	3-150; 1089-1169		De novo	3.8 - 6.0	Z	
	U6 snRNA		112	36,088	1-102		De novo	3.6 - 6.4	V	
	Prp19	U-box	1-51	5,713	1-51	3JB9	Homology modelled	~20	t,u,v,w	PRPF19/ <i>Cwf8</i>
		Coiled-coil	52-143	10,247	78-143	3JB9	Homology modelled	~20		
		WD40	144-503	40,646	171-501	3LRV	Docked	~25-30		
	Snt309		175	20,709	12-174	3JB9	Homology modelled	~20	s	BCAS2/ <i>Cwf7</i>
	Syf1		859	100,229	21-790		Idealised alpha helices	4.8 - 8	T	SYF1/ <i>Cwf3</i>
	Clf1	Core	1-271	32,396	1-271	3JB9	Homology modelled & rebuilt	3.8 - 6.4	S	CRNKL1/ <i>Cwf4</i>
NTR		Periphery	272-687	50,067	277-556		Idealised alpha helices	5.2 - 8.8		
	Cef1	N-terminal	1-191	21,868	12-191	3JB9	Homology modelled & rebuilt	3.8 - 6.2	O	CDCSL/ <i>Cdc5</i>
		Middle	192-505	65,905	-		Not modelled	-		
		C-terminal	506-590	9,994	506-590	3JB9	Homology modelled	~20		
	Isy1		235	32,992	1-96		De novo	3.8 - 6.2	G	ISY1/ <i>Cwf12</i>
	Prp45		379	42,483	32-224	3JB9	Homology modelled & rebuilt	4 - 8.4	K	SNW1/ <i>Prp45</i>
	Prp46		451	50,700	111-445	3JB9	Homology modelled & rebuilt	3.4 - 6.6	J	PLRG1/ <i>Prp5</i>
	Ecm2		364	40,925	6-324	3JB9	Homology modelled & rebuilt	4.0 - 7.0	N	RBM22/ <i>Cwf5</i>
	Cwc2		339	38,431	3-252	3U1L	Docked & rebuilt	3.6 - 6.0	M	RBM22/ <i>Cwf2</i>
	Cwc15		175	19,935	7-40	3JB9	Homology modelled & rebuilt	3.6 - 7.6	P	CWC15/ <i>Cwf15</i>
Splicing factors	Bud31		157	18,447	2-156	2MY1	Docked & rebuilt	3.6 - 6.8	L	BUD31/ <i>Cwf14</i>
	Yju2		278	32,312	2-115		De novo	3.8 - 5.4	D	CCDC94/ <i>Cwf16</i>
	Cwc21	N-terminal	1-64	7,057	2-50		De novo	3.8 - 7.4	R	SRRM2/ <i>Cwf21</i>
		Coiled-coil	65-135	8,724	64-111	2E62	Homology modelled	4.4 - 7.6		
	Cwc22	MIF4G	1-288	33,187	11-262	4C9B	Homology modelled & adjusted	4.6 - 8.2	H	CWC22/ <i>Cwf22</i>
		MA3	289-577	34,125	289-481		De novo	3.8 - 7.0		
	Cwc25		179	20,374	3-48		De novo	3.8 - 7.0	F	CWC25/ <i>Cwf25</i>
	Brr2		2,163	246,185	442-2163	4BGD	Docked	~13 - 20	B	200K/ <i>Brr2</i>
	Prp16		1,071	121,653	338-978	2XAU	Homology modelled & domains fitted	~12 - 15	Q	DHX38/ <i>Prp16</i>
	5'-exon		20	6,683	(-16) - (-1)		De novo	3.4 - 6.4	E	
Substrate	Intron		95	30,405	1-10; 54-76		De novo	3.4 - 7.2	I	

Resolution was calculated by averaging ResMap-calculated resolution voxels over each residue using Chimera. The resolution of residues at the 5th and 95th percentile for each chain then gave the resolution range for that chain. Da, Dalton.

# Structural basis for the antifolding activity of a molecular chaperone

Chengdong Huang<sup>1</sup>, Paolo Rossi<sup>1</sup>, Tomohide Saio<sup>1</sup> & Charalampos G. Kalodimos<sup>1</sup>

**Molecular chaperones act on non-native proteins in the cell to prevent their aggregation, premature folding or misfolding. Different chaperones often exert distinct effects, such as acceleration or delay of folding, on client proteins via mechanisms that are poorly understood. Here we report the solution structure of SecB, a chaperone that exhibits strong antifolding activity, in complex with alkaline phosphatase and maltose-binding protein captured in their unfolded states. SecB uses long hydrophobic grooves that run around its disk-like shape to recognize and bind to multiple hydrophobic segments across the length of non-native proteins. The multivalent binding mode results in proteins wrapping around SecB. This unique complex architecture alters the kinetics of protein binding to SecB and confers strong antifolding activity on the chaperone. The data show how the different architectures of chaperones result in distinct binding modes with non-native proteins that ultimately define the activity of the chaperone.**

Molecular chaperones rescue non-native proteins in the cell from aggregation and assist with their folding or unfolding to maintain a functional proteome<sup>1–4</sup>. Despite common features, different families of chaperones exhibit distinct activity and biological function<sup>5</sup>. Chaperones may exhibit foldase activity, whereby they accelerate folding of client proteins, or antifolding (holdase) activity, whereby they delay folding of client proteins, and the strength of the activity can vary significantly<sup>1,2</sup>. Molecular chaperones come in different sizes and a great variety of molecular shapes<sup>1–3</sup>. However, the scarcity of structural data of chaperones in complex with non-native proteins has impeded an understanding of how different chaperones engage these proteins and how distinct chaperone architectures may alter activity.

SecB is a multitasking molecular chaperone in the cytosol that exhibits an unusually strong antifolding activity<sup>6</sup>. SecB is responsible for maintaining secretory proteins in an unfolded, secretion-competent state<sup>7–10</sup>, as well as for their targeted delivery to the SecA ATPase<sup>7,11</sup>. SecB also acts as a generalized chaperone in the cell<sup>12–17</sup> and a *secB* null mutation results in severe protein aggregation<sup>15,18</sup>. Although extensively studied with biochemical and biophysical techniques<sup>6,10,19</sup>, the structural and mechanistic details of how SecB recognizes non-native proteins and how it exerts its antifolding activity are unknown. Recent advances in nuclear magnetic resonance (NMR) and isotope labelling approaches have enabled the characterization of large, dynamic protein complexes including molecular chaperones<sup>20–23</sup>. We have exploited these approaches to determine the solution structure of SecB in complex with client proteins captured in their unfolded state, revealing a unique binding architecture among protein–protein complexes.

## Recognition sites in SecB and client proteins

SecB exists as a tetramer organized as a dimer of dimers (dissociation constant,  $K_d$ , of tetramer–dimer equilibrium is  $\sim 20$  nM (ref. 24)) with an overall rectangular disk-like shape<sup>25,26</sup> (Fig. 1a). Each subunit consists of 155 residues (17.5 kDa) composed of a simple  $\alpha/\beta$  fold. The <sup>1</sup>H–<sup>15</sup>N- and <sup>1</sup>H–<sup>13</sup>C-correlated NMR spectra of the 70 kDa *Escherichia coli* SecB labelled in methyl-bearing (Ala, Ile, Met, Leu, Thr and Val) and aromatic (Phe, Trp and Tyr) residues are of high quality and near-complete assignment has been obtained (Methods and Extended Data Fig. 1a, b). We used maltose-binding protein (MBP)

(396 amino acids) and alkaline phosphatase (PhoA) (471 amino acids) as SecB protein substrates. NMR analysis (Extended Data Figs 1c, d and 2a) showed that there are five distinct SecB-recognition sites in PhoA (labelled a–e; Fig. 1b) and seven sites in MBP (labelled a–g; Fig. 1c), with all sites being enriched in hydrophobic and aromatic residues, as shown before<sup>13</sup>.

To determine the client-binding sites in SecB we sought to identify the SecB residues that show intermolecular nuclear Overhauser effects (NOEs) to short fragments of PhoA and MBP encompassing SecB-recognition sites. The SecB residues that interact with the substrates (Fig. 1d, e) collectively form long, continuous hydrophobic grooves that constitute the primary binding sites for non-native proteins (Fig. 1f). Most prominent is a shallow groove running along the surface, formed by helices  $\alpha 1$  and  $\alpha 2$ , the helix-connecting loop, the crossover loop and strand  $\beta 2$  (Fig. 1a, d–f). This groove, referred to as the primary client-binding site (Fig. 1f), is  $\sim 60$  Å long and exposes  $\sim 1,300$  Å<sup>2</sup> of hydrophobic surface, per SecB subunit. In addition, a smaller surface ( $\sim 600$  Å<sup>2</sup>) formed by residues emanating from helix  $\alpha 1$  and strands  $\beta 1$  and  $\beta 4$  also interacts with the unfolded proteins (Fig. 1e). This small surface, the secondary client-binding site (Fig. 1f), features several bulky non-polar amino acids. All four subunits combined, SecB exposes  $\sim 7,600$  Å<sup>2</sup> of hydrophobic surface that NMR has shown to interact with non-native proteins (Fig. 1f).

## SecB holds proteins in the unfolded state

We used NMR spectroscopy to monitor at the residue level the effect of SecB on the folding of PhoA and MBP. Urea-treated PhoA and MBP refold quickly to their native state upon removal of urea (Extended Data Fig. 2b, c). Notably, SecB prevents the folding of PhoA or MBP, with both proteins adopting an unfolded conformation when bound to SecB (Extended Data Fig. 2b, c). The NMR data indicate that SecB-bound PhoA and MBP lack a tertiary structure and the regions of the protein substrates in contact with SecB do not form any secondary structure.

## Client proteins wrap around SecB

To understand how SecB retains bound proteins in the unfolded state, we sought to structurally characterize the complexes of SecB with PhoA and MBP under native conditions. Multi-angle light scattering (MALS), isothermal titration calorimetry (ITC) and NMR all demonstrate that

<sup>1</sup>Department of Biochemistry, Molecular Biology & Biophysics, University of Minnesota, Minneapolis, Minnesota 55455, USA.



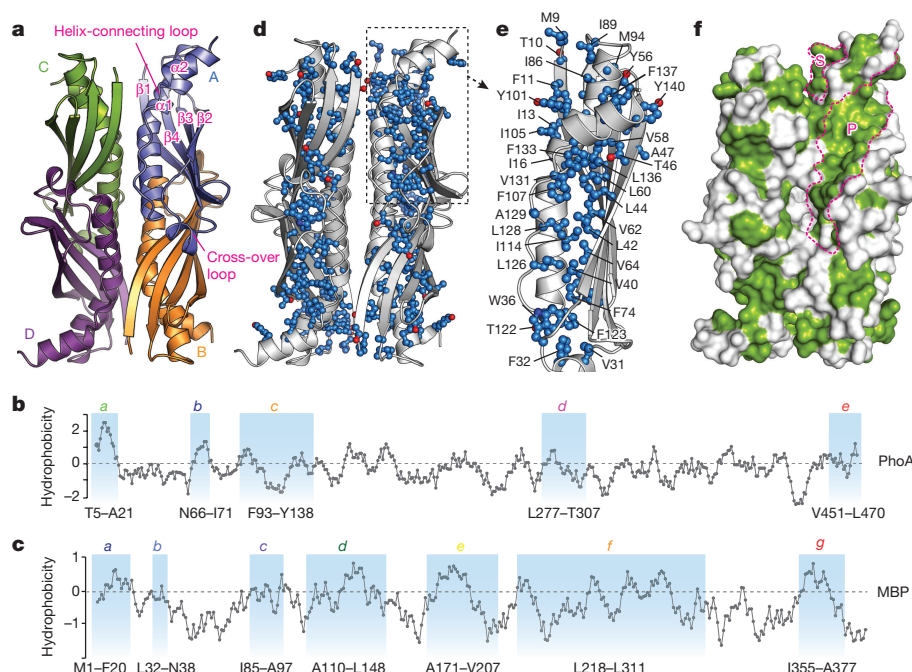


**Figure 1 | Recognition sites in SecB and client proteins.** **a**, Structure of *E. coli* SecB (Protein Data Bank accession number 1QYN). The four subunits (A–D) are coloured differently. The structural elements are labelled on subunit A. **b**, **c**, Hydrophobicity plot of PhoA (**b**) and MBP (**c**), as a function of their primary sequence. A hydrophobicity score (Roseman algorithm, window = 9) higher than zero denotes increased hydrophobicity. The sites identified by NMR to be recognized by SecB in PhoA (labelled *a–e*) and MBP (labelled *a–g*) are highlighted in blue and

the residue range is shown at the bottom. **d**, The SecB residues identified by intermolecular NOE data to interact with PhoA and MBP are shown in ball-and-stick and coloured blue. **e**, Expanded view of the binding sites in SecB subunit A is shown and the residues interacting with client proteins are labelled. **f**, The hydrophobic residues in SecB are coloured green, whereas all other residues are coloured white. The primary (P) and secondary (S) client-binding sites in SecB are marked and their boundaries delineated.

SecB forms stoichiometric complexes with PhoA and MBP (Extended Data Fig. 3), as is the case with other large client proteins including OmpA<sup>17,27</sup>. The structure of the SecB–PhoA complex (~120 kDa) was determined by NMR as detailed in Methods (Extended Data Figs 4 and 5 and Extended Data Table 1) and is shown in Fig. 2. The most remarkable feature is that PhoA wraps around SecB in an overall arrangement that maximizes the interacting surface between the client protein, which is held in an unfolded conformation, and the chaperone. All of the grooves, the primary client-binding sites in SecB, in the four subunits are occupied by specific PhoA sites (*a*, *c*, *d* and *e*) while the short PhoA site *b* binds to the smaller, secondary binding site (Fig. 2). The simultaneous engagement of all PhoA sites by SecB results in a significant enhancement in the affinity of the unfolded protein for SecB (Extended Data Fig. 3b, c), although the binding synergy is not strong. This is probably because the linkers tethering the SecB-recognition sites in PhoA are long and flexible (Fig. 1b and Extended Data Fig. 4a), thereby reducing the effective concentration of the sites and the measured avidity<sup>28</sup>.

Analysis of the SecB–PhoA structure revealed how SecB recognizes PhoA and how it accommodates all five PhoA sites (Fig. 1b) within one SecB molecule (Fig. 3). Most of the PhoA site *a* residues (Thr5–Ala21) are engaged in non-polar contacts with the SecB residues in the groove, burying a total of ~2,250 Å<sup>2</sup> of surface (~1,900 Å<sup>2</sup> non-polar and ~350 Å<sup>2</sup> polar). Interestingly, helix  $\alpha$ 2 in SecB, which acts as a lid of the binding groove, swings outwards by ~50° upon PhoA binding (Fig. 4a). Together with an outward displacement of the first two turns of the helix  $\alpha$ 1, the width of the hydrophobic groove increases significantly to accommodate the large non-polar side chains of the client (Figs 3 and 4a). Moreover, the rearrangement of several side chains lining the SecB groove allows some of the bulky PhoA residues (for example, Leu8, Leu11 and Phe15) to bury their side chains into the groove. Although most of the contacts are hydrophobic, several of the polar groups in PhoA site *a* are poised to form hydrogen bonds

with polar SecB residues lining the groove (Fig. 3). PhoA site *a* binds to SecB in an extended conformation, which maximizes the interacting surface. Of note, this region of PhoA forms an  $\alpha$ -helix when bound to a hydrophobic groove in the SecA ATPase<sup>29</sup>. Thus, SecB disfavors the formation of any regular secondary structure of the bound client.

PhoA site *c* is the longest SecB-recognition site in PhoA consisting of ~50 residues (Fig. 1b). It binds to SecB in an extended conformation spanning a distance of ~100 Å (Figs 2 and 3). The first 33 residues (Phe93–Ala125) of PhoA site *c* bind exclusively within the groove of one subunit, whereas the remaining PhoA<sup>c</sup> (the superscript denotes the corresponding site) residues (Ala126–Tyr138) extend across the surface at the tetramerization interface. The total surface buried by the binding of PhoA site *c* to SecB is ~5,150 Å<sup>2</sup> (~3,500 Å<sup>2</sup> non-polar and ~1,600 Å<sup>2</sup> polar). PhoA site *d* encompasses a stretch of 30 residues (Ala271–Thr309) and binds to SecB in an extended conformation, running along the entire groove and spanning a distance of ~70 Å (Figs 2 and 3). The buried surface amounts to a total of ~4,200 Å<sup>2</sup>, with ~2,800 Å<sup>2</sup> non-polar and ~1,400 Å<sup>2</sup> polar. PhoA site *e* (residues Asn450–Lys471) binds to SecB in a very similar manner to PhoA site *a*. PhoA site *e* is one of the regions that retains significant  $\alpha$ -helical structure in the unfolded PhoA<sup>20</sup>. It binds to SecB, however, in an extended conformation, further highlighting the tendency of SecB to disrupt any regular secondary structure.

SecB can adjust the structure of the primary binding grooves to allow longer substrates to fit in the groove. For example, whereas ~25 residues of the PhoA site *d* fit in the groove in an extended conformation, more than 40 residues of the PhoA site *c* fit within the same space (Fig. 4b). When the SecB helix  $\alpha$ 2 swings outwards upon client binding (Fig. 4a), the movement not only widens the binding groove but also exposes additional non-polar and polar surfaces that are available for binding by the unfolded client.

It should be noted that structure determination of isolated PhoA sites (PhoA<sup>a</sup>, PhoA<sup>c</sup>, PhoA<sup>d</sup> and PhoA<sup>e</sup>; Fig. 1b) in complex with SecB shows

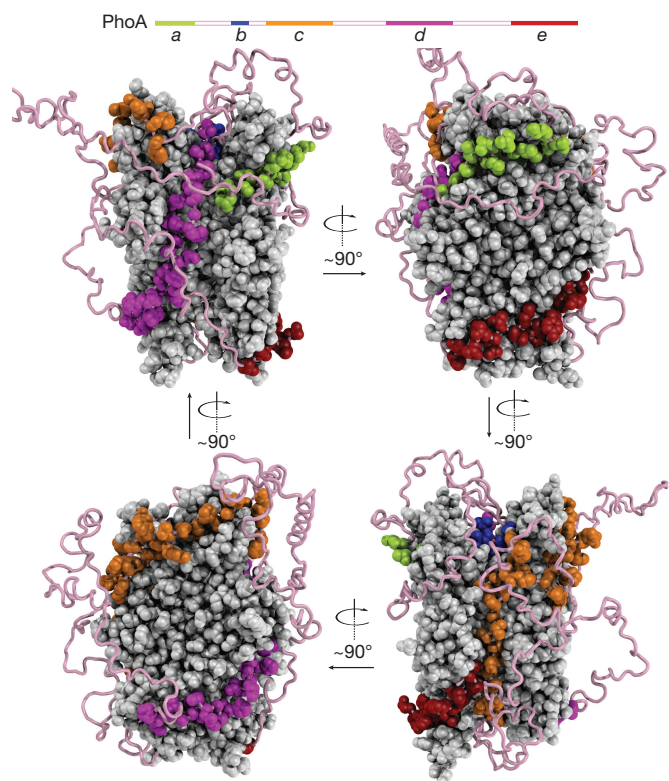


**Figure 2 | Structure of the SecB–PhoA complex.** Lowest-energy structure of the SecB–PhoA complex. SecB is shown as a space-filling model in grey. The five PhoA sites recognized by SecB are shown as space-filling models and coloured per the colour code in the graphic of the PhoA sequence at the top. The flexible regions of PhoA are shown as a pink ribbon. Four views of the complex are shown related by a rotation as indicated by the arrow. One PhoA molecule binds, which wraps around SecB. The NMR data show that the linkers tethering the binding sites in PhoA are flexible and do not interact with SecB (Extended Data Fig. 4a).

that multiple molecules of the individual sites can be accommodated within a SecB tetramer, owing to their relatively short length (Extended Data Figs 3c and 5).

NMR structure determination of MBP sites *d* and *e* in complex with SecB (SecB–MBP<sup>d</sup> and SecB–MBP<sup>e</sup> complexes; Extended Data Fig. 6 and Extended Data Table 1) showed that MBP binds to SecB in a very similar fashion to PhoA. Thus, non-native proteins share a similar binding mode for SecB. Analysis of the NMR spectra of labelled full-length MBP in complex with SecB demonstrated that all seven binding sites in MBP (Fig. 1c) are engaged by SecB in the SecB–MBP complex (Extended Data Fig. 7a). NMR-driven modelling of the SecB–MBP complex (Methods) shows that MBP, similarly to PhoA, wraps around SecB using the chaperone's entire binding surface (Extended Data Fig. 7b). Interestingly, the gain in avidity for MBP binding to SecB ( $K_d \approx 0.05$  M), compared with the isolated sites, appears to be an order of magnitude stronger than in the case of PhoA (Extended Data Fig. 3c, f). The reasons for the higher avidity are probably the larger interacting interface in the complex with MBP (~130 PhoA residues compared with ~240 MBP residues interacting with SecB) and the fact that the SecB-recognition sites in MBP are tethered with linkers that are much shorter in length than in the case of PhoA (Fig. 1b, c). Thermodynamic analysis reveals a large and favourable enthalpy of binding for both SecB–MBP and SecB–PhoA complexes, but with the overall affinity being reduced by unfavourable entropy of binding (Extended Data Fig. 3b, e).

Amino-acid substitutions at the client-binding sites in SecB resulted in a substantial decrease in the affinity for unfolded proteins and a marked decrease of its antifolding activity (Extended Data Fig. 8a–c).

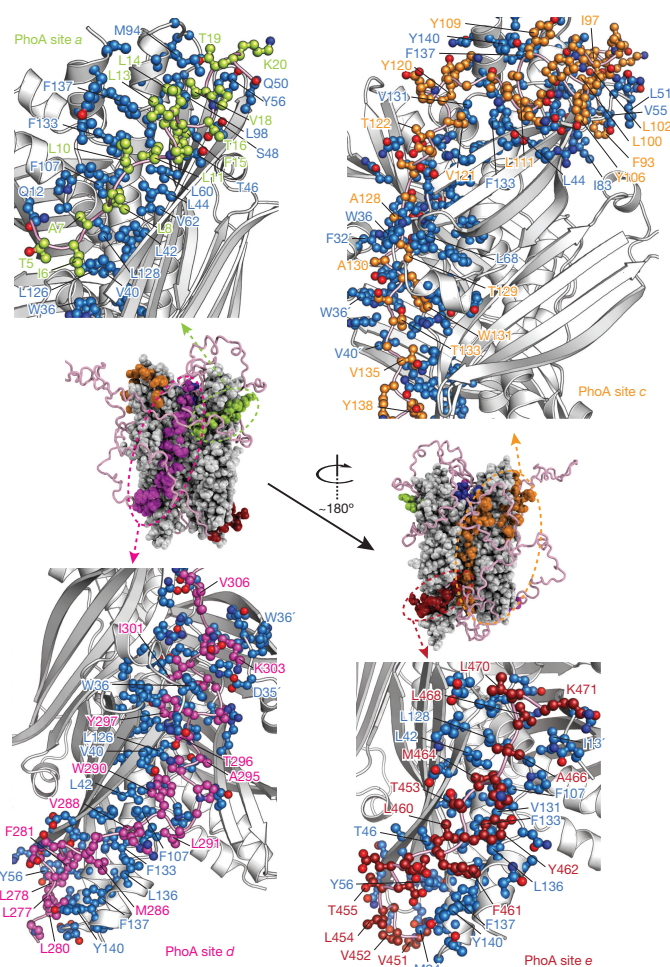


**Figure 3 | Recognition of non-native PhoA by SecB.** Expanded views of the SecB–PhoA complex highlighting the binding details and contacts that mediate recognition of the four PhoA sites (*a*, *c*, *d* and *e*) by SecB. The colour code of the PhoA sites, shown as ball-and-stick, is as in Fig. 2. SecB in the expanded views is shown as white ribbon and residues contacting PhoA are displayed as blue ball-and-stick.

### Chaperone–client binding mode modulates kinetics

SecB may prevent the folding of a protein altogether, whereas other chaperones such as trigger factor (TF) cannot typically do so (Fig. 5a). We used surface plasmon resonance (SPR) and bio-layer interferometry (BLI) to measure the kinetics of interaction between unfolded MBP and PhoA with the SecB and TF chaperones (Fig. 5b and Extended Data

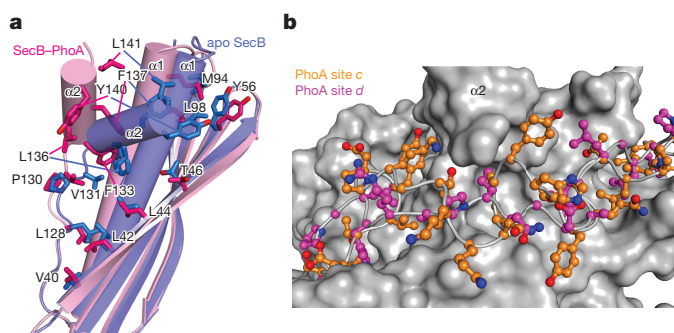


**Figure 4 | SecB structure adapts to client binding.** **a**, Superposition of SecB structures (only subunit A is shown) in the unliganded state (blue) and bound to PhoA (pink). PhoA is not shown for clarity. The SecB helix  $\alpha 2$  swings outward by  $\sim 50^\circ$  upon PhoA binding. See also Extended Data Fig. 4e. **b**, Superposition of the structure of SecB subunits in complex with PhoA site *c* coloured in orange and with PhoA site *d* coloured in magenta. SecB is shown as a solvent-exposed surface in white.



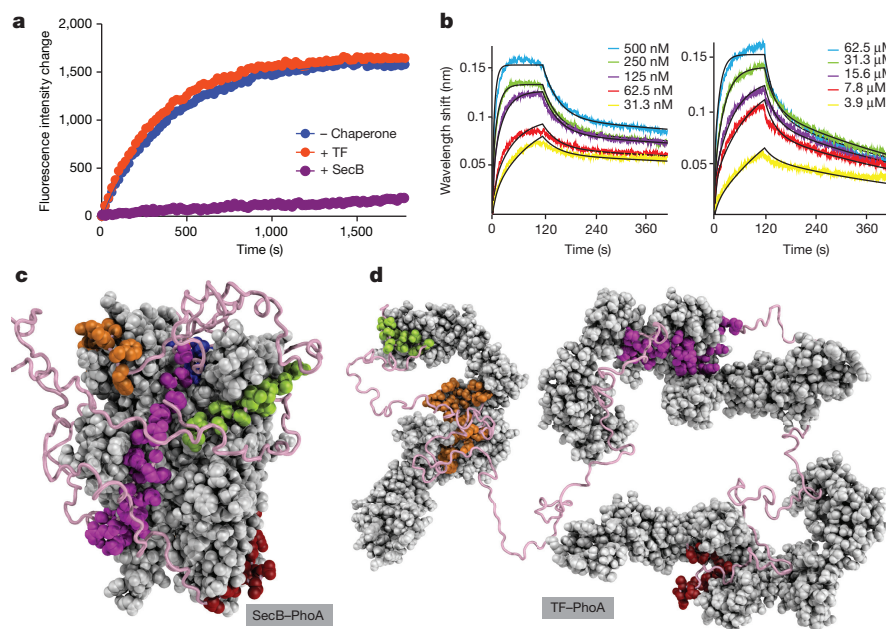


**Figure 5 | Effect of chaperone-client binding mode on kinetics and chaperone activity.** **a**, Folding of urea-denatured MBP (pre form) in the absence of a chaperone (blue) and in the presence of SecB (purple) or TF (orange). Folding was monitored by Trp fluorescence at 23 °C. SecB prevents the folding of MBP, whereas TF has a negligible effect. Both SecB and TF are in fourfold excess over MBP. **b**, Kinetic analysis by BLI of the

binding of MBP to SecB (left) and TF (right). **c**, Structure of SecB–PhoA and **d**, TF–PhoA complex<sup>20</sup>. In both structures, the chaperone and PhoA are rendered as in Fig. 2. TF can only accommodate ~50 interacting PhoA residues per TF molecule, whereas one SecB molecule can accommodate the entire PhoA.

Fig. 9a–f). Notably, MBP associates with SecB with an approximately tenfold higher rate ( $k_{\text{on}} \approx 10^6 \text{ M}^{-1} \text{ s}^{-1}$ ) than with TF ( $k_{\text{on}} \approx 10^5 \text{ M}^{-1} \text{ s}^{-1}$ ) and dissociates from SecB with an approximately fivefold slower rate ( $k_{\text{off}} \approx 0.01 \text{ s}^{-1}$ ) than from TF ( $k_{\text{off}} \approx 0.05 \text{ s}^{-1}$ ). Of note, SecB prevents folding<sup>8</sup> of the cytosolic pre-form of MBP (Fig. 5a and Extended Data Fig. 2c), but it cannot prevent folding of the mature (periplasmic) form of MBP, which lacks the amino (N)-terminal signal sequence (Extended Data Fig. 9g–i). This is because of the much faster intrinsic folding rate ( $k_f$ ) of the mature MBP ( $0.02 \text{ s}^{-1}$ ) compared with the  $k_f$  of the pre-form of MBP ( $0.003 \text{ s}^{-1}$ ) (Extended Data Fig. 9g, h). Interestingly, an MBP variant<sup>8</sup> with much slower folding rate ( $k_f \approx 0.0008 \text{ s}^{-1}$ ) allows even TF to delay its folding (Extended Data Fig. 9j), highlighting the importance of the kinetics of client intrinsic folding and binding to the chaperone.

### SecB rescues aggregation-prone folded proteins

To understand how SecB rescues cytosolic proteins<sup>6</sup> and increases the yield of natively folded proteins (Extended Data Fig. 9h), we used the aggregation-prone MBP<sup>G32D/I33P</sup> (hereafter MBP<sup>mut</sup>) variant<sup>20</sup> that has a high tendency to aggregate, especially at temperatures higher than 30 °C. Notably, in the presence of SecB, NMR shows that MBP<sup>mut</sup> remains folded and soluble even at temperatures as high as 50 °C (Extended Data Fig. 8d, e). At such high temperatures NMR showed that SecB binds to and shields the transiently exposed unfolded state of MBP<sup>mut</sup>, resulting in its protection from aggregation (Extended Data Fig. 8f, g). The aggregation-prone, transiently populated conformation of the otherwise folded MBP<sup>mut</sup> that is protected by SecB is only partly unfolded and dissociates rapidly from SecB, giving rise to an anti-aggregation effect as opposed to an antifolding effect.

### Conclusions

The present data demonstrate how the distinctive binding mode of SecB for non-native proteins (Fig. 2 and Extended Data Fig. 7b) enables the chaperone to prevent folding of bound proteins (Fig. 5a). Compared with TF (Fig. 5c, d), a chaperone for which its structure in complex with full length PhoA is known<sup>20</sup>, the structural data explain how the overall architecture of the chaperone and the way it engages non-native proteins give rise to different chaperone activities (Fig. 5a).

Although both SecB and TF prevent aggregation and misfolding, as most molecular chaperones do, SecB has a much stronger antifolding activity than TF. Each TF molecule can accommodate a stretch of up to ~50 interacting residues of an unfolded polypeptide, whereas SecB can accommodate as many as ~250 interacting residues (Fig. 5c, d and Extended Data Fig. 7b). Because SecB recognizes and binds to multiple regions within an unfolded protein, long client proteins wrap around SecB to maximize the binding interface, thereby altering the binding kinetics. The overall binding architecture appears to be unique among known protein–protein complexes. More structural data on complexes of chaperones with proteins<sup>30</sup> are needed to discover the full repertoire of binding architectures and how they influence chaperone activity.

**Online Content** Methods, along with any additional Extended Data display items and Source Data, are available in the online version of the paper; references unique to these sections appear only in the online paper.

**Received 9 March; accepted 24 June 2016.**

**Published online 8 August 2016.**

- Bukau, B., Weissman, J. & Horwich, A. Molecular chaperones and protein quality control. *Cell* **125**, 443–451 (2006).
- Kim, Y. E., Hipp, M. S., Bracher, A., Hayer-Hartl, M. & Hartl, F. U. Molecular chaperone functions in protein folding and proteostasis. *Annu. Rev. Biochem.* **82**, 323–355 (2013).
- Saibil, H. Chaperone machines for protein folding, unfolding and disaggregation. *Nature Rev. Mol. Cell Biol.* **14**, 630–642 (2013).
- Horwich, A. L. Molecular chaperones in cellular protein folding: the birth of a field. *Cell* **157**, 285–288 (2014).
- Mattoo, R. U. H. & Goloubinoff, P. Molecular chaperones are nanomachines that catalytically unfold misfolded and alternatively folded proteins. *Cell. Mol. Life Sci.* **71**, 3311–3325 (2014).
- Sala, A., Bordes, P. & Genevieux, P. Multitasking SecB chaperones in bacteria. *Front. Microbiol.* **5**, 666 (2014).
- Hartl, F. U., Lecker, S., Schiebel, E., Hendrick, J. P. & Wickner, W. The binding cascade of SecB to SecA to SecY/E mediates preprotein targeting to the *E. coli* plasma membrane. *Cell* **63**, 269–279 (1990).
- Hardy, S. J. & Randall, L. L. A kinetic partitioning model of selective binding of nonnative proteins by the bacterial chaperone SecB. *Science* **251**, 439–443 (1991).
- Wolff, N., Sapriel, G., Bodenreider, C., Chaffotte, A. & Delepelaire, P. Antifolding activity of the SecB chaperone is essential for secretion of HasA, a quickly folding ABC pathway substrate. *J. Biol. Chem.* **278**, 38247–38253 (2003).



10. Bechtluft, P. *et al.* Direct observation of chaperone-induced changes in a protein folding pathway. *Science* **318**, 1458–1461 (2007).
11. Zhou, J. & Xu, Z. Structural determinants of SecB recognition by SecA in bacterial protein translocation. *Nature Struct. Biol.* **10**, 942–947 (2003).
12. Ullers, R. S. *et al.* SecB is a bona fide generalized chaperone in *Escherichia coli*. *Proc. Natl Acad. Sci. USA* **101**, 7583–7588 (2004).
13. Knoblauch, N. T. *et al.* Substrate specificity of the SecB chaperone. *J. Biol. Chem.* **274**, 34219–34225 (1999).
14. Ullers, R. S., Ang, D., Schwager, F., Georgopoulos, C. & Genevieux, P. Trigger factor can antagonize both SecB and DnaK/DnaJ chaperone functions in *Escherichia coli*. *Proc. Natl Acad. Sci. USA* **104**, 3101–3106 (2007).
15. Sakr, S. *et al.* Lon protease quality control of presecretory proteins in *Escherichia coli* and its dependence on the SecB and DnaJ (Hsp40) chaperones. *J. Biol. Chem.* **285**, 23506–23514 (2010).
16. Calloni, G. *et al.* DnaK functions as a central hub in the *E. coli* chaperone network. *Cell Reports* **1**, 251–264 (2012).
17. Castanié-Cornet, M.-P., Bruel, N. & Genevieux, P. Chaperone networking facilitates protein targeting to the bacterial cytoplasmic membrane. *Biochim. Biophys. Acta* **1843**, 1442–1456 (2014).
18. Baars, L. *et al.* Defining the role of the *Escherichia coli* chaperone SecB using comparative proteomics. *J. Biol. Chem.* **281**, 10024–10034 (2006).
19. Tang, Y., Pan, X., Tai, P. C. & Sui, S.-F. The structure of SecB/OmpA as visualized by electron microscopy: The mature region of the precursor protein binds asymmetrically to SecB. *Biochem. Biophys. Res. Commun.* **393**, 698–702 (2010).
20. Saio, T., Guan, X., Rossi, P., Economou, A. & Kalodimos, C. G. Structural basis for protein antiaggregation activity of the trigger factor chaperone. *Science* **344**, 1250494 (2014).
21. Rosenzweig, R., Moradi, S., Zarrine-Afsar, A., Glover, J. R. & Kay, L. E. Unraveling the mechanism of protein disaggregation through a ClpB-DnaK interaction. *Science* **339**, 1080–1083 (2013).
22. Zhuravleva, A., Clérico, E. M. & Gierasch, L. M. An interdomain energetic tug-of-war creates the allosterically active state in Hsp70 molecular chaperones. *Cell* **151**, 1296–1307 (2012).
23. Kerfah, R., Plevin, M. J., Sounier, R., Gans, P. & Boisbouvier, J. Methyl-specific isotopic labeling: a molecular tool box for solution NMR studies of large proteins. *Curr. Opin. Struct. Biol.* **32**, 113–122 (2015).
24. Murén, E. M., Suciú, D., Topping, T. B., Kumamoto, C. A. & Randall, L. L. Mutational alterations in the homotetrameric chaperone SecB that implicate the structure as dimer of dimers. *J. Biol. Chem.* **274**, 19397–19402 (1999).
25. Xu, Z., Knafels, J. D. & Yoshino, K. Crystal structure of the bacterial protein export chaperone secB. *Nature Struct. Biol.* **7**, 1172–1177 (2000).
26. Dekker, C., de Kruijff, B. & Gros, P. Crystal structure of SecB from *Escherichia coli*. *J. Struct. Biol.* **144**, 313–319 (2003).
27. Burmann, B. M., Wang, C. & Hiller, S. Conformation and dynamics of the periplasmic membrane-protein-chaperone complexes OmpX-Skp and tOmpA-Skp. *Nature Struct. Mol. Biol.* **20**, 1265–1272 (2013).
28. Krishnamurthy, V. M., Semetey, V., Bracher, P. J., Shen, N. & Whitesides, G. M. Dependence of effective molarity on linker length for an intramolecular protein-ligand system. *J. Am. Chem. Soc.* **129**, 1312–1320 (2007).
29. Gelis, I. *et al.* Structural basis for signal-sequence recognition by the translocase motor SecA as determined by NMR. *Cell* **131**, 756–769 (2007).
30. Clare, D. K., Bakkes, P. J., van Heerikhuizen, H., van der Vies, S. M. & Saibil, H. R. Chaperonin complex with a newly folded protein encapsulated in the folding chamber. *Nature* **457**, 107–110 (2009).

**Acknowledgements** The work was supported by National Institutes of Health grant GM073854 to C.G.K.

**Author Contributions** C.H. and C.G.K. designed the project. C.H. performed protein purification, NMR data collection and analysis, structure determination, and kinetic and thermodynamic assays. P.R. assisted with structure determination. T.S. assisted with NMR analysis and kinetic assays. C.H. and C.G.K. wrote the manuscript.

**Author Information** Coordinate files for the SecB–PhoA and SecB–MBP complexes have been deposited in the Protein Data Bank under accession numbers 5JTL, 5JTM, 5JTN, 5JTO, 5JTP, 5JTQ and 5JTR. Reprints and permissions information is available at [www.nature.com/reprints](http://www.nature.com/reprints). The authors declare no competing financial interests. Readers are welcome to comment on the online version of the paper. Correspondence and requests for materials should be addressed to C.G.K. ([ckalodim@umn.edu](mailto:ckalodim@umn.edu)).

**Reviewer Information** *Nature* thanks L. Kay and the other anonymous reviewer(s) for their contribution to the peer review of this work.

## METHODS

No statistical methods were used to predetermine sample size. The experiments were not randomized. The investigators were not blinded to allocation during experiments and outcome assessment.

**Expression and preparation of proteins.** The *E. coli* SecB gene was cloned into the pET-16b vector (Novagen) containing a His<sub>6</sub>-tag and a tobacco etch virus (TEV) protease cleavage site at the N terminus. Protein samples of *E. coli* PhoA were produced as described before<sup>20</sup>. All *E. coli* MBP constructs were cloned into the pET-16b vector containing a His<sub>6</sub>-tag and a TEV protease cleavage site at the N terminus. The following MBP constructs were prepared in this study (residue numbers of the boundaries are in superscript): MBP<sup>1–396</sup>, mature MBP<sup>27–396</sup>, MBP<sup>29–99</sup>, MBP<sup>67–99</sup>, MBP<sup>97–164</sup>, MBP<sup>160–201</sup>, MBP<sup>198–265</sup>, MBP<sup>260–336</sup>, MBP<sup>331–396</sup>, and the MBP variants MBP<sup>G32D/133P</sup>, MBP<sup>Y283D</sup> and MBP<sup>V8G/Y283D</sup> (MBP mutants are numbered on the basis of the amino-acid sequence of the mature form of MBP). All constructs were transformed into BL21(DE3) cells. Isotopically unlabelled protein samples were produced in cells grown in Luria-Bertani (LB) medium at 37 °C in the presence of ampicillin (100 µg ml<sup>−1</sup>) to an absorbance at 600 nm ( $A_{600\text{ nm}}$ ) ≈ 0.8. Protein induction was induced by the addition of 0.2 mM isopropyl-β-D-1-thiogalactopyranoside (IPTG) and cells were allowed to grow for 16 h at 18 °C. Cells were harvested at  $A_{600\text{ nm}}$  ≈ 1.5 and resuspended in lysis buffer (50 mM Tris-HCl, 500 mM NaCl, pH 8 and 1 mM PMSF). Cells were disrupted by a high-pressure homogenizer and centrifuged at 50,000g. Proteins were purified using Ni Sepharose 6 Fast Flow resin (GE Healthcare), followed by tag removal by TEV protease at 4 °C (incubation for 16 h) and gel filtration using Superdex 75 16/60 or 200 16/60 columns (GE Healthcare). Protein concentration was determined spectrophotometrically at 280 nm using the corresponding extinction coefficient.

**MALS experiments.** MALS was measured using DAWN HELEOS-II (Wyatt Technology Corporation) downstream of a Shimadzu liquid chromatography system connected to a Superdex 200 10/300 GL (GE Healthcare) gel filtration column. The running buffer for SecB–PhoA complexes was 20 mM KPi (pH 7.0), 100 mM KCl, 4 mM βME, and 0.5 mM EDTA, whereas for SecB–MBP complexes was 20 mM HEPES, pH 7, 150 mM KOAc and 0.05% NaN<sub>3</sub>. Protein samples at a concentration of 0.05–0.2 mM were used. The flow rate was set to 0.5 ml min<sup>−1</sup> with an injection volume of 200 µl and the light scattering signal was collected at room temperature (~23 °C). The data were analysed with ASTRA version 6.0.5 (Wyatt Technology Corporation).

**ITC experiments.** ITC was performed using an iTC200 microcalorimeter (GE Healthcare) at temperatures ranging from 4 °C to 25 °C. All protein samples were extensively dialysed against the ITC buffer containing 50 mM KPi (pH 7.0), 50 mM KCl, 0.05% NaN<sub>3</sub> and 2 mM tris(2-carboxyethyl)phosphine (TCEP). All solutions were filtered using membrane filters (pore size, 0.45 µm) and thoroughly degassed for 20 min before the titrations. The 40-µl injection syringe was filled with ~0.05–1 mM of SecB solution and the 200-µl cell was filled with ~0.01–0.2 mM PhoA or MBP. To measure the binding affinity of MBP to SecB, the slowly folding MBP<sup>V8G/Y283D</sup> variant was used to measure the affinity of MBP for SecB. MBP<sup>V8G/Y283D</sup> was unfolded in 8 M urea, 20 mM HEPES, pH 7, 150 mM KOAc and 0.05% NaN<sub>3</sub>, and diluted 20 times to give a final concentration of 2.7 µM immediately before loading into the cell. The solution containing SecB was precisely adjusted to match the urea concentration. The titrations were performed with a preliminary 0.2-µl injection, followed typically by 15 injections of 2.5 µl each with time intervals of 3 min. The solution was stirred at 1,000 r.p.m. Data for the preliminary injection, which are affected by diffusion of the solution from and into the injection syringe during the initial equilibration period, were discarded. Binding isotherms were generated by plotting heats of reaction normalized by the moles of injectant versus the ratio of total injectant to total protein per injection. The data were fitted with Origin 7.0 (OriginLab Corporation).

**Protein isotope labelling for NMR studies.** Isotopically labelled samples for NMR studies were prepared by growing the cells in minimal (M9) medium. Cells were typically harvested at  $A_{600\text{ nm}}$  ≈ 1.0. U-[<sup>2</sup>H,<sup>13</sup>C,<sup>15</sup>N]-labelled samples were prepared for the backbone assignment of SecB and large MBP fragments by supplementing the growing medium with [<sup>15</sup>NH<sub>4</sub>Cl] (1 g l<sup>−1</sup>) and [<sup>2</sup>H<sub>7</sub>,<sup>13</sup>C<sub>6</sub>]-glucose (2 g l<sup>−1</sup>) in 99.9% <sup>2</sup>H<sub>2</sub>O (CIL and Isotec). The [<sup>1</sup>H-<sup>13</sup>C] methyl-labelled samples were prepared as described<sup>20,29,31</sup>. α-Ketobutyric acid (50 mg l<sup>−1</sup>) and α-ketoisovaleric acid (85 mg l<sup>−1</sup>) were added to the culture 1 h before the addition of IPTG. Met-[<sup>13</sup>CH<sub>3</sub>]- and Ala-[<sup>13</sup>CH<sub>3</sub>]-labelled samples were produced by supplementing the medium with [<sup>13</sup>CH<sub>3</sub>]-Met (50 mg l<sup>−1</sup>) and [<sup>2</sup>H<sub>2</sub>,<sup>13</sup>CH<sub>3</sub>]-Ala (50 mg l<sup>−1</sup>). For Thr labelling, a Thr-auxotrophic cell strain was used, and the medium was supplemented with [<sup>2</sup>H<sub>2</sub>,<sup>13</sup>CH<sub>3</sub>]-Thr (25 mg l<sup>−1</sup>). For Phe, Tyr, and Trp labelling, U-[<sup>1</sup>H,<sup>13</sup>C]-labelled amino acids were used. Alternative <sup>13</sup>C-labelling of aromatic residues

was performed as described<sup>32</sup>. All precursors and amino acids were added to the culture 1 h before the addition of IPTG, except Ala, which was added 30 min before induction.

**NMR spectroscopy.** NMR samples were typically prepared in 50 mM KPi (pH 7.0), 50 mM KCl, 0.05% NaN<sub>3</sub>, 5 mM βME and 7% D<sub>2</sub>O. NMR experiments were recorded on Bruker 900, 850 and 700 MHz spectrometers. NMR spectra were typically recorded at 10 °C for the isolated PhoA and MBP fragments and at 35 °C for SecB and its complexes. Protein sample concentration ranged from 0.1 to 1.0 mM. All NMR spectra were processed using NMRPipe<sup>33</sup> and analysed using NMRView (<http://www.onemoonscientific.com>).

**NMR assignment of SecB.** The SecB tetramer packs as a dimer of dimers and gives rise to two pairs of magnetically equivalent subunits: A and D give one set of resonances and subunits B and C give another set of resonances (Extended Data Fig. 1a). Sequential backbone assignment of SecB was achieved by the use of standard triple-resonance NMR pulse sequences. Three-dimensional (3D) <sup>1</sup>H-<sup>15</sup>N NOESY experiments were used to confirm and extend the backbone assignment within each subunit. Side-chain assignment for methyls and aromatic residues was accomplished using the following NMR experiments: 3D (<sup>1</sup>H)-<sup>13</sup>C heteronuclear multiple-quantum coherence (HMQC)-NOESY-<sup>1</sup>H-<sup>13</sup>C HMQC, <sup>13</sup>C-edited NOESY-HSQC, <sup>13</sup>C-edited HSQC-NOESY, <sup>15</sup>N-edited NOESY-HSQC, 3D (<sup>1</sup>H)-<sup>13</sup>C HSQC-NOESY-<sup>1</sup>H-<sup>15</sup>N HSQC, and 3D (<sup>1</sup>H)-<sup>15</sup>N HSQC-NOESY-<sup>1</sup>H-<sup>13</sup>C HSQC.

**NMR assignment of PhoA and MBP in the unfolded state.** We previously described the assignment strategy for unfolded PhoA<sup>20</sup>. We followed a similar strategy to assign MBP in the unfolded state by making use of several MBP fragments that remain soluble and unfolded when isolated (Extended Data Fig. 1c): MBP<sup>29–99</sup>, MBP<sup>67–99</sup>, MBP<sup>97–164</sup>, MBP<sup>160–201</sup>, MBP<sup>198–265</sup>, MBP<sup>260–336</sup> and MBP<sup>331–396</sup>. Isolated MBP fragments encompassing the first 26 N-terminal residues (signal sequence) were not stable and this region could only be assigned in complex with SecB. Overlay of the spectra of the MBP fragments with the spectra of full-length MBP in 4 M urea indicated very good resonance correspondence. This is expected because all of the fragments, as well as the MBP, in 4 M urea are unfolded. Resonance assignment obtained for the various fragments was transferred to full length MBP in urea, and ambiguities were resolved by the use of 3D NMR spectra. It should be noted that although resonance dispersion in unliganded PhoA and MBP is poor, complex formation with SecB alleviates this problem (for the PhoA and MBP residues in the SecB-binding regions) with the spectra being of high resolution (Extended Data Fig. 4c).

**Structure determination of SecB–PhoA and SecB–MBP complexes.**

Assignment of the resonances in SecB–PhoA was accomplished by first assigning the complexes between SecB and the individual PhoA sites (SecB–PhoA<sup>a</sup>, SecB–PhoA<sup>c</sup>, SecB–PhoA<sup>d</sup>, SecB–PhoA<sup>e</sup>). We used U-<sup>12</sup>C,<sup>15</sup>N-labelled samples that contained specifically protonated methyl groups of Ala, Val, Leu, Met, Thr and Ile (δ1) and protonated aromatic residues Phe, Tyr and Trp in an otherwise deuterated background. The high sensitivity and resolution of the methyl region, combined with the high abundance of these nine amino acids in SecB (Extended Data Fig. 1a) and in the SecB-binding sites of PhoA and MBP, provided a large number of intermolecular NOEs for the SecB–PhoA and SecB–MBP complexes (Extended Data Table 1). Because PhoA in complex with SecB provided higher quality spectra than the spectra of MBP in complex with SecB, we determined first the structure of the SecB–PhoA complex (~120 kDa) by NMR. We initially characterized the structure of the each PhoA site (a–e) individually in complex with SecB (Extended Data Fig. 5). The structures of SecB–PhoA<sup>a</sup>, SecB–PhoA<sup>c</sup>, SecB–PhoA<sup>d</sup>, and SecB–PhoA<sup>e</sup>, were determined by NMR and are presented in Extended Data Fig. 5. A large number of intermolecular NOEs were collected for each one of the complexes (Extended Data Table 1). Because of the relatively short length of the polypeptides encompassing the individual PhoA sites, multiple PhoA molecules bound to SecB, as shown in Extended Data Fig. 5. We also note that we detected the presence of a small number of intermolecular NOEs that were suggestive of alternative conformations of the PhoA sites bound to SecB. However, the intensity of these sets of NOEs was much weaker, indicating that the population of such alternative complexes is low. To solve the structure of the SecB–PhoA complex, we sought to determine how each one of the PhoA sites binds to SecB in the context of the full length PhoA. To circumvent the signal overlap in this large complex, we used samples where the two proteins were isotopically labelled in different amino acids. For example, in one of these samples SecB was labelled in the methyls of Leu, Val and Met, whereas PhoA in the methyls of Ile amino acids. Because of the distinct chemical shifts of <sup>1</sup>H and <sup>13</sup>C resonances of the methyls and the isotope labelling scheme, it was possible to measure specific intermolecular NOEs between SecB and PhoA (Extended Data Fig. 4b). Several of these samples were used to determine as many intermolecular NOEs as possible. As expected, the NOEs were compatible with the structure of each PhoA site in complex with SecB, with the

crucial difference that only one PhoA molecule could be accommodated in SecB. Owing to its short length, the isolated PhoA site *b* (PhoA<sup>b</sup>) binds to almost all of the exposed hydrophobic surface of SecB, as determined by NMR. In the SecB–PhoA complex with SecB, PhoA site *b* can only bind to the secondary binding site, as determined by NOEs. To further corroborate the structure of the SecB–PhoA complex we used PRE data (see below). The PRE-derived distances were fully compatible with the NOE data collected on SecB–PhoA. The structure of the SecB–PhoA complex was determined using the set of intermolecular NOEs collected directly in the complex and further refined using the intermolecular NOEs collected for the corresponding isolated PhoA sites in complex with SecB. It should be noted that because of the symmetry in SecB, the various PhoA sites may bind to any of the four SecB subunits. The final arrangement will be dictated by the length of the linkers tethering the SecB-recognition sites (as shown in Fig. 2), namely how far nearby recognition sites can bind from each other, and thus alternative routes of the polypeptide bound to SecB may be present. The only conceivable difference among the various conformations is the relative disposition of the PhoA sites. In all cases all of the SecB-recognition sites in PhoA are engaged by SecB in the complex and PhoA wraps around SecB. The NMR-driven structural model of the SecB–MBP complex (Extended Data Fig. 7b) was determined as follows: NMR analysis demonstrated that all seven recognition sites in MBP (labelled *a*–*g*) are bound to SecB in the SecB–MBP complex (Extended Data Fig. 7a). We have determined the high-resolution structure of MBP<sup>d</sup> and MBP<sup>e</sup> in complex with SecB (Extended Data Fig. 6). Because of their length and the short linker tethering the two sites, *d* and *e* sites most probably bind to the same side of SecB. MBP site *f* is the longest one, consisting of ~90 residues, and is thus entirely accommodated on the other side of SecB. With sites *d*, *e* and *f* occupying the primary binding sites, the other recognition sites (*a*, *b*, *c* and *g*), being much shorter, can be accommodated within the secondary client-binding sites on SecB. The structure of MBP sites *d* and *e* in complex with SecB was determined using the experimental intermolecular NOE data. The hydrophobic residues of the sites *a*, *b*, *c*, *f*, and *g*, showing the strongest effect upon SecB binding as determined by differential line broadening, were used to drive the docking of these sites to non-polar residues on SecB. The modelled structure shows that the entire MBP sequence can be accommodated within one SecB molecule. The structures of SecB in complex with PhoA and MBP were calculated with CYANA 3.97 (ref. 34), using NOE peak lists from 3D (<sup>1</sup>H)–<sup>13</sup>C HMQC–NOESY–<sup>1</sup>H–<sup>13</sup>C HMQC, 3D (<sup>1</sup>H)–<sup>15</sup>N HSQC–NOESY–<sup>1</sup>H–<sup>13</sup>C HSQC, <sup>13</sup>C-edited NOESY–HSQC, and <sup>15</sup>N-edited NOESY–HSQC. The <sup>13</sup>C<sub>α</sub>, <sup>13</sup>C<sub>β</sub>, <sup>13</sup>C′, <sup>15</sup>N and NH chemical shifts served as input for the TALOS+ program<sup>35</sup> to extract dihedral angles ( $\varphi$  and  $\psi$ ). The side chains of SecB residues within or nearby the PhoA and MBP binding sites were set flexible and their conformation was determined using intermolecular NOEs collected for each one of the complexes. The SecB regions remote to the binding sites were set rigid using the crystal structure coordinates for *E. coli* SecB<sup>26</sup>. The 20 lowest-energy structures were refined by restrained molecular dynamics in explicit water with CNS<sup>36</sup>. The percentage of residues falling in favoured and disallowed regions, respectively, of the Ramachandran plot is as follows: 99.4% and 0.6% for SecB–PhoA; 99.4% and 0.6% for SecB–PhoA<sup>a</sup>; 99.3% and 0.7% for SecB–PhoA<sup>b</sup>; 99.2% and 0.8% for SecB–PhoA<sup>d</sup>; 99.3% and 0.7% for SecB–PhoA<sup>e</sup>; 99.4% and 0.6% for SecB–MBP<sup>d</sup>; and 99.4% and 0.6% for SecB–MBP<sup>e</sup>.

**PRE experiments.** PRE experiments were used to confirm the position of each individual PhoA binding site in the SecB–PhoA complex. First, a ‘Cys-free’ variant of PhoA was prepared by mutating the four naturally occurring Cys residues in PhoA (Cys190, Cys200, Cys308 and Cys358) to Ser. We then introduced a Cys residue to either end of each SecB-binding site in PhoA and prepared a total of ten single-Cys mutants: T5C, T23C, K65C, M75C, G91C, G140C, Q274C, C308, N450C and C472. The protein purified from Ni-NTA column was quickly concentrated and loaded onto HiLoad 16/60 Superdex 200 gel filtration column (GE healthcare) using a buffer containing 50 mM KPi (pH 7.0), 150 mM NaCl and 0.05% Na<sub>2</sub>S<sub>2</sub>O<sub>3</sub>. Immediately after elution the purified single-Cys PhoA mutant was divided into two equal portions for parallel treatment with (1-oxyl-2,2,5,5-tetramethyl-3-pyrroline-3-methyl)-ethanethiosulfonate (MTSL, Toronto Research Chemicals, Toronto) and a diamagnetic MTSL analogue, in a tenfold molar excess at 4 °C for 16–20 h. MTSL was prepared in a 50 mM concentrated stock in acetonitrile. Free MTSL was removed by extensive buffer exchange using Centricon Centrifugal Filter with a MWCO of 10,000 (Millipore) at 4 °C. The MTSL-labelled PhoA protein samples were then concentrated and added into the <sup>2</sup>H-methyl-<sup>13</sup>CH<sub>3</sub>-labelled SecB at a final molar ratio of PhoA:SecB = 1:1. 2D <sup>1</sup>H, <sup>13</sup>C HMQC spectra were recorded at 28 °C. A sample of SecB in complex with PhoA cross-linked to a diamagnetic MTSL analogue was used as a reference. Residues experienced significant NMR signal intensity reduction (>50% intensity

loss) were identified as sites being within 20 Å of the paramagnetic centre whereas residues experiencing more than 90% intensity loss were identified as sites being within 14 Å of the paramagnetic centre.

**Protein folding assays.** Refolding experiments of MBP were performed as described before<sup>37</sup> with some modifications. Briefly, MBP was first denatured in 8 M urea, 100 mM HEPES, 20 mM KOAc, 5 mM Mg(OAc)<sub>2</sub>, pH 7.4, and 0.05% Na<sub>2</sub>S<sub>2</sub>O<sub>3</sub>. Refolding was initiated by rapid dilution (20 times dilution) in the urea-free buffer and the refolding process of MBP in the absence and presence of SecB or TF was monitored by the change in the intrinsic Trp fluorescence. Fluorescence intensity was measured using either a spectrofluorometer (FluoroMax-4, Horiba) or a microplate reader (Infinite 200 PRO, Tecan). The excitation and emission wavelengths were set to 295 nm and 345 nm, respectively. For measurement using the FluoroMax-4 instrument, the MBP concentration in the 1-ml cuvette was 0.4 μM, whereas for the microplate reader experiments the concentration of MBP was 4 μM in the 30 μl-plate well. All fluorescence measurements were performed at 25 °C. Data were fitted by the Prism 6 (GraphPad) software using the nonlinear regression analysis equation<sup>38</sup>.

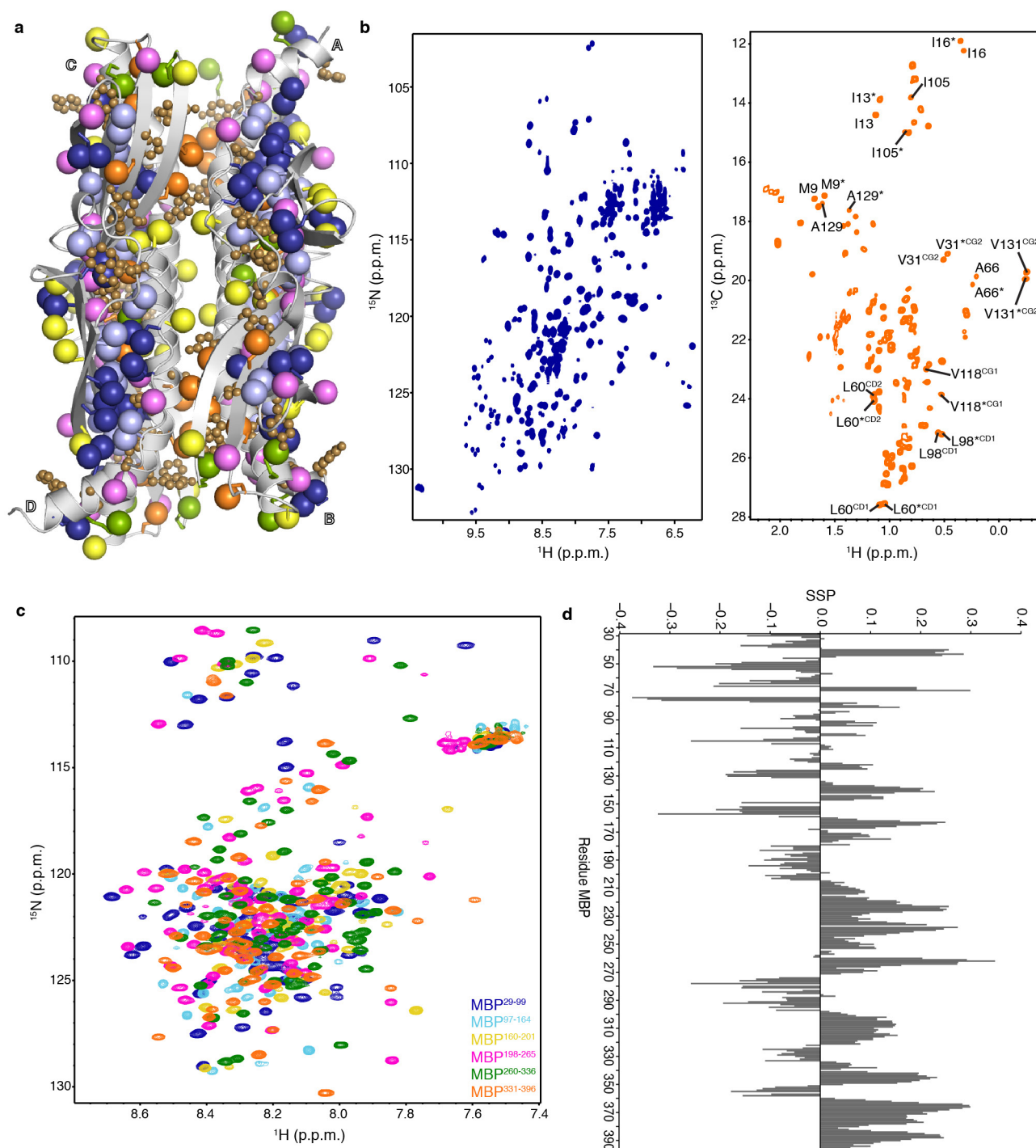
**Surface plasmon resonance (SPR).** All SPR experiments were performed on a Biacore T200 system (GE Healthcare) using a NTA-coated Sensor Chip NTA (GE Healthcare) at a flow rate of 50 μl min<sup>-1</sup>. The PhoA protein sample used for SPR experiments was genetically constructed with a His<sub>12</sub>-tag at the carboxy (C) terminus and a flexible (Gly-Ser)<sub>5</sub> linker repeat inserted in between to avoid steric hindrance. A single-cycle kinetic procedure was used to characterize the interaction of SecB and PhoA. The His-tagged PhoA was immobilized onto a NTA sensor chip, followed by washing with the running buffer containing 50 mM phosphate, 50 mM KCl, pH 7, 0.05% Na<sub>2</sub>S<sub>2</sub>O<sub>3</sub>, and 2 mM TCEP. The reducing agent (TCEP) ensured that PhoA was in the unfolded state<sup>20</sup>. SecB (analyte) at a range of concentrations (0.1–25.6 μM) was injected, and data for a period of 30 s of association and 60 s of dissociation were collected. MBP was prepared with a His<sub>10</sub>-tag at the N terminus followed by a flexible nine-residue linker to avoid steric hindrance. Multiple-cycle kinetic analysis was performed for the SPR experiments of the binding between MBP and SecB where each sample concentration was run in a separate cycle, and the surface was regenerated between each cycle using NTA regeneration buffer. His-tagged MBP was denatured in 8 M urea and immobilized onto a NTA sensor chip. Urea was quickly washed away by running buffer containing 20 mM HEPES, pH 7.4, 150 mM KOAc and 0.05% Na<sub>2</sub>S<sub>2</sub>O<sub>3</sub>. SecB was injected at concentrations ranging from 2.5 nM to 1.6 μM. The association and dissociation time for data collection was set as 90 s and 120 s, respectively. After urea was removed, MBP remained in the unfolded conformation for sufficient time to interact with SecB. This was confirmed by monitoring the refolding behaviour of MBP using an Infinite 200 PRO microplate reader (Tecan) at the temperature range of the experiments. All SPR experiments were repeated three times and highly reproducible data were obtained. The sensorgrams obtained from the assay channel were subtracted by the buffer control, and data were fitted using the Biacore T200 evaluation software (version 1.0).

**Bio-layer interferometry (BLI).** BLI experiments were performed using an Octet system (forteBIO) at room temperature (~23 °C). MBP was biotinylated using the biotinylation kit EZ-Link NHS-PEG4-Biotin (Thermo Fisher Scientific). Biotin label freshly dissolved in water was added to the protein solution to a final molar ratio of 1:1 in buffer containing 50 mM KPi, pH 7, 150 mM NaCl, 0.05% Na<sub>2</sub>S<sub>2</sub>O<sub>3</sub>, and the solution was mixed at room temperature for 45 min. Unlabelled biotin label was removed by extensive buffer exchange using Centricon Centrifugal Filter with a MWCO of 10,000 (Millipore) at 4 °C using a buffer containing 20 mM HEPES (pH 7), 150 mM KOAc and 0.05% Na<sub>2</sub>S<sub>2</sub>O<sub>3</sub>. Biotin-labelled MBP (200 nM) denatured in 8 M urea was immobilized onto the streptavidin (SA) biosensor, and the biosensors were subsequently blocked with biocytin in 8 M urea solution before a quick 30 s dip into the urea-free buffer. SecB or TF previously diluted was applied in a dose-dependent manner to the biosensors immobilized with MBP. Bovine serum albumin (BSA) powder (Sigma-Aldrich) was added to a final concentration of 2% to avoid non-specific interaction. Parallel experiments were performed for reference sensors with no MBP captured and the signals were subsequently subtracted during data analysis. The association and dissociation periods were set to 2 min and 5 min, respectively.

- Popovych, N., Tzeng, S. R., Tonelli, M., Ebright, R. H. & Kalodimos, C. G. Structural basis for cAMP-mediated allosteric control of the catabolite activator protein. *Proc. Natl Acad. Sci. USA* **106**, 6927–6932 (2009).
- Milbradt, A. G. *et al.* Increased resolution of aromatic cross peaks using alternate <sup>13</sup>C labeling and TROSY. *J. Biomol. NMR* **62**, 291–301 (2015).
- Delaglio, F. *et al.* NMRPipe: a multidimensional spectral processing system based on UNIX pipes. *J. Biomol. NMR* **6**, 277–293 (1995).

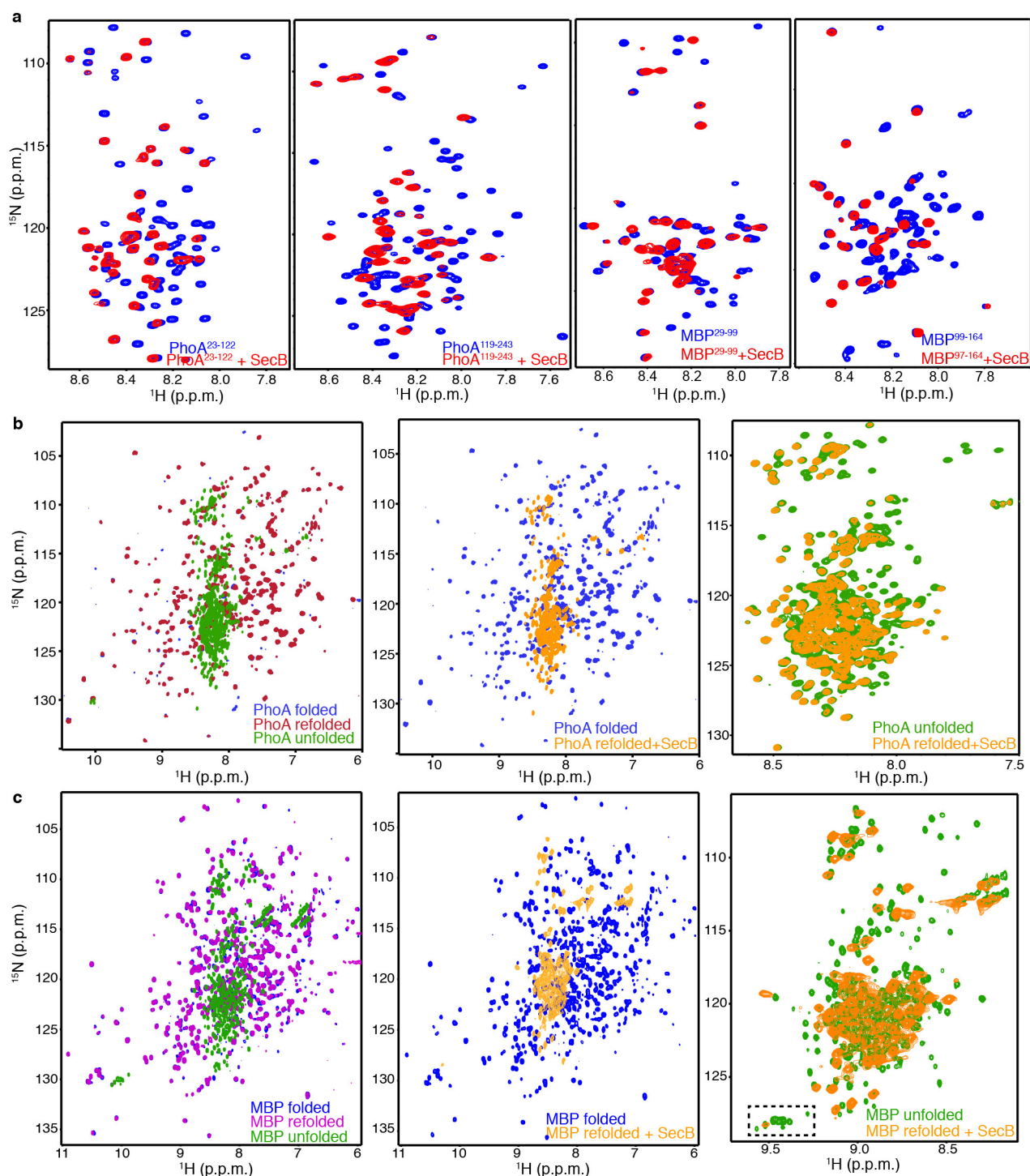


34. Güntert, P. Automated NMR structure calculation with CYANA. *Methods Mol. Biol.* **278**, 353–378 (2004).
35. Shen, Y., Delaglio, F., Cornilescu, G. & Bax, A. TALOS+: a hybrid method for predicting protein backbone torsion angles from NMR chemical shifts. *J. Biomol. NMR* **44**, 213–223 (2009).
36. Brunger, A. T. Version 1.2 of the Crystallography and NMR system. *Nature Protocols* **2**, 2728–2733 (2007).
37. Chun, S. Y., Strobel, S., Bassford, P., Jr & Randall, L. L. Folding of maltose-binding protein. Evidence for the identity of the rate-determining step in vivo and in vitro. *J. Biol. Chem.* **268**, 20855–20862 (1993).
38. Betton, J. M., Sassoone, N., Hofnung, M. & Laurent, M. Degradation versus aggregation of misfolded maltose-binding protein in the periplasm of *Escherichia coli*. *J. Biol. Chem.* **273**, 8897–8902 (1998).
39. Marsh, J. A., Singh, V. K., Jia, Z. & Forman-Kay, J. D. Sensitivity of secondary structure propensities to sequence differences between  $\alpha$ - and  $\gamma$ -synuclein: implications for fibrillation. *Protein Sci.* **15**, 2795–2804 (2006).
40. Camilloni, C., De Simone, A., Vranken, W. F. & Vendruscolo, M. Determination of secondary structure populations in disordered states of proteins using nuclear magnetic resonance chemical shifts. *Biochemistry* **51**, 2224–2231 (2012).
41. Betton, J. M. & Hofnung, M. Folding of a mutant maltose-binding protein of *Escherichia coli* which forms inclusion bodies. *J. Biol. Chem.* **271**, 8046–8052 (1996).
42. Tejero, R., Snyder, D., Mao, B., Aramini, J. M. & Montelione, G. T. PDBStat: a universal restraint converter and restraint analysis software package for protein NMR. *J. Biomol. NMR* **56**, 337–351 (2013).



**Extended Data Figure 1 | NMR characterization of SecB and unfolded MBP.** **a**, SecB is enriched in hydrophobic amino acids, such as methyl-bearing (Ala, Ile, Leu, Met, Thr and Val) and aromatic (Phe and Tyr). **b**,  $^1\text{H}$ - $^{15}\text{N}$  TROSY HSQC (left) and  $^1\text{H}$ - $^{13}\text{C}$  methyl HMQC (right) spectra of [ $^2\text{H}$ ; Ala- $^{13}\text{CH}_3$ ; Met- $^{13}\text{CH}_3$ ; Ile- $\delta 1$ - $^{13}\text{CH}_3$ ; Leu, Val- $^{13}\text{CH}_3$ / $^{13}\text{CH}_3$ ; Thr- $^{13}\text{CH}_3$ ]-labelled SecB. SecB packing gives rise to two pairs of spectroscopically equivalent subunits: one pair is formed by subunits A and D, and the other pair by subunits B and C. Select assignment is included in the methyl spectrum with the asterisk indicating the other pair. **c**,  $^1\text{H}$ - $^{15}\text{N}$  HSQC spectra of select MBP fragments spanning the entire

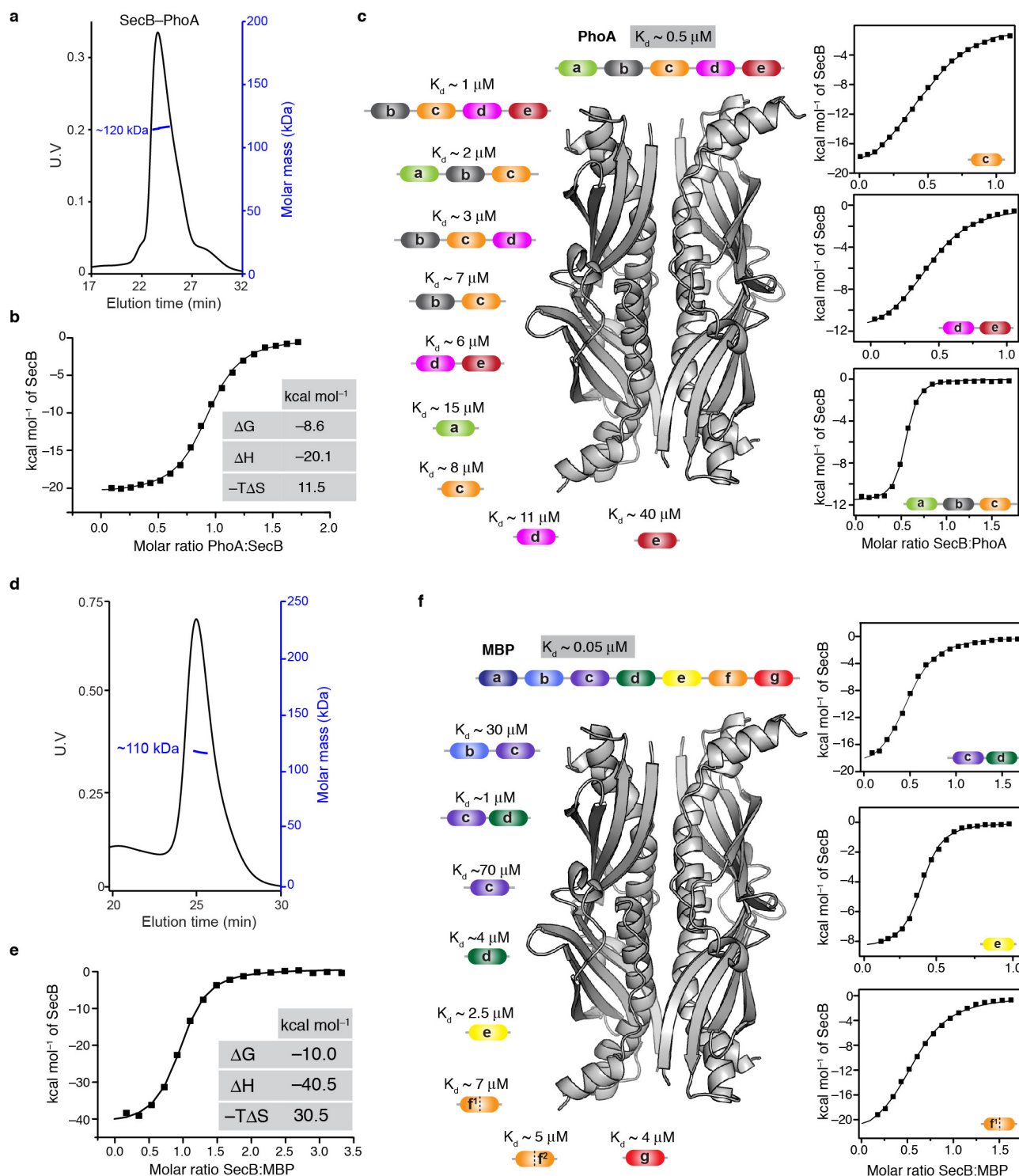
sequence of MBP. **d**, Secondary structure propensity (SSP) values<sup>39,40</sup> of unfolded MBP (extracted collectively from the fragments) plotted as a function of the amino-acid sequence. A SSP score at a given residue of 1 or -1 reflects a fully formed  $\alpha$ -helical or  $\beta$ -structure (extended), respectively, whereas a score of, for example, 0.5 indicates that 50% of the conformers in the native-state ensemble of the protein are helical at that position. The data show that several of the secondary structure elements in the folded MBP retain some transient secondary structure in the unfolded MBP fragments.



**Extended Data Figure 2 | NMR characterization of PhoA and MBP binding to SecB.** **a**, To determine the SecB-recognition sites within PhoA and MBP,  $^{15}\text{N}$ -labelled PhoA and MBP fragments were titrated with unlabelled SecB. Owing to the labelling scheme and the size of SecB, the intensity of the PhoA and MBP residues that are bound by SecB decreases dramatically or disappears. Several titration points were recorded but here only the spectra for the SecB:PhoA and SecB:MBP 1:1 are shown for two select fragments. The  $^1\text{H}$ - $^{15}\text{N}$  HSQC spectra of PhoA or MBP are shown

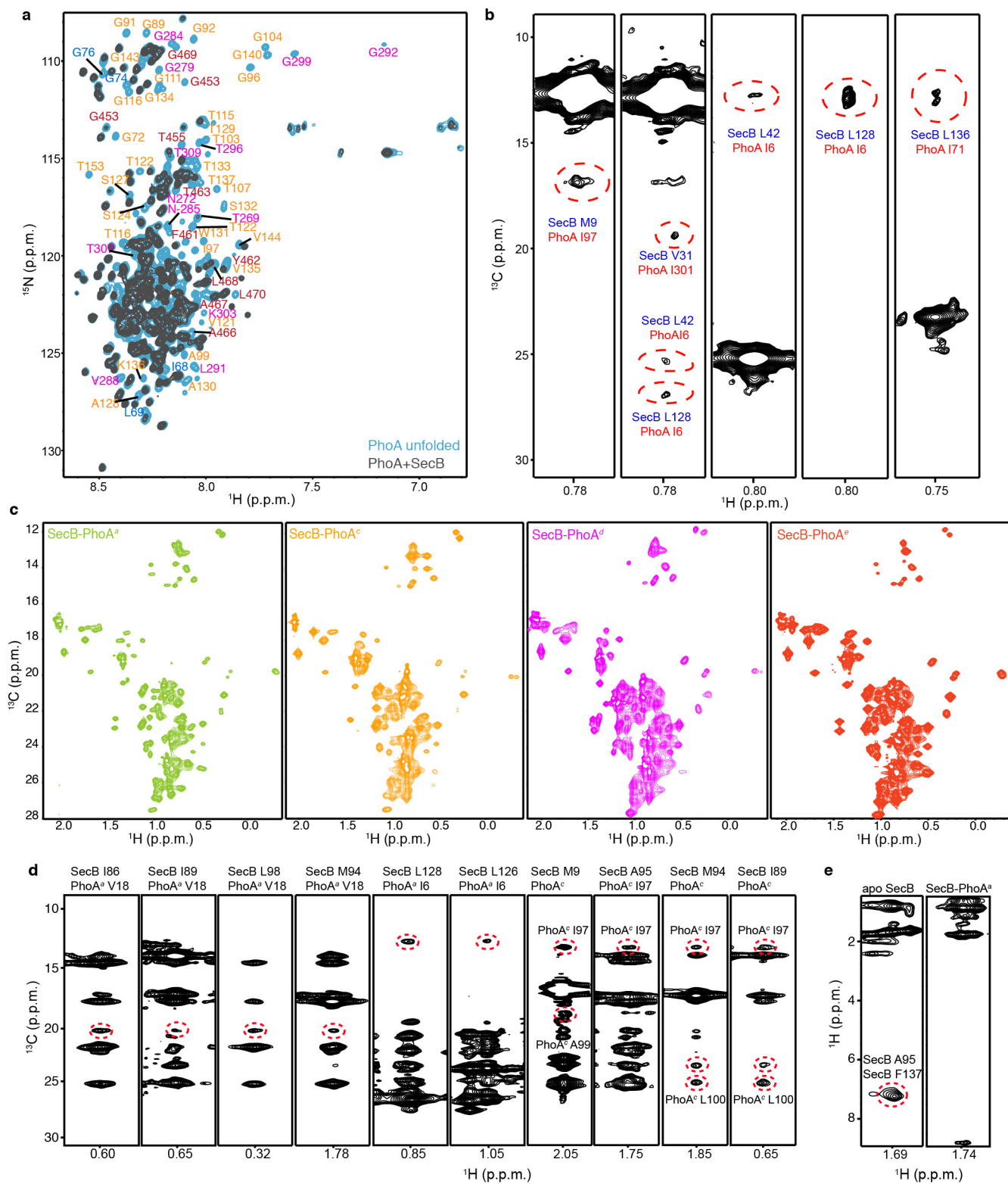
in the absence (blue) and presence (red) of SecB. **b**, **c**, PhoA (**b**) and MBP (**c**) refolding in the presence and absence of SecB monitored by  $^1\text{H}$ - $^{15}\text{N}$  HSQC spectra. Spectra of the 'refolded' state were recorded after rapid dilution of urea-treated MBP/PhoA in native buffer. Spectra of the 'unfolded' state were recorded in urea. MBP and PhoA refolded in their native structure in the absence of SecB but were retained in the unfolded state in the presence of SecB.





**Extended Data Figure 3 | Energetics of SecB interaction with PhoA and MBP.** **a**, MALS of SecB–PhoA complex showing a stoichiometry of 1:1. **b**, ITC of SecB binding to PhoA and the energetics of binding. **c**,  $K_d$  values for complexes between select PhoA fragments encompassing the five (a–e) SecB-recognition sites and SecB. **d**, MALS of SecB–MBP complex showing a stoichiometry of 1:1. **e**, ITC of SecB binding to MBP and the energetics of binding. **f**,  $K_d$  values for complexes between select

MBP fragments encompassing the seven (a–g) SecB-recognition sites and SecB. More than one of the smaller PhoA or MBP fragments (for example, PhoA<sup>c</sup>, PhoA<sup>d–e</sup>, MBP<sup>c–d</sup>) can be accommodated within SecB. Of note is the large favourable enthalpy of binding for the interaction of MBP and PhoA with SecB reflecting the large interacting surface. However, a large but unfavourable entropy diminishes the overall binding.

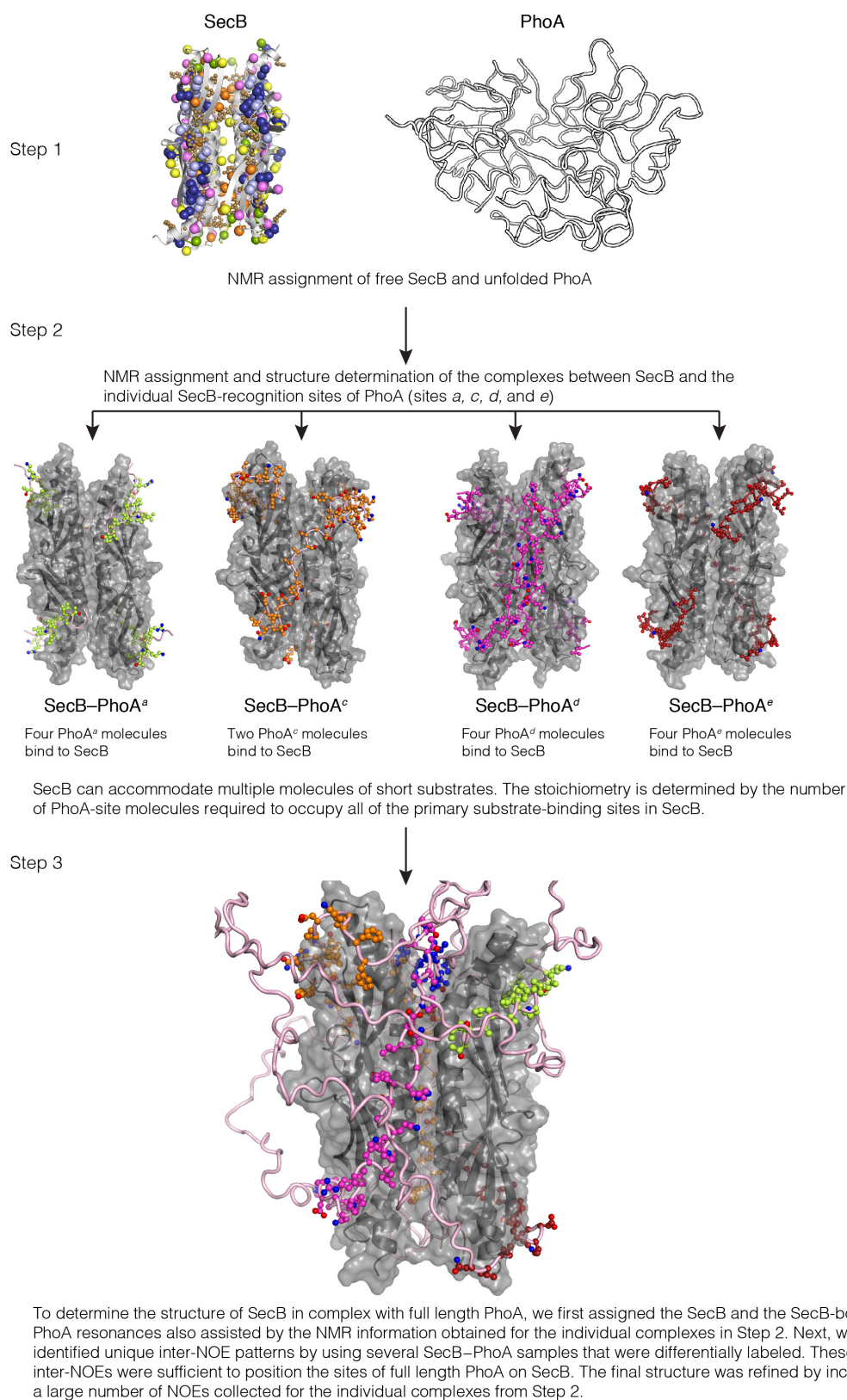


Extended Data Figure 4 | See next page for caption.

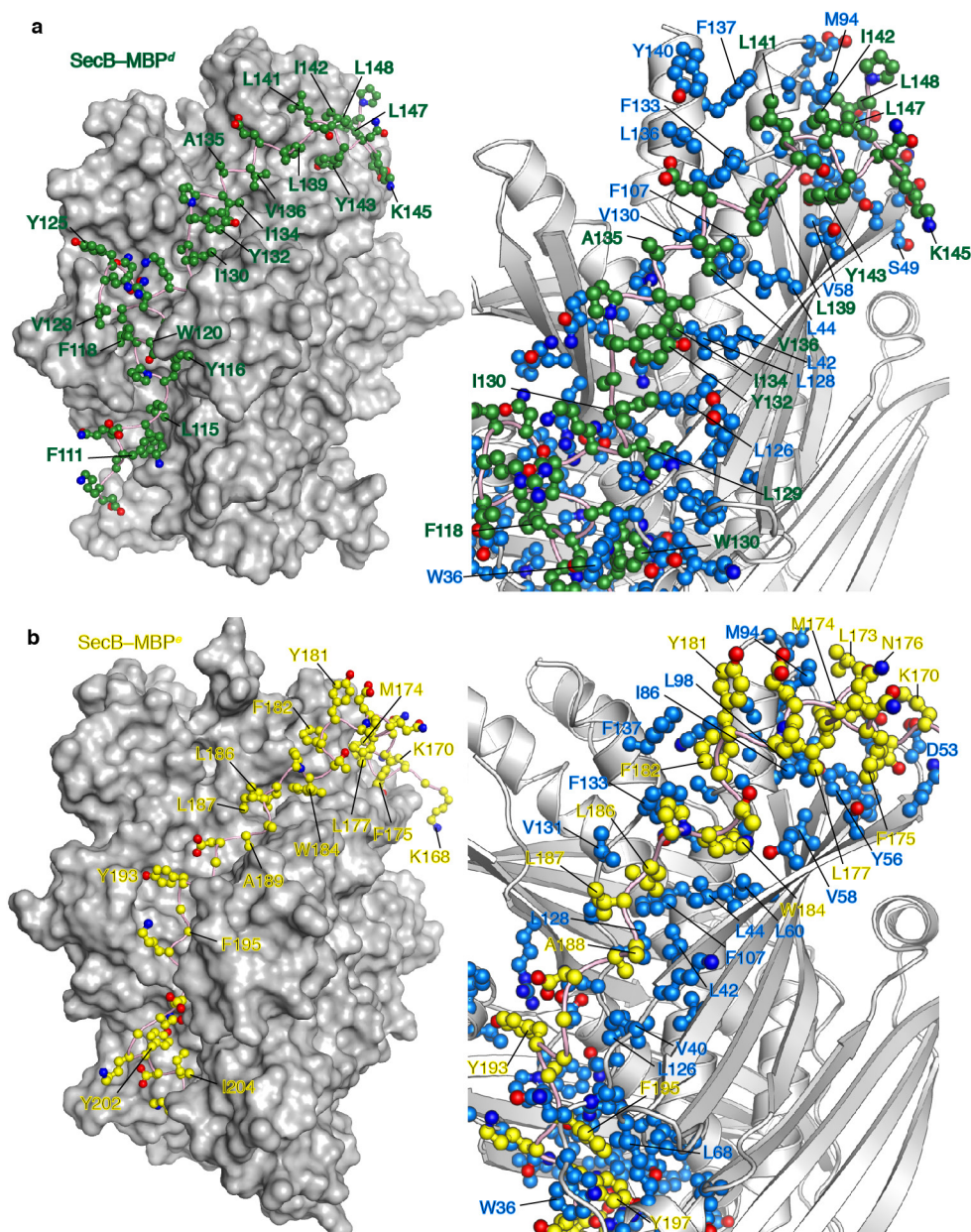
**Extended Data Figure 4 | NMR characterization of the SecB–PhoA complex.** **a**,  $^1\text{H}$ – $^{15}\text{N}$  TROSY HSQC spectra of PhoA in the unfolded state (light blue) and in complex with SecB (grey). The unfolded state was induced by the addition of reducing agent<sup>20</sup> or urea and assigned and characterized by NMR as shown before<sup>20</sup>. Select resonance assignment of SecB-recognition sites in PhoA is included (the colour is per the colour code for each SecB-recognition site within PhoA; see Fig. 1b). There is an excellent correspondence between the PhoA residues identified to bind to SecB using the various PhoA fragments (Extended Data Fig. 2a) and the residues of full-length PhoA that are bound to SecB in the SecB–PhoA complex. All five SecB-recognition sites in PhoA (a–e) are engaged by SecB in the SecB–PhoA complex. The PhoA regions that are not bound to SecB (they retain their intensity in the complex) are all in an unfolded conformation as suggested by their essentially identical chemical shifts to the unfolded PhoA. **b**, Select strips from  $^{13}\text{C}$ -edited NOESY experiments highlighting intermolecular NOEs in the SecB–PhoA complex. Owing to severe resonance overlap in the 120 kDa SecB–PhoA complex, to identify specific intermolecular NOEs we prepared samples wherein the two

protein partners are labelled in different methyl-bearing type of amino acids. In this example, SecB was labelled in Leu, Met and Val residues and PhoA in Ile residues. Thus, all NOEs detected between Leu/Val/Met and Ile methyls are intermolecular. **c**,  $^1\text{H}$ – $^{13}\text{C}$  methyl HMQC spectra of SecB in complex with PhoA fragments carrying the individual PhoA sites: PhoA<sup>a</sup> (green), PhoA<sup>c</sup> (orange), PhoA<sup>d</sup> (magenta) and PhoA<sup>e</sup> (red). Both SecB and PhoA fragments are [ $\text{U-}^2\text{H}$ ; Ala- $^{13}\text{CH}_3$ ; Met- $^{13}\text{CH}_3$ ; Ile- $\delta 1$ - $^{13}\text{CH}_3$ ; Leu,Val- $^{13}\text{CH}_3/^{13}\text{CH}_3$ ; Thr- $^{13}\text{CH}_3$ ]-labelled. **d**, Representative strips from  $^{13}\text{C}$ -edited NOESY–HSQC and HMQC–NOESY–HMQC NMR experiments. The NOE cross-peaks between SecB and residues of PhoA fragments are designated by a dashed-line red circle. **e**, Characteristic NOEs showing that the primary binding groove in SecA is enlarged by the displacement of helix  $\alpha 2$  as shown in Fig. 4a. For example, the NOE between SecB residues Ala95 and Phe137 is consistent with the closed conformation observed in apo SecB. This NOE is not present in the SecB–PhoA complex because the two SecB residues have moved apart as a result of the displacement of the helix  $\alpha 2$ .



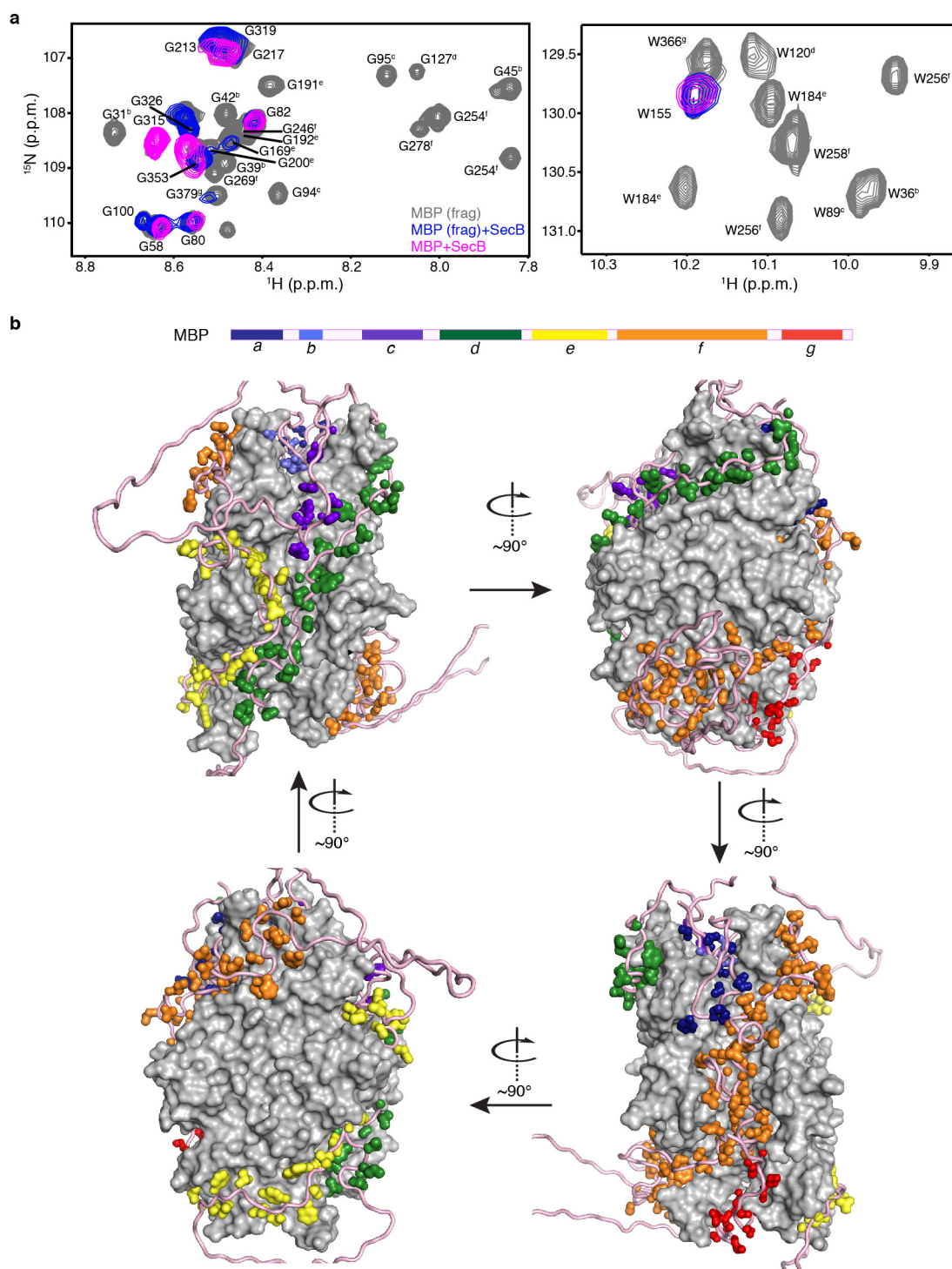


**Extended Data Figure 5 | Strategy for the structure determination of the SecB-PhoA complex.** The three main steps are briefly described here. More details can be found in Methods. The lowest-energy NMR structures of the SecB complexes with the individual PhoA sites *a*, *c*, *d* and *e* are shown. The structural and NMR statistics for each structure are shown in Extended Data Table 1 and Methods.



**Extended Data Figure 6 | Structures of SecB with MBP sites.** **a**, Lowest-energy structure of SecB in complex with a MBP fragment encompassing site *d* (MBP<sup>d</sup>, residues 105–152). **b**, Lowest-energy structure of SecB in complex with a MBP fragment encompassing site *e* (MBP<sup>e</sup>, residues 165–210). SecB is shown as grey solvent-accessible surface (left) or as

white cartoon (right). Expanded views (right) of the contacts between SecB and MBP. The SecB residues mediating contacts with MBP are shown as blue ball-and-stick. In both complexes an additional MBP molecule binds symmetrically to the opposite face of SecB but are not shown for clarity.

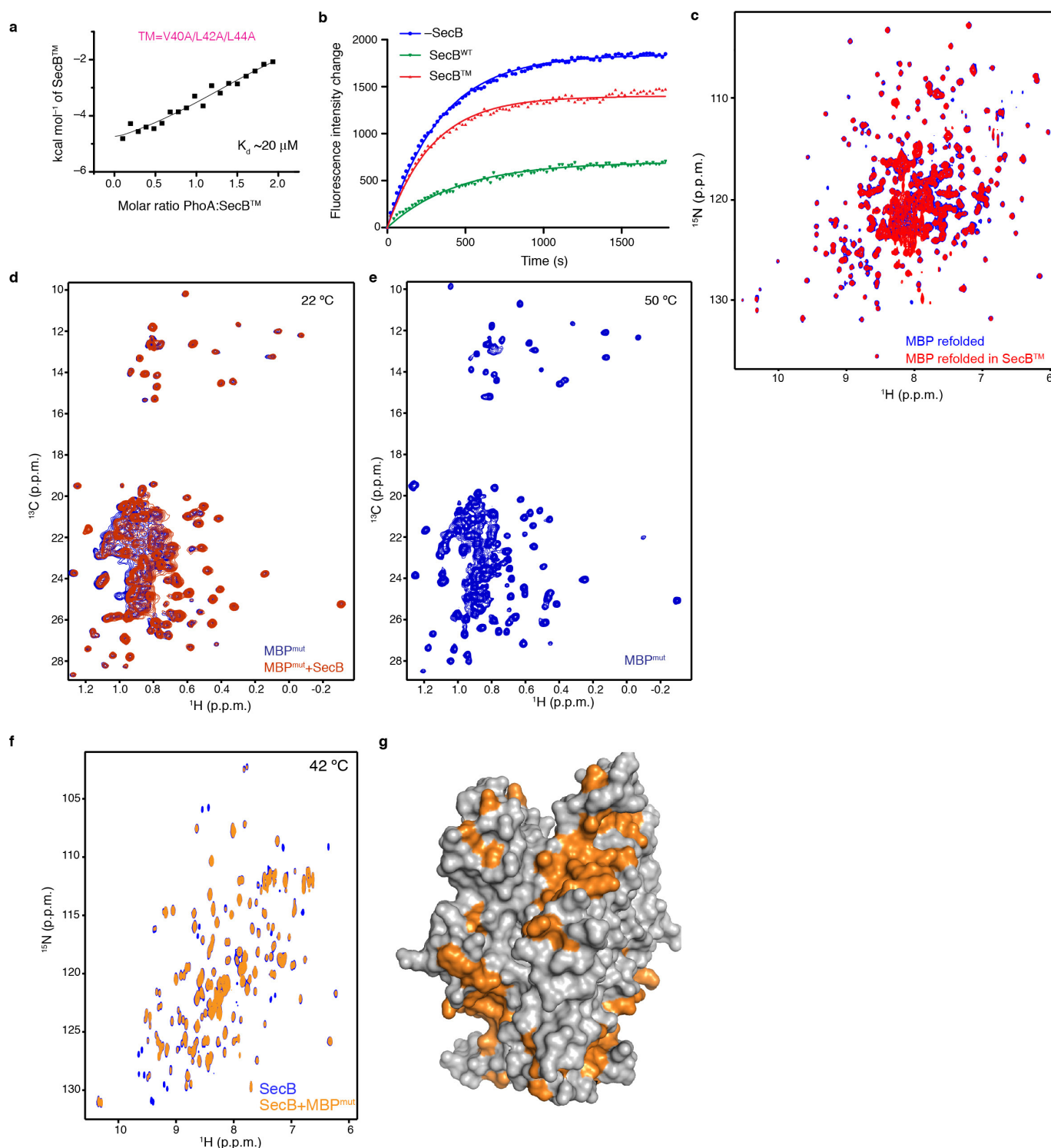


Extended Data Figure 7 | See next page for caption.



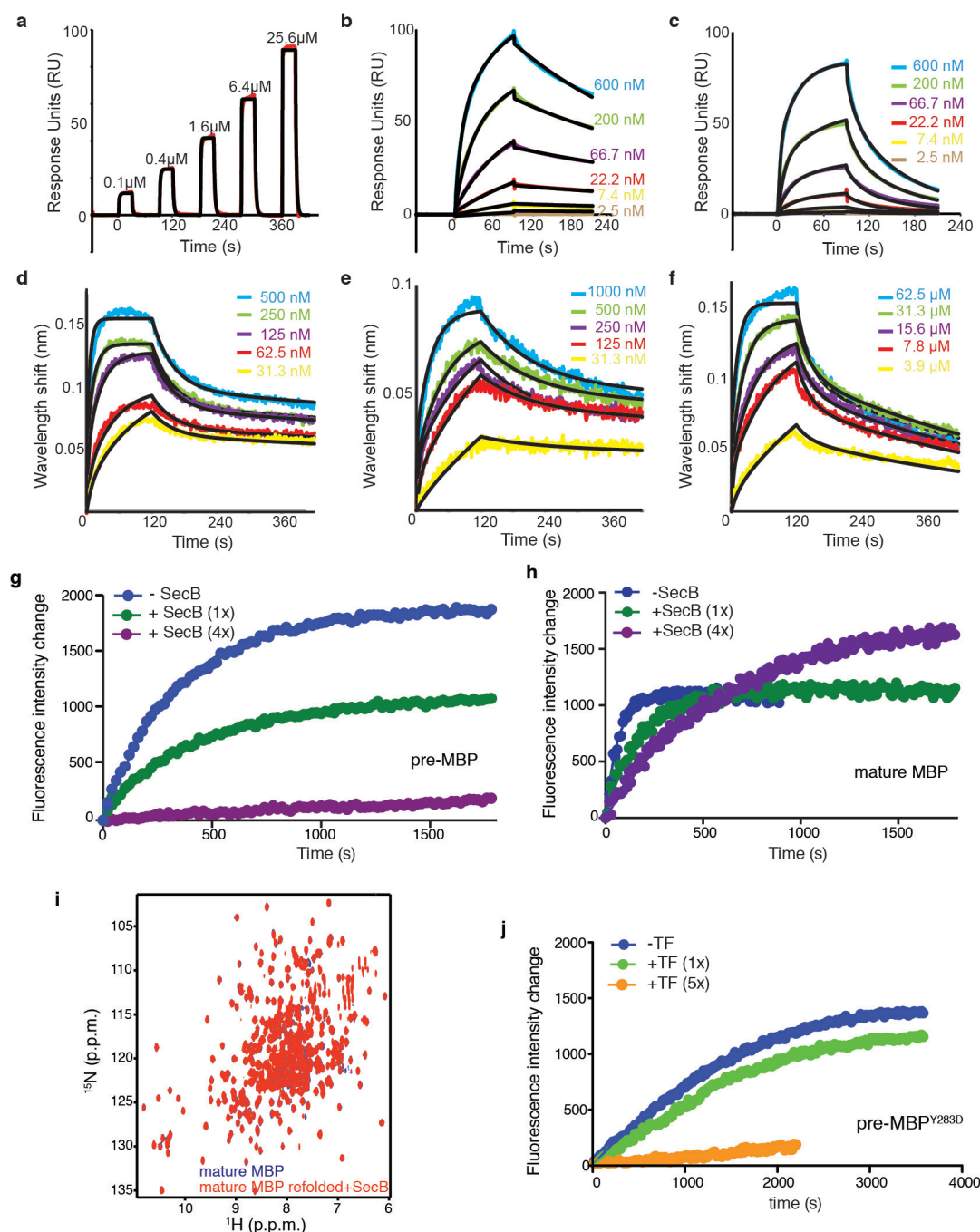
**Extended Data Figure 7 | NMR-driven model structure of SecB–MBP complex.** **a**,  $^1\text{H}$ – $^{15}\text{N}$  TROSY HSQC spectra of MBP fragments (grey), MBP fragments in complex with SecB (blue) and full-length MBP in complex with SecB (magenta). The Gly (left) and Trp N $\epsilon$  (right) regions are shown as examples because of the excellent dispersion and lack of severe resonance overlap. The various MBP fragments covering the entire MBP sequence (Extended Data Fig. 1c) are coloured grey and if they are located within a SecB-recognition site it is denoted in the superscript. The MBP residues that do not interact with SecB retain their intensity. These are residues located in regions that are not SecB-recognition sites (Fig. 1c). When these spectra are compared with the spectra of full-length MBP in complex with SecB (in magenta) a very good resonance correspondence is observed. Thus, two important observations can be made: first, all seven SecB-recognition sites (*a*–*g*) in MBP are engaged by SecB in the SecB–MBP complex; and, second, the MBP regions that do not interact with SecB in the SecB–MBP complex remain in an unfolded state. The Trp spectra (right) provide direct evidence in support of these observations: all Trp residues, with the exception of Trp155, are located in SecB-recognition sites and they all interact with SecB in the SecB–MBP complex. In contrast, Trp155 does not bind to SecB when the corresponding MBP fragment was used, and this was also the case for

MBP. **b**, Modelled structure of the SecB–MBP complex. SecB is shown as a solvent-exposed surface and MBP as a pink ribbon. The seven MBP sites recognized by SecB are shown as side-chain surface and coloured per the colour code in the graphic of the MBP sequence at the top. The structure of the complex was modelled as detailed in Methods. Briefly, as mentioned above, NMR analysis demonstrated that all seven recognition sites in MBP (labelled *a*–*g*) are bound to SecB in the SecB–MBP complex. We have determined the high-resolution structure of MBP<sup>*d*</sup> and MBP<sup>*e*</sup> in complex with SecB (Extended Data Fig. 6). Because of their length and the short linker tethering the two sites, *d* and *e*, most probably bind to the same side of SecB. MBP site *f* is the longest one, consisting of ~90 residues, and is thus entirely accommodated on the other side of SecB. With sites *d*, *e* and *f* occupying the primary binding sites, the other recognition sites (*a*, *b*, *c* and *g*), being much shorter, can be accommodated within the secondary client-binding sites on SecB. The structure of MBP sites *d* and *e* in complex with SecB was determined using the experimental intermolecular NOE data. The hydrophobic residues of the sites *a*, *b*, *c*, *f* and *g* showing the strongest effect upon SecB binding, as determined by differential line broadening, were used to drive the docking of these sites to non-polar residues on SecB. The modelled structure shows that the entire MBP sequence can be accommodated within one SecB molecule.



**Extended Data Figure 8 | Anti-aggregation activity of SecB.** **a**, A triple amino-acid substitution in the SecB (V40A/L42A/L44A) client-binding site was prepared and is referred to as the triple mutant SecB (SecB<sup>TM</sup>). ITC profile of the binding of PhoA to SecB<sup>TM</sup> to be compared with PhoA binding to wild-type SecB (Extended Data Fig. 3b). The triple substitution causes a 40-fold reduction in the affinity of SecB for PhoA. **b**, Fluorescence-monitored MBP folding in the absence of SecB (blue), in the presence of wild-type SecB (green) and in the presence of SecB<sup>TM</sup> (red). The triple mutant diminishes significantly the antifolding activity of SecB. **c**, <sup>1</sup>H-<sup>15</sup>N TROSY HSQC spectra of MBP refolded in the absence (blue) and presence of SecB<sup>TM</sup> (red). In contrast to wild-type SecB (Extended Data Fig. 2c), SecB<sup>TM</sup> cannot hold MBP in the unfolded state. **d**, <sup>1</sup>H-<sup>13</sup>C methyl HMQC spectra of MBP<sup>mut</sup> (blue) and in the presence of SecB (red) recorded at 22 °C. The MBP mutant (MBP<sup>mut</sup>) carries two amino-acid substitutions

(G32D/I33P) that renders the protein prone to aggregation<sup>41</sup>, especially at temperatures above 30 °C. No NMR signal of MBP<sup>mut</sup> can be detected at temperatures above 30 °C and the protein precipitates in the NMR tube. At 22 °C, MBP<sup>mut</sup> is folded, as evidenced by the resonance dispersion in the NMR spectra, and does not interact with SecB. **e**, <sup>1</sup>H-<sup>13</sup>C methyl HMQC spectrum of MBP<sup>mut</sup> in the presence of SecB recorded at 50 °C. MBP<sup>mut</sup> suffers heavy precipitation and aggregation at temperatures higher than 30 °C, but in the presence of SecB it is stable and folded even at temperatures as high as 50 °C. **f**, <sup>1</sup>H-<sup>15</sup>N TROSY HSQC spectra of SecB (blue) and in the presence of MBP<sup>mut</sup> (orange) at 42 °C, indicating binding. Because of the elevated temperature, a significant unfolded population of MBP<sup>mut</sup> is present, which binds to SecB (see main text). **g**, Mapping of the sites (orange) used by SecB to interact with MBP<sup>mut</sup>, on the basis of the chemical shift perturbation data from the spectra in **f**.



**Extended Data Figure 9 | Kinetics of PhoA and MBP interaction with SecB and TF.** **a–c**, SPR analysis of the interaction of SecB with PhoA (**a**) and MBP at 20 °C (**b**) and 30 °C (**c**). Single-cycle and multiple-cycle procedures were used for the SPR analysis of SecB with PhoA and MBP, respectively. **d–f**, BLI analysis of the binding of MBP to SecB (**d**), SecB<sup>TM</sup> (**e**) and TF (**f**). His-tagged PhoA or MBP (for SPR) or biotinylated MBP (for BLI) experiments was immobilized on an NTA chip (SPR) or streptavidin biosensor (BLI) and interactions were examined at different SecB or TF concentrations as indicated. Binding is reported in response units (RU) for SPR and wavelength shift (nanometers) for BLI as a function of time. **g, h**, Effect of SecB on the kinetics of MBP folding. **g**, Fluorescence-monitored folding of MBP (pre form) and

mature MBP (**h**) in the absence (blue) and presence of one- (green) and fourfold (purple) excess of SecB. SecB does not appreciably delay folding of mature MBP. In fact, SecB excess appears to increase the yield of soluble, folded mature MBP (purple). **i**, <sup>1</sup>H-<sup>15</sup>N TROSY HSQC spectra of mature MBP refolded in the absence (blue) and presence of SecB (red). SecB cannot retain the mature MBP unfolded. **j**, Fluorescence-monitored folding of the slowly folding MBP<sup>Y283D</sup> variant in the absence (blue), and presence of one- (green) and fivefold (orange) TF. As elaborated in the main text, TF does not delay folding of pre-MBP (Fig. 5a). However, it does delay folding of an inherently slowly folding MBP mutant (MBP<sup>Y283D</sup>), thus highlighting the importance of the intrinsic folding of the client protein and its association rate to the chaperone.



Extended Data Table 1 | NMR and refinement statistics for the SecB complexes with PhoA and MBP

	SecB- PhoA	SecB- PhoA <sup>a</sup>	SecB- PhoA <sup>c</sup>	SecB- PhoA <sup>d</sup>	SecB- PhoA <sup>e</sup>	SecB- MBP <sup>d</sup>	SecB- MBP <sup>e</sup>
<b>NMR distance and dihedral constraints</b>							
Distance restraints							
Total NOE	1362	1636	2151	1338	1043	1320	1446
Inter-residue							
Sequential ( $ i-j  = 1$ )	343	402	435	376	151	371	362
Non-sequential ( $ i-j  > 1$ )	1019	1234	1716	962	892	949	1084
Inter-molecule	171	33	52	54	27	25	22
Total dihedral angle restraints	1169	1004	996	1012	1012	1006	976
phi	583	502	498	506	506	503	488
psi	586	502	498	506	506	503	488
<b>Structure statistics</b>							
Violations (mean and s.d.)							
Distance constraints (Å)	0.012 ±0.047	0.015 ±0.052	0.015 ±0.052	0.016 ±0.052	0.018 ±0.055	0.013 ±0.045	0.016 ±0.054
Dihedral angle constraints (°)	0.42 ±1.4	0.26 ±0.85	0.26 ±0.85	0.28 ±0.89	0.23 ±0.79	0.027 ±0.85	0.31 ±0.96
Max. dihedral angle violation (°)	26.8	9.3	8.7	9.9	9.7	9.5	9.9
Max. distance constraint violation (Å)	1.11	0.86	0.89	0.80	0.83	0.95	0.95
Average pairwise r.m.s.d. (Å)							
Heavy	4.4	2.1	2.9	2.4	2.5	3.6	2.9
Backbone	4.0	1.5	2.1	1.7	1.7	2.8	2.1

Statistics for each structure were computed for the ensembles of 20 deposited structures. Ordered residue ranges ( $S(\varphi) + S(\psi) > 1.8$ ), 10–141 (of SecB subunits A, B, C and D); backbone (heavy atom) root mean squared deviation (r.m.s.d.) was ~1.0 (1.3) Å within the specified range for all complexes. Additionally, the r.m.s.d. within the PhoA fragments is reported for each structure. Average distance constraint violations were calculated with PDBStat<sup>42</sup>.

# Compression and ablation of the photo-irradiated molecular cloud the Orion Bar

Javier R. Goicoechea<sup>1</sup>, Jérôme Pety<sup>2,3</sup>, Sara Cuadrado<sup>1</sup>, José Cernicharo<sup>1</sup>, Edwige Chapillon<sup>2,4,5</sup>, Asunción Fuente<sup>6</sup>, Maryvonne Gerin<sup>3,7</sup>, Christine Joblin<sup>8,9</sup>, Nuria Marcelino<sup>1</sup> & Paolo Pilleri<sup>8,9</sup>

The Orion Bar is the archetypal edge-on molecular cloud surface illuminated by strong ultraviolet radiation from nearby massive stars. Our relative closeness to the Orion nebula (about 1,350 light years away from Earth) means that we can study the effects of stellar feedback on the parental cloud in detail. Visible-light observations of the Orion Bar<sup>1</sup> show that the transition between the hot ionized gas and the warm neutral atomic gas (the ionization front) is spatially well separated from the transition between atomic and molecular gas (the dissociation front), by about 15 arcseconds or 6,200 astronomical units (one astronomical unit is the Earth–Sun distance). Static equilibrium models<sup>2,3</sup> used to interpret previous far-infrared and radio observations of the neutral gas in the Orion Bar<sup>4–6</sup> (typically at 10–20 arcsecond resolution) predict an inhomogeneous cloud structure comprised of dense clumps embedded in a lower-density extended gas component. Here we report one-arcsecond-resolution millimetre-wave images that allow us to resolve the molecular cloud surface. In contrast to stationary model predictions<sup>7–9</sup>, there is no appreciable offset between the peak of the H<sub>2</sub> vibrational emission (delineating the H/H<sub>2</sub> transition) and the edge of the observed CO and HCO<sup>+</sup> emission. This implies that the H/H<sub>2</sub> and C<sup>+</sup>/C/CO transition zones are very close. We find a fragmented ridge of high-density substructures, photoablative gas flows and instabilities at the molecular cloud surface. The results suggest that the cloud edge has been compressed by a high-pressure wave that is moving into the molecular cloud, demonstrating that dynamical and non-equilibrium effects are important for the cloud evolution.

The Atacama Large Millimeter/submillimeter Array (ALMA) radio-telescope allows us to resolve the transition from atomic to molecular

gases at the edge of the Orion molecular cloud<sup>10–13</sup>, which is directly exposed to energetic radiation from the Trapezium stars (Fig. 1). The strong ultraviolet field drives a blister ‘H II region’ (hot ionized hydrogen gas or H<sup>+</sup>) that is eating its way into the parental molecular cloud. At the same time, flows of ionized gas stream away from the cloud surface at about 10 km s<sup>−1</sup> (roughly the speed of sound  $c_{\text{H II}}$  at  $T \approx 10^4$  K)<sup>10,11</sup>. The so-called photon-dominated or photodissociation region (PDR<sup>14</sup>; see Extended Data Fig. 1) starts at the H II region/cloud boundary where only far-ultraviolet radiation penetrates the ‘neutral’ cloud, that is, stellar photons with energies below 13.6 eV that cannot ionize H atoms but do dissociate molecules ( $\text{H}_2 + \text{photon} \rightarrow \text{H} + \text{H}$ ), and ionize elements such as carbon ( $\text{C} + \text{photon} \rightarrow \text{C}^+ + \text{electron}$ ). Inside the PDR, the far-ultraviolet photon flux gradually decreases due to dust grain extinction and H<sub>2</sub> line absorption, as do the gas and dust temperatures<sup>14</sup>. These gradients produce a layered structure with different chemical compositions as one moves from the cloud edge to the interior<sup>5,13</sup>. The ionized nebula (the H II region) can be traced by the visible light emission from atomic ions (such as the [S II] 6,731 Å electronic line). The ionization front is delineated by the [O I] 6,300 Å line of neutral atomic oxygen<sup>15</sup> (Fig. 1). Both transitions are excited by high-temperature collisions with electrons. Therefore, their intensities sharply decline as the electron abundance decreases by a factor of about 10<sup>4</sup> at the H<sup>+</sup>/H transition layer. In Fig. 1b, the dark cavity between the ionization front and the HCO<sup>+</sup>-emitting zone is the neutral ‘atomic layer’ ( $x(\text{H}) > x(\text{H}_2) \gg x(\text{H}^+)$ , where  $x$  is the species abundance with respect to H nuclei). This layer is very bright in mid-infrared polycyclic aromatic hydrocarbon emission, and cools via the far-infrared O and C<sup>+</sup> emission lines<sup>14</sup>. Although most of

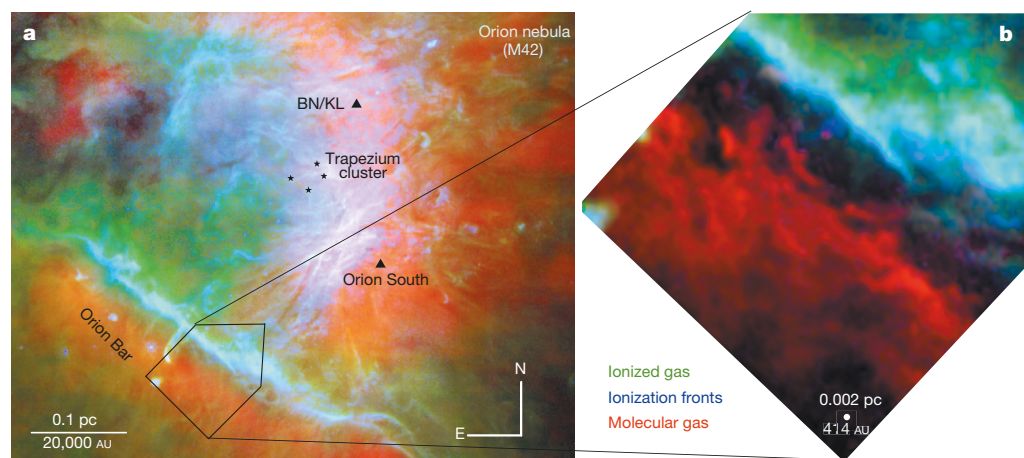


**Figure 1 | Multiphase view of the Orion nebula and molecular cloud.**

**a**, Overlay of the HCO<sup>+</sup>  $J=3-2$  emission (red) tracing the extended Orion molecular cloud. The hot ionized gas surrounding the Trapezium stars is shown by the [S II] 6,731 Å emission (green). The interfaces between the ionized and the neutral gas, the ionization fronts, are traced by the [O I] 6,300 Å emission (blue). Both lines were imaged with VLT/MUSE<sup>15</sup>. The size of the image is approximately  $5.8' \times 4.6'$ . BN/KL, Becklin–Neugebauer/Kleinmann–Low star-forming region. **b**, Close-up of the Orion Bar region imaged with ALMA in the HCO<sup>+</sup>  $J=4-3$  emission (red). The black region is the atomic layer.

<sup>1</sup>Grupo de Astrofísica Molecular, Instituto de Ciencia de Materiales de Madrid (CSIC), Calle Sor Juana Inés de la Cruz 3, E-28049 Cantoblanco, Madrid, Spain. <sup>2</sup>Institut de Radioastronomie Millimétrique (IRAM), 300 rue de la Piscine, F-38406 Saint Martin d'Hères, France. <sup>3</sup>Laboratoire d'Etudes du Rayonnement et de la Matière en Astrophysique et Atmosphères (LERMA), Observatoire de Paris, Centre National de la Recherche Scientifique (CNRS), Unité Mixte de Recherche (UMR) 8112, École Normale Supérieure, PSL Research University, 24 rue Lhomond, 75231, Paris Cedex 05, France. <sup>4</sup>Laboratoire d'Astrophysique de Bordeaux (LAB), Université de Bordeaux, UMR 5804, F-33270 Floirac, France. <sup>5</sup>CNRS, LAB, UMR 5804, F-33270 Floirac, France. <sup>6</sup>Observatorio Astronómico Nacional (OAN-IGN), Apartado 112, 28803 Alcalá de Henares, Spain. <sup>7</sup>Sorbonne Universités, Université Pierre et Marie Curie (UPMC), Université Paris 06, 75000, France. <sup>8</sup>Université de Toulouse, Université Paul-Sabatier-Observatoire Midi-Pyrénées (UPS-OMP), Institut de Recherche en Astrophysique et Planétologie (IRAP), 31028, Toulouse, France. <sup>9</sup>CNRS, IRAP, 9 Avenue du Colonel Roche, BP 44346, 31028 Toulouse, France.

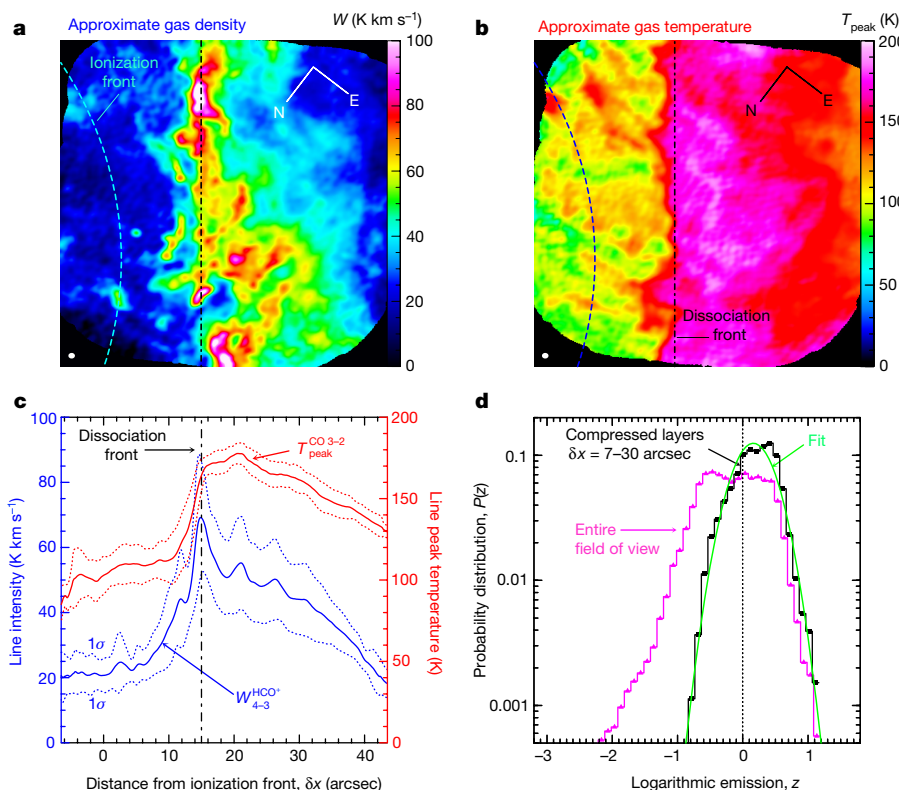


**Figure 2 | ALMA images of the Orion Bar.**

**a**, Integrated intensity of the  $\text{HCO}^+ J=4-3$  line. **b**,  $\text{CO } J=3-2$  line peak. Compared with Fig. 1, **a** and **b** have been rotated  $127.5^\circ$  anticlockwise to bring the incident ultraviolet radiation from the left (see Extended Data Fig. 1). The dashed curves and the vertical dot-dashed lines delineate the ionization and dissociation fronts, respectively<sup>1</sup>. **c**, Vertically averaged intensity cuts perpendicular to the Orion Bar in  $W_{\text{HCO}^+}^{4-3}$  (blue curve) and  $T_{\text{peak}}^{\text{CO } 3-2}$  (red curve). **d**, Probability distribution of  $W_{\text{HCO}^+}^{4-3}$  (proportional to the gas density) in the observed field (magenta triangles) and in the compressed layers (black squares).

the electrons are provided by the ionization of C atoms (thus  $x(e^-) \approx x(\text{C}^+) \approx 10^{-4}$ )<sup>14,16</sup>, the gas is mainly heated by collisions with energetic (about 1 eV) electrons photo-ejected from small grains and polycyclic aromatic hydrocarbons<sup>2,14</sup>. For the strong far-ultraviolet radiation flux impinging the Orion Bar<sup>3,5</sup>, which is approximately  $4.4 \times 10^4$  times the average flux in a local diffuse interstellar cloud<sup>16</sup>, a gas density  $n_{\text{H}} = n(\text{H}) + 2n(\text{H}_2)$  of  $(4-5) \times 10^4 \text{ cm}^{-3}$  in the atomic layer is consistent with the observed separation between the ionization and dissociation fronts<sup>3,4</sup>.

ALMA resolves the sharp edge where the  $\text{HCO}^+$  and CO emission becomes intense (Fig. 2). These layers spatially coincide with the brightest peaks of  $\text{H}_2$  vibrational emission ( $\text{H}_2^*$ ) tracing the  $\text{H}/\text{H}_2$  transition (Extended Data Fig. 2). Therefore, the  $\text{H}/\text{H}_2$  and the  $\text{C}^+/\text{C}/\text{CO}$  transition zones occur very close to each other. Static equilibrium models of a PDR with  $n_{\text{H}} = (4-5) \times 10^4 \text{ cm}^{-3}$  predict<sup>4,9,14</sup>, however, that the  $\text{C}^+/\text{CO}$  transition should occur deeper inside the molecular cloud because of the lower ionization potential of C atoms (11.3 eV) and because CO may not self-shield from photodissociation as effectively as  $\text{H}_2$ . The spatial coincidence of several  $\text{H}_2^*$  and  $\text{HCO}^+$  emission peaks shows that the formation of carbon molecules starts at the surface of the cloud (initiated by reactions of  $\text{C}^+$  with  $\text{H}_2$ ). This shifts the  $\text{C}^+/\text{CO}$  transition closer to the ionization front and suggests that dynamical effects are important<sup>17,18</sup>.

To zero order, the  $\text{CO } J=3-2$  (where  $J$  is the rotational quantum number) line intensity peak ( $T_{\text{peak}}^{\text{CO } 3-2}$  in K) is a measure of the gas temperature  $T$  in the molecular cloud ( $\delta x > 15''$  in Fig. 2c, where  $\delta x$  is the distance to the ionization front). The  $\text{HCO}^+ J=4-3$  integrated line intensity ( $W_{\text{HCO}^+}^{4-3}$  in  $\text{K km s}^{-1}$ ), however, scales with the gas density  $n_{\text{H}}$  (see Methods and Extended Data Fig. 3). Although the  $T_{\text{peak}}^{\text{CO } 3-2}$  image shows a relatively homogeneous temperature distribution, the  $W_{\text{HCO}^+}^{4-3}$  image shows small-scale structure (Fig. 2a, b). In particular, ALMA resolves several bright  $\text{HCO}^+$  emission peaks (filamentary substructures, some akin to globulettes) surrounding the dissociation front and roughly parallel to it. These substructures are surrounded by a lower-density gas component, with  $n_{\text{H}} \approx (0.5-1.0) \times 10^5 \text{ cm}^{-3}$ , producing an extended (ambient) emission<sup>4,5</sup>. The  $\text{HCO}^+$  substructures

(with a typical width of about  $2'' \approx 4 \times 10^{-3} \text{ pc}$ ) are located at the molecular cloud edge, and are different to the bigger ( $5''-10''$ ) condensations previously seen deeper inside the molecular cloud<sup>6,19</sup>.

To investigate the stratification of molecular emission inside the cloud, we constructed averaged emission cuts perpendicular to the Orion Bar. Three emission maxima are resolved in the  $W_{\text{HCO}^+}^{4-3}$  crosscuts at roughly periodic separations of about  $5''$  (approximately  $0.01 \text{ pc}$ ; Fig. 2c). Excitation models show that the average physical conditions that reproduce the mean CO and  $\text{HCO}^+$  intensities towards the dissociation front (at  $\delta x \approx 15''$ ) are  $T \approx 200-300 \text{ K}$  and  $n_{\text{H}} \approx (0.5-1.5) \times 10^6 \text{ cm}^{-3}$  (see Methods and Extended Data Fig. 3). Hence, the over-dense substructures have compression factors of about 5–30 with respect to the ambient gas component and are submitted to high thermal pressures ( $P/k = n_{\text{H}}T \approx 2 \times 10^8 \text{ K cm}^{-3}$ ). The three periodic maxima suggest that a high-pressure compression wave exists, and is moving into the molecular cloud. This wave may be associated with an enhanced magnetic field (several hundred microgauss; see Methods).

In the very early stages of an expansion of the  $\text{H II}$  region into molecular clouds, theory predicts that the ionization and dissociation fronts are co-spatial (an  $R$ -type front<sup>15,20</sup>). Soon after ( $t < 1,000 \text{ yr}$ ), the expansion slows down and the dissociation front propagates ahead of the ionization front and into the molecular cloud<sup>16,17</sup>. The ionization front changes to a  $D$ -type front (a compressive wave travels ahead of the ionization front<sup>16,20</sup> and the neutral gas becomes denser than the ionized gas). For a front advancing at a speed<sup>17,18</sup> of  $0.5-1.0 \text{ km s}^{-1}$ , the observed separation between the ionization and dissociation fronts in the Orion Bar implies a crossing time of 25,000–50,000 yr. Later in the expansion phase, when  $t$  is several times greater than the dynamical time  $t_{\text{dyn}}$  of the expanding  $\text{H II}$  region (the ratio of the initial radius of the  $\text{H II}$  region, the so-called the Strömgren radius, and  $c_{\text{H II}}$ ), the compressive wave slowly enters into the molecular cloud<sup>21,22</sup> ( $t_{\text{dyn}} \approx 0.2 \text{ pc per } 10 \text{ km s}^{-1} \approx 20,000 \text{ yr}$  for the Orion Bar). Observational evidence of such dynamical effects is scarce.

In the compressed layers suggested by ALMA (where  $\delta x$  is between  $7''$  and  $30''$  in Fig. 2a), the distribution of the gas densities follows a relatively narrow log-normal distribution (Fig. 2d). This is consistent



with magnetohydrodynamic simulations of non-gravitating turbulent clouds<sup>23,24</sup>. When the entire observed field is analysed, the shape of the distribution is closer to a double-peaked log-normal distribution. This resembles specific simulations in which the cloud compression is induced by the expansion of the ionized gas<sup>24,25</sup> (and not by a strong turbulence). Searching for further support for this scenario, we investigated the degree of turbulence and compared the different contributions of the gas pressure in the PDR (Extended Data Table 1). The inferred non-thermal (turbulent) velocity dispersion, about  $1 \text{ km s}^{-1}$ , results in a moderate Mach number of  $\leq 1$  (the ratio of the turbulent velocity dispersion to the local speed of sound)—that is, only a gentle level of turbulence. The thermal pressure exerted by the H II region at the H<sup>+</sup>/H interface<sup>1</sup> is several times higher than the turbulent and thermal pressures in the ambient molecular cloud. These pressure differences, together with the detection of over-dense substructures close to the cloud edge, agree with the ultraviolet radiation-driven compression scenario<sup>25,26</sup>. Whether these substructures could be the seeds of future star-forming clumps (for example, by merging into massive clumps) is uncertain<sup>22,27</sup>. Gravitational collapse is not apparent from their density distribution (no high-density power-law tail<sup>24,25</sup>). Indeed, their estimated masses (less than about  $0.005 M_{\odot}$ ; where  $M_{\odot}$  is the mass of the Sun) are much lower than the mass needed to make them gravitationally unstable. Even so, the increased ultraviolet shielding produced by the ridge of high-density substructures probably contributes to protecting the molecular cloud from photodestruction for longer periods.

The ALMA images also show CO emission ripples<sup>28</sup> along the surface of the molecular cloud (undulations separated by less than about  $5'' \approx 0.01 \text{ pc}$  in Fig. 2b), which are indicative of instabilities at the dissociation front. Such small-scale corrugations resemble the ‘thin-shell’ instability produced by the force imbalance between thermal (isotropic) and ram (parallel to the flow) pressures<sup>29</sup>. Characterizing these interface instabilities in detail would require new magnetohydrodynamic models that include mesh-resolutions that are well below the  $0.1\text{--}0.01 \text{ pc}$  scales achieved in current simulations<sup>25</sup> and include neutral gas thermochemistry.

Finally, ALMA reveals fainter HCO<sup>+</sup> and CO emission in the atomic layer (HCO<sup>+</sup> globulettes and plume-like CO features at  $\delta x < 15''$ , Fig. 2a, b). The dense gas HCO<sup>+</sup> emission structures must have survived the passage of the dissociation front<sup>30</sup>, whereas the CO plumes may trace either warm CO that reforms *in situ* in the atomic layer or molecular gas that advects or photoablates<sup>28</sup> from the surface of the molecular cloud. In the latter case, the pressure difference between the compressed molecular layers and the lower-density atomic layer would favour such a flow. Interestingly, molecular line profiles from the plumes typically show two velocity components, one of them identical to that of gas from inside the Orion Bar (Extended Data Fig. 4). This kinematic association supports the presence of photoablative flows through the atomic layer, and generally agrees with the suggested role of dynamical and non-equilibrium effects in ultraviolet-irradiated clouds.

**Online Content** Methods, along with any additional Extended Data display items and Source Data, are available in the online version of the paper; references unique to these sections appear only in the online paper.

**Received 13 February; accepted 8 June 2016.**

**Published online 10 August 2016.**

- Walmsley, C. M., Natta, A., Oliva, E. & Testi, L. The structure of the Orion Bar. *Astron. Astrophys.* **364**, 301–317 (2000).
- Tielens, A. G. G. M. & Hollenbach, D. J. Photodissociation regions. I: basic model. *Astrophys. J.* **291**, 722–754 (1985).
- Andree-Labsch, S., Ossenkopf, V. & Röllig, M. 3D modelling of clumpy PDRs: understanding the Orion Bar stratification. Preprint at <http://arxiv.org/abs/1405.5553> (2014).
- Tielens, A. G. G. M. *et al.* Anatomy of the photodissociation region in the Orion Bar. *Science* **262**, 86–89 (1993).
- Hogerheijde, M. R., Jansen, D. J. & van Dishoeck, E. F. Millimeter and submillimeter observations of the Orion Bar. I: physical structure. *Astron. Astrophys.* **294**, 792–810 (1995).

- Young Owl, R. C., Meixner, M. M., Wolfire, M., Tielens, A. G. G. M. & Tauber, J. HCN and HCO<sup>+</sup> images of the Orion Bar photodissociation region. *Astrophys. J.* **540**, 886–906 (2000).
- Sternberg, A. & Dalgarno, A. Chemistry in dense photon-dominated regions. *Astrophys. J. Suppl. Ser.* **99**, 565–607 (1995).
- Le Petit, F., Nehmé, C., Le Bourlot, J. & Roueff, E. A model for atomic and molecular interstellar gas: The Meudon PDR code. *Astrophys. J. Suppl. Ser.* **164**, 506–529 (2006).
- Röllig, M. *et al.* A photon dominated region code comparison study. *Astron. Astrophys.* **467**, 187–206 (2007).
- Genzel, R. & Stutzki, J. The Orion molecular cloud and star-forming region. *Annu. Rev. Astron. Astrophys.* **27**, 41–85 (1989).
- Goicoechea, J. R. *et al.* Velocity-resolved [CII] emission and [CII]/FIR mapping along Orion with Herschel. *Astrophys. J.* **812**, 75 (2015).
- O'Dell, C. R. The Orion Nebula and its associated population. *Annu. Rev. Astron. Astrophys.* **39**, 99–136 (2001).
- van der Werf, P. P., Goss, W. M. & O'Dell, C. R. Tearing the veil: interaction of the Orion Nebula with its neutral environment. *Astrophys. J.* **762**, 101 (2013).
- Hollenbach, D. J. & Tielens, A. G. G. M. Photodissociation regions in the interstellar medium of galaxies. *Rev. Mod. Phys.* **71**, 173–230 (1999).
- Weilbacher, P. M. *et al.* A MUSE map of the central Orion Nebula (M 42). *Astron. Astrophys.* **582**, A114 (2015).
- Draine, B. T. *Physics of the Interstellar and Intergalactic Medium* (Princeton Univ. Press, 2011).
- Bertoldi, F. & Draine, B. T. Nonequilibrium photodissociation regions: ionization-dissociation fronts. *Astrophys. J.* **458**, 222–232 (1996).
- Störzer, H. & Hollenbach, D. J. Nonequilibrium photodissociation regions with advancing ionization fronts. *Astrophys. J.* **495**, 853–870 (1998).
- Lis, D. C. & Schilke, P. Dense molecular clumps in the Orion Bar photon-dominated region. *Astrophys. J.* **597**, L145–L148 (2003).
- Spitzer, L. *Physical Processes in the Interstellar Medium* (Wiley, 1978).
- Hill, J. K. & Hollenbach, D. J. Effects of expanding compact H II regions upon molecular clouds: molecular dissociation waves, shock waves, and carbon ionization. *Astrophys. J.* **225**, 390–404 (1978).
- Hosokawa, T. & Inutsuka, S.-i. Dynamical expansion of ionization and dissociation front around a massive star. II: on the generality of triggered star formation. *Astrophys. J.* **646**, 240–257 (2006).
- Hennebelle, P. & Falgarone, E. Turbulent molecular clouds. *Astron. Astrophys. Rev.* **20**, 55 (2012).
- Federrath, C. & Klessen, R. S. On the star formation efficiency of turbulent magnetized clouds. *Astrophys. J.* **763**, 51 (2013).
- Tremblin, P., Audit, E., Minier, V., Schmidt, W. & Schneider, N. Three-dimensional simulations of globule and pillar formation around H II regions: turbulence and shock curvature. *Astron. Astrophys.* **546**, A33 (2012).
- Gorti, U. & Hollenbach, D. J. Photoevaporation of clumps in photodissociation regions. *Astrophys. J.* **573**, 215–237 (2002).
- Elmegreen, B. G. & Lada, C. J. Sequential formation of subgroups in OB associations. *Astrophys. J.* **214**, 725–741 (1977).
- Berné, O., Marcelino, N. & Cernicharo, J. Waves on the surface of the Orion molecular cloud. *Nature* **466**, 947–949 (2010).
- García-Segura, G. & Franco, J. From ultracompact to extended H II regions. *Astrophys. J.* **469**, 171–188 (1996).
- Lefloch, B. & Lazareff, B. Cometary globules. I: formation, evolution and morphology. *Astron. Astrophys.* **289**, 559–578 (1994).

**Acknowledgements** We thank the ERC for support under grant ERC-2013-Syg-610256-NANOCOSMOS. We also thank MINECO, Spain, for funding support under grants CSD2009-00038 and AY2012-32032. This work was in part supported by the French CNRS programme ‘Physique et Chimie du Milieu Interstellaire’. We thank P. Schilke and D. Lis for sharing their IRAM-PdBI observations of the H<sup>13</sup>CN  $J=1\text{--}0$  condensations inside the Orion Bar, and M. Walmsley for sharing his H<sub>2</sub>  $v=1\text{--}0$  S(1) and O I  $1.3 \mu\text{m}$  infrared images. ALMA is a partnership of the ESO (representing its member states), the NSF (USA) and NINS (Japan), together with the NRC (Canada), the NSC and ASIAA (Taiwan) and KASI (Republic of Korea) in cooperation with the Republic of Chile. The Joint ALMA Observatory is operated by the ESO, the AUI/NRAO and the NAJO. This Letter makes use of observations obtained with the IRAM 30 m telescope. IRAM is supported by the INSU/CNRS (France), the MPG (Germany), and the IGN (Spain).

**Author Contributions** J.R.G. was the principal investigator of the ALMA project. He led the scientific analysis, modelling and wrote the manuscript. J.P. and E.C. carried out the ALMA data calibration and data reduction. S.C. and N.M. carried out the single-dish maps observations with the IRAM 30 m telescope. All authors participated in the discussion of results, determination of the conclusions and revision of the manuscript.

**Author Information** We used the ALMA data ADS/JAO.ALMA#2012.1.00352.S available at [https://almascience.eso.org/aq/?project\\_code=2012.1.00352.S](https://almascience.eso.org/aq/?project_code=2012.1.00352.S). Reprints and permissions information is available at [www.nature.com/reprints](http://www.nature.com/reprints). The authors declare no competing financial interests. Readers are welcome to comment on the online version of the paper. Correspondence and requests for materials should be addressed to J.R.G. ([jrgoicoechea@icmm.csic.es](mailto:jrgoicoechea@icmm.csic.es)).

**Reviewer Information** Nature thanks R. Plume and the other anonymous reviewer(s) for their contribution to the peer review of this work.

## METHODS

**ALMA interferometric and IRAM 30-m single-dish observations.** ALMA Cycle-1 observations of the Orion Bar were carried out using 27 12 m antennae in band 7 at 345.796 GHz (CO  $J=3-2$ ) and 356.734 GHz (HCO<sup>+</sup>  $J=4-3$ ). The observations consisted of a 27-pointing (the array points to 27 different positions to cover the field) mosaic centred at right ascension  $\alpha(2000) = 5^{\text{h}} 35^{\text{m}} 20.6^{\text{s}}$ ; declination  $\delta(2000) = -05^{\circ} 25' 20''$ . The total field-of-view is  $58'' \times 52''$ . Baseline configurations from about 12 m to about 444 m were used (C32-3 antennae configuration). Lines were observed with correlators providing a resolution of approximately 500 kHz ( $\delta\nu \approx 0.4 \text{ km s}^{-1}$ ) over a 937.5 MHz bandwidth. The total observation time on the ALMA 12 m array was around 2 h. ALMA executing blocks were first calibrated in the CASA software (version 4.2.0) and then exported to GILDAS. To recover the large-scale extended emission filtered out by the interferometer, we used fully sampled single-dish maps as ‘zero-’ and ‘short-spacings’. Maps were obtained with the IRAM 30 m telescope (Pico Veleta, Spain) using the EMIR330 receiver under excellent winter conditions ( $<1 \text{ mm}$  of precipitable water vapour). On-the-fly scans of a  $170'' \times 170''$  region were obtained both along and perpendicular to the Orion Bar. The beam full-width at half-maximum power (FWHM) at 350 GHz is about  $7''$ . The GILDAS/MAPPING software was used to create the short-spacing visibilities<sup>31</sup> not sampled by ALMA. These visibilities were merged with the interferometric observations. Each mosaic field was imaged and a dirty mosaic was built. The dirty image was deconvolved using the standard Högbom CLEAN algorithm and the resulting cubes were scaled from Jansky per beam to a brightness temperature scale using the synthesized beam size of about  $1''$ . This resolution is a factor of approximately 9 higher than previous interferometric observations of the HCO<sup>+</sup>  $J=1-0$  line towards the Orion Bar<sup>6</sup>. The achieved root mean squared noise is about  $0.4 \text{ K per } 0.4 \text{ km s}^{-1}$  channel, with an absolute flux accuracy of about 10%. The resulting images are shown in Figs 1b and 2 and in Extended Data Fig. 2. Finally, the large-scale HCO<sup>+</sup>  $J=3-2$  (267.558 GHz) on-the-fly map shown in Fig. 1a was taken with the multi-beam receiver HERA, also at the IRAM 30 m telescope. The spectral and angular resolutions are approximately  $0.4 \text{ km s}^{-1}$  and  $9''$  (FWHM) respectively. The final images were generated using the GILDAS/GREG software.

**Saturation and extinction corrections for the near-infrared image.** To better understand the spatial distribution of the H<sub>2</sub>  $\nu=1-0$  S(1) line emission at  $\lambda=2.12 \mu\text{m}$  (H<sub>2</sub><sup>\*</sup>) presented in ref. 1 and shown in Extended Data Fig. 2, we note two effects that determine the resulting emission morphology. First, there is a bright star in the line of sight towards the Orion Bar ( $\Theta^2\text{A Ori}$  at  $\alpha(2000) = 5^{\text{h}} 35^{\text{m}} 22.9^{\text{s}}$ ;  $\delta(2000) = -05^{\circ} 24' 57.8''$ ) that saturates the near-infrared detectors in a slit of width approximately  $4''$  parallel to the Orion Bar (roughly between  $\delta x = 19''$  and  $23''$  in our rotated images). Hence, no H<sub>2</sub><sup>\*</sup> data are shown in this range. Therefore, the layers with H<sub>2</sub> vibrational emission are wider than suggested by Extended Data Fig. 2, and more H<sub>2</sub><sup>\*</sup> emission peaks may coincide with HCO<sup>+</sup> peaks in the blanked  $\delta x = 19''$ – $23''$  region. Older, near-infrared images with lower angular and spectral resolutions do show<sup>32</sup> that the H<sub>2</sub><sup>\*</sup> emission extends out to  $\delta x \approx 20''$ . Second, dust extinction (due to foreground dust in Orion’s Veil and also due to dust in the Orion Bar itself) may affect the apparent morphology of the near-infrared images. Such effects are often neglected<sup>1,32,33</sup> and are not included in Extended Data Fig. 2. The extinction towards the Orion Bar produced by the Veil is not greater than about 2 mag (ref. 34). Adopting a dust reddening appropriate to Orion<sup>11,35</sup>,  $R_V = A_V/E(B-V) = 5.5$ , and the  $A_K/A_V$  (where  $B$  and  $V$  stand for the blue and visible photometric filters at 4,400 and 5,500 Å respectively,  $A_V$  and  $A_K$  are the extinctions in the visible and in the K filter at  $2.2 \mu\text{m}$ ,  $E(B-V) = A_B - A_V$  is the reddening factor, and  $R_V$  is a dimensionless parameter that characterizes the slope of the extinction curve) value in ref. 35, we estimate that the H<sub>2</sub><sup>\*</sup> emission lines would only be approximately 30% brighter if foreground extinction corrections are taken into account. An additional magnitude of extinction due to dust in the atomic layer of the Bar itself results in a line intensity increase of about 50%. Therefore, minor morphological differences between the near-infrared and millimetre-wave images could reflect a small-scale or patchy extinction differences in the region<sup>1</sup>.

**Excitation and radiative transfer models for CO and HCO<sup>+</sup>.** To estimate the physical conditions of the HCO<sup>+</sup>-emitting gas near the dissociation front we run a grid of nonlocal, non-local thermodynamic equilibrium excitation and radiative transfer (Monte Carlo) models. This approach allows us to explore different column densities, gas temperatures and densities. Compared with most PDR models (using local escape probability approximations) our models take radiative pumping, line trapping and opacity broadening into account. This allows for the treatment of optically thick lines (see the appendix in ref. 36 for code details and benchmarking tests). Our models use the most recent inelastic collisional rates of HCO<sup>+</sup> with H<sub>2</sub> and with electrons, and of CO with both H<sub>2</sub> and H. The electron density,  $n_e$ , is an important factor in the collisional excitation of molecular cations in a far-ultraviolet-illuminated gas. For HCO<sup>+</sup>, collisions with electrons start to

contribute above  $n_e > 10 \text{ cm}^{-3}$  (or  $n_H > 10^5 \text{ cm}^{-3}$  if most of the electrons are provided by carbon atom ionization). In PDRs, collisions of molecules with H atoms can also contribute because the molecular gas fraction,  $f = 2n(\text{H}_2)/n_H = 2n(\text{H}_2)/[n(\text{H}) + 2n(\text{H}_2)]$ , is not 1 (a fully molecular gas). We adopted  $f = 0.8$  and varied  $x_e$  between 0 and  $10^{-4}$ . The H<sub>2</sub> ortho-to-para ratio was computed for each gas temperature  $T$ . Radiative excitation by the cosmic microwave background ( $T_{\text{CMB}} = 2.7 \text{ K}$ ) and by the far-infrared dust continuum in the Orion Bar<sup>37</sup> (simulated by optically thin thermal emission at  $T_{\text{dust}} = 55 \text{ K}$ ) were also included.

Column densities of  $N(\text{HCO}^+) = (5 \pm 1) \times 10^{13} \text{ cm}^{-2}$  and  $N(\text{CO}) = (1.0 \pm 0.5) \times 10^{18} \text{ cm}^{-2}$  were estimated using information from our IRAM 30-m telescope line-survey towards the dissociation front<sup>38</sup>. Several HCO<sup>+</sup>, H<sup>13</sup>CO<sup>+</sup>, HC<sup>18</sup>O<sup>+</sup> and C<sup>18</sup>O rotational lines were included in the estimation (the quoted dispersions in the column densities reflect the uncertainty obtained from least square fits to rotational population diagrams). They are consistent with previous observations in the region<sup>5,6</sup>. Radiative transfer models were run for  $N(\text{HCO}^+) = 5 \times 10^{13} \text{ cm}^{-2}$ ,  $N(\text{CO}) = 1.0 \times 10^{18} \text{ cm}^{-2}$ , and  $N_H = N(\text{H}) + 2N(\text{H}_2) \approx 2 \times 10^{22} \text{ cm}^{-2}$  (equivalent to  $A_V \approx 7 \text{ mag}$  for the dust properties in Orion). This results in  $x(\text{HCO}^+) \approx (2-3) \times 10^{-9}$  and  $x(\text{CO}) \approx (2.5-7.5) \times 10^{-5}$  abundances. In addition, the HCO<sup>+</sup>/H<sup>13</sup>CO<sup>+</sup> column density ratios derived from single-dish observations are similar to the  $^{12}\text{C}/^{13}\text{C} = 67$  isotopic ratio in Orion<sup>39</sup>. Thus, the H<sup>12</sup>CO<sup>+</sup> lines are not very opaque ( $\tau_{\text{line}} \approx 2$ ) otherwise the observed HCO<sup>+</sup>/H<sup>13</sup>CO<sup>+</sup> line intensity ratios would be considerably smaller. A non-thermal (turbulent) velocity dispersion ( $\sigma_{\text{nth}}$ ) of about  $1 \text{ km s}^{-1}$  reproduces the observed line widths. A similar value,  $1.0$ – $1.5 \text{ km s}^{-1}$ , is inferred directly from the observed line profiles ( $\sigma_{\text{nth}}^2 = \sigma_{\text{obs}}^2 - \sigma(T)_{\text{th}}^2$ , with  $\Delta\nu_{\text{FWHM}} = 2\sqrt{2\ln 2} \times \sigma_{\text{obs}} \approx 3.0 \pm 0.5 \text{ km s}^{-1}$  and  $T = 300 \text{ K}$ ). Hence, opacity broadening plays a minor role. The dispersion  $\sigma_{\text{nth}}$  is similar or lower than the local speed of sound at  $T = 100$ – $300 \text{ K}$  ( $c_{\text{PDR}} = (k_B T/m)^{1/2} = 1.0$ – $1.7 \text{ km s}^{-1}$ , where  $m$  is the mean mass per particle and  $k_B$  is the Boltzmann constant). This results in moderate Mach numbers  $M = \sigma_{\text{nth}}/c_{\text{PDR}} \leq 1$ .

Extended Data Fig. 3 shows model predictions for the CO  $J=3-2$  line intensity peak,  $T_{\text{peak}}^{\text{CO}3-2}$  (upper left panel), and HCO<sup>+</sup>  $J=4-3$  line integrated intensity,  $W_{4-3}^{\text{HCO}^+} = \int T_B dv$  (where  $T_B$  is the line brightness temperature) ( $\text{K km s}^{-1}$ ), for different  $T$  and  $n_H$  values. For optically thick lines ( $\tau_{\text{line}} \gg 1$ ),  $T_{\text{peak}}^{\text{CO}3-2}$  provides a good measure of the excitation temperature, with  $T_{\text{peak}} \approx J(T_{\text{ex}}) = E_{\text{up}}/k_B \times$

$\left[ \exp\left(\frac{E_{\text{up}}}{k_B T_{\text{ex}}}\right) - 1 \right]^{-1}$  (where  $T_{\text{ex}}$  is the excitation temperature of the transition and  $E_{\text{up}}$  is the upper level energy). In addition, for low-critical-density ( $n_{\text{cr}}$ ) transitions such as the low- $J$  CO transitions, the lines are close to thermalization at densities above about  $10^4 \text{ cm}^{-3}$ , thus  $T_{\text{ex}} \rightarrow T$  (with  $n_{\text{cr}} \equiv A_{ij}/\gamma_{ij}$ , where  $A_{ij}$  is the Einstein coefficient for spontaneous emission and  $\gamma_{ij}$  is the coefficient of the collisional de-excitation rate). In this case,  $T_{\text{peak}}^{\text{CO}3-2}$  is a good thermometer of the  $\tau_{\text{CO}3-2} \gg 1$  emitting layers. The HCO<sup>+</sup>  $J=4-3$  line, however, has much higher critical densities ( $n_{\text{cr,H}_2} > 5 \times 10^6 \text{ cm}^{-3}$  and  $n_{\text{cr,e}} \approx 10^3 \text{ cm}^{-3}$ ). For  $n_H < 2n_{\text{cr,H}_2}/\tau_{\text{line}}$  (sub-thermal excitation), the integrated line intensity  $W_{4-3}^{\text{HCO}^+}$  is approximately linearly proportional to  $N(\text{HCO}^+) = x(\text{HCO}^+)n_H l$  (where  $l$  is the cloud length along the line of sight) even if the line is moderately thick. PDR models<sup>6,7</sup> and CO observations respectively show that  $x(\text{HCO}^+)$  and  $T$  do not change substantially in the PDR layers around the H<sub>2</sub><sup>\*</sup> emission peaks (cloud depths between  $A_V \approx 1$  and 2 mag). In a nearly edge-on PDR, the spatial length along the line of sight does not change greatly either. We compute that for the inferred  $T$  and  $N(\text{HCO}^+)$  values in the region, the integrated line intensity  $W_{4-3}^{\text{HCO}^+}$  is proportional to the density in the  $n_H = 10^4$ – $10^6 \text{ cm}^{-3}$  range (the correlation coefficient is  $r \approx 0.98$  for models with  $x_e = 0$  and  $x_e = 10^{-4}$ ). Moreover,  $W_{4-3}^{\text{HCO}^+}$  still increases with a density of up to several  $10^6 \text{ cm}^{-3}$  ( $r \approx 0.94$ ). This reasoning justifies the use of  $W_{4-3}^{\text{HCO}^+}$  as a proxy for  $n_H$  in the region.

**Average physical conditions in the compressed structures.** The physical conditions that reproduce the mean CO  $J=3-2$  line peak and HCO<sup>+</sup>  $J=4-3$  integrated line intensity towards the compressed structures at  $\delta x \approx 15''$  ( $T_{\text{peak}}^{\text{CO}3-2} = 164 \pm 10 \text{ K}$  and  $W_{4-3}^{\text{HCO}^+} = 69 \pm 18 \text{ K km s}^{-1}$ ) are  $T = 200$ – $300 \text{ K}$  and  $n_H = (1.0 \pm 0.5) \times 10^6 \text{ cm}^{-3}$  (Extended Data Fig. 3). This implies high thermal pressures,  $P_{\text{th,comp}}/k = n_H T \approx (1.0$ – $4.5) \times 10^8 \text{ K cm}^{-3}$  (where  $P_{\text{th,comp}}$  is the pressure in the compressed gas component). The brightest HCO<sup>+</sup> emission peaks (with  $W_{4-3}^{\text{HCO}^+} \approx 100 \text{ K km s}^{-1}$ , Fig. 2a) probably correspond to specific gas density enhancements. For the range of column densities and physical conditions at  $\delta x \approx 15''$ , the gas temperature uncertainty is determined by the lack of higher- $J$  CO lines, observed at high angular resolution, to better constrain  $T$  from excitation models. The range of estimated gas densities is dominated by the dispersion (about 25%) of the mean  $W_{4-3}^{\text{HCO}^+}$  value.

The above physical conditions suggest that the cloud edge contains substructures that are denser than the atomic layer<sup>3,4</sup> ( $n_H = (4$ – $5) \times 10^4 \text{ cm}^{-3}$ ) and denser than the ambient molecular cloud<sup>5</sup> ( $n_H = (0.5$ – $1.0) \times 10^5 \text{ cm}^{-3}$ ). The equivalent



length of the substructures is small,  $l = N_{\text{H}}/n_{\text{H}} \approx (4-12) \times 10^{-3}$  pc (where  $N_{\text{H}}$  is the total column density of hydrogen nuclei along the line of sight) (about  $2''-6''$  at the distance to Orion, thus consistent with their apparent size in the ALMA image). The mass of a cylinder with  $n_{\text{H}}$  of a few  $10^6 \text{ cm}^{-3}$ ,  $2''-6''$  length and width of  $2''$  is  $\lesssim 0.005 M_{\odot}$  (that is, a mass per unit length of  $(0.3-1.0) M_{\odot} \text{ pc}^{-1}$ ). This is much lower than the virial and critical masses<sup>40</sup> needed to make them gravitationally unstable (approximately  $5 M_{\odot}$ , from the inferred gas temperature, density and velocity dispersion).  $\text{H}_2$  clumps of similar small masses (several  $0.001 M_{\odot}$ ) have been intuited towards the boundary of more evolved and distant H II regions<sup>41</sup>. Compression and fragmentation of ultraviolet-irradiated cloud edges must be a common phenomenon in the vicinity of young massive stars.

**Physical conditions in the ambient molecular cloud.** Deeper inside the molecular cloud,  $T_{\text{peak}}^{\text{CO}3-2}$  smoothly decreases from about 170 K to about 130 K. Therefore, these observations do not suggest temperature spikes at scales of a few arcseconds. Deeper inside the molecular cloud ( $\delta x > 30''$  in our rotated images), both  $N(\text{H}_2)$  and  $N(\text{HCO}^+)$  are expected to gradually increase<sup>5,6,7,37</sup>. For the expected  $N(\text{HCO}^+) \approx 2 \times 10^{14} \text{ cm}^{-2}$  column density<sup>5,6</sup>, excitation models show that the gas density in the ambient cloud is  $n_{\text{H}} \approx (0.5-1.0) \times 10^5 \text{ cm}^{-3}$  (dashed curves in Extended Data Fig. 3), in agreement with previous estimations<sup>2,5</sup>. Hence, the over-dense substructures have compression factors of approximately 5–30 with respect to the ambient molecular gas.

**Physical conditions in the atomic layer.** The decrease of both  $T_{\text{peak}}^{\text{CO}3-2}$  and  $W_{4-3}^{\text{HCO}^+}$  between the ionization and dissociation fronts is consistent with the expected sharp decrease of CO and  $\text{HCO}^+$  abundances in the atomic layer. The representative gas density in the atomic layer,  $n_{\text{H}} \approx (4-5) \times 10^4 \text{ cm}^{-3}$ , is constrained by the strength of the unattenuated far-ultraviolet flux at the Bar edge<sup>3,5</sup> ( $\chi \approx 4.4 \times 10^4$ , determined by the spectral type of the Trapezium stars) and by the current position of the dissociation front at  $\delta x \approx 15''$  (refs 1 and 33). The exact gas density value, however, depends on the assumed far-ultraviolet-extinction grain properties (which probably vary as function of cloud depth). In the context of stationary PDR models, larger-than-standard-size grains (lower far-ultraviolet absorption cross-sections) are often invoked<sup>33</sup>, otherwise the separation between the dissociation and ionization fronts would be smaller than the observed around  $15''$ . The lower densities in the atomic layer agree with the observed low  $\text{H}_2 v=1-0 \text{ S}(1)/v=2-1 \text{ S}(1) \approx 3$  line intensity ratio attributed to fluorescent  $\text{H}_2^*$  excitation<sup>32,42</sup>. We note that optically thin CO emission implies  $T_{\text{peak}}^{\text{CO}3-2} \ll T_{\text{ex}}$ . Hence,  $T_{\text{peak}}^{\text{CO}3-2}$  can no longer be used as a gas thermometer in the atomic layer where the CO abundance is low. The gas temperature close to the dissociation front is between  $T \approx 500$  K (from H I observations<sup>13</sup>) and  $T \approx 300$  K (from carbon radiorecombination<sup>43</sup> and [C II]  $158 \mu\text{m}$  (ref. 11) line observations).

**Emission probability distribution functions (PDF).** To study the distribution of gas densities in the region, approximated by the  $\text{HCO}^+ J=4-3$  emission, we analysed the probability distribution of the logarithmic emission, given by

$$z = \ln \left( W_{4-3}^{\text{HCO}^+} / \langle W_{4-3}^{\text{HCO}^+} \rangle \right), \text{ where } \langle W_{4-3}^{\text{HCO}^+} \rangle = \int T_{\text{B}} d\nu$$

observed field-of-view ( $37 \text{ K km s}^{-1}$ ). This is a common approach used to interpret (column) density maps, both from observations and MHD simulations<sup>24,44</sup>. The PDF is computed as the number of pixels (in the high signal-to-noise  $W_{4-3}^{\text{HCO}^+}$  image) per intensity bin divided by the total number of pixels. We first analysed the complete field-of-view observed by ALMA and selected  $W_{4-3}^{\text{HCO}^+}$  measurements above  $5\sigma$ , where we define  $\sigma = \text{rms}(2\delta\nu\Delta\nu_{\text{FWHM}})^{1/2}$ , with  $\delta\nu = 0.4 \text{ km s}^{-1}$  and  $\Delta\nu_{\text{FWHM}} = 3.0 \text{ km s}^{-1}$ . The resulting PDF is shown in Fig. 2d (magenta points). Second, we selected measurements only in the compressed layers region between  $\delta x = 7''$  and  $30''$  (with respect to the rotated images in Fig. 2). The resulting PDF (black points) is very close to a log-normal distribution with  $p(z) = \text{Nexp}(-(z - z_0)^2 / 2\sigma^2)$ , where  $z_0$  is the peak value and  $\sigma$  the standard deviation. We obtain  $z_0 = 0.165$  and  $\sigma = 0.31$  from a fit (green curve). If  $W_{4-3}^{\text{HCO}^+}$  is proportional to the gas density, these values imply that 99% of the observed positions in the compressed layers span a factor of about 6 in density. In MHD models,  $\sigma$  is a measure of how density varies in a turbulent cloud. Hence, it depends on the Mach number, the ratio of the thermal to magnetic pressure ( $\beta$ ) and the forcing characteristics of the turbulence<sup>24</sup>. The relatively modest  $\sigma$  value inferred in the  $\delta x = 7''-30''$  layer is consistent with the low Mach numbers in the PDR, and suggests an important role of magnetic pressure. We note that a similar analysis of the CO emission does not yield the same log-normal distribution. This is consistent with low- $J$  CO lines being optically thick and tracing gas temperatures rather than gas density variations. This reinforces that the log-normal shape of the  $W_{4-3}^{\text{HCO}^+}$  PDF in the compressed layer is a relevant observational result.

**Gas pressures, magnetic field and compression.** To support the cloud compression and gas photoablation scenario, we investigated the different contributions to the gas pressure in the region. The thermal pressure in the H II region near the ionization front<sup>1</sup> is  $P_{\text{th,H II}}/k = 2n_{\text{e}}T_{\text{e}} \approx 6 \times 10^7 \text{ K cm}^{-3}$ , about six times higher than

the turbulent ram pressure  $P_{\text{ram,amb}} = \rho\sigma_{\text{nth,amb}}^2$  in the ambient molecular cloud (Extended Data Table 1). As we find similar contributions from the thermal and non-thermal (turbulent) pressures in both the ambient cloud and the over-dense substructures ( $\alpha = P_{\text{nth,amb}}/P_{\text{th,amb}} \approx P_{\text{nth,comp}}/P_{\text{th,comp}} \approx 1$ ), it is reasonable to assume equipartition of thermal, turbulent and magnetic energies to quantify the magnetic pressure in the PDR ( $P_{\text{B}} = B^2/8\pi$ ). In particular, for  $\beta = P_{\text{B}}/P_{\text{th}} = 1$  we estimate the magnetic field strengths  $B$  to be  $200 \mu\text{G}$  and  $800 \mu\text{G}$  in the ambient and in the high-density substructures, respectively. Such strong magnetic fields at small scales need to be confirmed observationally (both the strength and the orientation) but seem consistent with the high values (approximately  $100 \mu\text{G}$ ) measured in the low-density foreground material<sup>45</sup> (the Orion Veil) confirming that  $B$  is particularly strong in the Orion complex. On much larger spatial scales, low-angular-resolution observations do suggest that  $B$  increases with density at H II/cloud boundaries ( $B \propto n_{\text{H}}^{0.5-1}$ ) (ref. 46).

A strong magnetic field would be associated with large magnetosonic speeds ( $v_{\text{ms}}$ ) in the PDR. If an ultraviolet radiation-driven shockwave is responsible for the molecular gas compression, its velocity is predicted to slow down to  $v_{\text{s}} \approx 3 \text{ km s}^{-1}$  once it enters the molecular cloud<sup>21</sup>. In such a slow, magnetized shock ( $v_{\text{s}} \ll v_{\text{ms}}$ ), compression waves can travel ahead of the shock front<sup>47</sup>. Thus, a high magnetic field strength may be related to the  $W_{4-3}^{\text{HCO}^+}$  undulations seen perpendicular to the Orion Bar (Fig. 2c). The inferred compression factor in the observed substructures ( $f = n_{\text{comp}}/n_{\text{amb}} = 5-30$ ) is consistent with slow shock velocities<sup>16</sup>,  $v_{\text{s}} = c_0 f^{0.5} \approx 1.5-4.0 \text{ km s}^{-1}$ , where  $c_0$  is the initial sound speed of the unperturbed molecular gas. The necessarily small  $v_{\text{s}}$  agrees with the relatively narrow molecular line-profiles ( $\Delta\nu_{\text{FWHM}} \lesssim 4 \text{ km s}^{-1}$ ) seen in PDRs<sup>14</sup> (including observations of face-on sources in which the shock would propagate in the line of sight). Owing to the high thermal pressure in the compressed structures, we also find that a pressure gradient, with  $P_{\text{th,comp}} \geq P_{\text{th,H II}}$  exists. This subtle effect is seen in simulations of an advancing shockwave around an H II region<sup>22,48</sup>.

**Molecular gas between the ionization and dissociation fronts.** ALMA reveals fainter  $\text{HCO}^+$  and CO emission in the atomic layer ( $\text{HCO}^+$  globulettes and plume-like CO features at  $\delta x < 15''$ , Fig. 2). Previous low-angular-resolution observations and models had suggested the presence of dense spherical clumps with sizes of  $5''-10''$  deeper inside the molecular cloud<sup>6,19</sup> (at  $\geq 15''-20''$  from the ionization front<sup>3,6,32</sup>). The dense substructures resolved by ALMA are smaller ( $\sim 2'' \times 4''$ ) and are detected at  $\delta x \geq 7''$  (even before the peak of the  $\text{H}_2$  vibrational emission).

The molecular line profiles towards the plumes typically show two velocity emission components (Extended Data Fig. 4): one centred at  $v_{\text{LSR}} \approx 8.5 \text{ km s}^{-1}$  (where  $v_{\text{LSR}}$  refers to the emission velocity with respect to the local standard of rest), the velocity of the background molecular cloud in the back-side of M 42 (ref. 11; not directly associated with the Orion Bar), and other at  $v_{\text{LSR}} \approx 11 \text{ km s}^{-1}$ , the velocity component of the molecular gas in the Orion Bar. In addition, despite the small size of the observed region, the crosscuts of the  $\text{HCO}^+ J=4-3$  line velocity centroid and of the FWHM velocity dispersion show gradients perpendicular to the Orion Bar (Extended Data Fig. 4). Moving from the ionization front to the molecular gas, the line centroid shifts to higher velocities (gas compression effects may, in part, contribute to this redshifted velocity). The velocity dispersion, however, shows its maximum between the ionization and the dissociation fronts, the expected layers for photoablative neutral gas flows. Both the kinematic association with the Orion Bar velocities and the higher velocity dispersion between the two fronts are consistent with the presence of gas flowing from the high-pressure compressed molecular layers ( $P_{\text{th,comp}}/k \approx 2 \times 10^8 \text{ K cm}^{-3}$ ) to the atomic layers ( $P_{\text{th,atomic}}/k \approx 5 \times 10^7 \text{ K cm}^{-3}$ ).

**$\text{HCO}^+$  chemistry and the  $\text{C}^+/\text{CO}$  transition zone.** Static equilibrium PDR models<sup>6</sup> appropriate to the ambient gas component ( $n_{\text{H}} \approx 5 \times 10^4 \text{ cm}^{-3}$ ) reproduce the separation between the ionization and dissociation fronts. However, they predict  $\text{HCO}^+$  abundances near the dissociation front that are too low ( $x(\text{HCO}^+)$  of a few  $5 \times 10^{-11}$ ) to be consistent with the bright ridge of  $\text{HCO}^+$  emission detected by ALMA. These models also predict that the  $\text{C}^+/\text{CO}$  transition should occur ahead of the H/ $\text{H}_2$  transition zone and deeper inside the molecular cloud (at  $\delta x \approx 20''$  from the ionization front<sup>3,4</sup>). However, our detection of bright CO and  $\text{HCO}^+$  emission towards the layers of bright  $\text{H}_2$  vibrational emission<sup>1</sup> implies that the  $\text{C}^+/\text{CO}$  transition occurs closer to the cloud edge, and nearly coincides with the H/ $\text{H}_2$  transition (at least it cannot be resolved at the approximately  $1''$  resolution of our observations). This is probably another signature of dynamical effects. Indeed, the presence of molecular gas near the cloud edge<sup>49</sup>, and a reduced  $\text{C}^+$  abundance deeper inside the molecular cloud<sup>50</sup>, may explain model and observation discrepancies of other chemically related molecules.

As an example, stationary PDR models applied to the fluorine chemistry<sup>51</sup> overestimate the  $\text{CF}^+$  column density observed towards the Orion Bar<sup>52</sup> by a factor of about 10. Given that HF readily forms as F atoms react with  $\text{H}_2$  molecules,  $\text{CF}^+$  must arise from layers where  $\text{C}^+$  and  $\text{H}_2$  overlap ( $\text{CF}^+$  forms through



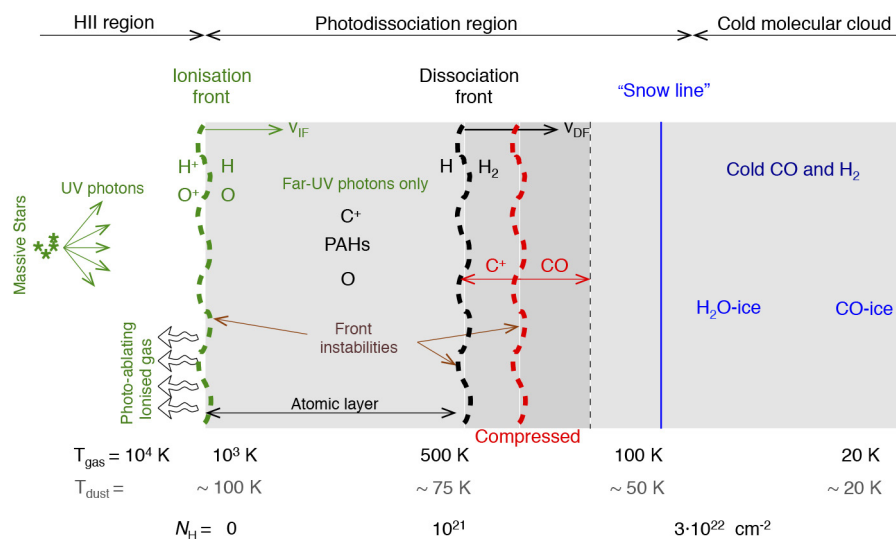
$\text{HF} + \text{C}^+ \rightarrow \text{CF}^+ + \text{H}$  reactions and is quickly destroyed by recombination with electrons<sup>51,53</sup>. Hence, the (lower-than-predicted) observed  $\text{CF}^+$  abundances probably reflect a dynamical PDR behaviour as well.

Stationary PDR models of strongly irradiated dense gas (with  $n_{\text{H}}$  values of a few  $10^6 \text{ cm}^{-3}$ ) have been presented in the literature<sup>3,6,7</sup>. The above densities are similar to those inferred in the compressed substructures at the Orion Bar edge. Thus they can be used to gain insight into the chemistry that leads to the formation of  $\text{HCO}^+$  and CO in ultraviolet-irradiated dense gas. Owing to the higher densities and enhanced  $\text{H}_2$  collisional de-excitation heating, the gas attains high temperatures. This triggers a warm chemistry in which endothermic reactions and reactions with energy barriers become faster. As a result, higher  $\text{HCO}^+$  abundances are predicted close to the dissociation front ( $x(\text{HCO}^+)$  of several  $10^{-9}$ ). Reactions of  $\text{C}^+$  with  $\text{H}_2$  (either far-ultraviolet-pumped or thermally excited) initiate the carbon chemistry<sup>54</sup>. This reaction triggers the formation of  $\text{CH}^+$  (explaining the elevated  $\text{CH}^+$  abundances detected by Herschel<sup>55</sup>) and reduces the abundance of  $\text{C}^+$  ions and  $\text{H}_2$  molecules near the dissociation front; that is, the  $\text{H}/\text{H}_2$  and the  $\text{C}^+/\text{CO}$  transition layers naturally get closer (in  $A_V$ )<sup>50</sup>. Fast exothermic reactions of  $\text{CH}^+$  with  $\text{H}_2$  subsequently produce  $\text{CH}_2^+$  and  $\text{CH}_3^+$ . Both hydrocarbon ions are 'burnt' in reactions with abundant oxygen atoms and contribute to the formation of  $\text{HCO}^+$  at the molecular cloud edge. This  $\text{HCO}^+$  formation route from  $\text{CH}^+$  can dominate over the formation of  $\text{HCO}^+$  from  $\text{CO}^+$  (after the  $\text{O} + \text{H}_2 \rightarrow \text{OH} + \text{H}$  reaction, followed by  $\text{C}^+ + \text{OH} \rightarrow \text{CO}^+ + \text{H}$ , and finally  $\text{CO}^+ + \text{H}_2 \rightarrow \text{HCO}^+ + \text{H}$ )<sup>5,6,32</sup>. Both OH and  $\text{CO}^+$  have been detected in the Orion Bar<sup>56,57</sup>, but high-angular-resolution maps do not exist. Recombination of  $\text{HCO}^+$  with electrons then drives CO production near the dissociation front<sup>6,7</sup>.

Extrapolating the above chemical scenario, the brightest  $\text{HCO}^+ J=4-3$  emission peaks in the Orion Bar should be close to  $\text{H}_2^+$  emission peaks. Extended Data Fig. 2a shows a remarkable spatial agreement between the  $\text{H}_2 v=1-0 \text{ S}(1)$  emission peaks and several  $\text{HCO}^+$  emission peaks. Detailed  $\text{H}_2$  excitation models (including both far-ultraviolet-pumping and collisions) show that for the conditions prevailing in the Orion Bar, the intensity of the  $\text{H}_2 v=1-0 \text{ S}(1)$  line is approximately proportional to the gas density<sup>42</sup>. Therefore, the  $\text{HCO}^+$  peaks that match the position of the  $\text{H}_2 v=1-0 \text{ S}(1)$  line peaks probably correspond to gas density enhancements as well. This agrees with the higher  $\text{H}_2 v=1-0 \text{ S}(1)/v=2-1 \text{ S}(1) \approx 8$  line intensity ratios observed at the dissociation front and consistent with efficient  $\text{H}_2$  collisional excitation<sup>32</sup>. The ALMA images thus confirm that in addition, or as a consequence of dynamical effects, reactions of  $\text{H}_2$  with abundant atoms and ions contribute to shift the molecular gas production towards the cloud edge. Even higher-angular-resolution observations of additional tracers will be needed to fully understand this, and to spatially resolve the chemical stratification expected in the over-dense substructures themselves. We note that if most of the carbon becomes CO at  $A_V \approx 2$  ( $N_{\text{H}}$  of several  $10^{21} \text{ cm}^{-2}$ ) in substructures with gas densities of a few  $10^6 \text{ cm}^{-3}$ , this depth is equivalent to a spatial length of several  $10^{15} \text{ cm}$ , or an angular-scale of about  $0.5''$  at the distance to Orion.

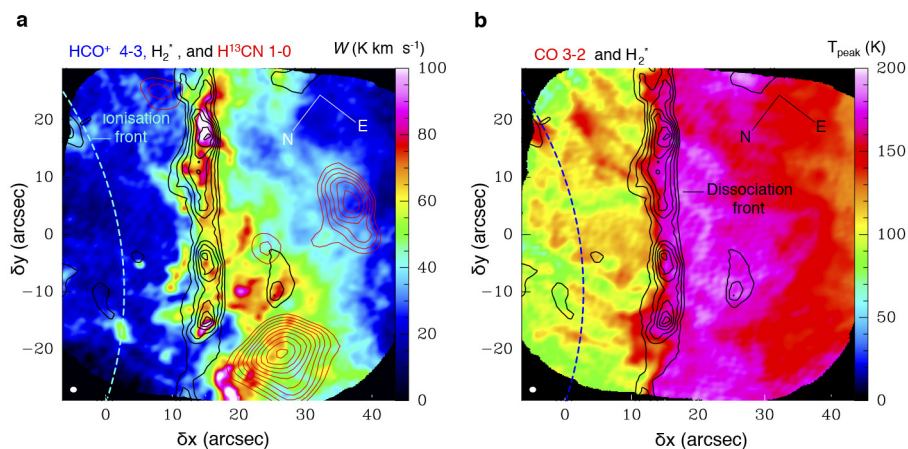
Deeper inside into the molecular cloud ( $\delta x > 30''$ ), the  $\text{CO}^+$ ,  $\text{CH}^+$ ,  $\text{CH}_2^+$  and  $\text{CH}_3^+$  abundances sharply decrease. The far-ultraviolet flux greatly diminishes, and the gas and dust grain temperatures accordingly decrease. The  $\text{HCO}^+$  abundance also decreases until the  $\text{CO} + \text{H}_3^+ \rightarrow \text{HCO}^+ + \text{H}$  reaction starts to drive the  $\text{HCO}^+$  formation at low temperatures. Gas-phase atoms and molecules gradually deplete and dust grains become coated by ices as the far-ultraviolet photon flux is attenuated at even larger cloud depths (see Extended Data Fig. 1).

31. Pety, J. & Rodríguez-Fernández, N. J. Revisiting the theory of interferometric wide-field synthesis. *Astron. Astrophys.* **517**, A12 (2010).
32. van der Werf, P. P., Stutzki, J., Sternberg, A. & Krabbe, A. Structure and chemistry of the Orion bar photon-dominated region. *Astron. Astrophys.* **313**, 633–648 (1996).
33. Allers, K. N., Jaffe, D. T., Lacy, J. H., Draine, B. T. & Richter, M. J.  $\text{H}_2$  pure rotational lines in the Orion Bar. *Astrophys. J.* **630**, 368–380 (2005).
34. O'Dell, C. R. & Yusef-Zadeh, F. High angular resolution determination of extinction in the Orion Nebula. *Astron. J.* **120**, 382–392 (2000).
35. Cardelli, J. A., Clayton, G. C. & Mathis, J. S. The relationship between infrared, optical, and ultraviolet extinction. *Astrophys. J.* **345**, 245–256 (1989).
36. Goicoechea, J. R. *et al.* Low sulfur depletion in the Horsehead PDR. *Astron. Astrophys.* **456**, 565–580 (2006).
37. Arab, H. *et al.* Evolution of dust in the Orion Bar with Herschel. I: radiative transfer modelling. *Astron. Astrophys.* **541**, A19 (2012).
38. Cuadrado, S. *et al.* The chemistry and spatial distribution of small hydrocarbons in UV-irradiated molecular clouds: the Orion Bar PDR. *Astron. Astrophys.* **575**, A82 (2015).
39. Langer, W. D. & Penzias, A. A.  $^{12}\text{C}/^{13}\text{C}$  isotope ratio across the Galaxy from observations of  $^{13}\text{C}^{18}\text{O}$  in molecular clouds. *Astrophys. J.* **357**, 477–492 (1990).
40. Inutsuka, S.-i. & Miyama, S. M. A production mechanism for clusters of dense cores. *Astrophys. J.* **480**, 681–693 (1997).
41. Noel, B., Joblin, C., Maillard, J. P. & Paumard, T. New results on the massive star-forming region S106 by BEAR spectro-imaging. *Astron. Astrophys.* **436**, 569–584 (2005).
42. Burton, M. G., Hollenbach, D. J. & Tielens, A. G. G. M. Line emission from clumpy photodissociation regions. *Astrophys. J.* **365**, 620–639 (1990).
43. Wyrowski, F., Schilke, P., Hofner, P. & Walmsley, C. M. Carbon radio recombination lines in the Orion Bar. *Astrophys. J.* **487**, L171–L174 (1997).
44. Tremblin, P. *et al.* Ionization compression impact on dense gas distribution and star formation. Probability density functions around HII regions as seen by Herschel. *Astron. Astrophys.* **564**, A106 (2014).
45. Brogan, C. L., Troland, T. H., Abel, N. P., Goss, W. M. & Crutcher, R. M. in *Astronomical Polarimetry: Current Status and Future Directions* (eds Adamson, A. *et al.*) 183–184 (ASP Conference Series 343, Astronomical Society of the Pacific, 2005).
46. Planck Collaboration. Planck intermediate results. XXXIV: The magnetic field structure in the Rosette Nebula. *Astron. Astrophys.* **586**, A137 (2016).
47. Roberge, W. G. & Draine, B. T. A new class of solutions for interstellar magnetohydrodynamic shock waves. *Astrophys. J.* **350**, 700–721 (1990).
48. Raga, A. C., Cantó, J. & Rodríguez, L. F. Analytic and numerical models for the expansion of a compact HII region. *Mon. Not. R. Astron. Soc.* **419**, L39–L43 (2012).
49. Hollenbach, D. J. & Natta, A. Time-dependent photodissociation regions. *Astrophys. J.* **455**, 133–144 (1995).
50. Bertoldi, F. *ISO: A Novel Look at the Photodissociated Surfaces of Molecular Clouds* 67–72 (Special Publication 419, European Space Agency, 1997).
51. Neufeld, D. A. & Wolfire, M. G. The chemistry of interstellar molecules containing the halogen elements. *Astrophys. J.* **706**, 1594–1604 (2009).
52. Neufeld, D. A. *et al.* Discovery of interstellar  $\text{CF}^+$ . *Astron. Astrophys.* **454**, L37–L40 (2006).
53. Guzmán, V. *et al.* The IRAM-30m line survey of the Horsehead PDR. I:  $\text{CF}^+$  as a tracer of  $\text{C}^+$  and as a measure of the fluorine abundance. *Astron. Astrophys.* **543**, L1 (2012).
54. Agúndez, M., Goicoechea, J. R., Cernicharo, J., Faure, A. & Roueff, E. The chemistry of vibrationally excited  $\text{H}_2$  in the interstellar medium. *Astrophys. J.* **713**, 662–670 (2010).
55. Nagy, Z. *et al.* The chemistry of ions in the Orion Bar. I.  $\text{CH}^+$ ,  $\text{SH}^+$ , and  $\text{CF}^+$ : the effect of high electron density and vibrationally excited  $\text{H}_2$  in a warm PDR surface. *Astron. Astrophys.* **550**, A96 (2013).
56. Goicoechea, J. R. *et al.* OH emission from warm and dense gas in the Orion Bar PDR. *Astron. Astrophys.* **530**, L16 (2011).
57. Stoerzer, H., Stutzki, J. & Sternberg, A.  $\text{CO}^+$  in the Orion Bar, M17 and S140 star-forming regions. *Astron. Astrophys.* **296**, L9–L12 (1995).



**Extended Data Figure 1 | Structure of a strongly ultraviolet-irradiated molecular cloud edge.** The incident stellar ultraviolet radiation comes from the left. The velocity of the advancing ionization and dissociation fronts are represented by  $v_{\text{IF}}$  and  $v_{\text{DF}}$  respectively. In the Orion Bar, the

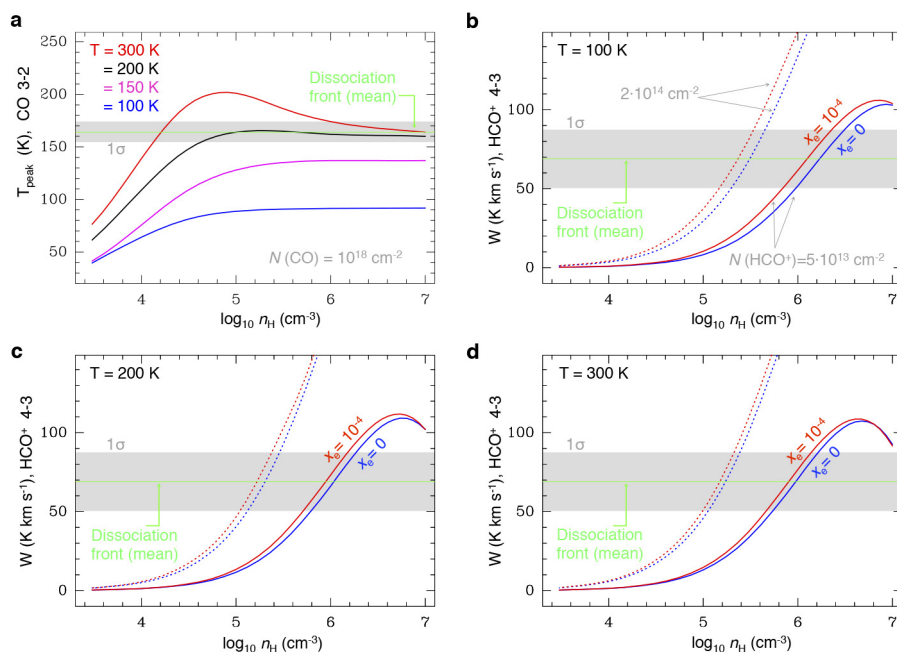
dissociation front is at about  $15''$  (about  $0.03 \text{ pc}$ ) from the ionization front. UV, ultraviolet; PAH, polycyclic aromatic hydrocarbons. The snow line refers to the inner cloud layers where molecular gases start to freeze and dust grains become coated by ices.



**Extended Data Figure 2 | Comparison with other tracers.** **a**, ALMA  $\text{HCO}^+ J=4-3$  line integrated intensity. **b**, ALMA  $\text{CO } J=3-2$  line peak (Orion Bar velocity component). The red contours represent the  $\text{H}^{13}\text{CN } J=1-0$  emission (from 0.08 to 0.026 in steps of  $0.02 \text{ Jy beam}^{-1} \text{ km s}^{-1}$ ) of dense condensations inside the Orion Bar<sup>19</sup>. The black contours show the

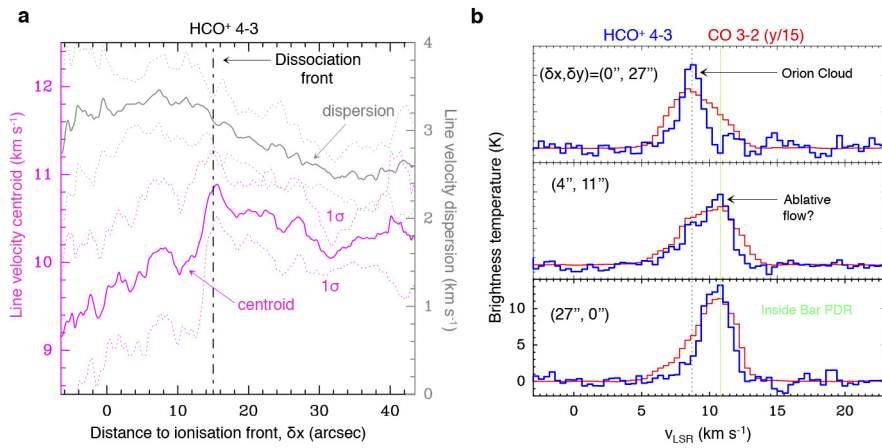
brightest regions of  $\text{H}_2 v=1-0 S(1)$  emission<sup>1</sup> (from 1.5 to 4.5 in steps of  $0.5 \cdot 10^{-4} \text{ erg s}^{-1} \text{ cm}^{-2} \text{ sr}^{-1}$ ). The  $\text{H}_2$  image is saturated between  $\delta x = 19''$  and  $23''$  (that is, no data are shown). Figures have been rotated  $127.5^\circ$  anticlockwise to bring the incident ultraviolet radiation from the left.





**Extended Data Figure 3 | Excitation models for different gas temperatures and densities.** **a**, CO  $J=3-2$  line peak (for  $N(\text{CO}) = 10^{18} \text{ cm}^{-2}$ ). **b–d**, HCO+  $J=4-3$  integrated line intensity at 100 K (**b**), 200 K (**c**) and 300 K (**d**). Each curve represents a different electron abundance model:  $x_e = 0$  (blue) and  $x_e = 10^{-4}$  (red).

Continuous curves are for  $N(\text{HCO}^+) = 5 \times 10^{13} \text{ cm}^{-2}$  and dotted lines for  $N(\text{HCO}^+) = 2 \times 10^{14} \text{ cm}^{-2}$  (appropriate for deeper inside the Orion Bar,  $\delta x > 30''$ ). The horizontal green dashed line represents the average  $T_{\text{peak}}^{\text{CO } 3-2}$  (**a**) and  $W_{4-3}^{\text{HCO}^+}$  (**b–d**) with their standard deviation (grey shaded) towards the dissociation front (at  $\delta x \approx 15''$ ).



**Extended Data Figure 4 | Line velocity centroid, dispersion and profiles.** **a**, Vertically averaged cuts perpendicular to the Orion Bar in the  $\text{HCO}^+ J=4-3$  line velocity centroid (magenta curve) and FWHM velocity dispersion (grey curve). **b**, CO and  $\text{HCO}^+$  spectra at representative positions. The top and middle plots show positions between the ionization

and dissociation fronts, the bottom plot is inside the molecular Orion Bar. Offsets are given with respect to the rotated images in Extended Data Fig. 2. The velocity of the background cloud is  $v_{\text{LSR}} \approx 8.5 \text{ km s}^{-1}$  (black dashed line), whereas the velocity of the Orion Bar is  $v_{\text{LSR}} \approx 11 \text{ km s}^{-1}$  (green line).

Extended Data Table 1 | Gas pressures and estimated magnetic field strengths

	Ionisation front	Atomic layer	Compressed structures	Ambient PDR component
Thermal pressure (K cm <sup>-3</sup> )	$P_{\text{th,IF}}/k \approx 6 \cdot 10^7$	$P_{\text{th,AL}}/k \leq 5 \cdot 10^7$	$P_{\text{th,comp}}/k \approx 2 \cdot 10^8$	$P_{\text{th,amb}}/k \approx 10^7$
Non-thermal pressure* (K cm <sup>-3</sup> )			$P_{\text{nth,comp}}/k \approx 2 \cdot 10^8$	$P_{\text{nth,amb}}/k \approx 10^7$
Magnetic field <i>B</i> (for $\beta=P_{\text{B}}/P_{\text{th}}=1$ )			$\approx 800 \text{ } \mu\text{Gauss}$	$\approx 200 \text{ } \mu\text{Gauss}$

All values are for a non-thermal velocity dispersion of  $\sigma_{\text{nth}} \approx 1 \text{ km s}^{-1}$ .



# Massive radius-dependent flow slippage in carbon nanotubes

Eleonora Secchi<sup>1</sup>, Sophie Marbach<sup>1</sup>, Antoine Niguès<sup>1</sup>, Derek Stein<sup>1,2</sup>, Alessandro Siria<sup>1</sup> & Lydéric Bocquet<sup>1</sup>

Measurements and simulations have found that water moves through carbon nanotubes at exceptionally high rates owing to nearly frictionless interfaces<sup>1–4</sup>. These observations have stimulated interest in nanotube-based membranes for applications including desalination, nano-filtration and energy harvesting<sup>5–10</sup>, yet the exact mechanisms of water transport inside the nanotubes and at the water–carbon interface continue to be debated<sup>11,12</sup> because existing theories do not provide a satisfactory explanation for the limited number of experimental results available so far<sup>13</sup>. This lack of experimental results arises because, even though controlled and systematic studies have explored transport through individual nanotubes<sup>7–9,14–17</sup>, none has met the considerable technical challenge of unambiguously measuring the permeability of a single nanotube<sup>11</sup>. Here we show that the pressure-driven flow rate through individual nanotubes can be determined with unprecedented sensitivity and without dyes from the hydrodynamics of water jets as they emerge from single nanotubes into a surrounding fluid. Our measurements reveal unexpectedly large and radius-dependent surface slippage in carbon nanotubes, and no slippage in boron nitride nanotubes that are crystallographically similar to carbon nanotubes, but electronically different. This pronounced contrast between the two systems must originate from subtle differences in

the atomic-scale details of their solid–liquid interfaces, illustrating that nanofluidics is the frontier at which the continuum picture of fluid mechanics meets the atomic nature of matter.

Measuring the pressure-driven flow of water through individual carbon nanotubes (CNTs) and boron nitride nanotubes (BNNTs) with well-defined radii ( $R_t$ ) and lengths ( $L_t$ ) requires overcoming two considerable challenges. First, when  $R_t$  decreases to the nanoscale, the flow rate through a tube drops too rapidly for even state-of-the-art flow-rate measurements to detect. Flow rates as low as a few picolitres per second have been measured through single nanocapillaries<sup>18</sup>, but such a rate is still about three orders of magnitude higher than the sensitivity required to probe mass flow through a single nanotube. Our approach avoids this problem by focusing instead on the flow that a fluid jet entrains outside a nanotube (see Fig. 1) and on the scaling property of the jet hydrodynamics<sup>19</sup>. The external flow is characterized by a driving force  $F_P$  that originates in the fluid momentum transfer at the tube opening<sup>20,21</sup> and scales linearly with  $R_t$ , so the flow velocities remain measurably large even when  $R_t$  shrinks to nanometre-scale dimensions. The second challenge is fabricating an experimental system for manipulating and using a single nanotube, in the form of a nanofluidic needle with a single nanotube protruding from the tip. To do this, we adapted a technique for selecting and manipulating nanotubes of known length

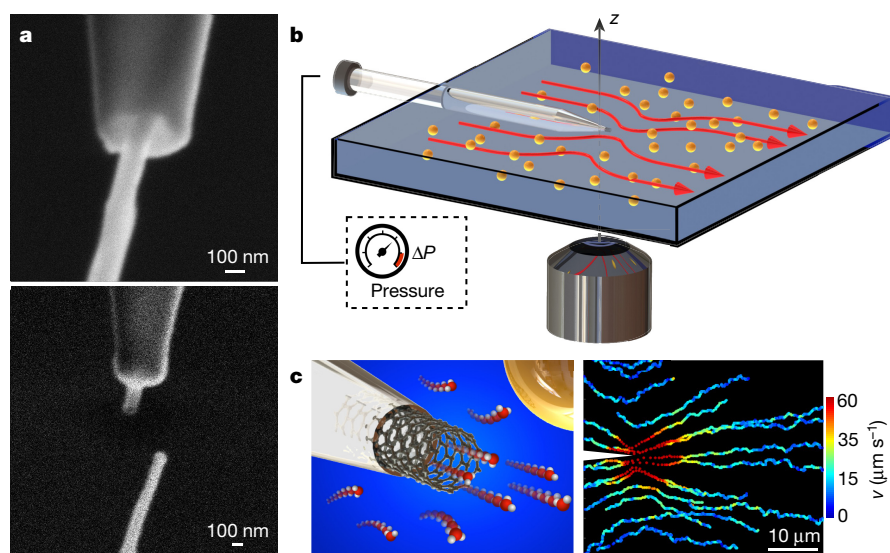


**Figure 1 | Nanojet experimental set-up.** **a**, SEM image of a CNT insertion into a nanocapillary (top) and after sealing (bottom). The CNT has dimensions of  $(R_t, L_t) = (50 \text{ nm}, 1,000 \text{ nm})$ . **b**, Sketch of the fluidic cell used to image the Landau–Squire flow set-up by nanojets emerging from individual nanotubes. Red arrows represent the Landau–Squire flow in the reservoir; orange spheres are tracer particles;  $z$  is the optical axis. **c**, Left, sketch of a nanotube protruding from a nanocapillary tip. The flow

of water molecules emerging from the nanotube is probed by the tracer particles. Right, trajectories of individual colloidal tracers in a Landau–Squire flow field in the outer reservoir. The colour scale quantifies the velocity  $v$  of the tracer particles. The flow is driven by a nanojet from a CNT with dimensions of  $(R_t, L_t) = (33 \text{ nm}, 900 \text{ nm})$ , with  $\Delta P = 1.7 \text{ bar}$ . Both reservoirs contained water with  $10^{-2} \text{ M KCl}$ .

<sup>1</sup>Laboratoire de Physique Statistique, Ecole Normale Supérieure, PSL Research University, 75005 Paris Cedex 05, France. <sup>2</sup>Physics Department, Brown University, Providence, Rhode Island 02912, USA.

and diameter with a nanomanipulator operating inside a scanning electron microscope (SEM)<sup>9</sup>; see Supplementary Methods 1 and Supplementary Video 1. We guided a nanotube into the tip of a laser-pulled glass nanocapillary with an orifice in the range 250–350 nm. The dimensions of the nanotubes were determined by ionic transport measurements and by electron microscopy (see Supplementary Methods 2 and 4). For this study we tested five different CNTs with dimensions (in nanometres) of  $(R_t, L_t) = (15, 700)$ ,  $(17, 450)$ ,  $(33, 900)$ ,  $(38, 800)$  and  $(50, 1,000)$ , and three different BNNTs with dimensions (in nanometres) of  $(R_t, L_t) = (23, 600)$ ,  $(26, 700)$  and  $(7, 1,300)$ ; see Supplementary Methods 2 and 4 and Supplementary Table 1.

The nanotube at the tip of the glass capillary bridged two macroscopic fluid reservoirs: one inside the capillary and another in the wide, transparent flow cell into which the capillary was placed (see Fig. 1b and Supplementary Methods 3). We filled both reservoirs with potassium chloride (KCl) solutions of a chosen concentration  $C_s$  and controlled pH, and seeded the flow cell with 500-nm polystyrene tracer particles. We then applied a pressure drop  $\Delta P$  to the capillary and tracked the resulting motion of the tracers under a microscope (see Fig. 1b) to map the velocity profile of the flow (see Figs 1c and 2). Flow measurements were performed with salt concentration  $C_s = 10^{-3}$  M or  $C_s = 10^{-2}$  M. Low salinity is required during the tracking experiments to prevent salt-induced colloid aggregation.

Ag/AgCl electrodes inserted into either reservoir were used to measure the ionic conductance across the nanotube before and after each fluidic experiment to ensure the integrity of the device, as well as to obtain information on the dimensions and the surface charge density

of the nanotube (see Supplementary Methods 4). These electrodes were grounded during flow measurements.

Owing to the needle geometry of the system, the pressure-driven flow through the nanotube sets up a flow in the outer reservoir called a Landau–Squire nanoflow<sup>18,20,21</sup>. The Landau–Squire solution of the Navier–Stokes equations at low Reynolds number predicts radial and angular components of the flow velocity of  $v_r = \frac{F_p \cos \theta}{4\pi\eta r}$  and  $v_\theta = -\frac{F_p \sin \theta}{8\pi\eta r}$ , respectively, where  $r$  is the radial distance from the tip,  $\theta$  is the angle relative to the symmetry axis of the jet and  $\eta$  is the viscosity<sup>20</sup>.  $F_p$  is the driving force of the jet applied at the origin. Figure 2a, b shows that our measurements of the flow field around single nanotubes agree well with the Landau–Squire prediction. The inset of Fig. 2b further highlights the long-range  $1/r$ -dependence of the Landau–Squire flow, which extends over tens of micrometres despite the nanometre-scale size of the source of the flow.

From our analysis of the Landau–Squire flow, we extracted experimental values of  $F_p$  for each nanotube and  $\Delta P$ . The results, presented in Fig. 2c, show a linear relationship between  $F_p$  and  $\Delta P$ . To gain insight into the permeability of the nanotubes, we begin by observing that the mass flow rate and  $F_p$  are both proportional to  $\Delta P$  and, hence, proportional to one another. The viscous origin of  $F_p$  at low Reynolds numbers as well as dimensional considerations motivate the definition  $F_p = \alpha\eta R_t v_{NT}$ , where  $\alpha = \mathcal{O}(1)$  is a geometry-dependent numerical prefactor and  $v_{NT}$  is the average fluid velocity inside the nanotube. The permeability of the tube  $k_{NT}$  is defined by  $v_{NT} = \frac{k_{NT} \Delta P}{\eta L_t}$ . Combining these expressions,  $F_p$ ,  $k_{NT}$  and  $\Delta P$  are related by  $F_p(\Delta P) = \frac{\alpha R_t k_{NT}}{L_t} \Delta P$ .

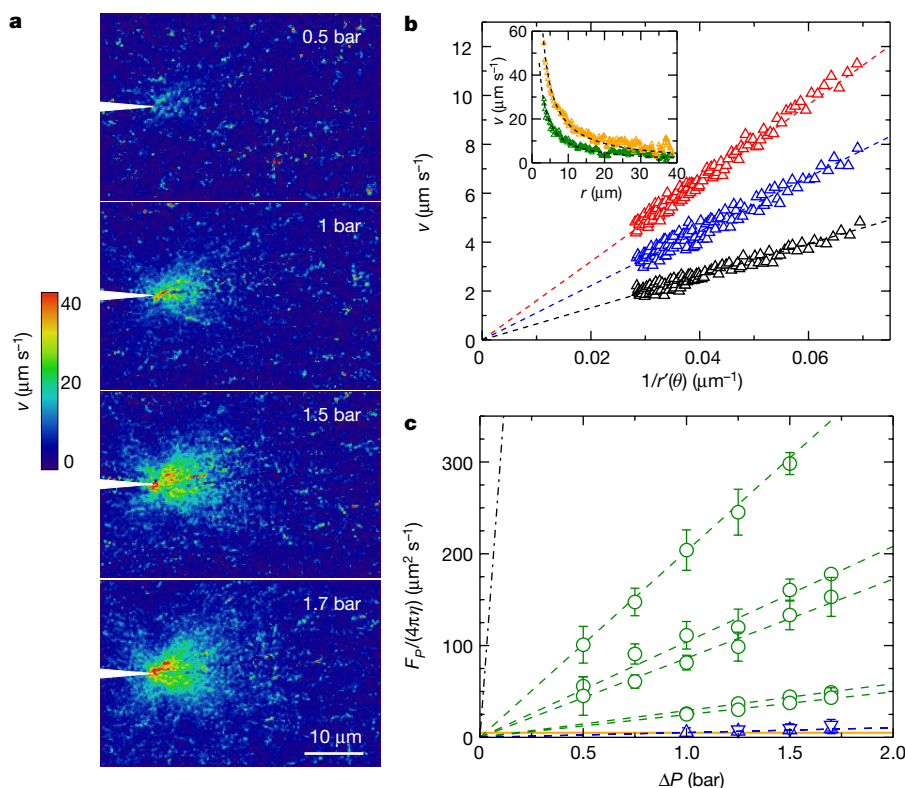


**Figure 2 | Measurement of Landau–Squire flows driven from nanotubes.** **a**, Maps of the velocity field near a CNT with  $(R_t, L_t) = (33 \text{ nm}, 900 \text{ nm})$  for various  $\Delta P$  as indicated ( $C_s = 10^{-2}$  M and pH 6). **b**, Magnitude of mean particle velocity  $v$  as a function of  $1/r'(\theta) = 2r/\sqrt{1 + 3\cos^2\theta}$  for  $\Delta P = 0.5$  bar (black),  $\Delta P = 1$  bar (blue) and  $\Delta P = 1.5$  bar (red). Dashed lines are fits of the Landau–Squire prediction. Inset, particle velocity along the jet axis ( $\theta = 0$ ) versus distance from the nanotube, for  $\Delta P = 0.75$  bar (green) and  $\Delta P = 1.7$  bar (orange); the dashed line is a  $1/r$  fit. **c**, Dependence of  $\frac{F_p}{4\pi\eta}$  on  $\Delta P$  for CNTs (green circles) and BNNTs (blue triangles). CNT dimensions (in nanometres) are,

from top to bottom,  $(R_t, L_t) = (50, 1,000)$ ,  $(33, 900)$ ,  $(38, 800)$ ,  $(15, 700)$  and  $(17, 450)$ ; BNNT dimensions (in nanometres) are  $(R_t, L_t) = (26, 700)$  and  $(23, 600)$ . The salt concentration is  $C_s = 10^{-3}$  M, except for the 33-nm CNT, which was studied at both  $C_s = 10^{-3}$  M and  $C_s = 10^{-2}$  M without a detectable difference. Dashed green lines are linear fits from which the permeability was calculated. The orange line indicates the lowest detectable flow strength. The black dashed line corresponds to the results of a control experiment using a nanocapillary without a nanotube (see Supplementary Methods 5). Error bars correspond to the uncertainty in the slope in **b**, estimated from at least three measurement replicates at each  $\Delta P$ .

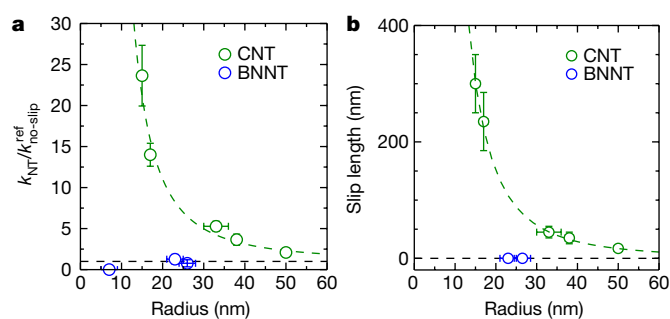


**Figure 3 | Permeability and slip length of individual CNTs and BNNTs.**

**a**, Normalized permeability ( $k_{\text{NT}}/k_{\text{NT}}^{\text{ref, no-slip}}$ ) of CNTs (green) and BNNTs (blue) as a function of nanotube radius  $R_t$ . The permeability of the BNNT with  $R_t = 7$  nm was below the experimental detection limit and is indicated as  $k_{\text{NT}} = 0$  for completeness. Error bars correspond to the experimental errors on  $F_p$ . **b**, Dependence of the experimentally determined slip length inside CNTs (green) and BNNTs (blue) on  $R_t$ . Error bars correspond to the uncertainty in the permeability. Salt concentration is  $C_s = 10^{-3}$  M, except for the 33-nm CNT, which was studied at both  $C_s = 10^{-3}$  M and  $C_s = 10^{-2}$  M without a detectable difference. In both panels, the horizontal dashed lines indicate the no-slip prediction ( $k_{\text{NT}}/k_{\text{NT}}^{\text{ref, no-slip}} = 1$ ) and the green dashed lines are guides to the eye. The error bars on the radius correspond to the experimental uncertainty in the electric characteristics (see Supplementary Methods 2 and 4). The values of the slip lengths are reported in Supplementary Tables 2 and 3.

According to this equation, the slope of the plots in Fig. 2c provides an estimate of the nanotube permeability, so we can already see that the permeability of CNTs is greatly enhanced as compared with BNNTs. But, to properly quantify the permeabilities, we need to know the value of  $\alpha$ . We calculated  $\alpha$  from the precise relationship between  $F_p$ ,  $v_{\text{NT}}$  and  $\Delta P$  that we obtained by numerically solving the full hydrodynamic Landau–Squire flow. Furthermore, because  $\alpha$  could be sensitive to details of the geometry of the nanotube and the tip, we repeated our calculations for every nanotube device, taking in account its particular geometry as measured by SEM (see Supplementary Methods 6). This exhaustive study, which combines numerical hydrodynamic calculations with experimental benchmarking using nanocapillaries, is summarized in Supplementary Methods 5. Our study showed that  $\alpha \approx 0.3$  for the nanotube devices considered in Fig. 2a, b, with only small variations between nanotubes. Having removed all uncertainty from the value of  $\alpha$ , we obtained accurate values for  $k_{\text{NT}}$  from the experimental dependence of  $F_p$  on  $\Delta P$ . Figure 3a presents the dependence of  $k_{\text{NT}}$  on  $R_t$  for every nanotube. The permeabilities are normalized by a simple no-slip reference,  $k_{\text{NT}}^{\text{ref, no-slip}} = R_t^2/8$ , corresponding to a nanotube of the same size with a no-slip boundary condition at its surface. Note that the flow from the smallest BNNT tube, with  $R_t = 7$  nm, was below the detection limit.

We attribute the enhanced permeability of the CNTs to hydrodynamic slippage at the carbon surface<sup>12,13,22,23</sup>. The fundamental way to account for this is to introduce a slip length  $b$  and to apply Navier's slip boundary condition to the fluid at the nanotube surface. We included the slip condition in our numerical analysis of the hydrodynamics of each nanotube device and obtained experimental  $b$  values by matching the computed flow rate enhancement due to surface slippage with the measured permeability data in Fig. 3a (see Supplementary Methods 6). This analysis, which uses the geometry of each nanotube device and takes into account hydrodynamic entrance effects at the nanotube ends, offers the most accurate estimation of  $b$  possible. The permeability and  $b$  can also be quantitatively obtained from an analytical model of hydrodynamic resistances in series, using the Sampson formula to account for both Poiseuille flow with slippage inside the nanotube and entrance effects<sup>24</sup>; see Supplementary Tables 2 and 3.

The peculiar nature of the water–carbon interface inside CNTs is revealed in Fig. 3b, which presents the experimentally determined slip

length as a function of  $R_t$ . A first key observation is that the slip length is strongly radius-dependent, reaching 300 nm inside the smallest CNT investigated here. This observation allows us to resolve a long-standing debate regarding the large difference in permeabilities reported previously<sup>2–4,25</sup> using large-scale CNT membranes. The results of those studies are consistent with a decreasing permeability enhancement factor for larger nanotubes, and the range of slip lengths they report is fairly compatible with what we have measured. Our results also explain why the slip lengths measured previously inside CNTs were consistently much larger than the values measured on planar hydrophobic and graphite surfaces<sup>13,26</sup>, for which  $b$  is typically a few tens of nanometres at most. From a theoretical perspective, the transport behaviour of water inside CNTs has been the subject of numerous studies, mostly using molecular dynamics simulations<sup>12,13</sup>. Radius-dependent slippage was predicted inside CNTs with  $R_t < 10$  nm (refs 22, 23) and rationalized in terms of curvature-dependent friction<sup>23</sup>. The results presented here confirm the predicted trend, but the measured slip lengths far exceed the numerical predictions. This discrepancy suggests that molecular dynamics simulations do not represent the interfacial dynamics well at a quantitative level, echoing similar limitations encountered in studies of slippage at hydrophobic surfaces<sup>13</sup>.

A second key feature of Fig. 3c is the vastly different behaviour of CNTs and BNNTs, with the latter showing no substantial slippage of water. The comparison is illuminating because CNTs and BNNTs have the same crystallography, but radically different electronic properties, with CNTs being semi-metallic and BNNTs insulating. That these nearly identical channels exhibit very different surface flow dynamics is unexpected: molecular dynamics simulations using semi-empirical interfacial parameters predict similar flow behaviour through CNTs and BNNTs<sup>27,28</sup>. More recent *ab initio* simulations predict that the friction of water on carbon surfaces is lower than on boron nitride surfaces<sup>29</sup>, but even these predictions strongly underestimate the difference observed here. The stark differences in flow behaviour must therefore originate in subtle atomic-scale details of the solid–liquid interface, including the electronic structure of the confining material. A more detailed understanding will require a systematic theoretical investigation of physico-chemical factors that could affect surface friction, such as chemical surface dissociation or specific ion adsorption. Useful information could also be gained by measuring the slip behaviour in CNTs at high salt concentrations, a regime in which the surface charge of CNTs is expected to increase<sup>15</sup>.

The unexpected slippage behaviour inside CNTs and BNNTs points to a hitherto not appreciated link between hydrodynamic flow and the electronic structure of the confining material. This opens up a new avenue for research that could bridge the gap between hard and soft condensed matter physics. We also expect that, with further improvements in sensitivity, the methods we have developed will enable the direct measurement of water transport through biological channels such as aquaporins.

Received 11 May; accepted 15 July 2016.

- Hummer, G., Rasaiah, J. C. & Noworyta, J. P. Water conduction through the hydrophobic channel of a carbon nanotube. *Nature* **414**, 188–190 (2001).
- Majumder, M., Chopra, N., Andrews, R. & Hinds, B. J. Nanoscale hydrodynamics: enhanced flow in carbon nanotubes. *Nature* **438**, 44 (2005); erratum **438**, 930 (2005).
- Holt, J. K. *et al.* Fast mass transport through sub-2-nanometer carbon nanotubes. *Science* **312**, 1034–1037 (2006).
- Whitby, M., Cagnon, L., Thanou, M. & Quirke, N. Enhanced fluid flow through nanoscale carbon pipes. *Nano Lett.* **8**, 2632–2637 (2008).
- Nair, R. R., Wu, H. A., Jayaram, P. N., Grigorieva, I. V. & Geim, A. K. Unimpeded permeation of water through helium-leak-tight graphene-based membranes. *Science* **335**, 442–444 (2012).
- Joshi, R. K. *et al.* Precise and ultrafast molecular sieving through graphene oxide membranes. *Science* **343**, 752–754 (2014).
- Park, H. G. & Jung, Y. Carbon nanofluidics of rapid water transport for energy applications. *Chem. Soc. Rev.* **43**, 565–576 (2014).
- Liu, H. *et al.* Translocation of single stranded DNA through single-walled carbon nanotubes. *Science* **327**, 64–67 (2010).



9. Siria, A. *et al.* Giant osmotic energy conversion measured in a single transmembrane boron nitride nanotube. *Nature* **494**, 455–458 (2013).
10. Geng, J. *et al.* Stochastic transport through carbon nanotubes in lipid bilayers and live cell membranes. *Nature* **514**, 612–615 (2014).
11. Guo, S., Meshot, E. R., Kuykendall, T., Cabrini, S. & Fornasiero, F. Nanofluidic transport through isolated carbon nanotube channels: advances, controversies, and challenges. *Adv. Mater.* **27**, 5726–5737 (2015).
12. Whitby, M. & Quirke, N. Fluid flow in carbon nanotubes and nanopipes. *Nat. Nanotechnol.* **2**, 87–94 (2007).
13. Bocquet, L. & Charlaix, E. Nanofluidics, from bulk to interfaces. *Chem. Soc. Rev.* **39**, 1073–1095 (2010).
14. Lee, C. Y., Choi, W., Han, J.-H. & Strano, M. S. Coherence resonance in a single-walled carbon nanotube ion channel. *Science* **329**, 1320–1324 (2010).
15. Secchi, E., Niguès, A., Jubin, L., Siria, A. & Bocquet, L. Scaling behavior for ionic transport and its fluctuations in individual carbon nanotubes. *Phys. Rev. Lett.* **116**, 154501 (2016).
16. Qin, X., Yuan, Q., Zhao, Y., Xie, S. & Liu, Z. Measurement of the rate of water translocation through carbon nanotubes. *Nano Lett.* **11**, 2173–2177 (2011).
17. Lorenz, U. & Zewail, A. Observing liquid flow in nanotubes by 4D electron microscopy. *Science* **344**, 1496–1500 (2014).
18. Laohakunakorn, N. *et al.* A Landau–Squire nanojet. *Nano Lett.* **13**, 5141–5146 (2013).
19. Eggers, J. & Villermaux, E. Physics of liquid jets. *Rep. Prog. Phys.* **71**, 036601 (2008).
20. Landau, L. D. & Lifshitz, E. M. *Fluid Mechanics* Vol. 6 of *Course of Theoretical Physics* 81–83 (Pergamon, 1959).
21. Squire, H. B. The round laminar jet. *Q. J. Mech. Appl. Math.* **4**, 321–329 (1951).
22. Thomas, J. A. & McGaughey, A. J. H. Reassessing fast water transport through carbon nanotubes. *Nano Lett.* **8**, 2788–2793 (2008).
23. Falk, K., Sedlmeier, F., Joly, L., Netz, R. R. & Bocquet, L. Molecular origin of fast water transport in carbon nanotube membranes: superlubricity versus curvature dependent friction. *Nano Lett.* **10**, 4067–4073 (2010).
24. Sampson, R. A. On Stokes's current function. *Phil. Trans. R. Soc. A* **182**, 449–518 (1891).
25. Mattia, D., Leese, H. & Lee, K. P. Carbon nanotube membranes: from flow enhancement to permeability. *J. Membr. Sci.* **475**, 266–272 (2015).
26. Maali, A., Cohen-Bouhacina, T. & Kellay, H. Measurement of the slip length of water flow on graphite surface. *Appl. Phys. Lett.* **92**, 053101 (2008).
27. Suk, M. E., Raghunathan, A. V. & Aluru, N. R. Fast reverse osmosis using boron nitride and carbon nanotubes. *Appl. Phys. Lett.* **92**, 133120 (2008).
28. Hilder, T. A., Gordon, D. & Chung, S.-H. Salt rejection and water transport through boron nitride nanotubes. *Small* **5**, 2183–2190 (2009).
29. Tocci, G., Joly, L. & Michaelides, A. Friction of water on graphene and hexagonal boron nitride from ab initio methods: very different slippage despite very similar interface structures. *Nano Lett.* **14**, 6872–6877 (2014).

**Supplementary Information** is available in the online version of the paper.

**Acknowledgements** L.B. and A.S. thank U. Keyser for discussions. E.S., A.N., S.M. and A.S. acknowledge funding from the European Union's H2020 Framework Programme/ERC Starting Grant agreement number 637748 — NanoSOFT. L.B. and D.S. acknowledge support from the European Union's FP7 Framework Programme/ERC Advanced Grant Micromegas. S.M. acknowledges funding from a J.-P. Aguilar grant. L.B. acknowledges funding from a PSL chair of excellence. We acknowledge funding from ANR project BlueEnergy.

**Author Contributions** L.B. and A.S. conceived and directed the research. A.N. and A.S. designed and fabricated the nanotube devices. E.S. and D.S. designed the fluidic cell. E.S. performed the measurements. The data were analysed by E.S., S.M. and L.B.; S.M. conducted the numerical analysis with input from the other authors. All authors contributed to the scientific discussions and the preparation of the manuscript.

**Author Information** Reprints and permissions information is available at [www.nature.com/reprints](http://www.nature.com/reprints). The authors declare no competing financial interests. Readers are welcome to comment on the online version of the paper. Correspondence and requests for materials should be addressed to L.B. ([lyderic.bocquet@lps.ens.fr](mailto:lyderic.bocquet@lps.ens.fr)) and A.S. ([alessandro.siria@lps.ens.fr](mailto:alessandro.siria@lps.ens.fr)).

**Reviewer Information** *Nature* thanks J. Eijkel and A. Michaelides for their contribution to the peer review of this work.

# Oxidative diversification of amino acids and peptides by small-molecule iron catalysis

Thomas J. Osberger<sup>1\*</sup>, Donald C. Rogness<sup>1\*</sup>, Jeffrey T. Kohrt<sup>2</sup>, Antonia F. Stepan<sup>3</sup> & M. Christina White<sup>1</sup>

Secondary metabolites synthesized by non-ribosomal peptide synthetases display diverse and complex topologies and possess a range of biological activities<sup>1,2</sup>. Much of this diversity derives from a synthetic strategy that entails pre-<sup>3</sup> and post-assembly<sup>2</sup> oxidation of both the chiral amino acid building blocks and the assembled peptide scaffolds. The vancomycin biosynthetic pathway is an excellent example of the range of oxidative transformations that can be performed by the iron-containing enzymes involved in its biosynthesis<sup>4</sup>. However, because of the challenges associated with using such oxidative enzymes to carry out chemical transformations *in vitro*, chemical syntheses guided by these principles have not been fully realized in the laboratory<sup>5</sup>. Here we report that two small-molecule iron catalysts are capable of facilitating the targeted C–H oxidative modification of amino acids and peptides with preservation of  $\alpha$ -centre chirality. Oxidation of proline to 5-hydroxyproline furnishes a versatile intermediate that can be transformed to rigid arylated derivatives or flexible linear carboxylic acids, alcohols, olefins and amines in both monomer and peptide settings. The value of this C–H oxidation strategy is demonstrated in its capacity for generating diversity: four ‘chiral pool’ amino acids are transformed to twenty-one chiral unnatural amino acids representing seven distinct functional group arrays; late-stage C–H functionalizations of a single proline-containing tripeptide furnish eight tripeptides, each having different unnatural amino acids. Additionally, a macrocyclic peptide containing a proline turn element is transformed via late-stage C–H oxidation to one containing a linear unnatural amino acid.

A synthetic strategy inspired by non-ribosomal peptide synthetases (NRPSs) was envisioned wherein a small-molecule-catalyst-mediated C–H oxidation of an amino acid in a monomer or peptide generates a versatile synthetic intermediate that may be transformed into numerous structural and functional group types with retained optical purity. Analogous strategies have successfully employed prefunctionalized pluripotent building blocks to generate structurally diverse compounds<sup>6,7</sup>. Limited examples of C–H oxidations of amino acid derivatives are known and of these few have been demonstrated in peptides<sup>8–11</sup>. Chelate-controlled C–H arylations are positionally limited to amino-terminal residues<sup>9</sup> and stoichiometric C–H hydroxylation methods suffer from operational difficulty, modest efficiency, and have no demonstrated chemoselectivity in peptide settings<sup>10,11</sup>. A survey of the possible products of C–H oxidation at the side chains of the proteinogenic amino acids led us to reason that targeting hydroxylation at C5 of proline would provide an excellent first example of our envisioned strategy (Fig. 1c). Oxidation of proline, a biomass chemical, to 5-hydroxyproline (5-HP) furnishes an intermediate having a highly synthetically versatile hemiaminal functional group that may be transformed to unnatural amino acids (UAAs) and UAA-containing peptides. 5-HP and 5-functionalized proline derivatives are currently accessed via multistep synthetic routes from

pre-functionalized glutamic acid or pyroglutamic acid derivatives<sup>12</sup>. Recently, methods have been developed to furnish  $\alpha$ -aryl pyrrolidines via iron salts<sup>13</sup> or photoredox catalysts<sup>14</sup> and chiral  $\alpha$ -nitrile pyrrolidines via biocatalysis<sup>15</sup>. These  $\alpha$ -amine functionalization methods generally proceed via generation of positively charged nitrogen via quaternization or amino radical cation formation followed by decarboxylation, deprotonation or abstraction of the  $\alpha$ -hydrogen of the homolytically and heterolytically weakest C–H bond. On a proline core, C–H abstraction may occur preferentially at the weakest  $\alpha$ -(C2)–H (bond dissociation enthalpy of about 87 kcal mol<sup>–1</sup>)<sup>16</sup> bond versus the  $\alpha$ -(C5)–H (bond dissociation enthalpy of about 90 kcal mol<sup>–1</sup>), leading to racemization. Free hydroxyl radical oxidations<sup>17</sup> and photoredox-mediated arylations<sup>14,18</sup> of proline form 2-pyrrolidone and racemic  $\alpha$ -arylated derivatives, respectively.

We sought a method for a direct (C5)–H hydroxylation of proline that would preserve its C2 stereocentre and those in every amino acid residue present in peptide settings. Additionally, we sought an oxidant that would be highly chemoselective for the target residue over the other amino acid side-chain C–H bonds. For these reasons, we evaluated the small-molecule non-haem iron catalysts Fe(PDP) (catalyst 1)<sup>19,20</sup> and Fe(CF<sub>3</sub>PDP) (catalyst 2)<sup>21</sup> (Fig. 1b). Such bulky, electrophilic C–H oxidation catalysts do not discriminate solely on the basis of C–H bond dissociation energies, but rather select between C–H bonds on the basis of their electronic, steric and stereoelectronic properties. This, along with observations of stereoretentive oxidations of an isoleucine derivative and dipeptide, suggested that site selectivity for C5 proline oxidation was likely, given that C2 is both sterically and electronically deactivated<sup>21</sup>. Additionally, in complex-molecule settings, catalyst 1 was shown to oxidize hyperconjugatively activated C–H bonds (for example, etheral C–H bonds) at faster rates than other aliphatic C–H bonds<sup>20</sup>, suggesting that regioselectivity for  $\alpha$ -(C5)–H proline, hyperconjugatively activated by the nitrogen lone pair, would effectively compete with C–H oxidation of aliphatic amino acid residues.

We began our investigations into this NRPS-inspired strategy with the evaluation of the oxidation reactivity of N-(4-nitrophenylsulfonyl)-(L)-proline methyl ester (–)-3 with Fe(PDP) (1) (Fig. 2a). Subjecting of (–)-3 to reported slow addition conditions<sup>20</sup> with 1 (25 mol%), AcOH, and H<sub>2</sub>O<sub>2</sub> at room temperature led to full oxidation at C5 of proline, affording the glutamic acid derivative (–)-4 in 77% yield, presumably via over-oxidation of singly oxidized 5-HP as its open-chain tautomer. We reasoned that a milder oxidation protocol may allow for selective oxidation of proline to the desired 5-HP, and found that by lowering the reaction temperature to 0 °C and decreasing the catalyst loading (iterative addition of 1, 15 mol%), it was possible to isolate 5-HP in good yield (62%) (see the Supplementary Information for details). A similarly encouraging result was observed with the less rigid proline homologue pipecolic acid, affording 6-hydroxypipicolic acid 5 in 53% yield. Interestingly, Boc-proline methyl ester (where

<sup>1</sup>Department of Chemistry, Roger Adams Laboratory, University of Illinois, Urbana, Illinois 61801, USA. <sup>2</sup>Pfizer Worldwide Research and Development, Groton Laboratories, Eastern Point Road, Groton, Connecticut 06340, USA. <sup>3</sup>Worldwide Medicinal Chemistry, Pfizer Worldwide Research and Development, Cambridge, Massachusetts 02139, USA.

\*These authors contributed equally to this work.

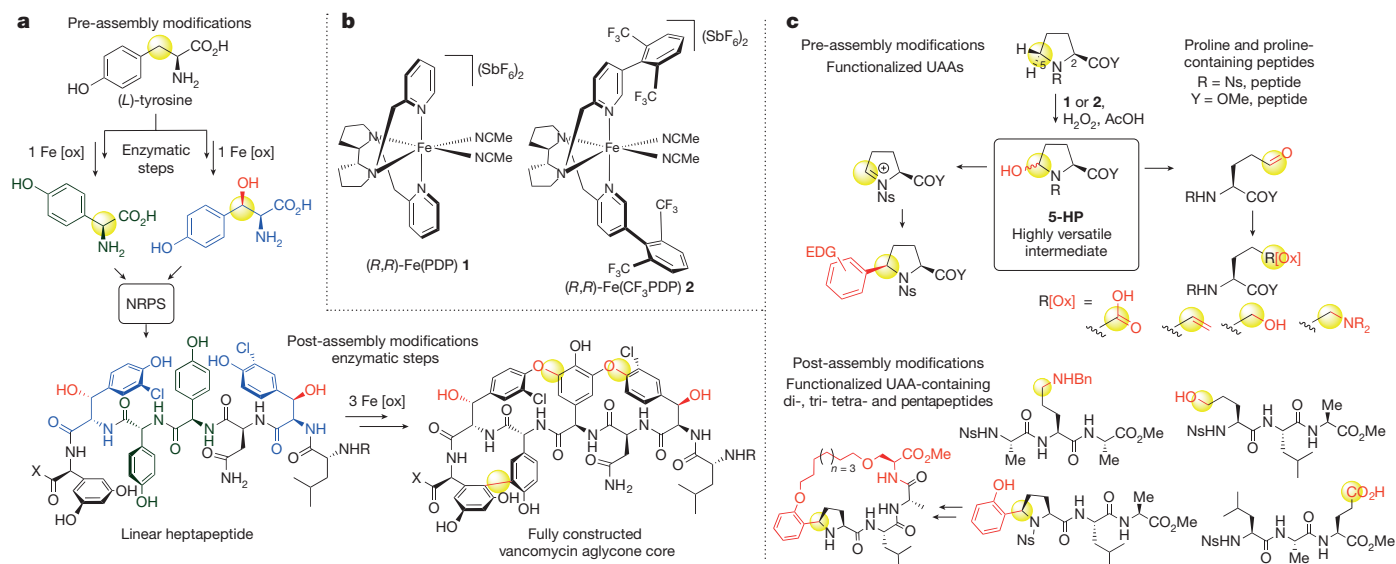


**Figure 1 | NRPS-inspired strategy for iron-catalysed C–H oxidative functionalization of amino acids and peptides.** **a**, Oxidative tailoring iron-enzyme pre- and post-assembly modifications in the biosynthesis of vancomycin. Iron enzymes diversify tyrosine into the two UAAs hydroxyphenylglycine and  $\beta$ -hydroxytyrosine, which are incorporated by the NRPS into a heptapeptide. Post-assembly oxidative tailoring by iron enzymes effects side-chain cross-linking to afford the vancomycin core. X = OH or the peptidyl carrier protein; R = H or methyl. **b**, The

small-molecule non-haem iron C–H oxidation catalysts Fe(PDP) **1** and Fe(CF<sub>3</sub>PDP) **2**. PDP = [N,N'-bis(2-pyridylmethyl)]-2,2'-bipyridoline. **c**, Iron catalysts **1** and **2** catalysed pre-assembly oxidative modification of proline to afford numerous classes of UAAs. Post-assembly oxidative modifications by **1** and **2** of proline-containing polypeptides to furnish UAA-functionalized polypeptides. Ns = 4-nitrophenylsulfonyl; Bn = benzyl; [ox], oxidation; yellow circles indicate sites of oxidative modification.

Boc = *tert*-butoxycarbonyl) gave oxidation to Boc-pyrogutamic acid methyl ester under the same conditions as the major isolated product (see the Supplementary Information for details). Gratifyingly, these experiments resulted in conditions for C5 oxidation of proline with control of the final oxidation state. Notably, we did not observe oxidation or racemization of the C2 stereocentre, even under the forcing conditions used to generate the glutamic acid analogue (–)-**4**.

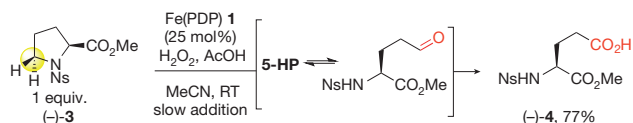
We questioned whether *in situ* derivatization of the hemiaminal functional group of **5-HP** could effect pre-assembly oxidative tailoring modifications, diversifying proline into non-proteinogenic amino acids. Arylated proline motifs are prevalent in medicinal agents<sup>22</sup>. Direct arylation at the 5-position of proline could be effected by a sequential proline oxidation/arylation procedure: crude **5-HP** generated by Fe(PDP) oxidation is treated with BF<sub>3</sub>OEt<sub>2</sub> to afford a highly reactive *N*-sulfonyl iminium ion intermediate that undergoes diastereoselective nucleophilic attack by an electron-rich arene (Fig. 2b). We first explored phenols as arenes in this transformation: phenol and 2-naphthol adducts (+)-**6** and (–)-**7** were isolated in high yields with >20:1 *syn*-stereochemistry, and with generally high regioselectivity (3.1:1.0 *ortho/para* for **6**, >20:1 for **7**). Using this oxidative arylation procedure, a novel crosslink (–)-**8** between proline and tyrosine was efficiently forged, reminiscent of the side-chain crosslinks between amino acids effected by oxidative tailoring enzymes (for example, vancomycin). Additionally, the intriguing natural product–amino acid conjugate (+)-**9** was produced when the polyphenol natural product resveratrol was employed as the arene. The scope of electron-rich arenes is not limited to phenols, as high yields and selectivities were observed with heteroarenes such as anthrone, indole, and benzothiophene, affording adducts **10–12**. The adducts were generally formed in *syn*-stereochemistry—possibly owing to steric factors introduced by the nosyl group—confirmed by single-crystal X-ray diffraction of adducts (–)-**7**, (+)-**11**, and (+)-**12** (see the Supplementary Information for details). Interestingly, the anthrone adduct (–)-**10** was furnished as the *anti*-diastereomer. Overall, this proline oxidation/arylation procedure efficiently furnishes stereochemically enriched (>20:1 diastereomeric ratio) 5-arylproline derivatives, presenting an array of structural features and functional groups.

To complement the synthetic versatility of **5-HP** as a precursor to rigid proline derivatives, we envisioned that *in situ* transformations of the open-chain aldehyde tautomer of **5-HP** could be a second avenue to access a variety of linear UAA structures that remain difficult synthetic targets<sup>23</sup> (see the Supplementary Information for details). We developed a one-pot approach starting with Fe(PDP) (**1**) oxidation of (–)-**3** to **5-HP** followed by either reduction, olefination or reductive amination to furnish linear terminal hydroxyl-, olefin- or amino-containing UAAs (Fig. 2c). For example, (–)-**3** was transformed to the 5-hydroxy-*L*-norvaline derivative (+)-**13** via Fe(PDP) (**1**) hydroxylation followed by *in situ* reduction with NaBH<sub>4</sub>. Alternatively, C–H hydroxylation followed by Wittig olefination of (*L*)- or (*D*)-proline furnished the chiral (*L*)-2-amino-5-enoic acid derivative (+)-**15** and its enantiomer (43% and 40%, respectively) (see the Supplementary Information for details). Similarly, performing this transformation on the proline homologue pipecolic acid generated the (*D*)-2-amino-6-heptenoic acid derivative (–)-**17**. The retention of stereochemistry at C2 of proline (–)-**3** over these sequences was established by synthetic derivatization and comparison of optical activity of products (–)-**4**, (+)-**13**, and (+)-**15** to known compounds (see the Supplementary Information for details).

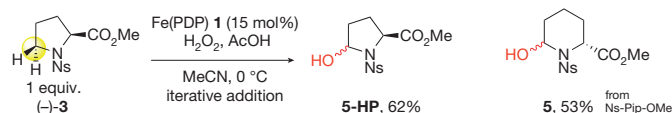
Fe(PDP) (**1**)-catalysed C–H hydroxylation followed by reductive amination afforded a general method of installing amines to furnish valuable UAAs, such as the chiral ornithine derivative (+)-**19**. The diversity of functionalized secondary and primary amines that may be used renders this a powerful transformation; for example, using 1-(2-aminopyridyl)-piperazine, a fluorescently labelled aminopyridine conjugated UAA (–)-**21** may be directly generated in an optically active form. The backbone amine of any suitably protected amino acid may be used to furnish backbone-to-side-chain linkages such as in the tryptophan derivative (+)-**22**. Utilization of less sterically encumbered primary amines results in reductive amination followed by intramolecular cyclization to afford optically enriched 3-aminopiperidinone scaffolds like (+)-**23**. Notably, additional reactive functionality can be united with the proline-derived backbone: proline oxidation/reductive amination with propargylamine furnished alkyne-substituted (+)-**24**, which may undergo a Cu-catalysed azide-alkyne cycloaddition to



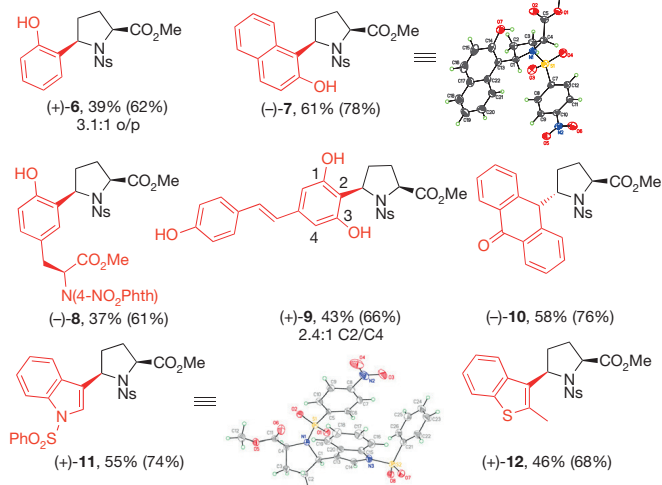
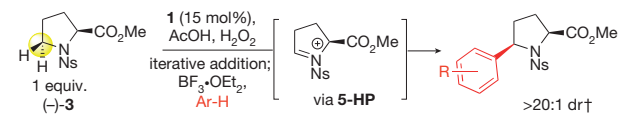
**a** Development of controlled oxidations of proline with Fe(PDP) 1  
Controlled over-oxidation of proline at RT



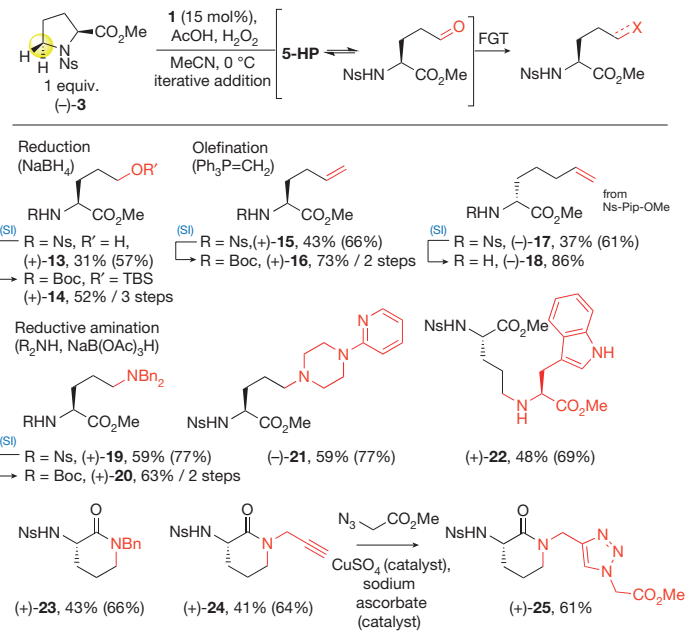
Selective oxidation of proline to 5-HP at 0 °C



**b** 5-Aryl proline derivatives via two-step oxidative arylation of proline



**c** Two-step oxidative modifications of proline to form UAAs



**d** Aliphatic C–H oxidation of amino acids and peptides

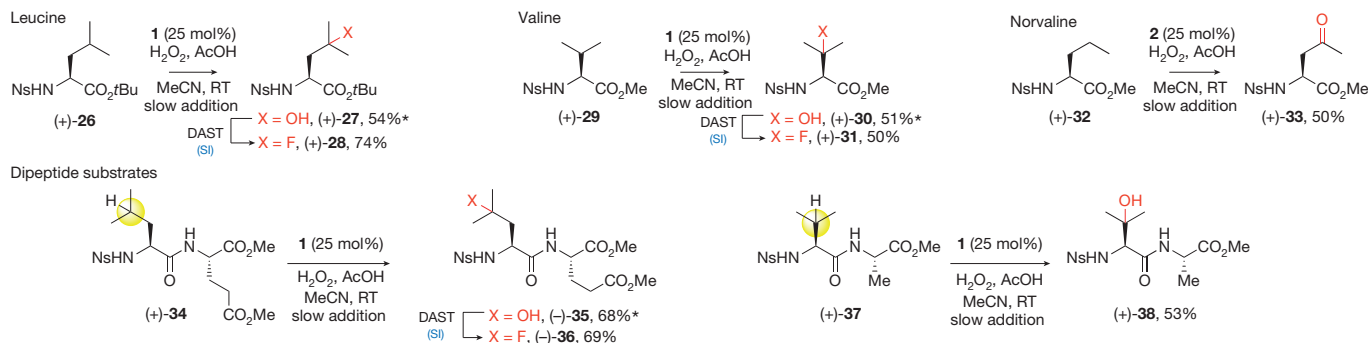


**Figure 2 | Four amino acids transformed to twenty-one chiral UAAs via small-molecule iron-catalysed C–H hydroxylations.** **a**, Oxidations to glutamic acid and 5-HP. Slow addition was as follows: AcOH (0.5–5 equiv.) was added to a MeCN solution of (–)-3. **1** (0.25 equiv. in CH<sub>3</sub>CN, 0.2 M) and H<sub>2</sub>O<sub>2</sub> (5–9 equiv. in CH<sub>3</sub>CN, 0.4–0.72 M) were added via syringe pump (75 min) simultaneously. Iterative addition: (–)-3 in MeCN was cooled to 0 °C. **1** (5 mol%) and AcOH (0.5 equiv.) were added, followed by dropwise addition (3 min) of 0 °C MeCN solution of H<sub>2</sub>O<sub>2</sub>

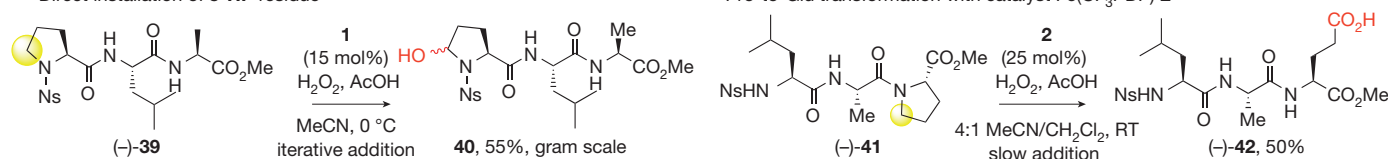
afford optically enriched triazole (+)-25. Significantly, these UAAs can be readily denosylated under mild conditions to furnish chiral amino esters with N-protecting groups common to peptide synthesis (for example, (+)-14, (+)-16, (–)-18, and (+)-20).

Additionally, we evaluated the generality of this method for the oxidation of chiral-pool amino acids possessing oxidizable aliphatic side-chain residues with stronger tertiary and secondary C–H bonds to enable direct routes to important UAAs (Fig. 2d). For example, exposure of leucine-, valine-, and *L*-norvaline-derived substrates to the reaction conditions with either **1** (tertiary oxidation) or **2** (secondary oxidation) at room temperature resulted in efficient aliphatic C–H oxidation, affording the tertiary hydroxyl derivatives (+)-27 and (+)-30 and the  $\delta$ -oxo derivative (+)-33 in good yields.

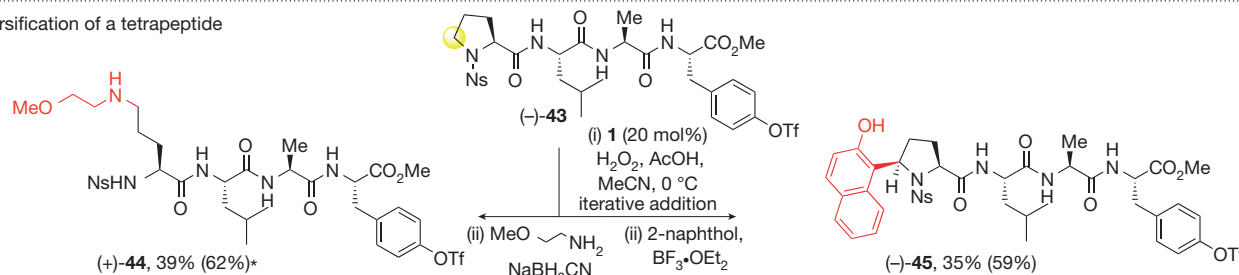
(1.9 equiv.). The addition of **1**, AcOH and H<sub>2</sub>O<sub>2</sub> was repeated twice, every 10 min. Crude 5-HP was passed through a silica gel plug and concentrated before arylation (in **b**) or reduction, olefination, or reductive amination (in **c**). **d**, Aliphatic C–H oxidation. \*Starting material recycled once. †dr, diastereomeric ratio, after isolation; o/p, ortho/para; RT, room temperature; DAST, diethylaminosulfur trifluoride; SI, Details for all methods can be found in the Supplementary Information. Yields represent the average of two experiments. Yields in parentheses are average yield per step.

These chiral hydroxylated amino acids are widely used in medicinal chemistry and as synthetic intermediates<sup>24</sup>. Importantly, the ability of catalysts **1** and **2** to selectively oxidize aliphatic side-chain C–H bonds of amino acids was not diminished when this method was applied to dipeptides possessing these residues, as similarly efficient oxidation of a leucine and valine residue were observed in these settings, see (–)-35 and (+)-38. The tertiary hydroxyl groups in (+)-27, (+)-30, and (–)-35 were converted to the fluorinated amino acids (+)-28 and (+)-31 and the fluorinated peptide (–)-36. Collectively, these results demonstrate a small-molecule-catalysed NRPS pre-assembly modification strategy, wherein a simple proline precursor and three other amino acids prone to oxidation are converted to twenty-one chiral UAAs representing seven distinct functional group

**a** Site-selective oxidative modifications of proline residues in peptides  
Direct installation of **5-HP** residue



**b** Diversification of a tetrapeptide



**c** Examination of reactivity at internal proline residues

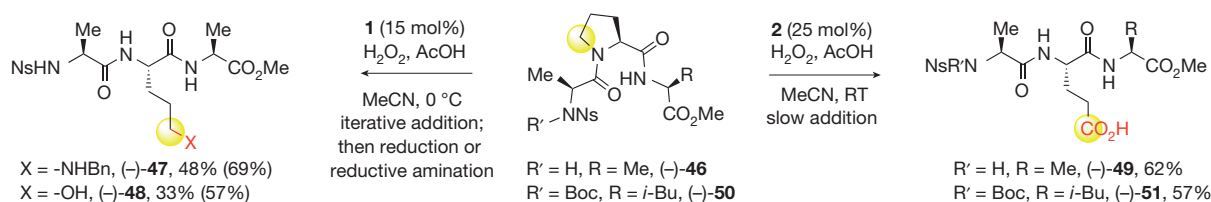


**Figure 3** | Direct oxidative modification of N-terminal, C-terminal and internal proline residues in peptides by small-molecule iron-catalysed C–H hydroxylation. **a**, Chemoselective oxidative modifications of N-terminal and C-terminal proline-containing peptides. **b**, Diversification of a tetrapeptide via chemoselective oxidation/functionalization

arrays: alcohols, fluorines, aryls, carboxylates, olefins, ketones and amines.

Post-assembly oxidative tailoring modifications in the more complex setting of a peptide were possible with catalysts **1** and **2** because of high functional group tolerance for amides in peptide settings, as well as high chemoselectivity in C5 oxidation of proline preferentially over other aliphatic C–H oxidations (Fig. 3a). For example, subjecting tripeptide (–)-**39** to oxidation with **1** at 0 °C led to the direct hydroxylation of the proline residue, with no observed off-site oxidation at the leucine residue. The use of catalyst **2** for proline over-oxidation in peptides was superior to catalyst **1**, possibly owing to the increased steric bulk around the iron centre of **2**, which minimizes off-site tertiary oxidation and deleterious coordination with the peptide. Underscoring the site selectivity and chemoselectivity that can be achieved with catalyst **2**, it is noteworthy that a +4 change in oxidation state of a methylene carbon in (–)-**41** to a carboxylic acid in (–)-**42** could be effected in the presence of an oxidizable tertiary C–H bond of a nearby leucine residue.

The Fe(PDP) C–H hydroxylation/arylation and reductive amination sequences were further tested in a challenging tetrapeptide setting (–)-**43** that included potentially oxidizable leucine, alanine, and tyrosine residues (Fig. 3b). Proline oxidation occurred with high site selectivity, and functionalization proceeded to efficiently furnish the amine (+)-**44** and the naphthol adduct (–)-**45**. We additionally examined the positional flexibility of proline oxidation, and found that catalyst **2** controlled over-oxidation of tripeptides containing an internal proline and furnished the corresponding glutamic acid derivatives (–)-**49** and (–)-**51** in excellent overall yields (62% and 57% yield, respectively; Fig. 3c). The internal proline of tripeptide (–)-**46** could also be transformed to the amine-containing residue (–)-**47** and the bishomoserine residue (–)-**48** via catalyst **1** oxidation followed by either reductive amination or reduction, respectively.

We sought to test our hypothesis that the ability to selectively install **5-HP** residues into proline-containing precursor peptides with catalyst **1**

sequences. \*Starting material recycled once. **c**, Direct oxidative opening of internal proline residues in tripeptides affords UAA- or glutamic-acid-containing tripeptides. Yields represent the average of two experiments. Yields in parentheses note the average yield per step. All slow additions were run with AcOH (0.5 equiv.)/H<sub>2</sub>O<sub>2</sub> (5 equiv.).

or catalyst **2** would enable a small-molecule-catalysed post-assembly oxidative strategy, affording late-stage diversification of peptides to new structures containing natural or unnatural amino acids (Fig. 4a). The tripeptide (–)-**39** was subjected to the full suite of proline oxidative modification reactions to install a phenol (oxidative arylation), carboxylic acid (controlled over-oxidation with catalyst **2**), alkene (Wittig olefination), alcohol (reduction), and four different amine functionalities (reductive amination), in good overall yields (average 40%, 63% per step) without observing epimerization of α-C–H bonds (chiral amino acid analysis of (–)-**53** indicated no epimerization to *D*-configuration of any residues; see the Supplementary Information for details). Strikingly, eight novel peptide sequences (**52**–**59**) were rapidly constructed from one peptide in one to two steps, underscoring the potential for such reactions to enable efficient diversification of native residues in a preassembled peptide setting. Alternative routes to make all eight peptides would involve eight separate syntheses from the respective amino acid building blocks, including the synthesis of UAAs.

Macrocyclic peptides are highly prevalent among NRPS natural products, and are valued as therapeutic candidates relative to their linear analogues owing to their increased stability against chemical and enzymatic degradation, increased receptor selectivity, and pharmacokinetic properties<sup>25–28</sup>. We sought to explore how the rapid installation of new functional groups in peptides from a simple proline residue could allow for the rapid construction and elaboration of macrocycles<sup>7</sup>. The phenol-, carboxylic acid- and olefin-derived tripeptides (**52**–**54**, see above) could be rapidly transformed into three macrocycles containing the ethereal (–)-**60**, amide (–)-**61**, and aliphatic (–)-**62** linkers, respectively, via short synthetic sequences (Fig. 4a) (see the Supplementary Information for details). The presence of functional groups on the linkage of stapled peptide-like structures like these has been shown to modulate the biological properties of the overall product<sup>29</sup>. Collectively, the small library of molecules rapidly synthesized from tripeptide (–)-**39** demonstrates the breadth of functionally

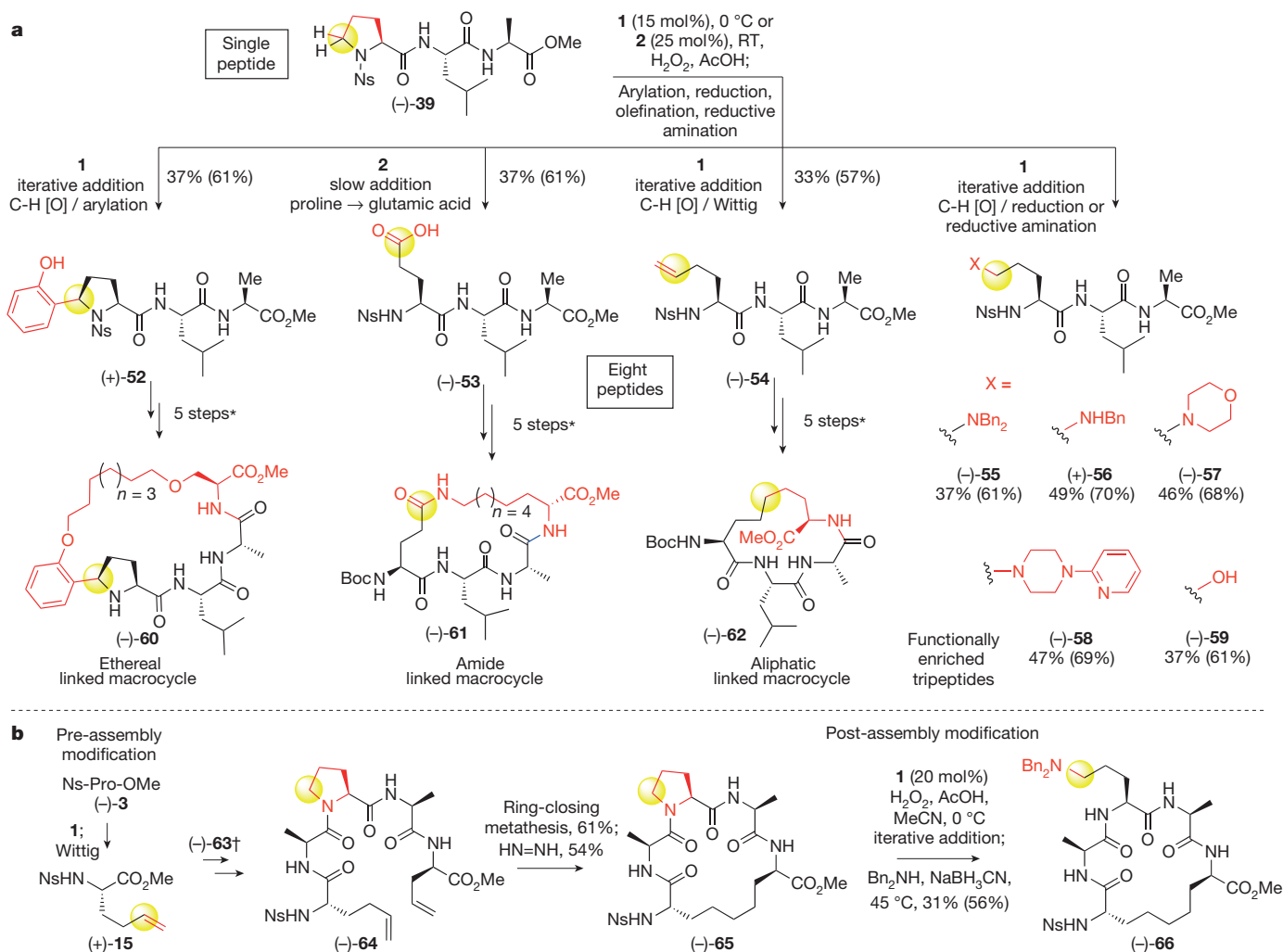


**Figure 4 | Small-molecule iron-catalysed oxidative diversification of tripeptides and macrocycles.** **a**, Fe(PDP) **1** and Fe(CF<sub>3</sub>PDP) **2** oxidative modifications of a single tripeptide enables synthesis of eight functionally diverse UAA-containing tripeptides. Slow addition was run with AcOH (0.5 equiv.)/H<sub>2</sub>O<sub>2</sub> (5 equiv.). \*Macrocycles **60–62** were prepared from tripeptides **52–54** using 5-step transformations involving alkene appendage to the UAA residue, coupling of a fourth alkene-containing amino acid to the C terminus, conversion of Nosyl to a Boc group,

ring-closing metathesis and hydrogenation. Individual routes vary in order. See the Supplementary Information for full details. **b**, Late-stage diversification of a proline-containing peptide macrocycle via post-assembly oxidation/reductive amination. †(-)-63 is Boc-Ala-Pro-Ala-(D)-Allylglycine-OMe. Yields generally represent the average of two experiments. Yields in parentheses indicate the average yield per step.

and structurally enriched molecules that can be accessed using our post-assembly oxidative strategy.

Proline has been used by synthetic chemists as a turning-element that helps to bring the ends of a linear peptide together to promote macrocyclizations<sup>30</sup>. We explored whether the NRPS-inspired C–H oxidation/functionalization strategy would enable internal proline residues, which serve as turn elements within a linear peptide sequence, to be transformed into a range of natural and unnatural acyclic amino acids. Encouraged by the high positional flexibility of proline oxidation (see above), we assembled a proline-containing linear pentapeptide (-)-**64**, using our pre-assembly modified UAA (+)-**15**, which was rapidly produced by C–H oxidation/olefination of proline (-)-**3**, and subjected it to ring-closing metathesis, which proceeded in good yield (61%) to furnish an 18-membered macrocycle. Reduction of the internal olefin with diimide provided the macrocyclic pentapeptide (-)-**65**. Application of the post-assembly C–H oxidation/functionalization with **1** to this macrocycle resulted in the late-stage conversion of the proline conformational element to a dibenzylornithine derivative (-)-**66**. This example underscores the potential for proline residues as diversifiable structural elements that may be functionally and structurally transformed at late stages in complex peptide settings.

The NRPS-inspired oxidation strategy described herein represents a powerful method for the direct diversification of amino acids and peptides via C–H oxidation. We anticipate that this strategy will benefit small-peptide therapeutics by enabling the rapid exploration of key physical properties (such as charge, polarity, and steric and stereochemical effects) and inspire the continued invention of non-directed, site-selective C–H oxidation reactions that unmask the potential for the pluripotent reactivity of C–H bonds in complex molecules.

Received 25 March; accepted 14 June 2016.

Published online 1 August 2016.

- Schwarzer, D., Finking, R. & Mahariq, M. Nonribosomal peptides: from genes to products. *Nat. Prod. Rep.* **20**, 275–287 (2003).
- Walsh, C. T. *et al.* Tailoring enzymes that modify nonribosomal peptides during and after chain elongation on NRPS assembly lines. *Curr. Opin. Chem. Biol.* **5**, 525–534 (2001).
- Wang, P., Gao, X. & Tang, Y. Complexity generation during natural product biosynthesis using redox enzymes. *Curr. Opin. Chem. Biol.* **16**, 362–369 (2012).
- Hubbard, B. K. & Walsh, C. T. Vancomycin assembly: nature's way. *Angew. Chem. Int. Ed.* **42**, 730–765 (2003).
- White, M. C. Adding aliphatic C–H bonds to synthesis. *Science* **335**, 807–809 (2012).



6. Burke, M. D. & Schreiber, S. L. A planning strategy for diversity-oriented synthesis. *Angew. Chem. Int. Ed.* **43**, 46–58 (2004).
7. Beckmann, H. G. *et al.* A strategy for the diversity-oriented synthesis of macrocyclic scaffolds using multidimensional coupling. *Nat. Chem.* **5**, 861–867 (2013).
8. Dangel, B. D., Johnson, J. A. & Sames, D. Selective functionalization of amino acids in water: a synthetic method via catalytic C–H bond activation. *J. Am. Chem. Soc.* **123**, 8149–8150 (2001).
9. Gong, W., Zhang, G., Liu, T., Giri, R. & Yu, J.-Q. Site-selective C(sp<sup>3</sup>)-H functionalization of di-, tri-, and tetrapeptides at the N-terminus. *J. Am. Chem. Soc.* **136**, 16940–16946 (2014).
10. Saladino, R. *et al.* A new and efficient synthesis of unnatural amino acids and peptides by selective 3,3-dimethyldioxirane side chain oxidation. *J. Org. Chem.* **64**, 8468–8474 (1999).
11. Rella, M. R. & Williard, P. G. Oxidation of peptides by methyl(trifluoromethyl)dioxirane: the protecting group matters. *J. Org. Chem.* **72**, 525–531 (2007).
12. Nájera, C. & Yus, M. Pyroglutamic acid: a versatile building block in asymmetric synthesis. *Tetrahedron Asymmetry* **10**, 2245–2303 (1999).
13. Ratnikov, M. O., Xu, X. & Doyle, M. P. Simple and sustainable iron-catalyzed aerobic C–H functionalization of *N,N*-dialkylanilines. *J. Am. Chem. Soc.* **135**, 9475–9479 (2013).
14. Zuo, Z. & MacMillan, D. W. C. Decarboxylative arylation of  $\alpha$ -amino acids via photoredox catalysis: one-step conversion of biomass to pharmacophores. *J. Am. Chem. Soc.* **136**, 5257–5260 (2014).
15. Turner, N. J. Enantioselective oxidation of C–O and C–N bonds using oxidases. *Chem. Rev.* **111**, 4073–4087 (2011).
16. Rauk, A. *et al.* Effect of structure on  $\alpha$ C–H bond enthalpies of amino acid residues: relevance to H-transfers in enzyme mechanism and protein oxidation. *Biochemistry* **38**, 9089–9096 (1999).
17. Uchida, K., Kato, Y. & Kawakishi, S. A novel mechanism for oxidative cleavage of prolyl peptides induced by the hydroxyl radical. *Biochem. Biophys. Res. Commun.* **169**, 265–271 (1990).
18. Shaw, M. H., Shurtleff, V. W., Terrett, J. A., Cuthbertson, J. D. & MacMillan, D. W. C. Native functionality in triple catalytic cross-coupling: *sp*<sup>3</sup> C–H bonds as latent nucleophiles. *Science* **352**, 1304–1308 (2016).
19. Chen, M. S. & White, M. C. A predictably selective aliphatic C–H oxidation reaction for complex molecule synthesis. *Science* **318**, 783–787 (2007).
20. Chen, M. S. & White, M. C. Combined effects on selectivity in Fe-catalyzed methylene oxidation. *Science* **327**, 566–571 (2010).
21. Gormisky, P. E. & White, M. C. Catalyst-controlled aliphatic C–H oxidations with a predictive model for site-selectivity. *J. Am. Chem. Soc.* **135**, 14052–14055 (2013).
22. Scola, P. M. *et al.* The discovery of Asunaprevir (BMS-650032), an orally efficacious NS3 protease inhibitor for the treatment of Hepatitis C virus infection. *J. Med. Chem.* **57**, 1730–1752 (2014).
23. Stevenazzi, A., Marchini, M., Sandrone, G., Vergani, B. & Lattanzio, M. Amino acidic scaffolds bearing unnatural side chains: an old idea generates new and versatile tools for the life sciences. *Bioorg. Med. Chem. Lett.* **24**, 5349–5356 (2014).
24. Seiple, I. B., Mercer, J. A. M., Sussman, R. J., Zhang, Z. & Myers, A. G. Stereocontrolled synthesis of *syn*- $\beta$ -hydroxy- $\alpha$ -amino acids by direct aldolization of pseudophenamine glycinamide. *Angew. Chem. Int. Ed.* **53**, 4642–4647 (2014).
25. Driggers, E. M., Hale, S. P., Lee, J. & Terrett, N. K. The exploration of macrocycles for drug discovery—an underexploited structural class. *Nat. Rev. Drug Discov.* **7**, 608–624 (2008).
26. Yudin, A. K. Macrocycles: lessons from the distant past, recent developments, and future directions. *Chem. Sci.* **6**, 30–49 (2015).
27. Schafmeister, C. E., Po, J. & Verdine, G. L. An all-hydrocarbon crosslinking system for enhancing the helicity and metabolic stability of peptides. *J. Am. Chem. Soc.* **122**, 5891–5892 (2000).
28. Miller, S. J., Blackwell, H. E. & Grubbs, R. H. Application of ring-closing metathesis to the synthesis of rigidified amino acids and peptides. *J. Am. Chem. Soc.* **118**, 9606–9614 (1996).
29. Lau, Y. H. *et al.* Functionalized staple linkages for modulating the cellular activity of stapled peptides. *Chem. Sci.* **5**, 1804–1809 (2014).
30. White, C. J. & Yudin, A. K. Contemporary strategies for peptide macrocyclization. *Nat. Chem.* **3**, 509–524 (2011).

**Supplementary Information** is available in the online version of the paper.

**Acknowledgements** Financial support for this work was provided by the NIH/ National Institute of General Medical Sciences (GM112492) and a grant from Pfizer to study the modification of natural products and medicinal compounds. T.J.O. is a Springborn Graduate Fellow. We thank L. Zhu for assistance with nuclear magnetic resonance spectroscopy, D. Gray and J. Bertke for X-ray crystallographic studies, A. I. Greenwood and J. Zhao for calculations on product (–)-**10**, W. A. van der Donk for use of his HPLC instrument, X. Yang and X. Zhao for assistance with Marfey’s reagent for chiral amino acid analysis of tripeptide (–)-**53**, C. Jiang for preliminary studies of amino acid oxidations, and G. S. Snapper for substrate synthesis.

**Author Contributions** T.J.O. and D.C.R. conducted the experiments and analysed the data. M.C.W. and T.J.O. wrote the manuscript. M.C.W., J.T.K., A.F.S., T.J.O. and D.C.R. designed the project. All authors provided comments on the experiments and manuscript during its preparation.

**Author Information** The crystal data have been deposited in The Cambridge Crystallographic Data Centre (<http://www.ccdc.cam.ac.uk>) under accession numbers 1478939, 1478940, and 1478941. Reprints and permissions information is available at [www.nature.com/reprints](http://www.nature.com/reprints). The authors declare no competing financial interests. Readers are welcome to comment on the online version of the paper. Correspondence and requests for materials should be addressed to M.C.W. ([mcwhite7@illinois.edu](mailto:mcwhite7@illinois.edu)).

# A progressively wetter climate in southern East Africa over the past 1.3 million years

T. C. Johnson<sup>1,2</sup>, J. P. Werne<sup>3</sup>, E. T. Brown<sup>1</sup>, A. Abbott<sup>4</sup>, M. Berke<sup>5</sup>, B. A. Steinman<sup>1</sup>, J. Halbur<sup>1</sup>, S. Contreras<sup>6</sup>, S. Grosshuesch<sup>1</sup>, A. Deino<sup>7</sup>, R. P. Lyons<sup>8†</sup>, C. A. Scholz<sup>8</sup>, S. Schouten<sup>9,10</sup> & J. S. Sinninghe Damsté<sup>9,10</sup>

African climate is generally considered to have evolved towards progressively drier conditions over the past few million years, with increased variability as glacial–interglacial change intensified worldwide<sup>1–3</sup>. Palaeoclimate records derived mainly from northern Africa exhibit a 100,000-year (eccentricity) cycle overprinted on a pronounced 20,000-year (precession) beat, driven by orbital forcing of summer insolation, global ice volume and long-lived atmospheric greenhouse gases<sup>4</sup>. Here we present a 1.3-million-year-long climate history from the Lake Malawi basin (10°–14° S in eastern Africa), which displays strong 100,000-year (eccentricity) cycles of temperature and rainfall following the Mid-Pleistocene Transition around 900,000 years ago. Interglacial periods were relatively warm and moist, while ice ages were cool and dry. The Malawi record shows limited evidence for precessional variability, which we attribute to the opposing effects of austral summer insolation and the temporal/spatial pattern of sea surface temperature in the Indian Ocean. The temperature history of the Malawi basin, at least for the

past 500,000 years, strongly resembles past changes in atmospheric carbon dioxide and terrigenous dust flux in the tropical Pacific Ocean, but not in global ice volume. Climate in this sector of eastern Africa (unlike northern Africa) evolved from a predominantly arid environment with high-frequency variability to generally wetter conditions with more prolonged wet and dry intervals.

Rainfall is the key metric for eastern African climate; annual temperature variations are limited, while moisture availability is far less predictable and profoundly affects distributions of vegetation and habitability across the landscape. Proxy records of northern and eastern African palaeoclimate reveal a trend towards drier conditions over the past few million years, overprinted by Milankovitch-scale cycles tied to Earth's orbit about the Sun<sup>1,2,5</sup>. However, it is unclear whether this trend holds for all of Africa. Our objectives were to determine how temperature and rainfall in the Malawi basin responded to orbital forcing of summer insolation, and whether they tracked global records of climate change, such as ice volume<sup>6</sup> and atmospheric carbon dioxide<sup>7</sup>,

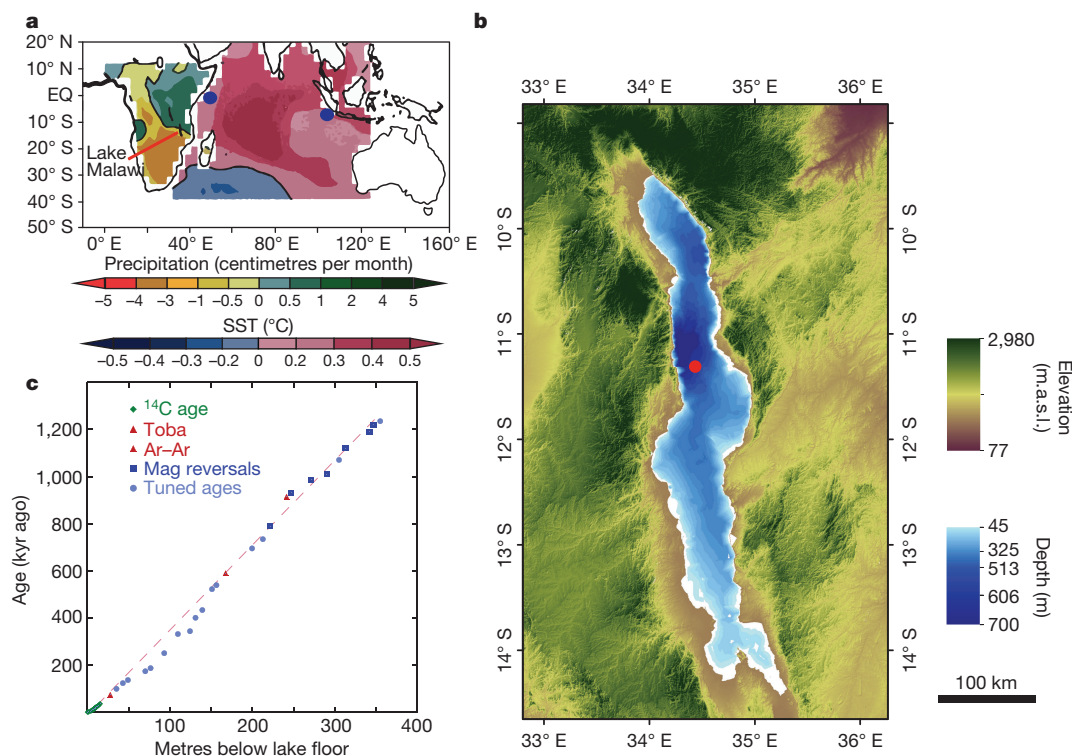


**Figure 1 | The location and bathymetry of Lake Malawi, African rainfall response to the Indian Ocean dipole, and the drill site age model.** **a**, Dominant patterns of precipitation variability over Africa and SST variability over the Indian Ocean for November–December–January of 1970–1992 (modified from ref. 24). The two blue dots depict the locations of two cores used to derive the history of west-minus-east SST gradient in Fig. 3 (see Methods). **b**, Bathymetric map of Lake Malawi, with location of drill site MAL05-1 (red dot), and digital elevation (metres above sea level, m.a.s.l.) map of the catchment. **c**, The age model for drill site MAL05-1.

<sup>1</sup>Large Lakes Observatory and Department of Earth and Environmental Sciences, University of Minnesota Duluth, Duluth, Minnesota 55812, USA. <sup>2</sup>Department of Geosciences, University of Massachusetts Amherst, Amherst, Massachusetts 01003, USA. <sup>3</sup>Department of Geology and Planetary Science, University of Pittsburgh, Pittsburgh, Pennsylvania 15260, USA. <sup>4</sup>Department of Earth and Planetary Sciences, Faculty of Science and Engineering, Macquarie University, Sydney, New South Wales 2109, Australia. <sup>5</sup>Department of Civil & Environmental Engineering & Earth Sciences, University of Notre Dame, 257 Fitzpatrick Hall, Notre Dame, Indiana 46556, USA. <sup>6</sup>Departamento de Química Ambiental and Centro de Investigación en Biodiversidad y Ambientes Sustentables (CIBAS), Universidad Católica de la Santísima Concepción, Casilla 297, Concepción, Chile. <sup>7</sup>Berkeley Geochronology Center, 2455 Ridge Road, Berkeley, California 94709, USA. <sup>8</sup>Earth Sciences Department, Syracuse University, 011a Heroy Geology Laboratory, Syracuse, New York 13244, USA. <sup>9</sup>NIOZ Netherlands Institute for Sea Research, Department of Marine Microbiology and Biogeochemistry, and Utrecht University, PO Box 59, 1790 AB Den Burg, The Netherlands. <sup>10</sup>Faculty of Geosciences, Department of Earth Sciences, Utrecht University, PO Box 80.021, 3508 TA Utrecht, The Netherlands. †Present address: Chevron Corporation, 1400 Smith Street, Houston, Texas 77002, USA.

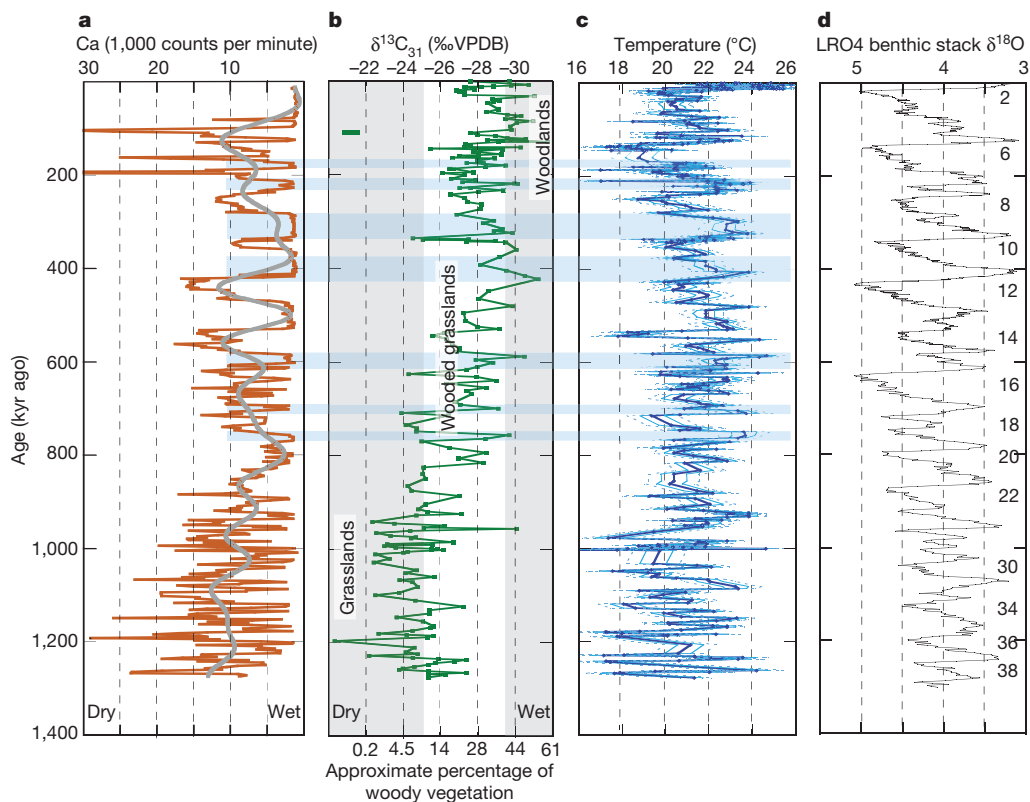


**Figure 2 | Vegetation (hydroclimate) and temperature history of the Lake Malawi basin.** **a**, Profile of calcium abundance ( $n = 22,010$ ), determined by X-ray fluorescence analysis at about 2-cm intervals, followed by a 20-point running mean. **b**, Profile of  $\delta^{13}\text{C}_{31}$  ( $n = 207$ ); each sample was run at least in duplicate and co-injected with squalane as an internal standard to monitor reproducibility of measurements. **c**, Profile of corrected temperature ( $n = 406$ ); roughly 10% of the samples were run in duplicate, and displayed average differences in  $\text{TEX}_{86}$  of 0.0076, corresponding to a  $2\sigma$  temperature value of  $0.8^\circ\text{C}$ . **d**, Profile of LR04 with marine isotope stage (MIS) numbers for glacial periods identified<sup>6</sup>

( $n = 950$ ). The heavy grey line in **a** represents a 100-kyr low-pass filter through the calcium data, which highlights the progressively wetter mean climate of the Malawi basin over the past 1.3 million years, as do the  $\delta^{13}\text{C}_{31}$  data. The green bar in the upper left corner of **b** indicates  $\pm 1\sigma$  analytical uncertainty in  $\delta^{13}\text{C}_{31}$ .  $1\sigma$  and  $2\sigma$  uncertainties in temperature due to analytical and lapse rate corrections (Methods) are indicated by the light blue solid and dashed lines, respectively, in **c**. Blue-shaded bars highlight some wet intervals, illustrating their correlation with warm temperatures during interglacial periods. Percentage woody vegetation is estimated from the  $\delta^{13}\text{C}_{31}$  correlation of ref. 16.

as well as the trends of increased aridity and variability observed farther north in Africa.

Although Lake Malawi (Fig. 1a) is an open basin today, its surface has dropped well below the elevation of its outlet on numerous occasions, creating closed-basin conditions with attendant shoreline migration and elevated water salinity<sup>8,9</sup>. We analysed sediment samples recovered by the Lake Malawi Drilling Project to produce records of temperature ( $\text{TEX}_{86}$ ) and aridity (calcium (Ca) content and leaf wax  $\delta^{13}\text{C}_{31}$ , where  $\text{C}_{31}$  indicates an  $n$ -alkane containing 31 carbon atoms) extending back to approximately 1.3 million years before present (Methods). Our age model for the sediment sequence is based on 15 radiocarbon dates, 3 dated tephra layers, and 6 palaeomagnetic reversals, supplemented by alignment of the  $\text{TEX}_{86}$  temperature record with the LR04 (the stacked record<sup>6</sup> of marine benthic foraminifera  $\delta^{18}\text{O}$ ) to assign ages between 75 and 590 thousand years (kyr) ago (Fig. 1c) (Methods).

A cyclic structure is apparent in the  $\text{TEX}_{86}$  temperature record after 600 kyr ago (Fig. 2, Extended Data Fig. 1). This is overprinted by considerable variability throughout the entire sediment sequence; we attribute this variability to the ill-defined ecology of freshwater *Thaumarchaeota*, which produce the  $\text{TEX}_{86}$  signal (such as the preferred water depth for *Thaumarchaeota*, dominant species in the archaeal community, seasonal variability<sup>10,11</sup>, and to inter-seasonal and inter-annual lake circulation dynamics. The temperature varies with an amplitude of about  $4^\circ\text{C}$ , between approximately  $19^\circ\text{C}$  and  $23^\circ\text{C}$ , displaying progressively larger-amplitude glacial–interglacial variations from marine isotope stage (MIS) 13 (about 500 kyr ago) to MIS 5 (about 125 kyr ago), after a remarkably cool MIS 14 (about 540 kyr ago) (Fig. 2c).

The degree of glacial cooling in the Malawi basin over the past 600 kyr does not match the amplitude of change in global ice volume as represented by the LR04 record (Fig. 2d). For example, Malawi basin glacial cooling was only about  $2^\circ\text{C}$  during MIS 12, when continental ice sheets were particularly extensive, but was  $4^\circ\text{C}$  during MIS 14, when global ice volume was relatively limited (Fig. 2c, d). However, the Malawi temperature record more closely matches the atmospheric carbon dioxide record for the past 600 kyr in the EPICA ice core<sup>7</sup> (Fig. 3a), and even more closely aligns ( $R^2 = 0.363$  and  $0.658$ ,  $P < 0.05$ , on raw and 100-kyr low-pass-filtered data, respectively) with a 500-kyr record of terrigenous dust flux to the central equatorial Pacific<sup>12</sup> (Fig. 3b). These relationships reflect carbon dioxide's key role in regulating tropical eastern African temperatures on a glacial–interglacial timescale, and suggest that atmospheric dust may also have contributed to temperature regulation on these timescales, despite its modest radiative impact, estimated at an order of magnitude lower than that of greenhouse gases<sup>13</sup>.

Calcium concentrations undergo a dramatic change from high-amplitude variability between calcareous and non-calcareous sediment (reflecting relatively arid and moist conditions, respectively) before 900 kyr ago to more prolonged periods of non-calcareous sediment and mainly lower-amplitude variations in the calcium values thereafter (Fig. 2a). Arid intervals were also longer after 900 kyr ago, including the most extreme ‘mega-drought’ of the past million years<sup>9,14</sup> which, if our tuned age model is correct, had its onset during MIS 6. Intriguingly, dry conditions when the lake surface was tens to hundreds of metres below outlet elevation (lowstand conditions) persisted intermittently well into



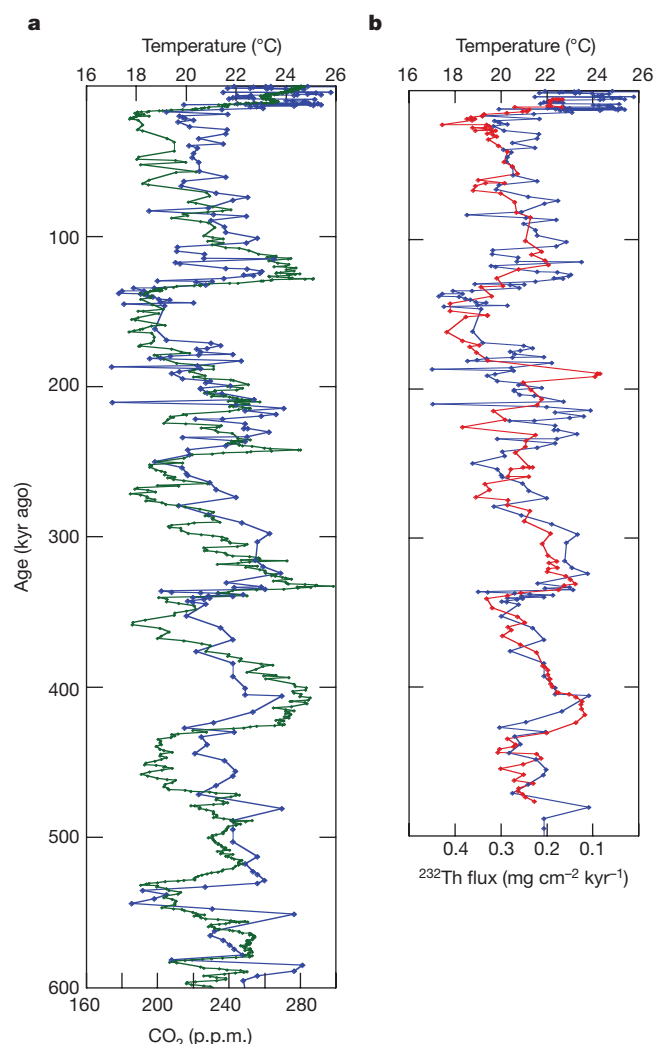


**Figure 3 | Correlation of the Malawi temperature record with atmospheric carbon dioxide and dust.** Temperature record for the Malawi basin (blue data points), plotted with atmospheric carbon dioxide (green data points)<sup>7</sup> (in a) and the dust flux to the central equatorial Pacific Ocean as represented by the depositional flux of  $^{232}\text{Th}$  (red data points)<sup>12</sup> (in b).

MIS 5, when a final recovery to hydrologically overfilled conditions developed (Fig. 2a).

$\delta^{13}\text{C}_{31}$  displays variability within a range of about 4‰ throughout the record, superimposed on a trend towards more negative mean values from around  $-24.5\text{‰}$  in the earlier part of the record to around  $-29\text{‰}$  in the last 100,000 years. We attribute this trend to a gradual shift to wetter conditions, and not to a change in catchment (other than its expansion when lake level dropped). From the perspective of basin evolution, we observe no evidence for major changes in catchment geometry (such as drainage capture), or large alterations of topographic gradients or the deformational regime over the interval of the drill core. Earlier in the Malawi rift valley's history, major shifts in catchment geometry and basin physiography would have occurred, owing to continental extension. On the basis of the extensive seismic reflection data set available from the basin<sup>15</sup>, such changes were unlikely in the most recent 15%–20% or so of the basin's history represented in our drill core.

$\delta^{13}\text{C}$  of vegetation can vary considerably, from about  $-24\text{‰}$  to  $-35\text{‰}$  for  $\text{C}_3$  and from  $-11\text{‰}$  to  $-14\text{‰}$  for  $\text{C}_4$  plants<sup>16</sup>. Nevertheless, an empirical relationship has been established between  $\delta^{13}\text{C}$  of soil organic matter and fractional cover of woody vegetation ( $r^2 = 0.77$ ) in eastern Africa<sup>17</sup>. This has been extended to  $\delta^{13}\text{C}$  of  $\text{C}_{31}$   $n$ -alkanes

preserved in lake sediment<sup>16</sup>. We use this relationship to estimate the vegetation in the Malawi catchment at the time of biomarker deposition. Our measured values of  $\delta^{13}\text{C}_{31}$  reflect substantial variations in the grassland cover, with less than 10% woody cover before 900 kyr ago, wooded grasslands consisting of 10%–40% woody plant cover and well developed ground cover of grasses and herbs from 900 kyr ago to the present, and occasional establishment of true woodlands, consisting of >40% woody plant cover in open or closed stands of trees, shrubs or thickets in the past 100 kyr (Fig. 2b).

After 900 kyr ago the calcium record displays intervals of carbonate-free sediment accumulation that lasted several tens of thousands of years, signifying open lake conditions during humid periods. These alternated with dry intervals, marked by carbonate accumulation, of comparable duration. The lake highstands correlate with periods of more negative  $\delta^{13}\text{C}_{31}$  and relatively warm temperatures (Fig. 2). Thus the Malawi basin experienced warm, wet interglacials and cooler (by about  $2\text{--}4^\circ\text{C}$ ), dry glacial periods, with a roughly 100-kyr periodicity, if our assumed age model is correct, over the past 900 kyr (Extended Data Fig. 2). It is noteworthy that during the megadrought initiated in MIS 6, when Lake Malawi was reduced to a saline lake <100 m deep<sup>9,14,18</sup>, the amplitude of the  $\delta^{13}\text{C}_{31}$  shift was relatively small, about 5‰ (Fig. 2b). However, the relationship between  $\delta^{13}\text{C}_{31}$  and landscape vegetation is nonlinear, so the relatively small 5‰ shift in  $\delta^{13}\text{C}_{31}$  represents a fourfold decrease in woody vegetation from  $\sim 40\%$  to  $\sim 10\%$  of the land cover.

Holocene climate shifts linked to precessional forcing are reported throughout northern Africa and much of tropical eastern Africa (including the so-called “African Humid Period”<sup>19</sup>), but the anti-phased response in the Southern Hemisphere (that is, an early Holocene arid period) appears to have been subdued and intermittent (for example, an early Holocene drop of about 120 m in the level of Lake Malawi<sup>20</sup> interspersed with highstands<sup>21</sup>; brief, early Holocene highstands of Lake Makgadikgadi at about  $20^\circ\text{S}$  (ref. 22) and Lake Chilwa at about  $15^\circ\text{S}$  (ref. 23). The apparent lack of an approximately 20-kyr cycle in the hydroclimate of the Lake Malawi basin over the past 900 kyr (Extended Data Fig. 2) is consistent with this more recent history.

We attribute the limited precessional signal in the Malawi record to the opposing effects of orbital influence on summer insolation and the Indian Ocean Dipole (IOD) pattern of sea surface temperature (SST) variability. At present, rainfall is enhanced in tropical eastern Africa but diminished in southern Africa during positive IOD phases (warm western equatorial Indian Ocean relative to the eastern Indian Ocean), and vice versa<sup>24</sup>. The IOD shows strong precessional variability, with the positive phase aligned with Northern Hemisphere summer insolation (Fig. 4) (Methods). Such a relationship enhances precessional variability in hydroclimate in the eastern African tropics north of the Equator because both factors contribute to increased rainfall. By contrast, the IOD is out of phase with summer insolation in the Southern Hemisphere, so the two factors have opposite effects on rainfall and thereby weaken precessional influence.

Lake Malawi is close to the present-day boundary of the dipolar African rainfall pattern that falls between tropical eastern Africa and southern Africa (Fig. 1a), with contrasting responses to the IOD. Tierney *et al.*<sup>25</sup> report a multidecadal relationship between eastern African rainfall and a positive IOD that differs from the aforementioned inter-annual pattern, with less rainfall over Lake Malawi and other lakes in the rift valley interior and wetter conditions closer to the eastern African coast and the Horn of Africa. In the Malawi record, precessional variation in precipitation may have been further obscured by changes due to migrations of the precipitation pattern boundary; these would have shifted the Malawi basin between the two IOD rainfall regimes.

Several interacting mechanisms may have contributed to the long-term trend towards a wetter climate in the Lake Malawi basin over the past million years. Aridification in the Horn of Africa has been attributed to Indian Ocean cooling due to the northward displacement

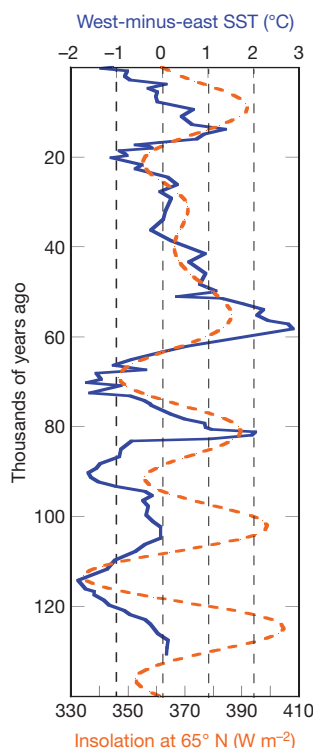


**Figure 4 | Northern Hemisphere summer insolation and the Indian Ocean SST gradient.** The west-minus-east SST gradient in the equatorial Indian Ocean (IOD) based on alkenone data from two core sites shown in Fig. 1a<sup>29,30</sup> (solid blue line), and Northern Hemisphere (at 65° N) summer insolation (dashed red line) over the past 140,000 years.

of New Guinea and narrowing of the Indonesian throughway over the past 3–4 million years<sup>26</sup>. An overall cooling of the Indian Ocean should result in a drier hydroclimate throughout eastern Africa, even in the Malawi basin. However, an anti-phased relationship in hydroclimate response to the IOD in the interior rift valley versus coastal eastern Africa and the Horn of Africa<sup>25</sup> suggests not only that the Indian Ocean became cooler, but that the IOD became progressively less positive over time. Model results suggest that this would be accompanied by a weakening of a localized Walker circulation over the Indian Ocean, less ascending air over the western Indian Ocean and coastal Africa, and more precipitation in the rift valley, including Lake Malawi<sup>25</sup>.

Lake Malawi sediment recorded a transition from a highly variable and predominantly arid climate before 900 kyr ago to a progressively more humid environment after the Mid-Pleistocene Transition, which was dominated by 100-kyr cycles consisting of warm, wet interglacial periods alternating with cooler, drier glacial periods. This shift towards more humid conditions contrasts with the well documented progression towards more aridity in northern Africa over the same period, as recorded in the carbon isotopic composition of soil carbonates and in dust fluxes to sediments in both the Atlantic Ocean and the Gulf of Aden (Extended Data Fig. 3)<sup>2</sup>. Yet another pattern is shown in a leaf-wax isotope record of South African vegetation (recovered from the tropical Atlantic Ocean) that displays a shift in dominant periodicity from about 40-kyr to about 100-kyr cycles through the Mid-Pleistocene Transition<sup>27</sup>, as observed in the Malawi record, but with no long-term trend towards either wetter or drier conditions. This growing body of evidence attests to a large regional variability in climate history over the African continent.

Regional differences in hydroclimate undoubtedly influenced the migration of our human ancestors<sup>28</sup>. As northern Africa became more arid over the past million years, the Malawi basin evolved towards a wetter, more hospitable environment, at least during interglacial times. The Malawi record raises key questions about African climate,

regarding how much of the rift valley shifted to wetter conditions over the past million years, whether MIS 14 was an unusually cold ice age throughout the region, and what role precessional forcing had on hydroclimate to the north of Malawi. Future drilling campaigns on the East African Great Lakes will offer unique opportunities to address these questions and to understand the changing landscape where our ancestors evolved, migrated and advanced their cultures.

**Online Content** Methods, along with any additional Extended Data display items and Source Data, are available in the online version of the paper; references unique to these sections appear only in the online paper.

**Received 10 December 2015; accepted 28 June 2016.**

**Published online 10 August 2016.**

1. Cerling, T. E. Development of grasslands, savannas in East Africa during the Neogene. *Palaeogeogr. Palaeoclimatol. Palaeoecol.* **97**, 241–247 (1992).
2. deMenocal, P. African climate change and faunal evolution during the Pliocene-Pleistocene. *Earth Planet. Sci. Lett.* **220**, 3–24 (2004).
3. Potts, R. Evolution and climate variability. *Science* **273**, 922–923 (1996).
4. Otto-Bliesner, B. *et al.* Coherent changes of southeastern equatorial and northern African rainfall during the last deglaciation. *Science* **346**, 1223–1227 (2014).
5. Trauth, M. H., Maslin, M. A., Deino, A. & Strecker, M. R. Late Cenozoic moisture history of East Africa. *Science* **309**, 2051–2053 (2005).
6. Liesecki, L. E. & Raymo, M. E. A Pliocene-Pleistocene stack of 57 globally distributed benthic  $\delta^{18}\text{O}$  records. *Paleoceanography* **20**, PA1003 (2004).
7. Lüthi, D. *et al.* High-resolution carbon dioxide concentration record 650,000–800,000 years before present. *Nature* **453**, 379–382 (2008).
8. Finney, B. P., Scholz, C. A., Johnson, T. C., Trumbore, S. & Southon, J. in *The Limnology, Climatology, and Palaeoclimatology of the East African Lakes* (eds Johnson, T. C. & Odada, E. O.) 495–508 (Gordon and Breach, 1996).
9. Scholz, C. A. *et al.* East African megadroughts between 135–75 kyr ago and implications for early human history. *Proc. Natl Acad. Sci. USA* **104**, 16416–16421 (2007).
10. Pearson, A. & Ingalls, A. E. Assessing the use of archaeal lipids as marine environmental proxies. *Annu. Rev. Earth Planet. Sci.* **41**, 359–384 (2013).
11. Schouten, S., Hopmans, E. C. & Sinninghe Damsté, J. S. The organic geochemistry of glycerol dialkyl glycerol tetraether lipids: a review. *Org. Geochem.* **54**, 19–61 (2013).
12. Winckler, G., Anderson, R. F., Fleisher, M. Q., McGee, D. & Mahowald, N. Covariant glacial-interglacial dust fluxes in the equatorial Pacific and Antarctica. *Science* **320**, 93–96 (2008).
13. Albani, S. *et al.* Improved dust representation in the Community Atmosphere Model. *J. Adv. Model. Earth Syst.* **6**, 541–570 (2014).
14. Lyons, R. P. *et al.* A continuous 1.3 million year record of East African hydroclimate, and implications for patterns of evolution and biodiversity. *Proc. Natl Acad. Sci.* **112**, 15568–15573 (2015).
15. Lyons, R. P., Scholz, C. A., Buoniconti, M. R. & Martin, M. R. Late Quaternary stratigraphic analysis of the Lake Malawi Rift, East Africa: an integration of drill-core and seismic-reflection data. *Palaeogeogr. Palaeoclimatol. Palaeoecol.* **303**, 20–37 (2011).
16. Magill, C. R., Ashley, G. M. & Freeman, K. H. Ecosystem variability and early human habitats in eastern Africa. *Proc. Natl Acad. Sci. USA* **110**, 1167–1174 (2013).
17. Cerling, T. E. *et al.* Woody cover and hominin environments in the past 6 million years. *Nature* **476**, 51–56 (2011).
18. Cohen, A. S. *et al.* Ecological consequences of early Late Pleistocene megadroughts in tropical Africa. *Proc. Natl Acad. Sci.* **104**, 16422–16427 (2007).
19. deMenocal, P. *et al.* Abrupt onset and termination of the African Humid Period: rapid climate responses to gradual insolation forcing. *Quat. Sci. Rev.* **19**, 347–361 (2000).
20. Finney, B. P. & Johnson, T. C. Sedimentation in Lake Malawi (East Africa) during the past 10,000 years: a continuous paleoclimate record from the southern tropics. *Palaeogeogr. Palaeoclimatol. Palaeoecol.* **85**, 351–366 (1991).
21. Van Bocxlaer, B., Salenbien, W., Praet, N. & Verniers, J. Stratigraphy and paleoenvironments of the early to middle Holocene Chippalawamba Beds (Malawi, Africa). *Biogeosciences* **9**, 4497–4512 (2012).
22. Burrough, S. L., Thomas, D. S. G. & Bailey, R. M. Mega-lake in the Kalahari: a Late Pleistocene record of the paleolake Makgadikgadi system. *Quat. Sci. Rev.* **28**, 1392–1411 (2009).
23. Thomas, D. S. G., Bailey, R., Shaw, P. A., Durcan, J. A. & Singray, J. S. Late Quaternary highstands at Lake Chilwa, Malawi: frequency, timing and possible forcing mechanisms in the last 44 ka. *Quat. Sci. Rev.* **28**, 526–539 (2009).
24. Goddard, L. & Graham, N. E. Importance of the Indian Ocean for simulating rainfall anomalies over eastern and southern Africa. *J. Geophys. Res.* **104**, 19099–19116 (1999).
25. Tierney, J. E., Smerdon, J. E., Anchukaitis, K. J. & Seager, R. Multidecadal variability in East African hydroclimate controlled by the Indian Ocean. *Nature* **493**, 389–392 (2013).
26. Cane, M. A. & Molnar, P. Closing of the Indonesian seaway as a precursor to east African aridification around 3–4 million years ago. *Nature* **411**, 157–162 (2001).

27. Schefuß, E., Schouten, S., Jansen, J. H. F. & Sinninghe Damsté, J. S. African vegetation controlled by tropical sea surface temperatures in the mid-Pleistocene period. *Nature* **422**, 418–421 (2003).
28. Trauth, M. H. *et al.* High- and low-latitude forcing of Plio-Pleistocene East African climate and human evolution. *J. Hum. Evol.* **53**, 475–486 (2007).
29. Mohtadi, M. *et al.* IGBP PAGES. [https://www.ncdc.noaa.gov/cdo/f?p=519:1:0:::P1\\_STUDY\\_ID:19139](https://www.ncdc.noaa.gov/cdo/f?p=519:1:0:::P1_STUDY_ID:19139) (NOAA World Data Center for Paleoclimatology, 2011).
30. Bard, E., Rostek, F. & Sonzogni, C. Interhemispheric synchrony of the last deglaciation inferred from alkenone palaeothermometry. *Nature* **385**, 707–710 (1997).

**Supplementary Information** is available in the online version of the paper.

**Acknowledgements** We thank the engineering and design team of the Lake Malawi Scientific Drilling Project for overcoming substantial technical challenges associated with drilling on Lake Malawi, especially the efforts of D. Schnurrenberger, M. Pardy and Lengeek Vessel Engineering. B. Otto-Bliesner and S. Albani provided advice on climate model results relevant to this study. J. King provided the palaeomagnetic reversal data that contributed substantially to the age model of the Malawi sediment record. We thank the scientists and technicians of LacCore, University of Minnesota, for their assistance in the splitting, initial analyses, sampling and archiving of the sediment cores obtained by the Lake Malawi Drilling Project. Financial support was provided

by the US National Science Foundation EAR and P2C2 programmes and by the International Continental Scientific Drilling Program. S.S. and J.S.S.D. were supported by the Netherlands Earth System Science Centre (NESSC), which is financially supported by the Dutch Ministry of Education, Culture and Science (OCW).

**Author Contributions** T.C.J., J.P.W. and E.T.B. conceptualized the project. C.A.S. and T.C.J. were two of the Principal Investigators on the Lake Malawi Drilling Project. J.P.W., J.S.S.D. and S.S. supervised and interpreted the biomarker analyses conducted by A.A., M.B., J.H., S.C. and S.G. E.T.B. supervised the X-ray fluorescence analyses for calcium. A.D. provided Ar–Ar dates on tephra. R.P.L. provided the lake level history. B.A.S. conducted the statistical analyses. T.C.J. and E.T.B. wrote the manuscript with substantial contributions from J.P.W., A.A., M.B., B.A.S., S.C., S.S. and J.S.S.D. All authors reviewed the paper prior to submission.

**Author Information** The data used in this study are available as Supplementary Data. Reprints and permissions information is available at [www.nature.com/reprints](http://www.nature.com/reprints). The authors declare no competing financial interests. Readers are welcome to comment on the online version of the paper. Correspondence and requests for materials should be addressed to T.C.J. ([tcj@d.umn.edu](mailto:tcj@d.umn.edu)).

**Reviewer Information** *Nature* thanks K. Freeman, P. Polissar and the other anonymous reviewer(s) for their contribution to the peer review of this work.



## METHODS

The Lake Malawi Drilling Project recovered a 380-m sediment sequence in 2005 from a water depth of 590 m. Cores MAL05-1B and MAL05-1C of the Drilling Project, and a nearby piston core M98-13P (Extended Data Table 1) were analysed for past temperature and rainfall. Seismic reflection profiles used to select the site portray an undisturbed sedimentary section that was not impacted by erosion, turbidity currents or mass wasting events<sup>15</sup>. Sediment samples were analysed to produce records of temperature (TEX<sub>86</sub>) and aridity (calcium content and leaf wax  $\delta^{13}\text{C}$ ).

**Palaeo-temperature derived from TEX<sub>86</sub>.** TEX<sub>86</sub> is a proxy for temperature in the upper water column, based on the distribution of glycerol dialkyl glycerol tetraether (GDGT) membrane lipids of *Thaumarchaeota* living in the water column<sup>31,32</sup>. *Thaumarchaeota* are ammonia oxidizers that live throughout the aerobic and sub-oxic water column, but have been found in many lake systems to have a maximum abundance just below the thermocline or chlorophyll maximum<sup>33,34</sup>. Indeed, in Lake Malawi the maximum abundance of the most labile GDGT produced by *Thaumarchaeota* has been identified at 50 m water depth<sup>34</sup>. Nevertheless, the distribution of their lipids is strongly related to surface water temperature in many lake systems<sup>31,35,36</sup>. The GDGTs used to determine TEX<sub>86</sub> are well preserved in sediments and have been identified intact in sediments as far back as the Cretaceous Period to estimate past ocean temperatures<sup>37</sup>.

Lipids were extracted from 577 freeze-dried, homogenized sediment samples using accelerated solvent extraction (Dionex ASE) using hexane/dichloromethane (DCM) 9:1 (v/v) at 100 °C and  $7.6 \times 10^6$  Pa to obtain a total lipid extract. The total lipid extract was then separated into neutral, free fatty acid, and phospholipid fatty acid fractions using an aminopropylsilyl bond elute column, cleaned before use with 10 ml successive rinses of methanol followed by 1:1 DCM:2-propanol. Eight millilitres each of 1:1 DCM:2-propanol, 4% glacial acetic acid in distilled ethyl ether, and methanol were used with the cleaned columns to elute the neutral, free fatty acid, and phospholipid fatty acid fractions, respectively. Short column chromatography with activated alumina as the stationary phase was used to further separate the neutral fraction into apolar and polar fractions using 9:1 hexane:DCM followed by 1:1 DCM: methanol as eluents for the two fractions, respectively. The polar fraction containing the GDGT lipids required for TEX<sub>86</sub> analysis was filtered (0.45  $\mu\text{m}$  filter), dried under N<sub>2</sub>, and then redissolved in 99:1 hexane:isopropanol for analysis. The apolar fraction containing *n*-alkanes was further separated into saturated and unsaturated hydrocarbons using Ag<sup>+</sup>-impregnated silica gel column chromatography as described in ref. 38.

GDGTs were analysed by high-performance liquid chromatography/atmospheric pressure chemical ionization mass spectrometry (HPLC/APCI-MS), using an Agilent 1100 series liquid chromatograph with an Alltech Prevail Cyano column (150 mm  $\times$  2.1 mm; 3  $\mu\text{m}$  diameter)<sup>39</sup>. Annual lake surface temperatures (ALST) in degrees Celsius were calculated using the TEX<sub>86</sub> ratio of GDGTs<sup>40</sup> and the lake sediment calibration of ref. 41:

$$\text{ALST} = 49.032(\text{TEX}_{86}) - 10.989 \quad (r^2 = 0.88; n = 16)$$

A global marine calibration for TEX<sub>86</sub> yields a mean error of 2.5 °C (ref. 42), and the global lake calibration yields a mean error of 3.6 °C (ref. 41). Although this is quite large relative to the rather small interannual variation in tropical temperature, the error of the global calibration is undoubtedly amplified by the differing composition of communities as well as differences in seasonality and depth habitat of *Thaumarchaeota* in different lakes. Within a single lake community, we suspect that the correlation between TEX<sub>86</sub> and ALST is much tighter.

The sampling interval for TEX<sub>86</sub> analyses averaged about 10 cm in the depth interval of 0–8 metres below lake floor (m.b.l.f.), 50 cm in the depth interval 8–18 m.b.l.f., and 1 m in the depth interval 18–379 m.b.l.f. Roughly 10% of the samples were run in duplicate, and displayed average differences in TEX<sub>86</sub> of 0.0076, corresponding to a 2 $\sigma$  temperature value of 0.8 °C.

**Acceptance criteria for TEX<sub>86</sub> data.** Palaeotemperature data derived from TEX<sub>86</sub> analysis may be compromised if the concentrations of the isomers used to calculate TEX<sub>86</sub> are too low, or if a substantial portion of the isoprenoid GDGTs used to calculate TEX<sub>86</sub> are derived from sources other than *Thaumarchaeota*, such as soil archaea in the catchment or methanogenic archaea living in the lower water column<sup>43</sup>. We accepted TEX<sub>86</sub> values for our palaeotemperature reconstructions as long as the following criteria were met:

- (1) The signal must be above the limit of quantitation<sup>39</sup>, which in our case corresponded to integral peak areas  $>10^4$  for the 1,300 and 1,292 ('cren') isomers.
- (2) The ratio of GDGT-0/crenarchaeol  $<2.0$  must exclude the impact of methanogen archaea.
- (3) The crenarchaeol isomer must be  $<10\%$  of the sum of the crenarchaeol and the crenarchaeol isomer and GDGT-2 must be  $<45\%$  of the total GDGTs to exclude influences of archaea other than *Thaumarchaeota*.
- (4) The BIT (branched and isoprenoid tetraether) index must be  $>0.5$  to exclude

the impact of soil-derived GDGTs (see refs 11 and 43 for further explanation and rationale for these criteria).

Using these criteria, we rejected 107 of the 584 analyses for TEX<sub>86</sub>. The rejected TEX<sub>86</sub> data yielded temperatures ranging between about 4 °C and 38 °C. Nearly all of them were associated with a BIT index  $>0.5$ , and most were warmer than adjacent temperatures that met our acceptance criteria (Extended Data Fig. 4). The temperatures derived from the accepted TEX<sub>86</sub> measurements fall within a range of  $\sim 18$ –28 °C (Extended Data Fig. 4).

Almost all of the TEX<sub>86</sub> values that were rejected correlate with depths where the sediments are calcareous and a lake-level index based on sediment composition<sup>14</sup> indicates relatively arid conditions with the lake at a lowstand. Under such conditions, the shoreline would have encroached upon the drill site, increasing the likelihood of terrestrially derived GDGT input from the catchment, a diminished aquatic production of GDGTs by *Thaumarchaeota*, proliferation of other archaeal species, and potential remobilization of previously deposited shallower water sediments.

**Temperature correction due to changing lake-surface elevation.** The remaining accepted temperatures were then corrected for the lapse rate effect of the lake's major lowstands. Lake Malawi has experienced drops of several hundred metres in lake level during prolonged arid periods in the past (referred to as "megadroughts" in ref. 9), and during such times of depressed lake level, water temperature would have risen owing to the temperature lapse rate alone, independent of any regional change in temperature. The lake-level history is not known precisely, but is best represented by principal component 1 (Lyons' PC1, or LPC1)<sup>14</sup>, derived from principal component analysis of four sediment parameters: natural gamma radiation, C/N ratio and  $\delta^{13}\text{C}$  of bulk organic matter, and reflected colour of the core digital image. We corrected the TEX<sub>86</sub> temperatures by using the linear relationship between LPC1 and lake-level depression (in metres) that Lyons *et al.*<sup>14</sup> derived from direct comparison of LPC1 with the depths of correlative lowstand deltas identified on seismic reflection profiles:

$$\Delta\text{LL} = -154.18(\text{LPC1}) - 247.05 \quad (R^2 = 0.9628)$$

where  $\Delta\text{LL}$  is the drop in lake level, in metres, from the present-day lake level.

Assuming a moist tropical lapse rate of 6 °C km<sup>-1</sup>, we multiplied negative values of  $\Delta\text{LL}$  by 0.006 to obtain the temperature correction to be subtracted from the original TEX<sub>86</sub> temperature to arrive at a temperature for constant lake elevation. In the few intervals where  $\Delta\text{LL}$  had a positive value (implying lake level higher than the present lake level), no temperature correction was applied because the lake cannot rise much above outlet elevation, and the lapse rate effect would be negligible. We applied the prediction uncertainty range of the Lyons *et al.*<sup>14</sup> PC1-to-lake-level relationship to estimate uncertainty in the lapse-rate-based temperature correction. The positive 2 $\sigma$  prediction uncertainty values were adjusted to not exceed a lake-surface elevation change  $\Delta\text{LL}$  of greater than zero (that is, during times of high lake level and overflow). The overall temperature uncertainty was calculated by adding in quadrature the analytical (2 $\sigma$  of 0.8 °C, described above) and lapse-rate correction uncertainties and resulted in average and maximum 2 $\sigma$  values of about 1.0 °C and 1.3 °C, respectively. The correction for lapse rate effect reduces the average temperature of the record by about 2 °C, but the overall amplitude of temperature shift and the occurrence of distinct intervals of relatively warm and relatively cold temperatures remain (Extended Data Fig. 1).

**Palaeo-aridity derived from  $\delta^{13}\text{C}$  of leaf-wax *n*-alkanes and calcium abundance.** Stable carbon isotopic compositions of C<sub>29</sub>–C<sub>33</sub> *n*-alkanes derived from fossil leaf waxes primarily reflect the relative abundances of C<sub>3</sub> (mostly trees, shrubs and herbs) and C<sub>4</sub> (mostly grass) vegetation<sup>16,32</sup>. An Agilent 6890N gas chromatograph (60-m HP-1 column, 0.32 mm inner diameter, 0.25  $\mu\text{m}$  film thickness) interfaced to a Thermo Finnigan Delta<sup>plus</sup> XP mass spectrometer via a combustion interface was used to determine the  $\delta^{13}\text{C}$  of *n*-alkanes. All  $\delta^{13}\text{C}$  values are reported as per mil deviations from the Vienna Pee Dee Belemnite (VPDB) standard using conventional delta notation. The gas chromatograph temperature program begins at 50 °C and increases at a rate of 50 °C min<sup>-1</sup> to 180 °C and next at a rate of 3 °C min<sup>-1</sup> to 320 °C. The final temperature of 320 °C is held for 6 min. The *n*-alkanes separated by the gas chromatography column are oxidized at 940 °C and converted to carbon dioxide. A standard mixture of *n*-alkanes of known  $\delta^{13}\text{C}$  values was analysed multiple times daily ('Mix-A' of C<sub>16</sub>–C<sub>30</sub> *n*-alkanes provided by A. Schimmelmann, Indiana University); from these replicate measurements, the typical precision of the  $\delta^{13}\text{C}$  measurements is  $\pm 0.5\%$  (1 $\sigma$ ). Each sample was run at least in duplicate and co-injected with squalane as an internal standard to monitor reproducibility of measurements. Replicates were analysed and plotted individually for each *n*-alkane sample, with a mean error of  $\pm 0.41\%$  for C<sub>31</sub> duplicates.

While C<sub>3</sub> herbs are found in both woodlands and grasslands,  $\delta^{13}\text{C}$  of C<sub>31</sub> *n*-alkanes in tropical eastern Africa generally reflect the restructuring of the landscape between woodlands dominated by C<sub>3</sub> vegetation, indicating relatively humid conditions, and by C<sub>4</sub> grasslands, representing relatively arid conditions in the lake basin<sup>16</sup>.

The trends of  $\delta^{13}\text{C}$  in the  $\text{C}_{29}$ ,  $\text{C}_{31}$ , and  $\text{C}_{33}$   $n$ -alkanes are broadly similar in timing and amplitude (Extended Data Fig. 5). Any one of these profiles could have been used to reflect the history of vegetation and hydroclimate on the landscape surrounding Lake Malawi, and would have been consistent with our interpretation of the environmental history of the region. We chose to reflect the terrigenous leaf-wax data as  $\delta^{13}\text{C}_{31}$ , which is usually the most abundant of the three  $n$ -alkanes and was chosen by ref. 16 to relate to  $\text{C}_3$  and  $\text{C}_4$  plant-type abundance in eastern Africa, which we utilize in Fig. 2. We find the down-core trend in  $\delta^{13}\text{C}_{31}$  to closely track the trend in  $\delta^{13}\text{C}_{\text{wax}}$ , the weighted mean average of the three  $n$ -alkanes that has been reported in previous studies in eastern Africa (see ref. 38) (Extended Data Fig. 5).

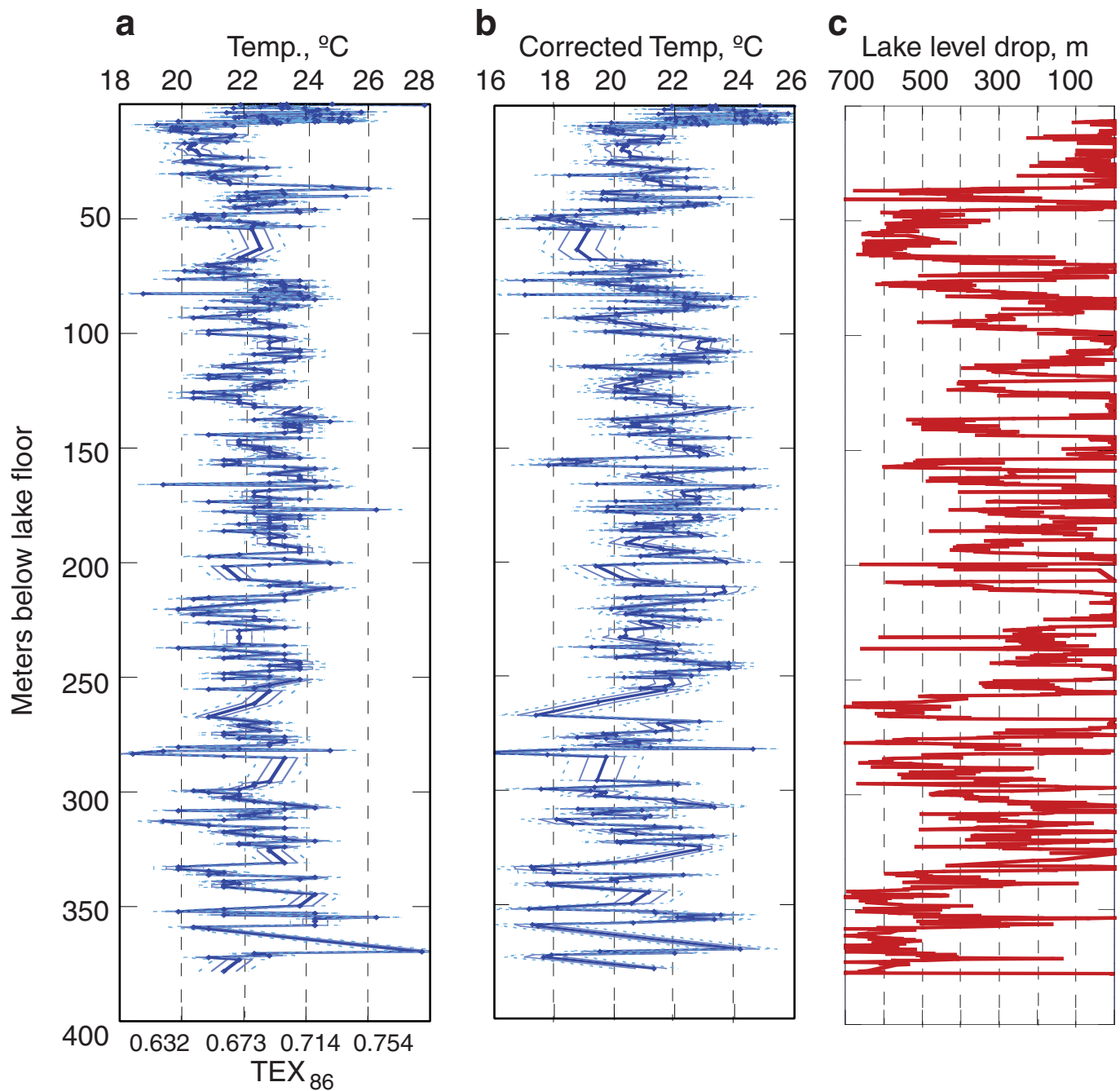
Calcium abundance in bulk sediment, determined by scanning X-ray fluorescence, was used as another indicator of past hydroclimate. The calcium signal is strongly bi-modal, exhibiting high values in calcareous sediments, which accumulate only during lake lowstands<sup>20,44</sup> and low values during wetter conditions when the lake overflows at its outlet, leaving the water column under-saturated with respect to calcite<sup>45</sup>.

**Refining the age model for the MAL05-1 drilling site.** Our age model (Fig. 1c) is based initially on 15 radiocarbon dates in the upper 16 m of core, the presence of the youngest Toba ash ( $75 \pm 1$  kyr ago) at 28.1 m.b.l.f. (ref. 46), Ar–Ar dates on tephra at 167.8 m.b.l.f. ( $590 \pm 20$  kyr ago) and 241.6 m.b.l.f. ( $915 \pm 8$  kyr ago), and six palaeomagnetic reversals beginning with the Brunhes–Matuyama at 222 m.b.l.f. (ref. 14) (Extended Data Fig. 6a, Extended Data Table 2). These dates indicate an average sedimentation rate of  $0.28 \text{ m kyr}^{-1}$  for the drill site, although they provide no age control in the interval between 75 kyr ago (Toba ash horizon) and 590 kyr ago (the younger of the two Ar–Ar dates). The corrected temperature versus depth-in-core record (Extended Data Fig. 1b) displays a statistically significant 33.6-m cycle, which corresponds to an eccentricity period of about 121 kyr, assuming a sedimentation rate of about  $0.28 \text{ m kyr}^{-1}$  (see statistics in Extended Data Fig. 6b). We note that the raw temperature data before correction for lapse rate also displays a significant cycle of 38.5 m (bandwidth is 0.0001 and 80% error estimate on the power spectrum is 0.626), which indicates that the lapse rate correction is not artificially introducing cyclicity into the temperature record. Consequently, we align the  $\text{TEX}_{86}$  corrected temperature record with the LR04 marine stacked benthic foraminiferal  $\delta^{18}\text{O}$  record to assign ages in the interval 75–590 kyr ago, recognizing that the periods of relatively warm temperature must have coincided with interglacials and relatively cool temperatures with glacial periods (Extended Data Fig. 6c). The resultant age assignments and sedimentation rates based on this alignment do not deviate dramatically from the initial age model (Extended Data Fig. 6a).

Employing our age model, we performed Blackman–Tukey spectral analysis on the lake-level history derived from LPC1 (Extended Data Fig. 2). A strong spectral peak corresponding to an approximately 100-kyr (eccentricity) cycle appears for the period from 900 kyr ago to the present, but not before 900 kyr ago. We conclude that: (1) the tuned age model is credible, and (2) a statistically significant shift to 100 kyr cycles in climate variability occurred at about 900 kyr ago (see statistics in Extended Data Fig. 2).

**Calculating the IOD for the past 130 kyr.** We examined variation in the IOD on a timescale of  $10^4$ – $10^5$  years by subtracting a 130-kyr alkenone record of SST in the eastern Indian Ocean (core GeoB 10038-4:  $5^\circ 56.25' \text{ S}$ ,  $103^\circ 14.76' \text{ E}$ ; ref. 29) from an alkenone SST record in the western Indian Ocean (core MD85668:  $0^\circ 01' \text{ N}$ ,  $46^\circ 02' \text{ E}$ ; ref. 30) (Extended Data Fig. 7).

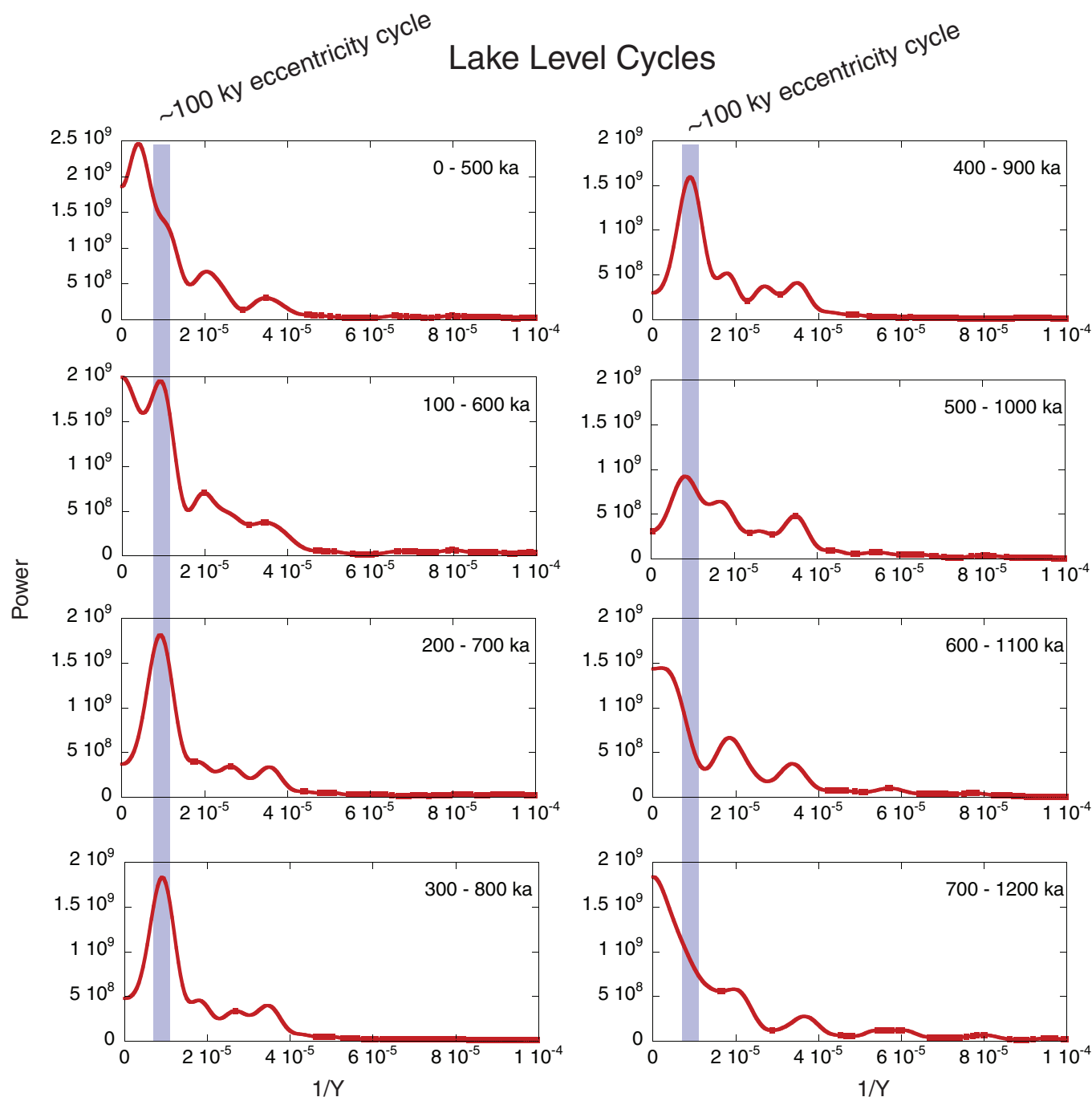
31. Powers, L. A. *et al.* Applicability and calibration of the  $\text{TEX}_{86}$  paleothermometer in lakes. *Org. Geochem.* **41**, 404–413 (2010).
32. Castañeda, I. S. & Schouten, S. A review of molecular organic proxies for examining modern and ancient lacustrine environments. *Quat. Sci. Rev.* **30**, 2851–2891 (2011).
33. Woltering, M. L. *et al.* Vertical and temporal variability in concentration and distribution of thaumarchaeotal tetraether lipids in Lake Superior and the implications for the application of the  $\text{TEX}_{86}$  temperature proxy. *Geochim. Cosmochim. Acta* **87**, 136–153 (2012).
34. Woltering, M. L. *Thaumarchaeota Distribution in the Water Column of Lake Superior and Malawi: Implications for the  $\text{TEX}_{86}$  Temperature Proxy*. <http://gradworks.umi.com/34/82/3482290.html>, PhD thesis, Univ. Minnesota (2011).
35. Blaga, C. I., Reichert, G.-J., Lotter, A. F., Anselmetti, F. S. & Sinninghe Damsté, J. S. A  $\text{TEX}_{86}$  lake record suggests simultaneous shifts in temperature in central Europe and Greenland during the last deglaciation. *Geophys. Res. Lett.* **40**, 948–953 (2013).
36. Blaga, C. I. *et al.* Seasonal changes in glycerol dialkyl glycerol tetraether concentrations and fluxes in a perialpine lake: implications for the use of the  $\text{TEX}_{86}$  and BIT proxies. *Geochim. Cosmochim. Acta* **75**, 6416–6428 (2011).
37. Schouten, S. *et al.* Extremely high sea-surface temperatures at low latitudes during the middle Cretaceous as revealed by archaeal membrane lipids. *Geology* **31**, 1069–1072 (2003).
38. Castañeda, I. S., Werne, J. & Johnson, T. C. Wet and arid phases in the southeast African tropics since the Last Glacial Maximum. *Geology* **35**, 823–826 (2007).
39. Schouten, S., Hugué, C., Hopmans, E. C., Kienhuis, M. V. M. & Sinninghe Damsté, J. S. Analytical methodology for  $\text{TEX}_{86}$  paleothermometry by high-performance liquid chromatography/atmospheric pressure chemical ionization-mass spectrometry. *Anal. Chem.* **79**, 2940–2944 (2007).
40. Schouten, S., Hopmans, E. C., Schefuss, E. & Sinninghe Damsté, J. S. Distributional variations in marine crenarchaeotal membrane lipids: a new tool for reconstructing ancient sea water temperatures? *Earth Planet. Sci. Lett.* **204**, 265–274 (2002).
41. Castañeda, I. S. & Schouten, S. Corrigendum to “A review of molecular organic proxies for examining modern and ancient lacustrine environments”. *Quat. Sci. Rev.* **125**, 174–176 (2015).
42. Kim, J.-H., Schouten, S., Hopmans, E. C., Donner, B. & Sinninghe Damsté, J. S. Global sediment core-top calibration of the  $\text{TEX}_{86}$  paleothermometer in the ocean. *Geochim. Cosmochim. Acta* **72**, 1154–1173 (2008).
43. Sinninghe Damsté, J. S., Ossebaard, J., Schouten, S. & Verschuren, D. Distribution of tetraether lipids in the 25-ka sedimentary record of Lake Challa: extracting reliable  $\text{TEX}_{86}$  and MBT/CBT palaeotemperatures from an equatorial African lake. *Quat. Sci. Rev.* **50**, 43–54 (2012).
44. Brown, E. T. Lake Malawi’s response to “megadrought” terminations: sedimentary records of flooding, weathering and erosion. *Palaeogeogr. Palaeoclimatol. Palaeoecol.* **303**, 120–125 (2011).
45. Ricketts, R. D. & Johnson, T. C. in *The Limnology, Climatology and Paleoclimatology of the East African Lakes* (eds Johnson, T. C. & Odada, E. O.) 475–493 (Gordon and Breach, 1996).
46. Lane, C., Chorn, B. & Johnson, T. C. Ash from the Toba supereruption in Lake Malawi shows no volcanic winter in East Africa at 75 ka. *Proc. Natl Acad. Sci. USA* **110**, 8025–8029 (2013).
47. Levin, N. E. Environment and climate of early human evolution. *Annu. Rev. Earth Planet. Sci.* **43**, 405–429 (2015).
48. deMenocal, P. B. Plio-Pleistocene African climate. *Science* **270**, 53–59 (1995).



**Extended Data Figure 1 | Correcting temperature data for lapse rate effect.** **a, b**, Uncorrected TEX<sub>86</sub> temperature (**a**) and temperature corrected for lapse rate effect (**b**) plotted against burial depth at drilling site MAL05-1. The light solid and dashed lines represent the 1 $\sigma$  and 2 $\sigma$  ranges of uncertainty in both graphs. **c**, Lake-level history, from LPC1<sup>14</sup>, which is the basis for the lapse-rate correction to temperature (Methods).

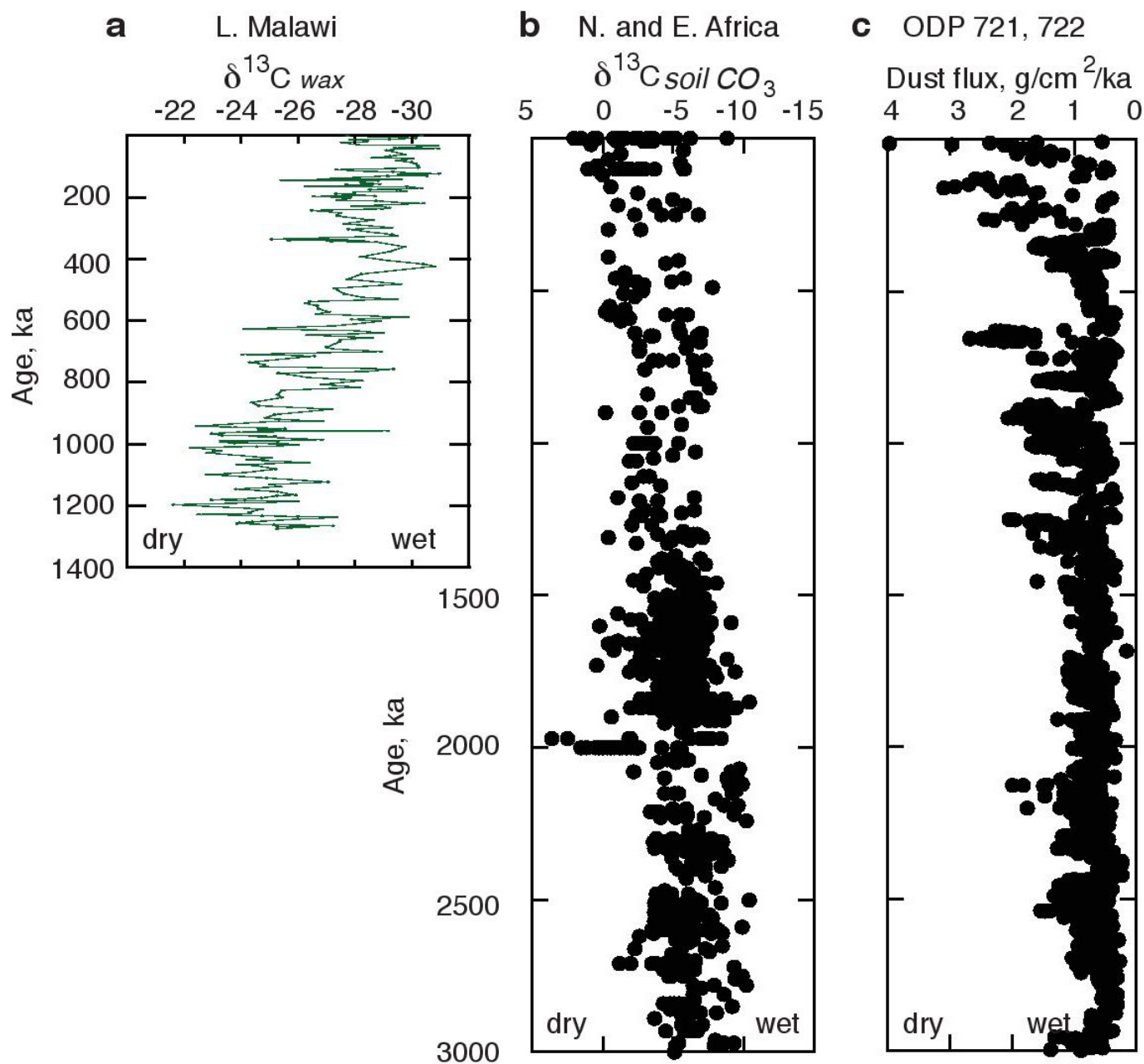


## Lake Level Cycles



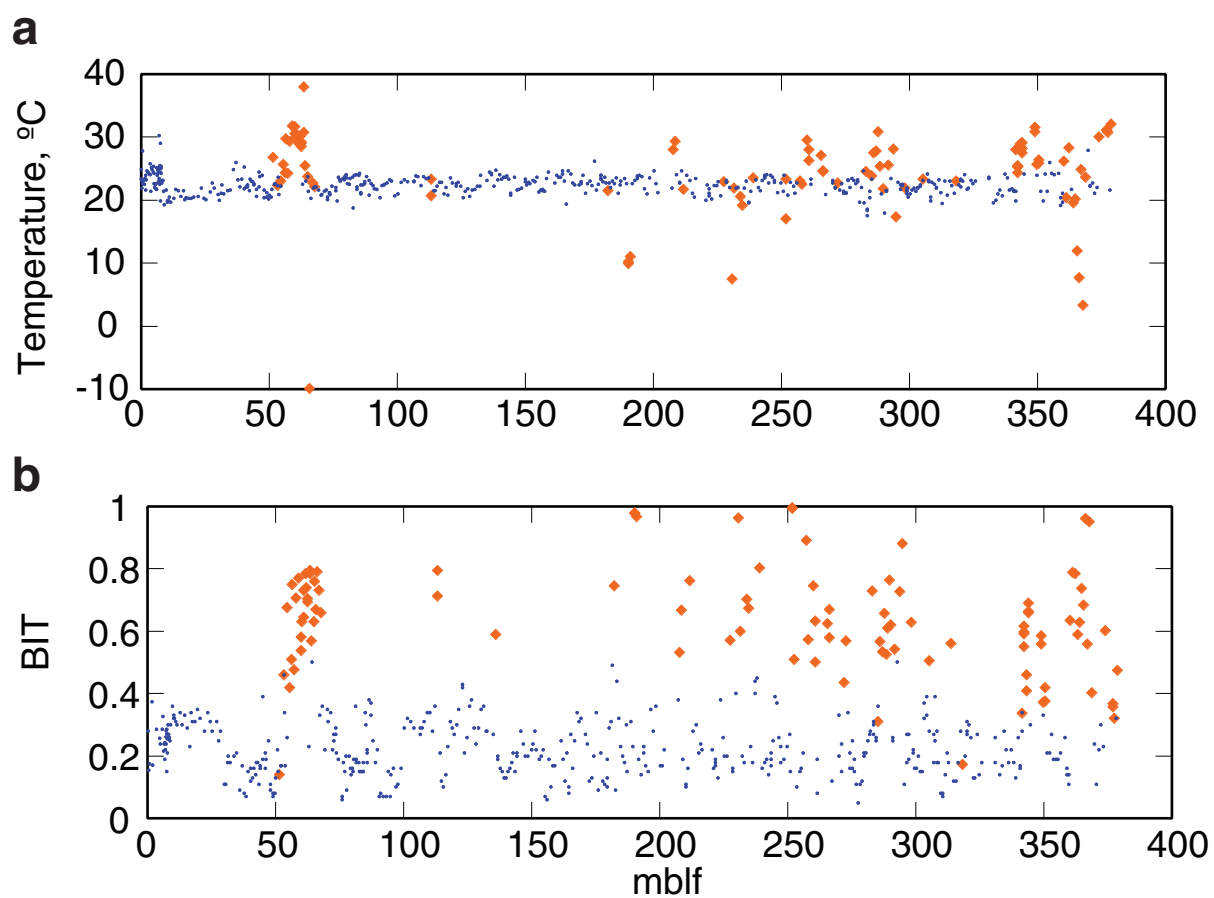
**Extended Data Figure 2 | A predominant 100-kyr (eccentricity) cycle in hydroclimate since the Mid-Pleistocene Transition.** Blackman–Tukey spectral power versus per year ( $1/Y$ ) of 500-kyr intervals from the present back to one million years ago, of the lake-level record portrayed in Extended Data Fig. 1, when dated with the tuned age model depicted in Extended Data Fig. 6. Bandwidth is 0.0001 and the 80% error estimate

on the power spectra is 0.626. We note the strong eccentricity cycle back to 900 kyr ago, and its diminishing influence before then. Whereas the temperature record would display this cycle simply because it was tuned to LR04, the lake level record was derived independently of the temperature data<sup>14</sup>.



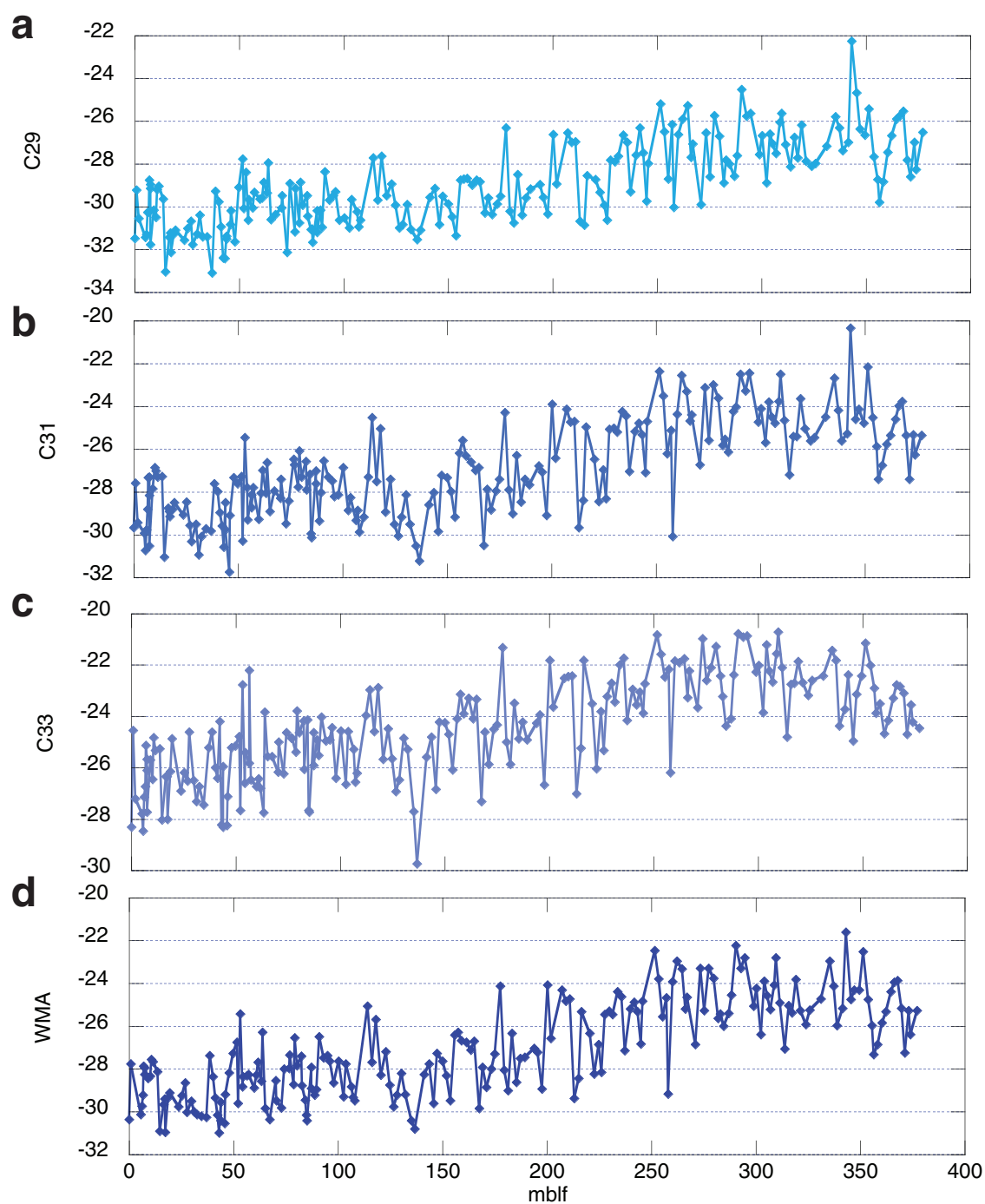
**Extended Data Figure 3 | A contrast in hydroclimate history on the African continent.** The leaf wax  $\delta^{13}\text{C}_{31}$  record indicates that the Malawi basin became progressively wetter since the Mid-Pleistocene Transition around 900 kyr ago (**a**), while much of the continent to the north of Lake Malawi maintained a trend towards drier conditions over the past

three million years or more, as indicated by soil carbonate  $\delta^{13}\text{C}$  values in northern Tanzania, Kenya and Ethiopia (summarized in ref. 47) (**b**) and in marine sediment records of terrigenous dust input from northern Africa<sup>48</sup>, as shown in ODP Sites 721 and 722 from the Gulf of Aden (**c**).

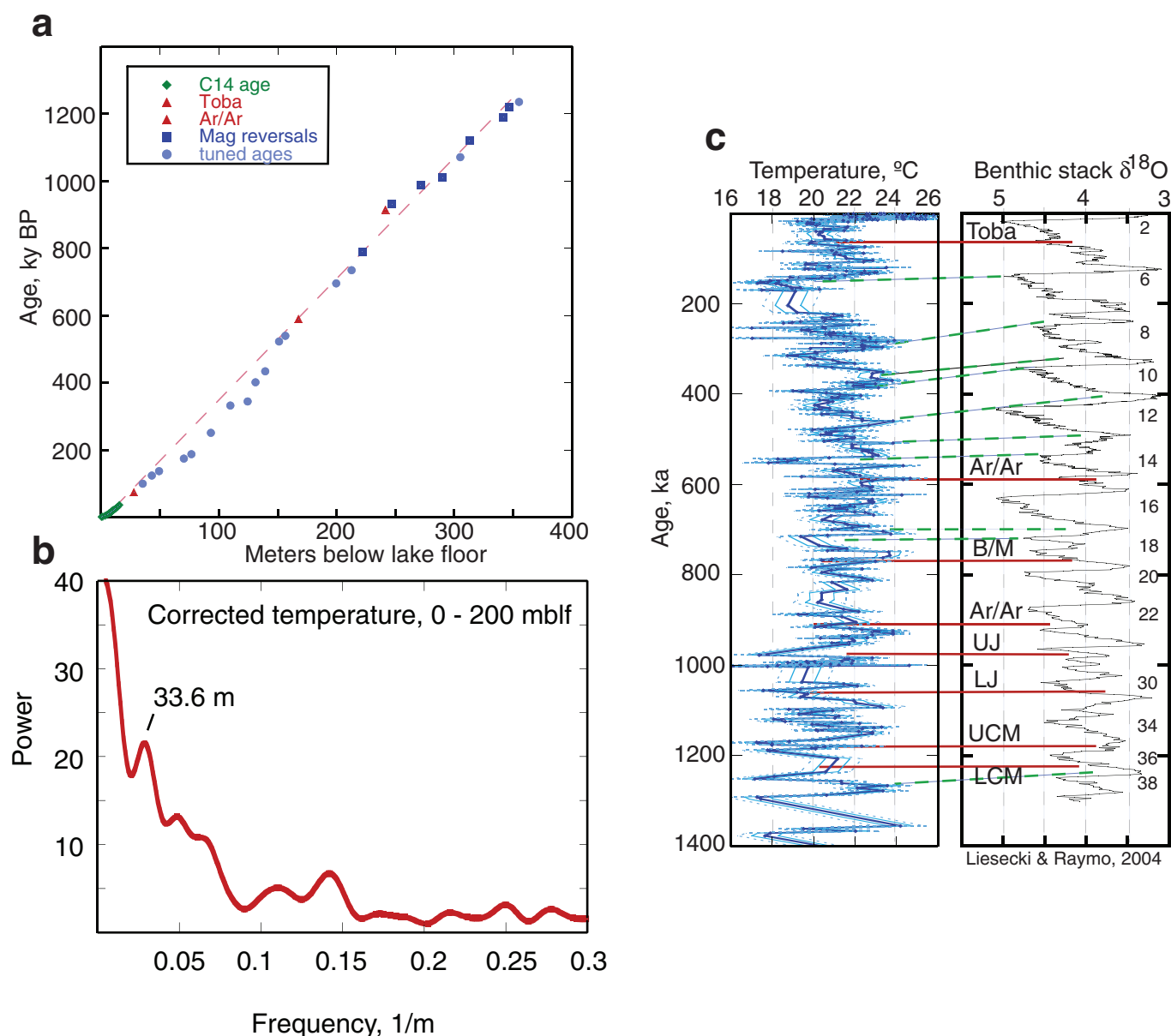


Extended Data Figure 4 | Accepted (blue) and rejected (orange) temperatures and BIT data. Acceptance criteria are explained in the Methods.



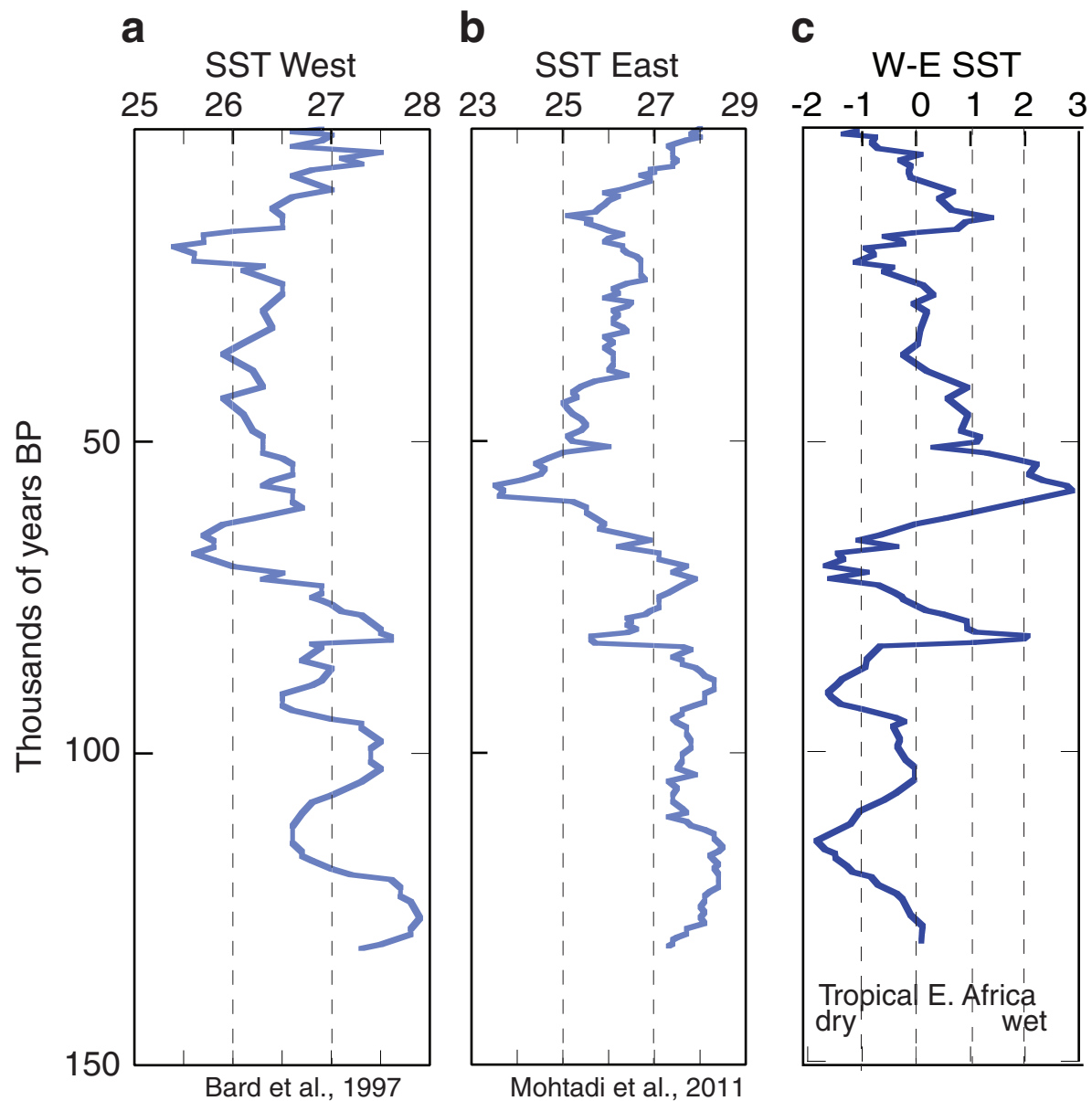


**Extended Data Figure 5 |  $\delta^{13}\text{C}$  of the  $\text{C}_{29}$ ,  $\text{C}_{31}$ ,  $\text{C}_{33}$   $n$ -alkanes.**  $\delta^{13}\text{C}$  of the  $\text{C}_{29}$ ,  $\text{C}_{31}$  and  $\text{C}_{33}$   $n$ -alkanes (a, b, c), and the weighted mean average (WMA) of these values (d).



**Extended Data Figure 6 | Aligning the temperature record to LR04 to refine the age model.** **a**, Age versus depth for drill site MAL05-1, depicting ages based on  $^{14}\text{C}$ , tephra, magnetic reversals and alignment (tuning) of corrected temperature with LR04. The dashed pink line is a linear fit through the dates derived from radiocarbon, tephra and magnetic reversals only, described by the equation: Age (in kyr before present) =  $-12.44 + 3.602z$  ( $r^2 = 0.9984$ ). **b**, Blackman–Tukey analysis (spectral power versus per metre) of the corrected temperature data in the upper 200 m of drill site MAL05-1, showing a 33.6-m cycle, which

corresponds to about 121 kyr. Bandwidth is 0.0001 and 80% error estimate on the power spectrum is 0.626. **c**, Temperature plotted against age based solely on radiocarbon, tephra and magnetic reversal dates aligned to the LR04 age scale (green dashed lines), in order to assign ages in MAL05-1 between 75 kyr ago (Toba ash horizon) and 590 kyr ago (Ar–Ar). The red lines depict tephra and magnetic reversal ages, which constrain the temperature alignment. B/M, Brunhes–Matuyama; UJ, Upper Jaramillo; LJ, Lower Jaramillo; UCM, Upper Cobb Mountain; LCM, Lower Cobb Mountain. Data are from ref. 14.



**Extended Data Figure 7 | The Indian Ocean west-minus-east gradient in SST since 130 kyr ago.** Alkenone records of SST in the western Indian Ocean (core MD85668: 0° 01' N, 46° 02' E) (a)<sup>30</sup> and the eastern Indian Ocean (core GeoB 10038-4: 5° 56.25' S, 103° 14.76' E) (b)<sup>29</sup>. The west-minus-east temperature gradient (IOD) derived from these two records is displayed in c.



Extended Data Table 1 | Locations of the cores analysed in this study

Site	Latitude	Longitude	Water Depth (m)	Core Length (m)
M98-13P	11°16' 0" S	34°26' 6" E	604	8.3
MAL05-1B	11°17'38" S	34°26'14" E	590	379.29
MAL05-1C	11°17'38" S	34°26'14" E	590	88.89

Extended Data Table 2 | Sediment dates that underlie the age model of this study

Meters below lake floor	Cal. Yrs. BP	Age basis
0.555	816	<sup>14</sup> C
1.70	1770	<sup>14</sup> C
3.70	4270	<sup>14</sup> C
5.46	7140	<sup>14</sup> C
6.71	11010	<sup>14</sup> C
7.51	12630	<sup>14</sup> C
7.90	13330	<sup>14</sup> C
8.51	14565	<sup>14</sup> C
9.46	18450	<sup>14</sup> C
9.56	18800	<sup>14</sup> C
10.55	21530	<sup>14</sup> C
11.52	23975	<sup>14</sup> C
12.46	26590	<sup>14</sup> C
14.09	30890	<sup>14</sup> C
15.81	36140	<sup>14</sup> C
28.09	75000	Toba ash
167.84	5.90e+05	Ar-Ar
222.00	7.90e+05	Brunhes-Matuyama
241.63	9.15e+05	Ar-Ar
247.00	9.32e+05	Santa Rosa
271.50	9.87e+05	Upper Jaramillo
290.00	1.07e+06	Lower Jaramillo
313.00	1.12e+06	Panaruu
342.00	1.19e+06	Cobb Mt. top
347.00	1.22e+06	Cobb Mt. bottom

Refer to Lyons *et al.*<sup>14</sup> for more detail. Ages are in calendar years before present.

# Digits and fin rays share common developmental histories

Tetsuya Nakamura<sup>1\*</sup>, Andrew R. Gehrke<sup>1\*</sup>, Justin Lemberg<sup>1</sup>, Julie Szymaszek<sup>1</sup> & Neil H. Shubin<sup>1</sup>

Understanding the evolutionary transformation of fish fins into tetrapod limbs is a fundamental problem in biology<sup>1</sup>. The search for antecedents of tetrapod digits in fish has remained controversial because the distal skeletons of limbs and fins differ structurally, developmentally, and histologically<sup>2,3</sup>. Moreover, comparisons of fins with limbs have been limited by a relative paucity of data on the cellular and molecular processes underlying the development of the fin skeleton. Here, we provide a functional analysis, using CRISPR/Cas9 and fate mapping, of 5' *hox* genes and enhancers in zebrafish that are indispensable for the development of the wrists and digits of tetrapods<sup>4,5</sup>. We show that cells marked by the activity of an autopodial *hoxa13* enhancer exclusively form elements of the fin fold, including the osteoblasts of the dermal rays. In *hox13* knockout fish, we find that a marked reduction and loss of fin rays is associated with an increased number of endochondral distal radials. These discoveries reveal a cellular and genetic connection between the fin rays of fish and the digits of tetrapods and suggest that digits originated via the transition of distal cellular fates.

The origin of tetrapod limbs involved profound changes to the distal skeleton of fins. Fin skeletons are composed mostly of fin rays<sup>6</sup>, whereas digits are the major anatomical and functional components of the distal limb skeleton. One of the central shifts during the origin of limbs in the Devonian period involved the reduction of fin rays coincident with an expansion of the distal endochondral bones of the appendage<sup>2,7</sup>. Because the distal skeletons of fins and limbs are composed of different types of bone tissue (dermal and endochondral, respectively) it remains unclear how the terminal ends of fish and tetrapod appendages are related and, consequently, how digits arose developmentally. Although the understanding of ectodermal signalling centres in fin buds and fin folds has advanced in recent years<sup>8–11</sup>, that of the cells that form the skeletal patterns has remained elusive.

*Hox* genes, namely those of the *HoxA* and *HoxD* clusters, have figured prominently in discussions of limb development and origins<sup>3,12–14</sup>. The 'early' and 'late' phases of *HoxD* and *HoxA* transcription are involved in specifying the proximal (arm and forearm) and distal (autopod) segments, respectively<sup>15</sup>. Both fate map assays and knockout phenotypes in mouse limbs reveal an essential role for *Hox13* paralogues in the formation of the autopod<sup>4,5</sup>. Mice engineered to lack *Hoxa13* and *Hoxd13* in limbs lack the wrists and digits exclusively<sup>4</sup>. Moreover, the lineage of cells expressing *Hoxa13* resides exclusively in the autopod of adult mice<sup>5</sup>. Together, these lines of evidence reveal the extent to which 5' *Hox* genes are involved in, and serve as markers for, the developmental pattern of the wrist and digits. Unfortunately, as no such studies have yet been performed in fish, the means to find antecedents of autopodial development in fins has been lacking.

Analyses of 5' *Hox* expression in phylogenetically diverse wild-type fish<sup>16–19</sup> as well as experimental misexpression in teleosts reveal that 5' *Hox* activity may be involved in patterning<sup>20</sup>, and defining the extent of, the distal chondrogenic region of fish fins<sup>21</sup>. Despite these advances, however, little is known about the contribution of different

*hox* paralogues—individually and in combination—to the adult fin phenotype and the origin of cells that give rise to the distal fin skeleton. While previous studies have shown that osteoblasts of the fin rays in the caudal fin of zebrafish are derived from either neural crest or paraxial mesoderm, the source of osteoblasts in pectoral fin rays is currently unknown<sup>22–24</sup>. Consequently, it remains unclear where the cellular and genetic markers of the autopod of the tetrapod limb reside in fish fins.

In order to bridge these gaps in knowledge, we followed the fates of cells marked by early and late phase *hox* enhancers to adult stages in pectoral fins. In addition, we engineered zebrafish that completely lacked each individual *hox13* gene, and bred stable lines with multiple gene knockout combinations of *hox* paralogues. The power of these experiments is twofold: 1) to our knowledge, they represent the first functional analyses of *hox* activity in fins, and 2) they enable a direct developmental comparison to experiments performed in tetrapod limbs.

We performed *in situ* hybridization of *hoxa13a*, *hoxa13b*, and *hoxd13a* genes from 48–120 h post fertilization (hpf) in zebrafish to determine whether active *hox* expression has a role in the development of the pectoral fin fold. *Hoxa13* genes in zebrafish are expressed in the distal fin mesenchyme at 48 hpf and weakly in the proximal portion of the pectoral fin fold from 72–96 hpf, indicating that *hoxa13* genes are not actively expressed in the developing fold<sup>18</sup> (Fig. 1a, b). *Hoxd13a* is expressed in the posterior half of the fin, but it becomes weak after 96 hpf (Fig. 1c). *Hox* expression is entirely absent in fins 10 days post fertilization (dpf) (Extended Data Fig. 1). As *hox13* genes do not appear to have a main role in zebrafish fin fold development past 72–96 hpf, we sought to determine what structures *hox*-positive cells populate in the developing and adult folds.

To follow the fates of cells that experience early phase activity in the zebrafish fin, we modified our previously reported transgenesis vector<sup>21</sup> to express Cre-recombinase driven by the zebrafish early-phase enhancer CNS65<sup>25</sup>. This enhancer activates expression throughout the endochondral disk of pectoral fins from 31 to ~38 hpf (Fig. 2a and Extended Data Fig. 1). Stable lines expressing CNS65x3–Cre were crossed to the lineage-tracing zebrafish line Tg(*ubi:Switch*) fish, in which cells that express Cre are permanently labelled with mCherry<sup>26</sup>. At 6 dpf mesenchymal cells in which expression was driven by CNS65 at 38 hpf make up the entire endochondral disk of the pectoral fin (Fig. 2b). We also found mCherry-positive cells in the fin fold at 6 dpf and extensively at 20 dpf (Fig. 2b). These cells contained filamentous protrusions extending distally as well as nuclei positioned at the posterior side, both of which suggest that the cells were migrating distally out of the endochondral disk (Fig. 2b).

To determine the fate of late phase cellular activity, we employed the same fate-mapping strategy but used a late phase *hoxa* enhancer (e16) from the spotted gar (*Lepisosteus oculatus*) genome<sup>21</sup>. We chose a *hoxa* enhancer because lineage-tracing data in mouse has shown that late phase *Hoxa13* cells in the limb make up the osteoblasts of the wrist and digits exclusively, making it a *bona fide* marker of the autopod<sup>5</sup>.

<sup>1</sup>Department of Organismal Biology and Anatomy, University of Chicago, Chicago, Illinois 60637, USA.

\*These authors contributed equally to this work.



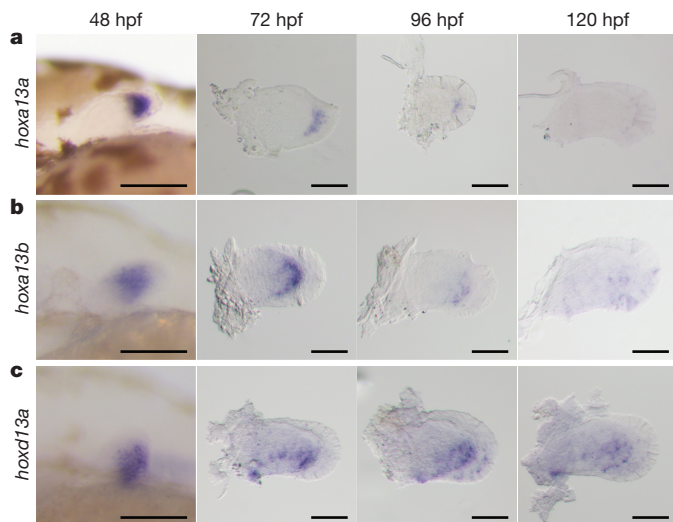


**Figure 1 | Expression patterns of *hox13* genes at 48–120 hpf.** **a**, *hoxa13a*. **b**, *hoxa13b*. **c**, *hoxd13a*. *Hoxa13a* is expressed in distal mesenchyme at 48 hpf, but expression continues in the proximal fin fold from 72 to 96 hpf (**a**). *Hoxa13b* is expressed in distal mesenchyme and expression can be observed at the distal part of the endochondral disk until 96 hpf (**b**). *Hoxd13a* is expressed in the posterior half of the mesenchyme at 48 hpf and expression continues in the posterior endochondral disk through 96 hpf. After 96 hpf, expression becomes weak (**c**). Scale bars are 100  $\mu$ m.  $n = 20$  embryos for each *in situ* hybridization at 48 hpf.  $n = 10$  embryos after 72 hpf.

In addition, *gar e16* (which has no sequence conservation in zebrafish) drives expression throughout the autopod in transgenic mice in a pattern that mimics the endogenous murine enhancer and *Hoxa13* expression<sup>21,27</sup>. In transgenic zebrafish, *gar e16* is active in the distal portion of the endochondral disk of the pectoral fin at 48 hpf, and ceases activity after approximately 55 hpf (Fig. 2a and Extended Data Fig. 1). When these transgenic zebrafish were crossed to *Tg(ubi:Switch)*, at 6 dpf we detected the majority of mCherry-positive cells in the developing fin fold with a small number of cells lining the distal edge of the endochondral disk (Fig. 2c). At 20 dpf, the fin fold contained nearly all of the mCherry-positive cells, which had formed tube-like cells that appeared to be developing actinotrichia (Fig. 2c). In adult fish (90 dpf), late phase cells were restricted to the adult structures of the fin fold, where they composed osteoblasts that make up the fin rays, among other tissues (Fig. 2d). As the *e16* enhancer is active only in the distal endochondral disk at 48 hpf, and the labelled cells end up in the fin rays of the adult, late phase *hox*-positive cells are likely to migrate from the endochondral portion of the fin into the fin fold, a hypothesis supported by extensive filopodia in mCherry-positive cells projecting in the direction of the distal edge of the fin (Fig. 2c).

To explore the function of *hox13* genes, we inactivated individual *hox13* genes from the zebrafish genome by CRISPR/Cas9 and also made combinatorial deletions through genetic crosses of stable lines (Extended Data Fig. 2 and Extended Data Table 2, 3 and 4). Homozygous null embryos for individual *hox13* genes exhibited embryonic pectoral fins that were comparable in size with the wild type at 72 hpf (Extended Data Fig. 3). The shape and size of the fin fold and endochondral disk were also assayed by *in situ* hybridization for *and1* and *shha*, which serve as markers for the developing fin fold and endochondral disk, respectively<sup>28</sup> (Extended Data Fig. 3). In adult fins (~120 dpf), we observed no detectable difference in the length of fin rays of *hoxd13a*<sup>-/-</sup> mutants when compared to wild-type fish (Fig. 3d and Extended Data Fig. 4). However, both *hoxa13a*<sup>-/-</sup> and *hoxa13b*<sup>-/-</sup> single mutant fish retained fin rays that were shorter than the wild type, suggesting a role for *hoxa13* genes in fin ray development (Fig. 3g, j and Extended Data Fig. 4). To determine the degree to which endochondral bones were affected, we used CT scanning technology

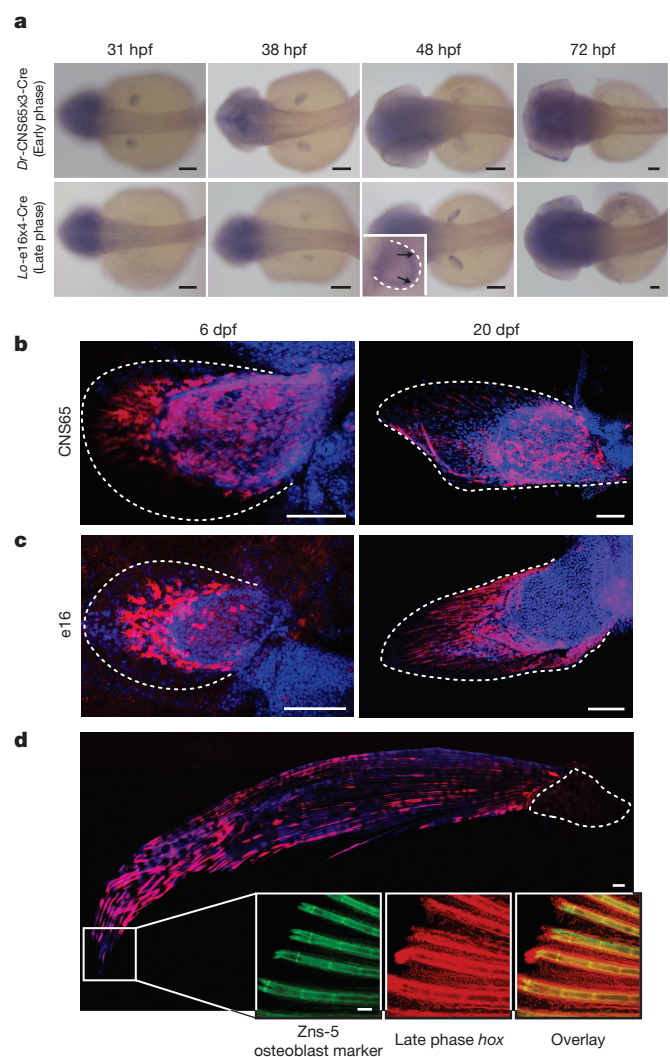


**Figure 2 | Fate mapping of cells marked by the activity of *hox* enhancers.** **a**, *In situ* hybridization of Cre in *Dr-CNS65x3-Cre* and *Lo-e16x4-Cre* exhibits expression dynamics of early and late phase enhancers used for fate mapping. Cre regulated by early phase *hox* enhancer *CNS65* is expressed throughout the fin from 31 to 38 hpf, whereas late phase expression (driven by *e16*) begins weakly in the distal fin at 38 hpf and ceases at ~55 hpf. Inset shows zoom in of the pectoral fin, black arrows point to the distal border of the endochondral disk. **b**, Lineage tracing of *Dr-CNS65x3-Cre* at 6 dpf and 20 dpf. Red: mCherry IF; blue: DAPI. Cells that experienced early phase expression (red) contribute to fin fold and endochondral disk. **c**, Lineage tracing of *Lo-e16x4-Cre* at 6 dpf and 20 dpf. Cells that underwent late phase expression are present mostly in the fin fold, though some cells are at the distal edge of the disk. Red cells at 6 dpf protrude filopodia in the distal direction, indicating that these cells are actively moving out into the fin fold. **d**, Lineage tracing of late phase *hox* cells in adult zebrafish fin (~120 dpf). mCherry cells are present only in the derivatives of the fin fold, and not in the endochondral disk. Inset: magnification of distal edge of fin rays. Green: Zns-5 osteoblast marker; red: Hox-positive; yellow: overlap of Zns5 and Cre. White dotted lines outline the fin (**b**, **c**) or endochondral bones in (**d**).  $n = 5$  for stable lines. All scale bars are 100  $\mu$ m except for the total fin in **d**, which is 500  $\mu$ m.

for wild-type and mutant adult fish. Each single mutant, *hoxa13a*<sup>-/-</sup>, *a13b*<sup>-/-</sup> or *d13a*<sup>-/-</sup>, had four proximal radials and 6–8 distal radials with similar morphology to those of wild-type zebrafish (Fig. 3c, f, i, l and Extended Data Fig. 4). We crossed heterozygous mutants to obtain fish that lacked all *hoxa13* genes (*hoxa13a*<sup>-/-</sup>, *a13b*<sup>-/-</sup>). The fin folds of *hoxa13a*<sup>-/-</sup>, *a13b*<sup>-/-</sup> embryos were ~30% shorter than the wild type at 72 and 96 hpf, whereas the number of cells in the endochondral disk was ~10% greater (Extended Data Fig. 5). Adult

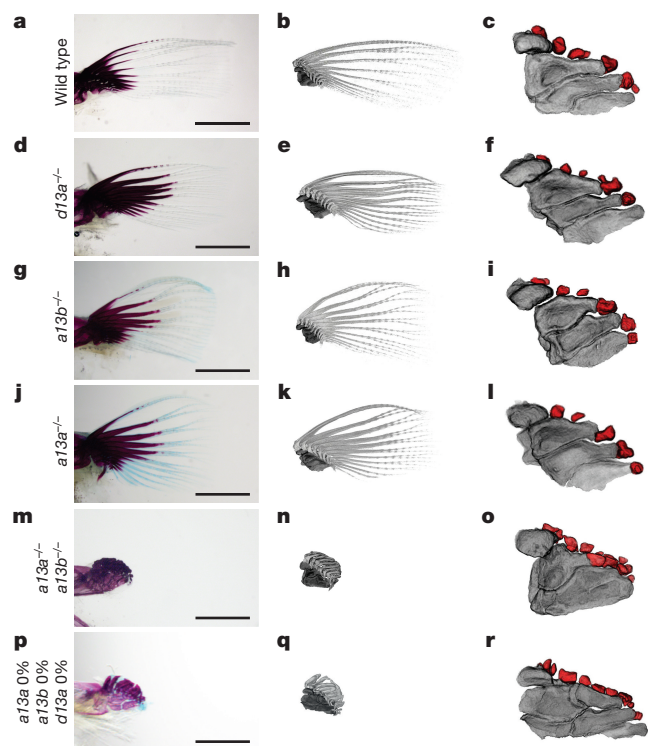


**Figure 3 | Adult fin phenotypes of *hox13* deletion series.** a–c, wild type. d–f, *hoxd13a*<sup>−/−</sup>. g–i, *hoxa13b*<sup>−/−</sup>. j–l, *hoxa13a*<sup>−/−</sup>. m–o, *hoxa13a*<sup>−/−</sup>, *a13b*<sup>−/−</sup>. p–r, *hoxa13a*<sup>0%</sup>, *a13b*<sup>0%</sup> and *d13a*<sup>0%</sup> (mosaic triple knockout; Methods and Extended Data Tables 3, 4). Each mutant *hox* sequence is found in Extended Data Tables 3, 4. a, d, g, j, m, p, Alizarin Red and Alcian Blue staining of pectoral fin. b, e, h, k, n, q, CT scanning of pectoral fins. Black: radials (endochondral bones); grey: fin rays (dermal bones). Note that *hoxa13* single (g, h, j, k), double (m, n), and mosaic triple (p, q) mutant fins show shorter fin rays than wild type (a, b). Fins were scaled according to the bone staining pictures. c, f, i, l, o, r, Enlarged images of CT scanning without fin rays to reveal endochondral patterns. Dark grey; proximal radials, red; distal radials. Upper left side is the anterior and bottom right is the posterior side in each picture. Double and triple knockout mutants have 10–13 distal radials (o and r; Extended Data Fig. 4, Supplementary Information). Third and fourth proximal radials started to fuse into one bone in *hoxa13a*<sup>−/−</sup>, *a13b*<sup>−/−</sup> (o). Note that posterior distal radials are stacked along proximodistal axis (o). Posterior proximal radials are broken down into small parts in mosaic triple knockout (r). Scale bars are 2 mm. The size of specimens are not scaled in c, f, i, l, o and r to display the detail of distal radials. *n* = 3 fish for single and double mutants and *n* = 5 fish for mosaic triple mutant.

*hoxa13a*<sup>−/−</sup>, *a13b*<sup>−/−</sup> fish exhibited greatly reduced fin rays (Fig. 3m, Extended Data Fig. 4 and Supplementary Information). In contrast to dermal reduction, the endochondral distal radials of double mutants were significantly increased to 10–13 in number, often stacked along the proximodistal axis (Fig. 3o, Extended Data Fig. 4 and Supplementary Information, *P* = 0.0014, *t*-test comparing the means). A similar pattern was seen in triple knockout fish (mosaic for *hoxa13b* and *hoxd13a*) (Fig. 3p–r and Extended Data Fig. 4) along with altered proximal radials, implying that late phase *Hox* genes are involved in patterning the proximal endochondral radials of fins, unlike their role in tetrapods (Fig. 3).

Despite being composed of different kinds of skeletal tissue, fin rays and digits share a common population of distal mesenchymal cells that experience late phase *Hox* expression driven by shared regulatory architectures and enhancer activities<sup>21</sup>. In addition, loss of 5' *Hox* activity results in the deletion or reduction of both of these structures. Whereas phylogenetic evidence suggests that rays and digits are not homologous in terms of morphology, the cells and regulatory processes in both the fin fold and the autopod share a deep homology that may be common to both bony fish and jawed vertebrates<sup>19</sup>.

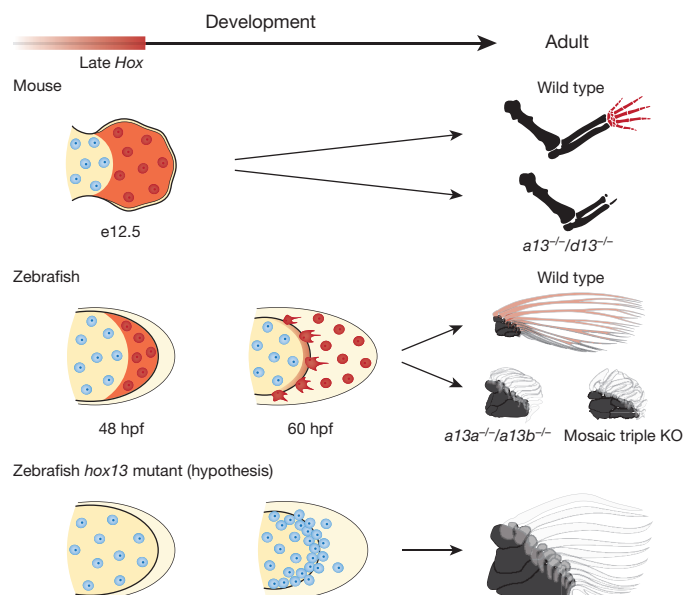


**Figure 4 | Shared developmental histories in fin rays and digits.** In mice (top row), late phase *Hox* expression (red) marks the distal cells of the limb bud that result in bones of the autopod (wrists and digits). Double knockout of *Hoxa13* and *Hoxd13* results in the loss of the autopod. In zebrafish wild-type fins (middle row), cells marked by late phase *hox* expression (red) end up in the fin fold and within osteoblasts of the dermal rays. *Hoxa13* double knockout fish (*hoxa13a*<sup>−/−</sup>, *a13b*<sup>−/−</sup>) and the triple knockout (mosaic for *hoxa13b* and *hoxd13a*) have extremely reduced fin rays with increased distal endochondral radials. Note that distal radials are stacked along the proximodistal axis in the posterior of the fins. The results lead to the hypothesis (bottom row) that the knockout phenotype results from a deficit in migration of mesenchymal cells with more cells left in the distal fin bud (increased number of cells in the endochondral disk of mutants fins, Extended Data Fig. 4) and fewer migrating to the fold, thereby resulting in a larger number of endochondral bones and reduced dermal ones. Red cells: cells that experienced late phase *hox* expression. Mouse limbs consist of only endochondral bones, but fish fins contain endochondral (black) and dermal (transparent; fin rays) bones.

Two major trends underlie the fin-to-limb transition—the elaboration of endochondral bones and the progressive loss of the extensive dermal fin skeleton<sup>2,7,20</sup>. In the combinatorial knockouts of *hox13* genes, which in tetrapods result in a loss of the autopod, distal endochondral radials were increased in number while fin rays were greatly reduced. As a common population of cells in the distal appendage is involved in the formation of rays and digits, the endochondral expansion in tetrapod origins may have occurred through the transition of distal cellular fates and differential allocation of cells from the fin fold to the fin bud<sup>18</sup> (Fig. 4). The two major trends of skeletal evolution in the fin-to-limb transition may be linked at cellular and genetic levels.

**Online Content** Methods, along with any additional Extended Data display items and Source Data, are available in the online version of the paper; references unique to these sections appear only in the online paper.

**Received 7 April; accepted 20 July 2016.**

**Published online 17 August 2016.**

- Clack, J. A. *Gaining Ground: The Origin and Evolution of Tetrapods*. Indiana University Press, Indiana (2012).
- Clack, J. A. The fin to limb transition: New data, interpretations, and hypotheses from paleontology and developmental biology. *Annu. Rev. Earth Planet. Sci.* **37**, 163–179 (2009).
- Schneider, I. & Shubin, N. H. The origin of the tetrapod limb: from expeditions to enhancers. *Trends Genet.* **29**, 419–426 (2013).
- Fromental-Ramain, C. *et al.* *Hoxa-13* and *Hoxd-13* play a crucial role in the patterning of the limb autopod. *Development* **122**, 2997–3011 (1996).
- Scotti, M., Kherdjemil, Y., Roux, M. & Kmita, M. A *Hoxa13:Cre* mouse strain for conditional gene manipulation in developing limb, hindgut, and urogenital system. *Genesis* **53**, 366–376 (2015).



6. Grandel, H. & Schulte-Merker, S. The development of the paired fins in the zebrafish (*Danio rerio*). *Mech. Dev.* **79**, 99–120 (1998).
7. Coates, M. I., Ruta, M. & Friedman, M. Ever since Owen: Changing perspectives on the early evolution of tetrapods. *Annu. Rev. Ecol. Syst.* **39**, 571–592 (2008).
8. Thorogood, P. *The Development of the Teleost Fin and Implications for Our Understanding of Tetrapod Limb Evolution*. (Springer US, 1991).
9. Fernandez-Teran, M. & Ros, M. A. The apical ectodermal ridge: morphological aspects and signaling pathways. *Int. J. Dev. Biol.* **52**, 857–871 (2008).
10. Zeller, R., López-Ríos, J. & Zuniga, A. Vertebrate limb bud development: moving towards integrative analysis of organogenesis. *Nat. Rev. Genet.* **10**, 845–858 (2009).
11. Yano, T., Abe, G., Yokoyama, H., Kawakami, K. & Tamura, K. Mechanism of pectoral fin outgrowth in zebrafish development. *Development* **139**, 2916–2925 (2012).
12. Sordino, P., van der Hoeven, F. & Duboule, D. Hox gene expression in teleost fins and the origin of vertebrate digits. *Nature* **375**, 678–681 (1995).
13. Woltering, J. M. & Duboule, D. The origin of digits: expression patterns versus regulatory mechanisms. *Dev. Cell* **18**, 526–532 (2010).
14. Gehrke, A. R. & Shubin, N. H. Cis-regulatory programs in the development and evolution of vertebrate paired appendages. *Semin. Cell Dev. Biol.* <http://dx.doi.org/10.1016/j.semcdb.2016.01.015> (2016).
15. Zakany, J. & Duboule, D. The role of Hox genes during vertebrate limb development. *Curr. Opin. Genet. Dev.* **17**, 359–366 (2007).
16. Freitas, R., Zhang, G. & Cohn, M. J. Biphasic Hoxd gene expression in shark paired fins reveals an ancient origin of the distal limb domain. *PLoS One* **2**, e754 (2007).
17. Davis, M. C., Dahn, R. D. & Shubin, N. H. An autopodial-like pattern of Hox expression in the fins of a basal actinopterygian fish. *Nature* **447**, 473–476 (2007).
18. Ahn, D. & Ho, R. K. Tri-phasic expression of posterior Hox genes during development of pectoral fins in zebrafish: implications for the evolution of vertebrate paired appendages. *Dev. Biol.* **322**, 220–233 (2008).
19. Tulenko, F. J. *et al.* HoxD expression in the fin-fold compartment of basal gnathostomes and implications for paired appendage evolution. *Sci. Rep.* **6**, 22720 (2016).
20. Freitas, R., Gómez-Marín, C., Wilson, J. M., Casares, F. & Gómez-Skarmeta, J. L. Hoxd13 contribution to the evolution of vertebrate appendages. *Dev. Cell* **23**, 1219–1229 (2012).
21. Gehrke, A. R. *et al.* Deep conservation of wrist and digit enhancers in fish. *Proc. Natl Acad. Sci. USA* **112**, 803–808 (2015).
22. Lee, R. T. H., Knapik, E. W., Thiery, J. P. & Carney, T. J. An exclusively mesodermal origin of fin mesenchyme demonstrates that zebrafish trunk neural crest does not generate ectomesenchyme. *Development* **140**, 2923–2932 (2013).
23. Lee, R. T. H., Thiery, J. P. & Carney, T. J. Dermal fin rays and scales derive from mesoderm, not neural crest. *Curr. Biol.* **23**, R336–R337 (2013).
24. Smith, M., Hickman, A., Amanze, D., Lumsden, A. & Thorogood, P. Trunk neural crest origin of caudal fin mesenchyme in the zebrafish *Brachydanio rerio*. *Proc. R. Soc. Lond. B* **256**, 137–145 (1994).
25. Braasch, I. *et al.* The spotted gar genome illuminates vertebrate evolution and facilitates human-teleost comparisons. *Nat. Genet.* **48**, 427–437 (2016).
26. Mosimann, C. *et al.* Ubiquitous transgene expression and Cre-based recombination driven by the ubiquitin promoter in zebrafish. *Development* **138**, 169–177 (2011).
27. Berlivet, S. *et al.* Clustering of tissue-specific sub-TADs accompanies the regulation of HoxA genes in developing limbs. *PLoS Genet.* **9**, e1004018 (2013).
28. Zhang, J. *et al.* Loss of fish actinotrichia proteins and the fin-to-limb transition. *Nature* **466**, 234–237 (2010).

**Supplementary Information** is available in the online version of the paper.

**Acknowledgements** We thank J. Westlund for figure preparation and construction, as well as maintenance of zebrafish facilities. M. Coates, M. Davis, R. Ho, I. Ruvinsky, J.-L. Gomez Skarmeta, and C. Tabin provided comments and advice. We thank L. I. Zon, C. Mosimann, and C. Lawrence for Tg(*ubi:Switch*) fish, M. L. Suster for the *pCR8GW-Cre-pA-FRT-kan-FRT* plasmid, R. Ho and S. Briscoe for insights regarding lineage-tracing experiments, V. Bindokas and the University of Chicago Integrated Light Microscopy Core Facility for assistance with imaging, L. Zhexi for use of the high-energy CT scanning facility of University of Chicago, M. E. Horb and M. C. Salanga of the National Xenopus Resource (RRID:SCR-013731) of the Marine Biological Laboratories for tutelage in applying CRISPR/Cas9, J. Gitlin, A. Latimer and R. Thomason for providing space for zebrafish CRISPR/Cas9 experiments and also maintaining juveniles, and the Marine Resource Center of the Marine Biological Laboratories for assistance with the transfer of mutant zebrafish between University of Chicago and the MBL. This study was supported by the Uehara Memorial Foundation Research Fellowship 2013, Japan Society for the Promotion of Science Postdoctoral Research Fellowship 2012–127, and Marine Biological Laboratory Research Award 2014 (to T.N.); National Institutes of Health Grant T32 HD055164 and National Science Foundation Doctoral Dissertation Improvement Grant 1311436 (to A.R.G.); and the Brinson Foundation and the University of Chicago Biological Sciences Division (to N.H.S.).

**Author Contributions** T.N., A.R.G. and N.H.S. designed research; T.N. and J.S. performed *in situ* hybridization and CRISPR experiments; A.R.G. did fate mapping of the *hox* enhancers; T.N. and J.L. obtained CT scanning data; T.N., A.R.G., J.L. and N.H.S. analyzed data; and T.N., A.R.G., J.L. and N.H.S. wrote the paper.

**Author Information** Reprints and permissions information is available at [www.nature.com/reprints](http://www.nature.com/reprints). The authors declare no competing financial interests. Readers are welcome to comment on the online version of the paper. Correspondence and requests for materials should be addressed to N.H.S. ([nshubin@uchicago.edu](mailto:nshubin@uchicago.edu)).

**Reviewer Information** *Nature* thanks S. Burgess and the other anonymous reviewer(s) for their contribution to the peer review of this work.



## METHODS

All zebrafish work was performed according to standard protocols approved by The University of Chicago (ACUP #72074). No statistical methods were used to predetermine sample size. The experiments were not randomized and the investigators were not blinded to allocation during experiments and outcome assessment.

**Whole-mount *in situ* hybridization.** *In situ* hybridization for the *hox13*, *Cre*, and *1* and *shha* genes were performed according to standard protocols<sup>29</sup> after fixation in 4% paraformaldehyde overnight at 4 °C. Probes for *hox13* and *shha* were as previously described<sup>18</sup>. Primers to clone *Cre* and *and1* into vectors can be found in Extended Data Tables 1 and 2. Specimens were visualized on a Leica M205FA microscope.

**Lineage tracing vector construction.** In order to create a destination vector for lineage tracing, we first designed a random sequence of 298 bp that contained a *SmaI* site to be used in downstream cloning. This sequence was ordered as a gBlocks fragment (IDT) and ligated into the pCR8/GW/TOPO TA cloning vector (Invitrogen). We then performed a Gateway LR reaction according to the manufacturers specifications between this entry vector and pXIG-cFos-GFP, which abolished an *NcoI* site present in the gateway cassette and introduced a *SmaI* site. We then removed the GFP gene with *NcoI* and *BglII* of the destination vector and ligated in *Cre* with (primers in Extended Data Table 1), using the 'pCR8GW-Cre-pA-FRT-kan-FRT' (kind gift of M. L. Suster, Sars International Center for Marine Molecular Biology, University of Bergen, Bergen, Norway) as a template for *Cre* PCR and Platinum Taq DNA polymerase High Fidelity (Invitrogen). In order to add a late phase enhancer to this vector, we first ordered four identical oligos (IDT gBlocks) of the core e16 sequence from gar, each flanked by different restriction sites. Each oligo was then ligated into pCR8/GW/TOPO, and sequentially cloned via restriction sites into a single pCR8/GW/TOPO vector. This entry vector was used as a template to PCR the final *Lo-e16x4* sequence and ligate it into the *Cre* destination vector using *XhoI* and *SmaI*, creating *Lo-e16x4-Cre*. The early phase enhancer *Dr-CNS65x3* was cloned into the destination vector using the same strategy. Final vectors were confirmed by sequencing. A full list of sequences and primers used can be found in Extended Data Table 1.

**Establishment of lineage tracing lines.** \*AB zebrafish embryos were collected from natural spawning and injected according to the Tol2 system as described previously<sup>21</sup>. Transposase RNA was synthesized from the pCS2-zT2TP vector using the mMessage mMachine SP6 kit (Ambion)<sup>21</sup>. All injected embryos were raised to sexual maturity according to standard protocols. Adult F0 fish were outcrossed to wild-type \*AB, and the total F1 clutch was lysed and DNA isolated at 24 hpf for genotyping (see Extended Data Table 1 for primers) to confirm germline transmission of *Cre* plasmids in the F0 founders. Multiple founders were identified and tested for the strongest and most consistent expression via antibody staining and *in situ* hybridization. One founder fish was identified as best, and all subsequent experiments were performed using offspring of this individual fish.

**Lineage tracing crossing and detection.** Founder *Lo-e16x4-Cre* and *Dr-CNS65x3-Cre* fish were crossed to the *Tg(ubi:Switch)* line (kind gift from L. I. Zon). Briefly, this line contains a construct in which a constitutively active promoter (*ubiquitin*) drives expression of a loxP flanked GFP protein in all cells of the fish assayed. When *Cre* is introduced, the GFP gene is removed and the *ubiquitin* promoter is exposed to mCherry, thus permanently labelling the cell. We crossed our founder *Cre* fish to *Tg(ubi:Switch)* and fixed progeny at different time points to track cell fate. In order to detect the mCherry signal, embryos or adults were fixed overnight in 4% paraformaldehyde and subsequently processed for whole-mount antibody staining according to standard protocols<sup>30</sup> using the following antibodies and dilutions: 1st rabbit anti-mCherry/DsRed (Clontech #632496) at 1:250, 1st mouse anti-Zns-5 (Zebrafish International Resource Center, USA) at 1:200, 2nd goat anti-rabbit Alexa Fluor 546 (Invitrogen #A11071) at 1:400, 2nd goat anti-mouse Alexa 647 (Invitrogen #A21235) at 1:400. Stained zebrafish were mounted under a glass slide and visualized using an LSM 710 confocal microscope (Organismal Biology and Anatomy, the University of Chicago). Antibody stains on adult zebrafish (90 dpf) fins were imaged on a Leica SP5 II tandem scanner AOBs Laser Scanning Confocal (the University of Chicago Integrated Light Microscopy Core Facility).

**CRISPR/Cas9 design and synthesis.** Two mutations were simultaneously introduced into the first exon of each *hox13* gene by CRISPR/Cas9 system as previously described in *Xenopus tropicalis*<sup>31</sup>. Briefly, two gRNAs that match the sequence of exon 1 of each *hox13* gene were designed by ZiFiT (<http://zifit.partners.org/ZiFiT/>). To synthesize gRNAs, forward and reverse oligonucleotides that are unique for individual target sequences were synthesized by Integrated DNA Technologies, Inc. (IDT). Each oligonucleotide sequence can be found in Extended Data Table 2. Subsequently, each forward and reverse oligonucleotide were hybridized, and double stranded products were individually amplified by PCR with primers that include a T7 RNA promoter sequence, followed by purification by NucleoSpin Gel and PCR Clean-up Kit (Macherey-Nagel). Each gRNA was synthesized

from the purified PCR products by *in vitro* transcription with the MEGascript T7 Transcription kit (Ambion). *Cas9* mRNA was synthesized by mMESSAGE mMACHINE SP6 Transcription Kit according to the manufacturer's instructions (Ambion).

**CRISPR/Cas9 injection and mutants selection.** Two gRNAs targeting exon 1 of each *hox* gene were injected with *Cas9* mRNA into zebrafish eggs at the one-cell stage. We injected ~2 nl of the injection solution (5 µl solution containing 1,000 ng of each gRNA and 500 ng *Cas9* diluted in nuclease-free water) into the single cell of the embryo. Injected embryos were raised to adulthood, and at three months were genotyped by extracting DNA from tail clips. Briefly, zebrafish were anaesthetized by Tricaine (0.004%) and tips of the tail fin (2–3 mm<sup>2</sup>) were removed and placed in an Eppendorf tube. The tissue was lysed in standard lysis buffer (10 mM Tris pH 8.2, 10 mM EDTA, 200 mM NaCl, 0.5% SDS, 200 µg/ml proteinase K) and DNA recovered by ethanol precipitation. Approximately 800–1,100 bp of exon 1 from each gene was amplified by PCR using the primers described in Extended Data Table 2. To determine whether mutations were present, PCR products were subjected to T7E1 (T7 endonuclease1) assay as previously reported<sup>32</sup>. After identification of mutant fish by T7E1 assay, detailed analysis of mutation patterns were performed by sequencing at the Genomics Core at the University of Chicago.

**Establishment of *hox13* single and double mutant fish.** Identified mutant fish were outcrossed to wild type to select frameshift mutations from mosaic mutational patterns and establish single heterozygous lines. Obtained embryos were raised to adults (~3 months), then analysed by T7E1 assay and sequenced. Among a variety of mutational patterns, fish that have frameshift mutations were used for assays as single heterozygous fish. We obtained several independent heterozygous mutant lines for each *hox13* gene to compare the phenotype among different frameshift mutations. To obtain *hoxa13a*<sup>+/-</sup>, *hoxa13b*<sup>+/-</sup> double heterozygous mutant fish, each single heterozygous mutant line was crossed with the other mutant line. Offspring were analysed by T7E1 assay and sequenced after three months, and double heterozygous mutant fish were selected. To generate double homozygous *hoxa13* mutant embryos and adult fish (*hoxa13a*<sup>-/-</sup>, *hoxa13b*<sup>-/-</sup>), double heterozygous fish (*hoxa13a*<sup>+/-</sup>, *hoxa13b*<sup>+/-</sup>) were crossed with each other. The ratio of each genotype from crossing heterozygous fish is summarized in Extended Data Table 4.

**Genotype of single (*hoxa13a*<sup>-/-</sup> or *hoxa13b*<sup>-/-</sup>) or double (*hoxa13a*<sup>-/-</sup>, *hoxa13b*<sup>-/-</sup>) mutant by PCR.** After mutant lines were established, single (*hoxa13a* or *hoxa13b*) or double (*hoxa13a*, *hoxa13b*) mutant embryos and adult fish were genotyped by PCR for each analysis. Primer sequences for PCR are listed in Extended Data Table 2. To identify an 8 bp deletion in exon 1 of *hoxa13a*, the PCR product was treated by *AvaI* at 37 °C for 2 h, because the 8 bp deletion produces a new *AvaI* site in the PCR product ('zebra *hoxa13a*\_8 bp del' primers, wild type; 231 bp, mutant; 111 bp and 119 bp). Final product size was confirmed by 3% agarose gel electrophoresis. To identify a 29 bp deletion in exon 1 of *hoxa13a*, the PCR product was confirmed by gel electrophoresis ('zebra *hoxa13a*\_29 bp del' primers, wild type; 110 bp, mutant; 81 bp). To identify a 14 bp insertion in exon 1 of *hoxa13b*, the PCR product was treated by *BccI* at 37 °C for 2 h, because the 14 bp insertion produces a new *BccI* site in the PCR product ('zebra *hoxa13b*\_14 bp ins' primers, wild type; 98 bp, mutant; 53 bp + 57 bp). The final product size was confirmed by 3% agarose gel electrophoresis. The details of the mutant sequence are summarized in Extended Data Table 3a–c.

**Combination of stable and transient deletion of all *hox13* genes by CRISPR / Cas9.** Two gRNAs targeting exon 1 of *hoxa13b* and two gRNAs targeting exon 1 of *hoxd13a* were injected with *Cas9* mRNA into zebrafish one-cell eggs that were obtained from crossing *hoxa13a*<sup>+/-</sup> and *hoxa13a*<sup>+/-</sup>, *hoxa13b*<sup>+/-</sup>, *hoxd13a*<sup>+/-</sup> (gRNAs were same as that were used to establish single *hox13* knockout fishes and found in Extended Data Table 2). Injected eggs were raised to adult fish and genotyped by extracting DNA from tail fins. PCR products of each *hox13* gene were cloned into pCRITOP (Invitrogen) and deep sequencing was performed (Genomic Core, the University of Chicago). At four months old, skeletal staining and CT scanning were performed to analyse the effect of triple gene deletions. The knockout ratios of each *hox13* allele were calculated from the results of deep sequencing.

**Measurement of the fin fold length.** Embryos were obtained by crossing *hoxa13a*<sup>+/-</sup>, *hoxa13b*<sup>+/-</sup> to each other and raised to 72 hpf or 96 hpf. After fixation by 4% PFA for 15 h, caudal halves were used for PCR genotyping. Pectoral fins of wild type and *hoxa13a*<sup>-/-</sup>, *hoxa13b*<sup>-/-</sup> were detached from the embryonic body and placed horizontally on glass slides. The fins were photographed with a Leica M205FA microscope, and the fin fold length along the proximodistal axis at the centre of the fin was measured using ImageJ. The resulting data were analysed by *t*-test comparing the means.

**Counting the cell number in endochondral disk.** Embryos were obtained by crossing *hoxa13a*<sup>+/-</sup>, *hoxa13b*<sup>+/-</sup> to each other and raised to 96 hpf. After fixation by 4% PFA for 15 h, caudal halves were used for PCR genotyping. Wild type

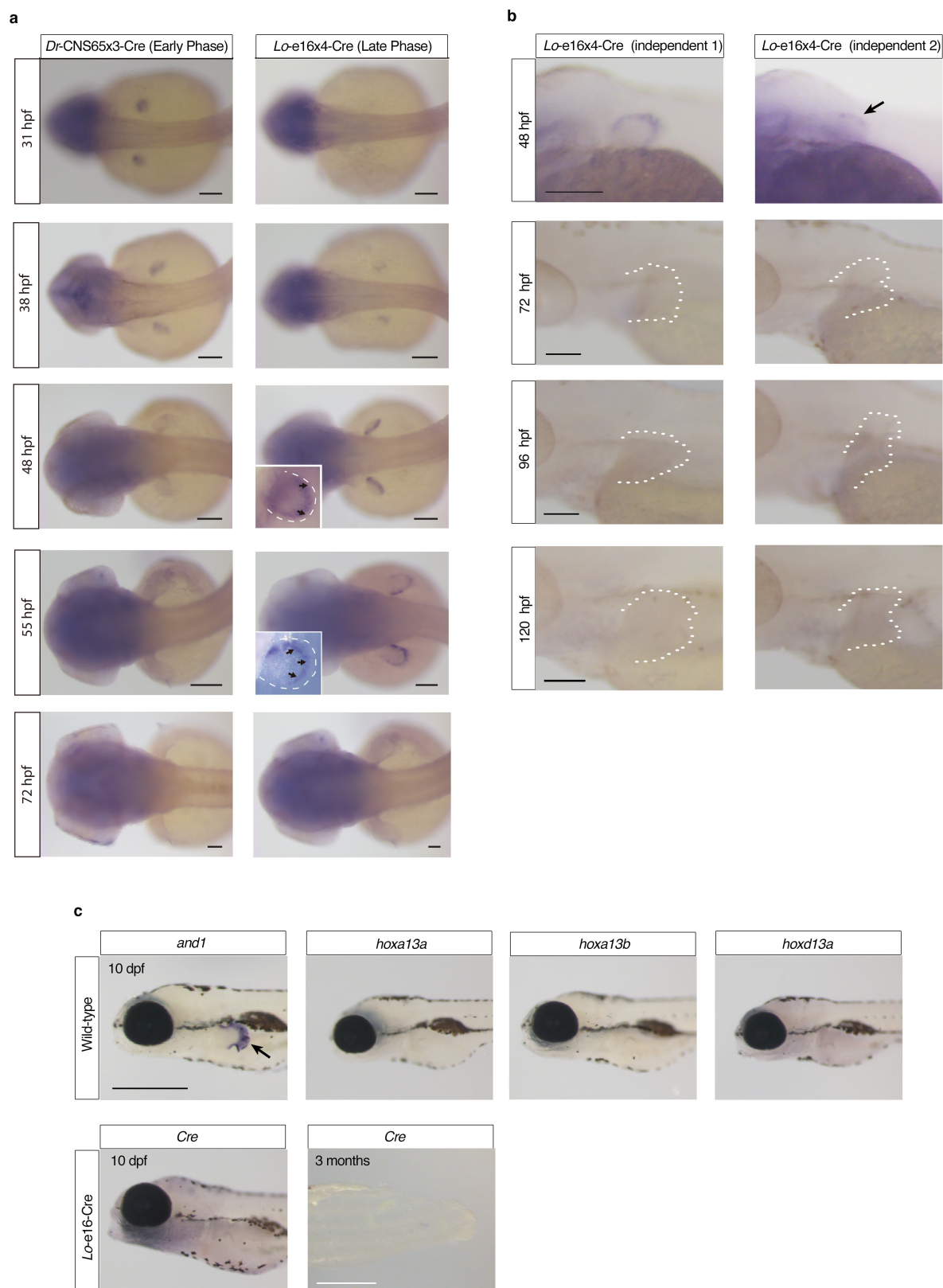
and *hoxa13a*<sup>-/-</sup>, *hoxa13b*<sup>-/-</sup> embryos were stained by DAPI (1:4,000 in PBS–0.1% Triton) for 3 h and washed for 3 h by PBS–0.1% Triton. Pectoral fins were detached from the embryonic body, placed on glass slides and covered by a coverslip. The DAPI signal was detected by Zeiss LSM 710 (Organismal Biology and Anatomy, the University of Chicago). Individual nuclei were manually marked using Adobe Illustrator and the number of nuclei was counted. The data were analysed by *t*-test comparing the means.

**Adult fish skeletal staining.** Skeletal staining was performed as previously described<sup>33</sup>. Briefly, fish were fixed in 10% neutral-buffered formalin overnight. After washing with milli-Q water, solutions were substituted by 70% EtOH in a stepwise fashion and then by 30% acetic acid/70% EtOH. Cartilage was stained with 0.02% alcian blue in 30% acetic acid/70% EtOH overnight. After washing with milli-Q water, the solution was changed to a 30% saturated sodium borate solution and incubated overnight. Subsequently, specimens were immersed in 1% trypsin/30% saturated sodium borate and incubated at room temperature overnight. Following a milli-Q water wash, specimens were transferred into a 1% KOH solution containing 0.005% Alzarin Red S. The next day, specimens were washed with milli-Q water and subjected to glycerol substitution. Three replicates for each genotype were investigated.

**PMA staining and CT scanning.** After skeletal staining, girdles and pectoral fins were manually separated from the body. Girdles and fins were stained with 0.5%

PMA (phosphomolybdic acid) in milli-Q water for 16 h and followed by washes with milli-Q water. Specimens were placed into 1.5 ml Eppendorf tubes with water and kept overnight to settle in the tubes. The next day, tubes containing specimens were set and scanned with the UChicago PaleoCT scanner (GE Phoenix v/tome/x 240kv/180kv scanner) (<http://luo-lab.uchicago.edu/paleoCT.html>), at 50 kVp, 160  $\mu$ A, no filtration, 5 $\times$ -averaging, exposure timing of 500 ms per image, and a resolution of 8  $\mu$ m per slice (512  $\mu$ m<sup>3</sup> per voxel). Scanned images were analysed and segmented using Amira 3D Software 6.0 (FEI). Three replicates for single and double homozygotes and five for mosaic triple knockout were investigated.

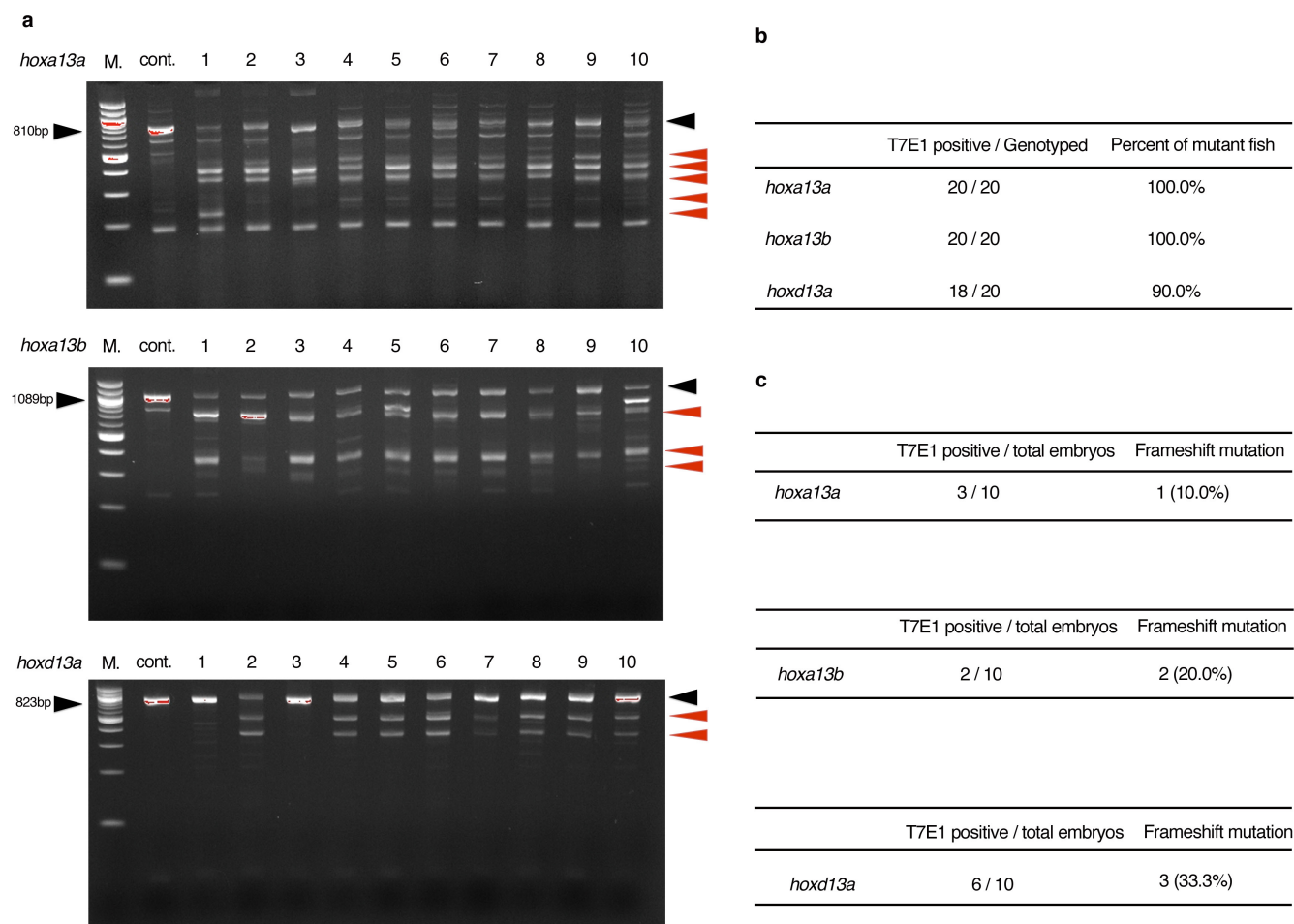
29. Thisse, C., Thisse, B. & Postlethwait, J. H. Expression of *snail2*, a second member of the zebrafish *snail* family, in cephalic mesendoderm and presumptive neural crest of wild-type and *spadetail* mutant embryos. *Dev. Biol.* **172**, 86–99 (1995).
30. Asharani, P. V. *et al.* Attenuated BMP1 function compromises osteogenesis, leading to bone fragility in humans and zebrafish. *Am. J. Hum. Genet.* **90**, 661–674 (2012).
31. Nakayama, T. *et al.* Simple and efficient CRISPR/Cas9-mediated targeted mutagenesis in *Xenopus tropicalis*. *Genesis* **51**, 835–843 (2013).
32. Jao, L.-E., Wente, S. R. & Chen, W. Efficient multiplex biallelic zebrafish genome editing using a CRISPR nuclease system. *Proc. Natl Acad. Sci. USA* **110**, 13904–13909 (2013).
33. Westerfield, M. *ZFIN: Zebrafish Book*. 4th ed. (Univ. of Oregon Press, 2000).



**Extended Data Figure 1 | Cre *in situ* hybridization of lineage tracing fish.** **a**, Cre is expressed only from 31 hpf to 38 hpf in *Dr-CNS65x3-Cre*, whereas it is expressed from 38 hpf to 55 hpf in *Lo-e16x4-Cre*. These temporal expression patterns of Cre indicate that our transgenic lineage tracing labelled the cells which experienced only early or late phase *hox*. Scale bars are 100  $\mu$ m. **b**, Cre expression pattern from 48–120 hpf in independent *Lo-e16x4-Cre* lines (different founders from **a**). The fin is outlined by a dashed white line. The expression patterns from different founders were investigated and all expression ceases before 72 hpf. Our *in situ* results indicate that *Lo-e16x4-Cre* marks only the cells that

experienced late phase *hox* expression from 38–55 hpf.  $n = 5$  embryos for all stages. Scale bars are 100  $\mu$ m. **c**, The expression pattern of *and1* and *hox13* genes in wild type (10 dpf) and also Cre in *Lo-e16x4-Cre* line (10 dpf and 3 months,  $n = 10$ ). Whereas *and1* expression can be observed in fin fold (positive control, black arrow), *hox13* genes are not expressed at 10 dpf in the wild type. Cre is not expressed at 10 dpf and at 3 months in the fin, indicating that *Lo-e16x4-Cre* activity is limited to only early embryonic development (38–55 hpf). Three month fins were dissected from the body of *Lo-e16x4-Cre* lines and subjected to *in situ* hybridization ( $n = 3$ ). Scale bars are 500  $\mu$ m at 10 dpf and 3 months.

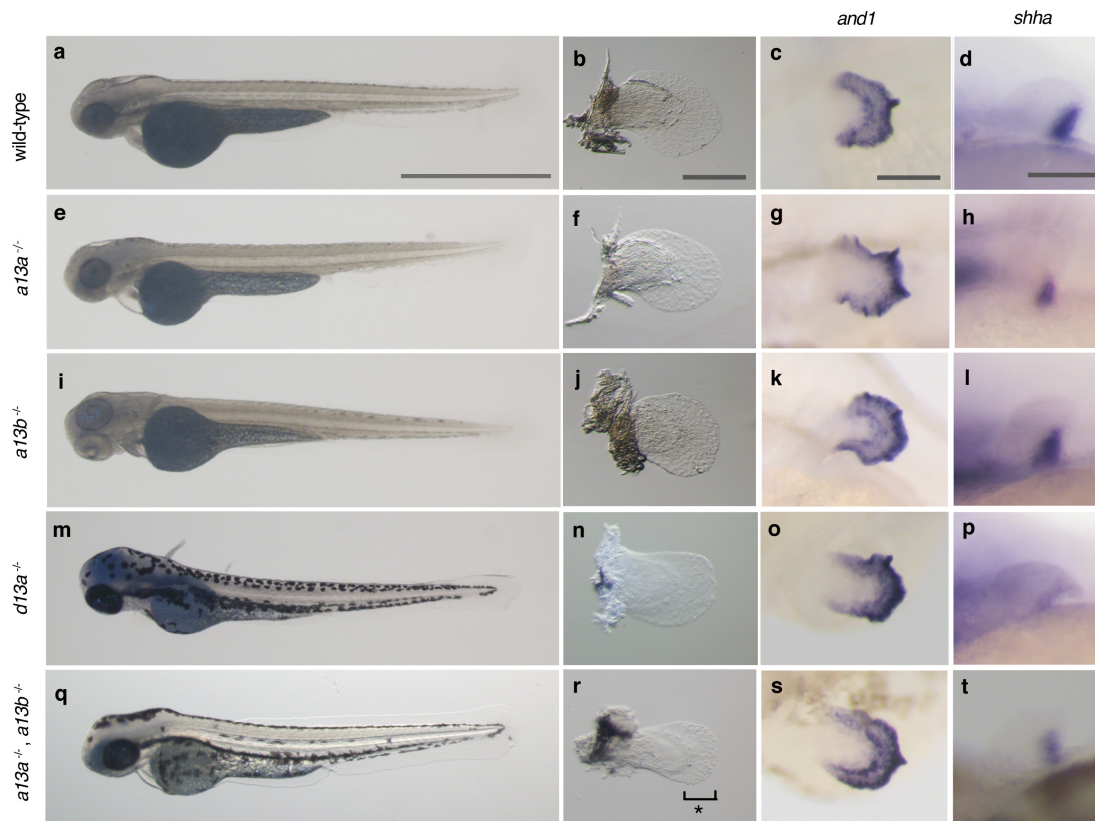




# Extended Data Figure 2 | T7E1 assay of F0 CRISPR/Cas9 adult fish.

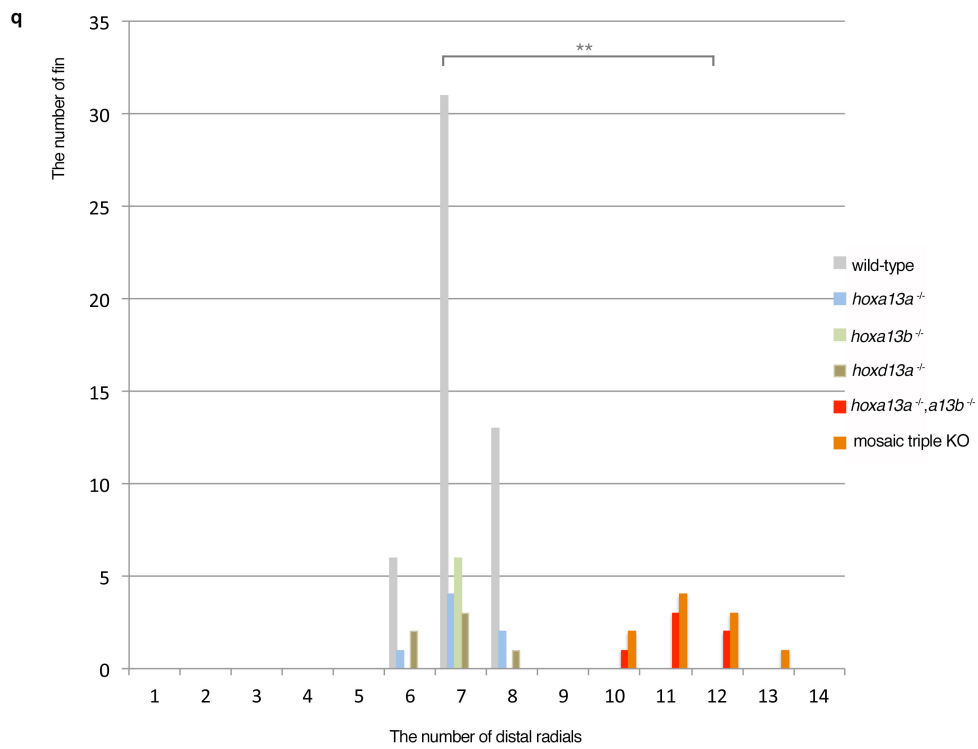
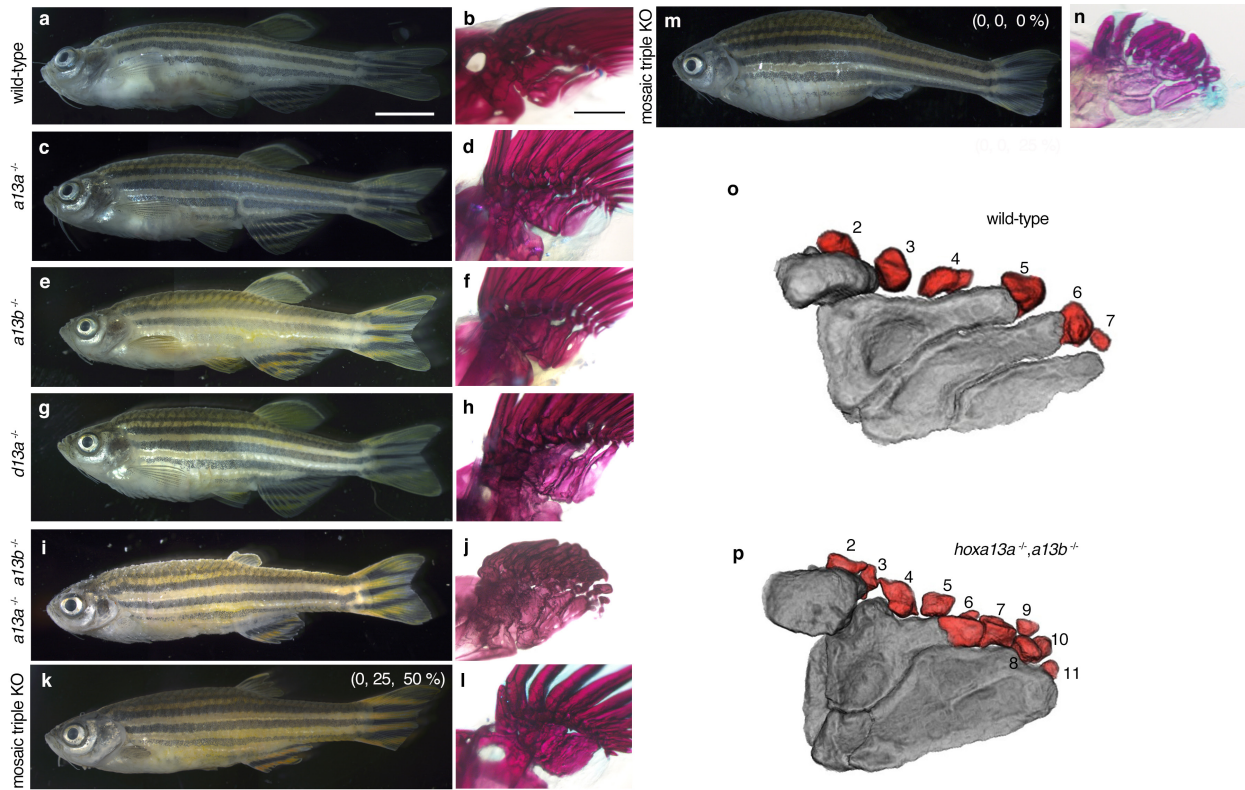
PCR products of *hoxa13a*, *hoxa13b* or *hoxd13a* were subjected to a T7E1 assay (Methods) and confirmed by gel electrophoresis. **a**, The result of the *hoxa13a*, *hoxa13b* or *hoxd13a* T7E1 assay for ten adult fish. 'M.' is a 100 bp DNA ladder marker (NEB). In the *hoxa13a* gel picture, 810 bp (black arrowhead) is the wild-type band as observed in cont. lane (wild type without gRNA injection). All ten fish showed smaller and bottom shifted products (red arrowheads) compared to negative control fish, indicating that all fish have mutations in the target region of *hoxa13a*. In the *hoxa13b* gel picture, 1,089 bp is the wild-type band. All ten fish into which *hoxa13b* gRNAs were injected showed smaller and bottom shifted products compared to negative control fish, indicating that all fish have

mutations in the target region of *hoxa13b*. In the *hoxd13a* gel picture, 823 bp is the wild-type band. Eight of ten fish showed smaller and bottom shifted products, indicating that 80% of fish have mutations in the target region of *hoxd13a*. **b**, The efficiency of CRISPR/Cas9 deletion for *hox13* in zebrafish. Almost all adult fish into which gRNAs and Cas9 mRNA were injected have mutations at the target positions. **c**, The efficiency of germline transmission of CRISPR/Cas9 mutant fish. Identified mutant fish were outcrossed to wild-type fish to obtain embryos and confirmed germline transmission. Obtained embryos were lysed individually at 48 hpf, genotyped by T7E1 assay and sequenced. Because of CRISPR/Cas9 mosaicism, some different mutation patterns, which result in a non-frameshift or frameshift mutation, were observed.



**Extended Data Figure 3 | Embryonic phenotypes of *hox13* deletion mutants.** **a, e, i, m, q,** Whole body pictures at 72 hpf. **a,** Wild type, **e,** *hoxa13a*<sup>-/-</sup> (4 bp del./4 bp del.), **i,** *hoxa13b*<sup>-/-</sup> (4 bp del./14 bp ins.), **m,** *hoxd13a*<sup>-/-</sup> (5 bp ins./17 bp del.), and **q,** *hoxa13a*<sup>-/-</sup>, *hoxa13b*<sup>-/-</sup> double homozygous embryo (8 bp del./29 bp del., 14 bp ins./14 bp ins.). The details of mutant sequences are summarized in Extended Data Table 3. Wild-type and single homozygous fish for *hoxa13a* or *hoxa13b* were treated by PTU to inhibit pigmentation. The body size and length of mutant embryos are relatively normal at 72 hpf. *n* = 5 embryos for all genotypes. **b, f, j, n, r,** Bright field images of pectoral fins. Pectoral fins were detached from the body and photographed (Methods). *Hoxa13a*<sup>-/-</sup>,

*a13b*<sup>-/-</sup> double homozygous embryo shows 30% shorter pectoral fin fold compared to wild type (**r**, see also Extended Data Fig. 5). *n* = 5 embryos for all genotypes. **c, g, k, o, s,** *and1* *in situ* hybridization at 72 hpf. *Hox13* mutants show normal expression patterns, which indicates that fin fold development is similar to wild type in these mutants. *n* = 3 embryos for all genotypes. **d, h, l, p, t,** *shha* *in situ* hybridization at 48 hpf. *Hox13* mutants show a normal expression pattern that is related to relatively normal anteroposterior asymmetry of adult fin (Fig. 3, Extended Data Fig. 4 and Supplementary Information). *n* = 3 embryos for all genotypes. Scale bars are 1 mm (**a**), 200  $\mu$ m (**b, c**) and 100  $\mu$ m (**d**).



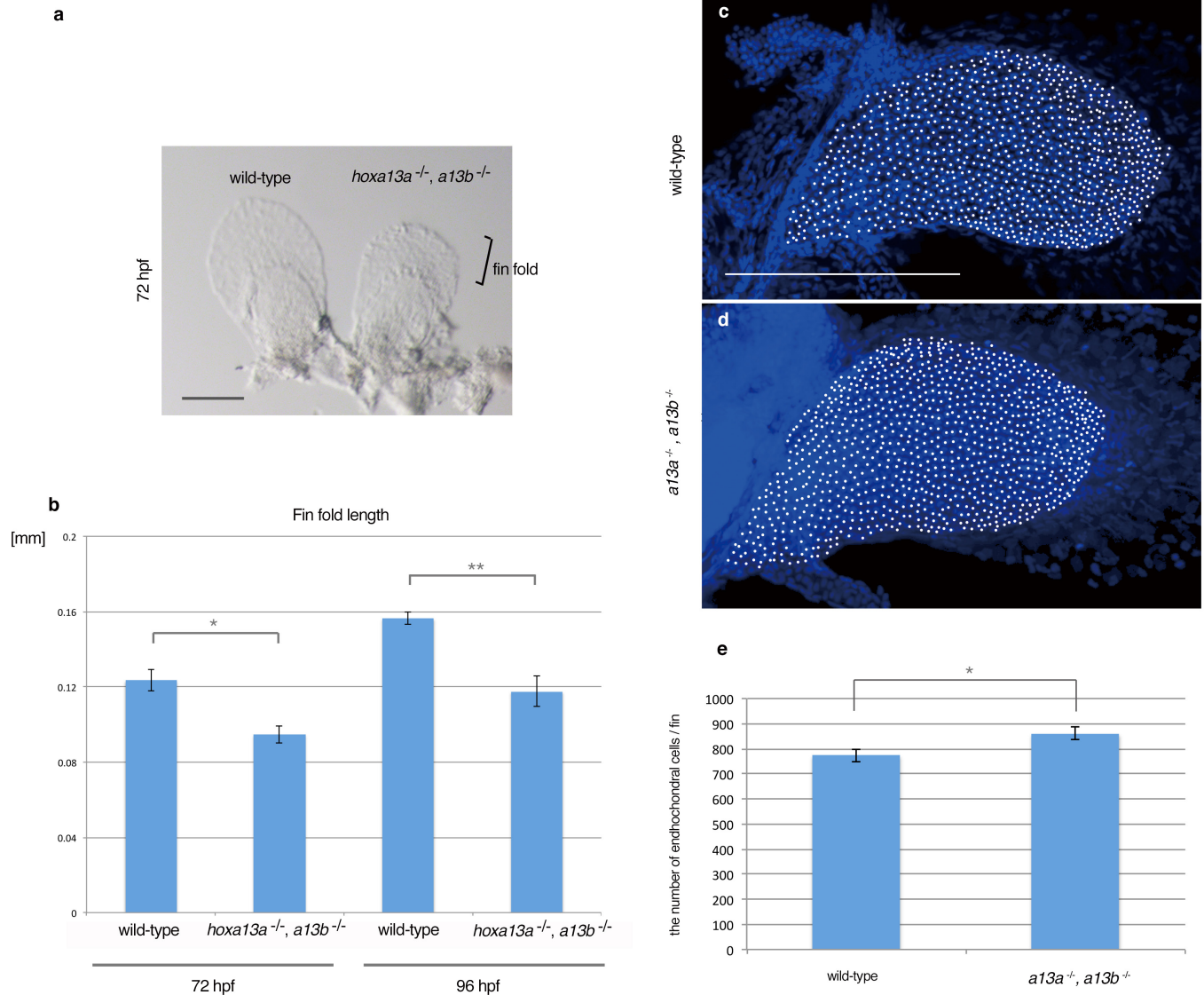
Extended Data Figure 4 | See next page for caption.



**Extended Data Figure 4 | Phenotype of adult *hox13* mutant fish.**

**a, c, e, g, i, k, m,** Whole body morphology of *hox13* deletion mutants were photographed at 4 months old; *hoxa13a*<sup>-/-</sup> (8 bp del./29 bp del.), *hoxa13b*<sup>-/-</sup> (4 bp del./14 bp ins.), *hoxd13a*<sup>-/-</sup> (5 bp ins./10 bp ins.), *hoxa13a*<sup>-/-</sup>, *hoxa13b*<sup>-/-</sup> double homozygous fish (8 bp del./29 bp del., 14 bp ins./14 bp ins.) and triple knockout (**k, m**, mosaic for *hoxa13a*, *hoxa13b* and *hoxd13a*) fish (Methods). *n* = 3 fish for wild type, single and double mutants and *n* = 5 fish for triple mosaic mutants (same specimens were used as in Fig. 3). The details of mutant sequences are summarized in Extended Data Table 3. Each homozygous mutant fish shows normal morphology at 4 months old except for slightly short pectoral fin rays of *hoxa13a*<sup>-/-</sup> or *a13b*<sup>-/-</sup> single mutants. *Hoxa13a*<sup>-/-</sup>, *hoxa13b*<sup>-/-</sup> double homozygous fish shows a severe reduction of fin rays in pectoral, pelvic, dorsal and anal fins compared with wild type. The triple knockout (mosaic for *hoxa13a*, *hoxa13b* and *hoxd13a*) fish also showed a reduction in fin rays. Scale bar is 5 mm. Owing to the size of the adult fish, three different pictures for anterior, centre and posterior of the body were merged to make whole-body pictures. **b, d, f, h, j, l, n,** Bone staining pictures of mutant fish. The endochondral bones of pectoral fins are shown. Whereas single homozygous fish show relatively normal proximal radials (**b, d, f, h** and Fig. 3), double homozygous mutants show fused third and fourth

proximal radials (**j**). One triple knockout (mosaic for *hoxa13a*, *hoxa13b* and *hoxd13a*, 0, 25, 50%) fish had fused third and fourth proximal radials (**i**), but another triple knockout (0, 0, 0%) had more broken down proximal radials (**n**). *n* = 3 fish for wild type, single and double mutants and *n* = 5 fish for triple mosaic mutants (same specimens were used as in Fig. 3). The scale bar is 500  $\mu$ m. **o, p,** Examples of counting distal radials in wild-type and *hoxa13a*<sup>-/-</sup>, *hoxa13b*<sup>-/-</sup> double homozygous fish. First distal radials are not shown in CT segmentation because of a fusion with first fin ray. **q,** The number variation of distal radials in mutant fish. Multiple fins were investigated in wild type (25 fish/50 fins), *hoxa13a*<sup>-/-</sup> (4 bp del./4 bp del., 3 fish/6 fins), *hoxa13b*<sup>-/-</sup> (4 bp del./14 bp ins., 3 fish/6 fins), *hoxd13a*<sup>-/-</sup> (5 bp ins./17 bp del., 3 fish/6 fins), *hoxa13a*<sup>-/-</sup>, *hoxa13b*<sup>-/-</sup> double homozygous (8 bp del./29 bp del., 14 bp ins./14 bp ins., 3 fish/6 fins) and triple knockout (mosaic for *hoxa13a*, *hoxa13b* and *hoxd13a*) fish (five fish/10 fins). The number of distal radials increased to 10 and 13 in double and triple mutants, respectively. The difference in distal radial number between wild-type and double homozygous or wild-type and triple knockout fish (mosaic for *hoxa13a*, *hoxa13b* and *hoxd13a*) is statistically significant ( $P = 0.0014$  or  $P = 0.00001$ , respectively, *t*-test comparing the means, two-tailed distribution).



**Extended Data Figure 5 | Analysis of embryonic fin fold and endochondral disk in *hoxa13a*<sup>-/-</sup>, *hoxa13b*<sup>-/-</sup> embryos.** **a**, A bright field image of wild-type and *hoxa13a*<sup>-/-</sup>, *hoxa13b*<sup>-/-</sup> pectoral fins at 72 hpf. Pectoral fins were detached from the body and photographed (Methods). Scale bar is 150  $\mu$ m. **b**, The difference in fin fold length between wild-type and *hoxa13a*<sup>-/-</sup>, *hoxa13b*<sup>-/-</sup> embryos. The length of the fin fold was measured in wild-type ( $n=8$ ) and *hoxa13a*<sup>-/-</sup>, *hoxa13b*<sup>-/-</sup> double homozygous ( $n=5$ ) embryos at 72 hpf and 96 hpf (Methods). The length of the fin folds was decreased to about 70% of wild

type in double homozygous embryos (72 hpf;  $P=0.006$ , 96 hpf;  $P=0.004$ ,  $t$ -test comparing the means, one-tailed distribution, see Source Data). The error bars indicate s.e.m. **c**, **d**, Images of DAPI staining of wild-type (**c**) and *hoxa13a*<sup>-/-</sup>, *hoxa13b*<sup>-/-</sup> mutant (**d**) pectoral fins captured by confocal microscopy. White circles indicate nuclei in the endochondral disks. Scale bar is 200  $\mu$ m. **e**, The average number of cells in the endochondral disk of wild-type and *hoxa13a*<sup>-/-</sup>, *hoxa13b*<sup>-/-</sup> mutant fins (see Methods and Source Data). The difference is statistically significant ( $P=0.041$  by Student's  $t$ -test, one-tailed distribution). The error bars indicate s.e.m.

### Extended Data Table 1 | Primers and oligos sequence for lineage tracing

## Lineage tracing oligos

CRE\_PCR\_F\_NcoI  
5'- CGGCCCTTCATGGATGGCCAATTACTGACCGTAC -3'  
CRE\_PCR\_R\_BglII  
5'- GTTCTTCTGAAGATCTCTCTGGGGTTCGGGGCTGCAGG -3'  
CRE\_Genotype\_F  
5'- CGTACTGACGGTGGGAGAAT -3'  
CRE\_Genotype\_R  
5'- ACCAGGCCAGGTATCTCTGA -3'  
CRE\_Probe\_F  
5'- ATGGCCAAATTACTGACCGTAC -3'  
CRE\_Probe\_R  
5'- CTAATCGCCATCTTCCAGCAGGCG -3'

Random\_Oligo\_Smal

5'- CTGCTCTGGTCAGCCCTCTAATGGCTGGTAGATAGCTAGCCGCTGGTAATCACTCGATGACCTCGGCTGCCCATTTGGTGCTACGGCGATTCTTGGAGAGCCAGCTGCGATCGCTAATGTGAGGACAGTGTAATATTAG  
CAAGCGATAGATGCCCACTGGTTGTGGCCCTTTGGAAAGTGAACCTTCAACATATGCTGTCTCACGACATATGCGATGGTTGGGACAAATTTGATTCAAGTCTGATCAACCTTACGTGCTTAGAATCAAAGCAGTGATCTC  
**CCGGGTGCGAAATAA-3'** SmaI site italicized in bold

Lo-e16\_Oligo\_1\_BamHI\_SmaI

5'- CCCCCAAAAATGACAAAACCTTGGAAATTATACGGCTTTGGCAATAGAGACGCGTTTTGGTGGGCAGTAAAGGTTTGATGTTACAGTATCGCCTTTAAATGCATTCATTCCTCTTTCATATGTGTGCAACTGTTAGATACATCATCAAAATGATGCACCATTAGGTTGCCCATTAGGCATTCACCGGTTCTCCCTCAGGCGCATGAGATAAATTTGGACACAGGTGATCCCTTCCTAGAAAGAGCCCTTGATGTCCTTGTGAATGAGTTGAAGCGGAGCTGTGATCGGCTTTCAGCAGGCATGAAGATGACCATAGAGTCGGGTGCAAAAGTCGCGCAGGCAGCATCTCATAGGAGCAGCTAGGCTTGCTGTGAAGCTGCCTTATTCACAGATCAGTTATGTGAAGGTACAGCAAAAAGGCAAGACATCTGATTTTGAATGACACAGCAAAAGTCGGTGC **GGATCCC**GAGTTTG **CCCGGGT**AGGCC -3'

BamHI and SmaI sites italicized in bold

Lo-e16\_Oligo\_2\_BamHI\_Sall\_SmaI

5'- CCCCCAAAAATGACAAAA**GGATCC**GAAATTATTACGGCTTTGGCAATAGAGACCGCTTTTGGGTGGC1CAGTAAAGGTTTGATGTTCCAGTATCGCCTTTAAATGCATTCATTCCTCTTCATATGTGTGCAACTGTT  
AGATACATCATAAAAATGTCCACATTGAGGTGCCCATAGGCATTACCCGTTCTCCTCCAGGCCATGAGAGATAAATGGACAGCGATGATCCCTCCTAGAGAAGCCCTTGATGTCTTCTGGTAATGAGTTGAAAGCGGAAG  
CTGTACGCTTCCAGCGGCATGAAGATGCAGTAATGAGCTGCGTCTCAAGGTCGCCAGCGCATCTCATAGGACAGCATAGCCTTGGTGTGAAGCTGCTTATTACAGATCAGTTATGTAAGGTCACAGCAAAAAGCAGACACT  
CGAATTTCGAATGACAGCAGCAAAAGT**GTGCACT**CTCCGAC**CCCGG**AAACTAGGCC-3' BamHI, SalI, and SmaI sites italicized in bold

Lo-e16\_Oligo\_3\_Sall\_BglII\_Smal

5'-CCCCCAAAAATGAC**GTGCAGC**TTGGAATTATACGGCTTTGGCAATAGAGACCGCTTTTGGGTGGCICAGTAAAGGTTTGATGTTCAAGTATCGCTTTTAAATGCATTCATCTCTTTCATATGTGTGCAACGTGTAGATACATCATAAAAATGACCAATGACAGGATCCCATAGGCATACCCCGGTCCTCCAGCGCCATGGAGATAAATTTGACACAGGGTATGCCCTCTGAGACAGGCCCTTGATGCTCTCTGGTAATGAGTGTAAAGCGGAAAGCTGTGACCGCTTCAGCAGCATAAGGATGCATTAAGCTGCGTGTCAAAGTCCCGCAGAGCTCTAAGAGCAGCATAGCCTTGGTGTAAAGCTGCTTATTAACAGATCAGTTATGTAAGGGTACAGCAAAAAGGCAAGACATCGATTTTGAATGACACAGCAAAGTCG**AGATCT**CTCCGAGT**CCCGGGA**CTACGCC -3'

Sall, BglII, and SmaI sites italicized in bold

Lo-e16\_Oligo\_4\_BglII\_SmaI

5'-CCCCCAAAATG**AGATC**TCTCTTGAATTATTACGCTTTGGCAATAGAGACCGCTTTTGGTGGCTCAGTAAAGGTTTGTATGTTACAGTATCGCCTTTTAAATGCATTCATCTCTTTTCATATGTGTGCAACTGTTT  
AGATACATCATAAAGATGTTACCAATTGAGGTGCCCATTAGGACTACACCGTCTCTCTCCAGGCCATGAGAGATAAATTTGGACAGGTGATCCCTCCTAGAAGAGCCCTTGATGTCTCTTGGAATGAGTTGAAAGCGGGAAG  
CTGCAGCCCTTCAGCAGGCATGAAGATCAATTAGGCTCGCTTCAAAGTGGCCAGGCAGCTCATAAGGAGCAGCTAGCTCTGTGTGAAGCTGCTTATTCACAGATCAGTTATGTAAGGTTACAGCAAAAAGCAGACACT  
CGATTTTGAATGACACAGCAAAAGT**CCCGGG**TTCTCCGAGAACTAGGCC -3'

BglII, and SmaI sites italicized in bold

Primers for final PCR to clone into destination vector:

e16x4\_F\_Xho1:  
5'- CAGGCTCCCTCGAGCCCCCAAAAATGACAAA -3'

e16x4\_R\_Smal:

5'- CGAATTCGGTCCCGGGACTTTGCTG -3'

Dr-CNS65\_Oligo\_1\_BamHI\_SmaI

[illegible]

Dr-CNS65\_Oligo\_2\_BamHI\_Sall\_SmaI

[illegible]

Dr-CNS65\_Oligo\_3\_Sall\_Smal

[illegible]

Primers for final PCR to clone into destination vector:

CNS65x3\_F\_XhoI:  
5'- GCAGGCTCCTCGAGGAGGTTACCTTTAACCA -3'

CNS54x3\_R\_Smal:

5'- AACGCTCACTTTCCCGGGTCTAGTGT -3'

PCR primers and oligos for construction of lineage tracing vectors are listed (See Methods). Restriction enzyme sites that were used for ligating oligos are highlighted in italics and bold in oligo sequence.



**Extended Data Table 2 | PCR primers for CRISPR/Cas9 deletion, T7E1 assay, genotypes and gene cloning**

## CRISPR gRNA oligos

zebra *hoxa13a*\_gRNA1\_F

5'- AATTAATACGACTCACTATAGGGCAATCACAACCAGTGGAGTTTATAGAGCTAGAAATAGC -3'

zebra *hoxa13a*\_gRNA2\_F

5'- AATTAATACGACTCACTATAGGCAGTAAAGACTCATGTGCGTTTATAGAGCTAGAAATAGC -3'

zebra *hoxa13b*\_gRNA1\_F

5'- AATTAATACGACTCACTATAGGATGATATGAGCAAAAACAGTTTATAGAGCTAGAAATAGC -3'

zebra *hoxa13b*\_gRNA2\_F

5'- AATTAATACGACTCACTATAGGACACTTCTGTTTCTGGAGGTTTATAGAGCTAGAAATAGC -3'

zebra *hoxd13a*\_gRNA1\_F

5'- AATTAATACGACTCACTATAGGCTCTGGCTCCTTCACGTTGTTTATAGAGCTAGAAATAGC -3'

zebra *hoxd13a*\_gRNA2\_F

5'- AATTAATACGACTCACTATAGGCGAACTCTTAAGCCAGCGTTTATAGAGCTAGAAATAGC -3'

zebra gRNA\_R

5'- AAAAGCACCGACTCGGTGCCACTTTTTCAAGTTGATAACGGACTAGCCTTATTTTAACTTGCTATTTCTAGCTCTAAAC -3'

## T7 assay primers

zebra *hoxa13a*\_Cont\_F

5'- CTGCAGCGGGTGATTCTG -3'

zebra *hoxa13a*\_Cont\_R

5'- CTCCTTTACCCGTCGGTTTT -3'

PCR product: 810 bp

zebra *hoxa13b*\_Cont\_F

5'- GAAGCTTATCACTAGAACTTTTACAGC -3'

zebra *hoxa13b*\_Cont\_R

5'- TTTTCTCAGGGCCTAAAGGT -3'

PCR product: 1089 bp

zebra *hoxd13a*\_Cont\_F

5'- AGCTGCCCCAATCACATGC -3'

zebra *hoxd13a*\_Cont\_R

5'- CGATTATAAATTCAGTTGCTCTTTAG -3'

PCR product: 823 bp

Genotype primers for single (*hoxa13a* or *a13b*) and double (*hoxa13a*, *a13b*) mutantszebra *hoxa13a*\_8 bp del\_F

5'- GCCAAGGAGTTTGCCTTGTA -3'

zebra *hoxa13a*\_8 bp del\_R

5'- TGACGACTCCACACGTTTC -3'

PCR product: wild-type 231 bp, mutant (cut by Ava1) 111 + 119 bp

zebra *hoxa13a*\_29 bp del\_F

5'- CAGGCAATAAGCGGGCCTT -3'

zebra *hoxa13a*\_29 bp del\_R

5'- GTGCAGTAGACCTGTCCGTT -3'

PCR product: wild-type 110 bp, mutant 81 bp

zebra *hoxa13b*\_14 bp ins\_F

5'- GATTGACCCGGTGATGTTTC -3'

zebra *hoxa13b*\_14 bp ins\_R

5'- TACACTGGTTCGAGCAAAA -3'

PCR product: wild-type 98 bp, mutant (cut by Bcc1) 53 + 57 bp

## Cloning primers

Danio\_*and1*\_F

5'-ACCTGCTCCTGCTCCAGTTA -3'

Danio\_*and1*\_R

5'- CACATCCTCTTGAGGGGAAA -3'

For synthesis of gRNAs, each forward primer and common reverse primer ('zebra gRNA\_R') were hybridized and used as templates. For genotype of single and double mutants, PCR products were treated by the enzymes indicated.

Extended Data Table 3 | List of *hox13* mutant sequences

a.

*hoxa13a*

TCCAGGCAATAAGCGGCCCTTGGGAGCCCC**CGACATGAGTCTTTACTGCC**GATGGAGAGTTACCAACCGT**GGGCAATCACAACCAAGTGGAT**TGGAAC **wild-type**  
 TCCAGGCAATAAGCGGCCCTTGGAGC-----GATGGAGAGTTACCAACCGT**GGGCAATCACAACCAAG**-----AAC **-22 -7 = 29 bp deletion**  
 TCCAGGCAATAAGCGGCCCTTGGAGCCCC**CGA**-----GTCTTTACTGCCGATGGAGAGTTACCAACCGT**GGGCAATCACA**-----GTGGATGGAAAC **-5 -3 = 8 bp deletion**  
 TCCAGGCAATAAGCGGCCCTTGGGAGCCCC-----**GAGTCTTTACTGCC**GATGGAGAGTTACCAACCGT**GGGCAATCACAACCAAGT**TGGATGGAAAC **-5 + 1 = 4 bp deletion**

b.

*hoxa13b*

CTATGACAACGGTTT**GGATGATATGAGCAAAAACAT**TGGAAGG-----TACAT**GGACACTTCTGTTCTGGAGAGGAGT** **wild-type**  
 CTATGACAACGGTTT**GGATGATATGAGCAAA**T**GGAGGATGAGAGC**JACATGGAAGG-----TACAT**GGACACTTCTGTTCTGGAGAGGAGT** (+1bp ins.) **14 bp insertion**  
 CTATGACAACGGTTT**GGATGATATGAGCAA**-----ATGGAAGG-----TACAT**GGACACTTCTGTTCTGGAGAGGAGT** **4 bp deletion**

c.

*hoxd13a*

ATCCAATAT**GGCTCTGGCTCCTTCACGTT**TGGATGCCATT-----CGGTGAAGCCTCCA**GCTGGCTTAAAGAGTTCGCCTTTTATCAAGG** **wild-type**  
 ATCCAATAT**GGCTCTGGCTCC**[**AAAAAA**]**TTCCGTT**TGGATGCCATT-----CGGTGAAGCCTCCA**GCTCT****CAAGCTTAAAGAGTTCGCCTTTTATCAAGG** **7 + 3 = 10 bp insertion**  
 ATCCAATAT**GGCTCTGGCTCCTTCAAA**T**GGCTCT**TGGATGCCATT-----CGGTGAAGCCTCCA**GCTGGCTTAAAGAGTTCGCCTTTTATCAAGG** **5bp insertion**  
 ATCCAATAT**GGCTCTGGCTCC**-----TTTGGATGCCATT-----CGGTGA-----GCTTAAAGAGTTCGCCTTTTATCAAGG **-11 -6 = 17 bp deletion**

d.

*hoxa13a*

TCCAGGCAATAAGCGGCCCTTGGGAGCCCC**CGACATGAGTCTTTACTGCC**GATGGAGAGTTACCAACCGT**GGGCAATCACAACCAAGTGGAT**TGGAAC **wild-type**  
 TCCAGGCAATAAGCGGCCCTTGGGAGCCCC**CGA**-----GTCTTTACTGCCGATGGAGAGTTACCAACCGT**GGGCAATCACA**-----GTGGATGGAAAC **-5 -3 = 8 bp deletion** **0%**

e.

*hoxa13b*

CTATGACAACGGTTT**GGATGATATGAGCAAAAACAT**TGGAAGG-----TACAT**GGACACTTCTGTTCTGGAGAGGAGT** **wild-type** **0%**  
 CTATGACAACGGTTT**GGATGATATGAGCAAA**T**GGAGGATGAGAGC**JACATGGAAGG-----TACAT**GGACACTTCTGTTCTGGAGAGGAGT** (+1bp ins.) **14 bp insertion** **50%**  
 CTATGACAACGGTTT**GGATGATATGAGC**-**AAATTTT**TGGAAGG-----TACAT**GGACACTTCTGTTCT**-----GAGT **-1 -6 = 7 bp deletion** **50%**

f.

*hoxd13a*

ATCCAATAT**GGCTCTGGCTCCTTCACGTT**TGGATGCCATT-----CGGTGAAGCCTCCA**GCTGGCTTAAAGAGTTCGCCTTTTATCAAGG** **wild-type** **0%**  
 ATCCAATAT**GGCTCTGGCTCCTT**-----TGGATGCCATT-----CGGTGAAGCCTCCA**GCTGGCTTAAAGAGTTCGCCTTTTATCAAGG** **6bp deletion** **14.3%**  
 ATCCAATAT**GGCTCTGGCTCCTT****CGCT****CGTT**TGGATGCCATT-----CGGTGAAGCCTCCA**GCTGGCTTAAAGAGTTCGCCTTTTATCAAGG** **4bp insertion** **28.5%**  
 ATCCAATAT**GGCTCTGGCTCCTTCAC**[**TCCAAATG**]**GT**TGGATGCCATT---CGGTGAAGCCTCCA**GCTGGCTTAAAGAGTTCGCCTTTTATCAAGG** **8bp insertion** **14.3%**  
 -----CGTTTGGATGCCATT-----CGGTGAAGCCTCCA**GCTGGCTTAAAGAGTTCGCCTTTTATCAAGG** **170bp deletion** **14.3%**  
 ATCCAATAT**GGCTCTGGCTCCTTCG**[**GCT**]**CGTT**TGGATGCCATT-----CGGTGAAGCCTCCA**GCTGGCTTAAAGAGTTCGCCTTTTATCAAGG** **3bp insertion** **14.3%**  
 ATCCAATAT**GGCTCTGGCTCCTTCAC**[**TCCAAATG**]**GT**TGGATGCCATT---CGGTGAAGCCTCCA-----GCTTAAAGAGTTCGCCTTTTATCAAGG **+ 8 - 4 = 4bp insertion** **14.3%**

g.

Figure 3, Extended Data Fig.4a-p (4 months adult)

	<i>hoxa13a</i>	<i>hoxa13b</i>	<i>hoxd13a</i>
<i>hoxa13a</i> -/-	8 bp del. / 29 bp del.		
<i>hoxa13b</i> -/-		4 bp del. / 14 bp ins.	
<i>hoxd13a</i> -/-			5bp ins. / 10 bp ins.
double homo	8 bp del. / 29 bp del.	14 bp ins. / 14 bp ins.	
Triple KO1	0%	25%	50%
Triple KO2	0%	0%	0%

Extended Data Fig.3, 5 (embryo), Extended Data Fig.4q (adults for radial count)

	<i>hoxa13a</i>	<i>hoxa13b</i>	<i>hoxd13a</i>
<i>hoxa13a</i> -/-	4 bp del. / 4 bp del.		
<i>hoxa13b</i> -/-		4 bp del. / 14 bp ins.	
<i>hoxd13a</i> -/-			5bp ins. / 17 bp del.
double homo	8 bp del. / 29 bp del.	14 bp ins. / 14 bp ins.	

Frame-shift mutation alleles that were used for each experiment are listed. The top sequence in each column show wild type with gRNA sequence in red. Green is insertional and blue is substitutional mutations. **a**, *hoxa13a* mutation patterns. Three types of mutations were used in this paper. Horizontal bars are deletional mutations. **b**, *hoxa13b* mutation patterns. Sequences flanked by two gRNAs are abbreviated by black horizontal bars. Additional 1 bp is inserted at 3' side of the gRNA target side in '14 bp insertion'. **c**, *hoxd13a* mutation patterns. Sequences flanked by two gRNAs are abbreviated by black horizontal bars. **d-f**, Mutational patterns in a triple knockout (mosaic for *hoxa13b* and *hoxd13a*) fish that is shown in Fig. 3p-r are listed. Sequence flanked by two gRNAs are abbreviated by horizontal bars in **e** and **f**. Each *hox13* gene shows some different mutations indicating that this fish is highly mosaic. The percentage of mutant alleles was calculated from the result of deep sequencing (Fig. 3 and Extended Data Table 4). **g**, Summary of genotype in all experiments. del. (deletion), ins. (insertion).

Extended Data Table 4 | Genotyping of progeny from mutant crosses

**a**

<i>hoxa13a</i> <sup>+/-</sup> x <i>hoxa13a</i> <sup>+/-</sup>				
	+/+	+/-	-/-	Total
Embryos (72 hpf)	9 (25.0%)	17 (47.2%)	10 (27.8%)	36
Adult	9 (21.4%)	20 (47.6%)	13 (31%)	42

<i>hoxa13b</i> <sup>+/-</sup> x <i>hoxa13b</i> <sup>+/-</sup>				
	+/+	+/-	-/-	Total
Embryos (72 hpf)	8 (25.0%)	20 (62.5%)	12 (37.5%)	32
Adult	20 (32.3%)	32 (51.6%)	10 (16.1%)	62

<i>hoxd13a</i> <sup>+/-</sup> x <i>hoxd13a</i> <sup>+/-</sup>				
	+/+	+/-	-/-	Total
Embryos (72 hpf)	8 (22.9%)	18 (51.4%)	9 (25.7%)	35
Adult	5 (26.3%)	11 (57.9%)	3 (15.8%)	19

**c**

	total adult fish	short finned fish	%
Negative control: <i>Cas9</i> only	96	0	0.00
<i>Cas9</i> , <i>hoxa13b</i> and <i>d13a</i> gRNAs	161	7	4.35

**b**

<i>hoxa13a</i> <sup>+/-</sup> , <i>a13b</i> <sup>+/-</sup> x <i>hoxa13a</i> <sup>+/-</sup> , <i>a13b</i> <sup>+/-</sup> (72hpf)					
<i>a13a</i> \ <i>a13b</i>	+/+	+/-	-/-	Total	
+/+	20 (11.0%)	25 (13.7%)	10 (5.5%)	55 (30.2%)	
+/-	23 (12.6%)	50 (27.5%)	10 (5.5%)	83 (45.6%)	
-/-	6 (3.3%)	28 (15.4%)	10 (5.5%)	44 (24.2%)	
Total	49 (26.9%)	103 (56.6%)	30 (16.5%)	182 (100.0%)	

<i>hoxa13a</i> <sup>+/-</sup> , <i>a13b</i> <sup>+/-</sup> x <i>hoxa13a</i> <sup>+/-</sup> , <i>a13b</i> <sup>+/-</sup> (Adult)					
<i>a13a</i> \ <i>a13b</i>	+/+	+/-	-/-	Total	
+/+	4	8	0	12 (22.2%)	
+/-	4	18	5	27 (50.0%)	
-/-	3	5	7	15 (27.8%)	
Total	11(20.4%)	31(57.4%)	12(22.2%)	54 (100.0%)	

**d**

Genotype of short fin fish (The percent of normal alleles are shown)

	#1	#2	#3	#4	#5	#6	#7
<i>hoxa13a</i>	20%	50%	0%	0%	25%	25%	0%
<i>hoxa13b</i>	20%	0%	25%	0%	0%	0%	0%
<i>hoxd13a</i>	100%	67%	50%	25%	30%	100%	0%

**a**, Breeding data in *hox13* single mutants. Single heterozygous fish were crossed with each other to obtain embryos and next generations. Embryos (72 hpf) or adult fish (3 months) were genotyped by T7E1 assay and sequenced. The number of each genotype and percentages are shown. The ratio of each genotype approximately follows Mendelian ratio. **b**, Breeding data for double *hoxa13* mutants. Double heterozygous fish (*hoxa13a*<sup>+/-</sup>, *hoxa13b*<sup>+/-</sup>) were crossed to obtain embryos and next generations. Embryos (72 hpf) or adult fish (three months) were genotyped by PCR followed by enzyme digestion (Methods) or sequencing. The number of each genotype and percentage are shown. The ratio of each genotype approximately follows Mendelian ratio. **c**, The efficiency of triple knockout (mosaic for *hoxa13a*, *hoxa13b* and *hoxd13a*) in zebrafish (See Methods). The number of normal adult fish and short-finned fish from negative control injection (*Cas9* mRNA without gRNAs) or triple knockout injection (*Cas9* mRNA with gRNAs) are shown. Genotypes for short-finned fish were calculated from deep sequencing of each allele and shown as a percentage of normal alleles in **d**.



# Proteasome inhibition for treatment of leishmaniasis, Chagas disease and sleeping sickness

Shilpi Khare<sup>1\*</sup>, Advait S. Nagle<sup>1\*</sup>, Agnes Biggart<sup>1</sup>, Yin H. Lai<sup>1</sup>, Fang Liang<sup>1</sup>, Lauren C. Davis<sup>1</sup>, S. Whitney Barnes<sup>1</sup>, Casey J. N. Mathison<sup>1</sup>, Elmarie Myburgh<sup>2,3</sup>, Mu-Yun Gao<sup>1</sup>, J. Robert Gillespie<sup>4</sup>, Xianzhong Liu<sup>1</sup>, Jocelyn L. Tan<sup>1</sup>, Monique Stinson<sup>1</sup>, Ianne C. Rivera<sup>1</sup>, Jaime Ballard<sup>1</sup>, Vince Yeh<sup>1</sup>, Todd Groessl<sup>1</sup>, Glenn Federe<sup>1</sup>, Hazel X. Y. Koh<sup>5</sup>, John D. Venable<sup>1</sup>, Badry Bursulaya<sup>1</sup>, Michael Shapiro<sup>1</sup>, Pranab K. Mishra<sup>1</sup>, Glen Spraggon<sup>1</sup>, Ansgar Brock<sup>1</sup>, Jeremy C. Mottram<sup>2,3</sup>, Frederick S. Buckner<sup>4</sup>, Srinivasa P. S. Rao<sup>5</sup>, Ben G. Wen<sup>1</sup>, John R. Walker<sup>1</sup>, Tove Tuntland<sup>1</sup>, Valentina Molteni<sup>1</sup>, Richard J. Glynn<sup>1</sup> & Frantisek Supek<sup>1</sup>

Chagas disease, leishmaniasis and sleeping sickness affect 20 million people worldwide and lead to more than 50,000 deaths annually<sup>1</sup>. The diseases are caused by infection with the kinetoplastid parasites *Trypanosoma cruzi*, *Leishmania* spp. and *Trypanosoma brucei* spp., respectively. These parasites have similar biology and genomic sequence, suggesting that all three diseases could be cured with drugs that modulate the activity of a conserved parasite target<sup>2</sup>. However, no such molecular targets or broad spectrum drugs have been identified to date. Here we describe a selective inhibitor of the kinetoplastid proteasome (GNF6702) with unprecedented *in vivo* efficacy, which cleared parasites from mice in all three models of infection. GNF6702 inhibits the kinetoplastid proteasome through a non-competitive mechanism, does not inhibit the mammalian proteasome or growth of mammalian cells, and is well-tolerated in mice. Our data provide genetic and chemical validation of the parasite proteasome as a promising therapeutic target for treatment of kinetoplastid infections, and underscore the possibility of developing a single class of drugs for these neglected diseases.

Kinetoplastid infections affect predominantly poor communities in Latin America, Asia and Africa. Available therapies suffer from multiple shortcomings, and new drug discovery for these diseases is limited by insufficient investment<sup>3</sup>. We sought low molecular weight compounds with a growth inhibitory effect on *Leishmania donovani*<sup>4,5</sup>, *Trypanosoma cruzi*<sup>6,7</sup> and *Trypanosoma brucei*<sup>5,8</sup>. Our approach was to test 3 million compounds in proliferation assays on all three parasites (Supplementary Information Tables 1–3), followed by triaging of active compounds (half-maximum inhibitory concentration value EC<sub>50</sub> < 10 µM) to select those with a clear window of selectivity (> fivefold)

with respect to growth inhibition of mammalian cells. An azabenzoxazole, GNF5343, was identified as a hit in the *L. donovani* and *T. brucei* screens. Although GNF5343 was not identified in the *T. cruzi* screen, we noted potent anti-*T. cruzi* activity of this compound in secondary assays.

Optimization of GNF5343 involved the design and synthesis of ~3,000 compounds, and focused on improving bioavailability and potency on inhibition of *L. donovani* growth within macrophages (Fig. 1). A critical modification involved replacement of the azabenzoxazole centre with C6-substituted imidazo- and triazolopyrimidine cores, which yielded compounds up to 20-fold more potent on intra-macrophage *L. donovani* (for example, GNF2636). Replacement of the furan group with a dimethylloxazole ring reduced the risk of toxicity associated with the furan moiety, and replacement of the chlorophenyl group with a fluorophenyl improved selectivity over mammalian cell growth inhibition (for example, GNF3849). These changes also resulted in low clearance and acceptable bioavailability. Further substitutions at the core C6 position led to GNF6702 and a 400-fold increase in intra-macrophage *L. donovani* potency compared to GNF5343.

*Leishmania donovani* parasites cause a majority of visceral leishmaniasis (VL) cases in East Africa and India<sup>9</sup>. In mice infected with *L. donovani*<sup>10</sup>, oral dosing with GNF6702 effected a more pronounced reduction in liver parasite burden than miltefosine, the only oral anti-leishmanial drug available in clinical practice<sup>5</sup> (Fig. 2a). The miltefosine regimen for VL efficacy studies was chosen to approximate the drug plasma concentration of the clinical regimen<sup>11</sup>. We noted a greater than three-log reduction in parasite load after

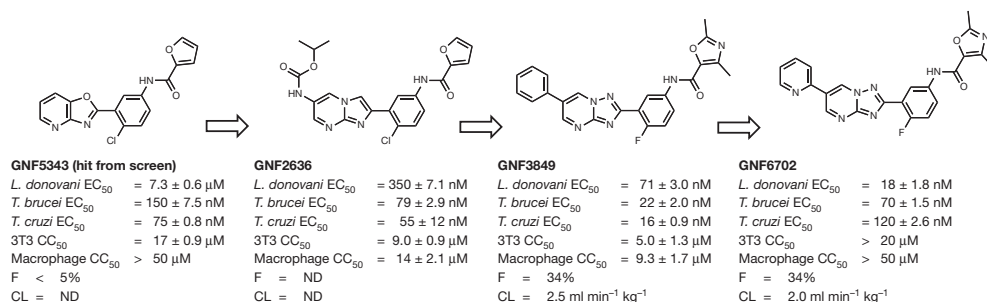


**Figure 1 | Chemical evolution of GNF6702 from the phenotypic hit GNF5343.** *Leishmania donovani*, amastigotes proliferating within primary mouse macrophages; *T. brucei*, the bloodstream form trypomastigotes; *T. cruzi*, amastigotes proliferating in 3T3 fibroblast cells; macrophage, mouse primary peritoneal macrophages; EC<sub>50</sub> and CC<sub>50</sub>, half-maximum

growth-inhibition concentration; F, oral bioavailability in mouse after administering single compound dose (20 mg kg<sup>-1</sup>) as a suspension; CL, plasma clearance in mouse after single i.v. bolus dose (5 mg kg<sup>-1</sup>); ND, not determined; all EC<sub>50</sub> and CC<sub>50</sub> values correspond to means ± s.e.m. (n = 4 technical replicates).

<sup>1</sup>Genomics Institute of the Novartis Research Foundation, 10675 John Jay Hopkins Drive, San Diego, California 92121, USA. <sup>2</sup>Wellcome Trust Centre for Molecular Parasitology, Institute of Infection, Immunity and Inflammation, College of Medical, Veterinary and Life Sciences, University of Glasgow, Glasgow G12 8TA, UK. <sup>3</sup>Centre for Immunology and Infection, Department of Biology, University of York, Wentworth Way, Heslington, York YO10 5DD, UK. <sup>4</sup>Department of Medicine, University of Washington, Seattle, Washington 98109, USA. <sup>5</sup>Novartis Institute for Tropical Diseases, 10 Biopolis Road, Singapore 138670.

\*These authors contributed equally to this work.

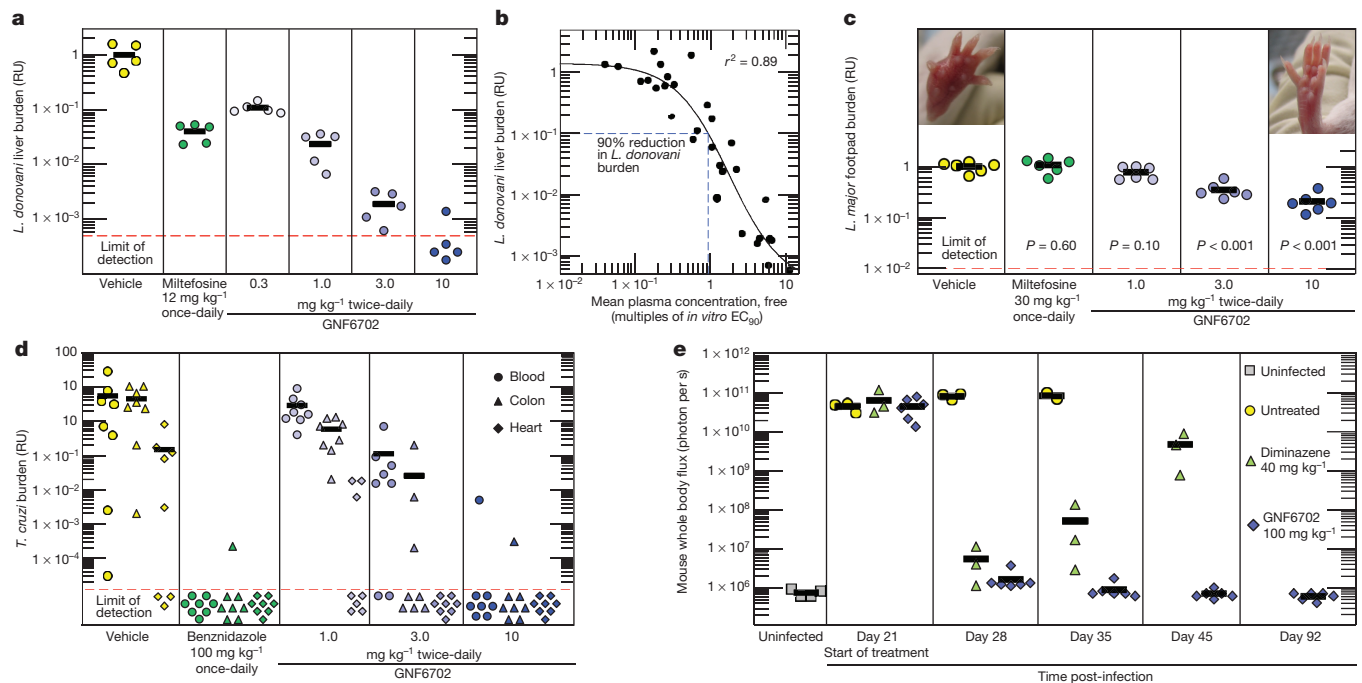


**Figure 2 | GNF6702 clears parasites in mouse models of kinetoplastid infections.** **a**, Post-treatment *L. donovani* liver burdens in mouse model of VL as assessed by qPCR ( $n = 5$  mice). **b**, PK/PD relationship for ten GNF6702 analogues, each administered at several doses; circles, mean liver burdens associated with individual compound regimens (30 regimens in total;  $n = 5$  mice per regimen) relative to vehicle; horizontal dotted line, 90% reduction in the liver *L. donovani* burden; vertical dotted line, 0.94-fold multiple of the mean free compound plasma concentration/ the *L. donovani* EC<sub>90</sub> value ratio. **c**, Post-treatment *L. major* footpad burdens in the BALB/c mouse model of CL as assessed by qPCR ( $n = 6$  mice); the  $P$  values (two-tailed distribution) relate parasite burdens in compound-treated mice with those from vehicle-treated mice; left inset picture, a representative mouse footpad after treatment with vehicle; right inset picture, a representative mouse footpad after treatment with GNF6702 10 mg kg<sup>-1</sup> twice-daily regimen. **d**, *T. cruzi* burden in mouse blood (circles), colon (triangles) and heart (diamonds) as assessed by qPCR after

eight-day treatment with 10 mg kg<sup>-1</sup> of GNF6702 twice-daily with the free concentration of GNF6702 (fraction unbound in plasma = 0.063) staying above the *L. donovani* EC<sub>99</sub> value (the concentration inhibiting 99% of intra-macrophage parasite growth *in vitro*) for the duration of the dosing period (Extended Data Fig. 1a). Characterization of efficacy of ten analogues in the series at various doses revealed a significant correlation ( $r^2 = 0.89$ ,  $P < 0.01$ ) between (i) the ratio of mean free plasma compound concentration to the *L. donovani* EC<sub>90</sub> value and (ii) reduction of the liver parasite burden. We found that 90% parasite burden reduction in the mouse model was achieved when the mean free compound plasma concentration during treatment equalled a 0.94-fold multiple of the *L. donovani* EC<sub>90</sub> value (Fig. 2b).

Cutaneous leishmaniasis (CL) affects about a million people per year, causing skin lesions that can resolve into scar tissue<sup>12</sup>. In parts of the Middle East, CL has reached epidemic proportions<sup>13</sup>. After footpad infection of BALB/c mice with the dermatotropic *L. major* strain<sup>14,15</sup>, treatment with GNF6702 at 10 mg kg<sup>-1</sup> twice-daily caused a fivefold decrease in footpad parasite burden and a reduction in footpad swelling (Fig. 2c). Both 3 mg kg<sup>-1</sup> and 10 mg kg<sup>-1</sup> twice-daily regimens of GNF6702 were superior to 30 mg kg<sup>-1</sup> once-daily miltefosine regimen ( $P < 0.01$ ), which translates into an approximately twofold higher miltefosine plasma concentration in mice than observed in clinical dosing<sup>11</sup>.

We further tested if GNF6702 can cure additional kinetoplastid parasite infections. An estimated 25% of the 8 million people infected with *T. cruzi* will develop chronic Chagas disease, manifesting as

20 days of treatment and four weeks of immunosuppression ( $n = 8$  mice). **e**, Whole-body *in vivo* imaging of bioluminescent *T. brucei* before and after treatment; *T. brucei*-infected mice were treated by a single intraperitoneal injection of diminazene aceturate ( $n = 3$  mice) or by oral administration of GNF6702 once-daily for 7 days ( $n = 6$  mice); filled symbols show whole-body bioluminescence values for individual mice; several mice from the untreated and diminazene aceturate-treated groups were euthanized between days 28 and 56 due to CNS infection symptoms; background bioluminescence values shown for uninfected mice (grey-filled squares;  $n = 4$ ) were collected independently from mice aged-matched for day 0 using the same acquisition settings. Red dotted lines in **a**, **c** and **d** show the limit of parasite detection by qPCR; plot symbols below the red dotted line, mice with no detectable parasites; data points below the limit of detection are 'jittered' to show number of animals in a group; thick horizontal lines, means of the treatment groups; RU, relative units (parasite burden relative to the mean burden of the vehicle-treated group).

cardiac or intestinal dysfunction<sup>16,17</sup>. Benznidazole is broadly used for treatment of acute and indeterminate stages of Chagas disease in Latin America<sup>18,19</sup>. However, benznidazole has side effects that frequently lead to treatment interruption<sup>18,20–22</sup> and a better tolerated drug is needed. To model treatment in the indeterminate disease stage, we infected mice with *T. cruzi* parasites and began treatment 35 days after infection, when the immune system of the mice had controlled parasite burden<sup>23</sup>. We increased the parasite detection sensitivity by immunosuppressing the mice after 20 days of treatment<sup>23,24</sup>. In this model, GNF6702 dosed twice-daily at 10 mg kg<sup>-1</sup> matched the efficacy of benznidazole at 100 mg kg<sup>-1</sup> once-daily; all but one of the treated mice had no detectable parasites in blood, colon or heart tissue, even after 4 weeks of immunosuppression (Fig. 2d).

Finally, we tested GNF6702 in a mouse model of stage II sleeping sickness (human African trypanosomiasis (HAT))<sup>25</sup>. Mortality of stage II HAT is caused by infection of the CNS and, in this mouse model, luciferase-expressing *T. brucei* parasites establish a CNS infection by day 21 post-infection. GNF6702 was administered at 100 mg kg<sup>-1</sup> once-daily to account for low exposure in the brain relative to the plasma (~10%, Extended Data Fig. 1b). Diminazene aceturate, a stage I drug that poorly crosses the blood-brain barrier, effected apparent clearance of parasites from the blood after a single dose, but did not prevent parasite recrudescence 21 days later. By contrast, treatment with GNF6702 for seven days caused a sustained clearance of parasites (days 42 and 92 post-infection in Fig. 2e, Extended Data Fig. 2a, Supplementary Information Tables 4 and 5). Importantly, mice treated

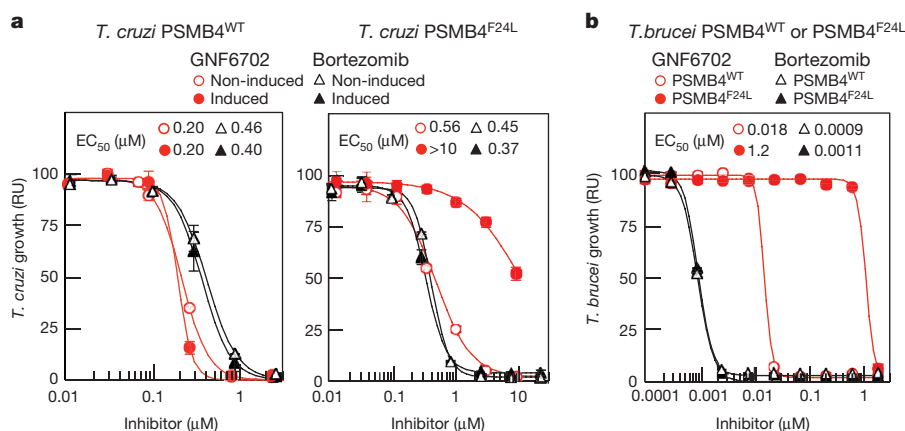


**Figure 3 | F24L mutation in proteasome  $\beta 4$  subunit confers selective resistance to GNF6702.** **a**, Growth inhibition of *T. cruzi* epimastigote strains ectopically expressing wild-type PSMB4 or PSMB4<sup>F24L</sup> protein by GNF6702 and bortezomib; non-induced/induced, culture medium without/with tetracycline to modulate expression of tetracycline-inducible PSMB4 genes. **b**, Growth inhibition of *T. brucei* bloodstream form trypomastigotes constitutively overexpressing wild-type PSMB4 or PSMB4<sup>F24L</sup> protein by GNF6702 and bortezomib. EC<sub>50</sub> values for

each strain/compound pair are listed inside **a** and **b** plot panels next to corresponding strain/compound symbol (defined in plot legends); means from  $n = 3$  technical replicates are shown; error bars represent s.e.m. values; for data points lacking error bars, s.e.m. values are smaller than circles representing means; owing to limited aqueous solubility, the highest tested GNF6702 concentration was 10  $\mu$ M. RU (relative units) in **a** and **b** corresponds to parasite growth relative to the DMSO control (%).

with GNF6702 had no detectable parasites in the brain at termination of the experiment, though parasites were clearly detected in the brains of mice treated with diminazene aceturate (Extended Data Fig. 2b, Supplementary Information Table 6).

As GNF6702 showed compelling efficacy in four mouse models of kinetoplastid infections: VL, CL, Chagas disease and stage II HAT, we reasoned that mechanistic studies of GNF6702 might identify a pan-kinetoplastid drug target that could inform target-based drug discovery efforts. We attempted to evolve *L. donovani* strains resistant to GNF3943 and GNF8000 (early analogues from the series, Extended Data Fig. 3) through 12 months of parasite culture under drug pressure without success. However, we were able to select two drug-resistant *T. cruzi* epimastigote isolates, one resistant to GNF3943, and another to GNF8000. Both *T. cruzi* lines exhibited at least 40-fold lower susceptibility to GNF6702 than wild-type *T. cruzi* (Extended Data Fig. 4a, b). Using whole-genome sequencing, we found that the GNF3943-resistant line had a homozygous mutation encoding a substitution of isoleucine for methionine at amino acid 29 in the proteasome  $\beta 4$  subunit (PSMB4<sup>I29M/I29M</sup>) and a heterozygous mutation P82L in dynein heavy chain gene. The GNF8000-resistant line had a heterozygous F24L mutation in PSMB4, and four other heterozygous mutations (Extended Data Table 1). We focused our attention on the proteasome as a likely target for the compound series because we found two independent mutations in the PSMB4 gene, and because the proteasome is an essential enzyme in eukaryotic cells. We also note that the *Plasmodium falciparum* proteasome has recently been the target of promising drug discovery efforts for malaria<sup>26</sup>.

We first asked whether two prototypic inhibitors of mammalian proteasome, bortezomib and MG132, could also block *T. cruzi* growth. Indeed, both compounds inhibited *T. cruzi* epimastigote proliferation with sub-micromolar potency. However, in contrast to GNF6702, bortezomib and MG132 inhibited proliferation of the two resistant lines (PSMB4<sup>I29M/I29M</sup>, PSMB4<sup>wt/F24L</sup>) with comparable potency to the wild-type parasites. Additionally, the PSMB4 mutant lines were not resistant to nifurtimox, an anti-kinetoplastid drug with an unrelated mechanism of action (Extended Data Fig. 4a, b). To determine whether the F24L mutation was sufficient to confer resistance to GNF6702, we engineered *T. cruzi* epimastigote lines that ectopically expressed either wild-type or F24L-mutated PSMB4. Overexpression of wild-type PSMB4 had little effect on the EC<sub>50</sub> value for GNF6702, whereas overexpression of PSMB4<sup>F24L</sup> caused a greater than tenfold reduction in GNF6702 potency, but not in that of bortezomib (Fig. 3a, Extended Data

Fig. 4c). Previously, bortezomib was also shown to inhibit the growth of *T. brucei*, suggesting that proteasome activity is essential for growth in this parasite as well<sup>27</sup>. To test whether PSMB4<sup>F24L</sup> can rescue growth inhibition by GNF6702 in *T. brucei*, we engineered two parasite strains that ectopically expressed wild-type and F24L-mutated PSMB4, respectively. Similar to *T. cruzi*, overexpression of PSMB4<sup>F24L</sup> in *T. brucei* conferred a high level of resistance to GNF6702 (~70-fold shift in EC<sub>50</sub> value), while having no effect on parasite susceptibility to bortezomib (Fig. 3b, Extended Data Fig. 4c).

We next asked whether GNF6702 could inhibit any of three *T. cruzi* proteasome proteolytic activities in biochemical assays. As predicted from the *T. cruzi* genome<sup>28</sup>, mass spectrometry analysis of purified *T. cruzi* proteasome identified seven alpha and seven beta proteasome subunits, including PSMB4 (Supplementary Tables 7 and 8). Using substrates that are specific for each of the chymotrypsin-like, trypsin-like and caspase-like proteolytic activities, we found that only the chymotrypsin-like activity of the *T. cruzi* proteasome was inhibited by GNF6702 (IC<sub>50</sub> = 35 nM), while the other two activities were not affected (IC<sub>50</sub> > 10  $\mu$ M). In contrast, bortezomib inhibited the chymotrypsin-like (IC<sub>50</sub> = 91 nM), the caspase-like (IC<sub>50</sub> = 370 nM) and the trypsin-like (IC<sub>50</sub> = 1.7  $\mu$ M) activities. We further found that the chymotrypsin-like activity of the PSMB4<sup>I29M</sup> *T. cruzi* proteasome was at least 300-fold less susceptible to GNF6702 (IC<sub>50</sub> > 10  $\mu$ M) and ~3-fold less susceptible to bortezomib (IC<sub>50</sub> = 0.26  $\mu$ M), while susceptibility of the other two mutant proteasome proteolytic activities to the two inhibitors were not affected (Fig. 4a, Extended Data Table 2).

We reasoned that if the primary mechanism of parasite growth inhibition by the compound series was through inhibition of the proteasome chymotrypsin-like activity, then the IC<sub>50</sub> values for this proteolytic activity should correlate with EC<sub>50</sub> values for parasite proliferation. Indeed, a tight correlation between the two parameters was observed for *L. donovani* axenic amastigotes and *T. brucei* bloodstream form trypomastigotes ( $r^2 = 0.78$  and  $r^2 = 0.67$ , respectively) over a 2,000-fold potency range for 317 analogues, thus indicating that inhibition of parasite proteasome activity was driving the anti-parasitic activity of these compounds. We observed a weaker correlation between IC<sub>50</sub> and EC<sub>50</sub> values for intracellular *T. cruzi* ( $r^2 = 0.36$ ,  $P < 0.01$ ), perhaps reflecting more complex cellular pharmacokinetics resulting from compounds having to access *T. cruzi* parasites within the cytosol of mammalian cells (Fig. 4b, Extended Data Fig. 5).

Both resistant *T. cruzi* lines retained sensitivity to bortezomib, which is a substrate-competitive inhibitor, suggesting that GNF6702 might



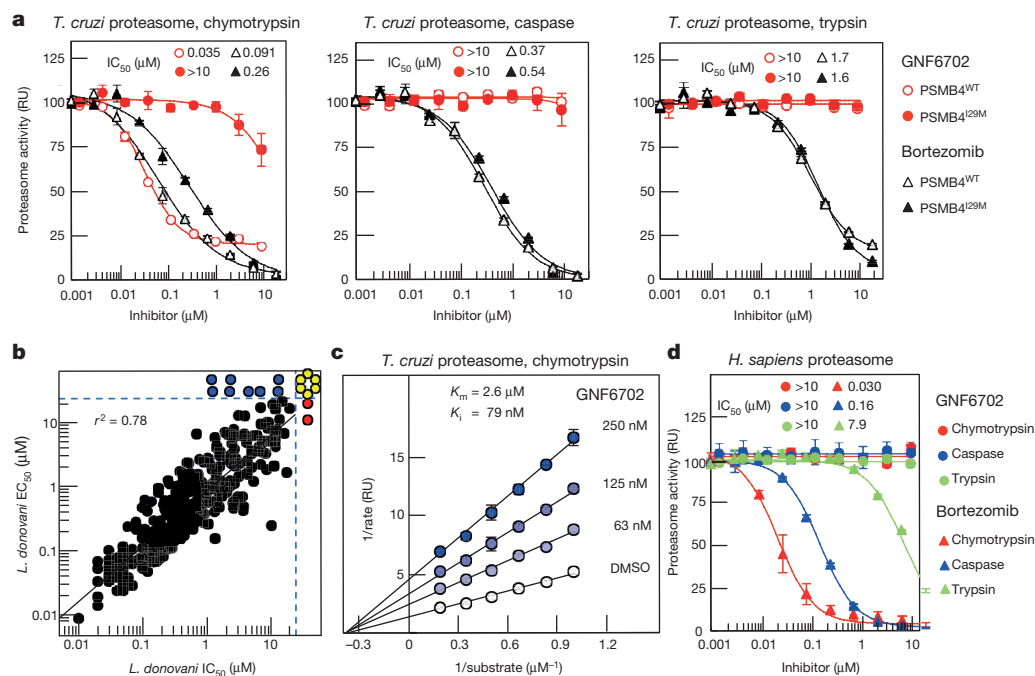


**Figure 4 | Compounds from GNF6702 series inhibit growth of kinetoplastid parasites by inhibiting parasite proteasome chymotrypsin-like activity.** **a**, Inhibition of three proteolytic activities of purified wild-type (PSMB4<sup>WT</sup>) and PSMB4<sup>I29M</sup> *T. cruzi* proteasomes by GNF6702 and bortezomib; IC<sub>50</sub> values for proteasome proteolytic activities are listed inside plots. **b**, Correlation between inhibition of chymotrypsin-like activity of purified *L. donovani* proteasome (IC<sub>50</sub>) and *L. donovani* axenic amastigote growth inhibition (EC<sub>50</sub>; data points correspond to means of 2 technical replicates); red circles, IC<sub>50</sub> > 20 μM; blue circles, EC<sub>50</sub> > 25 μM; yellow circles, IC<sub>50</sub> > 20 μM

have an alternative mode of inhibition. A Lineweaver–Burk plot of chymotrypsin-like activity at increasing concentrations of peptide substrate showed that GNF6702 has a non-competitive mode of inhibition clearly distinct from the competitive mechanism described for MG132 and bortezomib<sup>29,30</sup>. We were also able to extend these observations to proteasome from *L. donovani* (Fig. 4c, Extended Data Table 3). We further note that GNF6702 had no measurable activity on the human proteasome (Fig. 4d, Extended Data Table 2). Interestingly, human proteasome β4 subunit has a methionine at the 29th amino acid position, mirroring the I29M mutation in the GNF3943-resistant *T. cruzi* line (Extended Data Fig. 6a).

In summary, GNF6702 blocks the chymotrypsin-like activity harboured by the β5 subunit without competing with substrate binding, and mutations in the β4 subunit, which is in direct physical contact with the β5 subunit, confer resistance to this inhibition. Next we used homology modelling of the *T. cruzi* proteasome to look for evidence of an allosteric inhibitor binding site. In the *T. cruzi* proteasome model, the F24 and I29 β4 residues are positioned at the interface between the β4 and β5 subunits, on the outer limit of the β5 active site. Adjacent to these two β4 residues and the β5 active site is a plausible binding pocket for GNF6702 (Extended Data Fig. 6b, c).

Finally, we tested whether GNF6702 can inhibit proteasome activity in intact *T. cruzi* cells. Cellular proteins entering the proteasome degradation pathway are first tagged with ubiquitin, and proteasome inhibition results in intracellular accumulation of ubiquitylated proteins. Treatment of *T. cruzi* epimastigotes with GNF6702 led to substantial build-up of ubiquitylated proteins (Extended Data Fig. 7a) with the half-maximal effect (EC<sub>50</sub>) achieved at 130 nM compound concentration (Extended Data Fig. 7c). This EC<sub>50</sub> value correlated well with the half-maximal growth inhibitory concentration of GNF6702 on *T. cruzi* epimastigotes (EC<sub>50</sub> = 150 nM; Extended Data Fig. 4b). For comparison, similar experiments with bortezomib yielded comparable inhibitor

and EC<sub>50</sub> > 25 μM; data for 317 analogues are shown. **c**, Lineweaver–Burk plot of inhibition of *T. cruzi* proteasome chymotrypsin-like activity by GNF6702 at increasing concentrations of a peptide substrate. **d**, Effect of GNF6702 and bortezomib on three proteolytic activities of human constitutive proteasome; IC<sub>50</sub> values for proteasome proteolytic activities are listed inside plots. Data shown in **a**, **c** and **d** represent means ± s.e.m. ( $n = 3$  technical replicates; for data points lacking error bars, s.e.m. values are smaller than circles representing means). Owing to limited aqueous solubility, the highest tested GNF6702 concentration in experiments shown in **a** and **d** was 10 μM.

potencies in the two *T. cruzi* assays (ubiquitylation EC<sub>50</sub> = 62 nM versus growth inhibition EC<sub>50</sub> = 160 nM; Extended Data Figs 4b and 7c). We did not observe any detectable accumulation of ubiquitylated proteins in mammalian 3T3 cells treated with GNF6702 (Extended Data Fig. 7b, c), further confirming the high selectivity of this compound.

Validation of the parasite proteasome as the target of GNF6702 is supported through several lines of evidence: (i) point mutations in the PSMB4 gene are sufficient to confer resistance to biochemical proteasome inhibition and cellular *T. cruzi* growth inhibition; (ii) GNF6702 is a selective inhibitor of parasite proteasome activity and does not inhibit the human proteasome, mirroring the selective inhibition of parasite growth over mammalian cell growth; and (iii) potency of GNF6702 and analogues in parasite proteasome assays predict potency in parasite growth-inhibition assays.

In this work we show that in mouse disease models, GNF6702 was able to eradicate parasites from diverse niches that included the cytosol (*T. cruzi*), phagolysosome (*L. donovani*, *L. major*) of infected host cells, and brain (*T. brucei*). GNF6702 has also good pharmacokinetic properties, and the compound did not show activity in panels of human receptor, enzyme and ion channel assays (Supplementary Tables 9–11). Going forward, GNF6702, or analogues thereof, has potential to yield a new treatment for several kinetoplastid infections and it is currently being evaluated in preclinical toxicity studies. It is unclear if the clinical utility of GNF6702 could extend to the treatment of stage II HAT as GNF6702 was tested in the HAT mouse model only at one high dose (100 mg kg<sup>−1</sup> once-daily). We also note that identification of a broadly active pan-kinetoplastid drug might not be feasible (or desirable) as such a drug would need to reach high concentrations in varied tissues/subcellular compartments, and might carry increased toxicity risk. Instead, alternative analogues from this series with different pharmacological profiles might be needed for treatment of different kinetoplastid infections. Nevertheless, there are only scarce

resources for drug development in these diseases, and identification of a common target and chemical scaffold with potential across multiple indications provides new hope for improved treatment options for some of the world's poorest people.

**Online Content** Methods, along with any additional Extended Data display items and Source Data, are available in the online version of the paper; references unique to these sections appear only in the online paper.

**Received 23 December 2015; accepted 1 August 2016.**

**Published online 8 August 2016.**

- Research priorities for Chagas disease, human African trypanosomiasis and leishmaniasis. *World Health Organization, WHO Technical Report Series* 975, 1–100 (2012).
- El-Sayed, N. M. *et al.* Comparative genomics of trypanosomatid parasitic protozoa. *Science* **309**, 404–409 (2005).
- Bilbe, G. Infectious diseases. Overcoming neglect of kinetoplastid diseases. *Science* **348**, 974–976 (2015).
- Sundar, S. & Chakravarty, J. An update on pharmacotherapy for leishmaniasis. *Expert Opin. Pharmacother.* **16**, 237–252 (2015).
- Nagle, A. S. *et al.* Recent developments in drug discovery for leishmaniasis and human African trypanosomiasis. *Chem. Rev.* (2014).
- Bern, C. Chagas' Disease. *N. Engl. J. Med.* **373**, 456–466 (2015).
- Chatelain, E. Chagas disease drug discovery: toward a new era. *J. Biomol. Screen.* **20**, 22–35 (2015).
- Kennedy, P. G. Clinical features, diagnosis, and treatment of human African trypanosomiasis (sleeping sickness). *Lancet Neurol.* **12**, 186–194 (2013).
- Control of the leishmaniasis. *World Health Organization, WHO Technical Report Series* 949, 37–39 (2010).
- Yardley, V. & Croft, S. L. A comparison of the activities of three amphotericin B lipid formulations against experimental visceral and cutaneous leishmaniasis. *Int. J. Antimicrob. Agents* **13**, 243–248 (2000).
- Dorlo, T. P. *et al.* Pharmacokinetics of miltefosine in Old World cutaneous leishmaniasis patients. *Antimicrob. Agents Chemother.* **52**, 2855–2860 (2008).
- McGwire, B. S. & Satoskar, A. R. Leishmaniasis: clinical syndromes and treatment. *QJM* **107**, 7–14, (2014).
- Hotez, P. J. Combating the next lethal epidemic. *Science* **348**, 296–297 (2015).
- Sacks, D. & Anderson, C. Re-examination of the immunosuppressive mechanisms mediating non-cure of *Leishmania* infection in mice. *Immunol. Rev.* **201**, 225–238 (2004).
- Nelson, K. G., Bishop, J. V., Ryan, R. O. & Titus, R. Nanodisk-associated amphotericin B clears *Leishmania major* cutaneous infection in susceptible BALB/c mice. *Antimicrob. Agents Chemother.* **50**, 1238–1244 (2006).
- Nunes, M. C. *et al.* Chagas disease: an overview of clinical and epidemiological aspects. *J. Am. Coll. Cardiol.* **62**, 767–776 (2013).
- Coura, J. R. & Borges-Pereira, J. Chagas disease: 100 years after its discovery. A systemic review. *Acta Trop.* **115**, 5–13 (2010).
- Bern, C. Antitrypanosomal therapy for chronic Chagas' disease. *N. Engl. J. Med.* **364**, 2527–2534 (2011).
- Viotti, R. *et al.* Towards a paradigm shift in the treatment of chronic Chagas disease. *Antimicrob. Agents Chemother.* **58**, 635–639 (2014).
- Molina, I. *et al.* Randomized trial of posaconazole and benznidazole for chronic Chagas' disease. *N. Engl. J. Med.* **370**, 1899–1908 (2014).
- Morillo, C. A. *et al.* Randomized trial of benznidazole for chronic Chagas' cardiomyopathy. *N. Engl. J. Med.* **373**, 1295–1306 (2015).
- Viotti, R. *et al.* Side effects of benznidazole as treatment in chronic Chagas disease: fears and realities. *Expert Rev. Anti Infect. Ther.* **7**, 157–163 (2009).
- Khare, S. *et al.* Antitrypanosomal treatment with benznidazole is superior to posaconazole regimens in mouse models of Chagas disease. *Antimicrob. Agents Chemother.* **59**, 6385–6394 (2015).
- Bustamante, J. M., Bixby, L. M. & Tarleton, R. L. Drug-induced cure drives conversion to a stable and protective CD8<sup>+</sup> T central memory response in chronic Chagas disease. *Nature Med.* **14**, 542–550 (2008).
- Myburgh, E. *et al.* *In vivo* imaging of trypanosome-brain interactions and development of a rapid screening test for drugs against CNS stage trypanosomiasis. *PLoS Negl. Trop. Dis.* **7**, e2384 (2013).
- Li, H. *et al.* Structure- and function-based design of *Plasmodium*-selective proteasome inhibitors. *Nature* **530**, 233–236 (2016).
- Steverding, D. & Wang, X. Trypanocidal activity of the proteasome inhibitor and anti-cancer drug bortezomib. *Parasites & Vectors* **2**, 29 (2009).
- Ivens, A. C. *et al.* The genome of the kinetoplastid parasite, *Leishmania major*. *Science* **309**, 436–442 (2005).
- Li, X. *et al.* Effect of noncompetitive proteasome inhibition on bortezomib resistance. *J. Natl. Cancer Inst.* **102**, 1069–1082 (2010).
- Fernandez, Y. *et al.* Chemical blockage of the proteasome inhibitory function of bortezomib: impact on tumor cell death. *J. Biol. Chem.* **281**, 1107–1118 (2006).

**Supplementary Information** is available in the online version of the paper.

**Acknowledgements** This work was supported in part by grants from the Wellcome Trust (091038/Z/09/Z to R.J.G. and F.S., and 104976/Z/14/Z, 104111/15/Z to J.C.M. and E.M.) and NIH (A106850 to F.S.B.). We thank S. Croft, R. Don, L. Gredsted, A. Hudson and J. Mendlein for discussions, R. Tarleton for *T. cruzi* CL strain, and G. Cross for *T. brucei* Lister 427 strain. We thank A. Kreusch for help with proteasome purification, and F. Luna for help with *T. cruzi* whole-genome sequencing. We acknowledge technical assistance of O. Faghih in generating the plasmids for ectopic expression of PSMB4 in *T. cruzi*, R. Ritchie for IVIS *in vivo* imaging, and A. Mak, J. Matzen and P. Anderson for execution of high-throughput screens. We thank J. Isbell and T. Hollenbeck for profiling GNF6702 in ADME assays.

**Author Contributions** A.B., F.L., C.J.N.M., P.K.M., A.S.N., J.L.T. and V.Y. designed chemical analogues, and performed chemical synthesis and purification of synthesized analogues. F.S.B., J.B., J.R.G., S.K., H.X.Y.K., Y.H.L., S.P.S.R., F.S. and X.L. conducted and analysed data from *in vitro* growth-inhibition assays. L.C.D., X.L., J.C.M., E.M., I.C.R., S.P.S.R., M.S., F.S. and B.G.W. conducted and analysed data from *in vivo* efficacy assays. J.B., M.-Y.G., S.K. and F.S. conducted proteasome purification, proteasome inhibition assays and biochemical data analysis. S.W.B., G.F., S.K., F.S. and J.R.W. designed, conducted and analysed experiments resulting in identification of proteasome resistance mutations. G.S. and B.B. built the homology model of *T. cruzi* proteasome structure and performed GNF6702 docking. A.B. and J.D.V. analysed *T. cruzi* proteasome by mass spectrometry. A.N., T.G., M.S., F.S. and T.T. designed, conducted, and analysed PK data. A.N. and V.M. led the chemistry team. F.S. led the biology team. R.J.G. and F.S. supervised and led the overall project, and led the writing of the manuscript. All authors contributed to writing of the manuscript.

**Author Information** Reprints and permissions information is available at [www.nature.com/reprints](http://www.nature.com/reprints). The authors declare competing financial interests: details are available in the online version of the paper. Readers are welcome to comment on the online version of the paper. Correspondence and requests for materials should be addressed to F.S. ([fsupek@gnf.org](mailto:fsupek@gnf.org)).

**Reviewer Information** *Nature* thanks M. Phillips, S. Schreiber and the other anonymous reviewer(s) for their contribution to the peer review of this work.

## METHODS

No statistical methods were used to predetermine sample size.

**Ethics statement for animal models.** All procedures involving mice were performed in accordance with AAALAC standards or under UK Home Office regulations, and were reviewed and approved in accordance with the Novartis Animal Welfare Policy. Sample size was determined on the basis of the minimum number of animals required for good data distribution and statistics. Blinding was not possible in these experiments but animals were selected randomly for each group.

**Determination of IC<sub>50</sub>, EC<sub>50</sub>, and CC<sub>50</sub> values.** Reported IC<sub>50</sub>/EC<sub>50</sub>/CC<sub>50</sub> values were calculated by averaging IC<sub>50</sub>/EC<sub>50</sub>/CC<sub>50</sub> values obtained from individual technical replicate experiments (*n*; specified in relevant Figure captions and Methods sub-sections). Each technical replicate experiment was performed on a different day with freshly prepared reagents. Reported standard errors of mean (s.e.m.) were calculated using IC<sub>50</sub>/EC<sub>50</sub>/CC<sub>50</sub> values determined in individual technical replicate experiments. To calculate IC<sub>50</sub>/EC<sub>50</sub>/CC<sub>50</sub> values, measured dose response values were fitted with 4-parameter logistic function  $y = \frac{A + (B - A)}{1 + (\frac{x}{C})^D}$

(model 201, XLfit, IDBS), where *x* refers to compound concentration and *y* corresponds to an assay readout value.

**Leishmania donovani axenic amastigote growth-inhibition assay.** RPMI-1640 medium (HyClone) was supplemented with 20% heat-inactivated fetal bovine serum (Omega Scientific), 23 μM folic acid (Sigma-Aldrich), 100 μM adenosine (Sigma-Aldrich), 22 mM D-glucose (Sigma-Aldrich), 4 mM L-glutamine (Hyclone), 25 mM 2-(4-morpholino) ethanesulfonic acid (Sigma-Aldrich) and 100 IU penicillin/100 μg/ml streptomycin (HyClone), and adjusted to pH = 5.5 with 6 M hydrochloric acid (Fisher Scientific) at 37 °C. *Leishmania donovani* MHOM/SD/62/1 S-CL2D axenic amastigotes were cultured in 10 ml of this medium (Axenic Amastigote Medium) in T75 CELL-STAR flasks (Greiner Bio-One) at 37 °C/5% CO<sub>2</sub> and passaged once a week.

To determine compound growth inhibitory potency on *L. donovani* axenic amastigotes, 100 nl of serially diluted compounds in DMSO were transferred to the wells of white, solid bottom 384-well plates (Greiner Bio-One) by Echo 555 acoustic liquid handling system (Labcyte). Then,  $1 \times 10^3$  of *L. donovani* axenic amastigotes in 40 μl of Axenic Amastigote Medium were added to each well, and plates were incubated for 48 h at 37 °C/5% CO<sub>2</sub>. Parasite numbers in individual plate wells were determined through quantification of intracellular ATP. The CellTiter-Glo luminescent cell viability reagent (Promega) was added to plate wells, and ATP-dependent luminescence signal was measured on an EnVision MultiLabel Plate Reader (Perkin Elmer). Luminescence values in wells with compounds were divided by the average luminescence value of the plate DMSO controls, and used for calculation of compound EC<sub>50</sub> values as described above.

Axenic amastigote EC<sub>50</sub> values shown in Fig. 4b correspond to means of 2 technical replicates.

**Isolation and maintenance of Leishmania donovani splenic amastigotes.** Female BALB/c mice (Envigo) infected with *L. donovani* MHOM/ET/67/HU3 (ATCC) for 50–80 days were euthanized, and infected spleens were removed and weighed. The weight of an infected spleen ranged from 300 to 600 mg. For comparison, spleens from non-infected age-matched BALB/c mice weighed ~100 mg. Infected spleens were washed in Axenic Amastigote Medium (composition described above) and placed into Falcon 50 ml conical centrifuge tubes (Fisher Scientific) containing ice-cold Axenic Amastigote Medium (15 ml per infected spleen). Spleens were homogenized on ice in a Dounce homogenizer and centrifuged at 200g for 15 min at 4 °C to remove tissue debris. *Leishmania donovani* amastigotes present in the supernatant were pelleted by centrifugation at 1,750g for 15 min at 4 °C and re-suspended either in Axenic Amastigote Medium (when used for *in vitro* macrophage infections) or in Hanks' Balanced Salt Solution (when used for mouse infections; Hyclone). Suspensions of splenic amastigotes were kept on ice and used for *in vitro* or *in vivo* infections within 2–3 h. To propagate *L. donovani* amastigotes *in vivo*, 6–7-week-old female BALB/c mice were infected with  $8 \times 10^7$  purified splenic amastigotes in 200 μl of Hanks' Balanced Salt Solution by tail vein injection.

**Leishmania donovani intra-macrophage amastigote growth-inhibition assay.** *In vitro* compound potencies on intra-macrophage *L. donovani* MHOM/ET/67/HU3 were determined using primary murine peritoneal macrophages infected with *L. donovani* splenic amastigotes. Primary macrophages were elicited in female BALB/c mice for 72 h following the injection of 500 μl of sterile aqueous 2% starch (J. T. Baker) solution into the mouse peritoneal cavity. The protocol used for isolation of peritoneal macrophages was described in detail previously<sup>31</sup>. The isolated macrophages were re-suspended in Macrophage Infection Medium (RPMI-1640 medium supplemented with 2 mM L-glutamine, 10% heat-inactivated fetal bovine serum, 10 mM sodium pyruvate (Hyclone), and 100 IU penicillin/100 μg/ml streptomycin), and 50 μl of macrophage suspension ( $4 \times 10^5$  macrophages/ml) were

added to microscopy-grade, clear-bottom, black 384-well plates (Greiner Bio-One). Following overnight incubation at 37 °C/5% CO<sub>2</sub>, plate wells were washed with Macrophage Infection Medium to remove non-adherent cells using ELx405 Select microplate washer (BioTek), and then filled with 40 μl of Macrophage Infection Medium. *Leishmania donovani* HU3 splenic amastigotes isolated from infected spleens were re-suspended in Macrophage Infection Medium at a concentration of  $6 \times 10^7$  cells/ml, and 10 μl of the suspension were added to assay plate wells containing adherent macrophages. After a 24-h infection period at 37 °C/5% CO<sub>2</sub>, plate wells were washed with Macrophage Infection Medium to remove residual extracellular parasites and re-filled with 50 μl of the medium. *Leishmania donovani*-infected macrophages were subsequently treated with DMSO-dissolved compounds (0.5% final DMSO concentration in the assay medium) in dose response for 120 h at 37 °C/5% CO<sub>2</sub>. Next, treated macrophages were washed with the phosphate-buffered saline buffer (PBS; Sigma-Aldrich) supplemented with 0.5 mM magnesium chloride (Sigma-Aldrich) and 0.5 mM calcium chloride (Sigma-Aldrich), fixed with 0.4% paraformaldehyde (Sigma-Aldrich) in PBS, permeabilized with 0.1% Triton X-100 (Sigma-Aldrich) in PBS, and stained with SYBR Green I nucleic acid stain (Invitrogen, 1:100,000 dilution in PBS) overnight at 4 °C. Image collection and enumeration of macrophage cells and intracellular *L. donovani* amastigotes was performed using the OPERA QEHS automated confocal microscope system equipped with 20× water immersion objective (Evotec Technologies) and the OPERA Acapella software (Evotec Technologies) as described previously<sup>32</sup>.

All reported intra-macrophage *L. donovani* EC<sub>50</sub> values were calculated from at least 3 technical replicates (*n* = 3 or *n* = 4; specified in relevant figure captions).

**Trypanosoma brucei growth inhibition assay.** Bloodstream form *Trypanosoma brucei* Lister 427 parasites were continuously passaged in HMI-9 medium formulated from IMDM medium (Invitrogen), 10% heat-inactivated fetal bovine serum, 10% Serum Plus medium supplement (SAFC Biosciences), 1 mM hypoxanthine (Sigma-Aldrich), 50 μM bathocuproine disulfonic acid (Sigma-Aldrich), 1.5 mM cysteine (Sigma-Aldrich), 1 mM pyruvic acid (Sigma-Aldrich), 39 μg/ml thymidine (Sigma-Aldrich), and 14 μl/β-mercapthoethanol (Sigma-Aldrich); all concentrations of added components refer to those in complete HMI-9 medium. The parasites were cultured in 10 ml of HMI-9 medium in T75 CELL-STAR tissue culture flasks at 37 °C/5% CO<sub>2</sub>.

To determine compound growth inhibitory potency on *T. brucei* bloodstream form parasites, 100 nl of serially diluted compounds in DMSO were transferred to the wells of white, solid bottom 384-well plates (Greiner Bio-One) by Echo 555 acoustic liquid handling system. Then,  $5 \times 10^3$  of *T. brucei* parasites in 40 μl of HMI-9 medium were added to each well, and the plates were incubated for 48 h at 37 °C/5% CO<sub>2</sub>. Parasite numbers in individual plate wells were determined through quantification of intracellular ATP amount. The CellTiter-Glo luminescent cell viability reagent was added to plate wells, and ATP-dependent luminescence signal was measured on an EnVision MultiLabel Plate Reader. Luminescence values in wells with compounds were divided by the average luminescence value of the plate DMSO controls, and used for calculation of compound EC<sub>50</sub> values as described above.

*Trypanosoma brucei* EC<sub>50</sub> values shown in Fig. 1 and Extended Data Fig. 3 correspond to means of 4 technical replicates.

**Trypanosoma cruzi amastigote growth-inhibition assay.** NIH 3T3 fibroblast cells (ATCC) were maintained in RPMI-1640 medium (Life Technologies) supplemented with 10% heat-inactivated fetal bovine serum and 100 IU penicillin/100 μg/ml streptomycin at 37 °C/5% CO<sub>2</sub>. *Trypanosoma cruzi* Tulahuen parasites constitutively expressing *Escherichia coli* β-galactosidase<sup>33</sup> were maintained in tissue culture as an infection in NIH 3T3 fibroblast cells. Briefly,  $2 \times 10^7$  *T. cruzi* trypomastigotes were used to infect  $6 \times 10^5$  NIH 3T3 cells growing in T75 CELL-STAR tissue culture flasks and cultured at 37 °C/5% CO<sub>2</sub> until proliferating intracellular parasites lysed host 3T3 cells and were released into the culture medium (typically 6–7 days). During the infection, the tissue culture medium was changed every two days. Number of *T. cruzi* trypomastigotes present in 1 ml of medium was determined using a haemocytometer.

To determine compound potency on intracellular *T. cruzi* amastigotes, NIH 3T3 cells were re-suspended in phenol red-free RPMI-1640 medium containing 3% heat-inactivated fetal bovine serum and 100 IU penicillin/100 μg/ml streptomycin, seeded at 1,000 cells/well (40 μl) in white, clear bottom 384-well plates (Greiner Bio-One), and incubated overnight at 37 °C/5% CO<sub>2</sub>. The following day, 100 nl of each compound in DMSO were transferred to individual plate wells by Echo 555 acoustic liquid handling system. After one hour incubation,  $1 \times 10^6$  of tissue culture-derived *T. cruzi* trypomastigotes, in 10 μl of phenol red-free RPMI-1640 medium supplemented with 3% heat-inactivated fetal bovine serum and 100 IU penicillin/100 μg/ml streptomycin were added to each well. Plates were then incubated for 6 days at 37 °C/5% CO<sub>2</sub>. Intracellular *T. cruzi* parasites were quantified



by measuring the activity of parasite-expressed  $\beta$ -galactosidase. Ten microlitres of a chromogenic  $\beta$ -galactosidase substrate solution (0.6 mM chlorophenol red- $\beta$ -D-galactopyranoside/0.6% NP-40 in PBS; both reagents from Calbiochem) were added to each well and incubated for 2 h at room temperature. After incubation, absorption was measured at 570 nm on SpectraMax M2 plate reader (Molecular Devices). Measured absorbance values in wells with compounds were divided by the average absorbance value of the plate DMSO controls, and used for calculation of compound EC<sub>50</sub> values as described above.

*Trypanosoma cruzi* amastigote EC<sub>50</sub> values shown in Fig. 1 and Extended Data Fig. 3 correspond to means of 4 technical replicates.

***Trypanosoma cruzi* epimastigote proliferation assay.** *Trypanosoma cruzi* CL epimastigotes were continuously passaged in LIT medium containing 9 g/l liver infusion broth (Difco), 5 g/l bacto tryptose (Difco), 1 g/l sodium chloride, 8 g/l dibasic sodium phosphate (Sigma-Aldrich), 0.4 g/l potassium chloride (Sigma-Aldrich), 1 g/l D-glucose, 10% heat-inactivated fetal bovine serum and 10 ng/ml of hemin (Sigma-Aldrich). The medium was adjusted to pH = 7.2 with 6 M hydrochloric acid. The parasites were cultured in 10 ml of LIT medium in T75 CELL-STAR tissue culture flasks at 27 °C.

To determine compound growth inhibitory potency on *T. cruzi* epimastigotes, 100 nl of serially diluted compounds in DMSO were transferred to the wells of white, solid bottom 384-well plates (Greiner Bio-One) by an Echo 555 acoustic liquid handling system. Then,  $5 \times 10^3$  of *T. cruzi* epimastigotes in 40  $\mu$ l of LIT medium were added to each well, and the plates were incubated for 7 days at 27 °C. Parasite numbers in individual plate wells were determined through quantification of intracellular ATP amount. The CellTiter-Glo luminescent cell viability reagent was added to plate wells, and ATP-dependent luminescence signal was measured on an EnVision MultiLabel Plate Reader. Luminescence values in wells with compounds were divided by the average luminescence value of the plate DMSO controls, and used for calculation of compound EC<sub>50</sub> values as described above.

*Trypanosoma cruzi* epimastigote EC<sub>50</sub> values shown in Extended Data Fig. 4 correspond to means of 3 technical replicates.

**Mouse fibroblast NIH 3T3 growth-inhibition assay.** NIH 3T3 fibroblast cells were maintained in RPMI-1640 medium with glutamine (Life Technologies) supplemented with 5% heat-inactivated fetal bovine serum and 100 IU penicillin/100  $\mu$ g/ml streptomycin (3T3 medium) at 37 °C/5% CO<sub>2</sub>. NIH 3T3 fibroblast cells were purchased from ATCC. We did not perform cell line authentication and did not test the cells for mycoplasma contamination. This cell line is not listed in the database of commonly misidentified cell lines maintained by ICLAC and NCBI Biosample.

To determine compound potency, NIH 3T3 cells re-suspended in 3T3 medium were seeded at 1,000 cells/well (50  $\mu$ l) in white 384-well plates (Greiner Bio-One) and incubated overnight at 37 °C/5% CO<sub>2</sub>. The following day, 100 nl of each compound in DMSO were transferred to individual plate wells by Echo 555 acoustic liquid handling system and plates were incubated for five days at 37 °C/5% CO<sub>2</sub>. Cell numbers in individual plate wells were determined through quantification of intracellular ATP amount. The CellTiter-Glo luminescent cell viability reagent was added to plate wells, and ATP-dependent luminescence signal was measured on an EnVision MultiLabel Plate Reader. Luminescence values in wells with compounds were divided by the average luminescence value of the plate DMSO controls, and used for calculation of compound CC<sub>50</sub> values as described above.

NIH 3T3 CC<sub>50</sub> values shown in Fig. 1 and Extended Data Fig. 3 correspond to means of 4 technical replicates.

**Primary macrophage cytotoxicity assay.** Primary macrophage cell viability was determined on mouse peritoneal macrophages infected with *L. donovani* and was expressed as the ratio of the number of macrophage cells in wells treated with a compound to those in wells treated with DMSO. The number of macrophage cells in wells was determined by high content microscopy as described previously<sup>32</sup>.

All reported macrophage CC<sub>50</sub> values were calculated from 4 technical replicates ( $n = 4$ ; also specified in Fig. 1 and Extended Data Fig. 3 captions).

**Selection of GNF3943- and GNF8000-resistant *T. cruzi* mutants.** *Trypanosoma cruzi* epimastigotes cultures resistant to GNF3943 and GNF8000 were generated using a methodology described previously<sup>32</sup>. Briefly, epimastigotes were initially cultured in the presence of compound concentration equivalent to its EC<sub>20</sub> value (GNF3943 EC<sub>20</sub> = 1.5  $\mu$ M and GNF8000 EC<sub>20</sub> = 0.2  $\mu$ M in 0.2% DMSO) or 0.2% DMSO (control). Once a week, parasites were counted and growth rates were determined. If the parasite cultures exhibited a reduced growth rate compared to 0.2% DMSO-treated parasites, epimastigotes were cultured at the same compound concentration. Once the growth rates matched that of the control epimastigote culture (0.2% DMSO), parasites were transferred into medium containing twofold higher compound concentration. The process was repeated until substantial resistance was achieved (~10- to 20-fold increase in corresponding EC<sub>50</sub> value).

The time required for generation of cultures with such a level of resistance was approximately five months. Resistant clones were isolated by cloning by limiting dilution, and two independent clones were analysed by whole-genome sequencing.

***T. cruzi* whole-genome sequencing.** Chromosomal DNA isolation from GNF3943- and GNF8000-resistant *T. cruzi* clones, whole-genome sequencing and sequence analysis were performed as described previously<sup>32</sup>. Sequencing reads were aligned to the *T. cruzi* CL Brenner genome<sup>34</sup>.

**Generation of *T. cruzi* strains ectopically expressing proteasome  $\beta 4$  subunit variants.** *PSMB4* TcCLB503891.100 was amplified from *T. cruzi* CL Brenner genomic DNA using KOD Hot Start DNA Polymerase (EMD Millipore), and sense (5'-AAAGCGGCCGCATGTCGGAGACAACCATG-3') and antisense (5'-CCATGATCTTGATGTAATATAAGGCATTCAGCCCTGCTG-3') primers. The *PSMB4*<sup>F24L</sup> gene was generated from the wild-type *PSMB4* construct by site-directed mutagenesis using mutagenic sense (5'-CAGCAGGGCTGAATGCCTTATATTACATCAAGATCATGG-3') and antisense (5'-CCATGATCTTGATGTAATATAAGGCATTCAGCCCTGCTG-3') primers and QuikChange II Site-Directed Mutagenesis Kit (Stratagene). The sequences of the wild-type and mutant *PSMB4* genes were verified by sequencing and both gene versions were subcloned into the *T. cruzi* expression vector pTcIndex1 under control of a T7 promoter<sup>35</sup>. *Trypanosoma cruzi* CL Brenner epimastigotes were first transfected as described previously<sup>36</sup> with the pLEW13 plasmid<sup>37</sup> harbouring a tetracycline-inducible T7 RNA polymerase gene. Transfected epimastigotes were selected in medium supplemented with neomycin (G418) at 500  $\mu$ g/ml, and then transfected a second time with either pTcIndex1-*PSMB4*<sup>wt</sup> or pTcIndex1-*PSMB4*<sup>F24L</sup> plasmid. Double-transfected epimastigotes were selected in the presence of 500  $\mu$ g/ml of G418 (Sigma-Aldrich) and 500  $\mu$ g/ml of hygromycin (Sigma-Aldrich). Susceptibility of double transfected epimastigote cell lines to compounds was assessed using induced (+5 mg/ml of tetracycline) and non-induced parasite cultures after five days of compound treatment. Parasite viability was determined with AlamarBlue (ThermoFisher Scientific).

Reported EC<sub>50</sub> values for *T. cruzi* epimastigotes ectopically expressing *PSMB4* proteins were calculated from 3 technical replicates ( $n = 3$ ; also specified in the Fig. 3a caption).

**Generation of *T. brucei* strains ectopically expressing proteasome  $\beta 4$  subunit variants.** *PSMB4* (Tb927.10.4710) was amplified from *T. brucei* Lister 427 genomic DNA using PCR SuperMix High Fidelity (Invitrogen), sense (5'-GCAAGCTTATGGCAGAGACGACTATCGG-3') and antisense (5'-GCGGATCCCTAGCTTACAGATTGCACTC-3') primers. The *PSMB4*<sup>F24L</sup> gene was generated from the wild-type *PSMB4* construct by site-directed mutagenesis using mutagenic sense (5'-GCTCGGGGTTAAATGCGTTATACTACATTAAGATAACGG-3'), antisense (5'-CCGTATCTTAATGTAGTATAACGCATTTAACCCCGCAGC-3') primers and QuikChange II Site-Directed Mutagenesis Kit (Stratagene). The sequences of the wild-type and mutant *PSMB4* genes were verified by sequencing and both gene versions were cloned into the *T. brucei* expression vector pHD1034 under control of a ribosomal RNA promoter. Transfected *T. brucei* Lister 427 cells were selected in medium supplemented with puromycin at 1  $\mu$ g/ml. Susceptibility of transfected *T. brucei* cell lines to compounds was assessed after 2 days of compound treatment. Parasite viability was determined with CellTiter-Glo.

Reported EC<sub>50</sub> values for *T. brucei* parasites ectopically expressing *PSMB4* proteins were calculated from 3 technical replicates ( $n = 3$ ; also specified in the Fig. 3b caption).

**Purification of parasite 20S proteasomes.** *Trypanosoma cruzi* CL epimastigotes, *L. donovani* MHOM/SD/62/1 S-CL2D axenic amastigotes and *T. brucei* Lister 427 bloodstream form trypomastigotes were grown to log phase and harvested by centrifugation. The corresponding cell pellets were stored at -80 °C until further use. Prior to purification, 10 g of cell pellets were thawed, re-suspended in lysis buffer (50 mM Tris-HCl pH = 7.5, 1 mM TCEP, 5 mM EDTA, and 10  $\mu$ M E-64), and lysed by passing cell suspension three times through a needle (22 gauge) and by subsequent three freeze/thaw cycles. The lysate was first cleared of cellular debris by two centrifugation steps (15,000g at 4 °C for 15 min followed by 40,000g at 4 °C for 60 min) and then fractionated through ammonium sulphate precipitation. The protein fraction precipitated between 45% and 65% of ammonium sulphate saturation was re-suspended in 25 mM Tris-HCl pH = 7.5, 1 mM TCEP buffer, and dialysed overnight at 4 °C against the same buffer. Proteasomes were further purified by anion exchange chromatography (Resource Q column, GE Healthcare Life Sciences) and size-exclusion chromatography (Superose 6 column, GE Healthcare Life Sciences) as described elsewhere<sup>38</sup>. Active fractions from the latter purification step were pooled and used in proteasome biochemical assays.

**Subunit composition analysis of purified *T. cruzi* 20S proteasome by LC-MS/MS.** Purified *T. cruzi* proteasome sample was buffer-exchanged and concentrated into 100 mM trimethylamine bicarbonate-HCl pH = 8.0, 150 mM NaCl buffer

using a 10 kDa molecular weight cut-off micro-concentrator (Milipore Amicon Ultra). The resulting proteasome sample (200 µl, 1 mg/ml) was mixed with 5 µl of a TMTsixplex reagent (Pierce). After 60 s incubation to label primary amines, the reaction was stopped by adding 25 µl of 5% hydroxylamine. The labelled sample was run on 4–20% Bis-Tris PAGE gel (Invitrogen) to separate polypeptides. The gel was stained with eStain 2.0 (GenScript). Stained protein bands were cut out and in-gel-digested separately with elastase (Promega) and asparaginase (Roche). Peptides generated by the digestions were resolved by HPLC using a vented column setup with a 2 cm Poros 10 R2 (Life Technologies, Carlsbad, CA) self-packed pre-column, and a PepMap Easy-Spray C18 analytical column (15 cm × 75 µm ID, Thermo Scientific). Resin-bound proteolytic fragments were eluted with 2 to 40% acetonitrile / 0.1% formic acid operated at 300 nl/min for 120 min. Spectra of eluted peptide species were determined by a column-coupled Q Exactive hybrid quadrupole orbitrap mass spectrometer (Thermo Scientific). Proteome Discoverer v1.4 software (Thermo Scientific) was used to search the *T. cruzi* genome<sup>28</sup> with identified spectra for presence of 20S proteasome subunits (Supplementary Table 7). Search parameters included fixed carbamidomethyl modification of cysteine, and variable oxidation of methionine, deamidation of asparagine, pyroglut of N-terminal glutamine, and TMT(6-plex) modification of lysine residues.

**Measuring proteasome proteolytic activities.** The activity of purified parasite and human 20S proteasomes was monitored by measuring cleavage of various rhodamine-labelled fluorogenic substrates. Purified 20S proteasomes were diluted in proteasome assay buffer (25 mM Tris-HCl pH 7.5, 1 mM dithiothreitol (Sigma-Aldrich), 10 mM sodium chloride, 25 mM potassium chloride, 1 mM magnesium chloride, 0.05% (w/v) CHAPS (Sigma-Aldrich) and 0.9% DMSO) at a final concentration of 162 nM (parasite proteasomes) or 25 nM (human proteasome), and pre-incubated with compound (40 nM; 0.2% final DMSO concentration) for 1 h. Next, the following substrates (Biosynthon GmbH) were added at 3 µM final concentration to monitor specific proteolytic activities (Suc-LLVY-Rh110-dPro: chymotrypsin-like activity; Ac-RLR-Rh110-dPro: trypsin-like activity; Ac-GLD-Rh110-dPro: caspase-like activity). The reaction was allowed to proceed for two hours at room temperature and fluorescence as a measure of purified 20S proteasome activity was monitored using the EnVision plate reader (excitation at 485 nm/emission at 535 nm).  $K_m$  and  $K_i$  values were calculated using GraphPad Prism (GraphPad Software) 'non-competitive enzyme inhibition' function.

Data shown in Fig. 4a, c, d and Extended Data Table 3 represent means of 3 technical replicates ( $n = 3$ ). Data shown in Fig. 4b and Extended Data Fig. 5 represent means of 2 technical replicates ( $n = 2$ ).

**Monitoring accumulation of ubiquitylated proteins in intact cells.** Growing *T. cruzi* CL epimastigotes were seeded into 24-well tissue culture plate ( $1 \times 10^7$  cells per well) in LIT medium and treated for 2–12 h with DMSO (0.2%) or various concentrations of bortezomib and GNF6702 at 27 °C. Following the treatment, parasites were collected by centrifugation (3,500g for 6 min) and washed twice with phosphate-buffered saline (PBS). Epimastigotes were lysed by resuspending washed cells in a buffer containing 50 mM Tris-HCl pH = 7.4, 150 mM sodium chloride, 1% CHAPS, 20 µM E-64 (Sigma-Aldrich), 10 mM EDTA (Sigma-Aldrich), 5 mM N-ethylmaleimide (Sigma-Aldrich), 1 mM phenylmethylsulfonyl fluoride (Sigma-Aldrich), 10 µg/ml leupeptin (Sigma-Aldrich), 10 µg/ml aprotinin (Sigma-Aldrich), and incubating the suspension on ice for 20 min. Cell lysates were cleared by centrifugation at 21,000g for 30 min at 4 °C.

For 3T3 cells,  $2 \times 10^5$  cells/well were seeded into 24-well tissue culture plates in RPMI-1640 medium supplemented with 10% heat-inactivated fetal bovine serum, and incubated overnight at 37 °C to allow cells to attach. Attached cells were treated for 2 h with DMSO (0.25%) or various concentrations of bortezomib and GNF6702. Treated cells were washed twice with PBS and then lysed by incubating cells in modified RIPA buffer (50 mM Tris-HCl pH = 7.4, 1% Triton X-100, 0.2% sodium dodecylsulfate, 1 mM EDTA, 1 mM phenylmethylsulfonyl fluoride, 5 µg/ml aprotinin, 5 µg/ml leupeptin) for 30 min at 4 °C. Cell lysates were cleared by centrifugation at 21,000g for 30 min at 4 °C.

Protein concentration in cell extracts was determined with BCA assay (ThermoFisher), and 10 µg of cell extracts were loaded on NuPAGE Novex 4–12% Bis-Tris gel (Invitrogen). After electrophoresis, resolved proteins were transferred to nitrocellulose membrane. Ubiquitylated proteins were detected with polyclonal anti-ubiquitin primary antibody (Proteintech, catalogue number 10201-2-AP) and rabbit anti-mouse IgG-peroxidase antibody (Sigma-Aldrich, catalogue number A0545), and then imaged using ECL Prime Western Blotting Detection Reagent (Amersham) on Chemidoc XR+ imaging system (BioRad). Collected western blot images were quantified using Image Lab software (BioRad). Briefly, rectangles of identical size and shape were drawn around each blot lane to include inside the shape all ubiquitylated protein bands within 17–198 kDa molecular mass range. Next, integrated signal intensities within the rectangles (reported by the Image Lab software) were used for calculation of  $EC_{50}$  values. Three technical replicate

experiments ( $n = 3$ ) for each different dose response experiment (GNF6702 on *T. cruzi* epimastigotes; GNF6702 on 3T3 cells; bortezomib on *T. cruzi* epimastigotes; bortezomib on 3T3 cells) were performed.

**Trypanosoma cruzi proteasome modelling studies.** The homology model of *T. cruzi* 20S proteasome was built using 'Prime' protein structure prediction program (Schrödinger) and X-ray structure of bovine 20S proteasome (PDB accession code 1IRU)<sup>39</sup> as the template. The model was subjected to restrained minimization to relieve inter-chain clashes. 'SiteMap' program (Schrödinger) was used to identify pockets on a protein surface suitable for small molecule binding. Flexible ligand docking was performed using 'Glide 5.8' (Schrödinger). The grid box was centred in a middle of the identified pocket and extended by 10 Å, with outer box extending an additional 20 Å. The ligand was docked using the standard precision (SP) algorithm and scored using 'GlideScore' (Schrödinger). The GNF6702 GlideScore is equal to -8.5.

**Receptor, enzyme and ion channel assays.** GNF6702 profiling was performed at 10 µM concentration in a selectivity panel at Eurofins (www.eurofinspanlabs.com/Catalog/AssayCatalog/AssayCatalog.aspx). Listed values correspond to the assay readout values expressed relative to the DMSO control. To determine inhibition of a subset of human tyrosine kinases by GNF6702, the inhibitor was profiled on a panel of Ba/F3 cell lines expressing individual Tel-activated kinases as described previously<sup>40</sup>. All assays were performed as single technical repeats.

**Determination of GNF6702 thermodynamic solubility.** The solubility of GNF6702 was assessed in a high throughput thermodynamic solubility assay as described previously<sup>41</sup>. First, 25 µl of GNF6702 DMSO solutions were transferred to individual wells of a 96-well plate. DMSO was evaporated and 250 µl of 67 mM potassium phosphate buffer pH 6.8 were added to yield projected final compound concentrations from 1 µM to 100 µM. The plate was sealed to prevent solvent loss and shaken for 24 h at room temperature. The plate was then filtered to remove non-dissolved material. Concentration of GNF6702 in individual plate wells was determined by measuring solution UV absorbance with reference to a GNF6702 calibration curve.

**Determination of GNF6702 permeability in Caco-2 assay.** A 96-Multiwell Insert System (BD Biosciences) was used for the Caco-2 cell culture and permeability assay as described previously<sup>42</sup>. Caco-2 cells were seeded onto insert wells at a density of  $1.48 \times 10^5$  cells per ml and allowed to grow for 19–23 days before assays. To measure both absorptive (apical to basolateral (A–B)) and secretory (basolateral to apical (B–A)) compound transport, a solution of GNF6702 at 10 µM concentration in 0.5% DMSO were added to donor wells. The plate was incubated at 37 °C for 2 h, with samples taken at the beginning and end of the incubation from both donor and acceptor wells. The concentration of GNF6702 was determined by LC-MS/MS.

Apparent drug permeability ( $P_{app}$ ) was calculated using the following equation:

$$P_{app} = \frac{dQ}{dt} \times \frac{1}{A \times C_{in}}$$

where  $dQ/dt$  is the total amount of a test compound transported to the acceptor chamber per unit of time (nmol/s),  $A$  is the surface area of the transport membrane ( $0.0804 \text{ cm}^2$ ),  $C_{in}$  is the initial compound concentration in the donor chamber (10 µM), and  $P_{app}$  is expressed as cm/s.

**Determination of human CYP450 inhibition by GNF6702.** Extent of inhibition of major human CYP450 isoforms 2C9, 2D6 and 3A4 by GNF6702 was determined using pooled human liver microsomes and the known specific substrates of various CYP450 isoforms: diclofenac (5 µM), bufuralol (5 µM), midazolam (5 µM), and testosterone (50 µM). Probe substrate concentrations were used at concentrations equal to their reported  $K_m$  values. The CYP450 inhibition assays with probe substrates diclofenac (2C9) or midazolam (3A4) were incubated at 37 °C for 5 to 10 min using a microsomal protein concentration of 0.05 mg/ml. Probe substrates bufuralol (2D6) and testosterone (3A4) were incubated at 37 °C for 20 min using microsomal concentration 0.5 mg/ml. The test concentrations of GNF6702 ranged from 0.5 to 25 µM in the presence of 1% DMSO. The reactions were initiated by adding NADPH (1 mM final concentration; Sigma-Aldrich) after a 5-min preincubation. Incubations were terminated by the addition of 300 µl of acetonitrile to 100 µl of a sample. No detectable cytochrome P450 inhibition was observed. Extent of CYP450 isoform inhibition was determined by quantifying residual concentrations of individual CYP450 substrate probes at the end of reactions by LC-MS/MS.

**Determination of GNF6702 in vitro metabolic stability.** The intrinsic metabolic stability of GNF6702 was determined in mouse and human liver microsomes using the compound depletion approach and LC-MS/MS quantification. The assay measured the rate and extent of metabolism of GNF6702 by measuring the disappearance of the compound. The assay determined GNF6702 *in vitro* half-life



( $T_{1/2}$ ) and hepatic extraction ratios (ER) as described previously<sup>43</sup>. GNF6702 was incubated for 30 min at 1.0  $\mu$ M concentration in a buffer containing 1.0 mg/ml liver microsomes. Samples (50  $\mu$ l) were collected at 0, 5, 15 and 30 min and immediately quenched by addition of 150  $\mu$ l of ice-cold acetonitrile/methanol/water mixture (8/1/1). Quantification of GNF6702 in samples was performed by LC-MS/MS, and the *in vitro* intrinsic clearance was determined using the substrate depletion method. The intrinsic clearance,  $CL_{int}$  was calculated using the following equation:

$$CL_{int} = \frac{0.693}{T_{1/2}} \times \frac{V}{M}$$

where  $T_{1/2}$  is the *in vitro* half-life,  $V$  ( $\mu$ l) is the reaction volume, and  $M$  (mg) is the microsomal protein amount. Finally the hepatic extraction ratio is calculated as:

$$ER = \frac{CL_h}{Q_h}$$

where  $CL_h$  = hepatic clearance,  $Q_h$  = hepatic blood flow.

$CL_h$  was calculated using the following equation:

$$CL_h = \frac{Q_h \times f_u \times CL_{int}}{Q_h + f_u \times CL_{int}}$$

where  $f_u$  = fraction unbound to protein (assumed to be 1).

**Pharmacokinetic studies.** An outline of various *in vitro* and *in vivo* DMPK assays used in this study for compound profiling was summarized previously<sup>44</sup>. The pharmacokinetic properties of GNF compounds and calculation of pharmacokinetic parameters was performed as described previously<sup>23</sup>. Mean compound plasma concentrations were calculated from fitted functions approximating compound plasma profile throughout eight days of dosing. Blinding was not possible in these experiments.

**Bioanalysis of GNF6702 in plasma.** Plasma concentration of GNF6702 was quantified using a LC-MS/MS assay. Solution of 20 ng/ml of verapamil hydrochloride (Sigma-Aldrich) in acetonitrile/methanol mixture (3/1 by volume), was used as an internal standard. Twenty microlitres of plasma samples were mixed with 200  $\mu$ l of internal standard solution. The samples were vortexed and then centrifuged in an Eppendorf Centrifuge 5810R (Eppendorf) at 4,000 r.p.m. for 5 min at 4 °C to remove precipitated plasma proteins. The supernatants (150  $\mu$ l) were transferred to a 96-well plate and mixed with 150  $\mu$ l H<sub>2</sub>O. The samples (10  $\mu$ l) were then injected onto a Zorbax SB-C8 analytical column (2.1  $\times$  30 mm, 3.5  $\mu$ m; Agilent Technologies) and separated using a three step gradient (1st step: 1.5 ml of 0.05% formic acid in 10% acetonitrile; 2nd step: 0.5 ml of 0.05% formic acid in 100% acetonitrile; 3rd step: 0.5 ml of 0.05% formic acid in 10% acetonitrile) at flow rate of 700  $\mu$ l/min. GNF6702 and verapamil were eluted at retention time 1.19 and 1.17 min, respectively. The HPLC system, consisting of Agilent 1260 series binary pump (Agilent Technologies), Agilent 1260 series micro vacuum degasser (Agilent Technologies) and CTC PAL-HTC-xt analytics autosampler (LEAP Technologies) was interfaced to a SCIEX API 4000 triple quadrupole mass spectrometer (Sciex). Mass spectrometry analysis was carried out using atmospheric pressure chemical ionization (APCI) in the positive ion mode. GNF6702 (430.07 > 333.20) and verapamil (455.16 > 164.90) peak integrations were performed using AnalystTM 1.5 software (Sciex). The lower limit of quantification (LLOQ) in plasma was 1.0 ng/ml. Samples were quantified using seven calibration standards (dynamic range 1–5,000 ng/ml) prepared in plasma and processed as described above.

**Formulation of study drugs for *in vivo* efficacy experiments.** All compounds administered to mice during efficacy experiments were formulated as suspensions in distilled water containing 0.5% methylcellulose (Sigma-Aldrich) and 0.5% Tween 80 (Sigma-Aldrich). During a treatment course, each mouse received 0.2 ml of drug suspension per dose by oral gavage.

**Mouse model of visceral leishmaniasis.** Female BALB/c mice (Envigo; 6–8 weeks old) were infected by tail vein injection with  $4 \times 10^7$  *L. donovani* MHOM/ET/67/HU3 splenic amastigotes (protocol number P11-319). Seven days after infection, animals were orally dosed for eight days with vehicle (0.5% methylcellulose/ 0.5% Tween 80, miltefosine (12 mg/kg once-daily; Sigma-Aldrich), or a GNF compound (twice-daily). On the first day of dosing, three mice were used for collection of blood for PK determination and euthanized afterwards. On the last day of dosing, PK samples were collected from remaining five mice, which were also used for determination of compound efficacy ( $n = 5$  mice per group). Liver samples were collected from these five mice and *L. donovani* parasite burdens were quantified by qPCR as follows. Total DNA was extracted from drug-treated mice livers using the DNeasy Blood and Tissue Kit (Qiagen). Two types of DNA were quantified in parallel using the TaqMan assay: *L. donovani* major surface glycoprotein gp63 (Ldon\_GP63) and mouse *Gapdh*.

*Leishmania donovani* gp63 DNA was quantified with the following set of primers: TGCGGTTTATCCTCTAGCGATAT (forward), AGTCCATGAAGCGGAGATG (reverse), and TGGCAGTACTTCACGGAC (TaqMan MGB probe, 5'-FAM-labelled reporter dye, non-fluorescent quencher). Mouse *Gapdh* DNA was quantified with the following set of primers: GCCGCCATGTTGCAAAC (forward primer), CGAGAGGAATGAGGTTAGTCACAA (reverse primer), and ATGAATGAACCGCCGTTAT (TaqMan MGB probe, 5'-FAM-labelled reporter dye, non-fluorescent quencher). Each qPCR reaction (10  $\mu$ l) included 5  $\mu$ l of TaqMan Gene Expression Master Mix (Life Technologies), 0.5  $\mu$ l of a 20 $\times$  primer/probe mix (Life Technologies), and 4.5  $\mu$ l (50 ng) of total DNA from liver samples. DNA amount was quantified using the Applied Biosystems 7900HT instrument. *Leishmania donovani* parasite burden (RU: relative units) was expressed as the abundance of *L. donovani* gp63 DNA relative to the abundance of mouse *Gapdh* DNA.

**Mouse footpad model of cutaneous leishmaniasis.** *Leishmania major* MHOM/SA/85/JISH118 metacyclic promastigotes were generated and purified by the peanut agglutinin method as described elsewhere<sup>45</sup>. To establish the *L. major* footpad infection, female BALB/c mice (Envigo; 6–8 weeks old; protocol number P11-319) were injected with a suspension of *L. major* metacyclic promastigotes ( $1 \times 10^6$  parasites in 50  $\mu$ l) into their left hind footpads. After eight days of infection, animals were dosed with vehicle, miltefosine (30 mg/kg once-daily), or indicated regimens of GNF6702 for seven days ( $n = 6$  mice per group). The progress of infection was monitored by measuring the size (length and thickness) of hind footpad swelling using digital calipers. At the end of the study, the mice were euthanized, and the footpad tissues were extracted and used for genomic DNA isolation with the DNeasy Blood and Tissue kit (Qiagen). The *L. major* footpad burden was determined by qPCR quantification of kinetoplastid minicircle DNA (forward primer: 5'-TTTACACCTCCCCAGTTT-3'; reverse primer: 5'-CCCGTTCATAATTTCCCGAAA-3'; Taqman MGB probe: 5'-AGGCCAAAAATGG-3', 5'-FAM (6-carboxyfluorescein)-labelled reporter dye, non-fluorescent quencher). The amounts of mouse chromosomal DNA in extracted samples were quantified in parallel qPCR using a glyceraldehyde-3-phosphate dehydrogenase (*Gapdh*) TaqMan assay as described for mouse VL model above. *Leishmania major* burden in footpad was expressed as the ratio of kinetoplast minicircle DNA to mouse *Gapdh*. *P* values for the between-groups differences in efficacies were calculated with a Student's paired *t*-test with a two-tailed distribution.

**Mouse model of Chagas disease.** Compound efficacy in a mouse model of Chagas disease was determined as described previously<sup>23</sup>. Female C57BL/6 mice (Envigo; 6–8 weeks old; protocol number P11-316) were infected by intraperitoneal injection with  $10^3$  tissue culture-derived *T. cruzi* CL trypomastigotes. Starting at 35 days after infection, the animals were dosed orally once-daily with 100 mg/kg benznidazole (Sigma-Aldrich) and indicated doses of GNF6702 (1, 3, and 10 mg/kg twice-daily,  $n = 8$  per group) for 20 days. Ten days following the end of drug treatment, the mice underwent four cycles of cyclophosphamide immunosuppression, each cycle lasting one week. During each immunosuppression cycle, mice were dosed by oral gavage once-daily with 200 mg/kg cyclophosphamide (suspension in 0.5% methylcellulose/ 0.5% Tween80 aqueous solution) on day 1 and day 4 of the cycle. After the fourth immunosuppression cycle, blood samples were collected from the orbital venous sinus of each mouse, mice were euthanized and heart and colon samples were collected. Samples from treated mice were used for extraction of total DNA using the High Pure PCR template preparation kit (Roche). The amounts of *T. cruzi* satellite DNA (195-bp fragment) in extracted DNA samples were quantified by real-time qPCR TaqMan assay (Life Technologies) with the following set of primers: AATTATGAATGGCGGGAGTCA (forward primer), CCACTGTGTGAACACGCAAAC (reverse primer), and AGACACTCTCTTTCAATGTA (TaqMan MGB probe, 5'-FAM (6-carboxyfluorescein)-labelled reporter dye, non-fluorescent quencher). The amounts of mouse chromosomal DNA in extracted samples were quantified in parallel qPCR reactions using a *Gapdh* (glyceraldehyde-3-phosphate dehydrogenase) TaqMan assay as described for mouse VL model above. Each qPCR mixture (10  $\mu$ l) included 5  $\mu$ l of TaqMan Gene Expression master mix (Life Technologies), 0.5  $\mu$ l of a 20 $\times$  primer/probe mix (Life Technologies), and 4.5  $\mu$ l (50 ng) of total DNA extracted from blood samples. PCRs were run on the Applied Biosystems 7900HT instrument. *Trypanosoma cruzi* parasitemia was expressed as the abundance of *T. cruzi* microsatellite DNA relative to the abundance of mouse *Gapdh* DNA.

**Mouse model of stage II HAT.** Female CD1 (Charles River UK; ~8 weeks old; project license number PPL 60/4442) mice were infected by injection into the peritoneum with  $3 \times 10^4$  *T. brucei* (GVR35-VSL2) bloodstream form parasites<sup>46</sup>. Starting on day 21, mice were dosed by oral gavage once-daily with GNF6702 ( $n = 6$ ) at 100 mg/kg for 7 days or a single dose of diminazene aceturate (Sigma-Aldrich) at 40 mg/kg in

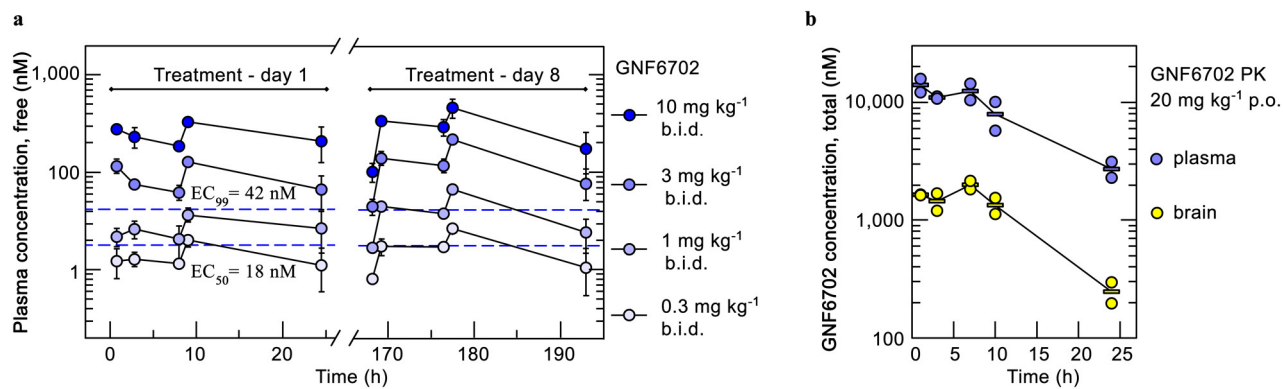


sterile water was administered by i.p. injection ( $n = 3$ ). A group of untreated mice ( $n = 3$ ) was included as controls.

Mice were monitored weekly for parasitemia from day 21 post-infection. *Trypanosoma brucei* was quantified in blood samples from the tail vein by microscopy, and *in vivo* bioluminescence imaging of infected mice was performed before treatment on day 21 post-infection and in weeks following the treatment (day 28, 35, 42, 56, 63, 72, 84, 92 post-infection). Imaging on groups of three mice was performed 10 min after i.p. injection of 150 mg D-luciferin (Promega)/kg body weight (in PBS) using an IVIS Spectrum (Perkin Elmer) as described previously<sup>25</sup>. A group of uninfected mice (aged-matched for day 0 time point;  $n = 4$ ) were imaged using the same acquisition settings to show the background bioluminescence (Fig. 2e, grey-filled squares) in the absence of luciferase-expressing *T. brucei* after day 92 of the experiment. Untreated and diminazene-treated mice were euthanized on days 32 and 35, and day 42, respectively, due to high parasitemia or the development of symptoms related to CNS infection. GNF6702-treated mice were euthanized on day 92. No parasitemia or clinical symptoms were observed at this point. At the specified endpoints mice were sacrificed by cervical dislocation, after which whole brains were removed and imaged *ex vivo* within 10 min after administration of 100  $\mu$ l of D-luciferin onto the brain surface. Data analysis for bioluminescence imaging was performed using Living Image Software (Perkin Elmer). The same rectangular region of interest (ROI) covering the mouse body was used for each whole-body image to show the bioluminescence in total flux (photons per second) within that region. Image panels of whole mouse bodies are composites of the original images with areas outside the ROI cropped out to save space. For *ex vivo* brain images the same oval shaped ROI was used to display the bioluminescence detected for each mouse brain at the respective endpoints.

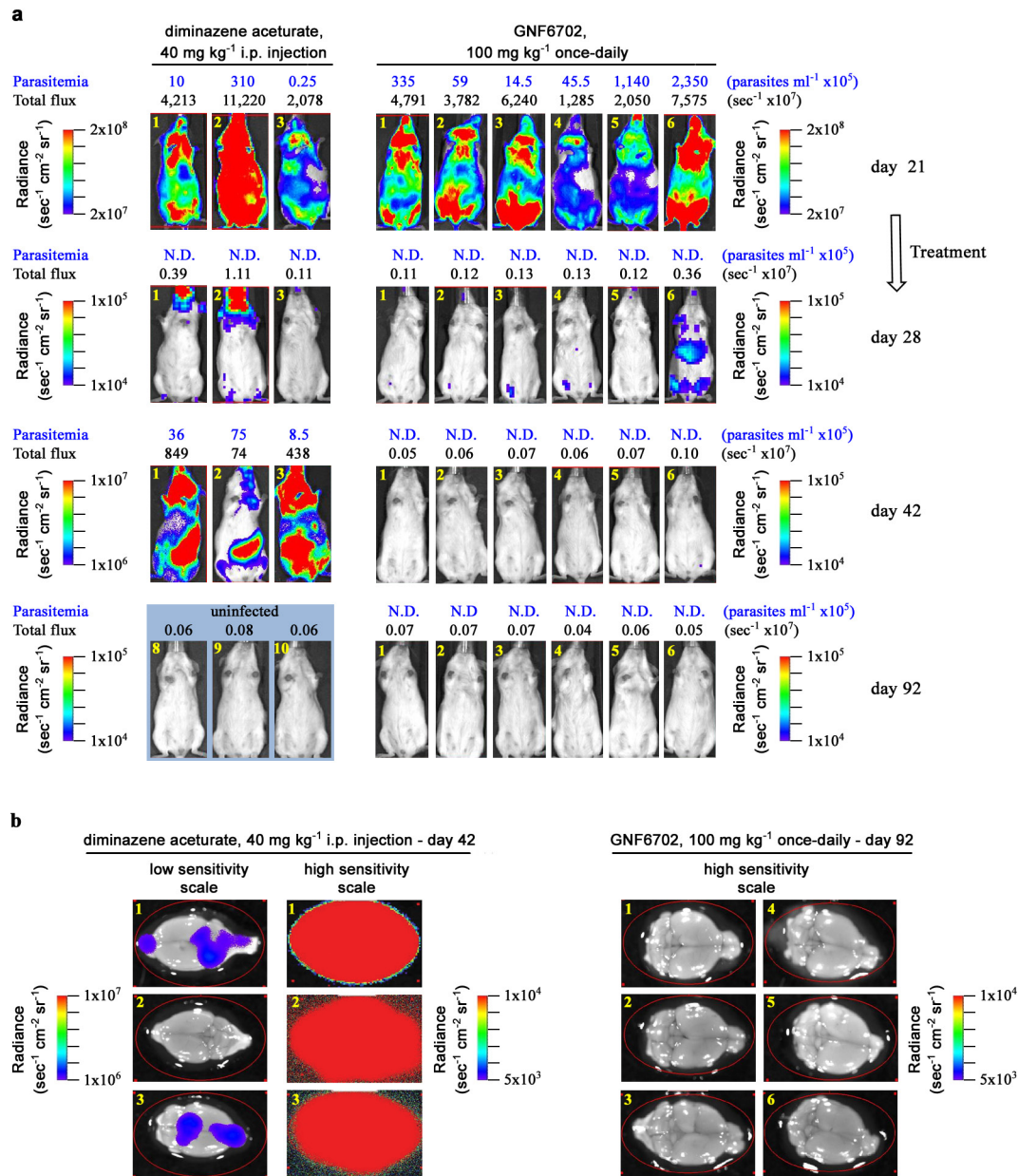
**Chemical synthesis.** The detailed procedures for chemical synthesis are presented in Supplementary Information.

31. Zhang, X., Goncalves, R. & Mosser, D. M. The isolation and characterization of murine macrophages. *Curr. Protoc. Immunol.* Chapter 14, Unit 14.1 (2008).
32. Khare, S. *et al.* Utilizing chemical genomics to identify cytochrome b as a novel drug target for Chagas disease. *PLoS Pathog.* **11**, e1005058 (2015).
33. Buckner, F. S., Verlinde, C. L., La Flamme, A. C. & Van Voorhis, W. C. Efficient technique for screening drugs for activity against *Trypanosoma cruzi* using parasites expressing beta-galactosidase. *Antimicrob. Agents Chemother.* **40**, 2592–2597 (1996).
34. Logan-Klumpler, F. J. *et al.* GeneDB—an annotation database for pathogens. *Nucleic Acids Res.* **40**, D98–D108 (2012).
35. Taylor, M. C. & Kelly, J. M. pTcINDEX: a stable tetracycline-regulated expression vector for *Trypanosoma cruzi*. *BMC Biotechnol.* **6**, 32 (2006).
36. Hariharan, S., Ajioka, J. & Swindle, J. Stable transformation of *Trypanosoma cruzi*: inactivation of the PUB12.5 polyubiquitin gene by targeted gene disruption. *Mol. Biochem. Parasitol.* **57**, 15–30 (1993).
37. Wirtz, E., Leal, S., Ochatt, C. & Cross, G. A. A tightly regulated inducible expression system for conditional gene knock-outs and dominant-negative genetics in *Trypanosoma brucei*. *Mol. Biochem. Parasitol.* **99**, 89–101 (1999).
38. Wilk, S. & Chen, W.-E. Purification of the eukaryotic 20S proteasome. *Curr. Protoc. Protein Sci.* Chapter 21 (2001).
39. Unno, M. *et al.* The structure of the mammalian 20S proteasome at 2.75 Å resolution. *Structure* **10**, 609–618 (2002).
40. Melnick, J. S. *et al.* An efficient rapid system for profiling the cellular activities of molecular libraries. *Proc. Natl Acad. Sci. USA* **103**, 3153–3158 (2006).
41. Waters, N. J., Jones, R., Williams, G. & Sohal, B. Validation of a rapid equilibrium dialysis approach for the measurement of plasma protein binding. *J. Pharm. Sci.* **97**, 4586–4595 (2008).
42. Wang, J. & Skolnik, S. Recent advances in physicochemical and ADMET profiling in drug discovery. *Chem. Biodivers.* **6**, 1887–1899 (2009).
43. Kalvass, J. C., Tess, D. A., Giragossian, C., Linhares, M. C. & Maurer, T. S. Influence of microsomal concentration on apparent intrinsic clearance: implications for scaling in vitro data. *Drug Metab. Dispos.* **29**, 1332–1336 (2001).
44. Li, C. *et al.* A modern *in vivo* pharmacokinetic paradigm: combining snapshot, rapid and full PK approaches to optimize and expedite early drug discovery. *Drug Discov. Today* **18**, 71–78 (2013).
45. Sacks, D. L. & Melby, P. C. Animal models for the analysis of immune responses to leishmaniasis. *Curr. Protoc. Immunol.* Chapter 19, Unit 19.12 (2001).
46. McLatchie, A. P. *et al.* Highly sensitive *in vivo* imaging of *Trypanosoma brucei* expressing “red-shifted” luciferase. *PLoS Negl. Trop. Dis.* **7**, e2571 (2013).



**Extended Data Figure 1 | Pharmacokinetic profile of GNF6702 in mouse.** **a**, Time profiles of mean free plasma concentration of GNF6702 in mouse model of visceral leishmaniasis; free GNF6702 concentration values were predicted from measured total plasma concentration values collected on day 1 and day 8 of treatment. Dashed blue lines correspond to intra-macrophage *L. donovani*

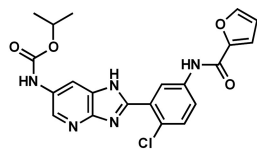
EC<sub>50</sub> of  $18 \pm 1.8$  nM and EC<sub>99</sub> of  $42 \pm 5.6$  nM. Circles, means  $\pm$  s.d.;  $n = 3$  mice for treatment day 1;  $n = 5$  mice for treatment day 8; fraction unbound in mouse plasma = 0.063. For data points lacking error bars, standard deviations are smaller than circles representing means. **b**, Time course of total GNF6702 concentration in mouse plasma and brain after single oral dose ( $20 \text{ mg kg}^{-1}$ );  $n = 2$  mice per time point; circles, measured values; rectangles, means.



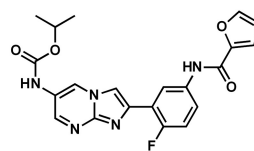
**Extended Data Figure 2 | GNF6702 clears parasites from mice infected with *T. brucei*.** **a**, *In vivo* quantification of bioluminescent *T. brucei* in infected mice before and after treatment. i.p., intraperitoneal; day 21, start of treatment; day 28, 24 h after last GNF6702 dose; day 42, evaluation of early parasite recrudescence in mice treated with diminazene aceturate ( $n = 3$ ); day 42 and 92, absence of parasite recrudescence in mice treated with GNF6702 ( $n = 6$ ). Images from uninfected mice (3 mice of 4 are shown) aged-matched for day 0 were collected independently using the same acquisition settings. Parasitemia (blue font) and whole mouse total flux (black font) values of each animal are shown above the image;

N.D., not detectable. Within each group the mouse numbers in yellow (top left in each image) refer to the same mouse imaged throughout. Complete sets of parasitemia and whole mouse total flux values collected on individual mice throughout the experiment are listed in Supplementary Tables 4 and 5. **b**, Brains from mice shown in **a** were soaked in luciferin and imaged for presence of bioluminescent *T. brucei* at the indicated time points. For three diminazene-treated mice, two images of each brain are shown, one at a lower sensitivity (left) and the other at a high signal intensity scale.



**GNF3943**

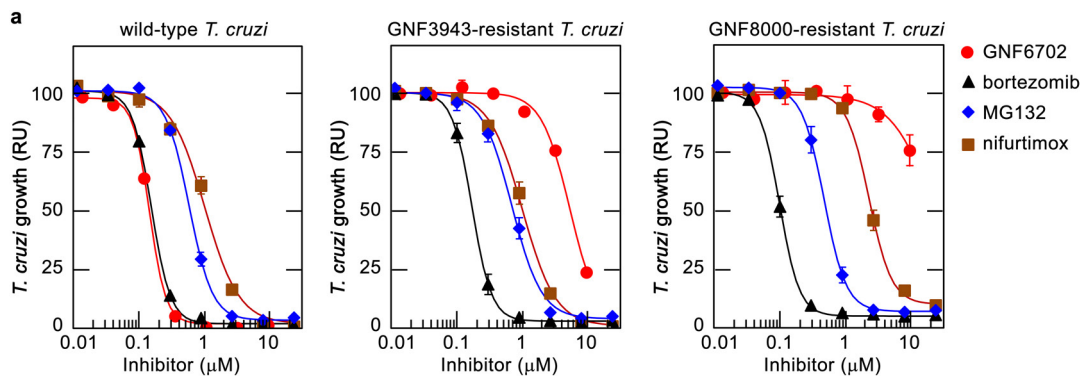
*L. donovani* EC<sub>50</sub> = 380 ± 23 nM  
*T. brucei* EC<sub>50</sub> = 33 ± 9.4 nM  
*T. cruzi* EC<sub>50</sub> = 120 ± 12 nM  
 3T3 CC<sub>50</sub> = 4.5 ± 0.9 μM  
 Macrophage CC<sub>50</sub> = 9.8 ± 2.4 μM  
 F = 75 %  
 CL = 17.7 ml min<sup>-1</sup> kg<sup>-1</sup>

**GNF8000**

*L. donovani* EC<sub>50</sub> = 320 ± 7.1 nM  
*T. brucei* EC<sub>50</sub> = 73 ± 2.9 nM  
*T. cruzi* EC<sub>50</sub> = 154 ± 12 nM  
 3T3 CC<sub>50</sub> > 20 μM  
 Macrophage CC<sub>50</sub> = 18 ± 2.1 μM  
 F = 10 %  
 CL = 8.8 ml min<sup>-1</sup> kg<sup>-1</sup>

**Extended Data Figure 3 | Structures and profiles of GNF3943 and GNF8000 used for selection of resistant *T. cruzi* lines.** *Leishmania donovani*, amastigotes proliferating within primary mouse macrophages; *T. brucei*, the bloodstream form trypomastigotes; *T. cruzi*, amastigotes proliferating in 3T3 fibroblast cells; macrophage, mouse primary

peritoneal macrophages; EC<sub>50</sub> and CC<sub>50</sub>, half-maximum growth-inhibition concentration; F, oral bioavailability in mouse after administering single compound dose (20 mg kg<sup>-1</sup>) as a suspension; CL, plasma clearance in mouse after single i.v. bolus dose (5 mg kg<sup>-1</sup>); all EC<sub>50</sub> and CC<sub>50</sub> values correspond to means ± s.e.m. (*n* = 4 technical replicates).



**b**

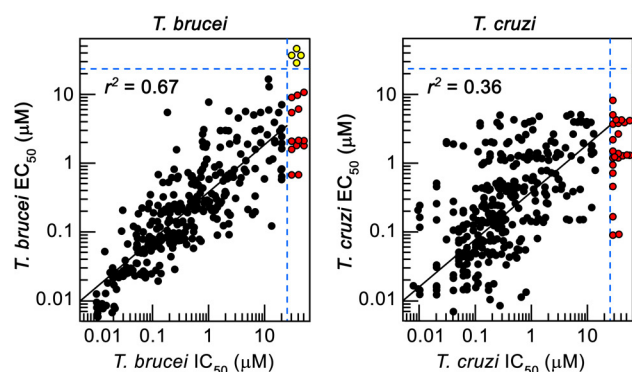
	wild-type <i>T. cruzi</i>	GNF3943 <sup>R</sup> <i>T. cruzi</i>	GNF8000 <sup>R</sup> <i>T. cruzi</i>
GNF6702 EC <sub>50</sub> (μM)	0.15 ± 0.002	5.5 ± 0.016	> 10
bortezomib EC <sub>50</sub> (μM)	0.16 ± 0.006	0.12 ± 0.020	0.10 ± 0.007
MG132 EC <sub>50</sub> (μM)	0.61 ± 0.015	0.76 ± 0.071	0.48 ± 0.052
nifurtimox EC <sub>50</sub> (μM)	1.0 ± 0.09	1.0 ± 0.11	2.4 ± 0.15

**c**

		<i>T. cruzi</i> ectopic PSMB4 <sup>WT</sup>		<i>T. cruzi</i> ectopic PSMB4 <sup>F24L</sup>		<i>T. brucei</i>	
		non-induced	induced	non-induced	induced	ectopic PSMB4 <sup>WT</sup> constitutive	ectopic PSMB4 <sup>F24L</sup> constitutive
GNF6702	(μM)	0.20 ± 0.007	0.20 ± 0.023	0.56 ± 0.029	> 10	0.018 ± 0.0018	1.2 ± 0.013
bortezomib	(μM)	0.46 ± 0.059	0.40 ± 0.057	0.45 ± 0.008	0.37 ± 0.015	0.00094 ± 0.00005	0.0011 ± 0.00026

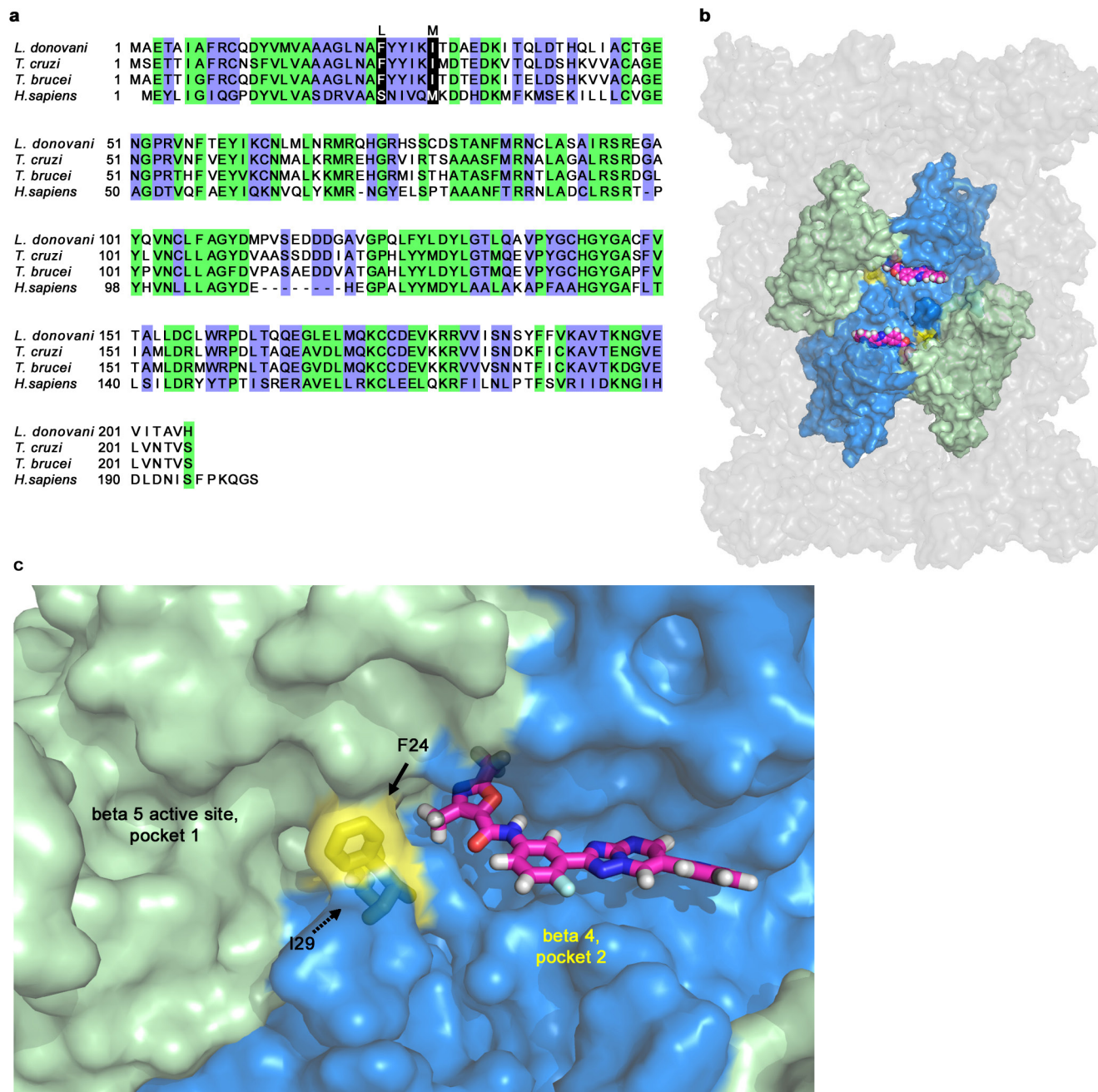
**Extended Data Figure 4 | Mutations in proteasome β4 subunit confer resistance to GNF6702 in *T. cruzi* and *T. brucei*.** **a**, Growth curves of wild-type, GNF3943-resistant and GNF8000-resistant *T. cruzi* epimastigote strains in the presence of increasing concentrations of GNF6702, nifurtimox, bortezomib and MG132; RU (relative units) corresponds to parasite growth relative to the DMSO control (%); for data points lacking error bars, standard errors are smaller than circles

representing means; owing to limited aqueous solubility, the highest tested GNF6702 concentration was 10 μM. **b**, Growth-inhibition EC<sub>50</sub> values of GNF6702, bortezomib, MG132 and nifurtimox on indicated *T. cruzi* strains. **c**, Growth-inhibition EC<sub>50</sub> values of GNF6702 and bortezomib on *T. cruzi* epimastigotes and *T. brucei* bloodstream form trypomastigotes overexpressing wild-type PSMB4 or PSMB4<sup>F24L</sup>. Data shown in panels **a**, **b** and **c** correspond to means ± s.e.m. (*n* = 3 technical replicates).



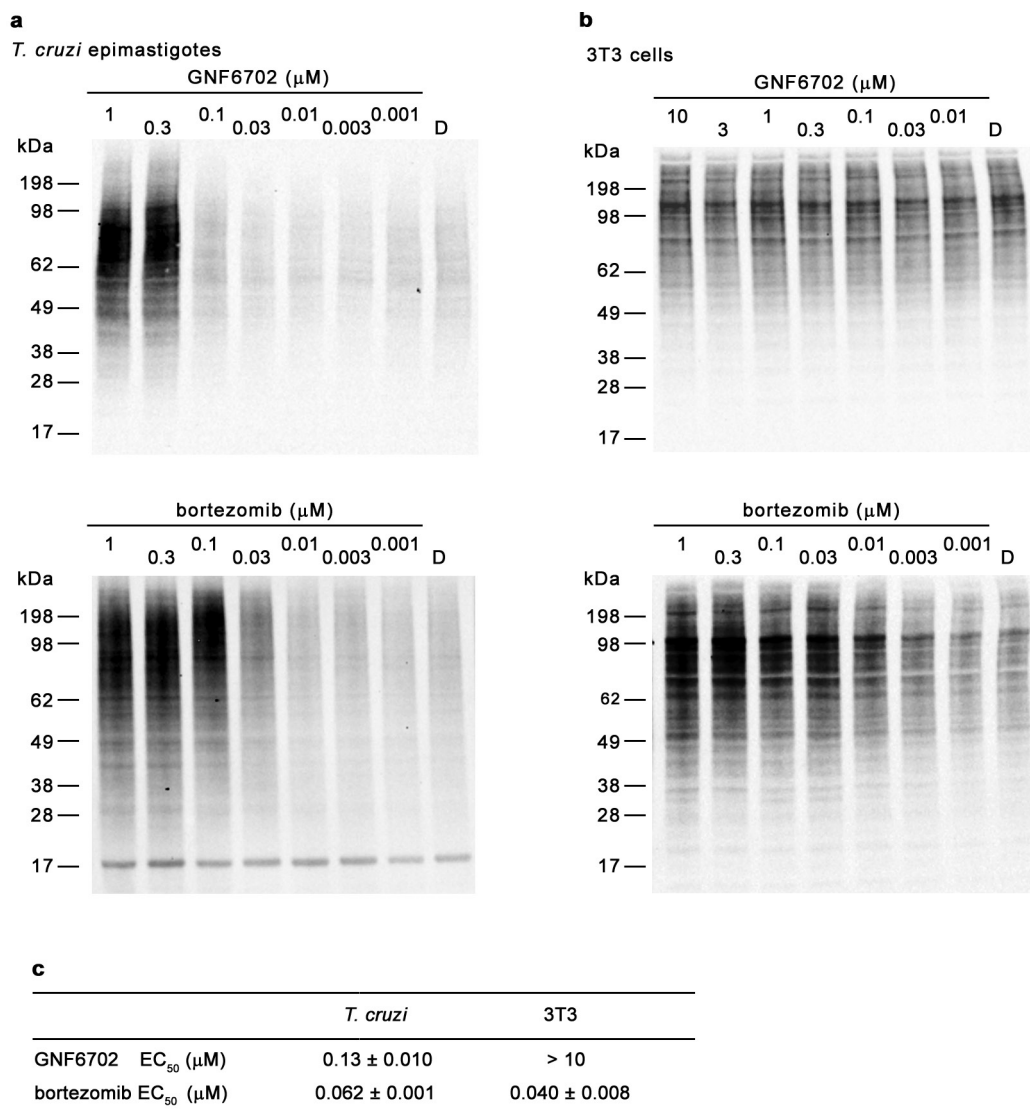
**Extended Data Figure 5 | Correlation between inhibition of parasite proteasome chymotrypsin-like activity and parasite growth inhibition by the GNF6702 compound series.** IC<sub>50</sub>, half-maximum inhibition of indicated parasite proteasome; *T. brucei* EC<sub>50</sub>, half-maximum growth inhibition on *T. brucei* bloodstream form trypomastigotes; *T. cruzi* EC<sub>50</sub>, half-maximum growth inhibition on *T. cruzi* amastigotes proliferating inside 3T3 cells; data points correspond to means of 2 technical replicates; red circles, IC<sub>50</sub> > 20 μM; yellow circles, IC<sub>50</sub> > 20 μM and EC<sub>50</sub> > 25 μM; data for 317 analogues are shown.





**Extended Data Figure 6 | Hypothetical model of GNF6702 binding to *T. cruzi* proteasome  $\beta 4$  subunit. a**, Alignment of amino acid sequences of proteasome  $\beta 4$  subunits (PSMB4) from *L. donovani*, *T. cruzi*, *T. brucei* and *Homo sapiens*. Green, amino acid residues conserved between human and kinetoplastid PSMB4 proteins; blue, amino acid residues conserved only among kinetoplastid PSMB4 proteins; black, amino acids mutated in *T. cruzi* mutants resistant to analogues from the GNF6702 series. **b**, Surface representation of the modelled *T. cruzi* 20S proteasome structure showing relative positions of the  $\beta 5$  and  $\beta 4$  subunits.  $\beta 4$  amino acid residues F24 and I29 (coloured yellow) are located at the interface of the two  $\beta$  subunits. GNF6702 is depicted in a sphere representation bound

into a predicted pocket on the  $\beta 4$  subunit surface with carbon, nitrogen, oxygen and hydrogen atoms coloured magenta, blue, red and grey, respectively. The other *T. cruzi* 20S proteasome subunits are coloured grey. **c**, Close-up of the  $\beta 5$  and  $\beta 4$  subunits. The  $\beta 5$  subunit active site (pocket 1, chymotrypsin-like activity) is coloured pale green. The predicted  $\beta 4$  pocket (pocket 2) with bound GNF6702 is coloured blue. The inhibitor is shown in a stick representation with atoms coloured as described in caption for **b**.  $\beta 4$  residues F24 and I29 are coloured yellow. The proteasome model shown in **b** and **c** was produced in the PyMol Molecule Graphics System, Version 1.8, Schrodinger, LLC.



**Extended Data Figure 7 | Effect of GNF6702 on accumulation of ubiquitylated proteins by *T. cruzi* epimastigotes and 3T3 cells.**

**a**, Western blot analysis of *T. cruzi* whole-cell extracts with anti-ubiquitin antibody after treatment with GNF6702 and bortezomib. **b**, Western blot analysis of 3T3 whole cell extracts with anti-ubiquitin antibody after treatment with GNF6702 and bortezomib. **c**, Concentrations of GNF6702 and bortezomib effecting half-maximum accumulation of ubiquitylated

proteins in *T. cruzi* and 3T3 cells (means  $\pm$  s.e.m.;  $n = 3$  technical replicates); total ubiquitin signal values in individual blot lanes shown in **a** and **b** were quantified and used for calculation of the listed  $\text{EC}_{50}$  values. In **a** and **b**, numbers above the blot lanes indicate compound concentrations and D indicates control, DMSO-treated cells. For western blot source data, see Supplementary Fig. 1.

Extended Data Table 1 | Point mutations identified by whole-genome sequencing in GNF3943- and GNF8000-resistant *T. cruzi* epimastigotes

	Gene ID	GNF3943 <sup>R</sup> mutant	GNF8000 <sup>R</sup> mutant
Number of reads (clone 1/ clone 2)		78x10 <sup>8</sup> / 63x10 <sup>8</sup>	48x10 <sup>6</sup> / 68x10 <sup>8</sup>
Mapped reads (clone 1/ clone 2) [%]		87/ 87	90/ 90
Average genome coverage (clone 1/ clone 2)		82x/ 66x	51x/ 66x
Proteasome beta 4 subunit	3540409	I29M/ I29M	wt/ F24L
Dynein heavy chain	3548195	wt/ P82L	wt/ wt
Trans-sialidase	3542504	wt/ wt	wt/ G90E
Trans-sialidase	3542504	wt/ wt	wt/ L93P
Hypothetical protein TCSYLVIO_005989	3547397	wt/ wt	wt/ L627P
Hypothetical protein TCSYLVIO_005986	3547401	wt/ wt	wt/ S55P



**Extended Data Table 2 | Enzyme inhibition IC<sub>50</sub> values of bortezomib and GNF6702 on three proteolytic activities of wild-type *T. cruzi*, PSMB4<sup>I29M</sup> *T. cruzi* and *H. sapiens* proteasomes**

		GNF6702 IC <sub>50</sub> (μM)*	bortezomib IC <sub>50</sub> (μM)*
<b>wild type <i>T. cruzi</i> proteasome</b>	<b>chymotrypsin</b>	0.035 ± 0.0013	0.091 ± 0.0075
	<b>caspase</b>	> 10	0.37 ± 0.012
	<b>trypsin</b>	> 10	1.7 ± 0.088
<b>PSMB4<sup>I29M</sup> <i>T. cruzi</i> proteasome</b>	<b>chymotrypsin</b>	> 10	0.26 ± 0.040
	<b>caspase</b>	> 10	0.54 ± 0.012
	<b>trypsin</b>	> 10	1.6 ± 0.058
<b><i>H. sapiens</i> constitutive proteasome</b>	<b>chymotrypsin</b>	> 10	0.030 ± 0.0070
	<b>caspase</b>	> 10	0.16 ± 0.007
	<b>trypsin</b>	> 10	7.9 ± 0.15

\*mean ± s.e.m.; *n* = 3 technical replicates.

Extended Data Table 3 | Inhibition kinetics parameters of GNF6702 on *L. donovani* and *T. cruzi* proteasomes

	chymotrypsin-like activity		caspase-like activity		trypsin-like activity	
	<i>L. donovani</i>	<i>T. cruzi</i>	<i>L. donovani</i>	<i>T. cruzi</i>	<i>L. donovani</i>	<i>T. cruzi</i>
Ki ± s.e.m. (μM)	0.055 ± 0.006*	0.079 ± 0.003*	> 10	> 10	> 10	> 10
Km ± s.e.m. (μM)	3.6 ± 0.60*	2.6 ± 0.15*	N.A.†	N.A.†	N.A.†	N.A.†
Mode of inhibition	non-competitive	non-competitive	N.A.†	N.A.†	N.A.†	N.A.†
R <sup>2</sup> (goodness of fit)	0.91	0.97	N.A.†	N.A.†	N.A.†	N.A.†

\*mean ± s.e.m.; *n* = 3 technical replicates.

†not applicable

# Germinal centre hypoxia and regulation of antibody qualities by a hypoxia response system

Sung Hoon Cho<sup>1</sup>, Ariel L. Raybuck<sup>1</sup>, Kristy Stengel<sup>2\*</sup>, Mei Wei<sup>1\*</sup>, Thomas C. Beck<sup>1</sup>, Emmanuel Volanakis<sup>3</sup>, James W. Thomas<sup>1,4</sup>, Scott Hiebert<sup>2,5,6</sup>, Volker H. Haase<sup>4,5,6,7</sup> & Mark R. Boothby<sup>1,4,5,6</sup>

Germinal centres (GCs) promote humoral immunity and vaccine efficacy. In GCs, antigen-activated B cells proliferate, express high-affinity antibodies, promote antibody class switching, and yield B cell memory<sup>1,2</sup>. Whereas the cytokine milieu has long been known to regulate effector functions that include the choice of immunoglobulin class<sup>3,4</sup>, both cell-autonomous<sup>5</sup> and extrinsic<sup>6,7</sup> metabolic programming have emerged as modulators of T-cell-mediated immunity<sup>8</sup>. Here we show in mice that GC light zones are hypoxic, and that low oxygen tension ( $p_{O_2}$ ) alters B cell physiology and function. In addition to reduced proliferation and increased B cell death, low  $p_{O_2}$  impairs antibody class switching to the pro-inflammatory IgG2c antibody isotype by limiting the expression of activation-induced cytosine deaminase (AID). Hypoxia induces HIF transcription factors by restricting the activity of prolyl hydroxyl dioxygenase enzymes, which hydroxylate HIF-1 $\alpha$  and HIF-2 $\alpha$  to destabilize HIF by binding the von Hippel–Landau tumour suppressor protein (pVHL)<sup>7</sup>. B-cell-specific depletion of pVHL leads to constitutive HIF stabilization, decreases antigen-specific GC B cells and undermines the generation of high-affinity IgG, switching to IgG2c, early memory B cells, and recall antibody responses. HIF induction can reprogram metabolic and growth factor gene expression. Sustained hypoxia or HIF induction by pVHL deficiency inhibits mTOR complex 1 (mTORC1) activity in B lymphoblasts, and mTORC1-haploinsufficient B cells have reduced clonal expansion, AID expression, and capacities to yield IgG2c and high-affinity antibodies. Thus, the normal physiology of GCs involves regional variegation of hypoxia, and HIF-dependent oxygen sensing regulates vital functions of B cells. We propose that the restriction of oxygen in lymphoid organs, which can be altered in pathophysiological states, modulates humoral immunity.

The micro-anatomy of secondary lymphoid organs and rapid proliferation of activated lymphocytes in them<sup>9</sup> prompted testing for hypoxia. Using flow cytometry, HIF levels were found to be increased in GC-phenotype B (GCB) cells compared to other B cells in the spleens of immunized mice (Fig. 1a; Extended Data Fig. 1a). Immunofluorescent microscopy revealed that HIF was most increased in GCs (Fig. 1b; Extended Data Fig. 1b). HIF is induced under low oxygen. However, HIF-1 $\alpha$  and HIF-2 $\alpha$  subunits can be stabilized at normoxic  $p_{O_2}$  (ref. 10), so we used chemical probes to mark hypoxic cells *in vivo*. Spleen, lymph nodes and Peyer's patches were analysed after injection of pimonidazole or EF5 (ref. 11) and staining with antibody that binds the adducts (Fig. 1c–e; Extended Data Fig. 1b–h). Fluorescence denoting hypoxia localized predominantly to the GC and the signal for each agent was weaker in the IgD<sup>+</sup> zone<sup>1</sup>. Flow cytometry detected EF5 only with GL7<sup>+</sup> GCB cells (Fig. 1e), and a hypoxia-related gene signature was enriched in GCB cells (Extended Data Fig. 1i). The EF5 and

pimonidazole signals only partially filled GCs, which are subdivided into light and dark zones between which B cells cycle iteratively to promote high-affinity antibodies. EF5 labelling predominantly overlapped a follicular dendritic cell marker (CD35) restricted to the light zone (Fig. 1f). B lymphoblasts proliferate rapidly in the dark zone, whereas cell cycling decreases in the light zone<sup>1</sup>. The most EF5-positive GCB cells had entered S-phase at lower rates (percentage BrdU<sup>+</sup>) (Fig. 1g, h) and more frequently activated an executioner caspase (Fig. 1i). Thus, activated B cells experience hypoxia in GCs, predominantly in their light zones. Notably, the more hypoxic GCB cells proliferated less and had increased apoptotic signalling.

To test the effect of hypoxia on antibody class switching, activated B cells cultured in hypoxia ( $p_{O_2}$  of 1%) were compared to controls cultured at atmospheric (~21%) or venous (5%)  $p_{O_2}$ , using conditions that promote IgG1 or the pro-inflammatory isotype IgG2c (Fig. 2a; Extended Data Fig. 2). Hypoxia restricted B cell population growth (Fig. 2a, b), with increased caspase-3 activation and lower BrdU incorporation (Extended Data Fig. 2a, b). Thus,  $O_2$  sufficiency promoted B cell proliferation by both improving survival and increasing cell cycling. These effects were paralleled by an altered balance in cell metabolism, as hypoxia promoted a higher glycolytic rate (Extended Data Fig. 2c) in activated B cells. Conversely, *in vitro* inhibition of prolyl hydroxyl dioxygenase (PHD) reduced  $O_2$  consumption, and gene expression profiling of fresh *ex vivo* B cells showed major differences between the non-GC and GC subsets (Extended Data Fig. 2d, e, respectively). Moreover, IgG<sup>+</sup> B cell frequencies were reduced at 1%  $p_{O_2}$  (Fig. 2a, Extended Data Fig. 2f). The enteric immune system is a site of physiological hypoxia<sup>12</sup>; notably, hypoxia did not decrease the frequency of IgA<sup>+</sup> B cells in IgA-promoting conditions (Fig. 2a, Extended Data Fig. 2f). Switching requires multiple B cell divisions<sup>13</sup>. When fluorescein partitioning was analysed along with switching to IgG2c, hypoxia reduced switching by B cells at the same division number (Fig. 2b). Thus, hypoxia at levels of the GC light zone altered antibody class switching by a direct influence on class choice in addition to reducing proliferation and reprogramming B cell metabolism and survival.

Class switch recombination is executed by AID, which is encoded by the *Aicda* gene<sup>1,3,4</sup>. In IgG switch conditions, *Aicda* mRNA and AID protein were reduced by hypoxia (Fig. 2c, d; Extended Data Fig. 2g). By contrast, AID was not reduced by hypoxia in IgA switch conditions (Fig. 2d). Switch recombinase is directed to the immunoglobulin heavy chain regions by transcription factors that create accessibility marked by germ-line transcripts (GLTs)<sup>3,4</sup>. Hypoxia decreased induction of the transcription factor T-bet and the T-bet-dependent I $\gamma$ 2c GLT<sup>14</sup> (Fig. 2e, f), whereas *Rora* mRNA and the I $\alpha$  GLT were not reduced in B cells at reduced  $p_{O_2}$  (Fig. 2e, f). The PHD inhibitor dimethylxylglycine (DMOG) reduced proliferation and increased apoptosis of B cells

<sup>1</sup>Department of Pathology, Microbiology and Immunology, Vanderbilt University, Nashville, Tennessee 37232, USA. <sup>2</sup>Department of Biochemistry, Vanderbilt University, Nashville, Tennessee 37232, USA. <sup>3</sup>Department of Pediatrics, Vanderbilt University, Nashville, Tennessee 37232, USA. <sup>4</sup>Department of Medicine, Vanderbilt University, Nashville, Tennessee 37232, USA. <sup>5</sup>Department of Cancer Biology, Vanderbilt University, Nashville, Tennessee 37232, USA. <sup>6</sup>Vanderbilt-Ingram Cancer Center, Vanderbilt University, Nashville, Tennessee 37232, USA. <sup>7</sup>Medical and Research Services, Department of Veterans Affairs, Tennessee Valley Healthcare System, Nashville, Tennessee 37212, USA.

\*These authors contributed equally to this work.



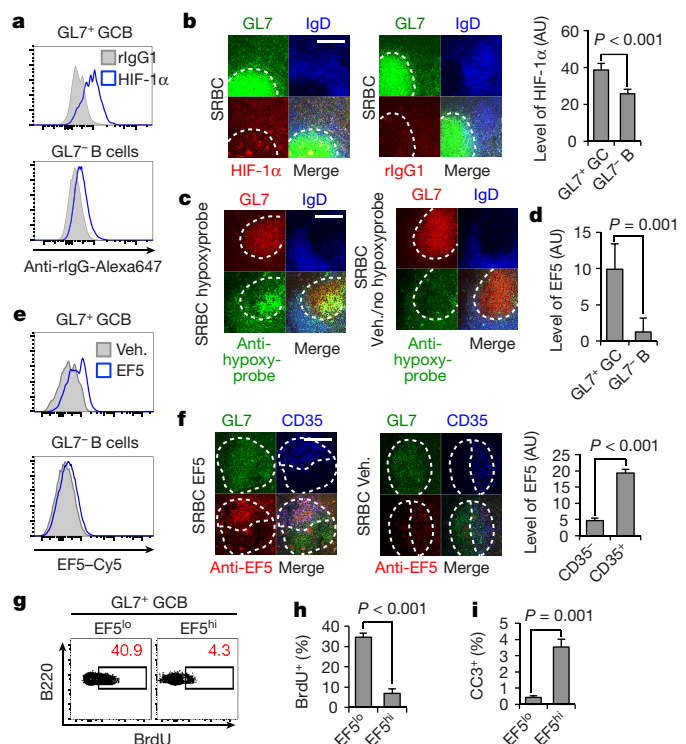


**Figure 1 | Hypoxia in GC light zones.** **a**, Flow cytometry of HIF-1α in GCBs (GL7<sup>+</sup> B220<sup>+</sup> gate) from sheep red blood cell (SRBC)-immunized mice, and in the GL7<sup>+</sup> B220<sup>+</sup> gate, compared to controls (rIgG1 instead of primary anti-HIF-1α antibody; Extended Data Fig. 1a, *Hif1a*<sup>Δ/Δ</sup> B cells stained with anti-HIF-1α). **b**, Left, immunofluorescent staining of HIF-1α or controls (rIgG1; as in **a**) in GCs (GL7<sup>+</sup> IgD<sup>+</sup>) and surrounding follicles (IgD<sup>+</sup> GL7<sup>+</sup>) ( $n = 12$  GCs, 4 spleens in 2 experiments). Scale bar in **b**, **c**, **f**, 100 μm. Right, HIF-1α signals quantified within GCs compared to the GL7<sup>+</sup> follicular cells (Extended Data Fig. 1b, *Hif1a*<sup>Δ/Δ</sup> B cells stained with anti-HIF-1α). AU, arbitrary units. **c–e**, GC hypoxia. Adducts, IgD and GL7 were stained after immunized mice were injected with EF5, pimonidazole (hypoxyprobe) or PBS (Veh.). **c**, Anti-pimonidazole staining of spleen sections (representative of 24 GCs in 9 sections from 3 independent experiments, quantified in Extended Data Fig. 1c). **d**, Quantified EF5 signals (Extended Data Fig. 1d) within GCs compared to the GL7<sup>+</sup> follicles, as in **b** ( $n = 19$  GCs from  $n = 5$  mice each condition, PBS and EF5; 3 independent experiments). **e**, A representative flow cytometry result ( $n = 3$  experiments) with anti-EF5 staining of spleen cells after intravital injection with EF5 or PBS, as in **c** and **d**, gated as in **a**. **f**, Hypoxia maps mostly to the light zone. Spleen sections as in **e**, stained for CD35, GL7 and EF5, and anti-EF5 signals in CD35<sup>+</sup> and CD35<sup>−</sup> regions, quantified as in **d**. **g**, Flow cytometric measurements of S-phase (BrdU<sup>+</sup>) GCB cells that were either hypoxic (EF5<sup>hi</sup>) or not (EF5<sup>lo</sup>), from mice as in **e** after BrdU injection. **h**, BrdU incorporation ( $n = 7$  samples in two independent experiments). **i**, Fractions of cleaved (activated) caspase-3-positive (CC3<sup>+</sup>) GCB cells, gated as in **g**. All data are mean ± s.e.m.

cultured at 21%  $p_{O_2}$  and severely restricted switching to IgG2c, whereas switching to IgA exhibited less impairment (Extended Data Fig. 3a, b). An inhibitor of HIF stabilization mitigated the reduction of IgG2c-switched B cells by low oxygen (1%  $p_{O_2}$ ) (Extended Data Fig. 3c). Akin to hypoxia, PHD inhibition and HIF stabilization impaired AID, T-bet, and Iγ2c GLT induction in the presence of the IgG2c switch cytokine IFNγ (Fig. 2c, e, f; Extended Data Fig. 4a–c). By contrast, levels of RNA for RORα and the Iα GLT were higher in DMOG-treated cells than in controls (Fig. 2c). Thus, hypoxia reduced AID and GLT induction in the conditions promoting IgG2c, whereas Iα and AID levels were maintained in IgA conditions, consistent with the relative effects on class-switched B cell antigen receptors (BCRs).

pVHL destabilizes HIF by targeting hydroxylated alpha subunits for rapid proteasomal degradation in most oxygen-sufficient

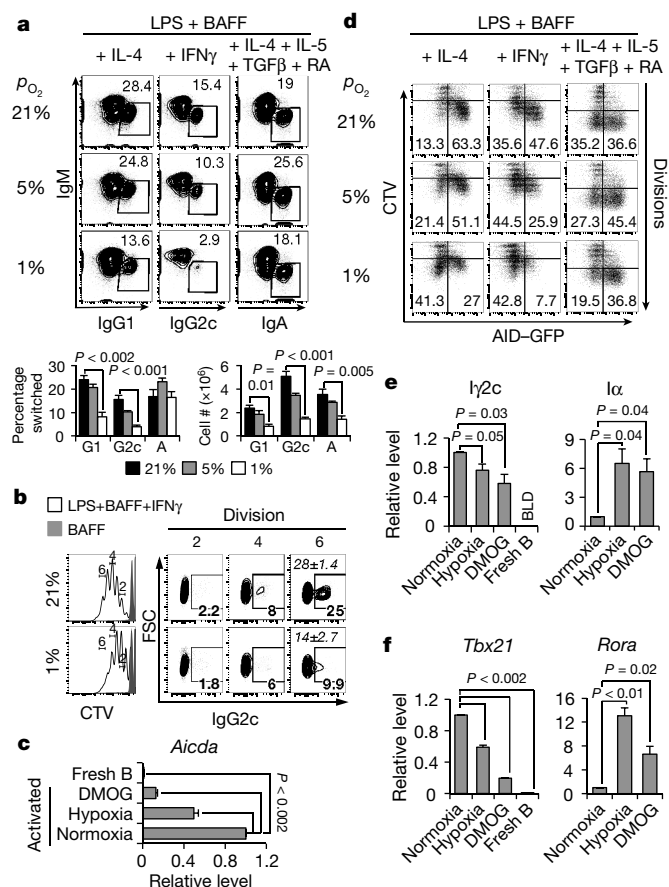


**Figure 2 | Hypoxia regulates B cell survival, proliferation and class switching.** **a**,  $O_2$  modulates the spectrum of antibody isotypes. Surface IgG1, IgG2c and IgA on B220<sup>+</sup>-gated cells, measured by flow cytometry after activation of purified B cells culture at  $p_{O_2}$  of 21% (normoxia), 5% or 1% (hypoxia) using conditions promoting IgG1, IgG2c or IgA. Flow cytometry data from one representative experiment (top) along with bar graphs showing aggregate results of cell numbers and switch efficiencies (bottom) ( $n = 4$  for 5%,  $n = 7$  for 1% and 21%  $p_{O_2}$ ). LPS, lipopolysaccharide. **b**, Flow cytometry of surface IgG2c (right) on B cells gated by division number (left) after activation of CellTrace Violet (CTV)-stained B cells and culture with IFNγ as in **a**. Inset numbers (bold font) denote the percentage of switched B cells at indicated division numbers in this analysis; mean (± s.e.m.) values from the independent replicate experiments ( $n = 3$ ) are italicized. Shaded overlay: CTV fluorescence of undivided cells cultured only in BAFF. **c**, **d**, AID regulated by oxygen sufficiency. **c**, *Aicda* mRNA was quantified in B cells activated and cultured as in **a**, or in the presence or absence of PHD inhibitor DMOG. **d**, Relative AID expression, measured as GFP fluorescence in AID-GFP transgenic B cells stained with CTV, activated and cultured in the conditions of **a** and **b**. Representative GFP fluorescence versus divisions for B220<sup>+</sup> cells quantified from four independent replicate analyses are in Extended Data Fig. 2g. **e**, **f**, Hypoxia and PHD inhibition reduce T-bet and Iγ2c GLT induction, but not Rora or Iα. Iγ2c GLT (**e**) and *Tbx21* (**f**) mRNA measured after B cell cultures in IgG2c conditions; Iα GLT (**e**) and *Rora* (**f**) mRNA in B cells cultured for IgA switching ( $n = 3$ –4 experiments). BLD, below limit of detection. Data are mean ± s.e.m.

environments<sup>7,15</sup>. To model persistent hypoxic signalling *in vivo*, we used conditional *Vhl* loss-of-function experiments. Mature B cells subjected to *Vhl* deletion yielded less antigen-binding GCB cells after immunization, less IgG2c antibodies, and a substantial decrease in cells secreting antigen-specific IgG2c in primary responses (Fig. 3a–c, Extended Data Figs 5, 6). Cycling between the light and dark zones in GCs promotes higher affinity antibodies<sup>16</sup>, so it was notable that for IgM and IgG1 pVHL depletion only impaired generation of high-affinity anti-4-hydroxy-3-nitrophenylacetyl (NP) antibodies

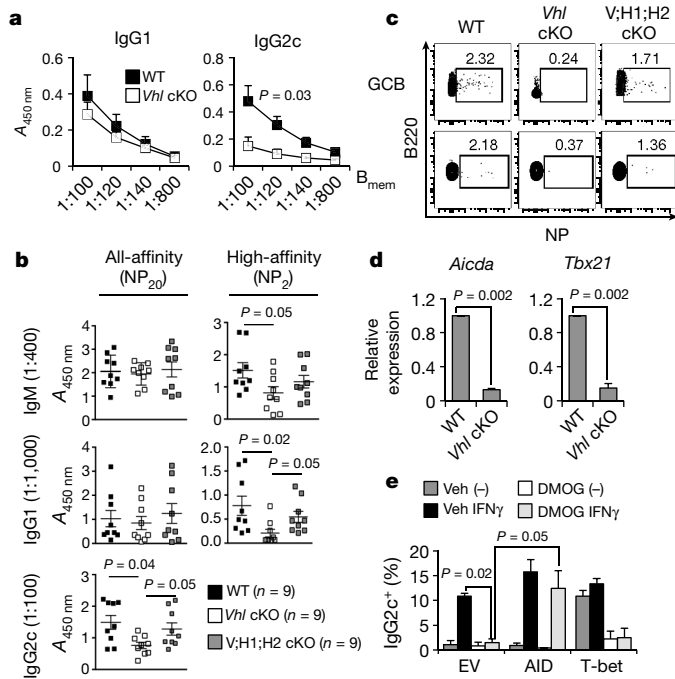


**Figure 3 | B cell-intrinsic role of pVHL in antibody response qualities.** **a–c**, In adoptive transfer experiments (schematic diagram, Extended Data Fig. 5a), B cells purified from tamoxifen-treated mice were transferred into recipients after mixing with CD4<sup>+</sup> T cells (polyclonal:OVA-specific OT-II cells = 4:1). Recipients were analysed after primary immunization, or, for memory responses (Extended Data Fig. 5d), after the primary and a recall immunization. **a**, Primary NP-specific IgG2c antibody response in *Rag*<sup>0</sup> recipients of wild-type (WT) or *Vhl*<sup>fl/f</sup>;ER<sup>T2</sup>-Cre (*Vhl* cKO) B cells from tamoxifen-treated donor mice ( $n = 5$  recipients of each genotype, distributed evenly between two independent replicate experiments). Other antibody isotypes are in Extended Data Fig. 5. **b**, High-affinity (NP<sub>2</sub>) or all-affinity (NP<sub>20</sub>) anti-NP antibodies of the indicated isotypes in sera from immunized recipients, measured by ELISA. Each dot represents one mouse ( $n = 9$  of each genotype, distributed evenly among 3 independent experiments). Horizontal lines denote the mean. WT, wild type; *Vhl* cKO, pVHL-depleted conditional knockout (*Vhl*<sup>Δ/Δ</sup>); V;H1;H2 cKO, pVHL-, HIF-1α- and HIF-2α-depleted conditional knockout (*Vhl*<sup>Δ/Δ</sup> *Hif1a*<sup>Δ/Δ</sup> *Epas1*<sup>Δ/Δ</sup>). **c**, HIF-dependent reduction of antigen-specific B cell populations. Flow cytometry results scoring NP-binding GCB cells (B220<sup>+</sup> GL7<sup>+</sup> IgD<sup>−</sup>) and early memory (B220<sup>+</sup> CD38<sup>+</sup> IgM<sup>+</sup> GL7<sup>−</sup> IgD<sup>−</sup>) phenotypes. One representative result from the same mice and experiments as shown in **b** (Extended Data Fig. 6c, d). **d**, VHL in B cells promotes *Aicda* and *Tbx21* expression. Wild-type and *Vhl*<sup>Δ/Δ</sup> B cells were activated, cultured and analysed as in Fig. 2c. **e**, B cells transduced with MIT, MIG, MIT-T-bet or pMx-GFP-AID retrovectors were cultured with BAFF and LPS ± IFN $\gamma$  in the presence or absence of DMOG. EV, empty retrovector. Frequencies of surface IgG2c<sup>+</sup> events among B220<sup>+</sup> cells analysed 4 days after transduction, with flow data from one experiment in Extended Data Fig. 4e ( $n = 3$  independent experiments). Data are mean  $\pm$  s.e.m.

(Fig. 3b). The defect in primary responses substantially reduced IgG2c of all affinities (Fig. 3b, Extended Data Fig. 6a), whereas antigen-specific IgA was unaffected (Extended Data Fig. 6b). The effects of pVHL depletion on IgG2c and high-affinity IgG1 antibody responses were HIF-dependent (Fig. 3b). Defects of antibody responses were heightened in recall (secondary) immunity when compared to primary responses (Extended Data Fig. 5c, d compared to Fig. 3a). pVHL loss reduced the population of antigen-binding memory B cells, an effect mitigated by concomitant HIF depletion (Fig. 3c, Extended Data Fig. 6d). *Aicda* mRNA induction in activated B cells was impaired in cells with increased HIF due to reduced *Vhl* (Fig. 3d, Extended Data Fig. 4c, d). *Tbx21* mRNA and T-bet protein levels were also lower in

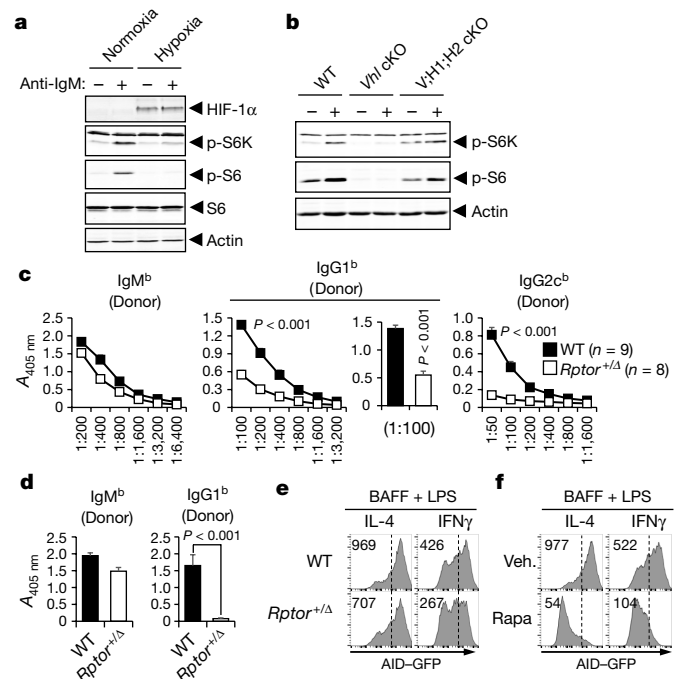


**Figure 4 | mTORC1 activity in B cells regulates antibody qualities but is attenuated by hypoxia.** **a**, Immunoblots of lysates prepared from activated B cells cultured overnight at 21% or 1%  $pO_2$ , before (−) and after (+) re-stimulation with anti-IgM. **b**, Immunoblots of B cell extracts as in **a**, using conditionally pVHL-depleted cells with either normal (*Vhl* cKO) or deficient (V;H1;H2 cKO) HIF expression. **c**, **d**, Raptor promotes generation of high-affinity antibodies and switch to IgG. IgH<sup>b</sup> (donor B-cell-derived)-allotype anti-NP antibodies were measured after immunization of IgH<sup>a</sup> allotype mice that had received wild-type or *Rptor*<sup>+/-Δ</sup> B cell transfers. ELISA results for all-affinity anti-NP IgG in primary response sera from recipient mice ( $n = 9$  WT,  $n = 8$  *Rptor*<sup>+/-Δ</sup>), captured on NP<sub>20</sub> (**c**), and high-affinity antibodies (IgM, 1:100; IgG1, 1:50) captured on NP<sub>2</sub> (**d**). IgG2c was undetectable, as in **c**. **e**, **f**, mTORC1 promotes AID expression. GFP in B220<sup>+</sup>-gated cells by flow cytometry after B cells were cultured for 4 days with LPS, BAFF and IL-4 or IFN $\gamma$  as indicated. **e**, *Rptor*<sup>+/-Δ</sup> (WT) or *Rptor*<sup>+/-Δ</sup> AID-GFP transgenic mice. **f**, *Rptor*<sup>+/-Δ</sup> AID-GFP cells cultured in the presence of mTORC1 inhibitor rapamycin (Rapa; 10 nM) or vehicle. Data are mean  $\pm$  s.e.m.; in **e**, **f**,  $n = 3, 4$  replicates, respectively.

pVHL-depleted B cells (Fig. 3d, Extended Data Fig. 4c). To test the impact of decreased AID and T-bet, we forced expression of these proteins in activated B cells. T-bet did not increase the frequency of IgG2c-positive B cells during PHD inhibition, although it bypassed the need for IFN $\gamma$  with control B cells (Fig. 3e, Extended Data Fig. 4e). By contrast, forcing AID expression normalized switching in these assays (Fig. 3e, Extended Data Fig. 4e). We conclude that the PHD/HIF/VHL axis regulates the qualities of antibody responses, with modulation of AID levels as a major mechanism for hypoxic influence on the Ig class preferences.

B cell activation, class switch recombination, and development into antibody-secreting cells are effected by receptors that stimulate mTOR. Hypoxia and HIF-1 have been shown to either inhibit or enhance mTORC1 activity in tumour or endothelial cells<sup>17,18</sup>. In hypoxic and DMOG-treated B cells, BCR engagement elicited less phosphorylation of proteins downstream from mTORC1 (Fig. 4a, Extended Data Fig. 7a). Depletion of pVHL also reduced BCR-stimulated mTORC1 by a HIF-dependent mechanism (Fig. 4b). Thus, hypoxia restrained mTORC1 in normal B cells. *In vitro* experiments suggest that HIF-mediated limitation of increased amino acid transport contributes to this effect. B cell activation increased leucine uptake and expression of transporters used for nutrient uptake; HIF stabilization impaired this induction (Extended Data Fig. 7b–e). Moreover, adequate supplies of leucine were crucial, and partially sufficient, for BCR re-activation of



mTORC1 in B lymphoblasts (Extended Data Fig. 7f). HIF depletion did not completely restore either the antibody response or amino acid uptake to normal in pVHL-deficient B cells. However, two additional mechanisms previously shown to suppress mTORC1 were evoked in hypoxic B cells *in vitro*—steady-state ATP pools were halved, accompanied by increased AMPK activity, and expression of the *Redd1* (also known as *Ddit4*) gene was increased (Extended Data Fig. 8a–c).

Disruption of mTOR function by means that impair both mTORC2 and mTORC1 altered the balance between class-switched and IgM antibody against specific antigen<sup>19,20</sup>. By contrast, HIF stabilization only partially inhibited mTORC1 and spared mTORC2 (Extended Data Fig. 8d, e). Accordingly, we tested whether partially reduced mTORC1 activity effects high-affinity antibody production, proliferation, AID levels, or biases of Ig class switching using disruption of *Rptor*, which encodes a protein essential for mTORC1 (ref. 21). *Rptor* haploinsufficiency in B cells reduced mTORC1 activity (Extended Data Fig. 9a), and yielded results of *in vitro* switching and humoral responses *in vivo* (Fig. 4c, d, Extended Data Fig. 9) similar to those obtained with hypoxia and the PHD/HIF/VHL axis. IgG2c reductions were more substantial than those of IgM or IgG1 (Fig. 4c), and NP-specific GCB cells and IgG2c anti-NP-antibody-secreting cells (Extended Data Fig. 9b–d) were reduced. Partial mTORC1 loss reduced switching to IgG2c (Extended Data Fig. 10a) and suppressed high-affinity IgG1 antibody production (Fig. 4d). IgG1 switch conditions promoted higher expression of a tracking allele, green fluorescent protein (GFP)-tagged AID, which was partially reduced by *Rptor* hemizygosity (Fig. 4e), whereas IgG2c conditions led to less AID in control cells and a greater reduction in *Rptor*<sup>+/-</sup> B cells. Moreover, *Rptor* haploinsufficiency led to reduced T-bet expression, and decreased mRNA levels of both *Tbx21* and *Aicda* in activated B cells (Extended Data Fig. 10b, c). Pharmacological inhibition of mTOR with rapamycin substantially reduced AID levels<sup>19,20</sup> (Fig. 4f) and switching to IgG2c, an effect mitigated by forced AID and T-bet expression (Extended Data Fig. 10d–f). Overall, localized hypoxia and HIF induction are normal features of GC microphysiology that modulate the output from lymphoid follicles, effects similar to those of restricting mTORC1 activity.

Low oxygen tension confronts B cells in GCs during an immune response. The findings reveal that restricted oxygen supply or persistent induction of HIF transcription factors in B cells limits proliferation, isotype switching, and levels of high-affinity antibodies. GCB cells undergo iterative selection to enhance antibody affinity<sup>1,2</sup> so that the most suitable B cells survive, further mature, and continue to multiply. Thus, the restriction of  $p_{O_2}$  of the GC may slow proliferation and set a more stringent threshold for crucial survival signals. In addition, the IgG2c isotype has particular functions in anti-microbial responses and inflammation owing to the affinities of its constant region with the spectrum of Fc receptors on cells<sup>22</sup>. Many patients with hypoxaemic lung disease exhibit lower serum IgG levels and heightened susceptibility to respiratory infection<sup>23</sup>. Hypoxia has also been recognized as a major aspect of inflammation in disease states. Intratumoral restrictions of oxygenation elicit indirect effects on immune function in cancer and may also act directly on T cells<sup>24,25</sup>. Moreover, hypoxia and neo-lymphoid tissue or tertiary lymphoid structures with GCs, plasma cells, and local antibody production are now recognized in a wide range of inflammatory settings in which the oxygen landscape is unexplored<sup>26</sup>. The hypoxia response program in intestinal epithelial cells limits local inflammation<sup>12,27,28</sup>, providing counter-regulation against activated neutrophils<sup>27</sup>. Analogous to this, the susceptibility of IgG2c to hypoxia may represent another means for limiting pathology from unchecked inflammation in normal immunity.

**Online Content** Methods, along with any additional Extended Data display items and Source Data, are available in the online version of the paper; references unique to these sections appear only in the online paper.

Received 8 September 2015; accepted 28 July 2016.

Published online 8 August 2016.

1. Vitorica, G. D. & Nussenzweig, M. C. Germinal centers. *Annu. Rev. Immunol.* **30**, 429–457 (2012).
2. Shlomchik, M. J. & Weisel, F. Germinal center selection and the development of memory B and plasma cells. *Immunol. Rev.* **247**, 52–63 (2012).
3. Xu, Z., Zan, H., Pone, E. J., Mai, T. & Casali, P. Immunoglobulin class-switch DNA recombination: induction, targeting and beyond. *Nat. Rev. Immunol.* **12**, 517–531 (2012).
4. Stavnezer, J., Guikema, J. E. & Schrader, C. E. Mechanism and regulation of class switch recombination. *Annu. Rev. Immunol.* **26**, 261–292 (2008).
5. Cui, G. *et al.* IL-7-induced glycerol transport and TAG synthesis promotes memory CD8<sup>+</sup> T cell longevity. *Cell* **161**, 750–761 (2015).
6. Munn, D. H. *et al.* Prevention of allogeneic fetal rejection by tryptophan catabolism. *Science* **281**, 1191–1193 (1998).
7. Kaelin, W. G. Jr. The von Hippel–Lindau tumour suppressor protein: O<sub>2</sub> sensing and cancer. *Nat. Rev. Cancer* **8**, 865–873 (2008).
8. Pearce, E. L., Poffenberger, M. C., Chang, C. H. & Jones, R. G. Fueling immunity: insights into metabolism and lymphocyte function. *Science* **342**, 1242454 (2013).
9. Spencer, J. A. *et al.* Direct measurement of local oxygen concentration in the bone marrow of live animals. *Nature* **508**, 269–273 (2014).
10. Patten, D. A. *et al.* Hypoxia-inducible factor-1 activation in nonhypoxic conditions: the essential role of mitochondrial-derived reactive oxygen species. *Mol. Biol. Cell* **21**, 3247–3257 (2010).
11. Koch, C. J. Importance of antibody concentration in the assessment of cellular hypoxia by flow cytometry: EF5 and pimonidazole. *Radiat. Res.* **169**, 677–688 (2008).
12. Colgan, S. P. & Taylor, C. T. Hypoxia: an alarm signal during intestinal inflammation. *Nat. Rev. Gastroenterol. Hepatol.* **7**, 281–287 (2010).
13. Rush, J. S., Liu, M., Odegard, V. H., Uniraman, S. & Schatz, D. G. Expression of activation-induced cytidine deaminase is regulated by cell division, providing a mechanistic basis for division-linked class switch recombination. *Proc. Natl Acad. Sci. USA* **102**, 13242–13247 (2005).
14. Peng, S. L., Szabo, S. J. & Glimcher, L. H. T-bet regulates IgG class switching and pathogenic autoantibody production. *Proc. Natl Acad. Sci. USA* **99**, 5545–5550 (2002).
15. Kaelin, W. G. Jr & Ratcliffe, P. J. Oxygen sensing by metazoans: the central role of the HIF hydroxylase pathway. *Mol. Cell* **30**, 393–402 (2008).
16. Bannard, O. *et al.* Germinal center centroblasts transition to a centrocyte phenotype according to a timed program and depend on the dark zone for effective selection. *Immunity* **39**, 912–924 (2013).
17. Wouters, B. G. & Koritzinsky, M. Hypoxia signalling through mTOR and the unfolded protein response in cancer. *Nat. Rev. Cancer* **8**, 851–864 (2008).
18. Krymskaya, V. P. *et al.* mTOR is required for pulmonary arterial vascular smooth muscle cell proliferation under chronic hypoxia. *FASEB J.* **25**, 1922–1933 (2011).
19. Keating, R. *et al.* The kinase mTOR modulates the antibody response to provide cross-protective immunity to lethal infection with influenza virus. *Nat. Immunol.* **14**, 1266–1276 (2013).
20. Zhang, S. *et al.* B cell-specific deficiencies in mTOR limit humoral immune responses. *J. Immunol.* **191**, 1692–1703 (2013).
21. Laplante, M. & Sabatini, D. M. mTOR signaling in growth control and disease. *Cell* **149**, 274–293 (2012).
22. Nimmerjahn, F. & Ravetch, J. V. Divergent immunoglobulin g subclass activity through selective Fc receptor binding. *Science* **310**, 1510–1512 (2005).
23. O’Keeffe, S. *et al.* Immunoglobulin G subclasses and spirometry in patients with chronic obstructive pulmonary disease. *Eur. Respir. J.* **4**, 932–936 (1991).
24. Gabrilovich, D. I. *et al.* Production of vascular endothelial growth factor by human tumors inhibits the functional maturation of dendritic cells. *Nat. Med.* **2**, 1096–1103 (1996).
25. Hatfield, S. M. *et al.* Immunological mechanisms of the antitumor effects of supplemental oxygenation. *Sci. Transl. Med.* **7**, 277ra30 (2015).
26. Konisti, S., Kiriakidis, S. & Paleolog, E. M. Hypoxia—a key regulator of angiogenesis and inflammation in rheumatoid arthritis. *Nat. Rev. Rheumatol.* **8**, 153–162 (2012).
27. Eltzschig, H. K. & Carmeliet, P. Hypoxia and inflammation. *N. Engl. J. Med.* **364**, 656–665 (2011).
28. Karhausen, J. *et al.* Epithelial hypoxia-inducible factor-1 is protective in murine experimental colitis. *J. Clin. Invest.* **114**, 1098–1106 (2004).

**Supplementary Information** is available in the online version of the paper.

**Acknowledgements** Research funding via National Institutes of Health (NIH) grants R01 AI113292, HL106812 to M.R.B., CA164605 to S.H.; Veterans Affairs Merit award I01 BX002348 to V.H.H., along with support of K.S. by American Cancer Society postdoctoral fellowship PF-13-303-01-DMC, and T.C.B. by T32 DK007563 are gratefully acknowledged, as are O. Davidoff and Q. Liu for expert help with mouse management and with hypoxia chamber usage, respectively,



K. Rathmell for critically reading and suggesting manuscript text, P. Young for use of an additional hypoxia chamber, H. Simkins and T. Laufer for guidance on making NP-conjugated fluors, N. Papavasiliou for the AID retrovector, C. Koch for hypoxia detection reagents, and scholarships via the Cancer Center Support Grant (CA068485) and Diabetes Research Center (DK0205930) to help pay for Vanderbilt University cores.

**Author Contributions** S.H.C., A.L.R., K.S., E.V., V.H.H., J.W.T. and M.R.B. conceived of and designed experiments; M.R.B. coordinated the research. S.H.C. and M.R.B. analysed all data, and wrote the manuscript, which K.S., J.W.T. and E.V. edited. S.H.C. performed and analysed the immunohistochemistry and flow cytometry for detection of GC hypoxia. S.H.C. and A.L.R. performed and analysed the adoptive transfer and immunization experiments. K.S. and S.H. conceived, performed and analysed RNA-seq experiments. M.W., A.L.R. and

S.H.C. performed and analysed class-switching experiments. S.H.C., A.L.R. and T.C.B. performed and analysed the metabolic assays. All other experiments and analyses were performed by S.H.C. and A.L.R.

**Author Information** The results of RNA-seq have been deposited in the NCBI Gene Expression Omnibus (GEO) database under accession code GSE77113. Reprints and permissions information is available at [www.nature.com/reprints](http://www.nature.com/reprints). The authors declare no competing financial interests. Readers are welcome to comment on the online version of the paper. Correspondence and requests for materials should be addressed to M.R.B. ([mark.boothby@vanderbilt.edu](mailto:mark.boothby@vanderbilt.edu)).

**Reviewer Information** *Nature* thanks H. Chi and the other anonymous reviewer(s) for their contribution to the peer review of this work.

## METHODS

**Mice and B cell transfer models.** Mice (C57BL/6 mice, CD45.1 congenic, Ig C<sub>H</sub> allotype-disparate (IgH<sup>a</sup>), *Rag*<sup>0</sup>, AID-GFP Tg, pVHL conditional knockout (*Vhl*<sup>fl/n</sup>, ER<sup>T2</sup>-Cre)<sup>29</sup>, pVHL; HIF-1 $\alpha$ ; HIF-2 $\alpha$  triple conditional knockout (*Vhl*<sup>fl/n</sup>; *Hif1a*<sup>fl/n</sup>; *Epas1*<sup>fl/n</sup>; ER<sup>T2</sup>-Cre), and raptor conditional knockout (*Rptor*<sup>fl/n</sup>; ER<sup>T2</sup>-Cre)<sup>30</sup>) were housed in ventilated micro-isolators under specified pathogen-free conditions in a Vanderbilt University mouse facility and used at 6–8 weeks of age following approved protocols. Healthy mice of useful genotype were randomly selected for the experiments, without preference to size, gender, or other potential confounding factor. All figures are based on data reproduced in independent biological replicates, typically conducted weeks or months apart in time and involving different cages of donor and recipient mice, and always with parallel handling and manipulation of the mice and cells of samples to be compared. For adoptive transfer experiments, B cells (from 1–2 donor mice of each genotype) were purified by depleting T cells using biotinylated anti-Thy1.2 antibody followed by streptavidin-conjugated microbeads (iMag; BD Biosciences). Pooled wild-type CD4<sup>+</sup> T cells and OT-II CD4<sup>+</sup> T cells ( $4 \times 10^6$  and  $1 \times 10^6$  cells per recipient, respectively, typically from two donor mice of each background) were purified by positive selection with L3T4 anti-CD4 microbeads and, in adoptive transfers into *Rag*<sup>0</sup> or Ig C<sub>H</sub> allotype-disparate (IgH<sup>a</sup>) mice, mixed with pools of wild-type, *Vhl* <sup>$\Delta/\Delta$</sup> , *Vhl* <sup>$\Delta/\Delta$</sup> ; *Hif1a* <sup>$\Delta/\Delta$</sup> ; *Epas1* <sup>$\Delta/\Delta$</sup> , or *Rptor* <sup>$\Delta/\Delta$</sup>  B cells ( $5 \times 10^6$  cells per recipient) and injected intravenously (i.v.) into *Rag*<sup>0</sup> or IgH<sup>a</sup> recipients. Recipient mice of similar ages (6–8 weeks) were randomly selected for the experiments, without preference to size or gender. Experiments using the conditional *Vhl* alleles (*Vhl* <sup>$\Delta/\Delta$</sup> ) were designed to avoid distortions rapidly imposed by systemic pVHL loss (for example, extra-medullary haematopoiesis<sup>29</sup>). Those using *Rptor*<sup>fl/fl</sup> drove excision with the same *Rosa26*;ER<sup>T2</sup>-Cre allele and with tamoxifen-initiated Cre activity so as to be more directly comparable to the *Vhl* experiments and because of distortions of B cell development observed even for heterozygotes with *mb1*-Cre (deletion at outset of B lymphoid ontogeny) (A.L.R. and M.R.B., unpublished observations).

**Reagents.** IFN $\gamma$ , IL-4 and monoclonal antibody (purified, biotinylated or fluorophore-conjugated) were from BD Pharmingen or Tonbo Biosciences unless otherwise indicated. IL-5 was from Peprotech, TGF $\beta$  and BAFF were from R&D Systems. NP-BSA (for capture ELISA), NP-OVA (4-hydroxy-3-nitrophenylacetyl hapten conjugated to ovalbumin, cat no. N-5051-100), and NP-O-succinimide (4-hydroxy-3-nitrophenylacetic acid active ester, or NP-Osu, for NP-allophycocyanin (APC) conjugation; cat no. N-1010) were obtained from Biosearch. SRBCs (sheep red blood cells), D-glucose, and 2-deoxyglucose were from Thermo Fisher Scientific. Tamoxifen, 4-hydroxy-tamoxifen, chicken ovalbumin, all-trans retinoic acid and LPS were from Sigma-Aldrich Chemicals. DMOG (HIF-hydroxylase inhibitor dimethylxallylglycine, Calbiochem cat no. 400091) and oligomycin were from EMD Millipore. Fluorescent proteins APC and (R)-phycoerythrin (rPE; Prozyme) were used for conjugation reactions with NP-O-succinimide to generate fluor-conjugated NP.

**Immunohistochemistry, flow cytometry and detection of hypoxia.** C57BL/6 mice were immunized with SRBCs ( $2 \times 10^8$  cells per mouse). At 1 week after immunization, mice were injected with EF5 (ref. 31) or pimonidazole HCl (hypoxyprobe). Spleen, lymph node and Peyer's patches were embedded in OCT reagent and snap frozen on dry ice. Sections of frozen tissue were fixed with 4% paraformaldehyde, permeabilized with 0.5% Triton X-100 in PBS, blocked with M.O.M. (Vector Laboratory) followed by incubation with GL7-FITC, IgD-PE, and anti-EF5-Cy5 antibodies at 4°C. For hypoxyprobe detection, frozen sections were stained with biotinylated anti-pimonidazole antibody followed by streptavidin-conjugated Alex647 antibody. Biotinylated anti-CD35 antibody (BD Pharmingen, clone 8C12) followed by streptavidin-conjugated phycoerythrin (PE) antibody was used for indirect immunofluorescent detection of follicular dendritic cells (FDC). Quantification of HIF-1 $\alpha$ , EF5 and hypoxyprobe fluorescence intensity within GCs (total or light zone as defined by CD35 staining) and follicular regions was performed using MetaMorph Image processing software. For the samples and negative controls, the regions were quantified *in toto* using the signal-averaged fluorescence intensity within each boundary (for example, CD35<sup>+</sup> or GL7<sup>+</sup>). After subtracting the background mean fluorescence intensity (MFI) from negative control samples, MFI values of HIF-1 $\alpha$ , EF5 and hypoxyprobe within GCs (CD35<sup>+</sup> and CD35<sup>-</sup> zones) and GL7<sup>-</sup> follicular region were obtained. Data are presented as mean ( $\pm$  s.e.m.) MFI values for the individual samples ( $n > 20$  GCs for each condition, drawing evenly on three independent experiments). In flow cytometric detection of hypoxic cells, BrdU incorporation, or cleaved caspase 3, cell surface markers were stained by fluor-conjugated monoclonal antibody, followed by fixation (4% paraformaldehyde), permeabilization with saponin (0.2%), and staining with anti-EF5-Cy5, or two-step staining of pimonidazole according to supplier's instructions. BrdU and cleaved caspase 3 were detected as described<sup>32</sup>. For these and other flow cytometric analyses, fluorescence emission data on cell

suspensions were collected on BD LSR or FACSCalibur flow cytometers driven by BD FACS Diva software, then processed using Flow-Jo software (TreeStar).

**Immunizations, and measurements of antibody responses.** After collection of pre-immune sera, mice were immunized with NP<sub>16</sub>-ovalbumin (OVA) (100  $\mu$ g intraperitoneally) in alum (Imject, Thermo Fisher Scientific) as described<sup>33</sup>. Alternatively, this primary immunogen was mixed with NP-modified SRBCs, followed by a boost with NP-OVA in alum. Relative levels of anti-NP antibodies in immune sera were assayed by ELISA on serial dilutions binding to either NP<sub>20</sub>-BSA (high valency, to capture all affinities of antibodies) or NP<sub>2</sub> (low valency, to restrict binding to the high-affinity antibody). Specific classes or isotypes were then detected using the series of isotype-specific second antibody of the SBA Clonotyping System (Southern Biotech), as described<sup>33</sup>. Data for antigen-specific antibodies are shown after subtraction of low absorbance (A) values from pre-immune controls analysed together with the immune sera and were separately determined to match values yielded by titration. Antibody-secreting cells were analysed by ELISpot as previously described<sup>33</sup> and quantitated using an ImmunoSpot Analyzer (Cellular Technology). Antigen-specific B cells were detected and enumerated using flow cytometry to score B lineage-marked cells binding to fluor (APC or rPE)-conjugated NP, using a dump channel (7-AAD and APC-conjugated monoclonal antibody against IgD, F4/80, Gr1, CD11b, CD11c, CD4, and CD8) to exclude non-specific signal.

**Gene expression profiling.** Mice were injected with SRBCs and euthanized 10 days after immunization. Single-cell suspensions from spleens were stained with anti-B220 (RA3-6B2) and anti-GL7. B220<sup>+</sup>GL7<sup>-</sup> and B220<sup>+</sup>GL7<sup>+</sup> splenocytes were sorted with TRIzol reagent (Ambion). Total RNA was isolated from biological replicates and provided to the Vanderbilt VANTAGE shared resource for library construction and sequencing. Briefly, libraries were constructed from poly-adenylated RNAs and sequenced with an Illumina HiSeq 2500 on an SR-50 run aiming for 30M reads/sample. Reads were aligned to the mm10 mouse transcriptome using TopHat and differential gene expression was determined using Cuffdiff as previously described<sup>34</sup>. Gene set enrichment analysis (GSEA) was performed using software available from the Broad Institute (<http://www.broadinstitute.org/gsea>), which tested for enrichment based on hypergeometric distribution with respect to published gene signatures. For hypoxia regulated gene signature, GSEA plots comparing a gene set pre-ranked by log<sub>2</sub> fold change in gene expression (GL7<sup>+</sup>B220<sup>+</sup> versus GL7<sup>-</sup>B220<sup>+</sup>) to a hypoxia signature published previously<sup>35</sup> were generated. A significant enrichment was defined as having a false discovery rate (FDR)  $q \leq 0.05$ .

**In vitro B cell cultures for class-switched antibody production.** Splenic B cells were purified (90–95%) by depleting T cells using biotinylated anti-Thy1.2 monoclonal antibody followed by streptavidin-conjugated microbeads. For IgG1, B cells ( $0.5 \times 10^6$  cells ml<sup>-1</sup>) were activated with LPS or F(ab')<sub>2</sub> anti-IgM (Southern Biotechnology) and anti-CD40 (BD Pharmingen), cultured with BAFF and IL-4. For IgG2c, B cells ( $0.5 \times 10^6$  cells ml<sup>-1</sup>) were activated with LPS or anti-IgM and anti-CD40, cultured with BAFF and IFN $\gamma$ . For IgA, B cells ( $0.5 \times 10^6$  cells ml<sup>-1</sup>) were activated with LPS ( $1 \mu$ g ml<sup>-1</sup>) or anti-IgM and anti-CD40 and cultured with BAFF (10 ng ml<sup>-1</sup>), TGF $\beta$  (5 ng ml<sup>-1</sup>), IL-4 (10 ng ml<sup>-1</sup>), IL-5 (10 ng ml<sup>-1</sup>), and all-trans retinoic acid (RA) (10 nM) in IMDM medium supplemented with 10% FBS, penicillin/streptomycin, L-glutamine, and  $\beta$ -mercaptoethanol. To analyse the partitioning of cell division, purified B cells were stained with CellTrace Violet (Thermo Fisher Scientific) according to manufacturer's instruction or CFDA-SE as described previously<sup>33</sup>. Cells were cultured (4 days) at  $pO_2$  of 21%, 5% or 1%, after which surface Ig was analysed by flow cytometry. In comparisons of all three oxygen tensions, experiments were performed by dividing one common pool of B cells and using two separate hypoxia chambers maintained at constant  $pO_2$  using nitrogen.

**Measurements of RNA and proteins.** RNA was isolated using TRIzol reagent (Invitrogen). After cDNA synthesis by reverse transcription, expression of genes was analysed in duplicate samples using SYBR green PCR master-mix (Qiagen) by quantitative reverse transcriptase PCR (qRT-PCR). Data are presented as values normalized to wild-type control, and averaged over PCR normalized to levels of internal control (actin). Primer pairs and cyclor conditions are freely available on request. Proteins in whole-cell extracts were separated by SDS-PAGE, transferred onto nylon membranes (Millipore), and then incubated with rabbit antibodies against p-S6 (S235/236), p-p70S6K (S371), p-Akt (S473), p-Akt (T308), p-ACC (S79), p-AMPK (T172) (Cell Signaling Technologies), or goat anti-actin (Santa Cruz) antibodies followed by the appropriate fluorophore-conjugated, species-specific secondary anti-Ig antibodies (Rockland Immunochemicals, and LI-COR). Proteins were visualized and quantitated by laser excitation and infrared imaging (Odyssey, LI-COR). For measurements of the induction of S6K, S6 and Akt phosphorylation, purified B cells were cultured 2 days in BAFF (10 ng ml<sup>-1</sup>) and F(ab')<sub>2</sub> anti-IgM ( $1 \mu$ g ml<sup>-1</sup>), washed, rested 18 h, and then re-stimulated (15 min)

in the presence or absence of F(ab')<sub>2</sub> anti-IgM (2.5 µg ml<sup>-1</sup>). To test the effect of amino acid supply on S6K and S6 phosphorylation, B lymphoblasts were washed, cultured in complete medium overnight, then rinsed, cultured in amino acid-free RPMI1640 (US Biological) for 1 h, and re-stimulated in the presence or absence of anti-IgM, with readdition of L-leucine (Sigma) or all 20 amino acids. For the induction of p-ACC and p-AMPK, purified B cells were cultured for 2 days in LPS, BAFF and IFNγ.

**Glycolysis and oxygen consumption assays.** Purified B cells were cultured for 2 days at 37 °C at *p*O<sub>2</sub> of 21% (normoxia) or *p*O<sub>2</sub> of 1% (hypoxia) in the presence of BAFF, LPS and IFNγ. To quantify glycolysis, 1 × 10<sup>6</sup> viable cells were washed, pulsed with 10 µCi of 5-[<sup>3</sup>H]glucose in 24-well plates (37 °C, 1 h), and returned to their previous oxygen condition. Glycolytic conversion was then quantitated as described<sup>32</sup>. Oxygen consumption rates were measured using Seahorse assays. Because this instrument cannot be used in a hypoxia chamber, purified B cells (1 × 10<sup>6</sup> cell ml<sup>-1</sup>) were activated with 1 µg ml<sup>-1</sup> LPS and cultured 48 h with 10 ng ml<sup>-1</sup> BAFF in complete IMDM medium supplemented as described<sup>32</sup> in the presence or absence of 0.5 mM DMOG. After 48 h, cultured B cells were washed twice, resuspended in XF Base Media (Seahorse Bioscience) supplemented with 2 mM L-glutamine, and equal numbers of Trypan Blue-excluding B cells (1.5 × 10<sup>5</sup>) were plated on extracellular flux assay plates (Seahorse Bioscience) coated with CellTak (Corning) according to the manufacturer's protocol. Before extracellular flux analysis, B cells were rested (25 min at 37 °C, atmospheric CO<sub>2</sub>) in XF Base Media. Oxygen consumption rate (OCR) and the extracellular acidification rate (ECAR) were measured using a XF96 extracellular flux analyser (Seahorse Bioscience) before and after the sequential addition of 10 mM D-glucose, 1 µM oligomycin, and 50 mM 2-deoxyglucose.

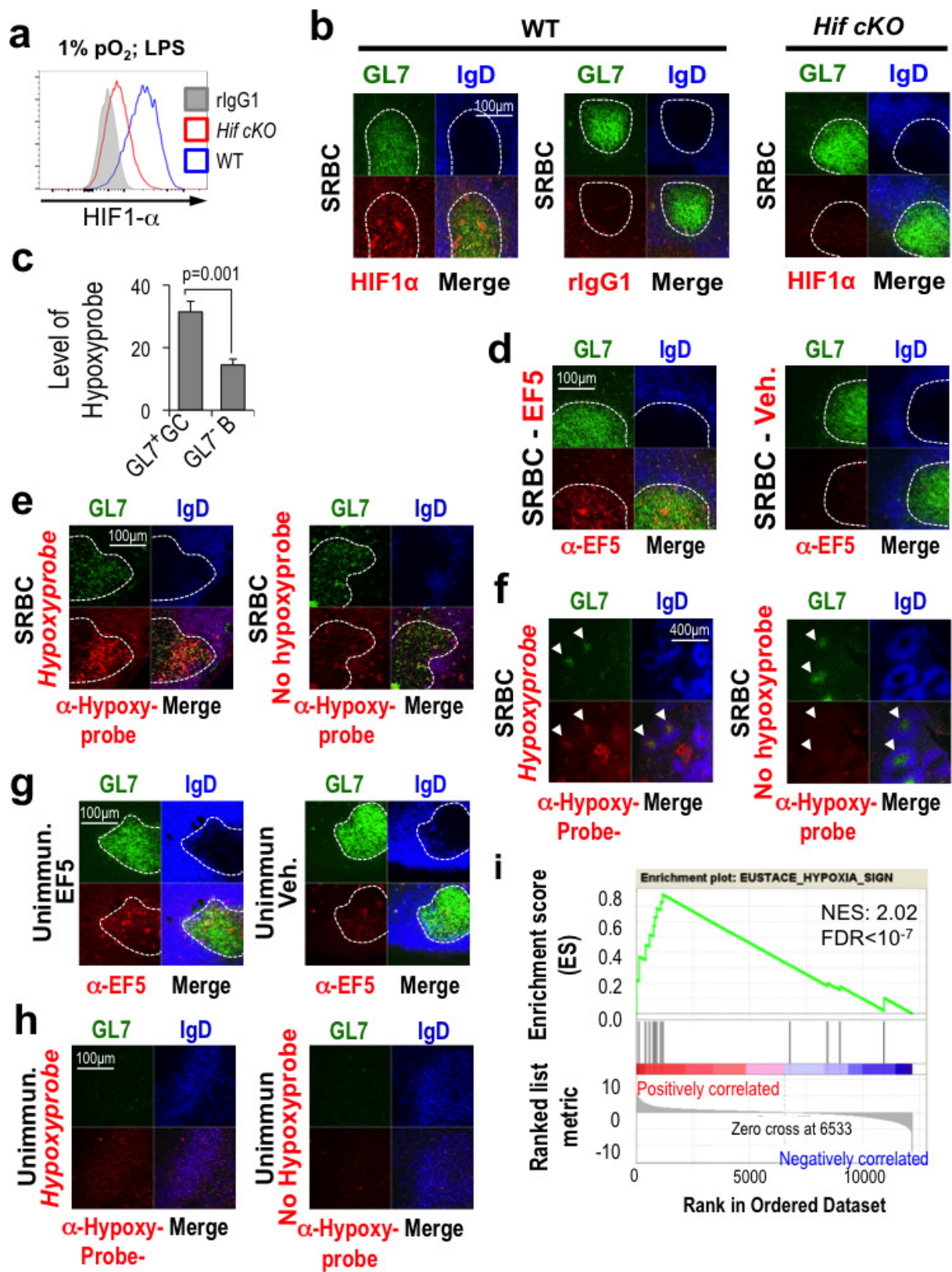
**Amino acid uptake assay.** Purified B cells were activated and cultured for 2 days with LPS and BAFF. Viable cells were washed and incubated with amino acid uptake buffer (5.4 mM KCl, 140 mM NaCl, 1.8 mM CaCl<sub>2</sub>, 0.8 mM MgSO<sub>4</sub>, 5 mM D-glucose, 25 mM HEPES, and 25 mM Tris, pH 7.5) for 30 min to deplete intracellular amino acids. Triplicate samples (1 × 10<sup>6</sup> cells per sample) were incubated with 1 µCi of L-[3, 4, 5-<sup>3</sup>H]leucine (American Radiolabelled Chemicals, Inc.) in amino acid uptake buffer for 2 min at room temperature and immediately spun through a layer of bromododecane (200 µl) into 8% sucrose/ 20% perchloric acid (25 µl). Tubes were frozen in a dry ice/ethanol bath and cut with dog nail clippers to separate the cells from unincorporated [<sup>3</sup>H]leucine. 25 µl of 10% Triton X-100 and liquid

scintillation cocktail were added and the cell-associated <sup>3</sup>H were measured by liquid scintillation counting.

**Statistical analysis.** The primary analyses were conducted on pooled data points from independent samples and replicate experiments (minimum two, generally three, biologically and temporally independent replicate experiments for all data, with multiple independent samples in the case of two biological replicates), using an unpaired two-tailed Student's *t*-test with post-test validation of its suitability. Welch's or Mann-Whitney testing were used instead of the *t*-test where indicated based on statistical analysis of the distribution of variances in the samples to be compared. Data are displayed as mean ± s.e.m., that is, 'centre values' were mean as 'average'. Results were considered statistically significant when the *P* value of for the null hypothesis of a comparison was <0.05. Since the extent or direction of difference between samples was unknown, and regulations mandate reducing the number of animals used to the lowest feasible level, no statistical methods were used to determine pre-specified sample sizes. The experiments were not randomized and the investigators were not blinded during the experiments. Corrections for multiple comparisons were not used. Statistical approaches for RNA-seq-related data are outlined in that section.

29. Liu, Q., Davidoff, O., Niss, K. & Haase, V. H. Hypoxia-inducible factor regulates hepcidin via erythropoietin-induced erythropoiesis. *J. Clin. Invest.* **122**, 4635–4644 (2012).
30. Guertin, D. A. *et al.* Ablation in mice of the mTORC components raptor, rictor, or mLST8 reveals that mTORC2 is required for signaling to Akt-FOXO and PKCα, but not S6K1. *Dev. Cell* **11**, 859–871 (2006).
31. Woods, M. L., Koch, C. J. & Lord, E. M. Detection of individual hypoxic cells in multicellular spheroids by flow cytometry using the 2-nitroimidazole, EF5, and monoclonal antibodies. *Int. J. Radiat. Oncol. Biol. Phys.* **34**, 93–101 (1996).
32. Cho, S. H. *et al.* Glycolytic rate and lymphomagenesis depend on PARP14, an ADP ribosyltransferase of the B aggressive lymphoma (BAL) family. *Proc. Natl Acad. Sci. USA* **108**, 15972–15977 (2011).
33. Cho, S. H. *et al.* B cell-intrinsic and -extrinsic regulation of antibody responses by PARP14, an intracellular (ADP-ribosyl)transferase. *J. Immunol.* **191**, 3169–3178 (2013).
34. Trapnell, C. *et al.* Differential gene and transcript expression analysis of RNA-seq experiments with TopHat and Cufflinks. *Nat. Protocols* **7**, 562–578 (2012).
35. Eustace, A. *et al.* A 26-gene hypoxia signature predicts benefit from hypoxia-modifying therapy in laryngeal cancer but not bladder cancer. *Clin. Cancer Res.* **19**, 4879–4888 (2013).

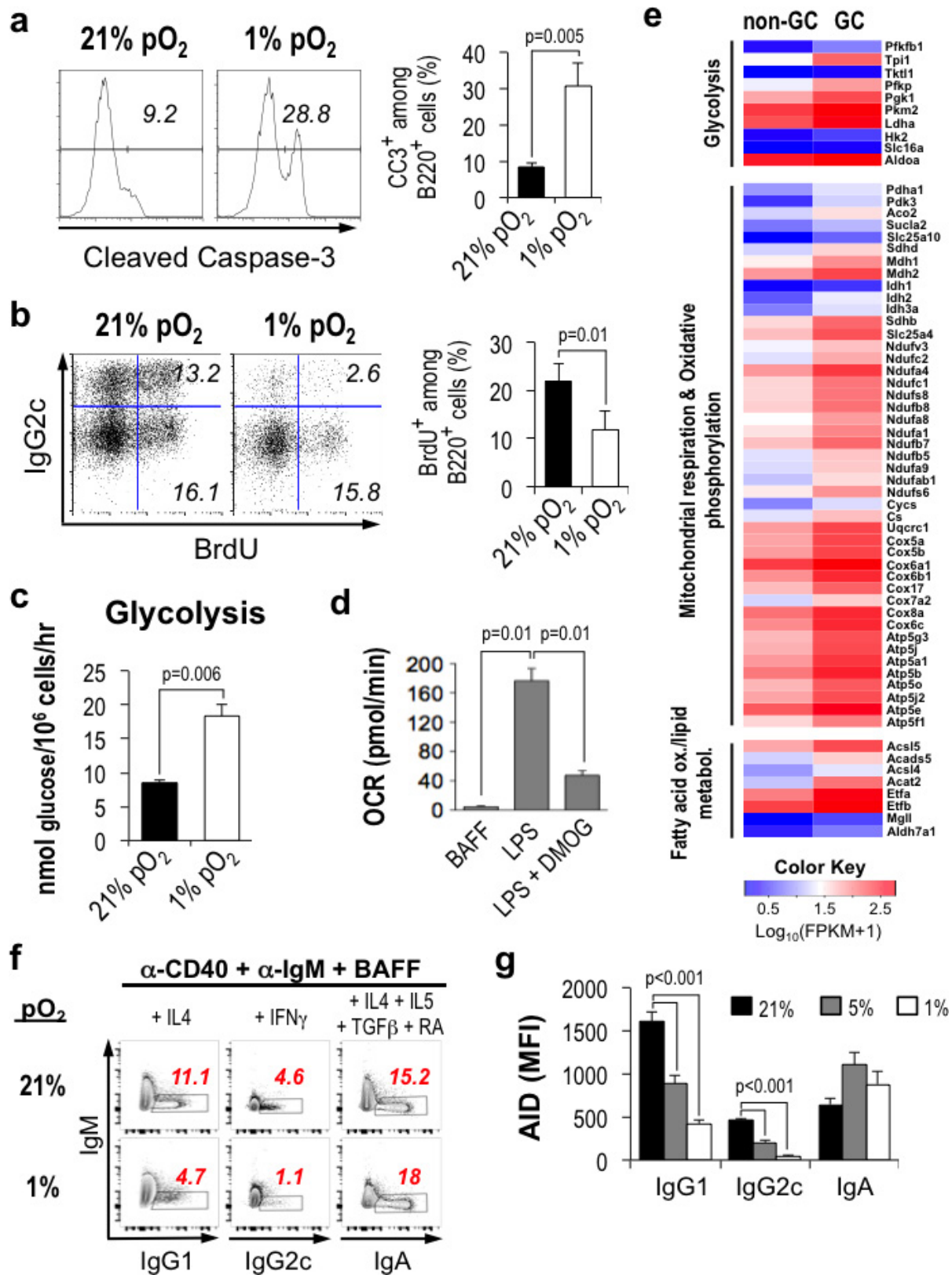




Extended Data Figure 1 | See next page for caption.

**Extended Data Figure 1 | Landscape of hypoxic cells in follicles and GCs of lymphoid organs.** **a, b**, Controls for anti-HIF-1 $\alpha$  antibody staining of GCs and portions of the surrounding splenic follicle, as in Fig. 1a, b, with fluorescent signals at the same intensity settings when analysing samples processed together, using SRBC immunization of wild-type and *Hif*-deleted mice and either anti-HIF-1 $\alpha$  sera or non-immune rabbit IgG (rIgG1), as indicated. Shown are flow cytometry results of intracellular staining performed after exposure of lymphoblasts of the indicated genotypes to 4-hydroxytamoxifen and hypoxia (**a**), and confocal images (original magnification,  $\times 40$ ) (**b**), as in Fig. 1a and b, respectively. **c**, Quantified data obtained from samples represented in Fig. 1c. Shown are the mean ( $\pm$  s.e.m.) specific fluorescence intensities of hypoxypromer (anti-pimonidazole) staining in GCs (delimited as GL7 $^{+}$ ) and GL7 $^{-}$  IgD $^{+}$  follicular B cell regions after subtracting background signal (mean fluorescence intensities in these regions after anti-pimonidazole staining of samples from PBS-injected control mice). **d**, Immunostaining of EF5-modified cells. Shown are confocal microscopic images of spleen sections from SRBC-immunized mice injected with EF5 (left) or PBS (right) 2 h before collection, followed by direct immunofluorescent staining of frozen sections with anti-GL7, anti-IgD and anti-EF5 antibodies,

representative of the quantified data presented in Fig. 1d ( $n = 7$  GC from 3 mice in biological replicate analyses). **e**, Representative images of mesenteric lymph nodes after injections and immunostaining as in Fig. 1c. **f**, Low magnification ( $\times 10$ ; panels are  $900\ \mu\text{m} \times 900\ \mu\text{m}$ ) image of anti-pimonidazole immunohistochemistry on spleen sections from SRBC-immunized mice injected with pimonidazole (left) or PBS (right) before collection. Among stained sections for both anti-pimonidazole and EF5,  $\sim 75\%$  of GC sections were unequivocally positive ( $n = 14$  sections from 4 spleens in biological replicate analyses). **g**, Representative images of Peyer's patches from non-immune, EF5-injected mice processed as in Fig. 1c ( $n = 6$  samples from 3 mice in biological replicate analyses). **h**, Representative images of spleen sections from unimmunized mice injected with hypoxypromer (left) or PBS (right) 3 h before collection, processed in parallel with sections from immunized mice injected with probe, and imaged by confocal microscopy at the same time and settings as for the sections from immunized mice (for each,  $n = 4$  sections from 2 spleens in independent biological replicates). **i**, GSEA plots comparing gene set pre-ranked by  $\log_2$ -fold change in relative expression (GL7 $^{+}$ /GL7 $^{-}$ ) in a hypoxia gene signature.



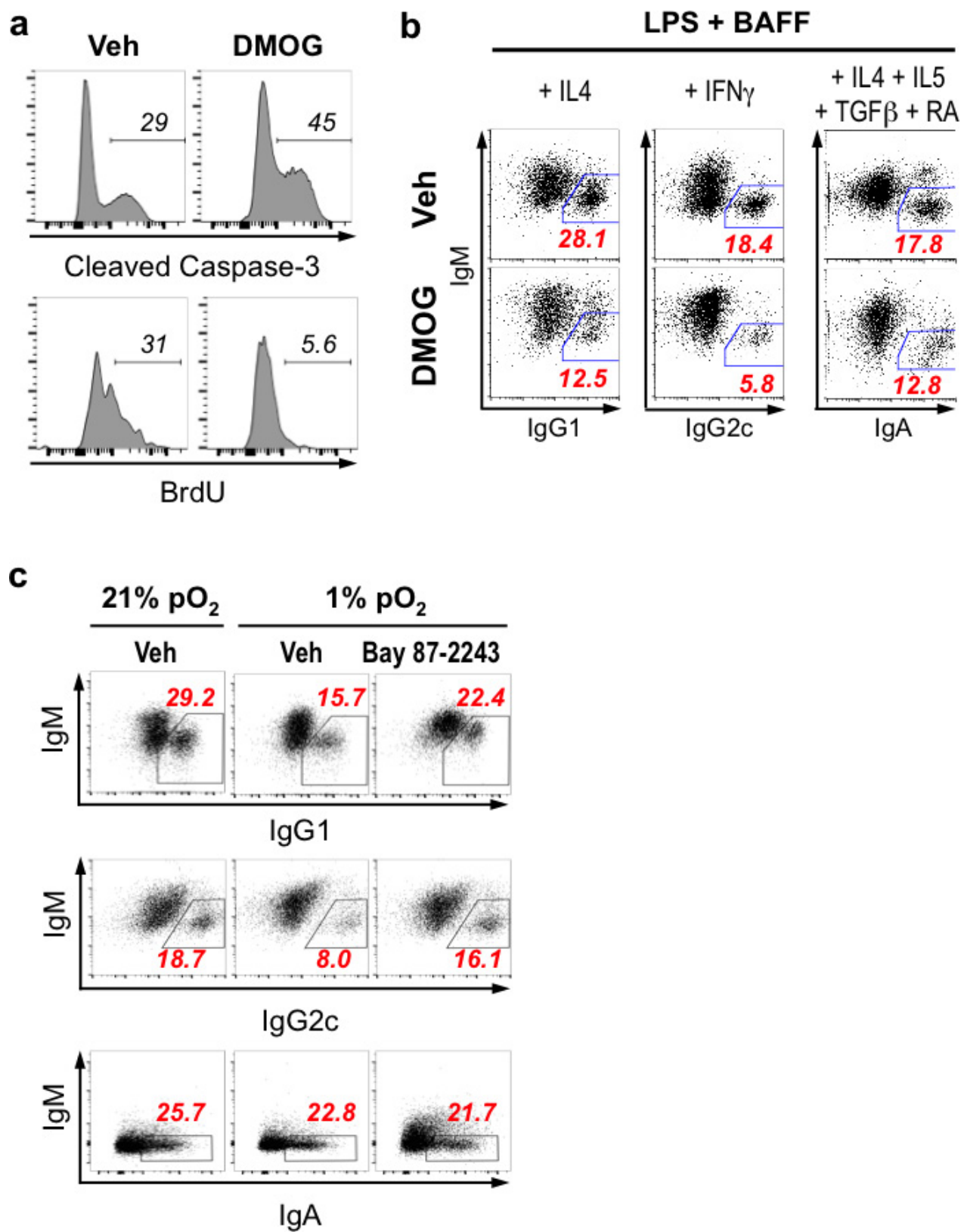
Extended Data Figure 2 | See next page for caption.



**Extended Data Figure 2 | Altered B cell survival, proliferation and metabolism in reduced  $P_{O_2}$ .**

**a**, Increased executioner caspase-3 activation in hypoxic B cells. Left, representative flow histograms of cleaved caspase-3 (CC3) in the B cell gate after activated B cells were cultured in  $P_{O_2}$  of 21% (normoxia) and 1% (hypoxia). B cells were stimulated with BAFF, LPS and  $IFN\gamma$ , cultured for 4 days at the indicated oxygen tension and processed for detection of activated caspase-3 using fluorescent-conjugated CC3 antibody. Right, quantitative data for the frequencies of B cells positive for caspase-3 cleavage in three independent replicate experiments (mean  $\pm$  s.e.m.). **b**,  $O_2$  sufficiency enhances cell cycle rates. As in **a**, but cells were pulsed with BrdU and frequencies of S-phase during the cultures are displayed in relation to IgG2c switching. Left, a representative result. Right, quantification of the overall B220<sup>+</sup> cell populations in three independent replicate experiments. B cells were cultured for 4 days with BAFF, LPS and  $IFN\gamma$  at the indicated oxygen levels, pulsed for 4 h with BrdU, and then stained with anti-IgG2c, -B220 and -BrdU antibodies after fixation, permeabilization and processing. **c**, **d**, Pools of purified wild-type B cells were stimulated with BAFF and LPS, divided and cultured for 2 days in  $P_{O_2}$  of 21% (normoxia) and 1% (hypoxia). **c**, Rates of glycolysis were measured after returning to their previous oxygen conditions, using equal numbers of surviving

B cells after culture as detailed in the Methods. Glycolysis rates were measured in three independent experiments (mean  $\pm$  s.e.m.). **d**, Inhibition of PHD activity decreases cellular respiration of B lymphoblasts. Purified B cells were activated and cultured for 2 days with LPS and BAFF in the presence or absence of DMOG (0.5 mM). The oxygen consumption rate (OCR) was measured with cultured viable B cells ( $1.5 \times 10^5$  cells) (see Methods). The OCR was measured from technical triplicates in one experiment representative of three independent replicates with similar results (mean  $\pm$  s.d.). **e**, Metabolic gene expression profile of GL7<sup>+</sup> GCB cells. Genes showing significant expression changes in GL7<sup>+</sup> GCB cells were mined for genes important for the indicated cellular processes. The heat map depicts values for the indicated genes shown as the value derived as  $\log_{10}$  of the fragments per kilobase per million (reads) after adding 1 to each value (FPKM + 1). **f**, Hypoxia limits switch to IgG among B cells activated via BCRs and CD40. As in Fig. 2a, except that the B cell preparations were activated by cross-linking their surface IgM and CD40 without addition of LPS. **g**, Quantified mean fluorescence intensities for GFP expression in the full set of replicate experiments conducted as in Fig. 2d, presented as mean ( $\pm$  s.e.m.) data for each condition of culture ( $P_{O_2}$  of 21, 5 or 1%, with cytokines and retinoic acid for Ig class switch conditions as indicated, and as for Fig. 2a, b).



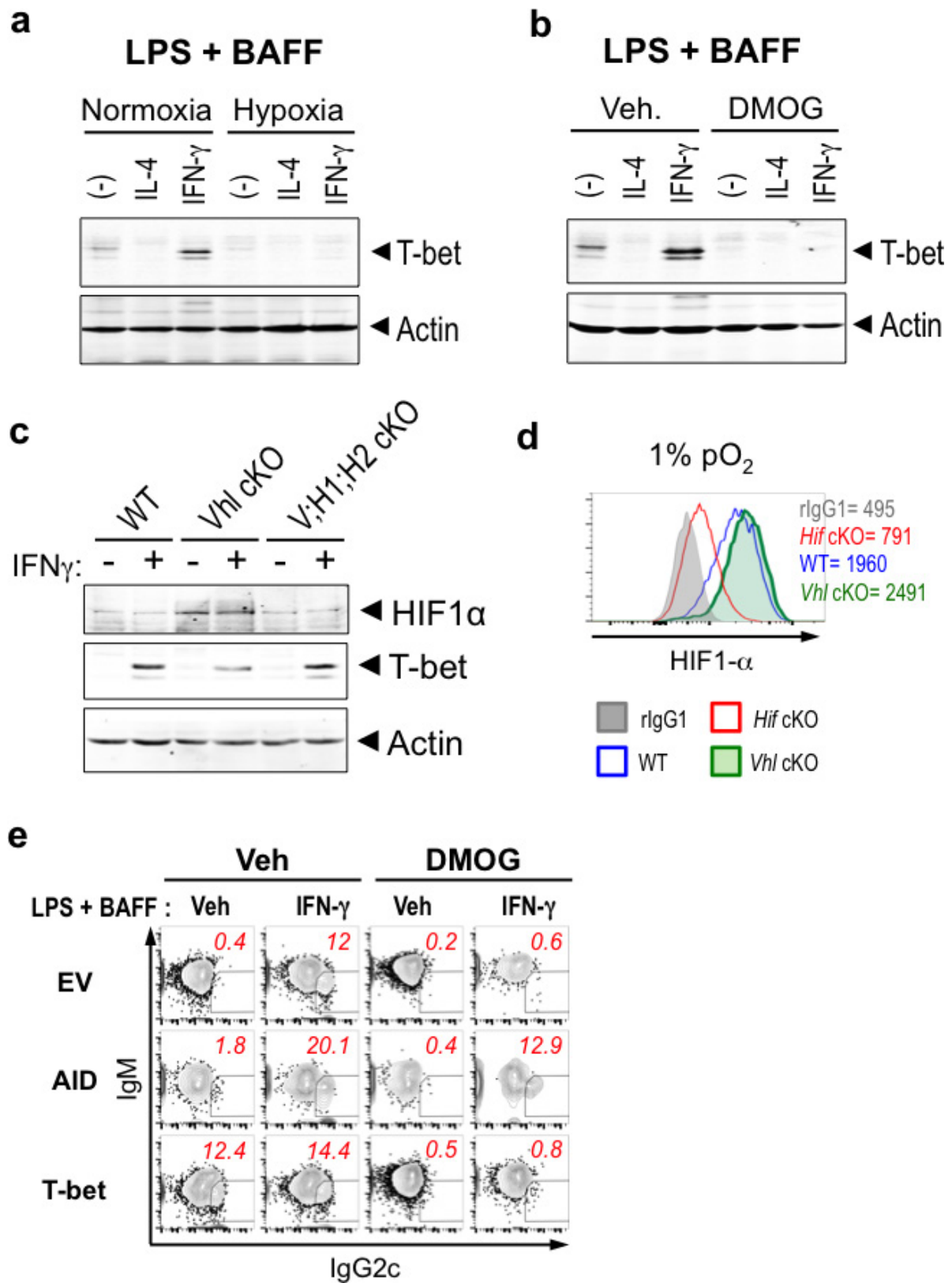
Extended Data Figure 3 | See next page for caption.

**Extended Data Figure 3 | HIF stabilization alters B cell survival, proliferation and class switched antibody level.** **a**, Purified wild-type B cells were activated and cultured for 4 days with LPS and BAFF in the presence or absence of DMOG, after which frequencies of cells with cleaved caspase 3 or BrdU uptake, as indicated, were measured as in Extended Data Fig. 2 (representative result from one experiment among  $n = 3$  independent replicate experiments). **b**, Purified wild-type B cells were activated and cultured in conditions for switching to IgG1, IgG2c and IgA, as in Fig. 2a, b, but at atmospheric (21%)  $P_{O_2}$  in the presence or absence of DMOG. The frequencies of surface IgG1, IgG2c and IgA among B220<sup>+</sup>-gated cells were measured as in Fig. 2 (see Methods). FACS plots

display the surface levels of IgG1, IgG2c and IgA on B220<sup>+</sup>-gated cells in one experiment representative of three independent replicates.

**c**, HIF inhibition impedes the hypoxia-induced alteration of antibody class switch choices. B cells were activated and cultured for 4 days with BAFF, LPS and the indicated switching conditions as in Fig. 2a (IL-4, IgG1; IFN $\gamma$ , IgG2c; retinoic acid, TGF $\beta$ , IL-4 and -5, IgA) at  $P_{O_2}$  of 21% (normoxia) or 1% (hypoxia) in the presence or absence of the HIF inhibitor Bay 87-2243. FACS plots displaying the surface levels of IgG1, IgG2c and IgA on B220<sup>+</sup>-gated cells in one representative result among three independent experiments are shown. Flow data shown in this figure were acquired on a BD FACScalibur but otherwise analysed as detailed in the Methods.

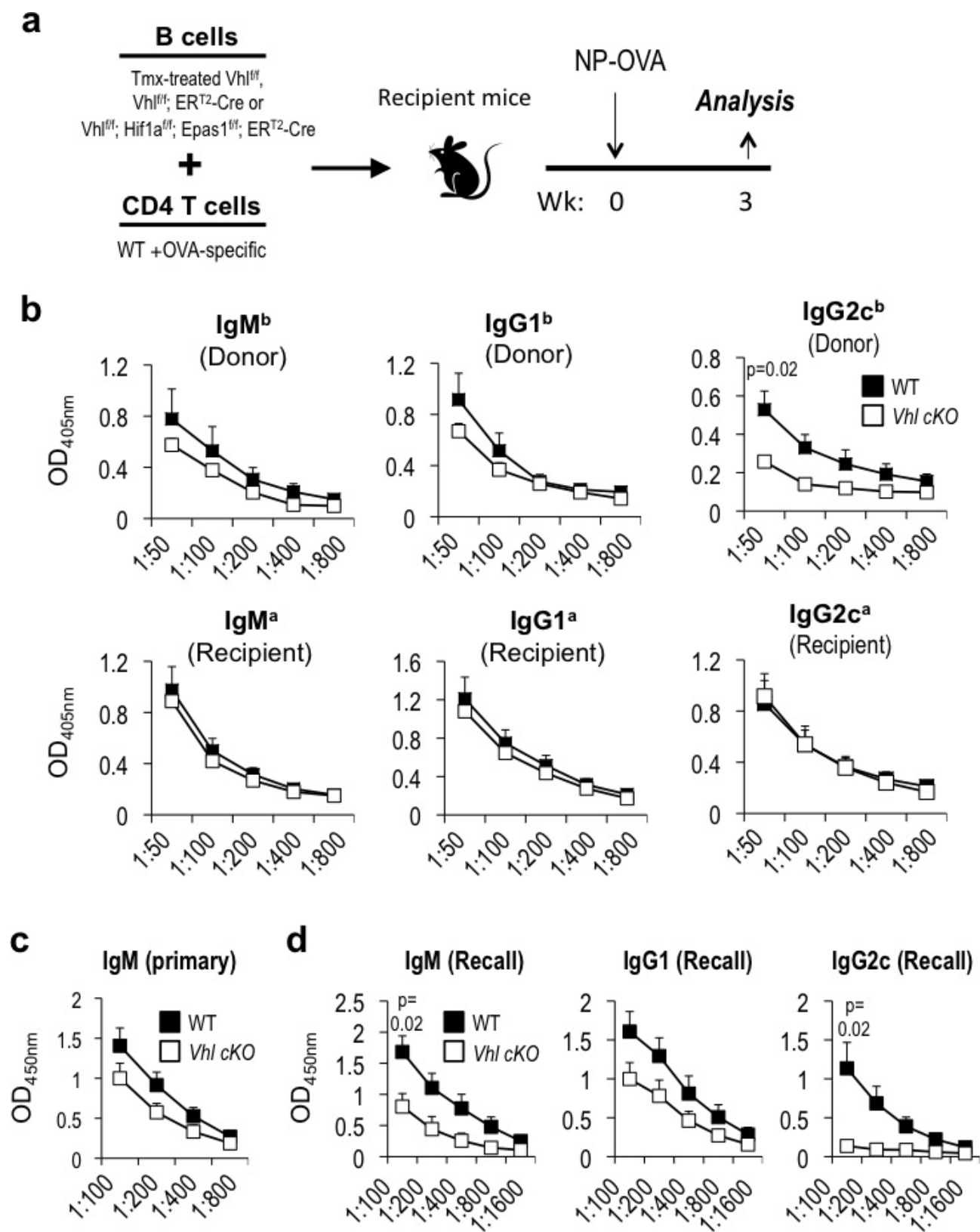




Extended Data Figure 4 | See next page for caption.

**Extended Data Figure 4 | Hypoxia and PHD inhibition repress T-bet induction.** **a, b**, B cells from wild-type mice were activated and cultured in LPS, BAFF and IL-4 or IFN $\gamma$  for 4 days under normoxic and hypoxic conditions (**a**) or cultured with and without DMOG at  $P_{O_2}$  of 21% (**b**). Shown are results of immunoblots using anti-T-bet antibody along with actin as a loading control. Shown is one representative result from three independent experiments. **c**, HIF-dependent regulation of T-bet expression by pVHL. B cells from wild-type or conditionally deleted *Vhl* $\Delta/\Delta$  and *Vhl* $\Delta/\Delta$  *Hif1* $\Delta/\Delta$  *Epas1* $\Delta/\Delta$  (*Vhl* and V;H1;H2 cKO, respectively) mice were activated and cultured for 4 days in LPS and BAFF in the presence or absence of IFN $\gamma$ , as indicated. Results of one representative immunoblot (from three independent experiments) probed for HIF-1 $\alpha$ , T-bet and actin are shown. **d**, HIF superinduction by pVHL depletion

in B cells at 1%  $P_{O_2}$ . Wild-type and B cells after conditional *Vhl*<sup>fl/f</sup> deletion were activated, cultured in 1%  $P_{O_2}$  as in Extended Data Fig. 1a, and analysed by flow cytometry after processing together for indirect immunofluorescent staining of intracellular HIF-1 $\alpha$  as in Fig. 1a and Extended Data Fig. 1a. Numbers denote the mean fluorescent intensity (MFI) of the B cells of each type. **e**, Flow cytometric data from one representative experiment as in Fig. 3e, in which B cells were transduced with MIT, MIG, MIT-T-bet or pMx-GFP-AID retrovectors, and cultured with BAFF and LPS  $\pm$  IFN $\gamma$  in the presence or absence of DMOG. The frequencies of surface IgG2c<sup>+</sup> events among B220<sup>+</sup> cells analysed 4 days after transduction are shown, with flow data from one experiment of three independent experiments.

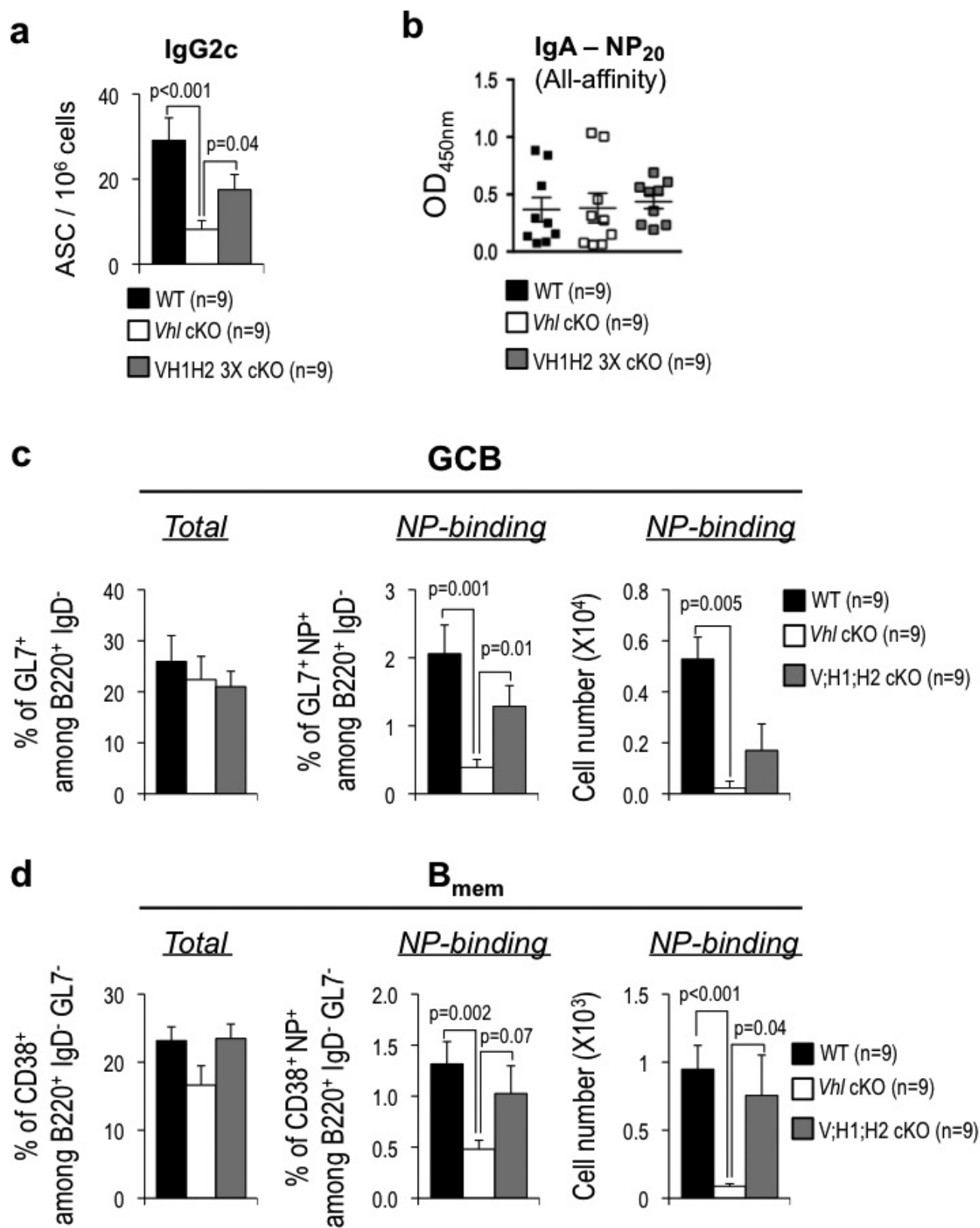


Extended Data Figure 5 | See next page for caption.



**Extended Data Figure 5 | VHL regulates antigen-specific antibody production.** **a**, Schematic outline of adoptive transfer experiments. B cells purified from tamoxifen-treated wild-type, *Vhl<sup>fl/fl</sup>*, or *Vhl<sup>fl/fl</sup>;Hif1a<sup>fl/fl</sup>;Epas1<sup>fl/fl</sup>;ER<sup>T2</sup>-Cre* mice were transferred into recipients after mixing with CD4<sup>+</sup> T cells (polyclonal:OVA-specific OT-II cells = 4:1). Recipients were analysed after primary immunization, or, for memory responses, after the primary and a recall immunization. **b**, As in Fig. 3a, except B cells from wild-type or conditionally deleted *Vhl* knockout mice were mixed with CD4<sup>+</sup> OT-II TCR transgenic T cells, transferred into Ig C<sub>H</sub> allotype-disparate (IgH<sup>a</sup>) recipient mice, followed by immunization with NP-OVA and collected 3 weeks after primary immunization. Donor- (b allotype) and recipient- (a allotype) derived NP-specific IgM and IgG1 levels in the sera were analysed by ELISA. The mean ( $\pm$  s.e.m.) absorbance data averaging independent samples ( $n = 8$  WT and  $n = 7$  *Vhl* cKO) obtained in two separate transfer experiments (measured

on the same ELISA plate) are shown. **c**, **d**, As in Fig. 3a, wild-type or *Vhl<sup>Δ/Δ</sup>* (*Vhl* cKO) B cells were mixed with wild-type CD4<sup>+</sup> T cells (polyclonal:OVA-specific OT-II cells = 4:1), and transferred into *Rag<sup>0</sup>* recipients that were then immunized with NP-OVA, and analysed for NP-specific antibody levels 3 weeks after primary immunization (**c**) or, for memory response, 9 weeks after the primary immunization and 1 week after a recall immunization (**d**) ( $n = 5$  independent recipients per genotype in two independent experiments) (**c**). Mean ( $\pm$  s.e.m.) ELISA data for all-affinity IgM anti-NP from the same samples as Fig. 3b are shown. **d**, Impaired immune memory follows interference with the B cell hypoxia response system. Terminal sera obtained from the recipient mice (Fig. 3a) 1 week after recall immunization were analysed by ELISA for all-affinity anti-NP antibodies of the indicated isotypes at the same time as the primary response samples (as in **c** and Fig. 3a).

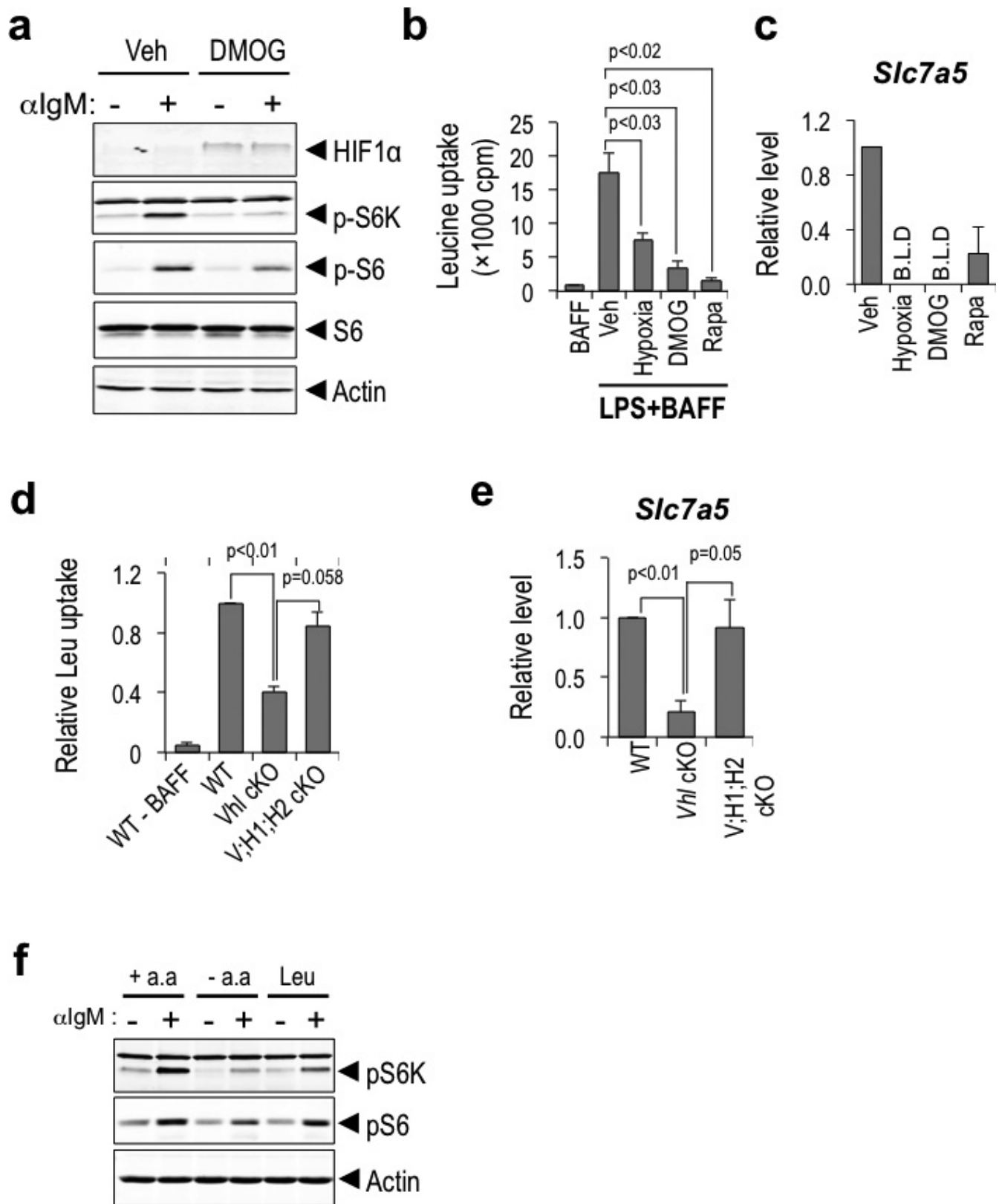


Extended Data Figure 6 | See next page for caption.

**Extended Data Figure 6 | HIF-dependent regulation of antigen-specific B cell population and antibody response by pVHL.** **a, b,** As in Fig. 3, wild-type, *Vhl*<sup>Δ/Δ</sup> (*Vhl* cKO), or *Vhl*<sup>Δ/Δ</sup> *Hifa*<sup>Δ/Δ</sup> *Epas1*<sup>Δ/Δ</sup> (V;H1;H2 cKO) B cells were mixed with wild-type CD4<sup>+</sup> T cells (polyclonal:OVA-specific OT-II cells = 4:1), transferred into *Rag*<sup>0</sup> recipients that were then immunized with NP-OVA and analysed for NP-specific antibody levels after primary immunization as in Fig. 3b, c. Using the same mice and samples as in Fig. 3b, c, cells in spleen secreting IgG2c anti-NP were quantified by ELISpot and averaged as frequencies of antibody-secreting cells (ASC) in the sample (**a**). Mean ( $\pm$  s.e.m.) frequencies for all samples ( $n = 9$  each) are shown. **b,** Anti-NP IgA levels in the sera of the samples used in Fig. 3b were quantified by ELISA. **c, d,** VHL regulation of antigen-specific GCs and memory B cells is HIF-dependent. As in Fig. 3b, c,

wild-type, *Vhl* cKO or V;H1;H2 cKO B cells were mixed with CD4<sup>+</sup> T cells (polyclonal:OVA-specific OT-II cells = 4:1), transferred into *Rag*<sup>0</sup> mice, immunized with NP-SRBC along with NP-OVA, boosted with NP-OVA at 3 weeks after primary immunization, and analysed at 1 week after the boost. Shown are the mean ( $\pm$  s.e.m.) frequencies or numbers of antigen (NP)-binding B cells of GC (IgD<sup>+</sup>GL7<sup>+</sup>) (**c**), and early memory (IgD<sup>+</sup>GL7<sup>+</sup>CD38<sup>hi</sup>) phenotypes (**d**) derived from each donor population and recovered in the recipient mice, as determined by enumeration and flow cytometric phenotyping with fluor-conjugated NP antibody. *P* values, as indicated in the figure, were derived using Welch's test for comparisons in **a**, **c** and **d**, where the variances were unequal but followed a normal (Gaussian) distribution.

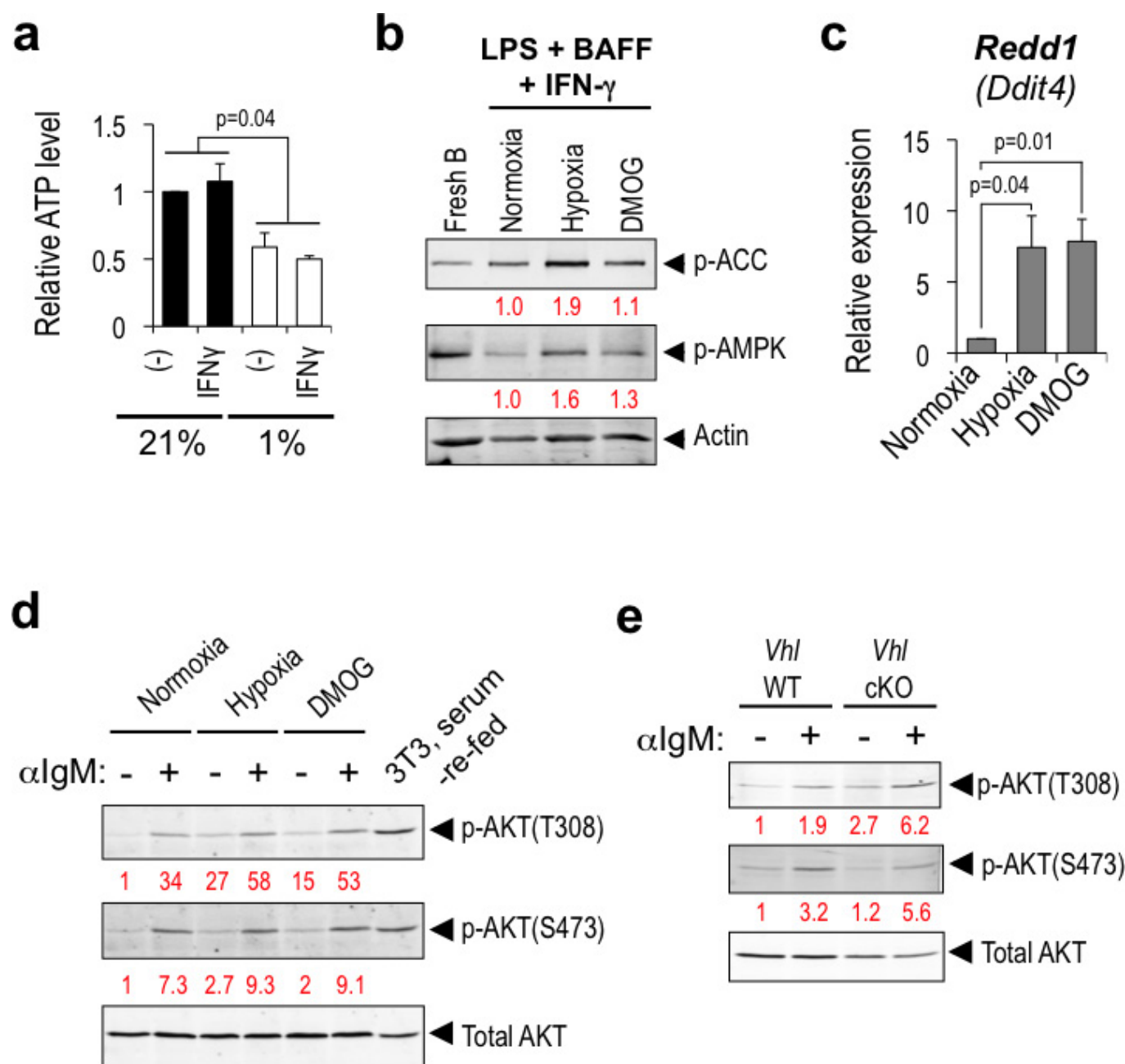




Extended Data Figure 7 | See next page for caption.

**Extended Data Figure 7 | Hypoxia interrupts impairs an activation-induced feed-forward loop in which mTORC1 increases leucine uptake by B cells.** **a**, PHD inhibition attenuates mTORC1 activity. Wild-type B cells were activated with anti-IgM and cultured for 2 days in BAFF, rested for 20 h in the presence or absence of DMOG, and then re-stimulated for 20 min with anti-IgM. Shown are immunoblots probed with anti-HIF-1 $\alpha$ , anti-p-S6K, anti-p-S6 and anti-S6 antibody along with anti-actin as a loading control. Data are the results from one representative experiment among three independent replicates. **b–f**, Hypoxia and HIF stabilization reduce leucine uptake and mTORC1 activation. **b**, **c**, Reduced leucine uptake (**b**) and *Slc7a5* mRNA encoding the large neutral amino acid transporter LAT1 (**c**) with inhibition of PHD proteins or mTOR. Wild-type cells were analysed after culture in 1% O<sub>2</sub> or at  $p_{O_2}$  of 21%, in presence of vehicle, DMOG or mTORC1 inhibitor (rapamycin) as indicated. **b**, B cell uptake of leucine, in  $n = 3$  independent experiments.

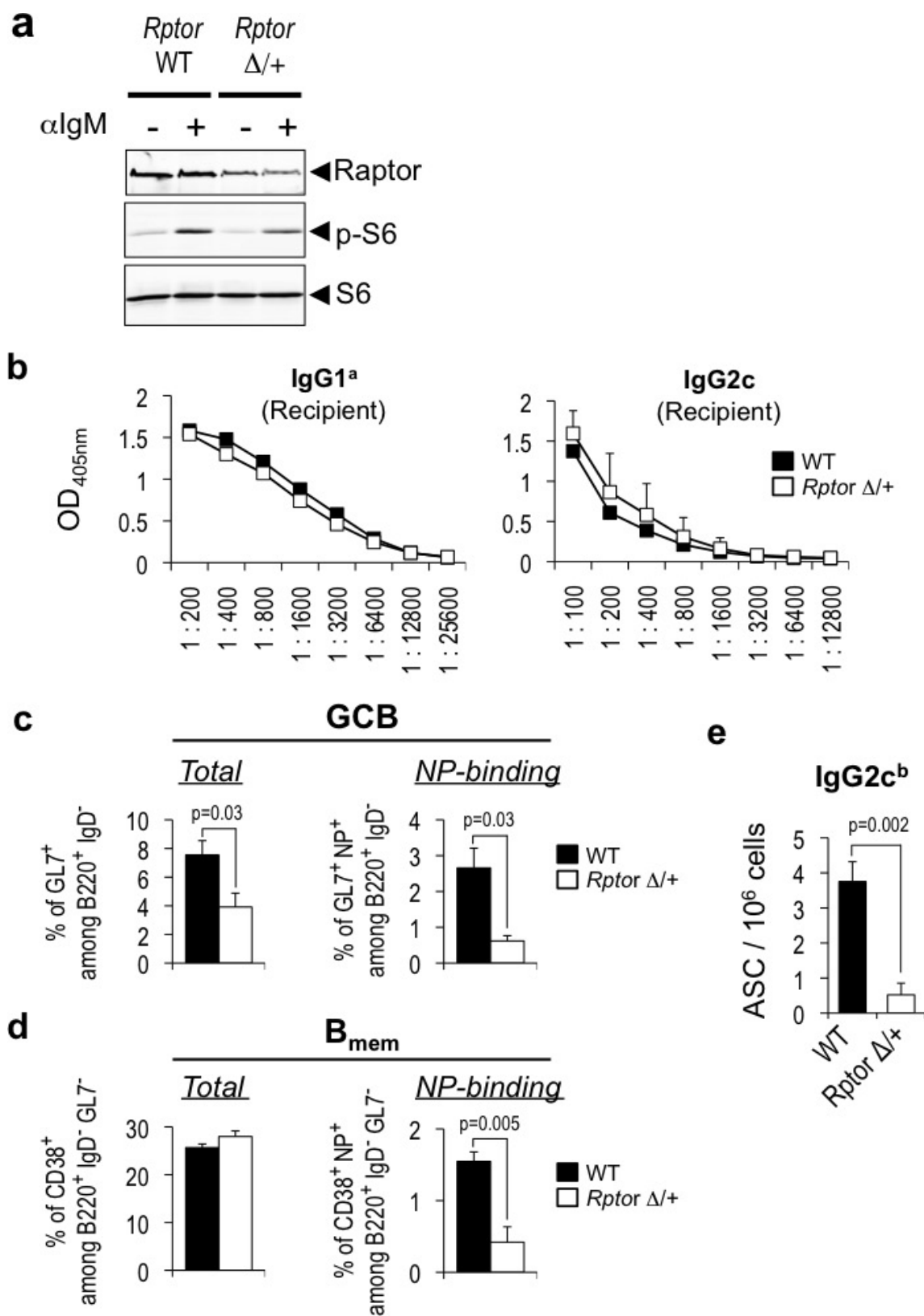
**c**, Relative mRNA level, normalized to actin ( $n = 3$  independent experiments). **d**, **e**, Activated B cells of the indicated genotypes were assayed for leucine uptake (**d**) and induction of the *Slc7a5* gene encoding a large neutral amino acid transporter (**e**). **d**, Leucine uptake by the cultured cells, normalized in each independent experiment ( $n = 3$ ) to activated wild-type cells. **e**, VHL loss leads to HIF-dependent attenuation of *Slc7a5* mRNA levels. Wild-type or conditional knockout B cells of the indicated genotypes were activated and cultured at 21% O<sub>2</sub> as in Fig. 3d. qPCR results normalized first to actin for level within a sample, and then to the wild-type control in each independent experiment ( $n = 3$ ). **f**, Leucine stimulates mTORC1 activity in activated B cells. Activated wild-type B cells, divided and cultured overnight in medium lacking or sufficient for the indicated amino acid, were restimulated and analysed as in Fig. 4a, b. Data are mean  $\pm$  s.e.m.



**Extended Data Figure 8 | Hypoxia promotes AMPK activity and induction of the mTORC1 inhibitor REDD1 without repressing mTORC2.** **a**, B cells were activated and grown for 2 days in LPS and BAFF at the indicated  $P_{O_2}$  and in the presence or absence of IFN $\gamma$  as indicated. ATP concentrations in equal numbers of cells were then assayed. In each of three replicate experiments with similar results, the [ATP] measured for cells at conventional (21%)  $P_{O_2}$  without IFN $\gamma$  was set as 1, and the mean ( $\pm$  s.e.m.) levels in each sample relative to this reference are shown for three biological replicates. **b**, Immunoblot results after probing membranes with anti-p-ACC, anti-p-AMPK (T172) and actin are shown for one representative experiment. Numbers indicate the level of signal for cells cultured in hypoxia or DMOG as compared to the reference value of the sample cultured in conventional (21%)  $P_{O_2}$ , after normalization of each sample according to its loading. **c**, Results of a representative qRT-PCR experiment measuring *Redd1* mRNA in wild-type B cells (activated and

cultured as in **b**), with each sample first normalized to *Actb* mRNA and then to vehicle-treated cells. **d**, **e**, Effect of VHL, hypoxia and DMOG on Akt phosphorylation in B cells. **d**, B cells were activated with anti-IgM and BAFF, cultured for 2 days and rested for 20 h under conditions of hypoxia or normoxia in the presence or absence of DMOG, after which cells were re-stimulated (20 min) with anti-IgM. **e**, As in **d**, B cells from wild-type or conditionally deleted *Vhl* knockout mice were activated with anti-IgM in the presence of BAFF, cultured for 2 days and rested for 20 h, after which cells were re-stimulated (20 min) with anti-IgM. Shown are results of immunoblots probed with antibodies directed against p-Akt (T308), p-Akt (S473), and Akt. Numbers show the quantification of signal relative to B cells that were not restimulated, after adjustment of each sample for loading as determined by total Akt. Data shown are from one representative experiment among three independent replicates.

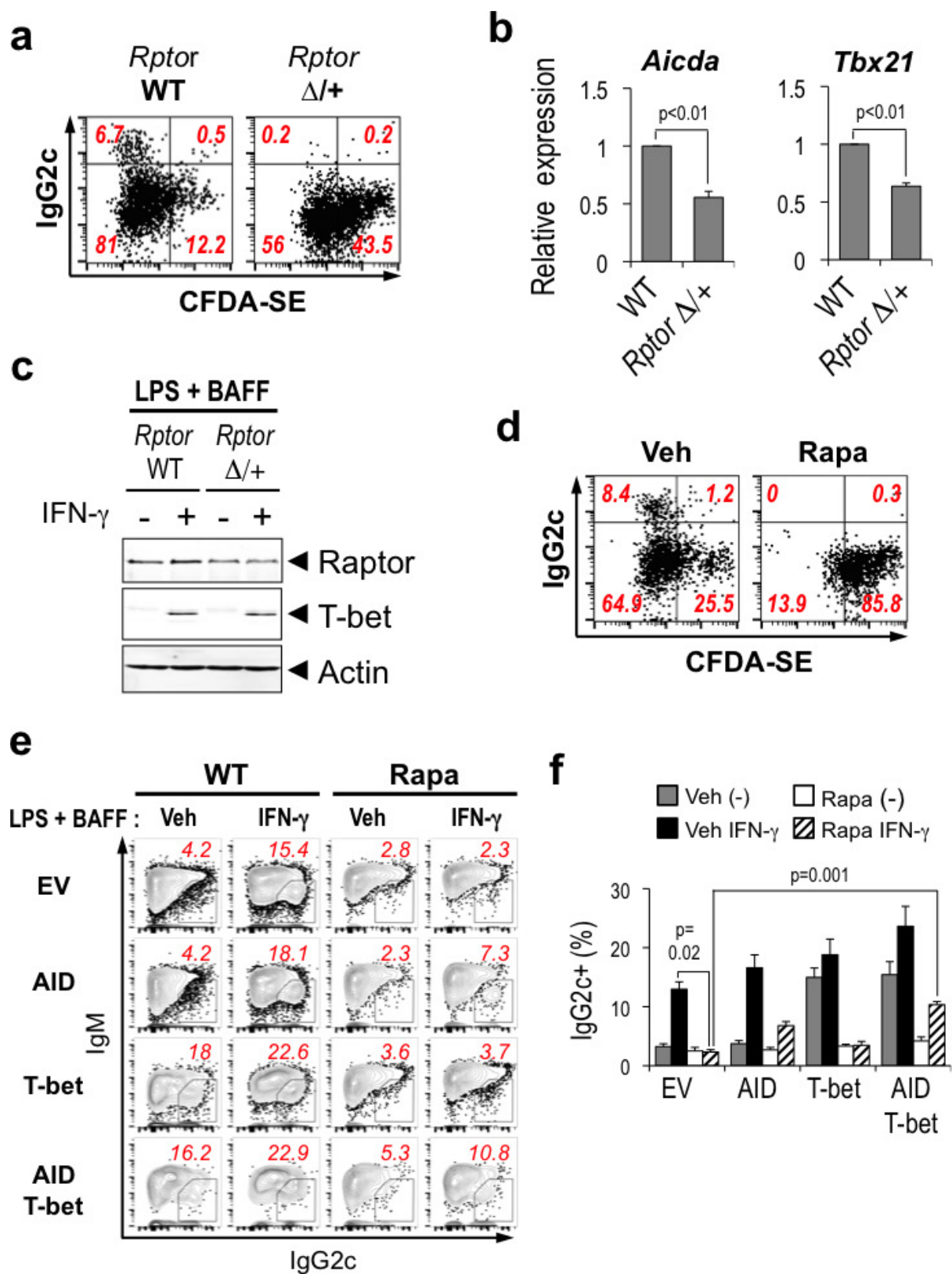




Extended Data Figure 9 | See next page for caption.

**Extended Data Figure 9 | mTORC1 regulates expansion of antigen-specific B cells and antibody class spectrum.** **a**, Results of immunoblots using anti-raptor and anti-p-S6 antibodies, with anti-S6 antibody as a loading control. B cells (wild-type or haploinsufficient for raptor) were activated with F(ab')<sub>2</sub> anti-IgM and BAFF, cultured for 2 days and rested for 20 h, after which cells were re-stimulated for 20 min with F(ab')<sub>2</sub> anti-IgM. Data shown are from one representative experiment among three independent replicates. **b**, Recipient antibody controls for effect of mTORC1 on class-switched antibody responses. As in Fig. 4c, wild-type or raptor-haploinsufficient B cells (from heterozygous mice that were *Rosa26;ER<sup>T2</sup>-Cre*, *Rptor<sup>fl/+</sup>* and converted to *Rptor<sup>+/-</sup>* by tamoxifen injections) were mixed with CD4<sup>+</sup> OT-II TCR transgenic T cells, transferred into Ig C<sub>H</sub> allotype-disparate recipient mice, immunized with NP-OVA, and obtained 3 weeks after primary immunization. Donor-derived (b allotype) (in Fig. 4) or recipient-derived (a allotype) NP-specific

IgG1 and IgG2c levels in the sera were analysed by ELISA. Absorbance data averaging samples ( $n = 9$  WT versus  $n = 8$  *Rptor<sup>+/-</sup>*) obtained in three separate experiments (measured on the same ELISA plate). **c–e**, Wild-type or *Rptor<sup>+/-</sup>* B cells were mixed with CD4<sup>+</sup> T cells (polyclonal:OVA-specific OT-II = 4:1) and transferred into *Rag<sup>0</sup>* mice and immunized with NP-OVA. Shown are the recoveries of antigen (NP)-binding wild-type versus *Rptor<sup>+/-</sup>* B cells of GC (B220<sup>+</sup> GL7<sup>+</sup> IgD<sup>-</sup>) (**c**) and early memory (B220<sup>+</sup> CD38<sup>+</sup> GL7<sup>-</sup> IgD<sup>-</sup>) (**d**) phenotypes. **e**, Generation of antigen-specific IgG2c-secreting cells depends on mTORC1. Mean ( $\pm$  s.e.m.) results of ELISpot assays quantitating NP-binding IgG2c (b allotype) antibody-secreting cells from the experiments in **b** and Fig. 4c, d, quantified as described in Extended Data Fig. 6a. *P* values were derived using Welch's test for comparisons in **c–e**, in which the variances were unequal but followed a normal (Gaussian) distribution.



Extended Data Figure 10 | See next page for caption.



**Extended Data Figure 10 | mTORC1 is rate-limiting for AID expression and switching to IgG2c.** **a**, A division-independent mechanism dependent on mTORC1 quantity in B cell switching to IgG2c. Flow cytometric data in the B cell gate, displaying carboxyfluorescein diacetate succinimidyl ester (CFDA-SE) partitioning (fluorescein emission intensities) versus IgG2c, were from one experiment representative of three independent biological replicates. Wild-type or *Rptor*<sup>+/Δ</sup> B cells were stained with CFSE and cultured with LPS, BAFF and IFN $\gamma$ , and analysed by flow cytometry. **b**, Wild-type or *Rptor*<sup>+/Δ</sup> B cells were cultured for 2 days with LPS, BAFF and IFN $\gamma$ . mRNA levels of the *Aidca* (left) and *Tbx21* (right) genes measured in three independent replicate experiments by qRT-PCR normalized to actin in the sample and then to the level in wild-type cells (set as relative level of 1). **c**, Immunoblots probed for raptor, T-bet

and actin, as indicated, using B cells as in **b** (representative of  $n = 3$  independent experiments). **d**, mTOR promotes switching to IgG by division-independent mechanisms. As in **a**, but CFSE-stained wild-type B cells were activated and cultured for 4 days with LPS, BAFF and IFN $\gamma$  in the presence or absence of rapamycin versus vehicle. **e**, **f**, mTORC1 regulation of AID level in collaboration with T-bet determines efficient switching to IgG2c. B cells were transduced with MIT, MIG, MIT-T-bet or pMx-GFP-AID retrovectors, and cultured with BAFF and LPS and/or IFN $\gamma$  in the presence or absence of rapamycin (5 nM). **e**, Representative flow data, from one experiment among three independent replicates, derived as in Extended Data Fig. 4e. **f**, Frequencies of surface IgG2c<sup>+</sup> events among B220<sup>+</sup> cells analysed 4 days after transduction are shown ( $n = 3$  independent experiments). Data are mean  $\pm$  s.e.m.

# The long non-coding RNA *Morrbid* regulates *Bim* and short-lived myeloid cell lifespan

Jonathan J. Kotzin<sup>1,2\*</sup>, Sean P. Spencer<sup>1,2\*†</sup>, Sam J. McCright<sup>1,2</sup>, Dinesh B. Uthaya Kumar<sup>3,4</sup>, Magalie A. Collet<sup>3</sup>, Walter K. Mowle<sup>1,2</sup>, Ellen N. Elliott<sup>3</sup>, Asli Uyar<sup>3</sup>, Michelle A. Makiya<sup>5</sup>, Margaret C. Dunagin<sup>6</sup>, Christian C. D. Harman<sup>7,8</sup>, Anthony T. Virtue<sup>1,2</sup>, Stella Zhu<sup>3</sup>, Will Bailis<sup>7</sup>, Judith Stein<sup>7,8</sup>, Cynthia Hughes<sup>7,8</sup>, Arjun Raj<sup>6</sup>, E. John Wherry<sup>2,9</sup>, Loyal A. Goff<sup>10,11</sup>, Amy D. Klion<sup>5</sup>, John L. Rinn<sup>12,13</sup>, Adam Williams<sup>3,4</sup>, Richard A. Flavell<sup>7,8</sup> & Jorge Henao-Mejia<sup>1,2,14</sup>

Neutrophils, eosinophils and 'classical' monocytes collectively account for about 70% of human blood leukocytes and are among the shortest-lived cells in the body<sup>1,2</sup>. Precise regulation of the lifespan of these myeloid cells is critical to maintain protective immune responses and minimize the deleterious consequences of prolonged inflammation<sup>1,2</sup>. However, how the lifespan of these cells is strictly controlled remains largely unknown. Here we identify a long non-coding RNA that we termed *Morrbid*, which tightly controls the survival of neutrophils, eosinophils and classical monocytes in response to pro-survival cytokines in mice. To control the lifespan of these cells, *Morrbid* regulates the transcription of the neighbouring pro-apoptotic gene, *Bcl2l1* (also known as *Bim*), by promoting the enrichment of the PRC2 complex at the *Bcl2l1* promoter to maintain this gene in a poised state. Notably, *Morrbid* regulates this process in *cis*, enabling allele-specific control of *Bcl2l1* transcription. Thus, in these highly inflammatory cells, changes in *Morrbid* levels provide a locus-specific regulatory mechanism that allows rapid control of apoptosis in response to extracellular pro-survival signals. As *MORRBID* is present in humans and dysregulated in individuals with hypereosinophilic syndrome, this long non-coding RNA may represent a potential therapeutic target for inflammatory disorders characterized by aberrant short-lived myeloid cell lifespan.

Neutrophils, eosinophils and 'classical' monocytes represent a first line of defense against nearly all pathogens<sup>1,2</sup>. However, these short-lived myeloid cells also contribute to the development of several inflammatory diseases<sup>1,2</sup>. Cytokines and metabolites tightly regulate the function and lifespan of these cells, but how these cues are translated into an optimal cellular lifespan is largely unknown. Emerging evidence indicates that certain long non-coding RNAs (lncRNAs) can integrate extracellular inputs with chromatin-modification pathways allowing cells to rapidly adapt to their environment<sup>3,4</sup>. As such, we investigated whether lncRNAs control the function or lifespan of short-lived myeloid cells in response to extracellular cues. We first analysed multiple RNA sequencing (RNA-seq) datasets for mouse lncRNAs that are preferentially expressed by mature short-lived myeloid cells<sup>5,6</sup>. We identified an uncharacterized lncRNA (*Gm14005*) that we termed *Morrbid* (myeloid RNA regulator of Bim-induced death). *Morrbid* is conserved across species, contains five exons, is poly-adenylated and is localized predominately to the nucleus bound to chromatin (Fig. 1a, b, Extended Data Fig. 1a–d). Importantly, *Morrbid* is highly and specifically

expressed by mature eosinophils, neutrophils and classical monocytes in both mice and humans (Fig. 1c, d, Extended Data Fig. 1e, f).

To investigate the role of *Morrbid* *in vivo*, we deleted the *Morrbid* locus to generate *Morrbid*-deficient mice (Extended Data Fig. 1g). Notably, and in accordance with the expression profile of *Morrbid*, we found that eosinophils, neutrophils and Ly6C<sup>hi</sup> classical monocytes were markedly reduced in the blood and tissues of these mice (Fig. 1e, Extended Data Fig. 1h, i). This defect was highly specific to these three cell types, as well as blood Ly6C<sup>lo</sup> monocytes (Extended Data Fig. 2a), which are suggested to be progeny of Ly6C<sup>hi</sup> monocytes<sup>7</sup>. All other lymphoid and myeloid cell types were unaffected (Extended Data Fig. 1i, 2a). Similarly, knockdown of *Morrbid* *in vivo* also led to a specific reduction in the frequency of short-lived myeloid cells in blood and spleen (Extended Data Fig. 2b–e). Finally, as these cells have a critical role in protective immunity and in the development of immunopathology, we found that *Morrbid*-deficient mice were highly susceptible to bacterial (*Listeria monocytogenes*) infection (Fig. 1f, g), and protected from eosinophil-driven allergic lung inflammation (Extended Data Fig. 2f–h). Altogether, these results support an important and selective role for *Morrbid* and potentially DNA elements within its locus in short-lived myeloid cell homeostasis.

Eosinophils, neutrophils and Ly6C<sup>hi</sup> monocytes originate from common progenitors in the bone marrow (BM)<sup>1,8</sup>, with extracellular cues driving the developmental programs needed to produce each of these cell types<sup>1,8</sup>. Using mixed BM chimaeras, we found that *Morrbid*-deficient BM cells have a significant defect in the generation of short-lived myeloid cells (Extended Data Fig. 3a–e), indicating that *Morrbid* acts in a cell-intrinsic manner. We next sought to determine whether *Morrbid* regulates short-lived myeloid cell development. Early progenitors of each of these cell types express low levels of *Morrbid* and its expression increases throughout development to reach maximal levels in fully mature eosinophils, neutrophils and Ly6C<sup>hi</sup> monocytes (Extended Data Fig. 3f–h). In accordance with this pattern of expression, the progenitors of each of these cell types were intact in *Morrbid*-deficient mice (Fig. 2a, Extended Data Fig. 3g–h). These results suggest that *Morrbid* regulates the frequency of mature eosinophils, neutrophils and monocytes, but not their progenitors.

Mature populations of myeloid cells are controlled by several mechanisms, including homeostatic proliferation, trafficking, and cell death. We found no defects in homeostatic proliferation in *Morrbid*-deficient mice (Extended Data Fig. 4a). Mature short-lived myeloid cells are

<sup>1</sup>Department of Pathology and Laboratory Medicine, University of Pennsylvania, Philadelphia, Pennsylvania 19104, USA. <sup>2</sup>Institute for Immunology, Perelman School of Medicine, University of Pennsylvania, Philadelphia, Pennsylvania 19104, USA. <sup>3</sup>The Jackson Laboratory for Genomic Medicine, Farmington, Connecticut 06032, USA. <sup>4</sup>Department of Genetics and Genomic Sciences, University of Connecticut Health Center, Farmington, Connecticut 06032, USA. <sup>5</sup>Laboratory of Parasitic Diseases, National Institute of Allergy and Infectious Diseases, National Institutes of Health, Bethesda, Maryland 20892, USA. <sup>6</sup>Department of Bioengineering, University of Pennsylvania, Philadelphia, Pennsylvania 19104, USA. <sup>7</sup>Department of Immunobiology, Yale University School of Medicine, New Haven, Connecticut 06520, USA. <sup>8</sup>Howard Hughes Medical Institute, Yale University, New Haven, Connecticut 06510, USA. <sup>9</sup>Department of Microbiology, Perelman School of Medicine, University of Pennsylvania, Philadelphia, Pennsylvania 19104, USA. <sup>10</sup>McKusick-Nathans Institute of Genetic Medicine, Johns Hopkins University, Baltimore, Maryland 21205, USA. <sup>11</sup>Department of Neuroscience, Johns Hopkins University, Baltimore, Maryland 21205, USA. <sup>12</sup>Biological and Biomedical Sciences, Harvard Medical School, Boston, Massachusetts 02115, USA. <sup>13</sup>Department of Stem Cell and Regenerative Biology, Harvard University, Cambridge, Massachusetts 02138, USA. <sup>14</sup>Division of Transplant Immunology, The Children's Hospital of Philadelphia, Philadelphia, Pennsylvania 19104, USA. <sup>†</sup>Present address: Department of Medicine, Massachusetts General Hospital, 55 Fruit St, Boston, Massachusetts 02114, USA.

\*These authors contributed equally to this work.

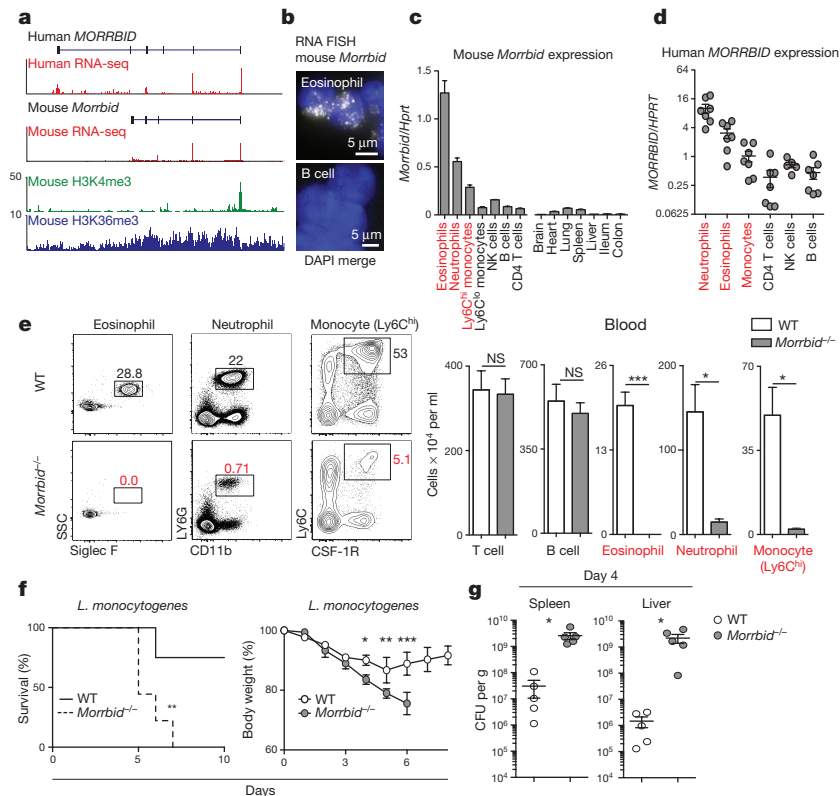


**Figure 1 | IncRNA *Morbid* is a critical regulator of eosinophils, neutrophils and Ly6C<sup>hi</sup> monocytes.** **a**, Human neutrophil and mouse granulocyte normalized RNA-seq and ChIP-seq tracks at the *Morbid* locus. **b**, Single molecule *Morbid* RNA fluorescence *in situ* hybridization (FISH). **c**, **d**, qPCR expression of mouse ( $n = 3$ ; representative of 3 independent experiments) (**c**) and human *Morbid* in indicated cell types and tissues ( $n = 7$ ) (**d**). **e**, Wild-type and *Morbid*-deficient flow cytometry

plots and absolute counts ( $n = 3$ –5; representative of 7 independent experiments). **f**, **g**, *L. monocytogenes* infection of wild-type and *Morbid*-deficient mice. **f**, Survival and weight loss ( $n = 9$ , representative of 3 independent experiments). **g**, Colony-forming units (CFUs) per g from indicated organs ( $n = 5$ ; representative of 3 independent experiments). Error bars show s.e.m. \* $P < 0.05$ , \*\* $P < 0.01$ , and \*\*\* $P < 0.001$  (two-sided *t*-test, **e**, **g**, **f** (right); Mantel–Cox test, **f** (left)).

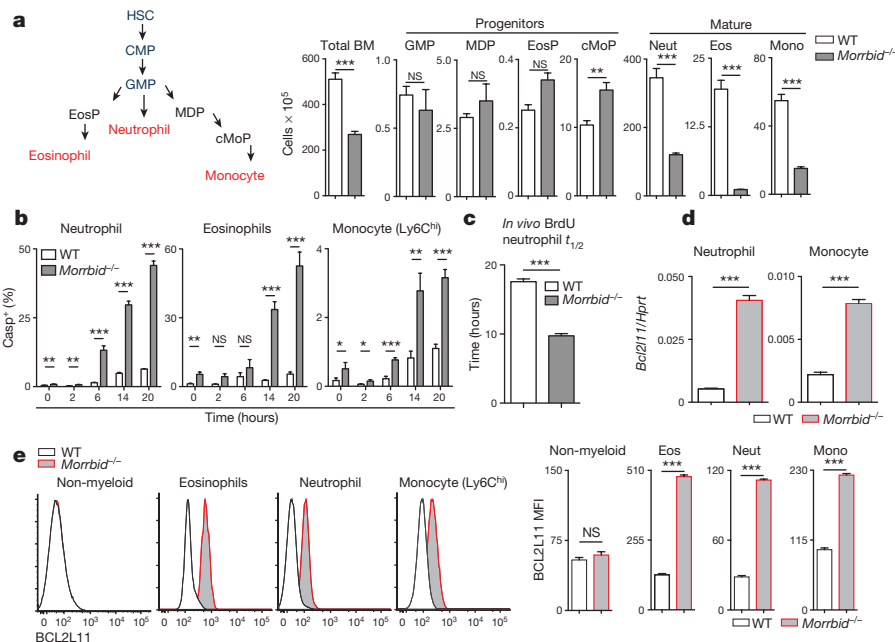


**Figure 2 | *Morbid* controls eosinophil, neutrophil and Ly6C<sup>hi</sup> monocyte lifespan.** **a**, Schematic of short-lived myeloid cell development and absolute numbers of the indicated cell types in BM from wild-type and *Morbid*-deficient mice ( $n = 3$ –5; representative of 3 independent experiments). **b**, Frequency of Casp<sup>+</sup> (Z-VAD-FMK<sup>+</sup>) cultured BM cells ( $n = 3$  mice; representative of 2 independent experiments). **c**, Half-life of BrdU pulse-labelled neutrophils in blood *in vivo* ( $n = 4$

mice; representative of 3 independent experiments). **d**, *Bcl2l1* qPCR expression in indicated cell types sorted from BM ( $n = 3$ ; representative of 2 independent experiments). **e**, BCL2L1 protein expression assessed by flow cytometry in indicated BM cell types. Left, representative histograms. Right, mean fluorescence intensity (MFI) quantification ( $n = 3$ –5 mice, representative of 3 independent experiments). Error bars show s.e.m. \* $P < 0.05$ , \*\* $P < 0.01$  and \*\*\* $P < 0.001$  (two-sided *t*-test).



substantially reduced in the BM of *Morrbid*-deficient mice and there was a near absence of *in vitro* BM-differentiated eosinophils<sup>9</sup> (Fig. 2a, Extended Data Fig. 4b, c), suggesting that *Morrbid* controls a dominant process independent of cell trafficking. Notably, *Morrbid*-deficient eosinophils, neutrophils and Ly6C<sup>hi</sup> monocytes were all highly prone to apoptosis in BM cultured *ex vivo* (Fig. 2b, Extended Data Fig. 4d). Furthermore, we observed significantly increased apoptosis *in vitro* in BM-derived eosinophils (Extended Data Fig. 4e), and *in vivo* during *L. monocytogenes* infection in the absence of *Morrbid* (Extended Data Fig. 4f). Given the close relationship between apoptosis and cellular lifespan, we hypothesized that *Morrbid* is a regulator of short-lived myeloid cell half-life. Using BrdU to label circulating neutrophils and determine their decay rate, we observed an ~2-fold decrease in the half-life of these cells (Fig. 2c, Extended Data Fig. 4g). These results indicate that *Morrbid* regulates short-lived myeloid cell lifespan through control of apoptosis.

Some lncRNAs regulate the expression of neighbouring genes<sup>10–13</sup>. The pro-apoptotic gene *Bcl2l1* (*Bim*) is located ~150-kb downstream of *Morrbid* (Extended Data Fig. 1a). *Bcl2l1* has been shown to be an important regulator of myeloid homeostasis<sup>14,15</sup>. Thus, we reasoned that *Morrbid* regulates short-lived myeloid cell lifespan through its control of *Bcl2l1* expression. Indeed, the protein and mRNA levels of *Bcl2l1* were markedly elevated in eosinophils, neutrophils and Ly6C<sup>hi</sup> monocytes from *Morrbid*-deficient mice (Fig. 2d, e, Extended Data Fig. 4h–k). In concordance with the pattern of *Morrbid* expression, *Bcl2l1* was maximally elevated in the mature state of each of these cell lineages in *Morrbid*-deficient mice (Extended Data Fig. 4l), and was not dysregulated in other myeloid and lymphoid cell populations (Extended Data Fig. 4m). Importantly, key myeloid lineage transcription factors and other genes neighbouring *Morrbid* were largely unaffected in the absence of *Morrbid* (Extended Data Fig. 5a–c). These results suggest that *Morrbid* represses *Bcl2l1* expression in short-lived myeloid cells.

To specifically address the role of *Morrbid* RNA in the regulation of *Bcl2l1* expression, we first established an *in vitro* eosinophil culture system in which we could study the function of *Morrbid* RNA in the absence of genetic disruptions<sup>9</sup> (Extended Data Fig. 6a). Using this system, we found that short hairpin RNA (shRNA)-mediated knockdown of *Morrbid* RNA results in a significant elevation in BCL2L1, which was accompanied by a substantial decrease in eosinophil survival (Figure 3a–c, Extended Data Fig. 6b–d). We observed similar results using transfection of locked nucleic acids (LNAs) as an independent knockdown technique (Extended Data Fig. 6e). We next sought to corroborate these results in a different cell type within the myeloid cell lineage. Interestingly, we found that lipopolysaccharide (LPS)-stimulated BM-derived macrophages (BMDMs) highly upregulated *Morrbid* (Extended Data Fig. 6f). Notably, LNA knockdown of *Morrbid*, deletion of the *Morrbid* promoter, or deletion of its locus in LPS-stimulated BMDMs resulted in a marked increase in *Bcl2l1* expression and apoptosis (Extended Data Fig. 6f–i). Altogether, these results indicate that *Morrbid* RNA is a critical regulator of *Bcl2l1* expression and short-lived myeloid cell survival.

Pro-survival cytokines can potentially influence the lifespan of immune cells. One well-described mechanism of this control is through the repression of *Bcl2l1* (refs 15, 16). We hypothesized that cytokines from the common  $\beta$ -chain receptor family (IL-3, IL-5 and GM-CSF), which are known to promote the survival of eosinophils, neutrophils and Ly6C<sup>hi</sup> monocytes, regulate *Bcl2l1* expression through the induction of *Morrbid*. To test this hypothesis, we first withdrew cytokines from cultured BM-derived eosinophils and observed a loss of *Morrbid* expression and an increase in *Bcl2l1* levels (Fig. 3d). Subsequent addition of IL-5, IL-3 or GM-CSF induced *Morrbid* expression, which was accompanied by *Bcl2l1* repression (Fig. 3d). Similarly, *ex-vivo*  $\beta$ -chain cytokine stimulation, but not G-CSF stimulation, significantly induced *Morrbid* and a corresponding repression of *Bcl2l1* in neutrophils and Ly6C<sup>hi</sup> monocytes (Fig. 3e, Extended Data Fig. 6m). Importantly, *Morrbid*-deficient neutrophils were unable to inhibit *Bcl2l1* expression

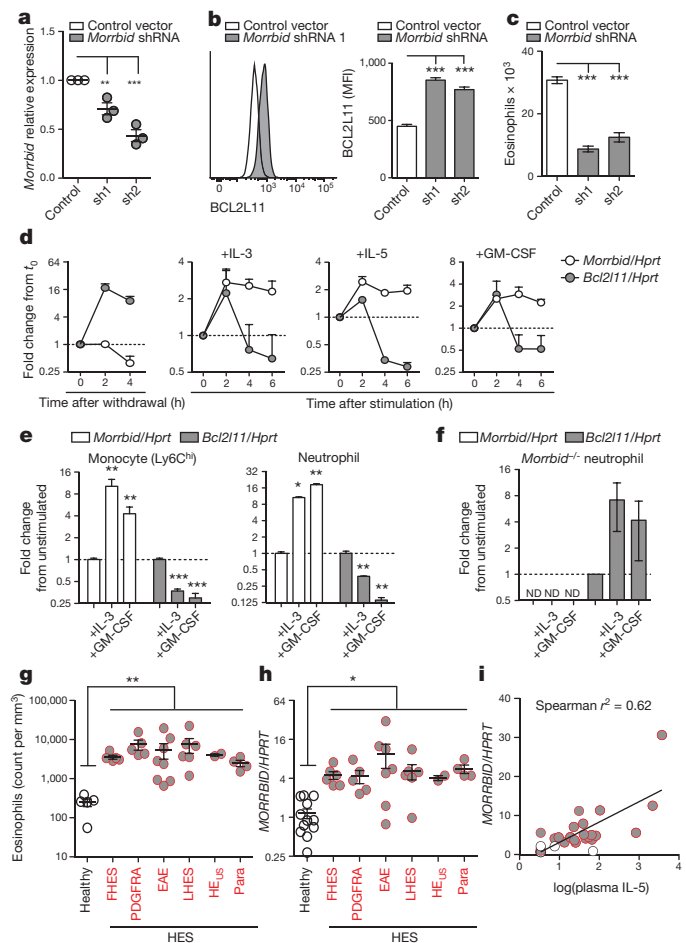


**Figure 3 | Pro-survival cytokines repress pro-apoptotic *Bcl2l1* through induction of *Morrbid* RNA.** a–c, BM-derived eosinophils transduced with control or *Morrbid*-specific shRNAs. a, *Morrbid* qPCR expression. b, c, BCL2L1 protein expression (b) and absolute eosinophil counts (c) ( $n = 3$  mice per group, representative of 2 independent experiments). d, *Morrbid* and *Bcl2l1* qPCR expression in BM-derived eosinophils following withdrawal/stimulation with indicated cytokines ( $n = 3$  mice, representative of 2 independent experiments). e, f, *Morrbid* and *Bcl2l1* qPCR expression in wild-type (e) and *Morrbid*-deficient (f) sorted BM cell types stimulated with indicated cytokines ( $n = 3–4$  mice, representative of 3 independent experiments). g–i, *MORRBID* expression in human hypereosinophilic syndrome (HES). Absolute eosinophil count (g), purified eosinophil *MORRBID* qPCR expression (h), and correlation between log(plasma IL-5) and *MORRBID* expression (i) (each dot represents one individual;  $n = 2–12$  per disease group). FHES, familial HES; PDGFRA, PDGFRA<sup>+</sup> HES; EAE, episodic angioedema and eosinophilia; LHES, lymphocytic variant HES; HE<sub>US</sub>, HES of undetermined significance; Para, parasitic infection. Error bars show s.e.m. \* $P < 0.05$ , \*\* $P < 0.01$ , and \*\*\* $P < 0.001$  (two-sided *t*-test, a–h; Spearman's correlation, i).

upon addition of  $\beta$ -chain cytokines (Fig. 3f). These results suggest that  $\beta$ -chain cytokines repress *Bcl2l1* expression in short-lived myeloid cells in a *Morrbid*-dependent manner.

Dysregulated immune cell survival is central to many human haematological and inflammatory diseases. Hypereosinophilic syndrome (HES) is a group of disorders characterized by eosinophilia and a wide range of clinical manifestations<sup>17</sup>. Several HES subtypes have been associated with increased production or responsiveness to IL-5 (ref. 17). We therefore reasoned that eosinophils from individuals with HES would overexpress *MORRBID*, and that this overexpression would positively correlate with IL-5 levels. We screened patients with varied subtypes of HES (Fig. 3g), and found that eosinophils from these patients expressed significantly higher levels of *MORRBID* than that of

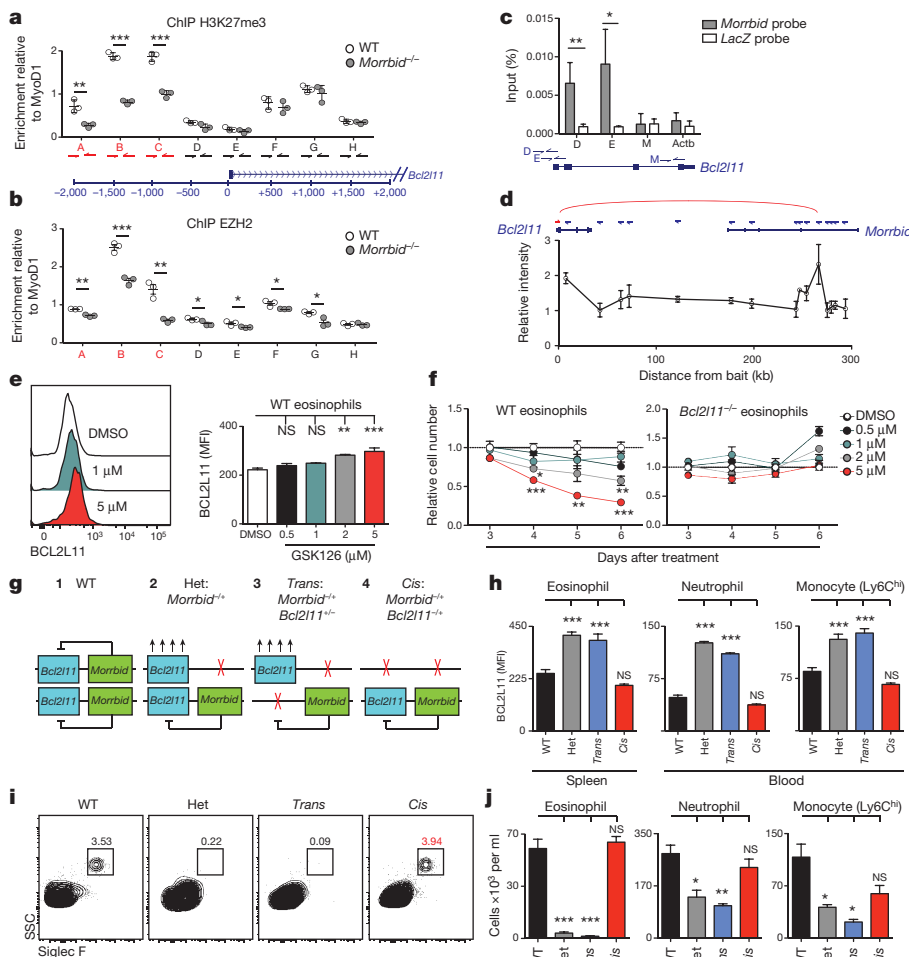


**Figure 4 | *Morrbid* represses *Bcl2l11* in cis by maintaining its bivalent promoter in a poised state.** **a, b**, ChIP-qPCR for H3K27me3 (**a**) and EZH2 (**b**) at the *Bcl2l11* promoter in sorted BM neutrophils (dots represents 1–2 pooled mice). **c**, ChIP-qPCR of *Morrbid* RNA occupancy. **d**, **e** and **f**, Wild-type and *Bcl2l11*-deficient BM-derived eosinophils treated with the EZH2 inhibitor GSK126. **e**, BCL2L11 protein expression on treatment day 5. **f**, Number of cells relative to DMSO treatment control ( $n = 3$  mice per dose, representative of 2 independent experiments). **g–j**, Allele-specific combinations of *Morrbid*- and *Bcl2l11*-deficient mice. **g**, Schema of generated allele-specific mutant mice. **h**, Quantification of BCL2L11 MFI of indicated cell types. **i**, Representative flow cytometry of blood eosinophils. **j**, Absolute counts of indicated splenic cell types ( $n = 3–9$  mice per group). Error bars show s.e.m. \* $P < 0.05$ , \*\* $P < 0.01$ , and \*\*\* $P < 0.001$  (two-sided  $t$ -test, **a–c**; one-way ANOVA with Tukey post-hoc test, **e, f, h, j**).

healthy controls (Fig. 3h). Additionally, we observed that *MORRBID* expression in eosinophils was positively correlated with plasma IL-5 levels (Fig. 3i). These results suggest a potential role for *MORRBID* in HES and other inflammatory diseases characterized by high levels of  $\beta$ -chain cytokines and altered short-lived myeloid cell lifespan.

Genes that require both tight regulation and the ability to be rapidly activated frequently have activating (H3K4me3) and repressive (H3K27me3) histone marks in their promoters, termed bivalent promoters<sup>18</sup>. The *Bcl2l11* gene has previously been described as having a bivalent promoter, which allows this pro-apoptotic gene to be maintained in a poised state<sup>19</sup>. A number of lncRNAs have been shown to repress gene expression by promoting the enrichment of polycomb repressive complex 2 (PRC2) at target genes, which in turn catalyzes the deposition of H3K27me3 (refs 20, 21). We therefore hypothesized that *Morrbid* represses *Bcl2l11* expression and prevents short-lived myeloid cell apoptosis by promoting PRC2 enrichment and H3K27me3 deposition at the bivalent promoter of *Bcl2l11*.

To test this hypothesis, we first performed chromatin immunoprecipitation followed by quantitative PCR (ChIP-qPCR) for total polymerase II (Pol II), H3K27me3 and the PRC2 subunit EZH2 in neutrophils from wild-type and *Morrbid*-deficient mice. In line with the elevated levels of *Bcl2l11* in *Morrbid*-deficient cells, we found that Pol II occupancy was significantly increased (Extended Data Fig. 7a), and the levels of H3K27me3 and EZH2 were markedly reduced at the promoter of *Bcl2l11* in the absence of *Morrbid* (Fig. 4a, b). We next asked whether the induction of *Morrbid* expression promotes the accumulation of PRC2 at the *Bcl2l11* promoter. Using the BMDM system in which *Morrbid* is induced upon LPS stimulation, we found that *Morrbid* levels and EZH2 occupancy at the *Bcl2l11* promoter concurrently increase in a *Morrbid*-dependent manner (Extended Data Fig. 7b). Finally, using

ChIP-seq and ATAC-seq (assay for transposase-accessible chromatin using sequencing), we did not detect changes in the activating histone marks H3K4me1 and H3K4me3, and only a modest increase in chromatin accessibility at the *Bcl2l11* promoter in the absence of *Morrbid* (Extended Data Fig. 7c–f). Altogether, these results indicate that *Morrbid* represses *Bcl2l11* expression in short-lived myeloid cells by promoting the deposition of H3K27me3 at the bivalent promoter of *Bcl2l11*.

lncRNAs have been suggested to promote the recruitment of PRC2 to target genes through direct lncRNA–PRC2 interactions or indirect mechanisms<sup>11,20–24</sup>. To understand further the mechanism by which *Morrbid* promotes PRC2 enrichment at the *Bcl2l11* promoter, we first examined whether *Morrbid* RNA associates with PRC2. Using a recently generated EZH2 photoactivatable ribonucleoside-enhanced crosslinking and immunoprecipitation (PAR-CLIP) dataset<sup>22</sup>, we found that *Morrbid* associates with EZH2 (Extended Data Fig. 8a). To further support this association, we performed RNA immunoprecipitation against EZH2 in myeloid cells and found that *Morrbid* significantly co-immunoprecipitates with this PRC2 subunit (Extended Data Fig. 8b). We next asked whether *Morrbid* RNA associates with chromatin regions within the *Bcl2l11* promoter, with which PRC2 also associates. We performed chromatin isolation by RNA purification (ChIRP)-qPCR in LPS-treated BMDMs. Using DNA probes that specifically and robustly retrieved *Morrbid* RNA (Extended Data Fig. 8c), we found that *Morrbid* association with chromatin was significantly enriched at the *Bcl2l11* promoter (Fig. 4c). Finally, we asked how *Morrbid* RNA comes into proximity of the *Bcl2l11* promoter. A number of lncRNA genes have been reported to loop into proximity with the genes that they regulate<sup>10–13,25</sup>; thus, we reasoned that the *Morrbid* and *Bcl2l11* loci interact with one another through DNA

looping. Using chromosome conformation capture (3C), we indeed observed a long-distance association between *Bcl2l11* and the *Morrbid* locus in short-lived myeloid cells (Fig. 4d, Extended Data Fig. 8d). Altogether, these results suggest a model in which *Morrbid* proximity to *Bcl2l11*, mediated through DNA looping, enables *Morrbid* RNA to promote PRC2 enrichment within the *Bcl2l11* promoter through direct *Morrbid*–PRC2 interactions and potentially through additional indirect mechanisms.

Our findings suggest an important role for PRC2 in *Morrbid*-dependent repression of *Bcl2l11*. Yet, whether short-lived myeloid cell survival depends on PRC2-mediated transcriptional repression of *Bcl2l11* is not known. We cultured eosinophils in the presence of a specific inhibitor of EZH2, GSK126. We observed a dose-dependent increase in BCL2L11 and eosinophil apoptosis upon PRC2 inhibition (Fig. 4e, f, Extended Data Fig. 8e, f). Importantly, *Bcl2l11*-deficient eosinophils were resistant to cell death following abrogation of PRC2 activity (Fig. 4f, Extended Data Fig. 8e, f). Altogether, these results demonstrate that PRC2 regulates short-lived myeloid cell survival specifically through repression of *Bcl2l11* expression, further supporting a critical role for *Morrbid* in the regulation of the lifespan of these highly inflammatory cells.

Finally, we found that *Morrbid*-heterozygous mice largely recapitulated the phenotype of mice lacking both alleles of *Morrbid* (Extended Data Fig. 8g). In light of this dominant heterozygous phenotype and the observed *Morrbid*–*Bcl2l11* DNA loop, we hypothesized that *Morrbid* functions in *cis* to repress *Bcl2l11*. As such, we expected that deletion of *Bcl2l11* on the same chromosome as that of the *Morrbid*-deficient allele will normalize *Bcl2l11* expression in short-lived myeloid cells and rescue their numbers, but that deletion of *Bcl2l11* on the opposite chromosome would not (Fig. 4g). We therefore generated all permutations of *Morrbid* and *Bcl2l11* double-heterozygous mice (Extended Data Fig. 9). Notably, deletion of *Bcl2l11* in *cis*, but not in *trans*, of the *Morrbid*-deficient allele normalized *Bcl2l11* expression (Fig. 4h) and rescued short-lived myeloid cell numbers (Fig. 4i, j, Extended Data Fig. 10a, b). Other cell types were largely unaltered in these genetic backgrounds (Extended Data Fig. 10b–d). This complete rescue in *cis* double-heterozygous mice indicates that *Morrbid* acts in an allele-specific manner to regulate *Bcl2l11* expression and short-lived myeloid cell lifespan.

Here we show that *Morrbid* integrates extracellular signals to control the lifespan of eosinophils, neutrophils and monocytes through allele-specific suppression of *Bcl2l11* expression (Extended Data Fig. 10e). As this lncRNA is present in humans and dysregulated in patients with HES, a better understanding of how *Morrbid* RNA and potentially DNA elements within its locus regulate *Bcl2l11* may provide new therapeutic approaches for several human inflammatory diseases. Finally, our results demonstrate that lncRNAs can function as highly cell-type specific local effectors of extracellular cues to control immunological processes that require rapid and strict regulation.

**Online Content** Methods, along with any additional Extended Data display items and Source Data, are available in the online version of the paper; references unique to these sections appear only in the online paper.

**Received 18 December 2015; accepted 8 August 2016.**

**Published online 15 August 2016.**

- Manz, M. G. & Boettcher, S. Emergency granulopoiesis. *Nat. Rev. Immunol.* **14**, 302–314 (2014).
- Ginhoux, F. & Jung, S. Monocytes and macrophages: developmental pathways and tissue homeostasis. *Nat. Rev. Immunol.* **14**, 392–404 (2014).
- Heo, J. B. & Sung, S. Vernalization-mediated epigenetic silencing by a long intronic noncoding RNA. *Science* **331**, 76–79 (2011).
- Xing, Z. *et al.* lncRNA directs cooperative epigenetic regulation downstream of chemokine signals. *Cell* **159**, 1110–1125 (2014).
- Boufffi, C. *et al.* Transcription factor repertoire of homeostatic eosinophilopoiesis. *J. Immunol.* **195**, 2683–2695 (2015).
- Luo, M. *et al.* Long non-coding RNAs control hematopoietic stem cell function. *Cell Stem Cell* **16**, 426–438 (2015).

- Yona, S. *et al.* Fate mapping reveals origins and dynamics of monocytes and tissue macrophages under homeostasis. *Immunity* **38**, 79–91 (2013).
- Geissmann, F. *et al.* Development of monocytes, macrophages, and dendritic cells. *Science* **327**, 656–661 (2010).
- Dyer, K. D. *et al.* Functionally competent eosinophils differentiated ex vivo in high purity from normal mouse bone marrow. *J. Immunol.* **181**, 4004–4009 (2008).
- Wang, K. C. *et al.* A long noncoding RNA maintains active chromatin to coordinate homeotic gene expression. *Nature* **472**, 120–124 (2011).
- Zhang, H. *et al.* Long noncoding RNA-mediated intrachromosomal interactions promote imprinting at the *Kcnq1* locus. *J. Cell Biol.* **204**, 61–75 (2014).
- Wang, L. *et al.* lncRNA *Dum* interacts with Dnmts to regulate *Dppa2* expression during myogenic differentiation and muscle regeneration. *Cell Res.* **25**, 335–350 (2015).
- Maass, P. G. *et al.* A misplaced lncRNA causes brachydactyly in humans. *J. Clin. Invest.* **122**, 3990–4002 (2012).
- Villunger, A., Scott, C., Bouillet, P. & Strasser, A. Essential role for the BH3-only protein Bim but redundant roles for Bax, Bcl-2, and Bcl-w in the control of granulocyte survival. *Blood* **101**, 2393–2400 (2003).
- Shinjo, T. *et al.* Downregulation of Bim, a proapoptotic relative of Bcl-2, is a pivotal step in cytokine-initiated survival signaling in murine hematopoietic progenitors. *Mol. Cell Biol.* **21**, 854–864 (2001).
- Bouillet, P. *et al.* Proapoptotic Bcl-2 relative Bim required for certain apoptotic responses, leukocyte homeostasis, and to preclude autoimmunity. *Science* **286**, 1735–1738 (1999).
- Simon, H.-U. *et al.* Refining the definition of hypereosinophilic syndrome. *J. Allergy Clin. Immunol.* **126**, 45–49 (2010).
- Voigt, P., Tee, W.-W. & Reinberg, D. A double take on bivalent promoters. *Genes Dev.* **27**, 1318–1338 (2013).
- Paschos, K., Parker, G. A., Watanatanasup, E., White, R. E. & Allday, M. J. BIM promoter directly targeted by EBNA3C in polycomb-mediated repression by EBV. *Nucleic Acids Res.* **40**, 7233–7246 (2012).
- Zhao, J., Sun, B. K., Erwin, J. A., Song, J.-J. & Lee, J. T. Polycomb proteins targeted by a short repeat RNA to the mouse X chromosome. *Science* **322**, 750–756 (2008).
- Rinn, J. L. *et al.* Functional demarcation of active and silent chromatin domains in human HOX loci by noncoding RNAs. *Cell* **129**, 1311–1323 (2007).
- Kaneko, S. *et al.* Interactions between JARID2 and noncoding RNAs regulate PRC2 recruitment to chromatin. *Mol. Cell* **53**, 290–300 (2014).
- Sarma, K. *et al.* ATRX directs binding of PRC2 to Xist RNA and Polycomb targets. *Cell* **159**, 869–883 (2014).
- Csorbai, T., Questa, J. I., Sun, Q. & Dean, C. Antisense COOLAIR mediates the coordinated switching of chromatin states at FLC during vernalization. *Proc. Natl Acad. Sci. USA* **111**, 16160–16165 (2014).
- Ranzani, V. *et al.* The long intergenic noncoding RNA landscape of human lymphocytes highlights the regulation of T cell differentiation by linc-MAF-4. *Nat. Immunol.* **16**, 318–325 (2015).
- Henao-Mejia, J. *et al.* Protocol for the generation of genetically modified mice using the CRISPR–Cas9 genome-editing system. *Cold Spring Harb. Protoc.* <http://dx.doi.org/10.1101/pdb.prot090704> (2016).

**Supplementary Information** is available in the online version of the paper.

**Acknowledgements** We thank several of our colleagues for critically reading our manuscript and their suggestions. J.H.-M. was supported by the Children's Hospital of Philadelphia, the IFI and IDOM pilot projects, and the COE at the University of Pennsylvania (J.H.-M.); A.W. and R.A.F. by NIH NIAID 1R21AI110776-01; C.C.D.H. and R.A.F. by Howard Hughes Medical Institute; J.J.K. by NIH NIDDK T32-DK00778017; S.P.S. by NIH NRSA F30-DK094708; W.K.M. by T32-AI05542803; A.R. and M.C.D. by New Innovator 1DP2OD008514, 1R33EB019767, NSF CAREER 1350601. This work was funded in part by the Division of Intramural Research, NIAID, NIH (M.A.M. and A.D.K.).

**Author Contributions** J.J.K., S.P.S., A.W., R.A.F. and J.H.-M. designed these experiments. J.J.K., S.P.S. and J.H.-M. wrote the manuscript. A.W. and R.A.F. edited the manuscript. L.G. and J.R. performed the bioinformatic analysis of lncRNA identification. J.S. and C.H. aided the generation novel mice. D.B.U.K. performed *in vitro* promoter targeting and eosinophil LNA transfection. M.A.C. and A.U. prepared and analysed the ChIP-seq and ATAC-seq. E.N.E. performed 3C. M.C.D. and A.R. performed FISH. M.A.M. and A.D.K. collected and aided in the analysis of HES patient samples. All other experiments and analyses were performed by J.J.K., S.P.S., S.J.M., J.H.-M. and A.W. with help from W.K.M., C.C.D.H., A.T.V., S.Z. and W.B.

**Author Information** ATAC-seq and ChIP-seq data have been deposited in the Gene Expression Omnibus under accession number GSE85073. Reprints and permissions information is available at [www.nature.com/reprints](http://www.nature.com/reprints). The authors declare no competing financial interests. Readers are welcome to comment on the online version of the paper. Correspondence and requests for materials should be addressed to A.W. ([adam.williams@jax.org](mailto:adam.williams@jax.org)), R.A.F. ([richard.flavell@yale.edu](mailto:richard.flavell@yale.edu)) or J.H.-M. ([jhena@mail.med.upenn.edu](mailto:jhena@mail.med.upenn.edu)).

**Reviewer Information** Nature thanks H. Y. Chang, S. Jung and the other anonymous reviewer(s) for their contribution to the peer review of this work.



## METHODS

**Mice.** All mice were bred and maintained under pathogen-free conditions at an American Association for the Accreditation of Laboratory Animal Care accredited animal facility at the University of Pennsylvania or Yale University. Mice were housed in accordance with the procedures outlined in the Guide for the Care and Use of Laboratory Animals under an animal study proposal approved by an institutional Animal Care and Use Committee. Male and female mice between 4 and 12 weeks of age were used for all experiments. Littermate controls were used whenever possible.

C57BL/6 (wild type) and B6.SJL-Ptpr<sup>c</sup> Pepc<sup>b</sup>/Boy (B6.SJL) mice were purchased from The Jackson Laboratory. We generated *Morrbid*-deficient mice and the *in cis* and *in trans* double heterozygous mice (*Morrbid*<sup>+/-</sup>, *Bcl2l1*<sup>+/-</sup>) mice using the CRISPR/Cas9 system as previously described<sup>26</sup>. In brief, to generate *Morrbid*-deficient mice, single guide RNAs (sgRNAs) were designed against regions flanking the first and last exon of the *Morrbid* locus (Extended Data Fig. 1g). Cas9-mediated double-stranded DNA breaks resolved by non-homologous end joining (NHEJ) ablated the intervening sequences containing *Morrbid* in C57BL/6N one-cell embryos. The resulting founder mice were *Morrbid*<sup>-/-</sup>, which were then bred to wild-type C57BL/6N and then intercrossed to obtain homozygous *Morrbid*<sup>-/-</sup> mice. One *Morrbid*-deficient line was generated. To control for potential off-target effects, mice were crossed for at least 5 generations to wild-type mice and then intercrossed to obtain homozygosity. Littermate controls were used when possible throughout all experiments.

To generate the *in cis* and *in trans* double heterozygous mice (*Morrbid*<sup>+/-</sup>, *Bcl2l1*<sup>+/-</sup>) mice, we first obtained mouse one-cell embryos from a mating between *Morrbid*<sup>-/-</sup> female mice and wild-type male mice. As such, the resulting one-cell embryos were heterozygous for *Morrbid* (*Morrbid*<sup>+/-</sup>). We then micro-injected sgRNAs designed against intronic sequences flanking the second exon of *Bcl2l1*, which contains the translational start site/codon, into *Morrbid*<sup>+/-</sup> one-cell embryos (Extended Data Fig. 9). Cas9-mediated double-stranded DNA breaks resolved by NHEJ ablated the intervening sequences containing the second exon of *Bcl2l1* in *Morrbid*<sup>+/-</sup> (C57BL/6N) one-cell embryos, generating founder mice that were heterozygous for both *Bcl2l1* and *Morrbid* (*Bcl2l1*<sup>+/-</sup>; *Morrbid*<sup>+/-</sup>). Founder heterozygous mice were then bred to wild-type C57BL/6N to interrogate for the segregation of the *Morrbid*-deficient and *Bcl2l1*-deficient alleles (Extended Data Fig. 9). Pups that segregated such alleles were named *in trans* and pups that did not segregate were labelled *in cis*. One line of *in cis* and *in trans* double heterozygous mice (*Bcl2l1*<sup>+/-</sup>; *Morrbid*<sup>+/-</sup>) lines were generated. To control for potential off-target effects, mice were crossed for at least 5 generations to wild-type (C57BL/6N) mice (for *in cis*) and to *Morrbid*<sup>-/-</sup> mice (for *in trans*) to maintain heterozygosity. To determine genetic rescue, samples from mice containing different permutations of *Morrbid* and *Bcl2l1* alleles (Fig. 4g–j) were analysed in a blinded manner by a single investigator not involved in the breeding or coding of these samples.

**Flow cytometry staining, analysis and cell sorting.** Cells were isolated from the indicated tissues (blood, spleen, bone marrow, peritoneal exudate, adipose tissue). Red blood cells were lysed with ACK. Single-cell suspensions were stained with CD16/32 and with indicated fluorochrome-conjugated antibodies. If run live, cells were stained with 7-AAD (7-amino-actinomycin D) to exclude non-viable cells. Otherwise, before fixation, Live/Dead Fixable Violet Cell Stain Kit (Invitrogen) was used to exclude non-viable cells. Active caspase staining using Z-VAD-FMK (CaspGLOW, eBiosciences) was performed according to the manufacturer's specifications. Apoptosis staining by annexin V+ (Annexin V Apoptosis Detection kit) was performed according to the manufacturer's recommendations. BrdU staining was performed using BrdU Staining Kit (eBioscience) according to the manufacturer's recommendations. For BCL2L1 staining, cells were fixed for 15 min in 2% formaldehyde solution, and permeabilized with flow cytometry buffer supplemented with 0.1% Triton X-100. All flow cytometry analysis and cell-sorting procedures were done at the University of Pennsylvania Flow Cytometry and Cell Sorting Facility using BD LSRII cell analysers and a BD FACSAria II sorter running FACSDiva software (BD Biosciences). FlowJo software (version 10 TreeStar) was used for data analysis and graphic rendering. All fluorochrome-conjugated antibodies used are listed in Supplementary Table 2.

**Western blotting.** 1 × 10<sup>6</sup> wild-type and *Morrbid*-deficient neutrophils sorted from mouse bone marrow were assayed for BCL2L1 protein expression by western blotting (Bim C34C5 rabbit monoclonal antibody, Cell Signaling), as previously described.

**ChIP-qPCR.** 2 × 10<sup>6</sup> wild-type and *Morrbid*-deficient neutrophils sorted from mouse bone marrow were cross-linked in a 1% formaldehyde solution for 5 min at room temperature while rotating. Crosslinking was stopped by adding glycine (0.2 M in 1 × PBS (phosphate buffered saline)) and incubating on ice for 2 min. Samples were spun at 2500g for 5 min at 4 °C and washed 4 times with 1 × PBS. The pellets were flash frozen and stored at -80 °C. Cells were lysed, and nuclei were isolated and sonicated for 8 min using a Covaris S220 (105 Watts, 2% duty cycle,

200 cycles per burst) to obtain approximately 200–500 bp chromatin fragments. Chromatin fragments were pre-cleared with protein G magnetic beads (New England Biolabs) and incubated with pre-bound anti-H3K27me3 (Qiagen), anti-EZH2 (eBiosciences), or mouse IgG1 (Santa Cruz Biotechnology) antibody-protein G magnetic beads overnight at 4 °C. Beads were washed once in low-salt buffer (20 mM Tris, pH 8.1, 2 mM EDTA, 50 mM NaCl, 1% Triton X-100, 0.1% SDS), twice in high-salt buffer (20 mM Tris, pH 8.1, 2 mM EDTA, 500 mM NaCl, 1% Triton X-100, 0.1% SDS), once in LiCl buffer (10 mM Tris, pH 8.1, 1 mM EDTA, 0.25 mM LiCl, 1% NP-40, 1% deoxycholic acid) and twice in TE buffer (10 mM Tris-HCl, pH 8.0, 1 mM EDTA). Washed beads were eluted twice with 100 µl of elution buffer (1% SDS, 0.1 M NaHCO<sub>3</sub>) and de-crosslinked (0.1 mg ml<sup>-1</sup> RNase, 0.3 M NaCl and 0.3 mg ml<sup>-1</sup> Proteinase K) overnight at 65 °C. The DNA samples were purified with Qiaquick PCR columns (Qiagen). qPCR was carried out on a ViiA7 Real-Time PCR System (ThermoFisher) using the SYBR Green detection system and indicated primers. Expression values of target loci were directly normalized to the indicated positive control loci, such as *MyoD1* for H3K27me3 and EZH2 ChIP analysis, and *Actb* for Pol II ChIP analysis. ChIP-qPCR primer sequences are listed in Supplementary Table 1.

**ATAC-seq preparation, sequencing, and analysis.** 50,000 wild-type and knock-out cells, in triplicate, were spun at 500g for 5 min at 4 °C, washed once with 50 µl of cold 1 × PBS and centrifuged in the same conditions. Cells were resuspended in 50 µl of ice-cold lysis buffer (10 mM Tris-HCl, pH 7.4, 10 mM NaCl, 3 mM MgCl<sub>2</sub>, 0.1% IGEPAL CA-630). Cells were immediately spun at 500g for 10 min at 4 °C. Lysis buffer was carefully pipetted away from the pellet, which was then resuspended in 50 µl of the transposition reaction mix (25 µl 2 × TD buffer, 2.5 µl Tn5 Transposase (Illumina), 22.5 µl nuclease-free water) and then incubated at 37 °C for 30 min. DNA purification was performed using a Qiagen MinElute kit and eluted in 12 µl of Elution buffer (10 mM Tris buffer, pH 8.0). To amplify library fragments, 6 µl of the eluted DNA was mixed with NEBnext High-Fidelity 2 × PCR Master Mix, 25 µM of customized Nextera PCR primers 1 and 2 (Supplementary Table 1), 100x SYBR Green I and used in PCR as follow: 72 °C for 5 min; 98 °C for 30 s; and thermocycling 4 times at 98 °C for 10 s; 63 °C for 30 s; 72 °C for 1 min. 5 µl of the 5 cycles PCR amplified DNA was used in a qPCR reaction to estimate the additional number of amplification cycles. Libraries were amplified for a total of 10–11 cycles and were then purified using a Qiagen PCR Cleanup kit and eluted in 30 µl of Elution buffer. The libraries were quantified using qPCR and bioanalyser data, and then normalized and pooled to 2 nM. Each 2 nM pool was then denatured with a 0.1 N NaOH solution in equal parts then further diluted to form a 20 pM denatured pool. This pool was then further diluted down to 1.8 pM for sequencing using the NextSeq500 machine on V2 chemistry and sequenced on a 1 × 75 bp Illumina NextSeq flow cell.

ATAC sequencing cells was done on Illumina NextSeq at a sequencing depth of ~40–60 million reads per sample. Libraries were prepared in triplicates. Raw reads were deposited under GSE85073. 2 × 75 bp paired-end reads were mapped to the mouse mm9 genome using 'bwa' algorithm with 'mem' option. Only reads that uniquely mapped to the genome were used in subsequent analysis. Duplicate reads were eliminated to avoid potential PCR amplification artifacts and to eliminate the high numbers of mtDNA duplicates observed in ATAC-seq libraries. Post-alignment filtering resulted in ~26–40 million uniquely aligned singleton reads per library and the technical replicates were merged into one alignment BAM file to increase the power of open chromatin signal in downstream analysis. Depicted tracks were normalized to total read depth. ATAC-seq enriched regions (peaks) in each sample was identified using MACS2 using the below settings:

```
MACS2-2.1.0.20140616/bin/macs2 callpeak -t <input tag file> -f BED -n <output peak file> -g 'mm' --nomodel --shift -100 --extsize 200 -B --broad
```

**ChIP-seq preparation, sequencing and analysis.** 10 × 10<sup>6</sup> wild-type and knock-out mice neutrophils were cross-linked in a 1% formaldehyde solution for 10 min at room temperature while rotating. Crosslinking was stopped by adding glycine (0.2 M in 1 × PBS) and incubating on ice for 2 min. Samples were spun at 2500g for 5 min at 4 °C and washed 4 times with 1 × PBS. The pellets were flash frozen and stored at -80 °C. Cells were lysed and sonicated (Branson Sonifier 250) for 9 cycles (30% amplitude; time, 20 s on, 1 min off). Lysates were spun at 18,400g for 10 min at 4 °C and resuspended in 3 ml of lysis buffer. A sample of 100 µl was kept aside as input and the rest of the samples were divided by the number of antibodies to test. Chromatin immunoprecipitation was performed with 10 µg of antibody-bound beads (anti-H3K27ac, H3K4me3, H3K4me1, H3K36me3 (Abcam) and anti-rabbit IgG (Santa Cruz), Dynal Protein G magnetic beads (Invitrogen)) and incubated overnight at 4 °C. Bead-bound DNA was washed, reverse cross-linked and eluted overnight at 65 °C, shaking at 950 r.p.m. Beads were removed using a magnetic stand and eluted DNA was treated with RNase A (0.2 µg µl<sup>-1</sup>) for 1 h at 37 °C shaking at 950 r.p.m., then with proteinase K (0.2 µg µl<sup>-1</sup>) for 2 h at 55 °C. 30 µg of glycogen (Roche) and 5 M of NaCl were added to the samples. DNA was extracted with 1 volume of phenol:chloroform:isoamyl alcohol

and washed out with 100% ethanol. Dried DNA pellets were resuspended in 30  $\mu$ l of 10 mM Tris HCl, pH 8.0, and DNA concentrations were quantified using Qubit. Starting with 10 ng of DNA, ChIP-seq libraries were prepared using the KAPA Hyper Prep Kit (Kapa Biosystems, Inc.) with 10 cycles of PCR. The libraries were quantified using qPCR and bioanalyser data then normalized and pooled to 2 nM. Each 2 nM pool was then denatured with a 0.1 N NaOH solution in equal parts then further diluted to form a 20 pM denatured pool. This pool was then further diluted down to 1.8 pM for sequencing using the NextSeq500 machine on V2 chemistry and sequenced on a 1  $\times$  75 bp Illumina NextSeq flow cell.

ChIP sequencing was done on an Illumina NextSeq at a sequencing depth of ~30–40 million reads per sample. Raw reads were deposited under GSE85073. 75 bp single-end reads were mapped to the mouse mm9 genome using 'bowtie2' algorithm. Duplicate reads were eliminated to avoid potential PCR amplification artifacts and only reads that uniquely mapped to the genome were used in subsequent analysis. Depicted tracks were normalized to control IgG input sample. ChIP-seq-enriched regions (peaks) in each sample was identified using MACS2 using the below settings:

```
MACS2-2.1.0.20140616/bin/macs2 callpeak -t <ChIP tag file> -c <control tag file> -f BED -g 'mm' --nomodel --extsize=250 --bdg --broad -n <output peak file>
```

**RIP-qPCR.**  $10^7$  immortalized BMDMs were collected by trypsinization and resuspended in 2 ml PBS, 2 ml nuclear isolation buffer (1.28 M sucrose; 40 mM Tris-HCl, pH 7.5; 20 mM MgCl<sub>2</sub>; 4% Triton X-100), and 6 ml water on ice for 20 min (with frequent mixing). Nuclei were pelleted by centrifugation at 2,500g for 15 min. Nuclear pellets were resuspended in 1 ml RNA immunoprecipitation (RIP) buffer (150 mM KCl, 25 mM Tris, pH 7.4, 5 mM EDTA, 0.5 mM DTT, 0.5% NP40; 100 U ml<sup>-1</sup> SUPERaseIn, Ambion; complete EDTA-free protease inhibitor, Sigma). Resuspended nuclei were split into two fractions of 500  $\mu$ l each (for mock and immunoprecipitation) and were mechanically sheared using a dounce homogenizer. Nuclear membrane and debris were pelleted by centrifugation at 15,800g for 10 min. Antibody to EZH2 (Cell Signaling 4905S; 1:30) or normal rabbit IgG (mock immunoprecipitation, SantaCruz; 10  $\mu$ g) were added to supernatant and incubated for 2 hours at 4°C with gentle rotation. 25  $\mu$ l of protein G beads (New England BioLabs S1430S) were added and incubated for 1 hour at 4°C with gentle rotation. Beads were pelleted by magnetic field, the supernatant was removed, and beads were resuspended in 500  $\mu$ l RIP buffer and repeated for a total of three RIP buffer washes, followed by one wash in PBS. Beads were resuspended in 1 ml of Trizol. Co-precipitated RNAs were isolated, reverse-transcribed to cDNA, and assayed by qPCR for the *Hprt* and *Morrbid*-isoform1. Primer sequences are listed in Supplementary Table 1.

**PAR-CLIP analysis.** EZH2 PAR-CLIP dataset (GSE49435) was analysed as previously described<sup>22</sup>. Adapter sequences were removed from total reads and those longer than 17 bp were kept. The Fastx toolkit was used to remove duplicate sequences, and the resulting reads were mapped using BOWTIE allowing for two mismatches. The four independent replicates were pooled and analysed using PARalyzer, requiring at least two T→C conversions per RNA-protein contact site. lncRNAs were annotated according to Ensemble release 67.

**Chromosome conformation capture (3C).**  $13 \times 10^6$  wild-type bone marrow derived mouse eosinophils were fixed with 1% formaldehyde for 10 minutes at room temperature, and quenched with 0.2 M glycine on ice. Eosinophils were lysed for 3–4 hours at 4°C (50 mM Tris, pH 7.4, 150 mM NaCl, 0.5% NP-40, 1% Triton X-100, 1  $\times$  Roche complete protease inhibitor) and dounce-homogenized. Lysis was monitored by Methyl-green pyronin staining (Sigma). Nuclei were pelleted and resuspended in 500  $\mu$ l 1.4  $\times$  NEB3.1 buffer, treated with 0.3% SDS for one hour at 37°C, and 2% Triton X-100 for another hour at 37°C. Nuclei were digested with 800 units BglII (NEB) for 22 hours at 37°C, and treated with 1.6% SDS for 25 minutes at 65°C to inactivate the enzyme. Digested nuclei were suspended in 6.125 ml of 1.25  $\times$  ligation buffer (NEB), and were treated with 1% Triton X-100 for one hour at 37°C. Ligation was performed with 1,000 units T4 DNA ligase (NEB) for 18 hours at 16°C, and crosslinks were reversed by proteinase K digestion (300  $\mu$ g) overnight at 65°C. The 3C template was treated with RNase A (300  $\mu$ g), and purified by phenol-chloroform extraction. Digested and undigested DNA were run on a 0.8% agarose gel to confirm digestion. To control for PCR efficiency, two bacterial artificial chromosomes (BACs) spanning the region of interest were combined in equimolar quantities and digested with 500 units BglII at 37°C overnight. Digested BACs were ligated with 100 units T4 Ligase HC (Promega) in 60  $\mu$ l overnight at 16°C. Both BAC and 3C ligation products were amplified by qPCR (Applied Biosystems ViiA7) using SYBR fast master mix (KAPA biosystems). Products were run side by side on a 2% gel, and images were quantified using ImageJ. Intensity of 3C ligation products was normalized to intensity of respective BAC PCR product.

**Listeria monocytogenes infections.** Mice were infected with 30,000 CFUs of *Listeria monocytogenes* (strain 10403s, obtained as a gift from E. J. Wherry) intravenously (i.v.). Mice were weighed and inspected daily. Mice were analysed at day 4 of infection to determine the CFUs of *L. monocytogenes* present in the spleen and liver.

**Papain challenge.** Papain was purchased from Sigma Aldrich and resuspended in at 1 mg ml<sup>-1</sup> in PBS. Mice were intranasally challenged with 5 doses of 20  $\mu$ g papain in 20  $\mu$ l of PBS or PBS alone every 24 hours. Mice were killed 12 hours after the last challenge. Bronchoalveolar lavage was collected in two 1 ml lavages of PBS. Cellular lung infiltrates were collected after 1 hour digestion in RPMI supplemented with 5% FCS, 1 mg ml<sup>-1</sup> collagenase D (Roche) and 10  $\mu$ g ml<sup>-1</sup> DNase I (Invitrogen) at 37°C. Homogenates were passed through a cell strainer and infiltrates separated with a 27.5%, Optiprep gradient (Axis-Shield) by centrifugation at 1,175g for 20 min. Cells were removed from the interface and treated with ACK lysis buffer.

**Bone marrow chimaeras.** Congenic C57BL/6 (wild-type) bone marrow expressing CD45.1 and CD45.2 and *Morrbid*-deficient bone marrow expression CD45.2 was mixed in a 1:1 ratio and injected into C57BL/6 hosts irradiated twice with 5 Gy 3 hours apart that express CD45.1 (B6.SJL-Ptpr<sup>c</sup> Pepc<sup>b</sup>/BoyJ). Mice were analysed between 4–9 weeks after injection.

**Bone-marrow-derived eosinophils.** Bone marrow was isolated and cultured as previously described<sup>9</sup>. Briefly, unfractionated bone marrow cells were cultured with 100 ng ml<sup>-1</sup> stem cell factor (SCF) and 100 ng ml<sup>-1</sup> FLT3-ligand (FLT3-L). At day 4, the media was replaced with media containing 10 ng ml<sup>-1</sup> interleukin (IL-5). Mature bone-marrow-derived eosinophils were analysed between day 10–14.

**Bone-marrow-derived macrophage cultures.** Bone marrow cells were isolated and cultured in media containing recombinant mouse M-CSF (10 ng ml<sup>-1</sup>) for 7–8 days. On day 7–8, cells were re-plated for use in experimental assays. Bone-marrow-derived macrophages were stimulated with LPS (250 ng ml<sup>-1</sup>) for the indicated periods of time.

**ChIRP-qPCR.** Briefly,  $40 \times 10^7$  immortalized bone-marrow-derived macrophages were fixed with 40 ml of 1% glutaraldehyde for 10 min at room temperature. Crosslinking was quenched with 0.125 M glycine for 5 min. Cells were rinsed with PBS, pelleted for 4 min at 2,000g, snap-frozen in liquid nitrogen, and stored at –80°C. Cell pellets were thawed at room temperature and resuspended in 800  $\mu$ l of lysis buffer (50 mM Tris-HCl, pH 7.0, 10 mM EDTA, 1% SDS, 1 mM PMSF, complete protease inhibitor (Roche), 0.1 U ml<sup>-1</sup> Suprase In (Life Technologies)). Cell suspension was sonicated using a Covaris S220 machine (Covaris; 100 W, duty factor 20%, 200 cycles per burst) for 60 minutes until DNA was in the size range of 100–500 bp. After centrifugation for 5 min at 16100g at 4°C, the supernatant was aliquoted, snap-frozen in liquid nitrogen, and stored at –80°C. 1 ml of chromatin was diluted in 2 ml hybridization buffer (750 mM NaCl, 1% SDS, 50 mM Tris HCl, pH 7.0, 1 mM EDTA, 15% formamide) and input RNA and DNA aliquots were removed. 100 pmoles of probes (Supplementary Table 1) were added and mixed by rotation at 37°C for 4 h. Streptavidin paramagnetic C1 beads (Invitrogen) were equilibrated with lysis buffer. 100  $\mu$ l washed C1 beads were added, and the entire reaction was mixed for 30 min at 37°C. Samples were washed five times with 1 ml of washing buffer (SSC 2  $\times$ , 0.5% SDS and fresh PMSF). 10% of each sample was removed from the last wash for RNA isolation. RNA aliquots were added to 85  $\mu$ l RNA PK buffer, pH 7.0, (100 mM NaCl, 10 mM TrisCl, pH 7.0, 1 mM EDTA, 0.5% SDS, 0.2 U  $\mu$ l<sup>-1</sup> proteinase K) and incubated for 45 min with end-to-end shaking. Samples were spun down, and boiled for 10 min at 95°C. Samples were chilled on ice, added to 500  $\mu$ l Trizol, and RNA was extracted according to the manufacturer's recommendations. Equal volume of RNA was reverse-transcribed and assayed by qPCR using *Hprt* and *Morrbid*-exon1-1 primer sets (Supplementary Table 1). DNA was eluted from remaining bead fraction twice using 150  $\mu$ l DNA elution buffer (50 mM NaHCO<sub>3</sub>, 1% SDS, 200 mM NaCl, 100  $\mu$ g ml<sup>-1</sup> RNase A, 100 U ml<sup>-1</sup> RNase H) incubated for 30 min at 37°C. DNA elutions were combined and treated with 15  $\mu$ l (20 mg ml<sup>-1</sup>) Proteinase K for 45 min at 50°C. DNA was purified using phenol: chloroform:isoamyl and assayed by qPCR using the indicated primer sequences (Supplementary Table 1).

**shRNA generation and transduction.** shRNAs of indicated sequences (Supplementary Table 1) were cloned into pGreen shRNA cloning and expression lentivector. Pseudotyped lentivirus was generated as previously described, and 293T cells were transfected with a packaging plasmid, envelop plasmid, and the generated shRNA vector plasmid using Lipofectamine 2000. Virus was collected 14–16 h and 48 h after transfection, combined, 0.4- $\mu$ m filtered, and stored at –80°C. For generation of *in vivo* BM chimaeras, virus was concentrated 6 times by ultracentrifugation using an Optiprep gradient (Axis-Shield).

For transduced BM-derived eosinophils, cultured BM cells on day 3 of previously described culture conditions were mixed 1:1 with indicated lentivirus and spininfected for 2 h at 260g at 25°C with 5  $\mu$ g ml<sup>-1</sup> polybrene. Cultures were incubated overnight at 37°C, and media was exchanged for IL-5 containing media at day 4 of culture as previously described<sup>9</sup>. Cells were sorted for GFP<sup>+</sup> cells on day 5 of culture, and then cultured as previously described for eosinophil generation. Cells were assayed on day 11 of culture.

For transduced *in vivo* BM chimaeras, BM cells were cultured at  $2.5 \times 10^6$  cells per ml in mL-3 (10 ng ml<sup>-1</sup>), mL-6 (5 ng ml<sup>-1</sup>) and mSCF (100 ng ml<sup>-1</sup>) overnight at 37°C. Culture was readjusted to 2 ml at  $2.5 \times 10^6$  cells per ml in a 6-well



plate, and spininfected for 2 h at 260g at 25 °C with 5 µg ml<sup>-1</sup> polybrene. Cells were incubated overnight at 37 °C. On the day before transfer, recipient hosts were irradiated twice with 5 Gy 3 hours apart. Mice were analysed between 4 and 5 weeks following transfer.

**Locked nucleic acid knockdown.** Bone marrow-derived macrophages (BMDMs) were transfected with pooled *Morrbid* or scrambled locked nucleic acid (LNA) antisense oligonucleotides of equivalent total concentrations using Lipofectamine 2000. *Morrbid* LNA pools contained *Morrbid* LNA 1–4 sequences at a total of 50 or 100 nM (Supplementary Table 1). After 24 h, the transfection media was replaced. The BMDMs were incubated for an additional 24 h and subsequently stimulated with LPS (250 ng ml<sup>-1</sup>) for 8–12 h.

Eosinophils were derived from mouse BM as previously described. On day 12 of culture,  $1 \times 10^6$  to  $2 \times 10^6$  eosinophils were transfected with 50 nm of *Morrbid* LNA 3 or scrambled LNA (Supplementary Table 1) using TransIT-oligo according to manufacturer's protocol. RNA was extracted 48 h after transfection.

***Morrbid* promoter deletion.** Guide RNAs (gRNAs) targeting the 5' and 3' flanking regions of the *Morrbid* promoter were cloned into Cas9 vectors pSPCas9(BB)-2A-GFP(PX458) (Addgene plasmid 48138) and pSPCas9(BB)-2A-mCherry (a gift from the Stitzel lab, JAX-GM) respectively. gRNA sequences are listed in Supplementary Table 1. The cloned Cas9 plasmids were then transfected into RAW 264.7, a mouse macrophage cell line using Lipofectamine 2000, according to manufacturer's protocol. Forty-eight hours post transfection the double positive cells expressing GFP and mcherry, and the double negative cells lacking GFP and mcherry were sorted. The bulk sorted cells were grown in a complete media containing 20% FBS, assayed for deletion by PCR, as well as for *Morrbid* and *Bcl2l1* transcript expression by qPCR.

**Ex vivo cytokine stimulation.** BM-derived eosinophils, or neutrophils or Ly6C<sup>hi</sup> monocytes sorted from mouse BM, were rested for 4–6 hours at 37 °C in complete media. Cells were subsequently stimulated with IL-3 (10 ng ml<sup>-1</sup>, Biolegend), IL-5 (10 ng ml<sup>-1</sup>, Biolegend), GM-CSF (10 ng ml<sup>-1</sup>, Biolegend), or G-CSF (10 ng ml<sup>-1</sup>, Biolegend) for 4–6 h. RNA was collected at each time-point using TRIzol (Life Technologies).

**GSK126 treatment.** Wild-type and *Bcl2l1*<sup>-/-</sup> BM-derived eosinophils were generated as previously described<sup>9</sup>. On day 8 of culture, the previously described IL-5 media was supplemented with the indicated concentrations of the EZH2-specific inhibitor GSK126 (Toronto Research Chemicals). Media was exchanged for fresh IL-5 GSK126 containing media every other day. Cells were assayed for numbers and cell death by flow cytometry every day for 6 days following GSK126 treatment.

**RNA extraction, cDNA synthesis and quantitative RT-PCR.** Total RNA was extracted from TRIzol (Life Technologies) according to the manufacturer's instructions. Gycogen (ThermoFisher Scientific) was used as a carrier. Isolated RNA was quantified by spectrophotometry, and RNA concentrations were normalized. cDNA was synthesized using SuperScript II Reverse Transcriptase (ThermoFisher Scientific) according to the manufacturer's instructions. Resulting cDNA was analysed by SYBR Green (KAPA SYBR Fast, KAPABiosystems) or Taqman-based (KAPA Probe Fast, KAPABiosystems) using indicated primers. Primer sequences are listed in Supplementary Table 1. All reactions were performed in duplicate using a CFX96 Touch instrument (BioRad) or ViiA7 Real-Time PCR instrument (ThermoFisher Scientific).

**RNA-seq and conservation analysis.** Reads generated from mouse (Gr1<sup>+</sup>) granulocytes (previously published GSE53928), human neutrophils (previously published GSE70068), and bovine peripheral blood leukocytes (previously published GSE60265) were filtered, normalized, and aligned to the corresponding host genome. Reads mapping around the *Morrbid* locus were visualized. For visualization of the high level of *Morrbid* expression in short-lived myeloid cells, reads from sorted mouse eosinophils (previously published GSE69707), were filtered, aligned to mm9, normalized using RPKM, and gene expression was plotted in descending order. For each human sample corresponding to the indicated stimulation conditions, the number of reads mapping to the human *MORRBID* locus per total mapped reads was determined.

For conservation across species, the genomic loci and surrounding genomic regions for the species analysed were aligned with mVista and visualized using the rankVista display generated with mouse as the reference sequence. Green highlights annotated mouse exonic regions and corresponding regions in other indicated species.

**RNA fluorescence in situ hybridization.** Single molecule RNA fluorescence *in situ* hybridization (FISH) was performed as previously described. A pool of 44 oligonucleotides (Biosearch Technologies) were labelled with Atto647N (Atto-Tec). For validation purposes, we also labelled subsets consisting of odd and even numbered oligonucleotides with Atto647N and Atto700, respectively, and looked for colocalization of signal. We designed the oligonucleotides using the online Stellaris probe design software. Probe oligonucleotide sequences are listed in Supplementary Table 1. Thirty Z-sections with a 0.3-µm spacing were taken for each field of view.

We acquired all images using a Nikon Ti-E widefield microscope with a 100× 1.4NA objective and a Pixis 1024BR cooled CCD camera. We counted the mRNA in each cell by using custom image processing scripts written in MATLAB.

**Cell fractionation.** For nuclear and cytoplasmic fractionation,  $5 \times 10^6$  BMDMs were stimulated with 250 ng ml<sup>-1</sup> LPS for 4 hours. Cells were collected and washed once with cold PBS. Cells were pelleted, resuspended in 100 µl cold NAR A buffer (10 mM HEPES, pH 7.9, 10 mM KCl, 0.1 mM EDTA, 1× complete EDTA-free protease inhibitor, Sigma; 1 mM DTT, 20 mM β-glycerophosphate, 0.1 U µl<sup>-1</sup> SUPERaseIn, Life Technologies), and incubated at 4 °C for 20 min. 10 µl 1% NP-40 was added, and cells were incubated for 3 min at room temperature. Cells were vortexed for 30 seconds, and centrifuged at 3,400g. for 1.5 min at 4 °C. Supernatant was removed, centrifuged at full speed for 90 min at 4 °C, and remaining supernatant was added to 500 µl Trizol as the cytoplasmic fraction. The original pellet was washed 4 times in 100 µl NAR A with short spins of 6,800g. for 1 min. The pellet was resuspended in 50 µl NAR C (20 mM HEPES, pH 7.9, 400 mM NaCl, 1 mM EDTA, 1× complete EDTA-free protease inhibitor, Sigma, 1 mM DTT, 20 mM β-glycerophosphate, 0.1 U µl<sup>-1</sup> SUPERaseIn, Life Technologies). Cells were vortexed every 3 min for 10 s for a total of 20 min at 4 °C. The sample was centrifuged at maximum speed for 20 min at room temperature. Remaining supernatant was added to 500 µl Trizol as the nuclear fraction. Equivalent volumes of cytoplasmic and nuclear RNA were converted to cDNA using gene specific primers and Super Script II RT (Life Technologies). Fraction was assessed by qPCR for *Morrbid*-exon1-1 and other known cytoplasmic and nuclear transcripts. Primer sequences are listed in Supplementary Table 1.

For cytoplasmic, nuclear, and chromatin fractionation, cell fractions  $5 \times 10^6$  to  $10 \times 10^6$  immortalized macrophages were activated with 250 ng ml<sup>-1</sup> LPS (Sigma) for 6 hours at 37 °C. Cells were washed 2× with PBS, and then resuspended in 380 µl ice-cold HLB (50 mM Tris-HCl, pH7.4, 50 mM NaCl, 3 mM MgCl<sub>2</sub>, 0.5% NP-40, 10% glycerol), supplemented with 100 U SUPERase In RNase Inhibitor (Life Technologies). Cells were vortexed 30 s and incubated on ice for 30 min, followed by a final 30 s vortex and centrifugation at 4 °C for 5 min × 1000g. Supernatant was collected as the cytoplasmic fraction. Nuclear pellets were resuspended by vortexing in 380 µl ice-cold MWS (50 mM Tris-HCl, pH7.4, 4 mM EDTA, 0.3 M NaCl, 1 M urea, 1% NP-40) supplemented with 100 U SUPERase in RNase Inhibitor. Nuclei were lysed on ice for 10 min, vortexed for 30 s, and incubated on ice for 10 more min to complete lysis. Chromatin was pelleted by centrifugation at 4 °C for 5 min × 1000g. Supernatant was collected as the nucleoplasmic fraction. RNA was collected as described previously and cleaned up using the RNeasy kit (Qiagen). Equivalent volumes of cytoplasmic, nucleoplasmic, and chromatin-associated RNA were converted to cDNA using random hexamers and Super Script III RT (Life Technologies). Fraction was assessed by qPCR for *Morrbid*-exon1-2 and other known cytoplasmic and nuclear transcripts. Primer sequences are listed in Supplementary Table 1.

**Copy number analysis.** *Morrbid* cDNA was cloned into reference plasmid (pCDNA3.1) containing a T7 promoter. The plasmid was linearized and *Morrbid* RNA was *in vitro* transcribed using the MEGashortscript T7 kit (Life Technologies), according to the manufacturer's recommendations, and purified using the MEGAclear kit (Life Technologies). RNA was quantified using spectrophotometry and serial dilutions of *Morrbid* RNA of calculated copy number were spiked into *Morrbid*-deficient RNA isolated from *Morrbid*-deficient mouse spleen. Samples were reverse transcribed in parallel with wild-type-sorted neutrophil RNA and B-cell RNA isolated from known cell number using gene-specific *Morrbid* primers, and the *Morrbid* standard curve and wild-type neutrophils and B cells were assayed using qPCR with *Morrbid*-exon 1 primer sets (Supplementary Table 1).

**Bromodeoxyuridine incorporation assay.** Cohorts of mice were given a total of 4 mg bromodeoxyuridine (BrdU; Sigma Aldrich) in 2 separate intraperitoneal (i.p.) injections 3 h apart and monitored over the subsequent 5 days, unless otherwise noted. For analysis cells were stained according to manufacturer protocol (BrdU Staining Kit, ebioscience; anti-BrdU, Biolgend). A one-phase exponential curve was fitted from the peak labelling frequency to 36 h after peak labelling within each genetic background, and the half-life was determined from this curve.

**Human samples. Human subject cohort 1.** Study subjects were recruited and consented in accordance with the University of Pennsylvania Institutional Review Board. Peripheral blood was separated by Ficoll–Paque density gradient centrifugation, and the mononuclear cell layer and erythrocyte/granulocyte pellet were isolated and stained for fluorescence-associated cell sorting as previously described. Neutrophils (live, CD16<sup>+</sup>F4/80<sup>int</sup>CD3<sup>-</sup>CD14<sup>-</sup>CD19<sup>-</sup>), eosinophils (live, CD16<sup>+</sup>F4/80<sup>hi</sup>CD3<sup>-</sup>CD14<sup>-</sup>CD19<sup>-</sup>), T cells (live, CD3<sup>+</sup>CD16<sup>-</sup>), monocytes (live, CD14<sup>+</sup>CD3<sup>-</sup>CD16<sup>-</sup>CD56<sup>-</sup>), natural killer (NK) cells (live, CD56<sup>+</sup>CD3<sup>-</sup>CD16<sup>-</sup>CD14<sup>-</sup>), B cells (live, CD19<sup>+</sup>CD3<sup>-</sup>CD16<sup>-</sup>CD14<sup>-</sup>CD56<sup>-</sup>). **Human subject cohort 2.** Samples from human subjects were collected on NIAID IRB-approved research protocols to study eosinophilic disorders (NCT00001406)

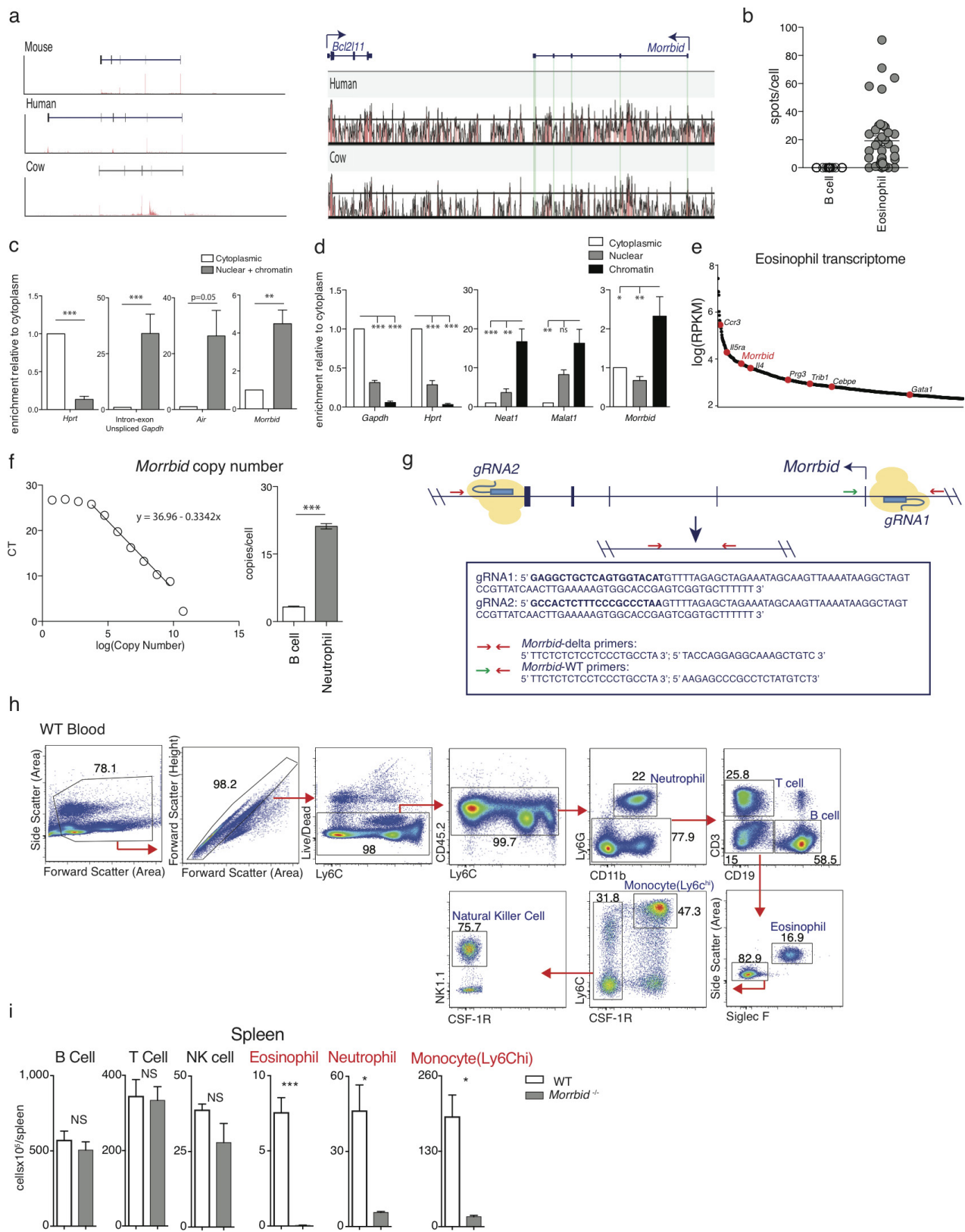


or to provide controls for in vitro research (NCT00090662). All participants gave written informed consent. Eosinophils were purified from peripheral blood by negative selection and frozen at  $-80^{\circ}\text{C}$  in TRIzol (Life Technologies). Purity was  $>97\%$  as assessed by cyto-spin. RNA was purified according to the manufacturer's instructions. Expression analysis by qPCR was performed in a blinded manner by an individual not involved in sample collection or coding of these of these samples. Plasma IL-5 levels were measured by suspension array in multiplex (Millipore). The minimum detectable concentration was  $0.1\text{ pg ml}^{-1}$ .

**Cell lines.** RAW 264.7 cells were obtained from ATCC and were not authenticated, but were tested for mycoplasma contamination biannually. Immortalized C57/B6 macrophages were obtained as a generous gift from I. Brodsky. These cells were not authenticated, but were tested for mycoplasma contamination biannually.

**Statistics.** Samples sizes were estimated based on our preliminary phenotyping of *Morbid*-deficient mice. Preliminary cell number analysis of eosinophils, neutrophils, and  $\text{Ly6C}^{\text{hi}}$  monocytes suggested that there were very large differences

between wild-type and *Morbid*-deficient samples, which would allow statistical interpretation with relatively small numbers and no statistical methods were used to predetermine sample size. No animals were excluded from analysis. All experimental and control mice and human samples were run in parallel to control for experimental variability. The experiments were not randomized. Experiments corresponding to Fig. 3g–i and Fig. 4g–j were performed and analysed in a single-blinded manner. All other experiments were not blinded to allocation during experiments and outcome assessment. Correlation was determined by calculating the Spearman correlation coefficient. Half-life was estimated by calculating the one-phase exponential decay constant from the peak of labelling frequency to 36 h after peak labelling. *P* values were calculated using a two-way *t*-test, Mann–Whitney *U*-test, one-way ANOVA with Tukey post-hoc analysis, Kaplan–Meier Mantel–Cox test, and false discovery rate (FDR) as indicated. FDR was calculated using trimmed mean of M-values (TMM)-normalized read counts and the DiffBind R package as described in Extended Data Fig. 7c, d. All error bars indicate mean plus and minus the standard error of mean (s.e.m.).

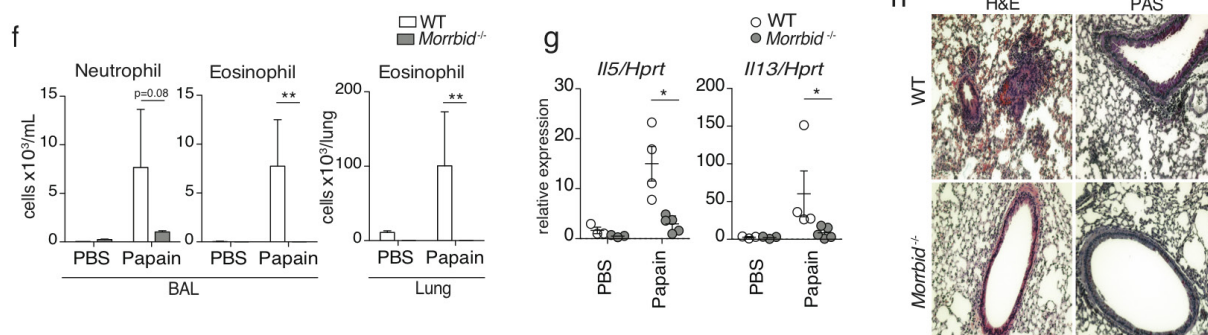


Extended Data Figure 1 | See next page for caption.

**Extended Data Figure 1 | *Morrbid* transcript expression, localization, and conservation across species.** **a**, Left: mouse, human and cow *Morrbid* transcripts. Human neutrophil, mouse granulocyte and cow peripheral blood RNA-seq data are represented as read density around the *Morrbid* transcript of each species. Right: the *Morrbid* loci and surrounding genomic regions of the indicated species were aligned with mVista and visualized using the rankVista display generated with mouse as the reference sequence. Green highlights annotated mouse exonic regions and corresponding regions in other indicated species. **b**, Quantification of *Morrbid* FISH spots per indicated cell population. Cells were stained with *Morrbid* RNA probes conjugated to 2 different fluorophores, and spots colocalizing in both fluorescent channels were quantified. **c**, Cytoplasmic and nuclear subcellular RNA fractionation of LPS-stimulated BMDMs with qPCR of indicated target transcripts ( $n = 3$  macrophages generated from independent mice). **d**, Cytoplasmic, nuclear and chromatin subcellular RNA fractionation of LPS-stimulated immortalized BMDMs with qPCR of indicated target transcripts (average of 4 independent experiments). **e**, Mature eosinophil transcriptome sorted in descending order of log(RPKM) gene expression,

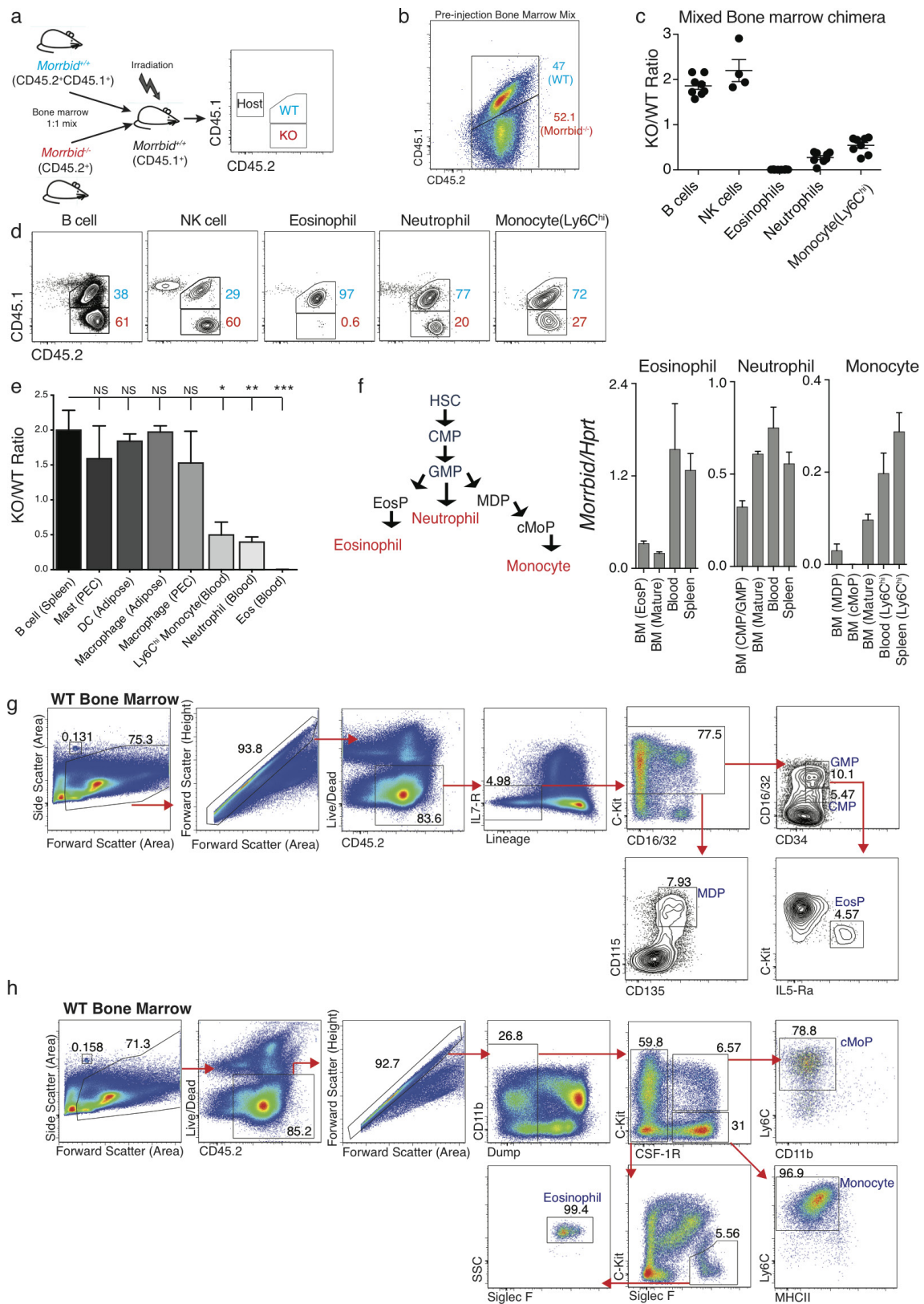
with annotated select reported eosinophil-associated genes. **f**, Average number of *Morrbid* RNA copies per cell in sorted neutrophils and B cells. Left: standard curve generated using *in vitro* transcribed *Morrbid* RNA spiked into *Morrbid*-deficient RNA isolated from spleen. Right: calculated per cell *Morrbid* RNA copies ( $n = 3$  replicates from independent mice). **g**, Representation of CRISPR-Cas9 targeting of the *Morrbid* locus with indicated guide RNA (gRNA) sequences and genotyping primer sets. Target gRNA sequences are bolded. **h**, Cells isolated from the blood of wild-type mice. Representative flow cytometry plots demonstrating the gating strategy for neutrophils ( $CD45^+CD11b^+LY6G^+$ ), T cells ( $CD45^+Ly6G^-CD3^+$ ), B cells ( $CD45^+Ly6G^-CD3^-CD19^+$ ), eosinophils ( $CD45^+CD3^-CD19^-Ly6G^-SiglecF^+SSC^{hi}$ ),  $Ly6C^{hi}$  monocytes ( $CD45^+CD3^-CD19^-Ly6G^-SSC^{lo}SiglecF^-Ly6C^{hi}CSF-1R^+$ ), NK cells ( $CD45^+CD3^-CD19^-Ly6G^-SSC^{lo}SiglecF^-CSF-1R^-NK1.1^+$ ). **i**, Total cell numbers of the indicated cell populations isolated from the spleen of wild-type and *Morrbid*-deficient mice ( $n = 3-5$  mice per group, results representative of 8 independent experiments). Error bars show s.e.m. \* $P < 0.05$ , \*\* $P < 0.01$ , and \*\*\* $P < 0.001$  (two-sided  $t$ -test, **c**, **f**, **i**; one-way ANOVA with Tukey post-hoc analysis, **d**).





**Extended Data Figure 2 | Myeloid cell populations in tissue following *Morrbid* deletion, and blood and spleen following *Morrbid* knockdown *in vivo*.** **a**, Representative flow cytometry plots and absolute counts of the indicated cell populations in wild-type and *Morrbid*-deficient mice ( $n = 3-5$  mice per group, representative of 3-7 independent experiments). **b**, shRNA knockdown of *Morrbid* RNA relative to control vector in BM-transduced with the indicated GFP vector, sorted on GFP, differentiated into eosinophils and assessed by qPCR (each dot represents eosinophils generated from independent mice). **c**, Schematic of control and *Morrbid* shRNA1 BM chimaera generation. **d, e**, Frequency of indicated cell

populations within total GFP<sup>+</sup> transduced cells from blood (**d**) and spleen (**e**) ( $n = 3-4$  mice per transduction group). **f-h**, Wild-type and *Morrbid*-deficient mice challenged with papain or PBS. **f**, Absolute numbers of indicated cell populations in lung tissue and bronchoalveolar lavage (BAL). **g**, qPCR expression in lung tissue. **h**, Representative haematoxylin and eosin (H&E) and periodic acid-Schiff (PAS) stain lung histology at 40 $\times$  magnification ( $n = 3-4$  mice per group; representative of two independent experiments). Error bars show s.e.m. \* $P < 0.05$ , \*\* $P < 0.01$ , and \*\*\* $P < 0.001$  (two-sided *t*-test, **a**, **b**, **d**, **e**; Mann-Whitney *U*-test, **f**, **g**).

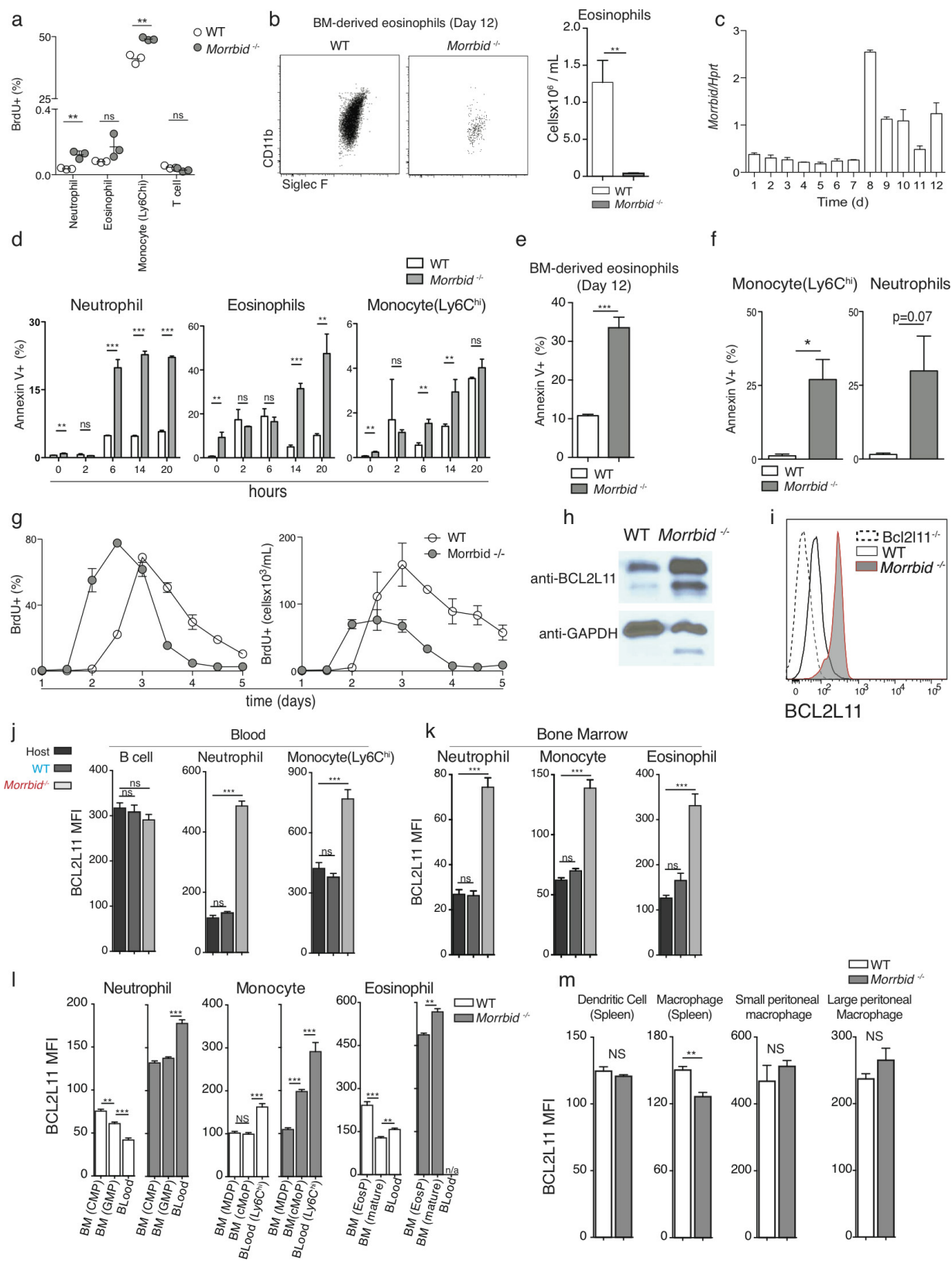


Extended Data Figure 3 | See next page for caption.

**Extended Data Figure 3 | *Morrbid* regulation of mature neutrophils, eosinophils and Ly6C<sup>hi</sup> monocytes is cell intrinsic.** **a–e**, *Morrbid*-deficient competitive BM chimaera generation. **a**, Schematic of mixed BM chimaera generation. Congenically labelled wild-type CD45.1<sup>+</sup>CD45.2<sup>+</sup> and *Morrbid*-deficient CD45.2<sup>+</sup> BM cells were mixed 1:1 and injected into an irradiated CD45.1<sup>+</sup> host. **b**, Ratio of mixed congenically labelled wild-type CD45.1<sup>+</sup>CD45.2<sup>+</sup> and *Morrbid*-deficient CD45.2<sup>+</sup> BM cells before injection into an irradiated CD45.1<sup>+</sup> host. **c**, **d**, Ratio of *Morrbid*-deficient to wild-type short-lived myeloid and control immune cells in blood (**c**) and representative flow cytometry plots of these cell populations (**d**). **e**, *Morrbid*-deficient to wild type ratio of additional immune cell populations ( $n = 4–8$  mice per group; pooled from two independent experiments). **f**, Schematic of myeloid differentiation and *Morrbid* qPCR expression in the indicated sorted progenitor and mature cells ( $n = 3–5$  mice per group; representative of 3 independent experiments). **g**, Cells isolated from the BM of wild-type mice. Representative flow cytometry

plots demonstrating the gating strategy for common myeloid progenitor (CMP): lineage<sup>−</sup>(Sca1, CD11b, GR-1, CD3, Ter-119, CD19, B220, NK1.1), IL7Ra<sup>−</sup>C-kit<sup>+</sup>CD34<sup>+</sup>CD16/32<sup>lo/int</sup>; granulocyte/monocyte progenitor (GMP): lineage<sup>−</sup>IL7Ra<sup>−</sup>C-kit<sup>+</sup>CD34<sup>+</sup>CD16/32<sup>hi</sup>; monocyte/dendritic cell progenitor (MDP): lineage<sup>−</sup>IL7Ra<sup>−</sup>C-kit<sup>+</sup>CD115<sup>+</sup>CD135<sup>+</sup>; eosinophil progenitor (EosP): lineage<sup>−</sup>IL7Ra<sup>−</sup>C-kit<sup>+</sup>CD34<sup>+</sup>CD16/32<sup>hi</sup>IL-5Ra<sup>+</sup>. **h**, Cells isolated from the BM of wild-type mice. Representative flow cytometry plots demonstrating the gating strategy for eosinophils: dump<sup>−</sup> (dump: CD3, NKp46, Ter119, CD19, Ly6G, Sca1), CSF-1R<sup>−</sup>C-kit<sup>−/lo</sup>SiglecF<sup>+</sup>SSC<sup>hi</sup>; monocytes: dump<sup>−</sup>CSF-1R<sup>+</sup>C-kit<sup>−</sup>MHCII<sup>−</sup>Ly6C<sup>hi</sup>; common monocyte progenitor (cMoP): dump<sup>−</sup>CSF-1R<sup>+</sup>C-kit<sup>+</sup>Ly6C<sup>hi</sup>CD11b<sup>lo</sup>. Flow cytometry count beads are visualized and gated by forward and side scatter area (**g**, **h**). Error bars show s.e.m. \* $P < 0.05$ , \*\* $P < 0.01$ , and \*\*\* $P < 0.001$  (one-way ANOVA with Tukey post-hoc test analysis).





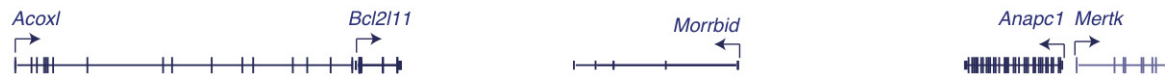
Extended Data Figure 4 | See next page for caption.

# Extended Data Figure 4 | *Morrbid* regulates neutrophil, eosinophil and Ly6C<sup>hi</sup> monocyte lifespan through cell-intrinsic regulation of *Bcl2l1*.

**a**, Flow cytometric analysis of percentage of BrdU incorporation in the indicated wild-type and *Morrbid*-deficient immune cell populations from blood. Mice were analysed 24 h after one dose of 2 mg BrdU ( $n = 3$  mice per group). **b**, Representative flow cytometry plots and absolute counts of mature eosinophils (live, CD45<sup>+</sup>SSC<sup>hi</sup>CD11b<sup>+</sup>Siglec F<sup>+</sup>) of BM-derived eosinophil culture on day 12 in wild-type and *Morrbid*-deficient mice ( $n = 3$  mice per group, results representative of 3 independent experiments). **c**, *Morrbid* expression of developing wild-type BM-derived eosinophils at indicated time points of *in vitro* culture ( $n = 3$  mice per group). **d**, Percentage of annexin V<sup>+</sup> wild-type and *Morrbid*-deficient BM cell populations at indicated time points of *ex vivo* culture ( $n = 3$  mice per group; data are representative of two independent experiments). **e**, Percentage of annexin V<sup>+</sup> eosinophils (gated on annexin-V<sup>+</sup>CD45<sup>+</sup>SSC<sup>hi</sup>CD11b<sup>+</sup>SiglecF<sup>+</sup>) of BM-derived eosinophil culture on day 12 in wild-type and *Morrbid*-deficient mice ( $n = 3$  mice per group, results representative of 3 independent experiments). **f**, Percentage of annexin V<sup>+</sup> wild-type and *Morrbid*-deficient neutrophils and Ly6C<sup>hi</sup> monocytes 4 days after *L. monocytogenes* infection ( $n = 3$  mice per group, representative of 2 independent experiments). **g**, Flow cytometric

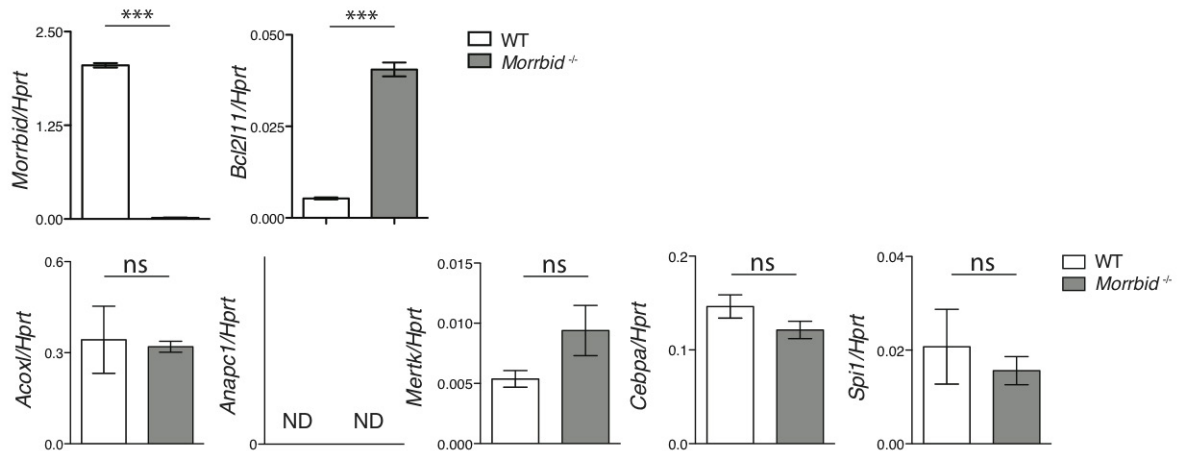
analysis of percentage and absolute number of blood neutrophils from wild-type or *Morrbid*-deficient mice that were pulsed two times with 2 mg BrdU 3 h apart and monitored over 5 days ( $n = 4$  mice per group; data are representative of three independent experiments). **h**, Western blot analysis of BCL2L1 protein expression in wild-type and *Morrbid*-deficient sorted BM neutrophils. **i**, BCL2L1 protein expression measured by flow cytometry in blood neutrophils from wild-type, *Morrbid*-deficient and *Bcl2l1*-deficient mice ( $n = 1-4$  mice per group). **j**, **k**, BCL2L1 protein expression in mixed BM chimaera model. Quantification of mean fluorescence intensity (MFI) of BCL2L1 protein expression in indicated cell populations from blood (**j**) and BM (**k**) ( $n = 4-8$  mice per group, results representative of two independent experiments). **l**, BCL2L1 protein expression in the indicated progenitors and mature cell types from wild-type and *Morrbid*-deficient mice. 'n/a' indicates that too few cells were present for MFI quantification ( $n = 3-5$  mice per group, results representative of 3 independent experiments). **m**, BCL2L1 expression measured in the indicated cell populations from wild-type and *Morrbid*-deficient mice ( $n = 3$ , results representative of two independent experiments). Error bars show s.e.m. \* $P < 0.05$ , \*\* $P < 0.01$ , and \*\*\* $P < 0.001$  (two-sided *t*-test).

a

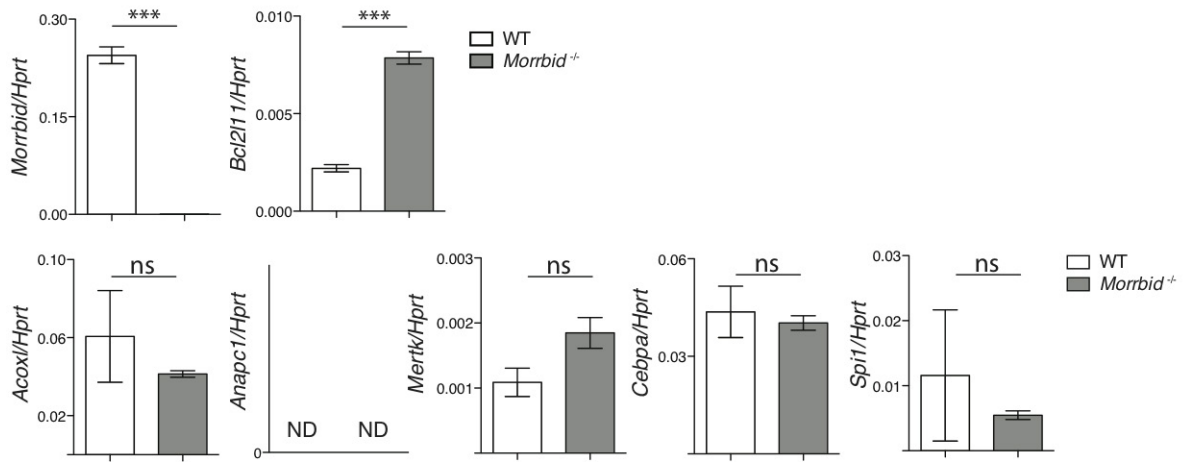


b

## Sorted bone marrow neutrophil expression



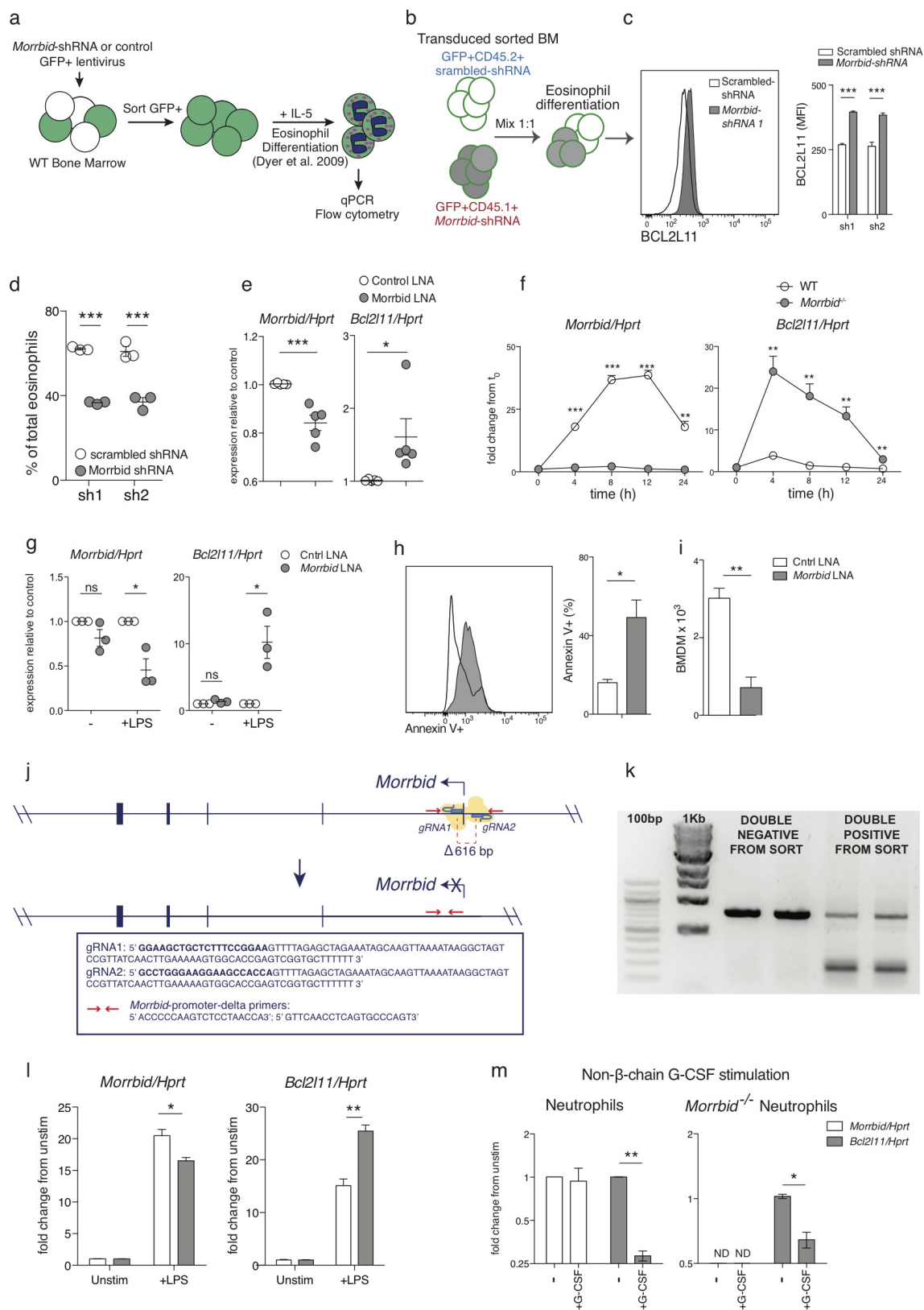
c

Sorted bone marrow monocyte (Ly6C<sup>hi</sup>) expression

**Extended Data Figure 5 | *Morrbid* specifically controls *Bcl2l11* expression.** **a**, Schematic representation of genes surrounding the *Morrbid* locus. **b**, **c**, Expression of indicated transcripts assessed by qPCR in neutrophils (**b**) and Ly6C<sup>hi</sup> (**c**) monocytes sorted from wild-type and

*Morrbid*-deficient mice. ND (not detected) indicates expression was below the limit of detection ( $n = 3$  mice per group, representative of 2 independent experiments). Error bars show s.e.m. \* $P < 0.05$ , \*\* $P < 0.01$ , and \*\*\* $P < 0.001$  (two-sided  $t$ -test).

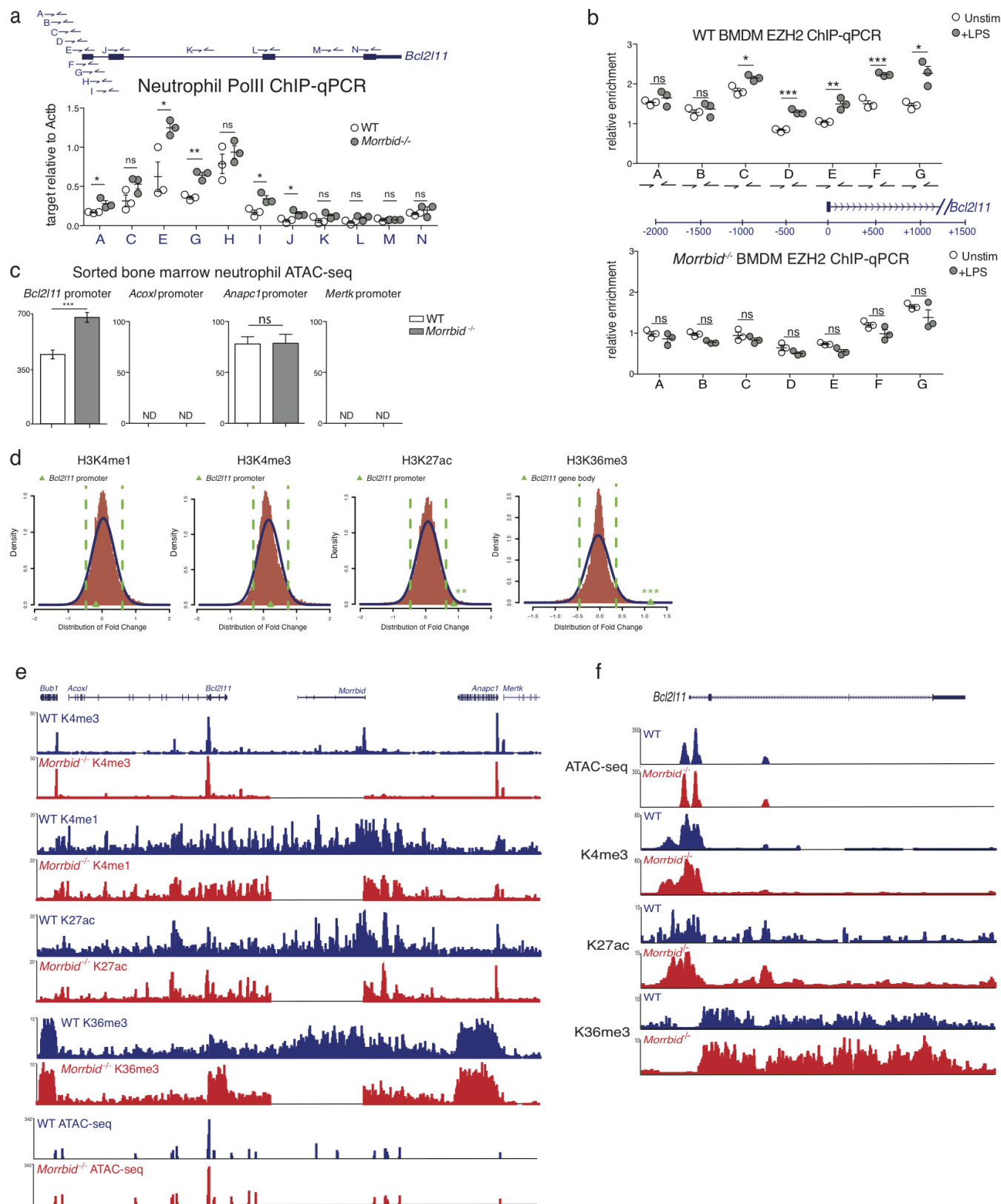




Extended Data Figure 6 | See next page for caption.

**Extended Data Figure 6 | Knockdown of *Morrbid* leads to *Bcl2l11* upregulation and cell death.** **a**, Schematic of shRNA-transduced BM-derived eosinophil system. **b–d**, *In vitro* shRNA BM-derived eosinophil competitive chimaera. **b**, Schematic of transduction of CD45.2<sup>+</sup> and CD45.1<sup>+</sup> BM cells transduced with GFP scrambled shRNA or GFP *Morrbid*-specific shRNA lentiviral vectors, respectively. GFP<sup>+</sup> cells were sorted, mixed 1:1, differentiated into eosinophils, and analysed by flow cytometry. **c**, Representative histogram and MFI quantification of BCL2L11 expression of mature eosinophils separated by congenic marker. **d**, Percentage of contribution of each congenic BM to the total mature eosinophil pool ( $n = 3$  mice per group, each dot represents eosinophils differentiated from the BM of 1 mouse, representative of 2 independent experiments). **e**, *Morrbid* and *Bcl2l11* expression of wild-type BM-derived eosinophils transfected with *Morrbid*-specific LNA 3 and control LNA (each dot represents the average of 2–3 biological replicates, data pooled from 5 independent experiments). **f**, *Morrbid* and *Bcl2l11* expression of wild-type and *Morrbid*-deficient BM-derived macrophages at the indicated time points following LPS stimulation. Expression is represented as fold change from time 0 ( $t_0$ ) ( $n = 3$  mice per group, representative of 3

independent experiments). **g–i**, LPS-stimulated BM-derived macrophages transfected with pooled *Morrbid*-specific (LNA 1–4) or scrambled (ctrl LNA) antisense LNAs. **g**, *Morrbid* and *Bcl2l11* qPCR expression; **h**, Annexin V<sup>+</sup> expression; **i**, absolute BM-derived macrophage numbers ( $n = 3$  mice per group, representative of 6 independent experiments). **j–l**, *Morrbid* promoter deletion in immortalized BMDMs. **j**, Diagram of *Morrbid* promoter targeting in immortalized BMDMs using CRISPR–Cas9. Immortalized BMDMs were transfected with GFP-expressing Cas9 and Cherry-expressing gRNA vectors of the indicated sequences. **k**, **l**, GFP<sup>+</sup>/Cherry<sup>+</sup> and GFP<sup>+</sup>/Cherry<sup>−</sup> expressing cells were sorted and assayed at the bulk level using PCR for verification of promoter deletion using the indicated primers (**j**, **k**) and qPCR for *Morrbid* and *Bcl2l11* expression following LPS stimulation for 6 hours (**l**) ( $n = 3$  LPS-stimulated cultures, average of 3 independent experiments). **m**, *Morrbid* and *Bcl2l11* transcript expression in wild-type and *Morrbid*-deficient sorted BM-derived neutrophils stimulated with G-CSF for 4 h. Expression is represented as fold change from unstimulated ( $n = 3$  mice, representative of 2 independent experiments). Error bars show s.e.m. \* $P < 0.05$ , \*\* $P < 0.01$ , and \*\*\* $P < 0.001$  (two-sided  $t$ -test).

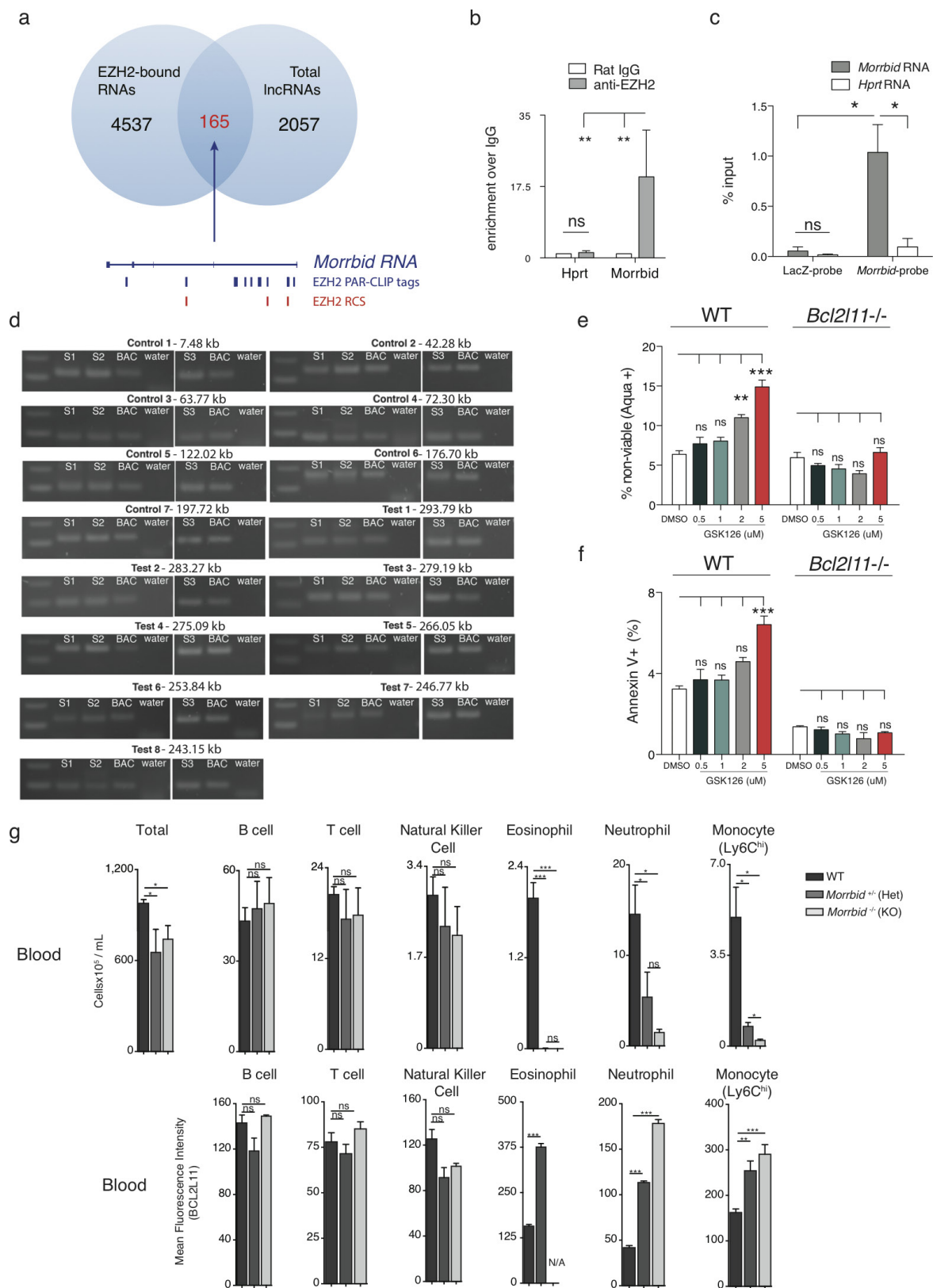


Extended Data Figure 7 | See next page for caption.



**Extended Data Figure 7 | Epigenetic effect of *Morrbid* deletion on its surrounding genomic region.** **a**, ChIP-qPCR analysis of total Pol II enrichment within the *Bcl2l1* promoter and gene body in wild-type and *Morrbid*-deficient neutrophils. Results are represented as *Bcl2l1* enrichment relative to control *Actb* enrichment within each sample. Each dot represents 1–2 pooled mice. **b**, ChIP-qPCR analysis of EZH2 enrichment within the *Bcl2l1* promoter in wild-type and *Morrbid*-deficient BMDMs stimulated with LPS for 12 hours. Results are represented as *Bcl2l1* enrichment relative to control *MyOD1* enrichment within each sample ( $n = 3$ , each dot represents BMDMs generated from 1 mouse). **c**, Relative chromatin accessibility levels at the *Bcl2l1*, *Acox1*, *Anapc1* and *Mertk* promoters in *Morrbid*<sup>-/-</sup> and wild-type neutrophils as assessed by ATAC-seq. Chromatin accessibility levels were estimated as an average trimmed mean of M-values (TMM)-normalized read count across the replicates. Statistics were obtained by differential open chromatin analysis using the DiffBind R package. The *Bcl2l1* promoter is more open in *Morrbid*<sup>-/-</sup> neutrophils with a 1.52-fold change with a FDR of < 0.1%. ND (not detected) indicates that no peak was present at the indicated

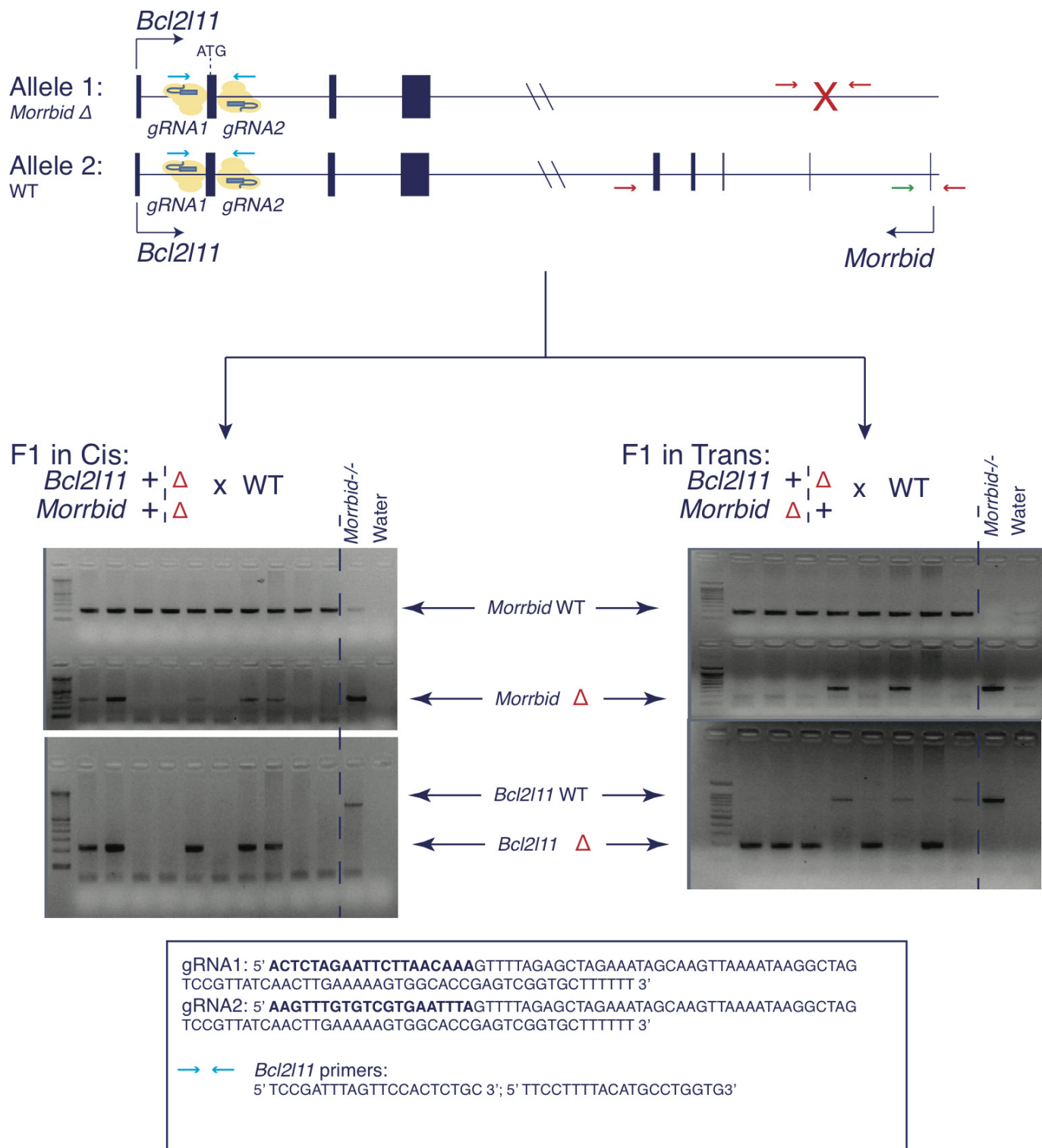
promoter. **d**, Density plot of log<sub>2</sub> fold-change distribution for H3K4me1, H3K4me3, H3K27ac and H3K36me3 levels between *Morrbid*<sup>-/-</sup> and wild-type neutrophils. Relative fold changes are estimated as the ratio of TMM-normalized read counts within consensus peak regions and were obtained using the DiffBind R package. Positive and negative fold changes indicate higher levels of ChIP binding in *Morrbid*<sup>-/-</sup> and wild-type neutrophils, respectively. Dashed green lines show the 5th and 95th percentiles. The green triangles on the  $x$  axis mark the change at the *Bcl2l1* promoter or gene body between wild-type and *Morrbid*<sup>-/-</sup> neutrophils. **e**, **f**, ATAC-seq and ChIP-seq for H3K4me1, H3K4me3, H3K27ac and H3K36me3 chromatin modifications were performed on neutrophils sorted from the bone marrow of wild-type and *Morrbid*-deficient mice. ATAC-seq and ChIP-seq are represented as read density surrounding the *Morrbid* locus (**e**) and at the *Bcl2l1* locus (**f**). ATAC-seq tracks are expressed as reads normalized to total reads, and chromatin modification tracks are expressed as reads normalized to input. Error bars show s.e.m. \* $P < 0.05$ , \*\* $P < 0.01$ , and \*\*\* $P < 0.001$  (two-sided  $t$ -test, **a**, **b**; FDR of fold change as described above, **c**, **d**).



**Extended Data Figure 8 | *Morrbid* represses *Bcl2l11* by maintaining its bivalent promoter in a poised state and phenotype of *Morrbid* heterozygous mice.** **a**, Venn diagram summary of EZH2 PAR-CLIP analysis, with representation of tags and RNA-protein contact sites as determined by PARalyzer mapping to *Morrbid*. RNA contact sites (RCS) are displayed in red. **b**, Co-immunoprecipitation of the PRC2 family member EZH2 and *Morrbid*. Nuclear extracts of immortalized wild-type BMDMs stimulated with LPS for 6–12 h were immunoprecipitated by IgG or anti-EZH2 antibodies. Co-precipitation of indicated RNAs were assayed by qPCR. Data are represented as enrichment over IgG control ( $n = 6$  biological replicates pooled from 2 independent experiments, representative of 3 independent experiments). **c**, Validation of *Morrbid* RNA pull-down over other RNAs using pools of *Morrbid* capture probes and LacZ probes ( $n = 3$ , average of 3 independent experiments).

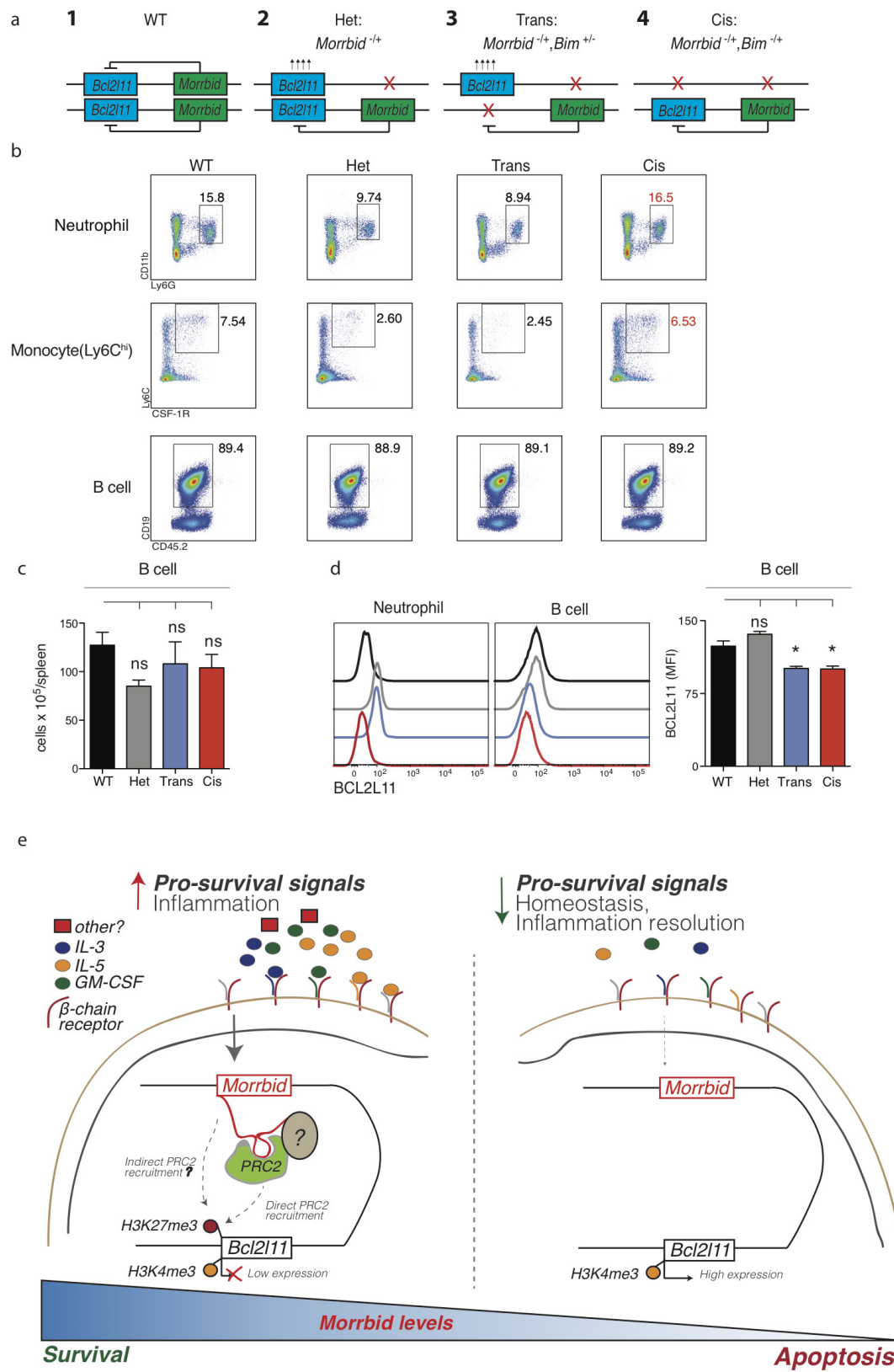
**d**, Visualized 3C PCR products from bait and indicated reverse primers using template from fixed and ligated BM-derived eosinophil DNA (S1, S2 and S3), BAC control (BAC) or water. The sequence of each reverse primer is listed in Supplementary Table 1. **e**, **f**, BM-derived eosinophils from wild-type and *Bcl2l11*<sup>-/-</sup> mice treated with EZH2 inhibitor GSK126 over time. Frequency of non-viable (Aqua<sup>+</sup>) (**e**) and annexin V (**f**) staining cells on day 5 following treatment with GSK126 ( $n = 3$  independently differentiated eosinophils per dose, results representative of 2 independent experiments). **g**, Total cell numbers (top) and BCL2L11 protein expression (bottom) of indicated cell populations from the blood of wild-type, *Morrbid*-heterozygous and *Morrbid*-deficient mice ( $n = 3$ –5 mice per group, results representative of 3 independent experiments). Error bars show s.e.m. \* $P < 0.05$ , \*\* $P < 0.01$ , and \*\*\* $P < 0.001$  (two-sided  $t$ -test, **c**, **g**; one-way ANOVA with Tukey post-hoc analysis, **e**, **f**; Mann-Whitney  $U$ -test, **b**).





**Extended Data Figure 9 | Generation of *Morrbid-Bcl2l11* double heterozygous mice.** Diagram of allele specific CRISPR–Cas9 targeting of *Bcl2l11*. *Bcl2l11* was targeted using indicated gRNA sequences in one-cell embryos from a wild-type by *Morrbid*-deficient breeding. F1 mice with allele-specific *Bcl2l11* deletions in *cis* or in *trans* of the *Morrbid*-deficient

allele were bred to a wild-type background to demonstrate linkage or segregation of *Bcl2l11* and *Morrbid* knockout alleles. Second-rightmost lanes of both gels contain *Morrbid*<sup>−/−</sup> *Bcl2l11*<sup>+/+</sup> DNA, and rightmost lanes contain water, as internal controls.



Extended Data Figure 10 | See next page for caption.

**Extended Data Figure 10 | *Morrbid* regulates *Bcl2l11* in an allele-specific manner and working model of the role of *Morrbid*.** **a**, Diagram of the allele-specific combinations of *Morrbid*- and *Bcl2l11*-deficient heterozygous mice studied. **b**, Representative flow cytometry plots of indicated splenic cell populations in the specified allele-specific deletion genetic backgrounds. Neutrophils ( $CD45^{+}CD11b^{+}LY6G^{+}$ ), monocytes ( $CD45^{+}CD3^{-}CD19^{-}Ly6G^{-}SSC^{lo}SiglecF^{-}Ly6C^{hi}CSF-1R^{+}$ ) and B cells ( $CD45^{+}Ly6G^{-}CD3^{-}CD19^{+}$ ). Wild-type (WT), *Morrbid* heterozygote (Het), *Bcl2l11* heterozygote and *Morrbid* heterozygote with deletions in *trans* (Trans), *Bcl2l11* heterozygote and *Morrbid* heterozygote with deletions in *cis* (Cis). **c**, **d**, Absolute counts (**c**) and BCL2L11 protein

expression (**d**) of indicated splenic cell populations in the specified genetic backgrounds ( $n = 3-9$  mice per genetic background). **e**, *Morrbid* integrates extracellular signals to control the lifespan of eosinophils, neutrophils and classical monocytes through the allele-specific regulation of *Bcl2l11*. Pro-survival cytokines induce *Morrbid*, which promotes enrichment of the PRC2 complex within the bivalent *Bcl2l11* promoter through direct and potentially indirect mechanisms to maintain this gene in a poised state. Tight control of the turnover of these short-lived myeloid cells by *Morrbid* promotes a balance of host anti-pathogen immunity with host damage from excess inflammation. Error bars show s.e.m. \* $P < 0.05$ , \*\* $P < 0.01$ , and \*\*\* $P < 0.001$  (one-way ANOVA with Tukey post-hoc analysis).



# PionX sites mark the X chromosome for dosage compensation

Raffaella Villa<sup>1</sup>, Tamas Schauer<sup>1</sup>, Pawel Smialowski<sup>2</sup>, Tobias Straub<sup>2</sup> & Peter B. Becker<sup>1</sup>

The rules defining which small fraction of related DNA sequences can be selectively bound by a transcription factor are poorly understood. One of the most challenging tasks in DNA recognition is posed by dosage compensation systems that require the distinction between sex chromosomes and autosomes. In *Drosophila melanogaster*, the male-specific lethal dosage compensation complex (MSL-DCC) doubles the level of transcription from the single male X chromosome, but the nature of this selectivity is not known<sup>1</sup>. Previous efforts to identify X-chromosome-specific target sequences were unsuccessful as the identified MSL recognition elements lacked discriminative power<sup>2,3</sup>. Therefore, additional determinants such as co-factors, chromatin features, RNA and chromosome conformation have been proposed to refine targeting further<sup>4</sup>. Here, using an *in vitro* genome-wide DNA binding assay, we show that recognition of the X chromosome is an intrinsic feature of the MSL-DCC. MSL2, the male-specific organizer of the complex, uses two distinct DNA interaction surfaces—the CXC and proline/basic-residue-rich domains—to identify complex DNA elements on the X chromosome. Specificity is provided by the CXC domain, which binds a novel motif defined by DNA sequence and shape. This motif characterizes a subclass of MSL2-binding sites, which we name PionX (pioneering sites on the X) as they appeared early during the recent evolution of an X chromosome in *D. miranda* and are the first chromosomal sites to be bound during *de novo* MSL-DCC assembly. Our data provide the first, to our knowledge, documented molecular mechanism through which the dosage compensation machinery distinguishes the X chromosome from an autosome. They highlight fundamental principles in the recognition of complex DNA elements by protein that will have a strong impact on many aspects of chromosome biology.

Previous work suggested that MSL2 may tether the MSL-DCC to DNA and that an intact CXC domain is required for X-chromosome discrimination<sup>5,6</sup>. To assess the DNA-binding specificity intrinsic

to MSL2 comprehensively, we surveyed the *Drosophila* genome for MSL2-binding sites *in vitro* by DNA immunoprecipitation (DIP)<sup>7,8</sup>. Recombinant MSL2 was incubated with sheared genomic DNA (gDNA) purified from male *Drosophila* S2 cells. MSL2-bound DNA was recovered and sequenced.

Considering the lack of X-chromosome binding selectivity seen in previous *in vitro* studies, we did not expect to find that MSL2 preferentially retrieved DNA from distinct genomic loci, with a notable enrichment of sequences from the X chromosome (Fig. 1a). On the X chromosome, the MSL2 binding pattern was remarkably similar to the *in vivo* pattern that marks the positions of high-affinity binding sites (HAS; or chromatin entry sites) of the MSL-DCC (Fig. 1b). A total of 57 DIP sites coincided with *in vivo* HAS, although they show different signal intensities (Extended Data Fig. 1a, b). The results were similar if DIP followed by sequencing (DIP-seq) was performed with gDNA extracted from female cells or synthesized *in vitro* by whole-genome amplification (excluding the contribution of male-specific RNA contaminants or DNA modifications) (Extended Data Fig. 1c, d). It therefore appears that recombinant MSL2 has an intrinsic ability to enrich X-chromosomal sequences from complex genomic DNA.

We next assessed the contribution of the three known MSL2 domains to DNA binding (Fig. 2a and Extended Data Fig. 2a). Deletion of the RING finger domain that mediates MSL2 interaction with MSL1 (ref. 9) and contains E3 ligase activity<sup>10</sup> had no obvious effect (Fig. 2b, c). Unexpectedly, however, deletion of a region rich in proline and basic amino acid residues (the Pro/Bas domain) that may bind RNA<sup>11</sup> resulted in the complete loss of DNA binding (Fig. 2b).

Upon deletion or mutation of the CXC domain, binding to a subset of sites was much reduced (Fig. 2b, c). Statistical analyses revealed 56 regions that specifically required a functional CXC domain for binding. Notably, these 'CXC-dependent' sites displayed a higher enrichment on the X chromosome (Fig. 2d and Extended Data Fig. 2b). A total of 37 sites mapped to MSL2 *in vivo* peaks (HAS) on

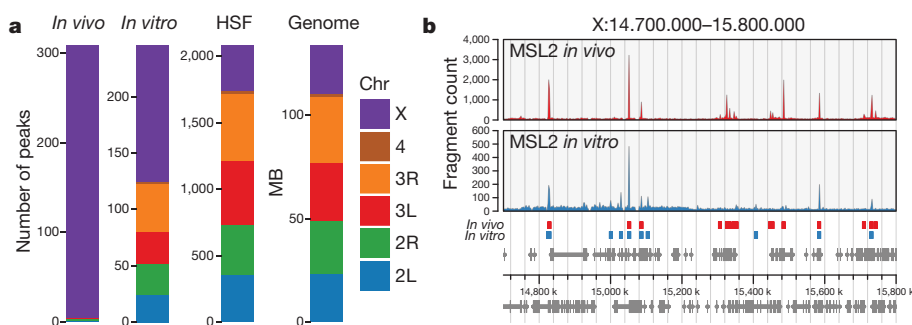


**Figure 1 | Genomewide MSL2 *in vitro* binding partially recapitulates the *in vivo* pattern.** **a**, Chromosomal distribution of robust *in vivo* and *in vitro* MSL2 binding peaks, each determined by two independent experiments. The DIP-seq profile of heat shock factor (HSF)<sup>8</sup> and the relative size of the chromosomes (genome) serve as references for

uniform distribution. **b**, Representative profiles of MSL2 chromatin immunoprecipitation with sequencing (ChIP-seq) and DIP-seq experiments in a 1.3-Mb window on the X chromosome. Red and blue bars indicate the positions of robust peaks. Gene models are depicted in grey at the bottom.

<sup>1</sup>Division of Molecular Biology, Biomedical Center and Center for Integrated Protein Science Munich, Ludwig-Maximilians-University, 82152 Planegg-Martinsried, Germany. <sup>2</sup>Bioinformatics Unit, Biomedical Center, Ludwig-Maximilians-University, 82152 Planegg-Martinsried, Germany.

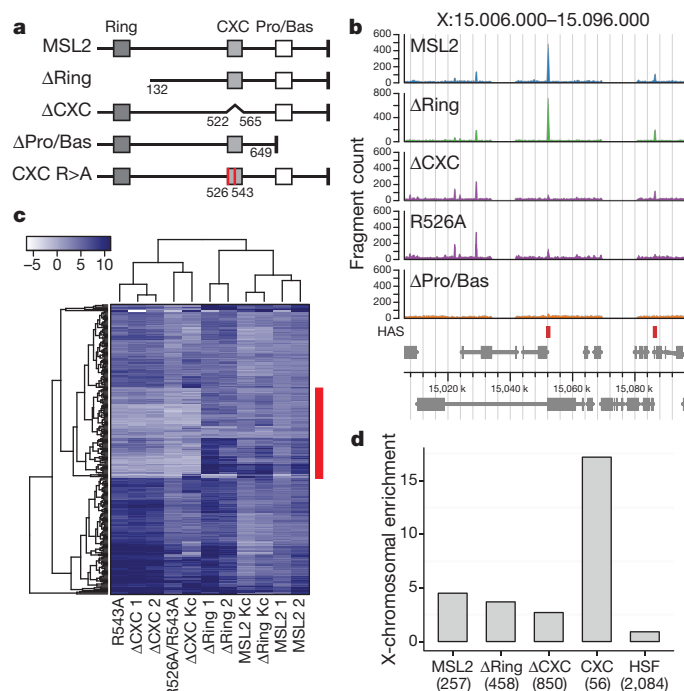


**Figure 2 | The CXC domain of MSL2 increases X-chromosomal specificity.** **a**, Linear representation of MSL2 domain organization and mutant proteins assayed in DIP. Point mutants in the CXC domain included a single (R543A) and double (R526A/R543A) mutant version. **b**, Representative DIP-seq profiles of wild-type and mutated MSL2 proteins in a region around the *hiw* gene. Red bars indicate HAS. **c**, Clustered heat map of DIP signals in all MSL2 *in vitro* peak regions. The red bar indicates a group of sites that show a prominent loss in signal upon CXC mutation. For some proteins, two independent replicates are shown. **d**, X-chromosomal enrichment over autosomes of robust wild-type and mutant MSL2 DIP-seq peaks. CXC indicates the peaks that significantly (false discovery rate (FDR) < 0.05) lose binding upon CXC depletion or mutation. The x-axis labels indicate the total number of peaks for each target in brackets.

the X chromosome, and 2 sites corresponded to rare cases of autosomal sites that show MSL2 enrichment *in vivo* (Extended Data Fig. 1e, Extended Data Table 1 and Supplementary Table 1). Our data suggest that MSL2 interacts with DNA via two domains, CXC and Pro/Bas, and that the CXC domain is the major determinant of the selectivity for the X chromosome. While binding-site specificity can be achieved by cooperation between different transcription factors<sup>12</sup>, our finding suggests that cooperation between two different DNA-binding surfaces within this one protein may also refine its overall binding specificity.

Sequence analyses within CXC-dependent and CXC-independent binding sites for MSL2 yielded two distinct motifs. Whereas the CXC-independent binding sites shared low-complexity GA repeats (Extended Data Fig. 3a), the CXC-dependent peaks centre around a more complex variation of the MSL response element (MRE), with a notable 5' extension (Figs 3a, 4c and Extended Data Fig. 3c). Remarkably, this novel motif can predict *in vivo* MSL2 binding (HAS) better than the MRE, as its position weight matrix (PWM) is superior in classifying whether MRE hit regions overlap HAS (Fig. 3b and Extended Data Fig. 3b, d). Applying low thresholds ( $q \leq 0.2$ ) we found 2,667 instances of this motif throughout the genome (Supplementary Table 1), with an approximately twofold enrichment on the X chromosome. Higher-scoring matches to the consensus sequence tend to be more strongly enriched on the X chromosome. For example, the 34 best matches are 9.8-fold enriched on the X chromosome (Extended Data Fig. 3e, f). However, 18 of those instances were not bound *in vitro* by MSL2 in a CXC-dependent manner, indicating that the recognition sequence represented by a PWM cannot fully explain this binding mode.

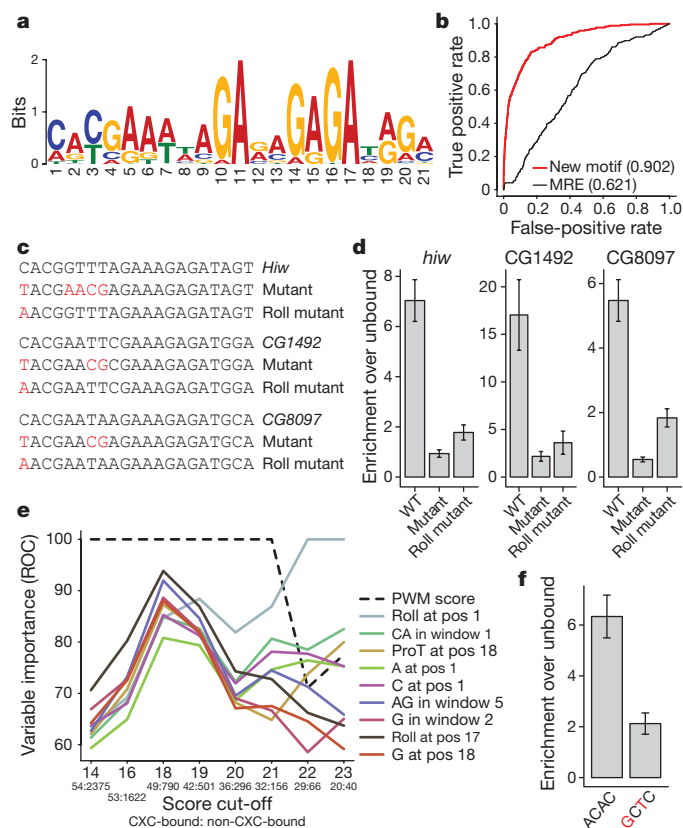


**Figure 3 | The CXC domain reads out nucleotide sequence and additional features.** **a**, Motif discovered by the MEME motif-discovery tool in CXC-dependent binding regions ( $E$ -value =  $3.9 \times 10^{-158}$ ). **b**, Receiver operating characteristic (ROC) curves representing the performance of MRE and the new motif PWMs in predicting whether genomic MRE instances (35,659) overlap with a HAS (266). Areas under the curves (AUCs) are provided in brackets. **c**, A list of oligonucleotides used in DIP experiments. Nucleotides highlighted in red are mutations introduced based on the predictions of our classification model. **d**, DIP experiments using synthetic DNA representing wild-type or mutated binding sites in the genomic context. Results from qPCR amplification were normalized for their input and shown as enrichment over an unbound fragment. Data are mean  $\pm$  s.e.m. for 3 biological replicates. **e**, Individual feature importance evaluated on sets of CXC-dependent motif instances defined by increasing score thresholds. For each feature a ROC analysis on CXC-dependent binding was performed. The AUCs of all features were scaled from 0 to 100 at each threshold level. Only features which ranked at least twice among the top five are reported. Numbers of instances (CXC-bound, non-CXC-bound) are provided underneath the x-axis tick labels. **f**, DIP experiments using the wild-type CG1492 sequence and a mutant in which the DNA roll at position +1 was reduced by mutating positions -1 and +2. Results from qPCR amplification were normalized for their input and shown as enrichment over an unbound fragment. Data are mean  $\pm$  s.e.m. for 4 biological replicates.

PWMs model the base readout of DNA sequences with the implicit assumption that each nucleotide at a given position contributes to binding independently of other positions. Physical interactions of neighbouring base pairs, however, alter the structural conformation of the DNA double helix (often referred to as the DNA shape), which may manifest as variations in the minor groove width, roll, helix twist, and propeller twist. Many proteins depend on both base identity and localized helix shape to recognize their binding site<sup>13–15</sup>. Using a pentamer-based model built from all-atom Monte Carlo simulations of DNA structures<sup>16</sup>, we calculated DNA shape parameters at each base position of the low-stringency motif hits, with 20-base-pair (bp) extensions on either side. To complement these position-centred features we also calculated regional mono- and dinucleotide frequencies ( $k$ -mers)

in 4-bp windows along the hit sequences. Principal component analysis (PCA) revealed that a combination of DNA shape and *k*-mer features was able to separate the two classes of sequences: those that were bound in a CXC-dependent manner (CXC-bound) and those that were not bound in a CXC-dependent manner (non-CXC-bound). Sequences in the latter group were either not bound at all (2,502) or were bound independently of the CXC domain (111) (Extended Data Fig. 4a and Supplementary Table 2). This suggested that at least some of the DNA features might improve binding prediction. Indeed, classification models constructed with our additional feature sets performed much better than a PWM-score model in predicting CXC-dependent binding sites on all motif hits (Extended Data Fig. 4b).

Guided by the good performance of our classification model using both the PWM-hit-score and *k*-mer features, we predicted mutations that would convert robust CXC-bound sites to non-CXC-bound sites. The model suggested that the best discriminating residues would localize to the 5' part of the motif and not to the GA-rich region (Fig. 3c). To test these predictions, we modified the DIP experiment by mixing appropriately diluted DNA oligonucleotides, representing either a native site or its mutated version, into the genomic DNA. The efficiency of DNA retrieval of experimental oligonucleotides and control genomic loci was quantified by quantitative PCR (qPCR). The results confirmed our predictions (Fig. 3d), leading us to conclude that the main determinants for CXC-dependent binding reside within the first eight bases at the 5' end of the consensus motif. Notably, this is the part of the motif that diverges most from the MRE.

To achieve a switch in the predicted class from CXC-bound to non-bound in the context of the unbalanced data set of low-threshold instances (54 bound sites, 2,613 non-bound sites) required at least three mutations. This inevitably affected the motif score, making it difficult to distinguish the effects of base and shape readout. To reduce class imbalance and to evaluate the contribution of shape features to CXC-dependent binding of sequences with high similarity to the motif consensus, we limited the analysis to fewer sites through the stepwise increase of motif score thresholds. Figure 3e reveals the relative success of the PWM score compared with a selection of additional features in predicting CXC-dependent binding. In a more balanced data set of motifs consisting of the 95 best motif hits (29 sequences CXC-bound, 66 non-bound) the PWM score was no longer a good predictor and DNA shape features became increasingly relevant. In particular, 'roll at position +1' (that is, the roll between the first two base pairs of the motif) turned into the best-performing predictor when sequences with

PWM scores higher than 21 were considered. We therefore focused on the 34 highest-scoring motif sequences ( $q < 0.05$ ), which are highly enriched on the X chromosome; however, only 16 of them are bound in a CXC-dependent manner by MSL2. We systematically scanned these high-scoring sequences for statistically significant shape differences between the CXC-bound and non-bound classes at any nucleotide position (Extended Data Fig. 4d). The results confirmed that 'roll at position +1' was appreciably different between the two classes. To test experimentally the importance of this feature we changed the degree of roll at position +1 from  $>4^\circ$  to  $<-2^\circ$  by either replacing cytosine at position +1 or the two adenines at positions -1 and +2. These mutations led to a clear reduction in MSL2 binding (Fig. 3c, d, f). We were also able to convert a sequence that was not efficiently bound by MSL2 into one that was by changing the roll at position +1 from  $<-1.9^\circ$  to  $>4^\circ$  (Extended Data Fig. 4c). Adding the DNA shape feature 'roll at position +1' to our PWM-hit-score classification model resulted in substantially improved performance when applied to the complete list of 2,667 motif hits (Extended Data Fig. 4b). We therefore conclude that the ability of MSL2 to distinguish true binding sites from a large collection of irrelevant elements with highly related sequences also relies on structural features.

To investigate further the role of MSL2-binding sites in X chromosome dosage compensation, we first attempted to monitor the interactions of MSL2 with HAS *in vivo*, with minimal contributions from other DCC subunits. Genetic studies had shown that the assembly of a mature MSL-DCC bound to the non-coding *roX* RNA in male flies is compromised by inactivating the RNA helicase maleless (MLE). Under those circumstances, the remaining MSL2-MSL1 sub-complex is bound to a small subset of HAS<sup>17</sup>. We recreated this scenario in S2 cells by using RNA interference (RNAi) against *mle* expression, and found that MSL2 binding was preferentially retained at HAS, corresponding to CXC-dependent binding sites (Extended Data Fig. 5b). The 25 HAS that were most resistant to MLE depletion (Fig. 4a) revealed a shared sequence, bearing a strong resemblance to the CXC-dependent motif (Fig. 4c). By contrast, the 25 sites most sensitive to MLE depletion (bound only by the complete DCC) shared a GA motif similar to the one found in CXC-independent *in vitro* binding sites (Extended Data Fig. 5a). This suggests that under physiological conditions, the MSL2-MSL1 sub-complex directly contacts a subset of HAS in a CXC-dependent manner in the absence of associated protein and RNA subunits.

It is possible that these chromosomal interactions represent an intermediate of MSL-DCC assembly. To test this hypothesis, we initiated

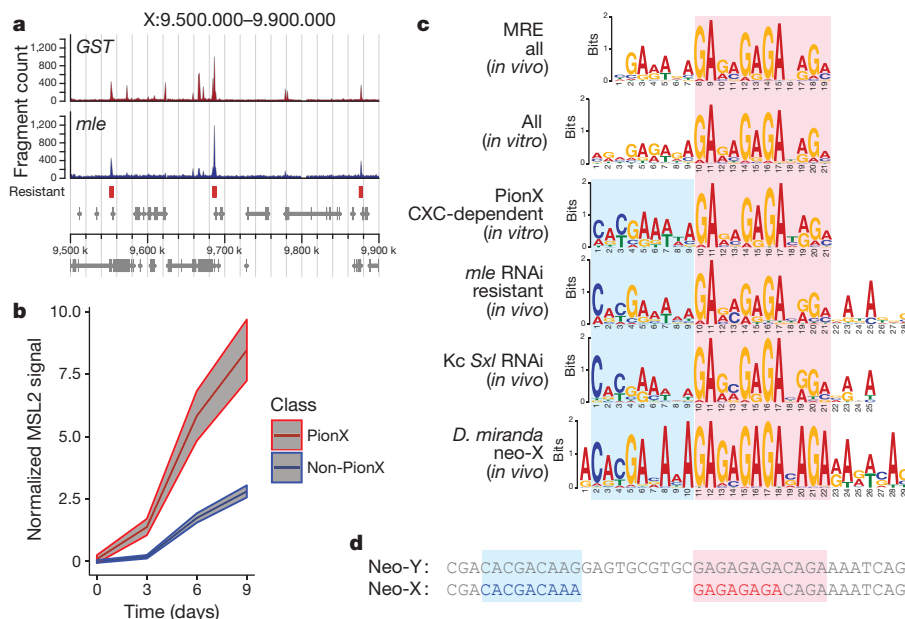


**Figure 4 | The CXC-dependent sites are pioneer HAS.** **a**, Representative profiles of MSL2 ChIP-seq from S2 cells treated with RNAi against *GST* (control) or *mle*. Red bars indicate binding sites that are maintained in the absence of MLE. **b**, MSL2 signal on 37 HAS matching CXC-dependent *in vitro* binding sites (PionX) or 272 non-matching ones (non-PionX) during SXL knockdown in Kc cells. Signals were averaged across 4 biological replicates and normalized to the mean signal at time point 0. Curves depict mean and s.e.m. across all sites within one class. **c**, Comparison of motifs found in MSL2-bound regions using different experimental approaches. See main text for details. Shown are the top scoring motifs except for 'all (in vitro)' which places second after a low-complexity GA-repeat similar to Extended Data Fig. 3a. **d**, Schematic representation of the 10-bp deletion that generated PionX motifs on the *D. miranda* neo-X chromosome<sup>21</sup>.



*de novo* MSL-DCC assembly in female Kc cells by reducing the expression of the sex-lethal gene *Sxl*. The SXL protein prevents MSL2 expression and thus the dosage compensation program in female cells. Upon depletion of SXL (Extended Data Fig. 5c, d), binding of newly expressed MSL2 to CXC-dependent HAS was stronger and occurred earlier when compared to CXC-independent ones (Fig. 4b). Consistent with this finding, hierarchical clustering of MSL2 signals from the common set of Kc and S2 peak regions revealed 30 sites that acquire strong MSL2 binding ability 3 days after SXL depletion (Extended Data Fig. 5d). *De novo* motif discovery on these sites revealed a consensus sequence that resembles the one in the CXC-dependent sites (Fig. 4c). Our data strongly suggest that those sites identified *in vitro* as CXC-dependent are pioneering binding sites for MSL2 *in vivo*. We therefore refer to them as PionX sites, and to their defining motif as the PionX motif.

The notion that PionX sites are important for dosage compensation is further supported by evolutionary considerations. *Drosophila miranda* represents a unique system to study how newly evolving X chromosomes acquired dosage compensation. The *D. miranda* neo-X chromosome is a sex chromosome that began to evolve just 1 million–2 million years ago<sup>18</sup>. Owing to the relatively short evolutionary time span, the neo-X chromosome still retains many autosomal features, but has already acquired partial dosage compensation. Recent work has identified the MSL-DCC-binding sites on all *D. miranda* X chromosomes<sup>19</sup>. *De novo* motif analysis yielded the typical GA-rich MREs for the older, fully compensated X-chromosomal arms XL and XR. Notably, though, the consensus sequence derived from the neo-X chromosome clearly resembled the PionX signature<sup>19</sup> (Fig. 4c).

The neo-Y chromosome originated from the fusion of one Müller-C chromosome to the Y chromosome, resulting in evolutionary pressure on the second Müller-C chromosome to become the neo-X chromosome. We found the PionX motif (but not the MRE) to be particularly enriched on the *D. miranda* neo-X chromosome but not on the related *Drosophila pseudoobscura* Müller C autosome, supporting the idea that this motif represents a new X-chromosome-specific feature (Extended Data Fig. 5e). Careful comparison of neo-X-chromosome sequences with the homologous regions in *D. pseudoobscura* revealed that the novel MSL-DCC-binding sites were acquired by diverse molecular mechanisms, including point mutations and short insertions/deletions of precursor sequences<sup>20</sup>. About half of them originated from precursor sequences contained in a *D. miranda*-specific helitron transposon<sup>21</sup>. The homologous neo-Y helitron does not contain PionX motifs—only precursor sequences in which the 5' CAC motif and the 3' GA-rich element are separated. On the neo-X chromosome these two parts are fused by a 10-bp deletion to form PionX consensus motifs<sup>19,21</sup> (Fig. 4d). The insertion of a PionX consensus motif derived from the *D. miranda* neo-X chromosome into an autosome of *D. melanogaster* led to strong, ectopic binding of the MSL-DCC. By contrast, the corresponding homologous neo-Y-chromosome sequence, in which the 5' and GA sequences are split by a 10-bp insertion, did not recruit the complex<sup>19,21</sup>. A similar experiment used the strongest DCC-binding site from the neo-X chromosome and the corresponding neo-Y-chromosomal fragment, showing MSL-DCC recruitment to the former, but not to the latter<sup>19</sup>. While the neo-Y-chromosomal fragment does not contain a PionX motif, the evolved neo-X chromosome contains nine of them (Extended Data Fig. 5f). Collectively, these observations suggest that PionX motifs play an important role in *de novo* acquisition of dosage compensation.

In summary, we provide three lines of argument suggesting that PionX sites are X-chromosome-specific determinants that function early in the series of events that lead to exclusive targeting of the X chromosome and correct dosage compensation. First, PionX sites are bound by an MSL2-MSL1 sub-complex in the absence of all other subunits, a state that may reflect an early intermediate of MSL-DCC assembly at HAS. Second, PionX sites are the first to be occupied during *de novo*

establishment of dosage compensation. Finally, PionX motifs arose during the early phase of neo-X-chromosome evolution in *D. miranda*.

A pertinent conceptual advance from our study is the understanding that not all HAS contain the same amount of information. The subset of PionX sites are not necessarily sites of highest MSL2 occupancy *in vivo* (Extended Data Fig. 1b), but contribute an important qualitative element of X-chromosomal discrimination. This discrimination is not wholly apparent from the consensus motif as it also relies on the shape of the DNA at the MSL2-binding site.

The initial recruitment of MSL2 to PionX sites on the X chromosome may trigger the distribution of the complex to nearby non-PionX HAS within the chromosomal territory, thereby further amplifying the difference in MSL2 occupancy between the X chromosome and the autosomes. It is likely that other factors contribute to the stability of the targeting system *in vivo*, such as the cooperativity of MSL2 domains within what is presumed to be a dimeric complex<sup>22</sup>; the assembly of functional complexes within the X-chromosomal territory owing to transcription of *roX* RNA from the X chromosome<sup>23</sup>; synergistic interactions between different MSL-DCC complexes and with the CLAMP protein at clustered MREs<sup>24</sup>; and a supportive organization of the conformation of the X chromosome<sup>25</sup>.

**Online Content** Methods, along with any additional Extended Data display items and Source Data, are available in the online version of the paper; references unique to these sections appear only in the online paper.

Received 14 December 2015; accepted 27 July 2016.

Published online 31 August 2016.

- Lucchesi, J. C. & Kuroda, M. I. Dosage compensation in *Drosophila*. *Cold Spring Harb. Perspect. Biol.* **7**, a019398 (2015).
- Alekseyenko, A. A. *et al.* A sequence motif within chromatin entry sites directs MSL establishment on the *Drosophila* X chromosome. *Cell* **134**, 599–609 (2008).
- Straub, T., Grimaud, C., Gilfillan, G. D., Mitterweger, A. & Becker, P. B. The chromosomal high-affinity binding sites for the *Drosophila* dosage compensation complex. *PLoS Genet.* **4**, e1000302 (2008).
- McElroy, K. A., Kang, H. & Kuroda, M. I. Are we there yet? Initial targeting of the Male-Specific Lethal and Polycomb group chromatin complexes in *Drosophila*. *Open Biol.* **4**, 140006 (2014).
- Fauth, T., Müller-Planitz, F., König, C., Straub, T. & Becker, P. B. The DNA binding CXC domain of MSL2 is required for faithful targeting of the Dosage Compensation Complex to the X chromosome. *Nucleic Acids Res.* **38**, 3209–3221 (2010).
- Zheng, S. *et al.* Structural basis of X chromosome DNA recognition by the MSL2 CXC domain during *Drosophila* dosage compensation. *Genes Dev.* **28**, 2652–2662 (2014).
- Gossett, A. J. & Lieb, J. D. DNA immunoprecipitation (DIP) for the determination of DNA-binding specificity. *CSH Protoc.* <http://dx.doi.org/10.1101/pdb.prot4972> (2008).
- Guertin, M. J., Martins, A. L., Siepel, A. & Lis, J. T. Accurate prediction of inducible transcription factor binding intensities *in vivo*. *PLoS Genet.* **8**, e1002610 (2012).
- Copps, K. *et al.* Complex formation by the *Drosophila* MSL proteins: role of the MSL2 RING finger in protein complex assembly. *EMBO J.* **17**, 5409–5417 (1998).
- Villa, R. *et al.* MSL2 combines sensor and effector functions in homeostatic control of the *Drosophila* dosage compensation machinery. *Mol. Cell* **48**, 647–654 (2012).
- Li, F., Schieman, A. H. & Scott, M. J. Incorporation of the noncoding *roX* RNAs alters the chromatin-binding specificity of the *Drosophila* MSL1/MSL2 complex. *Mol. Cell. Biol.* **28**, 1252–1264 (2008).
- Jolma, A. *et al.* DNA-dependent formation of transcription factor pairs alters their binding specificity. *Nature* **527**, 384–388 (2015).
- Abe, N. *et al.* Deconvolving the recognition of DNA shape from sequence. *Cell* **161**, 307–318 (2015).
- Joshi, R. *et al.* Functional specificity of a Hox protein mediated by the recognition of minor groove structure. *Cell* **131**, 530–543 (2007).
- Zhou, T. *et al.* Quantitative modeling of transcription factor binding specificities using DNA shape. *Proc. Natl Acad. Sci. USA* **112**, 4654–4659 (2015).
- Zhou, T. *et al.* DNASHape: a method for the high-throughput prediction of DNA structural features on a genomic scale. *Nucleic Acids Res.* **41**, W56–62 (2013).
- Dahlsveen, I. K., Gilfillan, G. D., Shelest, V. I., Lamm, R. & Becker, P. B. Targeting determinants of dosage compensation in *Drosophila*. *PLoS Genet.* **2**, e5 (2006).
- Lucchesi, J. C. Gene dosage compensation and the evolution of sex chromosomes. *Science* **202**, 711–716 (1978).
- Alekseyenko, A. A. *et al.* Conservation and *de novo* acquisition of dosage compensation on newly evolved sex chromosomes in *Drosophila*. *Genes Dev.* **27**, 853–858 (2013).

20. Zhou, Q. *et al.* The epigenome of evolving *Drosophila* neo-sex chromosomes: dosage compensation and heterochromatin formation. *PLoS Biol.* **11**, e1001711 (2013).
21. Ellison, C. E. & Bachtrog, D. Dosage compensation via transposable element mediated rewiring of a regulatory network. *Science* **342**, 846–850 (2013).
22. Hallacılı, E. *et al.* Msl1-mediated dimerization of the dosage compensation complex is essential for male X-chromosome regulation in *Drosophila*. *Mol. Cell* **48**, 587–600 (2012).
23. Park, Y., Kelley, R. L., Oh, H., Kuroda, M. I. & Meller, V. H. Extent of chromatin spreading determined by roX RNA recruitment of MSL proteins. *Science* **298**, 1620–1623 (2002).
24. Soruco, M. M. *et al.* The CLAMP protein links the MSL complex to the X chromosome during *Drosophila* dosage compensation. *Genes Dev.* **27**, 1551–1556 (2013).
25. Ramírez, F. *et al.* High-affinity sites form an interaction network to facilitate spreading of the MSL complex across the X chromosome in *Drosophila*. *Mol. Cell* **60**, 146–162 (2015).

**Supplementary Information** is available in the online version of the paper.

**Acknowledgements** This work was supported by the European Research Council under the European Union's Seventh Framework Programme

(FP7/2007-2013)/ERC grant agreement number 293948 (PBB) and the German Research Council (CRC 1064, T.St.). We thank P. Korber for suggesting the DIP experiment, F. Gebauer for sharing her antibody against SXL, and S. Schunter, V. Flynn, S. Krause and A. Zabel for technical assistance. We thank N. Gompel for critical reading of the manuscript and S. Krebs and H. Blum for their sequencing service.

**Author Contributions** R.V. and T.St. conceived the project. R.V. conducted all the experiments except for the ones in Kc cells that were performed by T.Sc. All bioinformatics analyses were conducted by T.St. with the exception of machine learning procedures that were performed by P.S. P.B.B. supervised the experiments and provided intellectual support toward design and interpretation of the results. R.V., T.St. and P.B.B. wrote the manuscript.

**Author Information** The next-generation sequencing data have been deposited at the Gene Expression Omnibus (GEO) under accession number GSE75033. Reprints and permissions information is available at [www.nature.com/reprints](http://www.nature.com/reprints). The authors declare no competing financial interests. Readers are welcome to comment on the online version of the paper. Correspondence and requests for materials should be addressed to P.B.B. ([pbecker@med.uni-muenchen.de](mailto:pbecker@med.uni-muenchen.de)) or T.St. ([tstraub@med.uni-muenchen.de](mailto:tstraub@med.uni-muenchen.de)).

**Reviewer Information** *Nature* thanks J. Larsson, R. Rohs and the other anonymous reviewer(s) for their contribution to the peer review of this work.

## METHODS

No statistical methods were used to predetermine sample size. The experiments were not randomized and investigators were not blinded to allocation during experiments and outcome assessment.

**Protein purification.** MSL2 proteins were expressed in Sf21 cells and purified by Flag affinity chromatography as described<sup>5</sup>.

**Genomic DNA preparation.** The pellet from  $6 \times 10^7$  S2 or Kc cells was suspended in 1.2 ml of lysis buffer (10 mM Tris pH 8, 100 mM NaCl, 25 mM EDTA pH 8, 0.5% SDS, 0.15 mg ml<sup>-1</sup> of proteinase K) and incubated at 56 °C overnight. After addition of sodium acetate to a final concentration of 0.3 M, the nucleic acids were extracted with phenol–chloroform and precipitated with an equal volume of isopropanol at –20 °C for 1 h. Precipitated nucleic acids were centrifuged and washed with 70% ethanol. Dried pellets were resuspended in TE buffer and sonicated with Covaris AFA S220 (microTUBEs, peak incident power 175 W, duty factor 10%, cycles per burst 200, 430 s) to generate 200-bp fragments. After RNase digestion (0.1 mg ml<sup>-1</sup>, 1 h at 37 °C), DNA was purified with the GenElute kit (Sigma). Synthetic DNA was produced using the Repli-g kit (Qiagen) with 20 ng of gDNA as starting material.

**DIP-seq.** DIP-seq experiments were performed as in ref. 7 with few modifications. In brief, 400 ng of gDNA was incubated with either 80 nM of MSL2–Flag or mutated recombinant protein at 26 °C for 30 min in 100 µl of binding buffer (100 mM KCl, 2 mM MgCl<sub>2</sub>, 2 mM Tris–HCl pH 7.5, 10% glycerol, 10 µM ZnCl<sub>2</sub>). For DIP experiments in the presence of synthetic DNA, 10 pM of the specified synthetic DNA was added to the reaction. 10% of the reactions was taken as input material and subjected to quantitative PCR and/or deep sequencing. DNA–protein complexes were immunoprecipitated using 15 µl of Flag bead slurry (M2, Sigma) for 15 min at room temperature and washed twice with 100 µl of binding buffer to eliminate unbound DNA. After digestion with proteinase K (0.5 mg ml<sup>-1</sup>, 1 h at 56 °C), DNA was purified with the GenElute kit (Sigma) and subjected to qPCR and/or deep sequencing. The DIP experiments in presence of synthetic DNA were performed using the deltaRING construct (three different protein preps).

**Cells, RNAi, ChIP-seq.** All cells used in this study were authenticated performing karyotyping and staining for the MSL–DCC and regularly tested for mycoplasma contamination.

Double-stranded RNAi fragments were generated from PCR products obtained using the following oligonucleotides: *mle* RNAi: 5′-TTAATACG ACTCACTATAGGGAGAATGGATATAAAATCTTTTGTACCAATTTTG-3′; 5′-TTAATACGACTCACTATAGGGAGAACAGGGCGCATGACTTGCT-3′. *Sxl* RNAi-1: 5′-TAATACGACTCACTATAGGGAGAGATACACGCCGTGTCC-3′; 5′-TAATACGACTCACTATAGGGAGATACCGAATTAAGAGCAAATAATAA-3′. *Sxl* RNAi-2: 5′-TAATACGACTCACTATAGGGAGACCCTATTCAGAGCCAT TGGA-3′; 5′-TAATACGACTCACTATAGGGAGAGTTATGGTACGCGGC AGATT-3′.

The culture of *Drosophila* male S2 (subclone L2-4, provided by P. Heun), female Kc cells and RNAi against *mle* and *Sxl* were performed as previously described<sup>3</sup> with modifications. At days 3, 6 and 9 after the initial treatment with dsRNA, *Sxl* RNAi cells were split and either collected for ChIP experiments and western blot analyses or treated again with *Sxl* dsRNA. For S2 cells, ChIP experiments were performed using a Covaris AFA S220 (PIP 100 W, DF 20%, 200 CB for 30 min) to generate chromatin fragments of sizes averaging 180 bp. For Kc cells, ChIP experiments were performed as before<sup>26</sup> with modifications. In brief, about  $4 \times 10^7$  cells were suspended in ice-cold homogenization buffer and fixed with 1% formaldehyde for 10 min at room temperature. After quenching with 125 mM glycine, the cells were collected and washed three times with ice-cold RIPA buffer (1% Triton X-100, 0.1% Na deoxycholate, 0.1% SDS, 140 mM NaCl, 10 mM Tris–HCl pH 8, 1 mM EDTA). Fixed nuclei were sonicated in RIPA buffer with a Covaris sonifier (PIP: 140, DF 20%, CB: 200) for 30 min.

**Antibodies.** MSL2, MLE and Lamin antibodies were previously described<sup>10</sup>. The SXL antibody was obtained from F. Gebauer.

**Library preparation and sequencing.** The Diagenode MicroPlex library kit was used to prepare libraries from 1–2 ng of input, DIP or ChIP DNA quantified using the Qubit dsDNA HS Assay kit (Life Technologies Q32851). The libraries were sequenced on a HighSeq 1500 (Illumina) instrument to yield roughly 15 million–25 million reads of 50-bp single-end sequences per sample.

**Oligonucleotides.** Double-stranded synthetic DNA fragments were obtained by annealing equimolar concentrations (10 µM) of complementary oligonucleotides. All oligonucleotides used in the DIP studies are listed in Extended Data Table 2.

**Data analysis.** If not indicated otherwise, data were processed using R (<http://www.r-project.org/>) or Bioconductor (<http://www.bioconductor.org/>) and function calls with default parameters. For hierarchical clustering of binding sites based on MSL2 signals, we applied the complete method on Euclidean distances.

**Read processing, coverage and normalized coverage.** Sequence reads were aligned to the *D. melanogaster* release 6 reference genome using Bowtie<sup>27</sup> version 1.1.1 allowing only for single matches to the reference (parameter –m 1).

We extended the matched reads to a total of 200 bp and calculated for each sample a per-base genomic coverage vector by cumulating the total spans of all sequenced fragments.

We defined target signal enrichment as the standardized difference between normalized immunoprecipitate and corresponding normalized input coverage using:

$$\text{normalized coverage}_i = \arcsin \left( \sqrt{\frac{\text{coverage}_i}{\sum_{i=1}^n \text{coverage}_i}} \right)$$

in which  $i$  denotes genomic position, and coverage denotes number of fragments covering  $i$ .

**Peak calling, definition of robust peak sets and chromosomal enrichment.** Peaks were called using Homer<sup>28</sup> findPeaks version 4.7.2 with the parameters: style = factor; size = 200; fragLength = 200; inputFragLength = 200 and C = 0. All peaks were called using the corresponding input samples as controls. We defined peaks as robust if the region was called in at least two biologically replicated samples. X-chromosomal enrichment describes the ratio of X-chromosomal peak density to autosomal peak density, with density being the number of peaks divided by length of chromosome(s).

**Definition of CXC-dependent sites (PionX).** We first defined a robust set of *in vitro* MSL2-binding regions by combining the peaks called in the two MSL2 DIP-seq experiments performed on S2 gDNA and the one performed on Kc gDNA. We calculated the average signal enrichment over the input for the profiles described in Fig. 2c. We then tested for signal differences in samples with intact CXC domain against the ones with a deleted or mutated CXC domain using a linear model (R package, limma) including the cell type (origin of gDNA) as random effect. CXC-dependent sites were defined with an FDR threshold of < 0.05 and a fold change < 0.

**De novo motif discovery and genome-wide motif searches.** We searched for enriched motifs in peak regions using MEME<sup>29</sup>, with the zero or one occurrence per sequence (zoops) model, except for searches in *D. Mirando*. Here we applied the any number of repetitions (anr) model, given the extreme amplification of motifs in some of the peak regions. Genome-wide searches were performed with FIMO<sup>29</sup> version 4.10.0 and an initial  $P$ -value cutoff of  $1 \times 10^{-5}$ .

**Definition of HAS and MRE.** MSL2 *in vivo* peaks were called on two published high-quality profiles (GEO accession codes GSM929148 and GSM929149). A total of 309 overlapping peak regions (304 on the X chromosome, 5 on the autosomes) were defined as HAS. MEME-based *de novo* motif discovery using the zoops model yielded a consensus sequence that we refer to as MRE. This MRE closely matches the original definition<sup>2,3</sup> (Extended Data Fig. 3c).

**Performance comparison of MRE and PionX PWM.** On each of the genome-wide 36,410 MRE hits we calculated the score of the PionX PWM after extending the hit region by 2 bp 5′ to the MRE consensus. We then determined the overlap of the hit regions with the 309 HAS. If more than one MRE hit matched to the same HAS, we kept the hit with the highest PionX score. We determined the ROC of each PWM by continuous thresholding of the respective scores using the match to a HAS as response. The analysis comprises 35,659 instances mapping to 266 HAS.

**Definition of *mle* RNAi-resistant sites.** Average MSL2 enrichment was calculated on all 309 robust MSL2 *in vivo* binding sites (HAS) in control and MLE RNAi ChIP-seq samples (3 biological replicates each). We then tested for difference in signals between the two experimental groups using limma (R). We defined the most resistant as the 25 sites with the highest moderated  $t$  values. Accordingly, the 25 sites with the lowest  $t$  values were defined as most sensitive sites.

**Definition of strong MSL2-binding sites upon *Sxl* RNAi in Kc cells.** Average MSL2 enrichment was calculated for all 309 HAS including the 90 robust peak regions arising in Kc cells (4 biological replicates for the *Sxl* RNAi at each time point, 2 for the controls). The signals were clustered hierarchically. Two clusters with the strongest gain were combined to constitute a set of 30 sites.

**DNA shape calculation and extended feature description.** The initial set of regions subjected to extended feature analysis was defined by applying low thresholds ( $q \leq 0.2$ ) on FIMO motif searches for the PionX motif. We obtained 2,667 hits (Supplementary Table 1), 54 of which were bound in a CXC-dependent manner by MSL2, 111 bound in a CXC-independent manner by MSL2 and 2,502 were unbound in our *in vitro* DIP-seq experiments. We refer to unbound instances as well as CXC-independently bound ones as non-CXC-bound.

DNA shape parameters were calculated with the DNashape program<sup>16</sup>. While minor groove width and propeller twist refer to specific nucleotide positions, roll and helix twist specify structural parameters between adjacent bases. For the sake of simplicity, we assigned the values of roll and helical twist to the preceding base ('roll at position 1' actually specifies the roll between the bases of nucleotides at position 1 and 2).



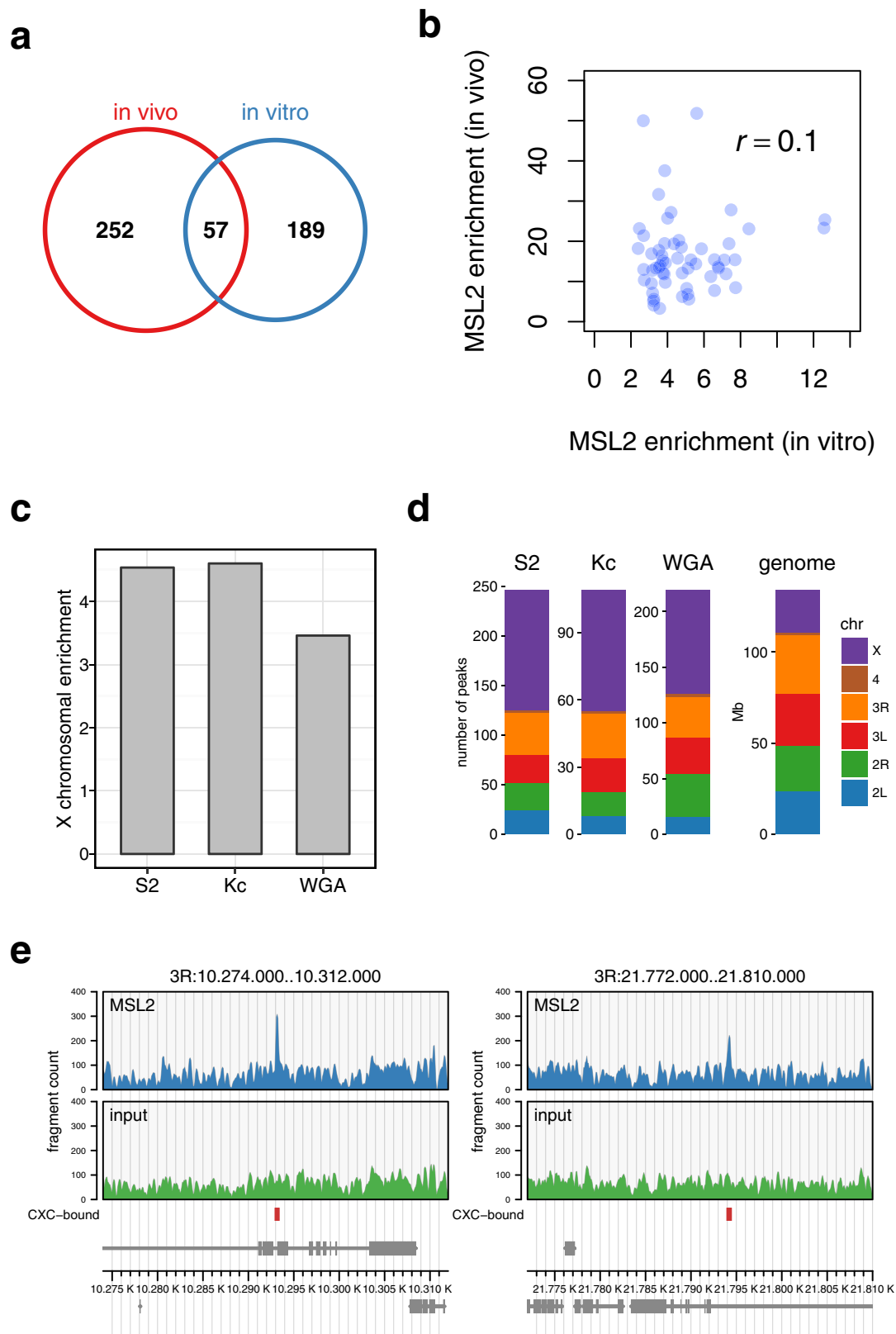
The total set of features considered in this study (with the number of variables in brackets) comprise: the PWM-hit-score (1), nucleotide composition at each position from  $-20$  bp to  $+20$  bp around the motif (244), minor groove width from  $-18$  bp to  $+18$  bp around the motif (57), roll from  $-19$  bp to  $+18$  bp around the motif (58), helix twist from  $-19$  bp to  $+18$  bp around the motif (57), propeller twist from  $-18$  bp to  $+18$  bp around the motif (57), nucleotide frequencies in six consecutive 4-bp windows starting at position 1 of the motif (24), dinucleotide frequencies in six consecutive 4-bp windows starting at position 1 of the motif (96). Minor groove width, roll, twist and propeller twist constitute the shape features (230). Mono- and dinucleotide frequencies constitute the  $k$ -mer features (120). The total number of features was 595.

**Machine learning.** Classification models for feature evaluation were built using simple logistic classifier<sup>30</sup>. ROC curves of the classifiers were based on tenfold cross-validation.

The importance of all features were ranked by measuring their correlation (Pearson's) with the class label on the whole set of PionX PWM hits with a  $q \leq 0.2$ . Features selected as relevant for and present at CXC-dependent binding of the *hiw*,

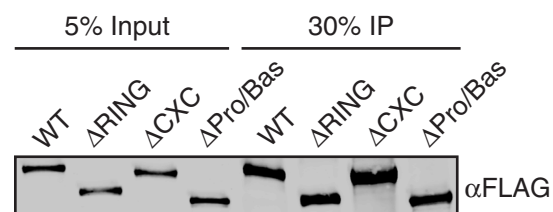
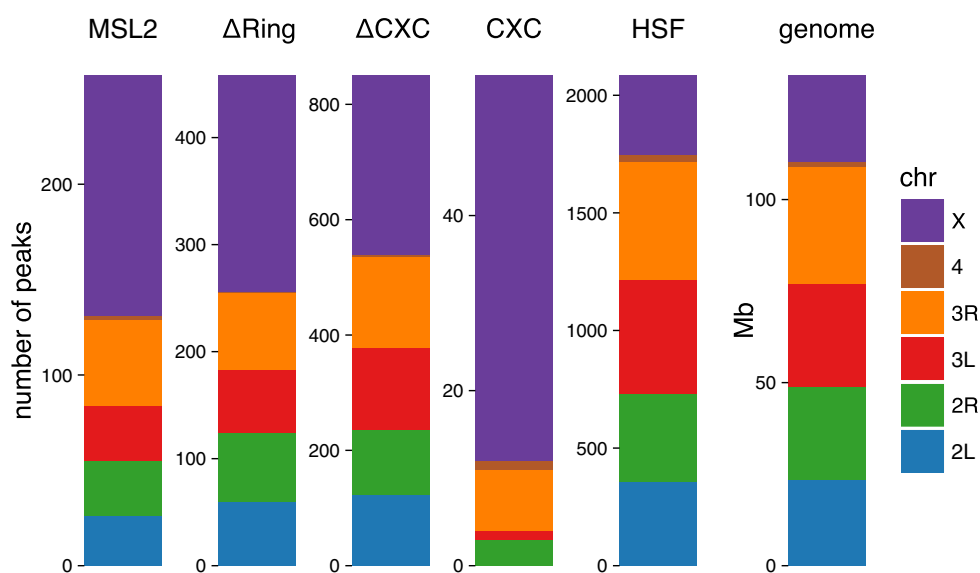
CG8097 and CG1492 genes were: 'CA in window 1', 'TT at window 2' and 'T at window 2'. Mutations were proposed based on the results of feature selection and the presence of respective  $k$ -mers in the sites selected for mutation. The proposed mutations were evaluated by simple logistic classifier trained using the PWM score and  $k$ -mers on the full data set. Modified sites were designed to result in the switch of the predicted class from CXC-bound to not CXC-bound.

26. Schauer, T. *et al.* CAST-ChIP maps cell-type-specific chromatin states in the *Drosophila* central nervous system. *Cell Reports* **5**, 271–282 (2013).
27. Langmead, B., Trapnell, C., Pop, M. & Salzberg, S. L. Ultrafast and memory-efficient alignment of short DNA sequences to the human genome. *Genome Biol.* **10**, R25 (2009).
28. Heinz, S. *et al.* Simple combinations of lineage-determining transcription factors prime cis-regulatory elements required for macrophage and B cell identities. *Mol. Cell* **38**, 576–589 (2010).
29. Bailey, T. L. *et al.* MEME SUITE: tools for motif discovery and searching. *Nucleic Acids Res.* **37**, W202–W208 (2009).
30. Sumner, M., Frank, E. & Hall, M. *Speeding Up Logistic Model Tree Induction* 675–683 (Springer, 2005).



**Extended Data Figure 1 | Analysis of *in vitro* versus *in vivo* MSL2-binding sites.** **a**, Venn diagram showing the genome-wide overlap of robust MSL2 *in vivo* and *in vitro* DNA binding peaks. **b**, MSL2 enrichment (immunoprecipitate (IP) over input) of all 57 overlapping peaks from *in vitro* DIP-seq and *in vivo* ChIP-seq experiments. The average of two biological replicates is shown, and the Pearson correlation coefficient is indicated. **c**, X-chromosomal enrichment over autosomes of MSL2 DIP-seq peaks using genomic DNA from S2 cells, Kc cells or synthetic gDNA (whole-genome amplified). S2 peaks correspond to an overlapping

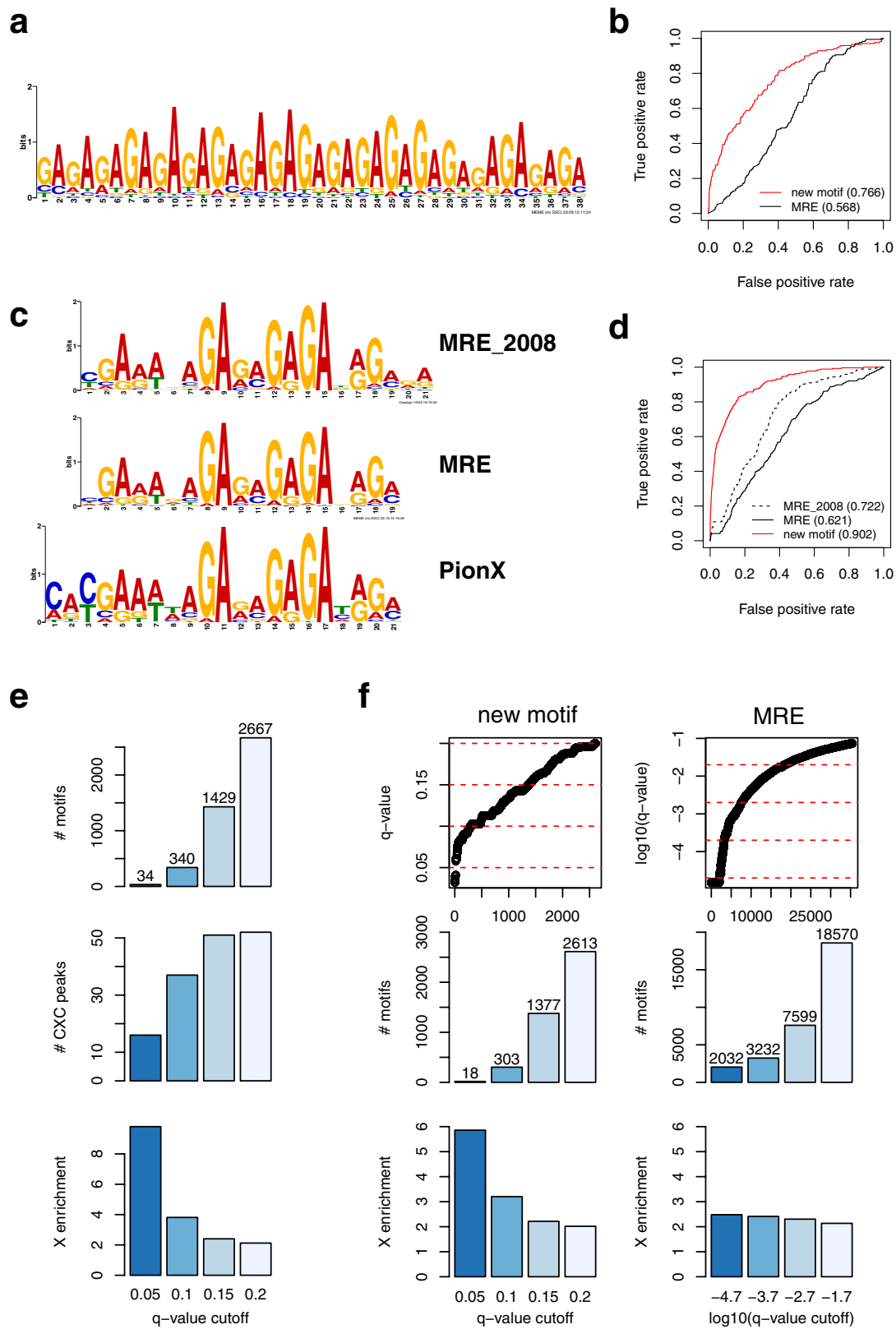
set of two biological replicate experiments; Kc cell and whole-genome amplification experiments were performed once. **d**, Chromosomal distribution of MSL2 DIP-seq peaks of experiments shown in **c**. The relative size of chromosomes and the genome serve as a reference for uniform distribution. **e**, Representative profiles of *in vivo* MSL2 ChIP-seq and the corresponding chromatin input on chromosome 3R. Red bars indicate the positions of CXC-dependent *in vitro* binding sites. Gene models are depicted in grey at the bottom.

**a****b**

**Extended Data Figure 2 | Analysis of MSL2 mutants in DIP-seq assays.**  
**a.** Western blots showing input and anti-Flag immunoprecipitated MSL2 proteins from a representative DIP experiment (for gel source data

see Supplementary Fig. 1). **b.** Chromosomal distribution of DIP-seq peaks obtained with MSL2, MSL2 mutants and HSF<sup>8</sup> (see Fig. 2d). The chromosomal size distribution (genome) is provided for reference.

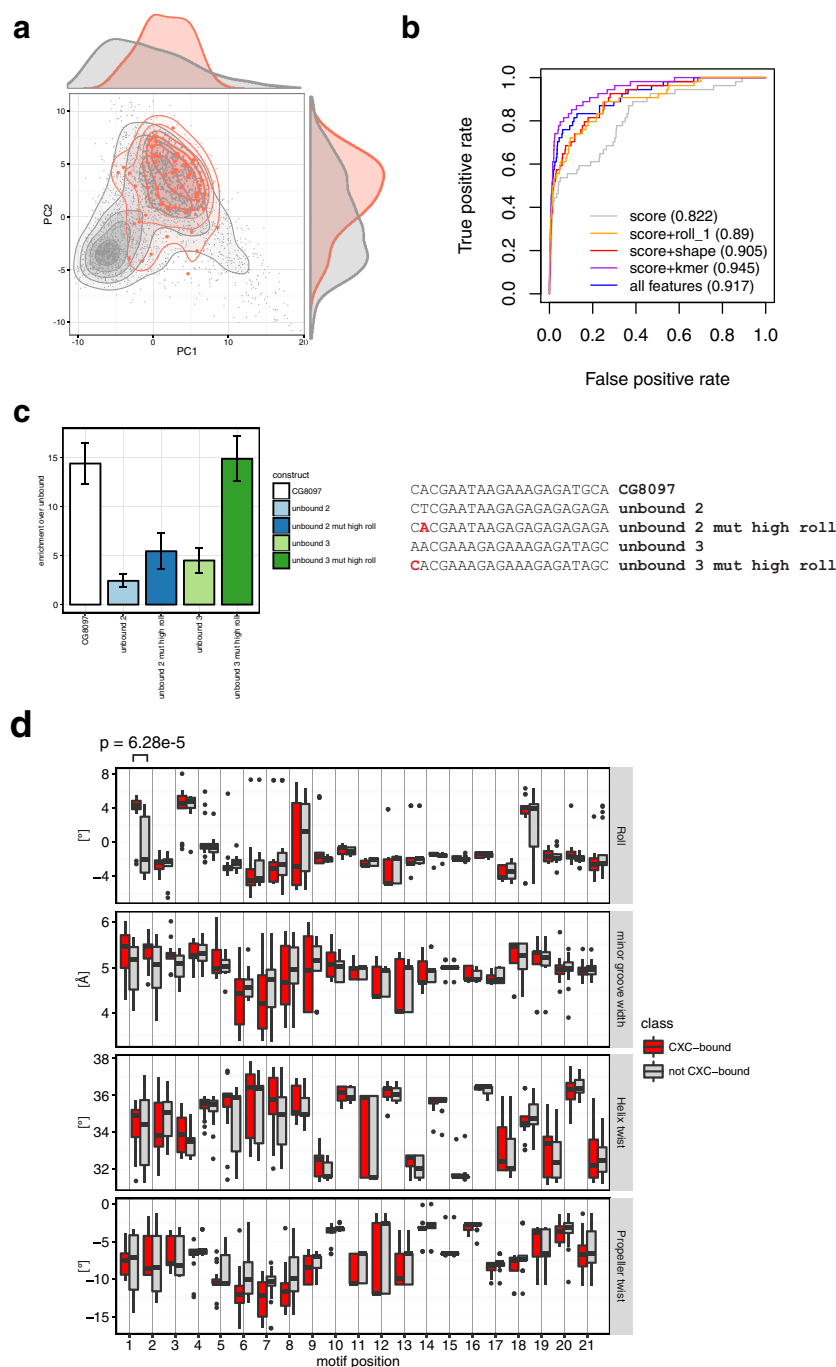




Extended Data Figure 3 | See next page for caption.

**Extended Data Figure 3 | Comparison between the CXC-dependent motif and the MRE.** **a**, Consensus motif in CXC-independent binding regions (present in 164 out of 201 regions;  $E = 2.0 \times 10^{-1,191}$ ). **b**, ROC curves representing the PWM performances of MRE and the new motif in predicting whether an instance of the new motif ( $n = 2,651$ ) will overlap with HAS (170). AUCs are provided in brackets. As our method slightly penalizes the MRE performance estimation (see Methods), this figure represents a symmetrical analysis of the new motif hits of Fig. 3b. **c**, Top, motif logos of MRE as reported previously<sup>2</sup>. Middle, MRE as reported in this study (see also Fig. 4c, top). Bottom, PionX motif as reported in this study (Fig. 3a). **d**, ROC curves representing the PWM performance comparison analogous to the result presented in Fig. 3b, including the MRE as reported previously<sup>2</sup> (labelled MRE 2008), the MRE as reported

in this study (labelled MRE) and the PionX motif (labelled new motif) in classifying MRE instances (35,659) within HAS (266) or not. AUCs are provided in brackets. **e**, Genome-wide search with the PWM of the new motif using FIMO.  $q$ -value cut-off relation with the total number of genomic hits (top), the number of CXC-dependent *in vitro* binding sites (middle) and the X-chromosomal enrichment of motif hits (bottom). **f**, To ensure that the enrichment is not solely due to performing *de novo* motif discovery on mainly X-chromosomal sequences, we performed the analysis as presented in **e** excluding the training regions. We conducted the same analysis for the new motif (left) as well as the MRE (right). Top panels depict the  $q$ -value distribution and the cut-offs used. The total numbers of genomic hits are displayed in the centre panels, with the corresponding X-chromosomal enrichments displayed at the bottom.



**Extended Data Figure 4 | Importance of *k*-mer frequencies and DNA shape for CXC-dependent MSL2 *in vitro* binding.** **a**, PCA on the set of all extended features in 2,667 genomic hit regions of the new motif ( $q \leq 0.2$ ). Scatter plots and corresponding scaled density plots of PC1 versus PC2. 2,613 sites not bound *in vitro* in a CXC-dependent manner and 54 bound in a CXC-dependent manner are coloured grey and red, respectively. **b**, ROC curves depicting the performance of simple logistic classifiers for CXC-dependent binding on 2,667 low-stringency motif hits ( $q \leq 0.2$ ; 54 sites CXC-bound, 2,613 sites non-CXC-bound) based on different combinations of motif PWM scores and extended features. AUCs are provided in brackets. **c**, DIP experiments testing the binding affinities of DNA oligonucleotides representing two unbound sites (unbound 2 and 3)

and their respective mutated sites (unbound 2 mut and unbound 3 mut) to increase the roll at position +1. Results from qPCR amplification were normalized for their input and shown as enrichment over an unbound fragment. Data are mean  $\pm$  s.e.m for 4 biological replicates. **d**, DNA shape features at each base position comparing CXC-bound motifs ( $n = 16$ ) to non-CXC-bound ones ( $n = 18$ ) in the highest-scoring hit regions of the new motif ( $q < 0.05$ ). Differences of shape features at all positions were evaluated by applying Wilcoxon exact rank tests with two-sided alternatives. Only roll at position +1 had  $P < 0.001$ . As roll and helix twist specify inter-base structural features, the corresponding bar graph representations have been centred between the respective nucleotide positions.





Extended Data Table 1 | CXC-dependent sites (PionX)

Release Dm6 coordinates		
Chromosome	Start	End
X	253666	253909
X	762263	762467
X	798142	798353
X	2024836	2025054
X	2599191	2599424
X	4628553	4628776
X	5759739	5759964
X	6083151	6083363
X	6370871	6371095
X	7288123	7288377
X	8248450	8248658
X	8689224	8689451
X	10347710	10347917
X	11580085	11580334
X	11703168	11703386
X	12010823	12011036
X	12649470	12649672
X	12715985	12716233
X	13200918	13201126
X	13263388	13263594
X	13420994	13421248
X	14103895	14104106
X	14117342	14117604
X	14585023	14585225
X	14828410	14828624
X	15052054	15052262
X	15086257	15086486
X	15584177	15584395
X	15730624	15730842
X	15875723	15875949
X	15996469	15996701
X	17655454	17655699
X	17821583	17821832
X	17926738	17926952
X	18495583	18495801
X	18849100	18849328
X	19489957	19490201
X	19730579	19730791
X	19968088	19968315
X	20024562	20024819
X	20794352	20794555
X	21317751	21317980
X	22535550	22535752
X	23100209	23100436
2R	3129113	3129339
2R	4970222	4970435
2R	13913696	13913908
3R	2556412	2556628
3R	4052724	4052974
3R	7075728	7075953
3R	10293064	10293265
3R	10516992	10517205
3R	21794080	21794326
3R	30080869	30081093
3L	3762195	3762399
4	292171	292388

Extended Data Table 2 | List of oligonucleotides used in the DIP experiments

Name	Sequence
Hiw wt	ATACGGCGACCACCGAGATAAGAACACGGTTTAGAAAGAGATAGTATTAC ACTCGTATGCCGTCTTCTGCTTG
Hiw mut	ATACGGCGACCACCGAGATAAGAATACGAACGAGAAAGAGATAGTATTAC AC TCGTATGCCGTCTTCTGCTTG
Hiw Roll mut	ATACGGCGACCACCGAGATAAGAAAACGGTTTAGAAAG GATAGTATTACACTCGTATGCCGTCTTCTGCTTG
CG8097 wt	ATACGGCGACCACCGAGATAGAAAACACGAATAAGAAAGAGATGCAAAAC ATG TCGTATGCCGTCTTCTGCTTG
CG8097 mut	ATACGGCGACCACCGAGATAGAAAATACGAACGAGAAAGAGATGCAAAAC ATG TCGTATGCCGTCTTCTGCTTG
CG8097 Roll mut	ATACGGCGACCACCGAGATAGAAAAACGAATAAGAAAGAGATGCAAAAC ATG TCGTATGCCGTCTTCTGCTTG
CG1492 wt	ATACGGCGACCACCGAGATATTTACACGAATTCGAAAGAGATGGAAATA TGC TCGTATGCCGTCTTCTGCTTG
CG1492 mut	ATACGGCGACCACCGAGATATTTCAACGAACGCGAAAGAGATGGAAATA TGC TCGTATGCCGTCTTCTGCTTG
CG1492 roll mut	ATACGGCGACCACCGAGATATTTCAAACGAATTCGAAAGAGATGGAAATA TGC TCGTATGCCGTCTTCTGCTTG
CG1492 Roll mut2	ATACGGCGACCACCGAGATATTTCGCTCGAATTCGAAAGAGATGGAAATA TGC TCGTATGCCGTCTTCTGCTTG
Unbound	ATACGGCGACCACCGAGATAATAAAATGAAAAAGAAAAAGAAAAAGAAAC ACTCGTATGCCGTCTTCTGCTTG
Unbound 2	ATACGGCGACCACCGAGATATTGCACTCGAATAAGAGAGAGAGAGAGCC ACCT TCGTATGCCGTCTTCTGCTTG
Unbound 2mut	ATACGGCGACCACCGAGATATTGCACACGAATAAGAGAGAGAGAGAGCC ACCT TCGTATGCCGTCTTCTGCTTG
Unbound 3	ATACGGCGACCACCGAGATACAGAAAACGAAAGAGAAAGAGATAGCGTTA G TCGTATGCCGTCTTCTGCTTG
Unbound 3mut	ATACGGCGACCACCGAGATACAGAAACACGAAAGAGAAAGAGATAGCGTT AG TCGTATGCCGTCTTCTGCTTG

Adapters are highlighted in yellow, mutations in blue.

# Insights from biochemical reconstitution into the architecture of human kinetochores

John R. Weir<sup>1\*</sup>, Alex C. Faesen<sup>1\*</sup>, Kerstin Klare<sup>1\*</sup>, Arsen Petrovic<sup>1</sup>, Federica Basilico<sup>1</sup>, Josef Fischböck<sup>2</sup>, Satyakrishna Pentakota<sup>1</sup>, Jenny Keller<sup>1</sup>, Marion E. Pesenti<sup>1</sup>, Dongqing Pan<sup>1</sup>, Doro Vogt<sup>1</sup>, Sabine Wohlgemuth<sup>1</sup>, Franz Herzog<sup>2</sup> & Andrea Musacchio<sup>1,3</sup>

**Chromosomes are carriers of genetic material and their accurate transfer from a mother cell to its two daughters during cell division is of paramount importance for life. Kinetochores are crucial for this process, as they connect chromosomes with microtubules in the mitotic spindle<sup>1</sup>. Kinetochores are multi-subunit complexes that assemble on specialized chromatin domains, the centromeres, that are able to enrich nucleosomes containing the histone H3 variant centromeric protein A (CENP-A)<sup>2</sup>. A group of several additional CENPs, collectively known as constitutive centromere associated network (CCAN)<sup>3–6</sup>, establish the inner kinetochore, whereas a ten-subunit assembly known as the KMN network creates a microtubule-binding site in the outer kinetochore<sup>7,8</sup>. Interactions between CENP-A and two CCAN subunits, CENP-C and CENP-N, have been previously described<sup>9–11</sup>, but a comprehensive understanding of CCAN organization and of how it contributes to the selective recognition of CENP-A has been missing. Here we use biochemical reconstitution to unveil fundamental principles of kinetochore organization and function. We show that cooperative interactions of a seven-subunit CCAN subcomplex, the CHIKMLN complex, determine binding selectivity for CENP-A over H3-nucleosomes. The CENP-A:CHIKMLN complex binds directly to the KMN network, resulting in a 21-subunit complex that forms a minimal high-affinity linkage between CENP-A nucleosomes and microtubules *in vitro*. This structural module is related to fungal point kinetochores, which bind a single microtubule. Its convolution with multiple CENP-A proteins may give rise to the regional kinetochores of higher eukaryotes, which bind multiple microtubules. Biochemical reconstitution paves the way for mechanistic and quantitative analyses of kinetochores.**

Kinetochores are one of the largest and most functionally intricate molecular machines of eukaryotic cells<sup>12</sup>. As many as 100 or more proteins reside at human mitotic kinetochores, a fraction of them are core structural components, while others play accessory regulatory roles. Kinetochores perform two related and essential functions. First, they bind to spindle microtubules to promote the bi-orientation of the sister chromatids in mitosis and meiosis II, and of their homologues in meiosis I. Second, they control the spindle assembly checkpoint, a cell cycle checkpoint that prevents chromosome segregation before completion of bi-orientation, thus ensuring genome stability during cell division<sup>1,13</sup>.

The centromere is the genetic locus, unique to each chromosome, upon which the kinetochore is established<sup>2,14</sup> (Fig. 1a). In most eukaryotes, maintenance of centromere identity does not require specific DNA sequences, but relies on epigenetic mechanisms. Crucial for this process is the deposition of new CENP-A at mitotic exit, which repopulates the CENP-A pool after its equal partition to the sister chromatids during DNA replication. Part of the machinery involved in this reaction has been identified and a molecular understanding of this process is emerging<sup>2,14</sup>. Among other requirements, the

recognition of CENP-A by other kinetochore proteins appears to play a fundamental role in the epigenetic specification of centromeres<sup>2,14</sup>. Previous studies established that CENP-C and CENP-N recognize the divergent C-terminal tail and the CENP-A-targeting domain (CATD) of CENP-A, respectively<sup>10,11</sup> (Extended Data Fig. 1). Whether CENP-C and CENP-N act in a complex on single or distinct CENP-A nucleosomes, and whether other CCAN subunits contribute to their interactions with CENP-A, is not known. To shed light on this problem and on additional functional and structural aspects of kinetochore function, we embarked on a biochemical reconstitution of human kinetochores *in vitro* with purified components (Fig. 1b and Extended Data Fig. 1; for gel source data, see Supplementary Fig. 1). Here, we report the main conclusions emerging from this effort.

Similarly to their *Saccharomyces cerevisiae* homologues<sup>15</sup>, human CENP-L and CENP-N formed a stoichiometric complex (Extended Data Fig. 2a). After solid-phase immobilization, CENP-LN interacted preferentially with octameric CENP-A nucleosome core particles (CENP-A<sup>NCP</sup>) compared with H3 nucleosome core particles (H3<sup>NCP</sup>) (Fig. 1c). Analogous results were obtained with electrophoretic mobility shift assays (EMSA; Extended Data Fig. 3a). In size-exclusion chromatography (SEC) experiments, which separate macromolecules on the basis of their size and shape, a recombinant construct encompassing residues 1–544 of CENP-C (CENP-C<sup>1–544</sup>), which embeds the first nucleosome-binding motif of CENP-C; Extended Data Figs 1 and 2b), co-eluted with CENP-A<sup>NCP</sup> but not with H3<sup>NCP</sup> (both reconstituted on a 145-bp fragment of ‘601’ DNA (ref. 16)) (Fig. 1d and Extended Data Fig. 2e, f). SEC also demonstrated that CENP-LN binds directly to CENP-C<sup>1–544</sup> (Fig. 1e, light blue trace), in line with two recent studies<sup>17,18</sup>, and directly, but more weakly, to the four-subunit CCAN subcomplex CENP-HIKM (ref. 19) (Fig. 1e, green trace). Together with our previous demonstration that CENP-C<sup>1–544</sup> binds CENP-HIKM (ref. 20), these interactions suggest that CENP-LN, CENP-HIKM, and CENP-C<sup>1–544</sup> bind in a single complex. SEC readily confirmed this hypothesis (Fig. 1e, orange trace). We refer to this seven-subunit complex as the ‘CHIKMLN’ complex (note that ‘C’ implies CENP-C<sup>1–544</sup>, not full-length CENP-C). Molecular mass estimates obtained by sedimentation velocity analytical ultracentrifugation (AUC) indicated that there is a single copy of each subunit in the HIKM and CHIKMLN complexes (Table 1 and Extended Data Fig. 4a, b).

Both CENP-C<sup>1–544</sup> and CENP-LN bind CENP-A. We therefore asked whether their presence in the same complex increases the binding affinity for CENP-A compared with individual binders. We incubated CENP-A<sup>NCP</sup> with growing concentrations of CENP-C<sup>1–544</sup>, CENP-HIKM, CENP-LN, or the CHIKMLN complex and determined relative binding affinities by EMSA assays (Fig. 2a). These experiments revealed that, besides CENP-C and CENP-LN, CENP-HIKM also binds CENP-A<sup>NCP</sup>. However, CENP-HIKM did not bind CENP-A<sup>NCP</sup> with

<sup>1</sup>Department of Mechanistic Cell Biology, Max Planck Institute of Molecular Physiology, Otto-Hahn-Straße 11, 44227 Dortmund, Germany. <sup>2</sup>Gene Center Munich, Ludwig-Maximilians-Universität München, Feodor-Lynen-Straße 25, 81377 Munich, Germany. <sup>3</sup>Centre for Medical Biotechnology, Faculty of Biology, University Duisburg-Essen, Universitätsstraße, 45141 Essen, Germany.

\*These authors contributed equally to this work.



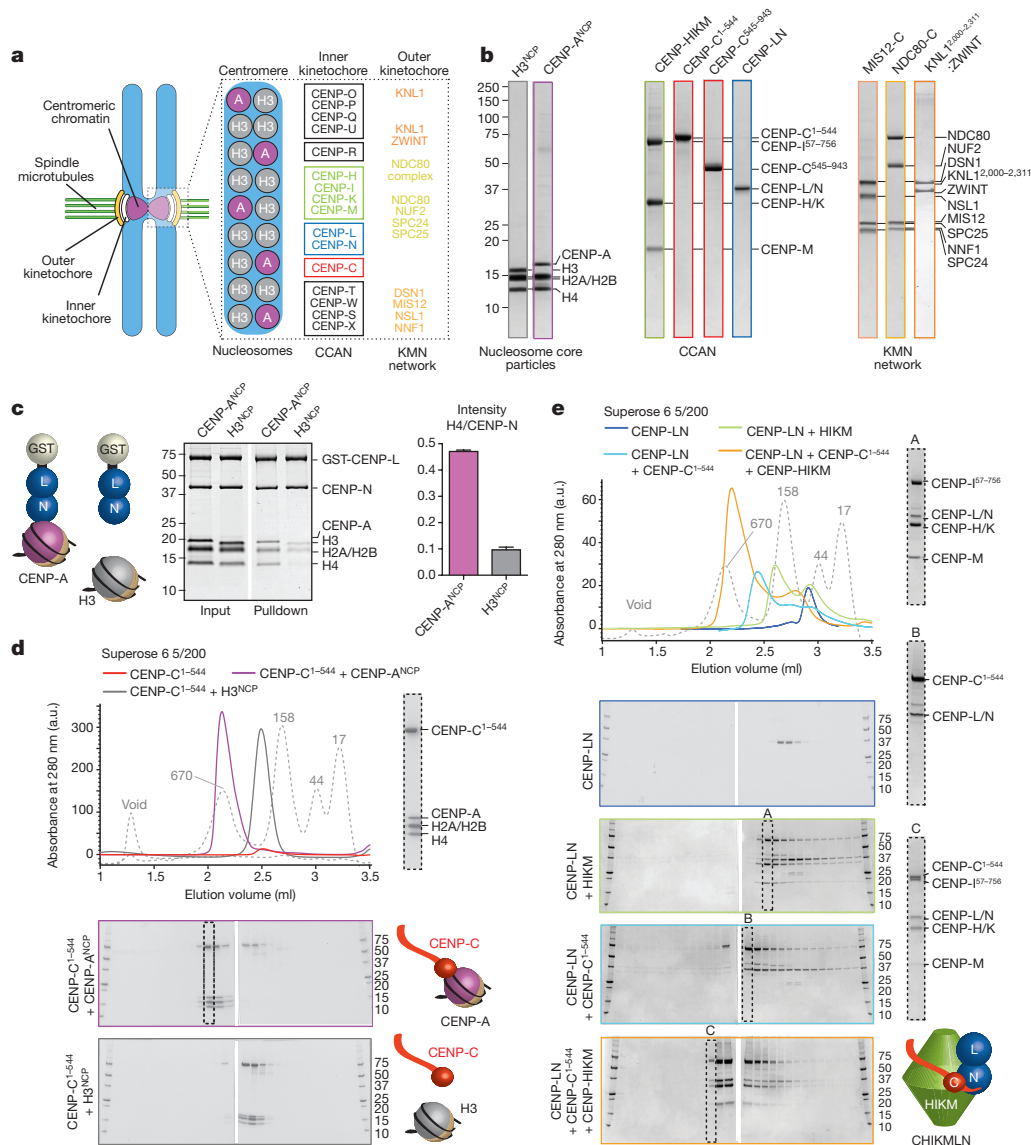


**Figure 1 | Reconstitution of the CHIKMLN complex.** **a**, Layered organization of the kinetochore with schematic depiction of subcomplexes. Those in coloured boxes were included in the reconstitution.

**b**, Coomassie-stained SDS-PAGE of recombinant proteins used in this study. **c**, CENP-LN binds preferentially to CENP-A over H3. GST-tagged CENP-L in complex with CENP-N on GSH-sepharose beads was combined with either CENP-A<sup>NCP</sup> or H3<sup>NCP</sup>. Data from three independent experiments were quantified. Shown are mean  $\pm$  s.d. **d**, CENP-C1-544 binds preferentially to CENP-A<sup>NCP</sup> over H3<sup>NCP</sup>. SEC elution profiles of

an affinity sufficient for co-elution in SEC experiments (not shown), binding with apparently similar affinity to free DNA and to H3<sup>NCP</sup> (Extended Data Fig. 3b). Notably, when bound in a single complex, the CCAN subunits showed the highest affinity for CENP-A<sup>NCP</sup>, indicative of cooperative binding (Fig. 2a). CHIKMLN co-eluted with CENP-A<sup>NCP</sup> in a single high-molecular-mass complex from an SEC column, while a much more modest shift was observed with H3<sup>NCP</sup>, demonstrating that the interaction is selective for CENP-A<sup>NCP</sup> (Fig. 2b). Additional binding experiments, shown in Extended Data Fig. 3c–e, confirmed the selectivity of the interaction of the CHIKMLN complex with CENP-A<sup>NCP</sup>.

Using AUC, we showed that a single CENP-A<sup>NCP</sup> binds two CENP-LN or CHIKMLN complexes (Table 1 and Extended Data Fig. 4). Chemical crosslinking coupled with mass spectrometry (XL-MS, ref. 21) identified an extensive network of interactions of the CHIKMLN subunits with themselves and with CENP-A<sup>NCP</sup>.

CENP-C1-544 (red trace), CENP-C1-544 mixed to CENP-A<sup>NCP</sup> (purple), and CENP-C1-544 mixed to H3<sup>NCP</sup> (grey). Shift in the elution profile indicates binding of CENP-C1-544 to CENP-A<sup>NCP</sup>. a.u., arbitrary units. **e**, CENP-LN (dark blue trace) forms a complex when mixed with CENP-C1-544 (light blue trace) or CENP-HIKM (light green trace). These interactions are compatible and lead to formation of a seven-subunit 'CHIKMLN' complex (orange trace). Elution of individual proteins or complexes is shown in Extended Data Fig. 2.

CENP-C1-544, which may be largely intrinsically disordered, contacts all other subunits, with the exclusion of histone H2A, thus emerging as the backbone of CHIKMLN (Fig. 2c and Supplementary Table 1). In line with the EMSA assays in Fig. 2a, we found several crosslinks between the CENP-HIKM complex and CENP-A<sup>NCP</sup>.

We asked if the network of interactions linking the CHIKMLN subunits and the CENP-A nucleosome correlated with localization co-dependencies in HeLa cells. Individual depletions of CENP-C, CENP-H, CENP-L, or CENP-M by RNA interference (RNAi) led to a near-complete disappearance of the other CHIKMLN subunits from kinetochores during interphase (Fig. 2d and Extended Data Fig. 5a–c). Significant levels of CENP-A were present on kinetochores at the time of fixation for indirect immunofluorescence, suggesting that the loss of CHIKMLN subunits is not caused by complete co-depletion of CENP-A, but rather by the co-dependency of CHIKMLN subunits for stable kinetochore recruitment. Collectively, our observations indicate

**Table 1 | Sedimentation velocity AUC of selected kinetochore complexes.**

Experiment	Complex	Predicted mass (kDa)	Observed mass (kDa)	Frictional ratio	Condition	Sedimentation coefficient (S)	Predicted stoichiometry
1	CENP-HIKM	160	145	1.6	A	4.2	1:1:1:1
2	CENP:CHIKMLN*	301	266	1.7	A	6.2	1:1:1:1:1:1
3	CENP-A <sup>NCP</sup>	200	206	1.4	B	10.7	octamer
4	CENP-LN + CENP-A <sup>NCP</sup>	357	360	1.76	B	10.9	2 CENP-LN:1 octamer
5	CENP-A <sup>NCP</sup>	200	ND	ND	C	7.1	ND
6	CENP-LN + CENP-A <sup>NCP</sup>	357	ND	ND	C	7.9	ND
7	CENP:CHIKMLN† + CENP-A <sup>NCP</sup>	760	ND	ND	C	16.2	ND
8	Chimeric BFP-tagged H3/CENP-A <sup>NCP</sup>	252	293	1.3	C	12.1	octamer
9	CENP:CHIKMLN† + Chimeric‡ BFP-tagged H3/CENP-A <sup>NCP</sup>	812	799	1.35	C	18.4	2 CENP:CHIKMLN:1 octamer

ND, not determined. Condition A: 20 mM HEPES pH 7.6, 300 mM NaCl, 2.5% (v/v) glycerol, 1 mM TCEP. Buffer density 1.01365 g ml<sup>-1</sup> and viscosity 1.307 centipoise (cP). Run was performed at 10 °C. Condition B: 20 mM HEPES pH 7.5, 10% glycerol, 150 mM NaCl, 1 mM EDTA, 2 mM TCEP. Buffer density 1.03503 g ml<sup>-1</sup> and viscosity of 1.002 cP. Runs were performed at 20 °C. Condition C: 20 mM Tris pH 8.5, 150 mM NaCl, 2.5% (v/v) glycerol, 1 mM TCEP. Buffer density 1.01365 g ml<sup>-1</sup> and viscosity 1.307 cP. Run was performed at 10 °C. CENP-HIKM = CENP-HI<sup>57-756</sup>KM; CENP-CHIKMLN\* = CENP-C<sup>1-544</sup>HI<sup>57-756</sup>KMLN; CENP-CHIKMLN† = CENP-C<sup>189-544</sup>HI<sup>57-756</sup>KMLN.

‡The chimera includes an N-terminal histidine tag, followed by the N-terminal region of H3.1, followed by the C-terminal region of CENP-A: 6His-H3.1(Ala2-Ile75)/CENP-A(Cys75-Gly140).

that the stability of the CHIKMLN complex, as well as its binding affinity and selectivity for the CENP-A<sup>NCP</sup>, arise from the reciprocal interactions of its subunits.

CENP-T and CENP-W, two additional CCAN subunits (Fig. 1a), contain histone-fold domains and form a tight dimer that further

associates with a dimer of two additional histone-fold-domain proteins, the CENP-SX complex<sup>5</sup>. The CENP-TWSX complex has been proposed to form a CENP-C-independent (but CENP-A-dependent) axis of kinetochore assembly<sup>22</sup>, but other reports have suggested that kinetochore localization of the CENP-TWSX complex depends on

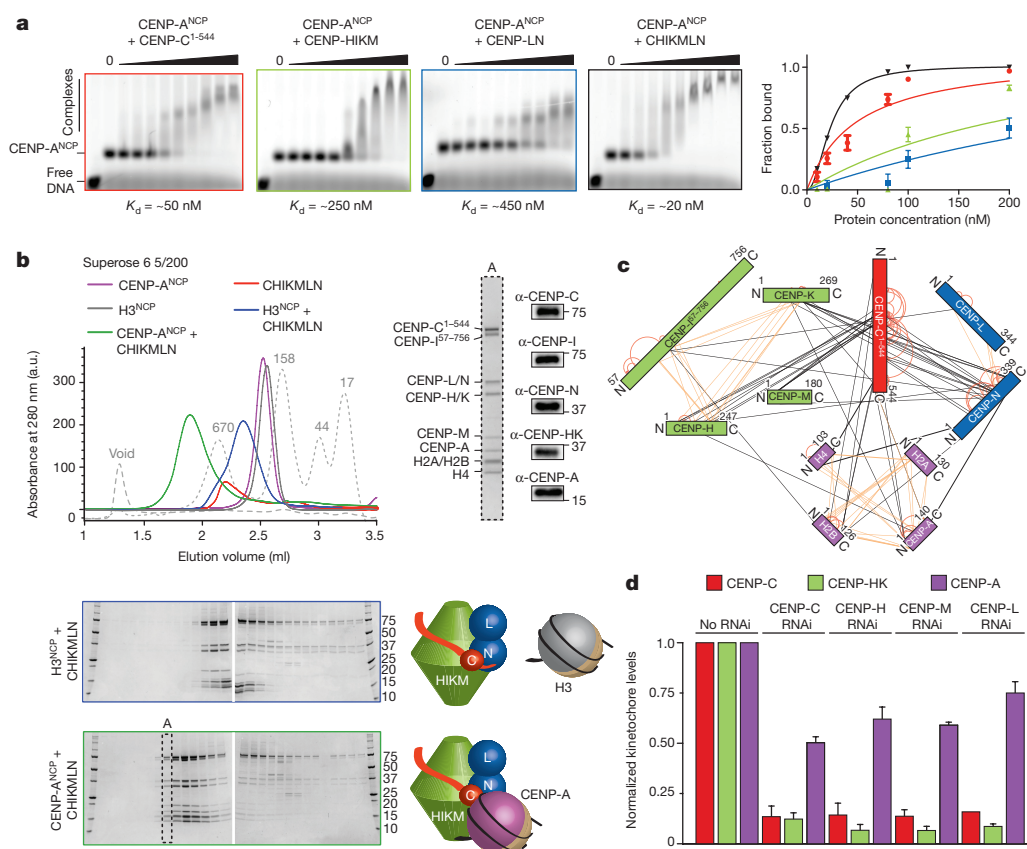


**Figure 2 | Selective cooperative binding of CHIKMLN to CENP-A mononucleosomes.** **a**, EMSA assays with the binding species indicated. Shown is mean  $\pm$  s.d. from three independent experiments. **b**, CHIKMLN complex (red trace) binds to CENP-A (green trace) but not H3 (blue trace). The composition of the CENP-A<sup>NCP</sup>:CHIKMLN complex was confirmed by the western blotting of several subunits. **c**, Topology of the CENP-A<sup>NCP</sup>:CHIKMLN complex. XL-MS revealed a network of crosslinked peptides. Intra-protein crosslinks are shown as red lines, intra-subcomplex crosslinks are shown as orange lines, inter-subcomplex crosslinks are shown as black lines. Proteins are coloured according to subcomplex (CENP-C, red; CENP-LN, blue; CENP-HIKM, green;

CENP-A<sup>NCP</sup>, purple). **d**, Cooperative localization of CHIKMLN to kinetochores. Quantification of kinetochore levels of CENP-C (red bars), CENP-HK (green bars), and CENP-A (purple bars) measured by immunofluorescence (IF) in control HeLa cells (left) or after depletion of the indicated CCAN subunits by short interfering RNAs (siRNAs) (see Methods). Localizations of CENP-C and CENP-HK are significantly perturbed, despite relatively high residual CENP-A levels. Graphs and bars indicate mean  $\pm$  s.e.m. of 2 or 3 independent experiments quantifying between 514 and 1,249 kinetochores in 13–25 cells. Representative immunofluorescence images are shown in Extended Data Fig. 5.

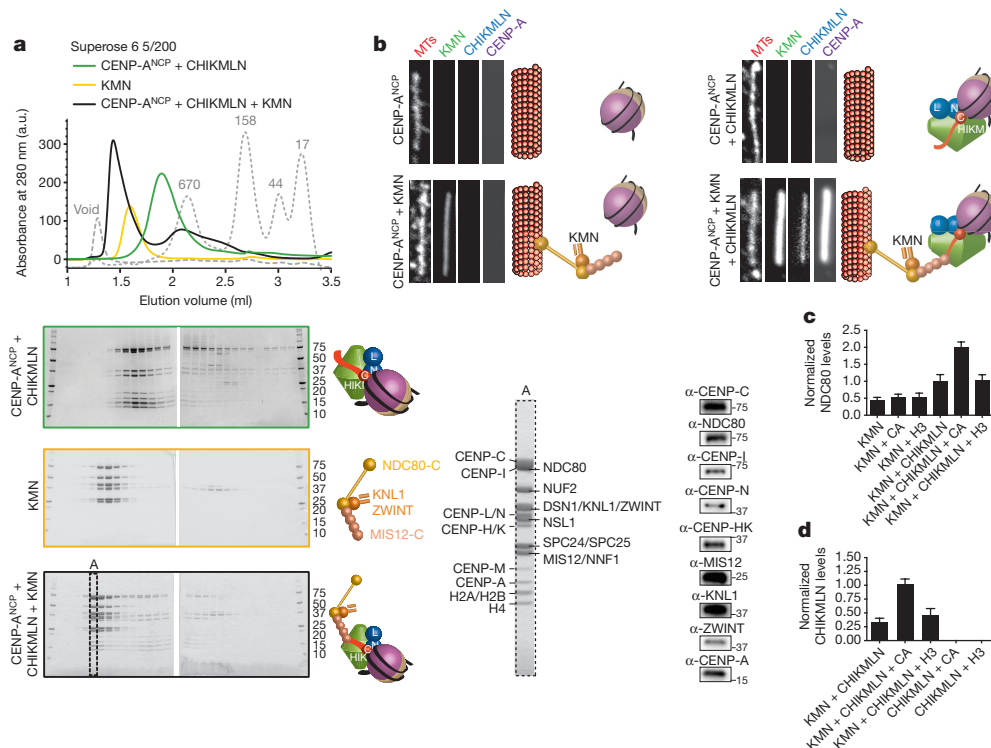


**Figure 3 | KMN and CHIKMLN connect CENP-A to microtubules.**

**a**, The CHIKMLN:CENP-A<sup>NCP</sup> complex (green trace) and the KMN (yellow trace) were mixed, run on a Superose 6 SEC column (black trace), and analysed by SDS-PAGE. All 17 components of the kinetochore and the 4 subunits of the CENP-A<sup>NCP</sup> shift together. Analysis of peak fraction (boxed and marked 'A') by Coomassie staining and western blot demonstrates co-elution of all subunits. **b**, Microtubule binding assay. Rhodamine-labelled microtubules (red channel) were tethered

CENP-C<sup>9,19</sup>. In agreement with the latter, recruitment of CENP-TWSX complex to CENP-A<sup>NCP</sup> requires both CENP-C<sup>1-544</sup> and the CENP-HIKM complex (Extended Data Fig. 6).

The KMN network is made of three subcomplexes, the KNL1 complex (KNL1-C), the MIS12 complex (MIS12-C), and the NDC80 complex (NDC80-C). It forms the outer kinetochore and binds microtubules<sup>7,8</sup> (Fig. 1a). After characterizing CHIKMLN as the CENP-A<sup>NCP</sup>-associated complex, we asked if it was also competent to recruit the outer kinetochore components. The CENP-A<sup>NCP</sup>:CHIKMLN complex readily bound to a reconstituted 10-subunit KMN network complex and all components co-eluted from a SEC column, forming a 17-subunit kinetochore complex bound to an octameric CENP-A<sup>NCP</sup> (Fig. 3a, black trace). XL-MS of this complex revealed an extensive network of interactions around a hub represented by the MIS12 complex (Extended Data Fig. 7 and Supplementary Table 2). The MIS12 complex formed crosslinks to several outer-kinetochore subunits, as well as to inner-kinetochore subunits, including CENP-C<sup>1-544</sup>, CENP-K, and CENP-N.

We asked if reconstituted kinetochore particles could translocate centromeric chromatin onto microtubules. After immobilizing microtubules on a coverslip, we tested the ability of fluorescently labelled kinetochore components to interact with them (Fig. 3b and Extended Data Fig. 8a, b). The KMN network bound microtubules in the absence of other components, fitting with its well-established role as a microtubule receptor at the kinetochore<sup>7,8,23</sup>. Neither CHIKMLN nor CENP-A<sup>NCP</sup>, either together or in isolation, decorated microtubules in the absence of the KMN network (Fig. 3b). Conversely, when the KMN network was added alongside the CHIKMLN complex and CENP-A<sup>NCP</sup>, they strongly decorated microtubules (Fig. 3b), demonstrating that the KMN network and the CHIKMLN complex create a direct bridge between centromeres and microtubules. Only

to glass coverslips and incubated in the presence of green fluorescent protein (GFP)-KMN (green), Alexa-405-labelled CHIKMLN (blue), or Alexa-647-labelled CENP-A<sup>NCP</sup> (purple), and combinations thereof. **c**, **d**, Quantification of fluorescence data (see Extended Data Fig. 8 and Methods). 'CA' and 'H3' indicate CENP-A<sup>NCP</sup> and H3<sup>NCP</sup>, respectively. Shown for each channel is mean  $\pm$  s.e.m. from at least 20 microtubules in at least 2 independent experiments.

weak binding to microtubules was observed when CENP-A<sup>NCP</sup> was replaced with H3<sup>NCP</sup> (Extended Data Fig. 8a–c). Addition of CHIKMLN enhanced KMN binding to microtubules (Fig. 3c), a phenomenon whose mechanistic basis will require further investigation. Addition of CENP-A<sup>NCP</sup>, but not of H3<sup>NCP</sup>, further increased the binding affinity of the KMN for microtubules (Fig. 3b–d). It is likely that this effect reflects multivalency arising from the incorporation of two CHIKMLN complexes on a single CENP-A<sup>NCP</sup> (AUC analysis in Table 1 and Extended Data Fig. 4), which probably allows for the binding of two KMN assemblies to the same particle. Because CENP-TW recruits additional NDC80-C to kinetochores<sup>22,24,25</sup>, it may contribute to further enhancements of the microtubule-binding capacity.

CENP-C<sup>545-943</sup>, like CENP-C<sup>1-544</sup>, contains a nucleosome-binding element (the CENP-C motif; Extended Data Fig. 1), reported to bind NCPs with a moderate preference for CENP-A<sup>NCP</sup> over H3<sup>NCP</sup> (ref. 11). *In vitro*, C-terminal segments of CENP-C interacted with CENP-A<sup>NCP</sup> but did not recapitulate any of the interactions with CHIKMLN subunits observed with CENP-C<sup>1-544</sup> (Extended Data Fig. 9a, b, summarized in Fig. 4a). The specific topology of the CENP-C protein and its interactions are shown in Extended Data Fig. 9c.

The point kinetochore of *Saccharomyces cerevisiae* consists of a single CENP-A (also known as Cse4) nucleosome associated with proteins that are evolutionarily related to the CCAN subunits of humans<sup>12</sup> (Fig. 4b). Our finding that the human CCAN subunits and the KMN network form a single, apparently stoichiometric complex on a CENP-A<sup>NCP</sup> suggests that the human and *S. cerevisiae* kinetochores form a unit of similar architecture. At regional centromeres, which may extend over several megabases of genomic DNA, up to 200 CENP-A nucleosomes intersperse with conventional H3 nucleosomes at an approximate ratio of 1 CENP-A nucleosome over 25 H3 nucleosomes<sup>26</sup>. We therefore propose that kinetochores built on regional centromeres represent the



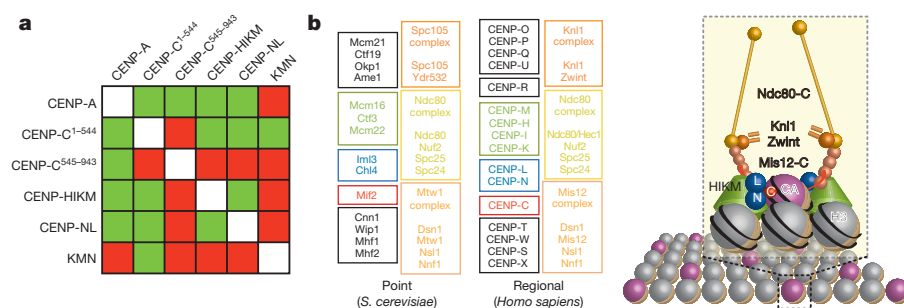


**Figure 4 | Centromere and kinetochore assembly and propagation.** **a**, Matrix of intra-kinetochore interactions. An observed physical interaction is highlighted in green, lack of interaction in red. **b**, Similar subunit composition suggests conservation of a structural module that is present in only one copy at 'point' centromeres/kinetochores, which bind a single microtubule, and that is instead present in multiple copies at 'regional' centromeres/kinetochores, which bind multiple microtubules<sup>12</sup>. As few as 1 in 25 nucleosomes at centromeres may contain CENP-A<sup>26</sup>.

convolution with multiple CENP-A nucleosomes of the structural unit identified by our *in vitro* reconstitution (Fig. 4b).

Here we have reported the production of entirely synthetic kinetochores that specifically bind centromeric chromatin while mediating a simultaneous connection to microtubules. We note in this context that the reconstitution of functional kinetochore particles on an octameric CENP-A<sup>NCP</sup> may set a benchmark to resolve an ongoing discussion on the actual structure of the CENP-A nucleosome<sup>27</sup>. Our efforts complement previous studies with kinetochore particles isolated from *S. cerevisiae*<sup>28,29</sup> or reconstitutions on CENP-A arrays in extracts of *Xenopus laevis*<sup>30</sup>. Synthetic kinetochores have the potential to drive new inroads into the structural characterization of kinetochore architecture, which remains largely unknown. The manipulation of recombinant kinetochores *in vitro* may allow molecular insight into crucial kinetochore functions including the regulation of microtubule binding, of the spindle assembly checkpoint and of new CENP-A deposition.

**Online Content** Methods, along with any additional Extended Data display items and Source Data, are available in the online version of the paper; references unique to these sections appear only in the online paper.

**Received 23 September 2015; accepted 25 July 2016.**

**Published online 31 August 2016.**

- Foley, E. A. & Kapoor, T. M. Microtubule attachment and spindle assembly checkpoint signalling at the kinetochore. *Nature Rev. Mol. Cell Biol.* **14**, 25–37 (2013).
- Fukagawa, T. & Earnshaw, W. C. The centromere: chromatin foundation for the kinetochore machinery. *Dev. Cell* **30**, 496–508 (2014).
- Izuta, H. *et al.* Comprehensive analysis of the ICEN (interphase centromere complex) components enriched in the CENP-A chromatin of human cells. *Genes Cells* **11**, 673–684 (2006).
- Foltz, D. R. *et al.* The human CENP-A centromeric nucleosome-associated complex. *Nature Cell Biol.* **8**, 458–469 (2006).
- Hori, T. *et al.* CCAN makes multiple contacts with centromeric DNA to provide distinct pathways to the outer kinetochore. *Cell* **135**, 1039–1052 (2008).
- Okada, M. *et al.* The CENP-H-I complex is required for the efficient incorporation of newly synthesized CENP-A into centromeres. *Nature Cell Biol.* **8**, 446–457 (2006).
- DeLuca, J. G. *et al.* Kinetochore microtubule dynamics and attachment stability are regulated by Hec1. *Cell* **127**, 969–982 (2006).
- Cheeseman, I. M., Chappie, J. S., Wilson-Kubalek, E. M. & Desai, A. The conserved KMN network constitutes the core microtubule-binding site of the kinetochore. *Cell* **127**, 983–997 (2006).
- Carroll, C. W., Milks, K. J. & Straight, A. F. Dual recognition of CENP-A nucleosomes is required for centromere assembly. *J. Cell Biol.* **189**, 1143–1155 (2010).
- Carroll, C. W., Silva, M. C., Godek, K. M., Jansen, L. E. & Straight, A. F. Centromere assembly requires the direct recognition of CENP-A nucleosomes by CENP-N. *Nature Cell Biol.* **11**, 896–902 (2009).
- Kato, H. *et al.* A conserved mechanism for centromeric nucleosome recognition by centromere protein CENP-C. *Science* **340**, 1110–1113 (2013).
- Westermann, S. & Schleiffer, A. Family matters: structural and functional conservation of centromere-associated proteins from yeast to humans. *Trends Cell Biol.* **23**, 260–269 (2013).
- London, N. & Biggins, S. Signalling dynamics in the spindle checkpoint response. *Nature Rev. Mol. Cell Biol.* **15**, 736–748 (2014).
- Catania, S. & Allshire, R. C. Anarchic centromeres: deciphering order from apparent chaos. *Curr. Opin. Cell Biol.* **26**, 41–50 (2014).
- Hinshaw, S. M. & Harrison, S. C. An Iml3-Chl4 heterodimer links the core centromere to factors required for accurate chromosome segregation. *Cell Reports* **5**, 29–36 (2013).
- Lowary, P. T. & Widom, J. New DNA sequence rules for high affinity binding to histone octamer and sequence-directed nucleosome positioning. *J. Mol. Biol.* **276**, 19–42 (1998).
- Naggal, H. *et al.* Dynamic changes in CCAN organization through CENP-C during cell-cycle progression. *Mol. Biol. Cell* **26**, 3768–3776 (2015).
- McKinley, K. L. *et al.* The CENP-L-N complex forms a critical node in an integrated meshwork of interactions at the centromere-kinetochore interface. *Mol. Cell* **60**, 886–898 (2015).
- Basilico, F. *et al.* The pseudo GTPase CENP-M drives human kinetochore assembly. *eLife* **3**, e02978 (2014).
- Klare, K. *et al.* CENP-C is a blueprint for constitutive centromere-associated network assembly within human kinetochores. *J. Cell Biol.* **210**, 11–22 (2015).
- Herzog, F. *et al.* Structural probing of a protein phosphatase 2A network by chemical cross-linking and mass spectrometry. *Science* **337**, 1348–1352 (2012).
- Gascoigne, K. E. *et al.* Induced ectopic kinetochore assembly bypasses the requirement for CENP-A nucleosomes. *Cell* **145**, 410–422 (2011).
- Ciferri, C. *et al.* Implications for kinetochore-microtubule attachment from the structure of an engineered Ndc80 complex. *Cell* **133**, 427–439 (2008).
- Schleiffer, A. *et al.* CENP-T proteins are conserved centromere receptors of the Ndc80 complex. *Nature Cell Biol.* **14**, 604–613 (2012).
- Suzuki, A., Badger, B. L. & Salmon, E. D. A quantitative description of Ndc80 complex linkage to human kinetochores. *Nature Commun.* **6**, 8161 (2015).
- Bodor, D. L. *et al.* The quantitative architecture of centromeric chromatin. *eLife* **3**, e02137 (2014).
- Westhorpe, F. G. & Straight, A. F. The split personality of CENP-A nucleosomes. *Cell* **150**, 245–247 (2012).
- Gonen, S. *et al.* The structure of purified kinetochores reveals multiple microtubule-attachment sites. *Nature Struct. Mol. Biol.* **19**, 925–929 (2012).
- Akiyoshi, B. *et al.* Tension directly stabilizes reconstituted kinetochore-microtubule attachments. *Nature* **468**, 576–579 (2010).
- Guse, A., Carroll, C. W., Moree, B., Fuller, C. J. & Straight, A. F. *In vitro* centromere and kinetochore assembly on defined chromatin templates. *Nature* **477**, 354–358 (2011).

**Supplementary Information** is available in the online version of the paper.

**Acknowledgements** We are grateful to F. Martino and D. Rhodes for help in setting up NCP preparations, to A. F. Straight for providing plasmids for expression of CENP-A:H4, to K. A. Davey for plasmids to produce the '601' 145-bp nucleosomal DNA, to C. Smith for setting up conditions for CENP-H depletion, to G. Ossolengo of the antibody facility at the European Institute of Oncology in Milan (Italy) for help with antibody production, and all other members of the Musacchio laboratory for discussions. A.C.F. is supported by an EMBO long-term fellowship (ALTF 1096-2012) and Marie Curie Intra-European Fellowship. A.M. acknowledges funding by the European Union's 7th Framework Program Integrated Project MitoSys, the Horizon 2020 ERC agreement RECIANCE, and the DFG's Collaborative Research Centre 1093. F.H. is supported by the European Research Council (MolStruKT StG number 638218) and by an LMU excellent junior grant.

**Author Contributions** J.R.W., K.K., A.C.F. and A.M. designed the experiments. J.R.W., K.K., A.C.F., F.B., J.K., A.P., S.W., M.P. and S.P. purified proteins. D.V. and F.B. purified nucleosomes. D.P. created the engineered nucleosomes used in AUC experiments. J.R.W. performed gel filtration experiments. A.P. performed AUC experiments. K.K. performed cell biology experiments. A.C.F. performed microtubule binding experiments. J.F. and F.H. performed crosslinking and mass-spec experiments. A.M. coordinated the working team. J.R.W. and A.M. wrote the paper.

**Author Information** Reprints and permissions information is available at [www.nature.com/reprints](http://www.nature.com/reprints). The authors declare no competing financial interests. Readers are welcome to comment on the online version of the paper. Correspondence and requests for materials should be addressed to J.R.W. ([john.weir@mpi-dortmund.mpg.de](mailto:john.weir@mpi-dortmund.mpg.de)) or A.M. ([andrea.musacchio@mpi-dortmund.mpg.de](mailto:andrea.musacchio@mpi-dortmund.mpg.de)).

**Reviewer Information** Nature thanks A. Desai and the other anonymous reviewer(s) for their contribution to the peer review of this work.



## METHODS

No statistical methods were used to predetermine sample size. The experiments were not randomized. The investigators were not blinded to allocation during experiments and outcome assessment.

**Production of recombinant proteins.** CENP-LN was produced as a GST fusion construct from insect cells using the MultiBac expression system<sup>31</sup>. Specifically, a coding sequence expressing 3C cleavable GST-tagged CENP-L was sub-cloned into MCS2, and the coding sequence of CENP-N was sub-cloned into MCS1 of pFL. Bacmid was then produced from EMBAcy cells<sup>31</sup>, and subsequently used to transfect Sf9 cells and produce baculovirus. Baculovirus was amplified through three rounds of amplification and used to infect Tnao38 cells<sup>32</sup>. Cells infected with the GST- CENP-L/CENP-N virus were cultured for 72 h before harvesting. Cells were washed and resuspended in lysis buffer (50 mM Na-HEPES, 300 mM NaCl, 10% glycerol, 4 mM 2-mercaptoethanol, 1 mM MgCl<sub>2</sub>, pH 7.5). Resuspended cells were lysed by sonication in the presence of Benzonase before clearance at 100,000g at 4 °C for 1 h. Cleared lysate was passed over GSH-Sepharose, before extensive washing with lysis buffer. GST-CENP-L/CENP-N complex was then eluted in lysis buffer + 20 mM reduced glutathione. Eluted protein was concentrated in a 30 kDa Amicon-Ultra-15 Centrifugal Filter (Millipore) in the presence of GST-tagged 3C protease. Concentrated protein was then loaded onto a Superdex 200 16/600 column equilibrated in 20 mM Na- HEPES pH 7.5, 300 mM NaCl, 2.5% glycerol. A 5 ml GSH-Sepharose FF column was connected in series after the Superdex 200 column to trap GST, un-cut GST-CENP-L/CENP-N and GST-tagged 3C protease. Peak fractions corresponding to CENP-L/CENP-N were collected and again concentrated in a 30 kDa MWCO concentrator to approximately 50–100 μM before being flash frozen in liquid N<sub>2</sub> and stored at –80 °C.

Synthetic, codon-optimized DNA (Genent), encoding the human CENP-C<sup>1–544</sup>His, CENP-C<sup>189–544</sup>, or CENP-C<sup>545–943</sup> was sub-cloned into pFL or pFG (containing an N-terminal 3C cleavable GST) vectors, respectively, by restriction cloning with the enzymes BamHI and SalI. A non-cleavable histidine tag comprising six histidines (His6-tag) was introduced C-terminally of CENP-C<sup>1–544</sup>His, a tobacco etch virus (TEV) cleavage site was introduced N-terminal of CENP-C<sup>545–943</sup>. Tnao38 cells expressing CENP-C<sup>1–544</sup>His, CENP-C<sup>189–544</sup>, or CENP-C<sup>545–943</sup> were resuspended in lysis buffer (20 mM HEPES pH 7.5, 500 mM NaCl, 10% glycerol, 2 mM β-mercaptoethanol) and lysed by sonication before centrifugation at 100,000g at 4 °C for 1 h. The cleared lysates were incubated with Ni-NTA Agarose beads (for CENP-C<sup>1–544</sup>His), GST-Trap affinity column (GE Healthcare, for CENP-C<sup>189–544</sup>) or Glutathione Sepharose 4 Fast Flow beads (for CENP-C<sup>545–943</sup>) at 4 °C for 2 h. After washing with 70 column volumes of lysis buffer, CENP-C<sup>1–544</sup>His was eluted with lysis buffer supplemented with 200 mM Imidazole, CENP-C<sup>189–544</sup> was eluted in lysis buffer supplemented with 30 mM reduced glutathione, and CENP-C<sup>545–943</sup> was cleaved off the beads in 16 h at 4 °C by addition of TEV protease. After elution, proteins were diluted in buffer A (20 mM HEPES pH 7.5, 5% glycerol, 1 mM TCEP, to achieve a final concentration of 300 mM NaCl), loaded onto a pre-equilibrated HiTrap Heparin HP column, and eluted with a linear gradient of buffer B (20 mM HEPES pH 7.5, 2 M NaCl, 5% glycerol, 1 mM TCEP) in a gradient from 300 to 1200 mM NaCl. Fractions containing CENP-C<sup>1–544</sup>His and CENP-C<sup>545–943</sup> were loaded onto a Superdex 200 16/60 SEC column pre-equilibrated in SEC buffer (10 mM HEPES pH 7.5, 300 mM NaCl, 2.5% glycerol, 2 mM TCEP). For CENP-C<sup>189–544</sup>, the GST tag was cleaved using 3C protease and the protein concentrated in a 10 kDa MWCO concentrator. The protein was then further purified by SEC as described for the other two constructs. SEC fractions containing CENP-C<sup>1–544</sup>His, CENP-C<sup>189–544</sup>, or CENP-C<sup>545–943</sup> were concentrated, flash-frozen in liquid nitrogen, and stored at –80 °C.

NDC80-GFP complexes were constructed with a C-terminal fusion of GFP to HEC1. The unlabelled NDC80 complex was constructed with an N-terminal fusion of a His6-tag to SPC25. Construct for insect cell expression exploited the MultiBac baculovirus expression system<sup>31</sup>. Bacmid was then produced from EMBAcy cells, and subsequently used to transfect Sf9 cells and produce baculovirus. Baculovirus was amplified through three rounds of amplification and used to infect Tnao38 cells. Cells infected with virus expressing untagged NDC80 were cultured for 72 h before harvesting. Cells were washed and resuspended in lysis buffer (25 mM Na-HEPES, 300 mM NaCl, 10% glycerol, 1 mM TCEP, 1 mM MgCl<sub>2</sub> pH 7.5 and 1 mM PMSF). Resuspended cells were lysed by sonication in the presence of Benzonase before clearance at 100,000g at 4 °C for 1 h. Cleared lysate was passed over Ni-Sepharose, before extensive washing with lysis buffer. The Ndc80 complex was then eluted in lysis buffer + 250 mM imidazole. Eluted protein was diluted to 50 mM NaCl using buffer A (25 mM Na-HEPES, 10% glycerol, 1 mM TCEP) and loaded on a ResQ anion-exchange column. The NDC80-GFP was eluted using a salt gradient over 30 column volumes to 500 mM NaCl using buffer B (25 mM Na-HEPES, 1,000 mM NaCl, 10% glycerol, 1 mM TCEP). The eluted protein was concentrated in a 30-kDa Amicon-Ultra-15 Centrifugal Filter

(Millipore) and the concentrated protein was then loaded onto a Superdex 200 16/600 column equilibrated in 10 mM Na- HEPES pH 7.5, 150 mM NaCl, 2.5% glycerol, pH 7.5. Peak fractions containing the NDC80 complex were collected and again concentrated in a 30 kDa MWCO concentrator to approximately 10 μM before being flash frozen in liquid N<sub>2</sub> and storage at –80 °C.

Codon-optimized human CENP-1<sup>57–756</sup> (57-C) was subcloned in a MultiBac pFL-derived vector<sup>31</sup> with an N-terminal TEV cleavable His6-tag, under the control of the *polh* promoter. A complementary DNA (cDNA) segment encoding human CENP-M isoform 1 was subcloned in the second MCS of the same vector, under the control of the p10 promoter. Simultaneously, a second pFL-based vector was created with untagged CENP-H and CENP-K under the control of the *polh* and *p10* promoters, respectively. The CENP-I/M vector was then linearized with BstZ171, and the expression region of the CENP-H/K vector was PCR amplified with primers designed for sequence and ligation independent cloning (SLIC) of the PCR fragment into the linearized CENP-I/M vector. The SLIC reaction was then performed to produce a single pFL-based vector with four expression cassettes. Constructs were sequence verified. Baculovirus was then produced and amplified with three rounds of amplification.

Expression of CENP-HI<sup>57–C</sup>KM complex was performed in Tnao38 cells, using a virus:culture ratio of 1:40. Infected cells were incubated for 72 h at 27 °C. Cell pellets were harvested, washed in 1 × PBS, and finally resuspended in a buffer containing 50 mM HEPES 7.5, 300 mM NaCl, 1 mM MgCl<sub>2</sub>, 10% glycerol, 5 mM imidazole, 2 mM β-mercaptoethanol, 0.1 mM AEBSE, and 2.5 units per millilitre Benzonase (EMD/Millipore). Cells were lysed by sonication, and cleared for 1 h at 100,000g. Cleared cell lysate was then run over a 5 ml Talon superflow column (Clontech) and then washed with 50 mM HEPES 7.5, 1 M NaCl, 10% glycerol, 5 mM imidazole, and 2 mM β-mercaptoethanol. CENP-HI<sup>57–C</sup>KM complex was eluted with a gradient of 5–300 mM imidazole, and the fractions containing CENP-HI<sup>57–C</sup>KM pooled, and the His tag cleaved overnight at 4 °C. CENP-HI<sup>57–C</sup>KM in solution was then adjusted to a salt concentration of 100 mM and a pH of 6.5, before loading on a 6 ml Resource S ion-exchange column (GE Healthcare), equilibrated in 20 mM MES 6.5, 100 mM NaCl, 2 mM β-mercaptoethanol. CENP-HI<sup>57–C</sup>KM was then eluted with a gradient of 100–1,000 mM NaCl over 20 column volumes, and peak fractions corresponding to CENP-HI<sup>57–C</sup>KM were pooled and concentrated in a 50 kDa MW Amicon concentrator (Millipore). CENP-HI<sup>57–C</sup>KM was then loaded onto a Superdex 200 16/600 (GE Healthcare) in 20 mM HEPES 7.5, 150 mM NaCl, 2.5% glycerol, 2 mM TCEP. The sample was concentrated and flash frozen in liquid N<sub>2</sub> before use. CENP-HI<sup>57–C</sup>KM complex was labelled using the Alexa Fluor 405 C5 Maleimide kit (Thermo Fisher Scientific).

A cDNA segment encoding residues 459–561 (the histone fold, HF) of human CENP-T isoform 1, was subcloned in pGEX-6P-2rbs vector as a C-terminal fusion to GST, with an intervening 3C protease site. A cDNA segment encoding human CENP-W was subcloned in the second cassette of the same vector. Similarly, a synthetic cDNA segment encoding human CENP-X isoform 1, codon-optimized for expression in bacteria, was subcloned in pGEX-6P-2rbs vector as a C-terminal fusion to GST, with an intervening 3C protease site. Also, a cDNA segment encoding human CENP-S isoform 1, was subcloned in the second cassette of the same vector. Constructs were sequence-verified. The expression and purification procedure was the same for CENP-T/CENP-W and CENP-S/CENP-X complexes. *Escherichia coli* BL21 Rosetta cells harbouring vectors expressing GST-CENP-T/CENP-W or GST-CENP-X/CENP-S were grown in Terrific Broth at 37 °C to an absorbance at 600 nm (*A*<sub>600 nm</sub>) of 0.6–0.8, then 0.3 mM IPTG was added and the culture was grown at 20 °C overnight. Cell pellets were resuspended in lysis buffer (25 mM Tris/HCl pH 7.5, 300 mM NaCl, 10% glycerol, 1 mM DTT) supplemented with protease inhibitor cocktail (Serva), lysed by sonication, and cleared by centrifugation at 48,000g at 4 °C for 1 h. The cleared lysate was applied to Glutathione Sepharose 4 Fast Flow beads (GE Healthcare) pre-equilibrated in lysis buffer, incubated at 4 °C for 2 h, washed with 70 volumes of lysis buffer and subjected to an overnight cleavage reaction with 3C protease. A heparin column (GE Healthcare) was pre-equilibrated in a mixture of 85% buffer A (20 mM Tris/HCl pH 7.5, 5% glycerol, 1 mM DTT) and 15% buffer B (20 mM Tris/HCl pH 7.5, 2 M NaCl, 5% glycerol, 1 mM DTT). The eluate from glutathione beads was directly loaded onto the heparin column and eluted with a linear gradient of buffer B from 300 to 1,200 mM NaCl in ten bed column volumes. Fractions containing CENP-T(HF)/CENP-W or CENP-S/CENP-X were concentrated in 10-kDa-cut-off Vivaspin concentrators (Sartorius) and loaded onto a Superdex 75 size-exclusion chromatography (SEC) column (GE Healthcare) pre-equilibrated in SEC buffer (20 mM HEPES pH 7.5, 300 mM NaCl, 5% glycerol, 1 mM TCEP). SEC was performed under isocratic conditions at a flow rate of 0.5 ml/min. Fractions containing CENP-T(HF)/CENP-W or CENP-S/CENP-X were concentrated. To form the T(HF)WSX complex, T(HF)W was added to SX at a 1.5 molar excess, incubated for 1 h on ice, and then subjected to separation on a Superdex 200 size-exclusion column to separate tetrameric T(HF)SX complex from T(HF)

W dimers. Fractions containing the tetrameric T(HF)WSX complex were then concentrated in a 10-kDa MWCO concentrator to a concentration of 50–250  $\mu$ M, and flash-frozen.

**H3 containing NCPs.** Plasmids for the production of *X. laevis* H2A, H2B, H3 and H4 histones were a gift from D. Rhodes. *X. laevis* histone expression and purification, refolding of histone octamers or H2A:H2B dimers, and reconstitution of H3 containing mononucleosomes were performed precisely as described<sup>33</sup>. Plasmids for the production of the '601' 145-bp DNA were a gift from C. A. Davey. DNA production was performed as described<sup>33</sup> with no modifications. For Alexa-647-labelled nucleosomes, the 145-bp DNA fragments (601-Widom) were amplified using fluorescently labelled primers (Sigma-Aldrich). Biotinylated nucleosomes were reconstituted using commercial synthetic 145-bp DNA fragments (601-Widom) (Epiccypher).

**CENP-A containing NCPs.** Plasmids for the production of human CENP-A:H4 histone tetramer were a gift of A. F. Straight. Preparations of CENP-A-containing NCPs were performed precisely as described<sup>34</sup>. For Alexa-647-labelled nucleosomes, the 145-bp DNA fragments (601-Widom) were amplified using fluorescently labelled primers (Sigma-Aldrich, St. Louis, Missouri, USA). Biotinylated nucleosomes were reconstituted using commercial synthetic 145-bp DNA fragments (601-Widom) (Epiccypher, Durham, North Carolina, USA).

**H3.1/CENP-A-chimaera with H2B-BFP histone octamer.** Polycistronic-coexpression plasmid pETDuet-6HisH3.1/CENP-A-H4-6His-H2A-H2B-BFP was generated on the basis of the strategy described previously<sup>35</sup> with human histone sequences. The coding sequences of the open reading frames of 6His-H3.1(Ala2-Ile75)/CENP-A(Cys75-Gly140), H4, 6His-H2A1B, and H2B1J-TagBFP were sub-cloned between NcoI and XhoI sites of pETDuet-1 using conventional cloning techniques and the Gibson cloning<sup>36</sup>. The H3 and CENP-A segments of the chimaera paste within the  $\alpha$ 1-helix in a structurally seamless manner. One ribosome-binding site was placed upstream of each open reading frame of these four recombinant histones. A TEV protease site was placed between 6His-tag and H3.1/CENP-A-chimaera and a PreScission protease site was placed between 6His-tag and H2A1B to allow tag-removal during protein purification.

Protein expression and purification of BFP-labelled H3.1/CENP-A-chimaera histone octamer followed a previous study<sup>35</sup> with minor modifications. Purification of the octamer was done according to the previous study<sup>35</sup> with minor modifications. After Ni-affinity purification, the octamers were incubated for 15 h at 4 °C with His-TEV protease and His-PreScission protease in buffer A containing 20 mM Tris-HCl pH 8.0, 1.0 M sodium chloride, 1 mM tris(2-carboxyethyl)-phosphine (TCEP). The tag-removed octamers were concentrated in buffer B (20 mM Tris-HCl pH 8.0, 2.0 M sodium chloride, 1 mM TCEP) and further purified using Superdex 200 10/300 GL gel-filtration column (GE Healthcare) equilibrated with buffer B. Fractions containing the octamers were pooled, concentrated and stored at –80 °C until used for nucleosome reconstitution.

**Analytical SEC analysis.** Analytical SEC was performed on a custom-made Superose 6 5/200 in a buffer containing 20 mM HEPES, 300 mM NaCl, 2.5% glycerol, 2 mM TCEP, pH 7.5 on an ÄKTAmicro system. As indicated, the following additional columns were used: Superdex 200 5/150 Increase and Superose 6 5/150. All samples were eluted under isocratic conditions at 4 °C in SEC buffer (20 mM HEPES pH 7.5, 300 mM NaCl, 2.5% glycerol, 2 mM TCEP) at a flow rate of 0.2 ml/min. Elution of proteins was monitored at 280 nm. Fractions (100  $\mu$ l) were collected and analysed by SDS-PAGE and Coomassie blue staining. To detect the formation of a complex, proteins were mixed at the indicated concentrations in 50  $\mu$ l, incubated for at least 2 h on ice and then subjected to SEC.

**Kinetochore-microtubule binding assay.** Coverslips and glass slides were cleaned by sonication in isopropanol and 1 M KOH or 1% Hellmanex and 70% ethanol, respectively. After functionalization of coverslips with 5% biotinylated poly-L-lysine-PEG for 30 min, flow cells were created with a volume of 10–15  $\mu$ l. Flow cells were passivated with 1% pluronic F-127 for 1 h and coated with avidin for 30–45 min. After incubation with 10 nM microtubules (10% biotinylated, 10% rhodamine labelled, Cytoskeleton, polymerized according to the manufacturer's instructions) for 10–20 min, proteins (400 nM) were added in 80 mM Pipes (pH 6.8), 125 mM KCl, 1 mM EGTA, 1 mM MgCl<sub>2</sub> and 20  $\mu$ M Taxol. Flow cells were sealed with wax and imaged with spinning disk confocal microscopy on a 3i Marianas system (Intelligent Imaging Innovations, Göttingen, Germany) equipped with Axio Observer Z1 microscope (Zeiss, Oberkochen, Germany), a CSU-X1 confocal scanner unit (Yokogawa Electric Corporation, Tokyo, Japan), Plan-Apochromat 100 $\times$ /1.4 numerical aperture DIC oil objective (Zeiss), Orca Flash 4.0sCMOS Camera (Hamamatsu, Hamamatsu City, Japan) and controlled by Slidebook Software 6.0 (Intelligent Imaging Innovations). Images were acquired as z-sections at 0.27  $\mu$ m and maximal intensity projections were made with Slidebook Software 6.0 (Intelligent Imaging Innovations).

**GST pulldown assays.** GST pulldown experiments were performed using pre-blocked GSH Sepharose beads in pulldown buffer (10 mM HEPES pH 7.5, 200 mM

NaCl, 0.05% Triton, 2.5% glycerol, 1 mM TCEP). GST-CENP-LN as bait at a 1  $\mu$ M concentration was incubated with NCPs as prey at a 3  $\mu$ M concentration. The bait was loaded to 12  $\mu$ l preblocked beads, before the prey was added. At the same time, 1  $\mu$ g of each protein was added into Laemmli sample loading buffer for the input gel. The reaction volume was topped up to 40  $\mu$ l with buffer and incubated at 4 °C for 1 h under gentle rotation. Beads were spun down at 500g for 3 min. The supernatant was removed and beads washed twice with 250  $\mu$ l buffer. Supernatant was removed completely, samples boiled in 15  $\mu$ l Laemmli sample loading buffer and run on a 14% SDS-PAGE gel. Bands were visualized with Coomassie brilliant blue staining. Preblocking of GSH sepharose beads 750  $\mu$ l of GSH Sepharose beads were washed twice with 1 ml washing buffer (20 mM HEPES pH 7.5, 200 mM NaCl) and incubated in 1 ml blocking buffer (20 mM HEPES pH 7.5, 500 mM NaCl, 500  $\mu$ g/ml BSA) overnight at 4 °C rotating. Beads were washed five times with 1 ml washing buffer and resuspended in 500  $\mu$ l washing buffer to have a 50/50 slurry of beads and buffer.

**RNAi interference.** For CENP-C silencing, we used a single siRNA (target sequence: 5'-GGAUCAUCAGAAUAGAA-3'; obtained from Sigma-Aldrich), targeting the coding region of endogenous CENP-C mRNA. For an efficient depletion, siRNA for CENP-C was transfected at a concentration of 60 nM for 72 h. For CENP-M silencing, we used a combination of three siRNA duplexes (target sequences: 5'-ACAAAAGGUCUGUGGCUA-3'; 5'-UUAAGCAGCUGGCGUGUUA-3'; 5'-GUGCUGACUCCAUAAACAU-3'; purchased from Thermo Scientific, Carlsbad, California, USA) targeting the 3'-UTR of endogenous CENP-M. CENP-M siRNA duplexes were used at 20 nM each for 72 h as published<sup>3</sup>. For CENP-H a single siRNA (target sequence: 5'-CUAGUGUCUACUGGAUAA-3' obtained from Dharmacon) targeting the coding region of endogenous CENP-H mRNA was used at 100 nM for 72 h. For CENP-L a single siRNA (target sequence: 5'-UUUAUCAGCCACAAGAUUA-3' obtained from Dharmacon) targeting the coding region of endogenous CENP-L was used at 100 nM for 72 h. Transfections of RNAi were performed with HyPerFect (QIAGEN) according to the manufacturer's instructions. Phenotypes were analysed 96 h after first siRNA addition and protein depletion was monitored by western blotting or immunofluorescence.

**Mammalian plasmids.** Constructs were created by cDNA subcloning in pcDNA5/FRT/TO-mCherry-IRES vector, a modified version of pcDNA5/FRT/TO vector (Invitrogen). pcDNA5/FRT/TO vector (Invitrogen) is a tetracycline-inducible expression vector designed for use with the Flp-In T-REX system. It carries a hybrid human cytomegalovirus/TetO2 promoter for high-level, tetracycline-regulated expression of the target gene.

**Cell culture.** Parental Flp-In T-REX HeLa cells used to generate stable doxycycline-inducible cell lines were a gift from S. Taylor (University of Manchester, Manchester, UK). They were grown at 37 °C in the presence of 5% CO<sub>2</sub> in Dulbecco's Modified Eagle's Medium (DMEM; PAN Biotech) supplemented with 10% Tet-free Fetal Bovine Serum (Invitrogen) and 2 mM L-glutamine (PAN- Biotech, 250  $\mu$ g/ml hygromycin (Invitrogen, Carlsbad, California, USA) and 4  $\mu$ g/ml blasticidin (Invitrogen, Carlsbad, California, USA). The cell line was regularly tested for mycoplasma contamination.

**Immunoblotting.** RNAi-depleted cells for various CCAN components were harvested by trypsinization and lysed by incubation in lysis buffer (75 mM HEPES pH 7.5, 150 mM KCl, 1.5 mM EGTA, 1.5 mM MgCl<sub>2</sub>, 10% glycerol, 0.075% NP-40, 90 U/ml benzonase (Sigma)), protease inhibitor cocktail (Serva) at 4 °C for 15 min followed by sonication and centrifugation. Cleared lysate was washed with lysis buffer, resuspended in Laemmli sample buffer, boiled, and analysed by western blotting using 12% NuPAGE gels (Life Technologies). The following antibodies were used: anti-Vinculin (mouse monoclonal, clone hVIN-1; 1:15,000; Sigma-Aldrich, V9131), anti- $\alpha$ -tubulin (mouse monoclonal, Sigma-Aldrich T9026), anti-CENP-C (rabbit polyclonal antibody SI410 raised against residues 23–410 of human CENP-C; 1:1,200; ref. 10), anti-CENP-HK (rabbit polyclonal antibody SI0930 raised against the full length human CENP-HK complex; 1:1,000), anti-CENP-M (rabbit polyclonal antibody raised against the full length human CENP-M), anti-CENP-L (rabbit polyclonal, Acris antibodies 17007-1-AP). Secondary antibodies were affinity-purified anti-mouse (Amersham, part of GE Healthcare), anti-rabbit or anti-mouse (Amersham) conjugated to horseradish peroxidase (1:10,000). After incubation with ECL western blotting system (GE Healthcare), images were acquired with ChemiDoc™ MP System (BioRad). Levels were adjusted with ImageJ and Photoshop and images were cropped accordingly.

**Immunofluorescence and quantification.** Flp-In T-REX HeLa cells were grown on coverslips pre-coated with 0.01% poly-L-lysine (Sigma). Cells were fixed with PBS/PHEM- paraformaldehyde 4% followed by permeabilization with PBS/PHEM-Triton 0.5%. The following antibodies were used for immunostaining: CREST/anti-centromere antibodies (human auto-immune serum, 1:100; Antibodies, Davis, California), anti-CENP-C (SI410; 1:1,000, or the directly Alexa488 conjugated form of this antibody 1:400), anti-CENP-A mouse monoclonal (Gene



Tex GTX13939, 1:500) anti-CENP-HK (SI0930; 1:800 or the Alexa488 directly conjugated form of this antibody 1:800). Rodamine Red-conjugated, DyLight405-conjugated secondary antibodies were purchased from Jackson ImmunoResearch Laboratories, West Grove, Pennsylvania, USA. Alexa Fluor 647-labelled secondary antibodies were from Invitrogen. Coverslips were mounted with Mowiol mounting media (Calbiochem). All experiments were imaged under identical conditions at room temperature using the spinning disk confocal microscopy of a 3i Marianas system (Intelligent Imaging Innovations, Denver, Colorado, USA) equipped with an Axio Observer Z1 microscope (Zeiss, Oberkochen, Germany), a CSU-X1 confocal scanner unit (Yokogawa Electric Corporation, Tokyo, Japan), Plan-Apochromat 63 $\times$  or 100 $\times$ /1.4 numerical aperture objectives (Zeiss) and Orca Flash 4.0 sCMOS Camera (Hamamatsu, Hamamatsu City, Japan) and converted into maximal intensity projections TIFF files for illustrative purposes. Quantification of kinetochore signals was performed on unmodified Z-series images using Imaris 7.3.4 software (Bitplane, Zurich, Switzerland). Z-stacks of single cells were processed in Imaris by creating an ellipsoid of 0.3  $\mu$ m width and 1  $\mu$ m height, which was positioned on the CREST signal to cover most of the kinetochore signal in all channels. Four background points with equal ellipsoid size and shape were set between kinetochore dots. Intensity values of single kinetochores were exported in a Microsoft Excel file and the average of the background values was subtracted from every kinetochore value. The mean of all kinetochore signals was taken. For each signal, the mean of the corrected values in mock-depleted cells was set to 1. All other values in perturbation experiments were then normalized to this value to derive the fraction of signal for each measured kinetochore protein compared with control cells.

**Chemical crosslinking and mass spectrometry.** Cross-linking analysis of CENP-A<sup>NCP</sup>:CHIKMLN:KMN complex or CENP-A<sup>NCP</sup>:CHIKMNL complex was performed with an equimolar mixture of light and heavy-labelled (deuterated) bis[sulfosuccinimidyl] suberate (BS3-d0/d12, Creative Molecules). The complex was incubated with 0.8 mM BS3 for 30 min at 30 °C and the crosslinking reaction was quenched by adding ammonium bicarbonate to a final concentration of 100 mM. Digestion with lysyl endopeptidase (Wako) was performed at 35 °C, 6 M urea for 2 h (at enzyme–substrate ratio of 1:50 w/w) and was followed by a second digestion with trypsin (Promega) at 35 °C overnight (also at 1:50 ratio w/w). Digestion was stopped by the addition of 1% (v/v) trifluoroacetic acid (TFA). Cross-linked peptides were enriched on a Superdex Peptide PC 3.2/30 column (300  $\times$  3.2 mm) at a flow rate of 25  $\mu$ l min<sup>-1</sup> and water/acetonitrile/TFA, 75:25:0.1 as a mobile phase. Fractions were analysed by liquid chromatography coupled to tandem mass spectrometry using a hybrid LTQ Orbitrap Elite (Thermo Scientific) instrument. Cross-linked peptides were identified using xQuest11. False discovery rates (FDRs) were estimated by using xProphet12 and results were filtered according to the following parameters: FDR = 0.05, min delta score = 0.85, MS1 tolerance window of -4 to 4 ppm, Id-score >22. The crosslinks were visualized using the webserver xVis (<http://xvis.genzentrum.lmu.de/>) (ref. 37).

**EMSA assays.** EMSA were performed using either Alexa-647-labelled NCPs, or unlabelled NCPs, at 10 nM. Proteins or protein complexes were added to the nucleosomes at the concentrations indicated and incubated in buffer containing 10 mM HEPES, 150 mM NaCl, 2 mM TCEP, 1% glycerol, 1% Ficoll, 2 mg/ml BSA in 10  $\mu$ L volume. Samples were then run on 0.75% agarose gel in 0.5 $\times$  TBE at 4 °C. Gels of unlabelled nucleosomes were stained with SYBRGold (Thermo Fisher Scientific, Waltham, MA, USA) according to the manufacturer's instructions. Gels were imaged using a TyphoonTrio scanner (GE Healthcare, Chicago, Illinois, USA). Quantification was performed using ImageJ, and analysis using Prism (Graphpad, La Jolla, California, USA). CENP-A binding data were fitted with a quadratic binding equation. For CENP-A binding by CHIKMLN, a Hill equation with Hill coefficient of 2.07 was applied, without changes in the apparent  $K_d$ .

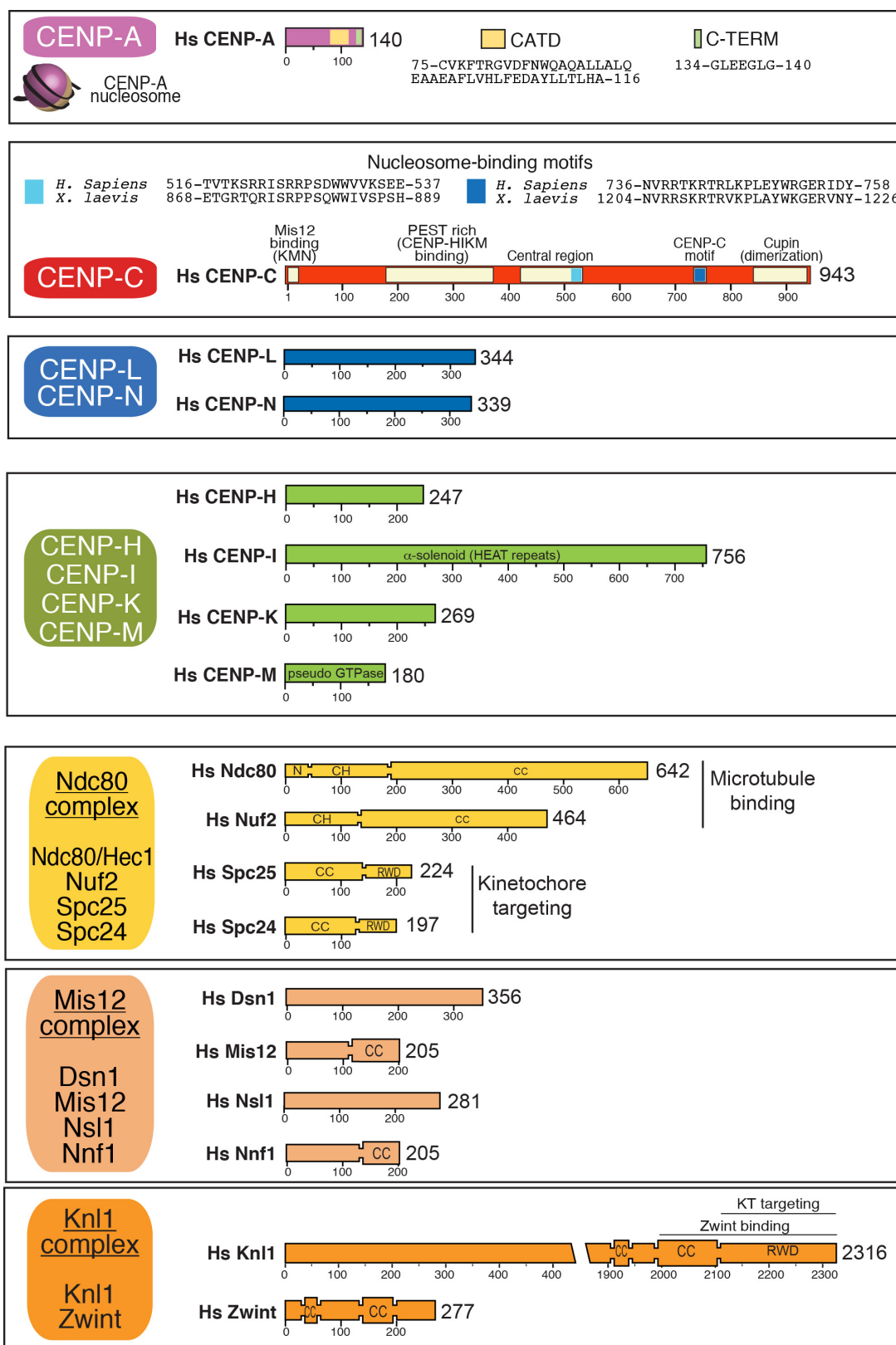
**AUC.** Sedimentation velocity experiments were performed in an Optima XL-A analytical ultracentrifuge (Beckman Coulter, Palo Alto, California, USA) with Epon charcoal-filled double-sector quartz cells and an An-60 Ti rotor (Beckman Coulter, Palo Alto, California, USA). Samples were centrifuged at 203,000g at 10 °C or 20 °C and 500 radial absorbance scans at either 280 nm or at 497 nm (for samples containing CENP-HI<sup>57-C</sup>KM complex labelled with Alexa Fluor 488) and collected with a time interval of 1 min. Data were analysed using the SEDFIT software<sup>38</sup> in terms of continuous distribution function of sedimentation coefficients (c(s)). The protein partial specific volume was estimated from the amino-acid sequence using the program SEDNTERP. Data were plotted using the program GUSI in the SEDFIT software<sup>38</sup>. The GUSI software is also freely available from <http://biophysics.swmed.edu/MBR/software.html>.

Analysis of NCPs or NCPs bound to CENP-LN was performed at 20 °C in 20 mM HEPES pH 7.5, 10% glycerol, 150 mM NaCl, 1 mM EDTA and 2 mM TCEP (leading to values of buffer density of 1.03503 g/ml and viscosity of 1.002 cP). All other experiments were performed at 10 °C in 10 mM HEPES pH 7.5, 2.5% glycerol and 0.3 M NaCl (leading to values of buffer density 1.02001 g/ml and viscosity of 1.307 cP). To calculate the value of the partial specific volume ( $\bar{V}$ ,

inverse of density) for nucleosomes, we took the value of the 0.55 ml/g for the DNA. This gave a value of  $\bar{V}$  = 0.6565 ml/g for the nucleosomes at 20 °C (or 0.65423 ml/g at 10 °C). The value of the partial specific volume for the CENP-LN bound to CENP-A NCPs is 0.692 ml/g at 20 °C (assuming 2:1 stoichiometry). The value for the CHIKMLN and CENP-A NCPs is 0.71666 ml/g at 10 °C (assuming 2:1 stoichiometry). The value for the HIKM is 0.7394 ml/g at 10 °C and the value for CHIKMLN is 0.73380 ml/g at 10 °C.

**Biotinylated NCP pulldown assays.** Biotinylated NCPs (0.5  $\mu$ M) were incubated with prey proteins (1.5  $\mu$ M or as indicated) for 30 min on ice in a buffer containing 20 mM HEPES, 200 mM NaCl, 0.05% Triton-X100, 2.5% glycerol, 2 mM TCEP in a reaction volume of 40  $\mu$ L. Ten microlitres of the protein mix were taken as an input. Ten microlitres of pre-equilibrated streptavidin beads (GE Healthcare, Chicago, IL, USA) were then added to the samples and incubated for 2 min. The samples were then spun down, the supernatant removed, and the beads washed once. Laemmli buffer (1 $\times$ ) was then added to the beads, and heated to 95 °C for 1 min to release all the streptavidin from the beads.

- Bieniossek, C., Imasaki, T., Takagi, Y. & Berger, I. MultiBac: expanding the research toolbox for multiprotein complexes. *Trends Biochem. Sci.* **37**, 49–57 (2012).
- Hashimoto, Y., Zhang, S., Zhang, S., Chen, Y. R. & Blissard, G. W. Correction: BTI-Tnao38, a new cell line derived from *Trichoplusia ni*, is permissive for AcMNPV infection and produces high levels of recombinant proteins. *BMC Biotechnol.* **12**, 12 (2012).
- Dyer, P. N. et al. Reconstitution of nucleosome core particles from recombinant histones and DNA. *Methods Enzymol.* **375**, 23–44 (2004).
- Guse, A., Fuller, C. J. & Straight, A. F. A cell-free system for functional centromere and kinetochore assembly. *Nature Protocols* **7**, 1847–1869 (2012).
- Shim, Y., Duan, M. R., Chen, X., Smerdon, M. J. & Min, J. H. Polycistronic coexpression and nondenaturing purification of histone octamers. *Anal. Biochem.* **427**, 190–192 (2012).
- Gibson, D. G. et al. Enzymatic assembly of DNA molecules up to several hundred kilobases. *Nature Methods* **6**, 343–345 (2009).
- Grimm, M., Zimniak, T., Kahraman, A. & Herzog, F. xVis: a web server for the schematic visualization and interpretation of crosslink-derived spatial restraints. *Nucleic Acids Res.* **43** (W1), W362–W369 (2015).
- Brown, P. H. & Schuck, P. Macromolecular size-and-shape distributions by sedimentation velocity analytical ultracentrifugation. *Biophys. J.* **90**, 4651–4661 (2006).
- Black, B. E. et al. Structural determinants for generating centromeric chromatin. *Nature* **430**, 578–582 (2004).
- Przewlaka, M. R. et al. CENP-C is a structural platform for kinetochore assembly. *Curr. Biol.* **21**, 399–405 (2011).
- Scrapanti, E. et al. Direct binding of CENP-C to the Mis12 complex joins the inner and outer kinetochore. *Curr. Biol.* **21**, 391–398 (2011).
- Cohen, R. L. et al. Structural and functional dissection of Mif2p, a conserved DNA-binding kinetochore protein. *Mol. Biol. Cell* **19**, 4480–4491 (2008).
- Dambacher, S. et al. CENP-C facilitates the recruitment of M18BP1 to centromeric chromatin. *Nucleus* **3**, 101–110 (2012).
- Milks, K. J., Moree, B. & Straight, A. F. Dissection of CENP-C-directed centromere and kinetochore assembly. *Mol. Biol. Cell* **20**, 4246–4255 (2009).
- Wei, R. R., Al-Bassam, J. & Harrison, S. C. The Ndc80/HEC1 complex is a contact point for kinetochore-microtubule attachment. *Nature Struct. Mol. Biol.* **14**, 54–59 (2007).
- Kiyomitsu, T., Iwasaki, O., Obuse, C. & Yanagida, M. Inner centromere formation requires hMis14, a trident kinetochore protein that specifically recruits HP1 to human chromosomes. *J. Cell Biol.* **188**, 791–807 (2010).
- Petrovic, A. et al. Modular assembly of RWD domains on the Mis12 complex underlies outer kinetochore organization. *Mol. Cell* **53**, 591–605 (2014).
- Hornung, P. et al. Molecular architecture and connectivity of the budding yeast Mt11 kinetochore complex. *J. Mol. Biol.* **405**, 548–559 (2011).
- Petrovic, A. et al. The MIS12 complex is a protein interaction hub for outer kinetochore assembly. *J. Cell Biol.* **190**, 835–852 (2010).
- Maskell, D. P., Hu, X. W. & Singleton, M. R. Molecular architecture and assembly of the yeast kinetochore MIND complex. *J. Cell Biol.* **190**, 823–834 (2010).
- Ghongane, P., Kapanidou, M., Asghar, A., Elowe, S. & Bolanos-Garcia, V. M. The dynamic protein Knl1 - a kinetochore rendezvous. *J. Cell Sci.* **127**, 3415–3423 (2014).
- Moree, B., Meyer, C. B., Fuller, C. J. & Straight, A. F. CENP-C recruits M18BP1 to centromeres to promote CENP-A chromatin assembly. *J. Cell Biol.* **194**, 855–871 (2011).
- Hayashi, T. et al. Mis16 and Mis18 are required for CENP-A loading and histone deacetylation at centromeres. *Cell* **118**, 715–729 (2004).
- Jansen, L. E., Black, B. E., Foltz, D. R. & Cleveland, D. W. Propagation of centromeric chromatin requires exit from mitosis. *J. Cell Biol.* **176**, 795–805 (2007).
- Dunleavy, E. M., Almouzni, G. & Karpen, G. H. H3.3 is deposited at centromeres in S phase as a placeholder for newly assembled CENP-A in G<sub>1</sub> phase. *Nucleus* **2**, 146–157 (2011).

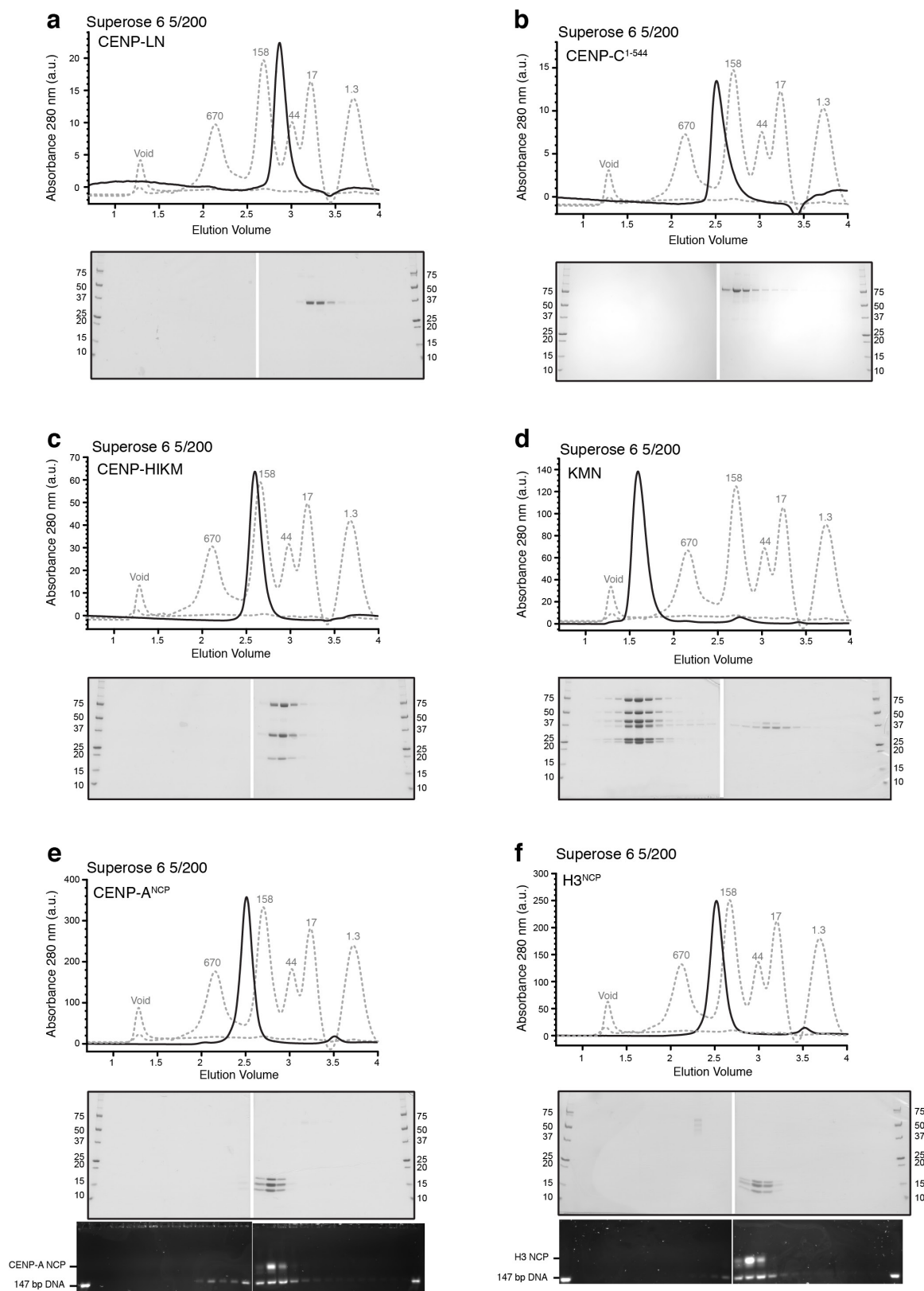


Extended Data Figure 1 | See next page for caption.



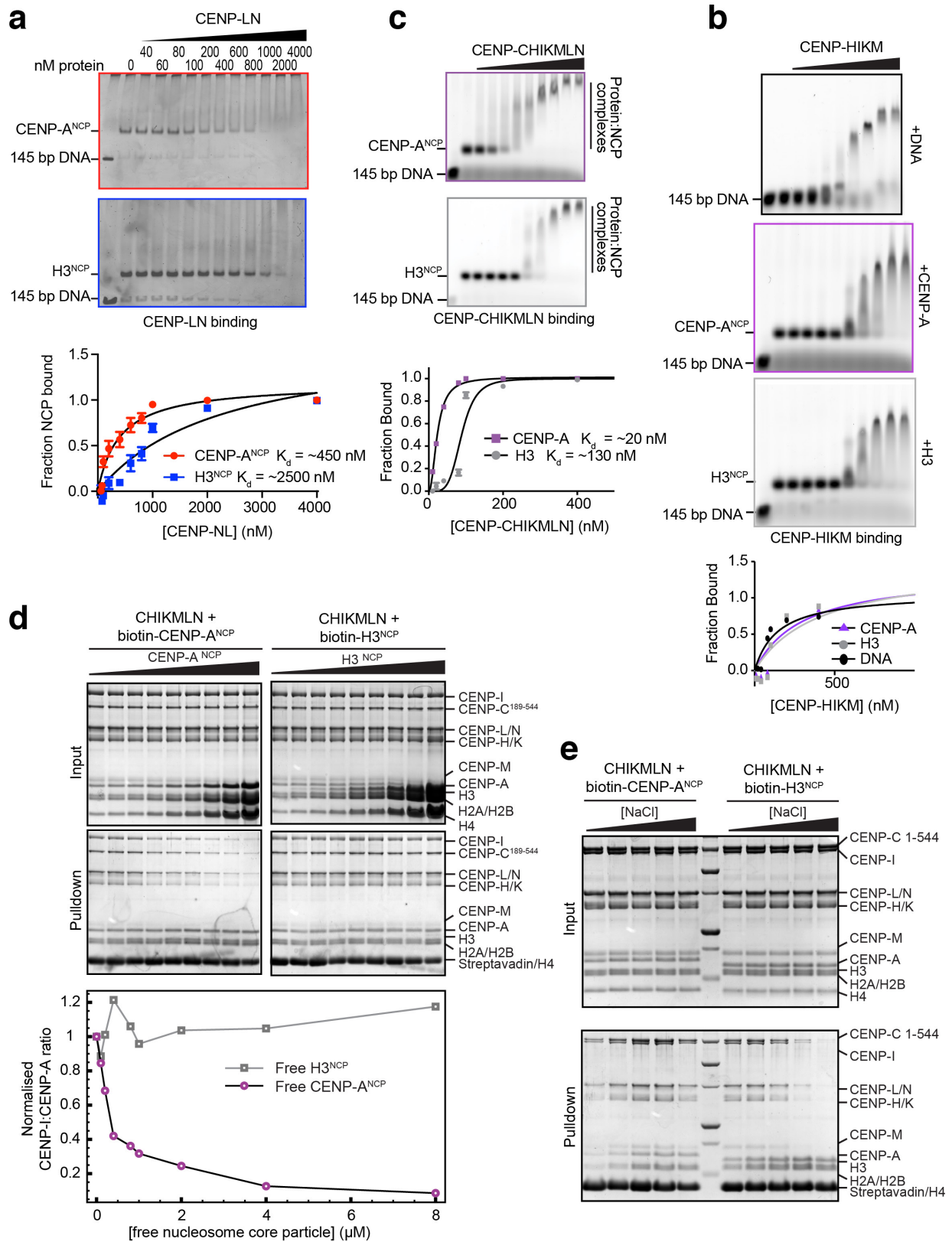
**Extended Data Figure 1 | Building blocks of the kinetochore.** Schematic organization of protein and subcomplexes used in this study, with essential structural features. CENP-A is a histone H3 variant. Crucial to its function in kinetochore assembly are the so-called CATD box and the C-terminal region, which are believed to interact with CENP-N and CENP-C, respectively<sup>10,11,39</sup>. For our reconstitution studies, we reconstituted human CENP-A:H4 tetramers and combined them with *X. laevis* H2A:H2B dimers. Nucleosome core particles containing histone H3 were reconstituted with *X. laevis* H3, H4, H2A, and H2B (see Methods). CENP-C can be thought of as a blueprint for kinetochore assembly, with binding motifs for outer and inner kinetochore subunits ordered from the N to the C terminus. The N-terminal region starts with a binding site for the Mis12 complex<sup>40,41</sup>, followed by a binding site for the CENP-HIKM complex<sup>19</sup>. Two related nucleosome-binding motifs have been identified, in the so-called 'central region' and 'CENP-C motif'<sup>11</sup>. The nucleosome-binding motifs interact with the H2A:H2B dimer and with the C-terminal region of CENP-A<sup>11</sup>. Finally, the dimerization motif has a cupin-like fold<sup>42</sup>. The C-terminal region also binds to M18BP1 (refs 43, 44), which is involved in CENP-A deposition. The two subunits of the CENP-LN complex have similar size and are structurally related, as revealed by the crystal structure of their *S. cerevisiae* homologues<sup>15</sup>. The four-subunit CENP-HIKM complex contains a tight subcomplex of the CENP-H and CENP-K subunits<sup>19</sup>. CENP-M is a pseudo-Ras-like small GTPase that has lost the ability to bind GTP<sup>19</sup>. It interacts with CENP-I

and is required for its stability<sup>19</sup>, but no CENP-M orthologue has been identified in *S. cerevisiae*, whereas Ctf3 is the CENP-I orthologue in this organism (see Fig. 4a). Structurally, CENP-I may resemble the HEAT-repeat  $\alpha$ -solenoid structure of Importin- $\beta$  (ref. 19). The four-subunit NDC80 complex is crucial for microtubule-binding by kinetochores<sup>7,8</sup>. It is a dumbbell-shaped, elongated protein with large coiled-coil domains<sup>23,45</sup>. Calponin-homology (CH) domains near the N terminus of the NDC80 and NUF2 subunits have been implicated in microtubule-binding<sup>23,45</sup>. The RWD domains of the SPC24 and SPC25 subunits target the NDC80 complex to the kinetochore<sup>46,47</sup> through interactions with the MIS12 complex. The four-subunit MIS12 complex remains structural uncharacterized, except for low-resolution negative-stain electron microscopy analyses<sup>47–50</sup>. It is a hub of interactions, including interactions with the CENP-C complex (discussed above), the NDC80 complex (also discussed above), and the Knl1 subunit of the Knl1 complex<sup>49</sup>. The two-subunit Knl1 complex plays a crucial role in spindle assembly checkpoint signalling<sup>51</sup>. The C-terminal region of Knl1, the largest known core kinetochore subunits, consists of tandem RWD domains and is sufficient with an interaction with the MIS12 complex<sup>47,49</sup>. A longer region, comprising approximately the last 300 residues, is also sufficient for tight binding to ZWINT. For our studies, we used a construct encompassing residues Knl1<sup>2000–2311</sup> that was endowed with the ability to bind the MIS12 complex and ZWINT.



**Extended Data Figure 2 | SEC analyses.** The indicated samples (at a concentration of 10  $\mu$ M, 5  $\mu$ M for nucleosome core particles) were loaded on the indicated SEC column and the resulting elution fractions were analysed by SDS-PAGE. **a**, CENP-LN complex. Note that CENP-L and CENP-N migrate identically in these gels because of their almost

identical mass. They can be distinguished by selective addition of a tag, as shown in Fig. 1c. **b**, CENP-C<sup>1-544</sup> complex. **c**, CENP-HIKM. **d**, KMN network. **e**, CENP-A<sup>NCP</sup>; the lower panel is a MidoriGreen-stained agarose gel of the same fractions analysed by SDS-PAGE in the upper panel. **f**, H3<sup>NCP</sup>; bottom panel as in **e**.



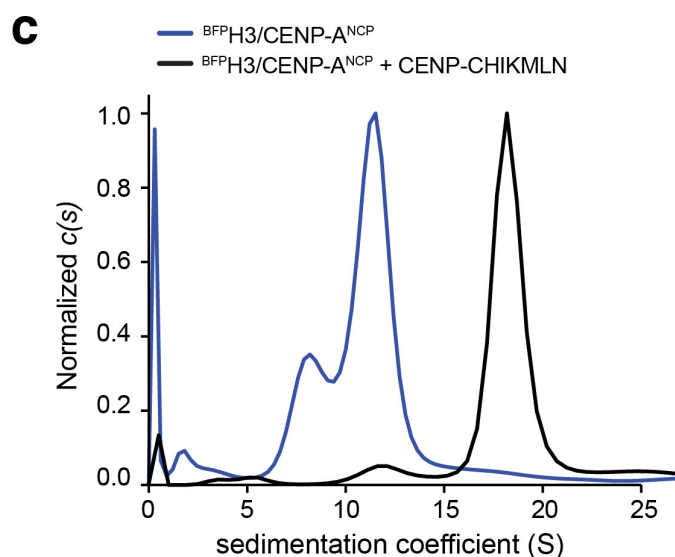
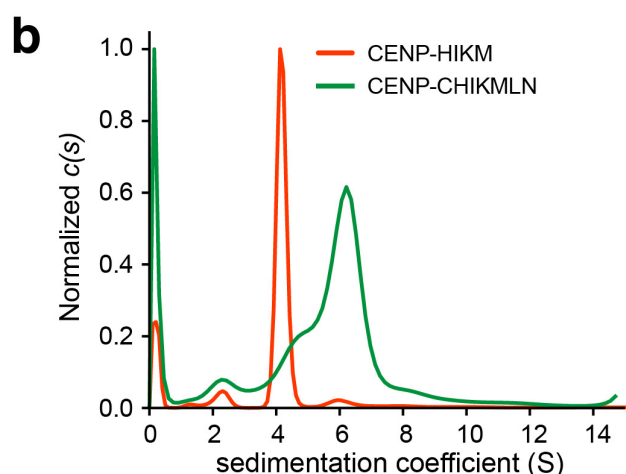
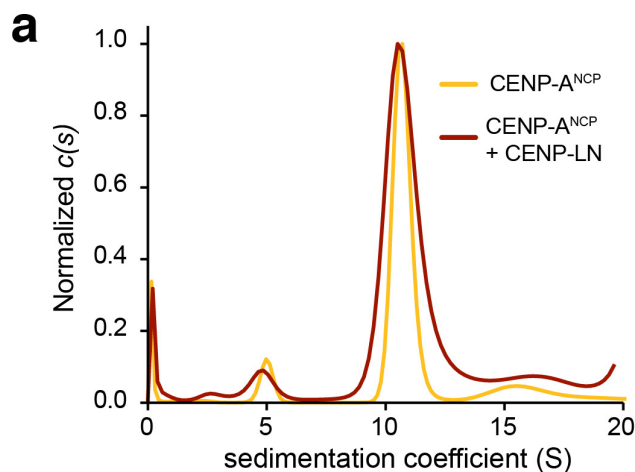
Extended Data Figure 3 | See next page for caption.

**Extended Data Figure 3 | Additional CENP-A binding experiments.**

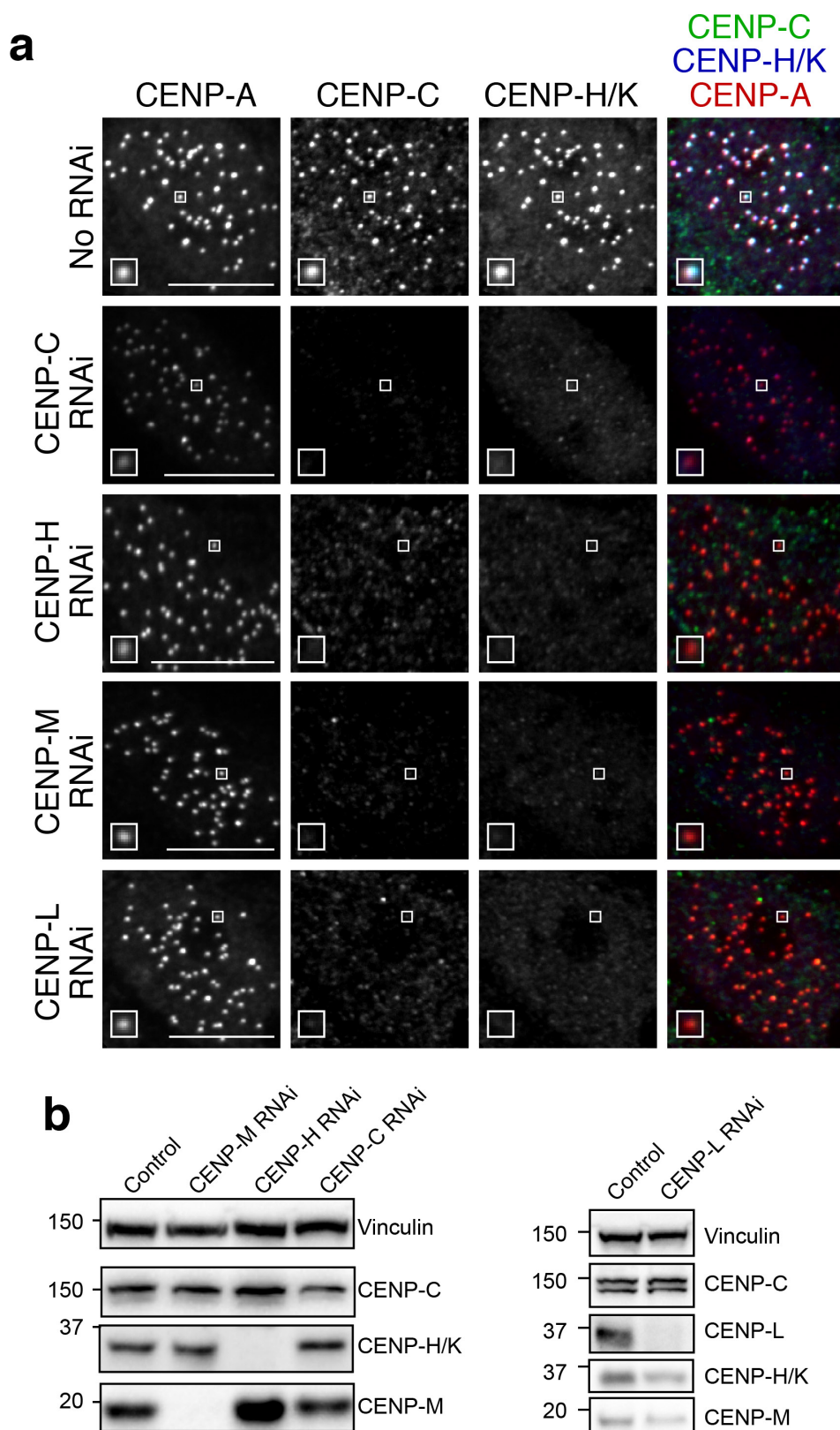
**a**, EMSAs were used to assess relative binding affinity of H3 or CENP-A NCPs to the CENP-LN complex. Quantification of binding data predicts the indicated dissociation constants. In quantifications of **a–c**, the mean  $\pm$  s.d. from three independent experiments is shown. **b**, CENP:CHIKMLN was titrated against Alexa-647-labelled CENP-A NCPs (purple trace) or H3 NCPs (grey trace) in an EMSA assay. Experimental triplicates were performed, and the approximate dissociation constant determined. CENP:CHIKMLN binds with approximately sevenfold higher affinity to CENP-A NCPs than to H3 NCPs. **c**, EMSA assays were performed using Alexa-647-labelled DNA in free form (black trace), in complex with H3 containing octamers (grey trace), or in complex with CENP-A containing octamers (purple trace). CENP-HIKM complex was titrated against the DNA or NCPs. No binding preference emerged. **d**, Biotinylated CENP-A NCPs were used as bait to pull down

CENP:CHIKMLN complex. Interactions were then competed for using an increasing concentration of free (non-biotylated) CENP-A NCPs (left) or H3 NCPs (right). The ratio of CENP-I to CENP-A was plotted in the lower graph. Free CENP-A NCPs effectively compete off biotinylated CENP-A NCPs from the CHIKMLN complex. Free H3 NCPs are unable to do so, even at concentrations 20-fold the biotinylated bait. The assay was performed in 200 mM NaCl, and used a shorter construct of CENP-C (189–544) owing to the greater stability of this construct at lower salt concentrations and to better separation of the CENP-C and CENP-I bands on SDS–PAGE for analysis. **e**, Biotinylated nucleosomes were used as bait to pull down CENP:CHIKMLN complex. Pull-downs were performed at increasing salt concentrations from 100–300 mM NaCl. CENP-A nucleosomes maintained a strong interaction with CENP:CHIKMLN in 300 mM salt. H3 NCPs lost the interaction with CENP:CHIKMLN at NaCl concentrations above 200 mM.





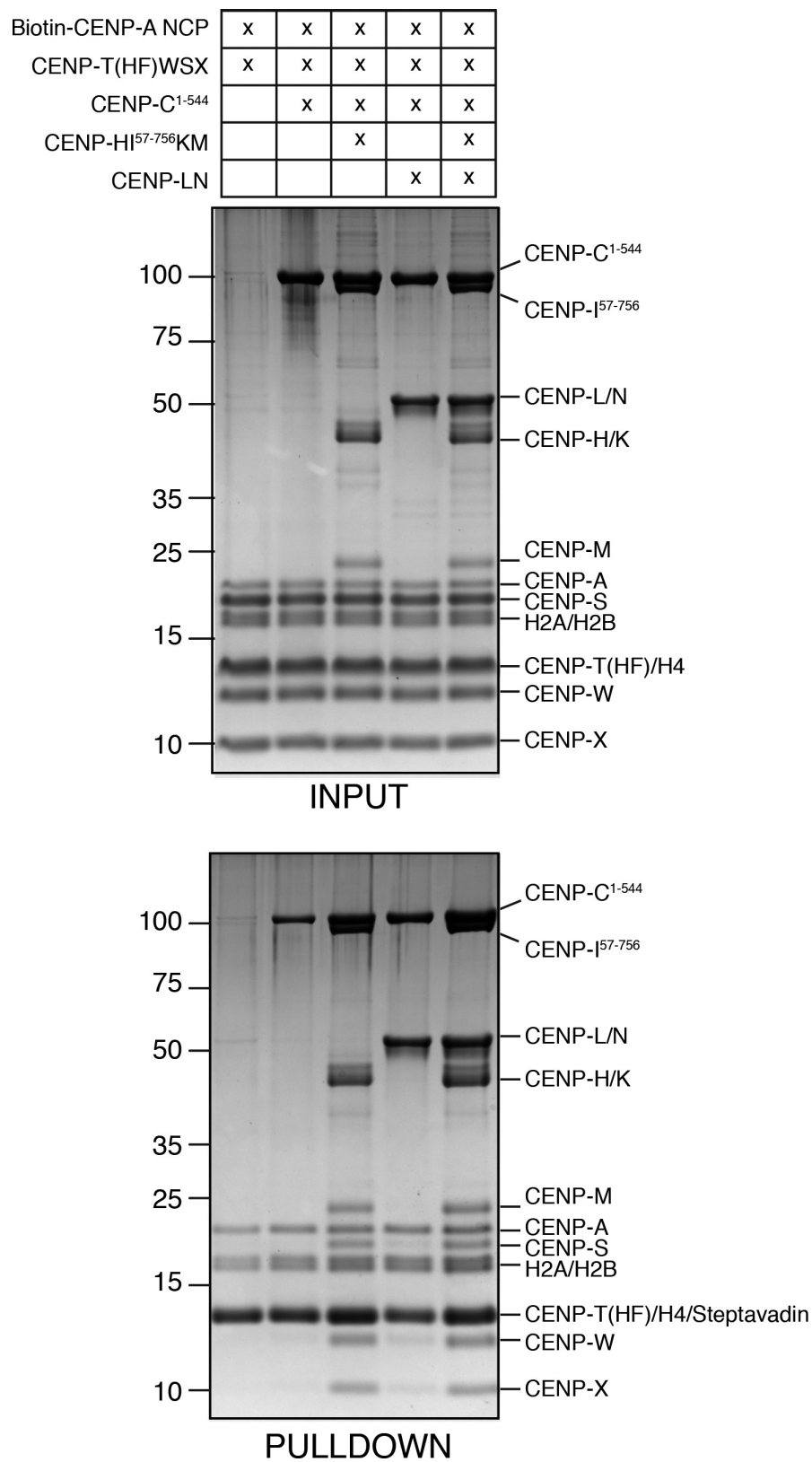
**Extended Data Figure 4 | Binding assays and analytical ultracentrifugation.** **a**, Normalized sedimentation coefficient ( $c(s)$ ) distributions of the respective sedimentation velocity runs. The data were collected at 280 nm and the size distribution analysis of the sedimentation coefficient was performed with SEDFIT<sup>38</sup> software using a continuous  $c(s)$  model. The rotor was spun at 42,000 rpm and equilibrated at 20 °C for 1 h before the start of the run. **b**, Normalized  $c(s)$  distributions of the indicated sedimentation velocity runs. The data were collected at 497 nm (thus analysing signals from CENP-HI<sup>57-CKM</sup> complex labelled with Alexa Fluor 488) and the size distribution analysis of the sedimentation coefficient was performed with SEDFIT using a continuous  $c(s)$  model. The rotor was spun at 42,000 rpm and equilibrated at 10 °C for 2 h before the start of the run. We were unable to carry out runs with isolated CENP-C<sup>1-544</sup>, CENP-C<sup>189-544</sup>, or CENP-LN complex, owing to sample instability during the centrifugation experiments. **c**, Normalized  $c(s)$  distributions of the indicated sedimentation velocity runs. The data were collected at 401 nm to monitor sedimentation of blue fluorescent protein (BFP) in chimaeric nucleosomes consisting of residues 2–75 of histone H3.1 and residues 75–140 of CENP-A (see Methods). The chimaeric nucleosomes were mixed with a threefold excess of CHIKMLN complex (containing CENP-C<sup>189-544</sup>; that is, a construct devoid of the binding domain for the MIS12 complex) to saturate binding.



#### Extended Data Figure 5 | Kinetochores localization studies.

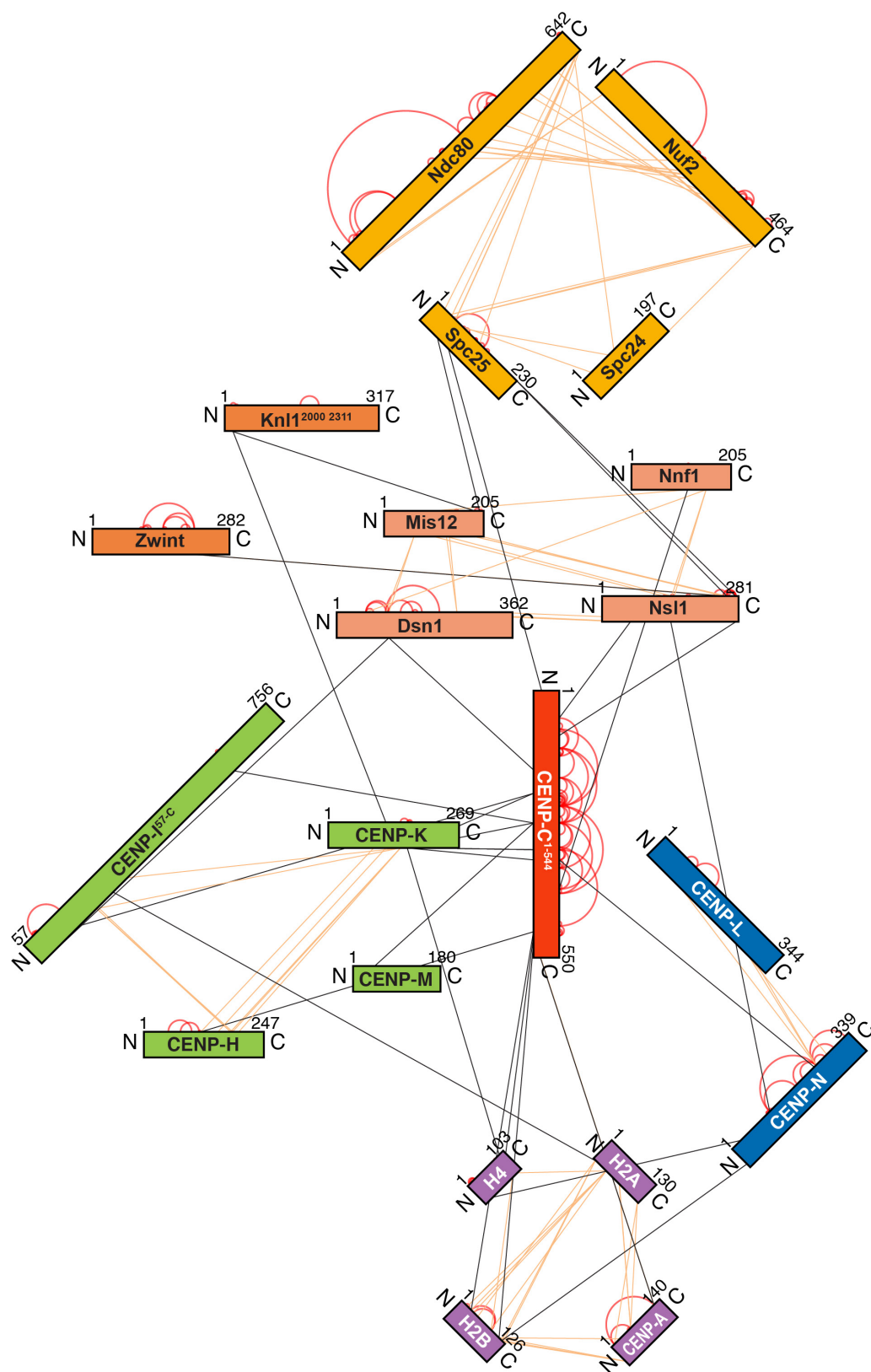
**a**, Representative images showing kinetochores levels in interphase cells of CENP-A, CENP-C, and CENP-HK (with an antibody raised against the CENP-HK complex) in Flp-In T-REx HeLa cells upon RNAi-based depletion of the indicated proteins. Kinetochores were visualized with anti-CENP-A sera. Scale bar, 10  $\mu$ m. Magnification 630 $\times$ . **b**, Western blots documenting protein depletion. RNAi-based depletion of CENP-C

appears incomplete by western blotting, whereas it appears to be very penetrant in immunofluorescence experiments. We have described this phenomenon before<sup>20</sup>, and found that decreased CENP-C silencing correlates with the higher degree of cell confluence (~80%) for the relatively large-scale RNAi preparations required for western blotting compared with immunofluorescence (where we start with cells at ~30% confluence).



**Extended Data Figure 6 | Incorporation of CENP-TWSX.** In an *in vitro* pull-down assay, CENP-A<sup>NCP</sup> reconstituted with biotinylated DNA were incubated with streptavidin-coated beads and the other recombinant kinetochore species indicated in the INPUT (top) panel of the figure. Beads were recovered by centrifugation and washed, and proteins bound

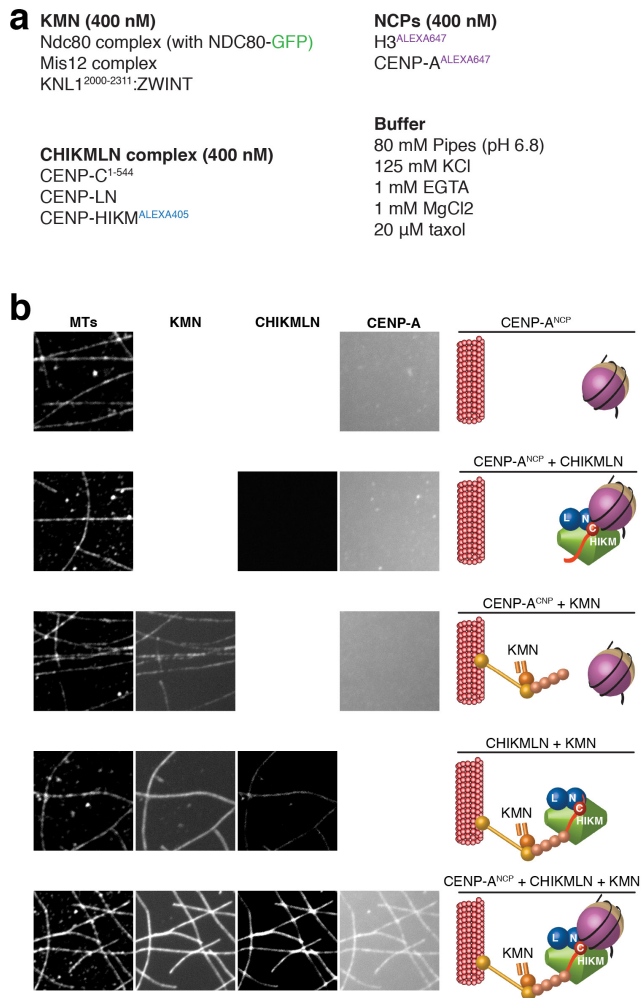
to the solid phase (PULLDOWN, bottom) were visualized by SDS-PAGE followed by Coomassie blue staining. Binding of CENP-TWSX tetramer (which contains only the histone fold domain of CENP-T) was contingent to binding of CENP-C<sup>1-544</sup> and CENP-HI<sup>57-756</sup>KM.



**Extended Data Figure 7 | Topology of the kinetochore.** Using XL-MS, the inter-peptide interactions within the kinetochore sample were analysed. Intra-protein crosslinks are shown in red, intra-subcomplex crosslinks are shown in orange, inter-subcomplex crosslinks in black.

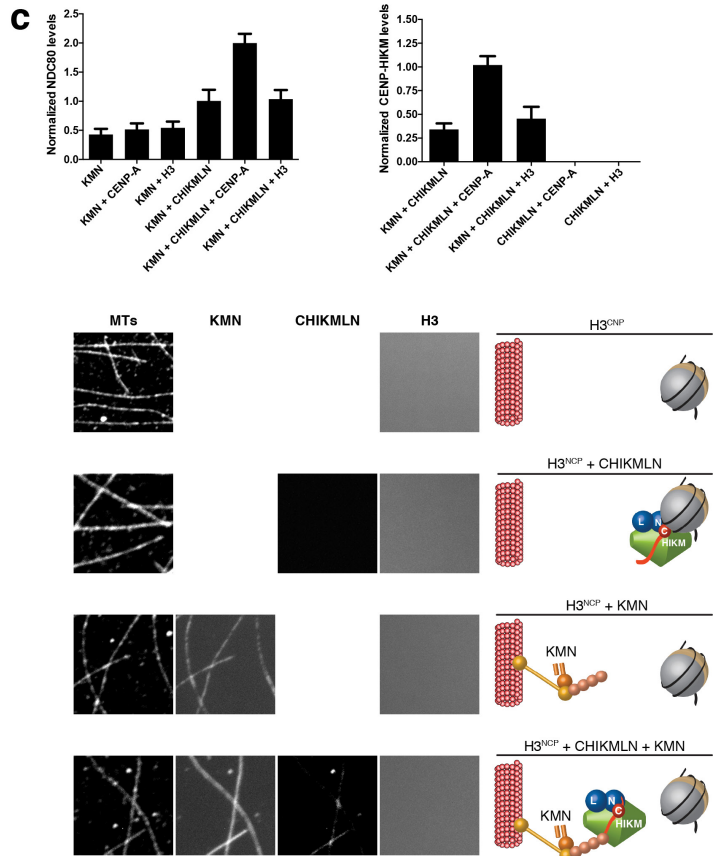
Proteins are coloured according to their subcomplex: CENP-A<sup>NCP</sup>, purple; CENP-C<sup>1-544</sup>, red; CENP-HIKM, green; CENP-LN, blue; MIS12-C, peach; KNL1-C, orange; NDC80-C, yellow.



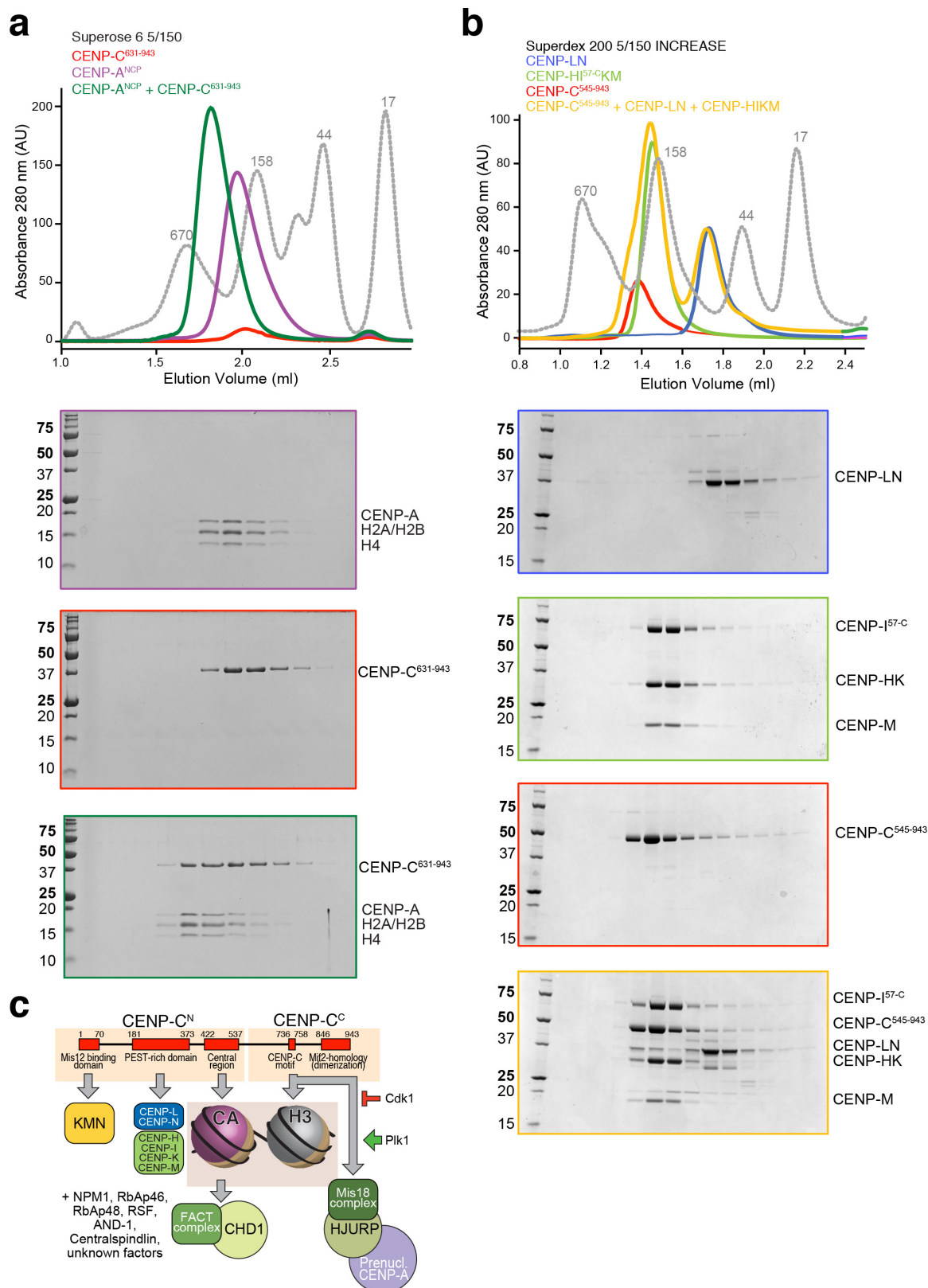


### Extended Data Figure 8 | Microtubule-binding experiments.

**a**, Description of reagents and buffer used in experiments in **b** and in Fig. 3b. **b**, Rhodamine-labelled microtubules (red channel) were tethered to glass coverslips and incubated in the presence of GFP-KMN (green), Alexa-405-labelled CHIKMLN (blue), or Alexa-647-labelled CENP-A<sup>NCP</sup> or H3<sup>NCP</sup> (purple), and combinations thereof. Only CENP-A<sup>NCP</sup>



translocated to microtubules, whereas H3<sup>NCP</sup> did not. Single microtubules from these images have already been shown in Fig. 3b. **c**, Quantification of experiments, already shown in Fig. 3b. **c**. Shown for each channel is mean  $\pm$  s.e.m. from at least 20 microtubules in at least 2 independent experiments.



**Extended Data Figure 9 | CENP-C<sup>545-943</sup> does not interact with CCAN subunits.** **a**, SEC analysis of CENP-A<sup>NCP</sup> (purple), CENP-C<sup>631-943</sup> (red trace), and their combination (green trace) shows a stoichiometric interaction. **b**, SEC analysis of CENP-LN (blue trace), CENP-HI<sup>57-C</sup>KM (green trace), CENP-C<sup>545-943</sup> (red trace), and their combination (orange trace). No apparent shift of CENP-C<sup>545-943</sup> was observed. **c**, Summary of known interactions at the centromere-kinetochore interface. The N-terminal region of CENP-C (exemplified by CENP-C<sup>1-544</sup>) binds the KMN, the CHIKMLN, and a CENP-A nucleosome. The C-terminal

region of CENP-C (exemplified by CENP-C<sup>545-943</sup>) does not bind core kinetochore components (this study) but interacts with CENP-A loading machinery, including the Mis18 complex, which in turn recruits the CENP-A chaperone HJURP<sup>52,53</sup>. Each half of CENP-C contains a nucleosome-binding motif, and has therefore the potential to interact with two adjacent nucleosomes. After DNA replication, when CENP-A levels are halved, CENP-A is replaced with H3 (H3.3, refs 54, 55). After mitosis, the C-terminal region of CENP-C contributes to recruit machinery that replaces H3 with CENP-A.

## CORRIGENDUM

doi:10.1038/nature18962

### Corrigendum: Enhancer loops appear stable during development and are associated with paused polymerase

Yad Ghavi-Helm, Felix A. Klein, Tibor Pakozdi, Lucia Ciglar, Daan Noordermeer, Wolfgang Huber & Eileen E. M. Furlong

*Nature* **512**, 96–100 (2014); doi:10.1038/nature13417

In Fig. 2d of this Letter, two different representative stage 11 embryos were mistakenly shown for the green (*scyl*) and red (*chrb*) channels. The merge image showed the signal of both genes in the ‘*scyl*’ embryo. This has now been corrected in Fig. 1 of this Corrigendum, which shows the expression of both genes in the same embryo. Both genes are highly co-expressed, even more so than previously reported.

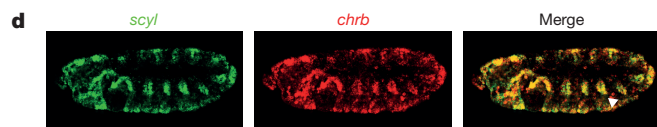


**Figure 1** | This figure shows the corrected Fig. 2d of the original Letter.

# CORRECTIONS & AMENDMENTS

---

## CORRIGENDUM

doi:10.1038/nature18931

### Corrigendum: Malaria: Thermoregulation in a parasite's life cycle

Jun Fang & Thomas F. McCutchan

*Nature* **418**, 742 (2002); doi:10.1038/418742a

In the first paragraph of this Brief Communications, accession numbers are provided for four rRNAs. The database that they refer to is incorrect (it should be the European Nucleotide Archive (ENA) rather than GenBank), the order in which the accessions are indicated is also incorrect, and there is an extra '3' in one the of accession numbers. The text should say: "...two mature A-type rRNAs (A1, A2; ENA accession numbers, AF503871 and AF503870) and two mature S-type rRNAs (S1, S2; ENA accession numbers, AF503869 and AF503868)...".



# CAREERS

**STAR STRUCK** An astronomer crunches data for Hollywood **p.257**

**LINKEDIN** A beginner's guide to the networking site [go.nature.com/2c4wg7v](http://go.nature.com/2c4wg7v)

**NATUREJOBS** For the latest career listings and advice [www.naturejobs.com](http://www.naturejobs.com)



BY EMILY SOHN

When biologist Adrian Smith chose to study ants, he approached the field with ambitious questions and big dreams of discovering how animal societies work. The reality was much less glamorous.

To capture ant colonies to study in the lab, he digs human-sized holes and then plucks out thousands of insects, one by one. After six hours or more of this backbreaking work, Smith, who works at the North Carolina Museum of Natural Sciences in Raleigh, and his teammates sometimes discover that the queen is missing, or they've inadvertently cut her in half. They then have to start over again.

Such mind-numbing work occupies researchers' time in most specialties. By nature, science depends on intensive data collection, repetition and replication. To cope with the tedium, experienced scientists have found tricks for making the work more pleasurable, such as getting to know colleagues who are in the same trenches and keeping long-term goals in mind.

Given the intense focus required for the bulk of their work, many scientists learn to value brainless tasks that allow them to zone out and indulge in free thinking. That can lead to creative research ideas or ways to boost efficiency. Faced with day after day of doing the same thing, researchers who appreciate boredom can gain insight into their goals and priorities.

## SURVIVAL GAME

Boredom is a typical part of the process of scientific discovery, which rarely happens in a day. Even when intriguing results emerge, it can take many months to write a paper, get it peer reviewed and complete multiple revisions, and then wait for publication before sharing discoveries with the world. The first step towards coping successfully can be simply to accept the drill.

"We wouldn't be on the edge of discovery if it was easy," Smith says. "Sometimes, you're in places where no one has really looked, or you're seeing something no one has seen before. To get to that point, it takes some tedious work."

At such times, it can help to remember that the work might eventually bring bursts of exhilaration or, sometimes, a real thrill of discovery, says David Burnham, a palaeontologist at the University of Kansas Biodiversity Institute & Natural History Museum in Lawrence. He regularly digs for dinosaur bones — an experience that resembles a notorious description of war, he says — it entails "long periods of boredom, interspersed with high excitement". ▶

## LAB LIFE

# Daydream and discover

*Tedious daily work might feel frustrating, but idle thoughts can drum up just the right spark of scientific inspiration.*

► Every trip begins months beforehand with much tiresome preparation, such as filling out forms to get excavation permits. Once his team arrives in the field, the group has to organize gear, drive on bumpy dirt roads and hike to a site where the researchers set up tents and equipment. Then comes the slow process of digging, often in hot or otherwise uncomfortable conditions. The work starts with shovels and picks, but when fossil evidence begins to appear, the palaeontologists switch to smaller, more delicate tools to unearth what might end up being just unidentifiable shards of bone. Any finds that could add to the overall puzzle must be carefully wrapped and meticulously documented before being taken to the lab, where an even more delicate process of excavation and investigation continues.

As the hours disappear, Burnham keeps in mind the possibility that he might at any moment find a motherlode of bones or a fossil that will change everything. Equally motivating are sporadic discoveries that shed light on big questions. Sometimes, the pay-off can be huge. On one memorable dig in China, Burnham's team found a raptor that turned out to be a new species. During the monotonous fact-checking process required to verify the find, the team compared the new bones to those of a related raptor and realized that the relative had grooved teeth, which suggested that it was venomous. That realization led to a paper, published in the *Proceedings of the National Academy of Sciences*<sup>1</sup> in 2010, that described the first venomous raptor ever known.

Finds such as those are rewarding enough, he says, to confer a surprisingly high tolerance for boredom or similar discomfort. "That one piece of excitement is so exhilarating," he says. "It just gets into your blood and you have to keep going."

Telling others about your grand goals can be another way to endure tedium, suggests

David Hadley, an epidemiologist in Tampa, Florida, who does both academic and industrial research. He is developing a programme that would help oncologists to settle on the best course of care for patients with cancer on the basis of treatment data from previous patients and other information such as their ages, gender and genetic variations. To get it right, he has to run a lot of computer simulations and then wait as a computer crunches data, sometimes for up to a week. Often, results reveal mistakes that need to be fixed before the next simulation can be run. "It really helps to talk to other people about the big picture, not necessarily about what you are doing day to day, but about what you are trying to achieve overall," he says. "In my case, it's trying to help sick kids. That is why I'm motivated to do it."

### GRUNT WORK TO GROWTH

Just as musicians need to learn scales before they can improvise, grunt work is a necessary step towards designing studies to answer big questions, adds William Stoops, a behavioural pharmacologist at the University of Kentucky in Lexington. He has spent many hours supervising research subjects as they interact with a computer to earn doses of addictive drugs, with the goal of working out what drives drug use and abuse, and finding treatments. "If you can't understand what a subject is supposed to do in a session, and you design an experiment that's just not feasible, it will fail," he says. "Every graduate student and postdoc learns this stuff from the ground up."

Frequently reminding yourself of the potential pay-off can make delayed gratification more palatable, Smith says. "It sucks until it doesn't" is a mantra that he repeated to himself on a trip this year to Florida, where he spent eight long, hot days roaming around forests getting bitten by mosquitoes while crawling on his hands and knees to look for ants. It was tough going until



Biologist Karen Warkentin counts frog eggs.

he found what he was looking for: colonies of *Formica archboldi*, a species that preys on other ants and litters its nests with their carcasses. He wanted to take them to his lab to study their prey preferences and possible predatory behaviours.

It could always be worse, adds neuroscientist Dean Burnett, who, as a graduate student at Cardiff University, UK, watched many rats navigate many mazes, tallying which direction the rats chose at each turn, to try to understand how they retrieved memories. Without a way to automate data collection, he would remind himself of the glamour of his previous job: embalming corpses for a medical school.

He recommends starting work with your eyes open and the expectation that some tasks will be less fun than others. "People want to do science, and they have big lofty goals," he says. "A lot is day-to-day work. There can't be many jobs that are generally enjoyable all day, every day."

To make monotonous work more bearable, it can also be useful to schedule repetitive tasks to match your own ebbs and flows of energy, says Karen Warkentin, an integrative biologist at Boston University in Massachusetts. To do her work, she has forced herself to stay awake many nights in a dark lab, waiting for snakes to wake up and eat frog eggs. She has walked around a pond counting bundles of dozens of eggs, often recounting and recounting. And she has measured thousands of frogs as they grew from tadpoles to adults, all in the name of understanding plasticity in the early-life stages of amphibians, among other goals. After handling frogs all day, she spent evenings plugging numbers into spreadsheets and checking columns — clocking 16-hour work days in what she calls a "crazy marathon" of an experiment.

She prefers different times for different tasks. For her, early morning is usually best for creative work, such as writing. When her brain feels fried, often after lunch or in the evening, she finds satisfaction in repetitive jobs. "You can feel like, 'Hey, I'm still being productive,'" she says.

Warkentin likes to work in silence, but many researchers distract themselves by listening to music, podcasts or books on tape (see "Tunes for tedium"). Tedious times can also be a bonding experience, Burnham says. While digging

## BEATING BOREDOM

### Tunes for tedium

When work gets boring, many researchers tune out by tuning in — enduring repetitive work by listening to music or stories. Deciding what's best to listen to during tedious tasks depends on the kind of work. For tasks that require some attention but not full focus, behavioural ecologist Margaret Couvillon, who will soon teach entomology at the Virginia Polytechnic Institute and State University in Blacksburg, recommends choosing familiar audio books. But to survive long stretches of nothing punctuated by busy periods, she prefers podcasts that are easy to pause and resume. Favourites include: *This American Life*, *Invisibilia*, *Science Friday* and *Wait Wait Don't Tell Me*.

Adrian Smith, an ant researcher at the North Carolina Museum of Natural Sciences in Raleigh, North Carolina, likes podcasts, too, and recommends ones that match outside interests. He enjoys comedy and pop-culture themes: *Bullseye*, *WTF*, the *Memory Palace* and the *Bret Easton Ellis Podcast*.

Music is another option. David Hadley, an epidemiologist in Tampa, Florida, likes to listen to stuff that's familiar to him. UK neuroscientist Dean Burnett prefers classic mainstream pop that drowns out distractions without being too stimulating. He also points to a common belief that video-game theme music is ideal for boosting motivation. **E.S.**

SEAN MATTSOON/SMITHSONIAN TROPICAL RESEARCH INSTITUTE



for dinosaur bones, his field crew chats and jokes around, creating memories and forging friendships. “The best way to endure it is to put together a field crew of people who are like-minded and enthusiastic and really want to be there,” he says. “Then you can sit around and have fun.”

### BUILDING WITH BOREDOM

Boredom isn't just something to endure: it can carry value of its own, giving the brain uninhibited space to wander and wonder. As a graduate student, Smith had an idea while watching ants (*Novomessor cockerelli*) move around in a box for hours: what if he reunited a group of isolated worker ants with the queen instead of with the rest of the colony, as he had done in other experiments? The results were surprising: the queen attacked the main worker and rallied the rest of the workers to gang up on it. The discovery spawned two publications: one in the German journal *Naturwissenschaften*<sup>2</sup> in 2011, and the other in *Animal Behavior*<sup>3</sup> in 2012.

Smith also credits boredom for some unexpected twists in his career. During bouts of daydreaming and podcast-listening while doing menial tasks, he decided to create a series of YouTube videos and launch a podcast, *Age of Discovery*, in which he interviews biologists about their careers. Developing those multimedia skills helped him to land his current job, which includes outreach and communications. “I spent countless hours thinking about whether I wanted to commit to things that were tangential to my research but turned out to not be tangential to my career,” he says. “That stuff wouldn't have happened if I was just occupied in front of the computer writing all the time or whatever.”

Boredom can also spark creative ways to minimize it. Frustrated with how long it took to run computer simulations for his software, Hadley more than once boosted his efficiency by rewriting programs created by others. “If you are only doing something once or twice, you can afford to wait a couple of seconds,” he says. “When you are doing permutations two million times, that's two million seconds lost. It helps me reduce my downtime.”

These kinds of stories are being documented in an emerging field of research on the value of boredom. In one study<sup>4</sup>, Jennifer Hunter, a PhD student at York University in Toronto, and her colleagues found that — after accounting for traits such as extroversion — people who are prone to boredom also report being curious types, adding to growing evidence that boredom can breed innovation. “I think it can be a huge catalyst,” she says. “Don't ignore your boredom. It can tell you really powerful things about what you're doing.”

As a career evolves, boredom can become a state of comfort. Although Warkentin's frog-counting work might sound tedious, she doesn't mind it — instead, she finds it

satisfying to be in the natural world and enjoy serendipitous experiences with wildlife. She looks for the same personality fit when fielding applicants for her team. “When I'm recruiting students,” she says, “I'm like, ‘Does this sound like your idea of a good time?’”

The answer might be ‘no’, and those feelings are worth paying attention to, says Margaret Couvillon, a behavioural ecologist who recently completed a postdoc at the University of Sussex, UK, and will soon begin teaching entomology at the Virginia Polytechnic Institute and State University in Blacksburg. Couvillon started out as a neurobiology PhD student, and found herself staring at slices of bird brains. As she slowly inserted probes into the tissue to find neurons, she became discontented. Her true interest was animal behaviour, and she realized that she really wanted to watch animals in action, not study their brains in the lab.

When she transferred to an ecology programme elsewhere, she discovered that her experiments included plenty of tedious elements, too. She has spent “many, many, many hours” watching videos of dancing bees (*Apis mellifera*) and timing and measuring their movements to determine where they forage. She has also spent a lot of time sitting in front of honeybee feeders, counting insects that visit and waiting for long stretches when none come by. But Couvillon has discovered that she's much happier enduring boring work when it addresses the questions that truly interest her. And with so much of her time taken up by mentally exhausting tasks, she has come to cherish the chance to sit by a honeybee feeder on a nice day. She suggests keeping expectations realistic — after all, nobody has a job that delivers eureka moments every day.

She also recommends shadowing a variety of scientists to see whether the daily reality seems appealing before committing to a speciality. “Not all dirty work is created the same,” Couvillon says. “You have to have an everyday life you can handle.” ■

**Emily Sohn** is a freelance journalist in Minneapolis, Minnesota.

1. Gong, E., Martin, L. D., Burnham, D. A. & Falk, A. R. *Proc. Natl Acad. Sci. USA* **107**, 766–768 (2010).
2. Smith, A. A., Hölldobler, B. & Liebig, J. *Naturwissenschaften* **98**, 237–240 (2011).
3. Smith, A. A., Hölldobler, B. & Liebig, J. *Animal Behav.* **83**, 587–593 (2012).
4. Hunter, J. A., Abraham, E. H., Hunter, A. G., Goldberg, L. C. & Eastwood, J. D. *Thinking Skills Creativity* **22**, 48–57 (2016).

### CORRECTION

The Careers feature ‘Visa to visit’ (*Nature* **536**, 365–366; 2016) wrongly stated that Kelsey Glennon asked students from indigenous tribes not to stand so close to her. She actually made the request of all her students.

## TRADE TALK

### Star selector



As an astronomy PhD student at Harvard University in Cambridge, Massachusetts, Nathan Sanders learnt statistical modelling to analyse supernova explosions. Now, he

works for *Legendary Entertainment* in nearby Boston, applying those quantitative skills to predict which stars and story lines can make a film into a commercial success.

### When did you consider leaving astronomy?

I had learned a new computational framework in a statistics course. As I applied those techniques for my thesis, I realized that I loved what I was doing, and the reason had more to do with the statistical models than the astronomy applications. That made me open to new opportunities. I thought I would be doing a disservice to myself if I didn't explore them.

### What appealed to you about this position?

When I was hired in 2013, *Legendary* had just launched its applied-analytics division in Boston. It felt like an opportunity to rethink and reinvent the way that companies pick which films to make and how to build support for them. The goal was to be the first in Hollywood to make decisions on the basis of data and evidence rather than on intuition.

### Besides technical skills, what do you look for in candidates when you recruit?

Communication is key. You have to be comfortable with diverse concepts, and talk to business people, filmmakers and technical colleagues.

### How did you hear about this position?

I emphasize the importance of volunteering and getting out into the community. As a first-year graduate student, I started a project called *Astrobites*, a collaborative writing project that creates a *Reader's Digest* version of astronomy literature. I also volunteered with an organization doing live science demonstrations. The executive director was a friend of the chief analytics officer at *Legendary Entertainment*. It was one of those random connections that so often creates a job opportunity, but that can be hard for scientists to foster if they are completely focused on their thesis work. ■

### INTERVIEW BY MONYA BAKER.

This interview has been edited for length and clarity. See [go.nature.com/2bix4y7](http://go.nature.com/2bix4y7) for more.



# TRY CATCH THROW

BY ANDREW NEIL GRAY / ILLUSTRATION BY CHRIS MALBON



SCIENCE. FICTION.  
A *Nature* special issue  
[nature.com/scifispecial](http://nature.com/scifispecial)



# TRY

THE FIRST THING MARIELLE DOES IS RESET THEIR LIVES TO THE NIGHT SAM HAS THE IDEA THAT WILL DESTROY THE WORLD.

## RESET



Andrew Neil Gray has published work in Apex Magazine, IGMS and has a novella forthcoming with Tor.com. He won second place in the 2015 Quantum Shorts Competition.



THEY ARE AT CHIANTI'S ON WEST 4TH. A SMALL TABLE NEAR THE BACK. HE'D TOLD HER THAT THEIR CONVERSATION DURING THE DATE PLANTED THE SEED OF HIS EXPERIMENT.

SO SHE IS HERE TO UPROOT IT.



# CATCH

"I THINK WE SHOULD MOVE IN TOGETHER."

SAM NEARLY SPITS OUT HIS WINE.

IT'S A DRAMATIC WAY TO DERAIL HIS TRAIN OF THOUGHT - THEY'VE BEEN DATING FOR ONLY SIX WEEKS.

IN THEIR PREVIOUS LIFE, IT TOOK NEARLY THREE YEARS TO REACH THIS POINT. AFTER THE MESS HER PARENTS HAD MADE, ALL ROMANTIC RELATIONSHIPS SEEMED PROVISIONAL. SAM IS A COMMITTER THOUGH. EYES LIT.

"YOU'RE NOT PULLING MY CHAIN?"  
"NO CHAIN," SHE SAYS.  
"NO STRINGS."





# TRY

IT BUYS HER EIGHT MONTHS. AN APARTMENT ON MAPLE STREET. TWO TOOTHBRUSHES IN THE CUP. SHE ALMOST FORGETS THE LIFE THEY'D ALREADY LIVED. THEN ONE EVENING SHE COMES HOME LATE AND HE'S AT THE KITCHEN TABLE SURROUNDED BY FAMILIAR-LOOKING DIAGRAMS.

THE FLOOR DROPS OUT FROM UNDER HER.

"YOU HAD AN IDEA,"  
MARIELLE SAYS.

"I TOTALLY HAD AN IDEA.  
WAIT TILL I TELL YOU."

"BEFORE YOU DO, CAN YOU  
REMEMBER WHEN YOU HAD IT?"



# CATCH

SAM AND ANDY WONG CARPOOL WHEN MARIELLE HAS TO STAY LATE AT THE SUPERCOMPUTING CENTRE WHERE THEY ALL WORK. AND OF COURSE THEY'VE BEEN TALKING ABOUT HOW TO PROVE THE SIMULATION HYPOTHESIS.

SHE RESETS A DAY AND DRIVES SAM HOME INSTEAD.

NOT ENOUGH.

THE CONVERSATION HAS BEEN ONGOING. SHE TRIES A WEEK. A MONTH. STILL THE DIAGRAMS ON THE TABLE LAYING OUT A PATH TO THE END OF EVERYTHING.

FINALLY, SHE RESETS TO BEFORE THE CARPOOL BEGAN AND CREATES A CONVINCING PAPER TRAIL THAT SUGGESTS ANDY WONG LIED TERRIBLY ON HIS CV.

SHE SENDS IT ANONYMOUSLY TO THE HEAD OF RESEARCH.

## RESET

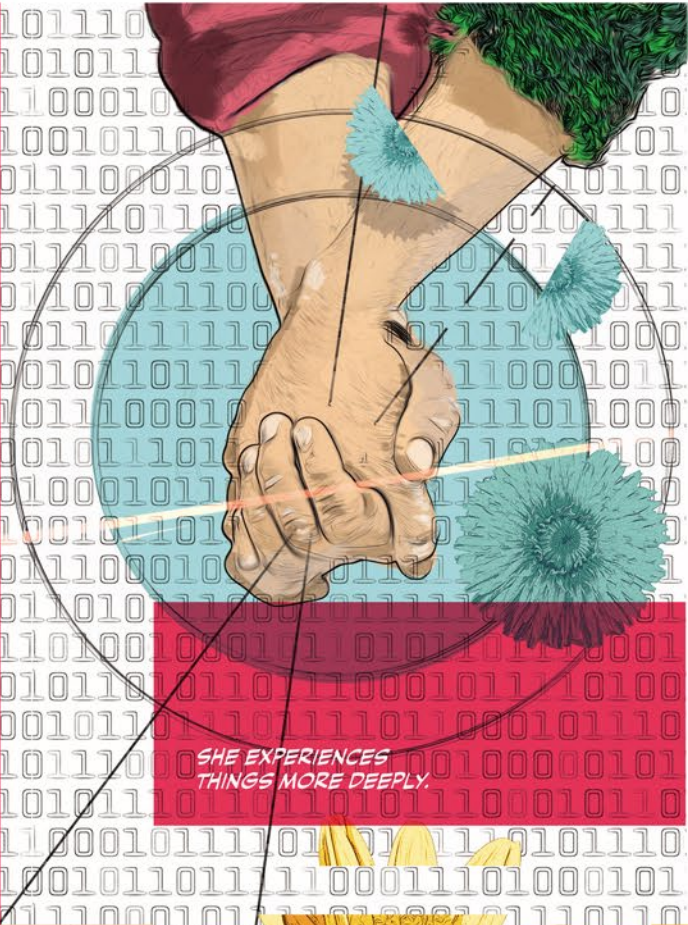
SAM CARPOOLS WITH KRISTIN KANZ, THE OFFICE MANAGER. THEY SHARE AN INTEREST IN POLICE DRAMAS. THEY DO NOT DISCUSS COMPUTATIONAL PHYSICS.



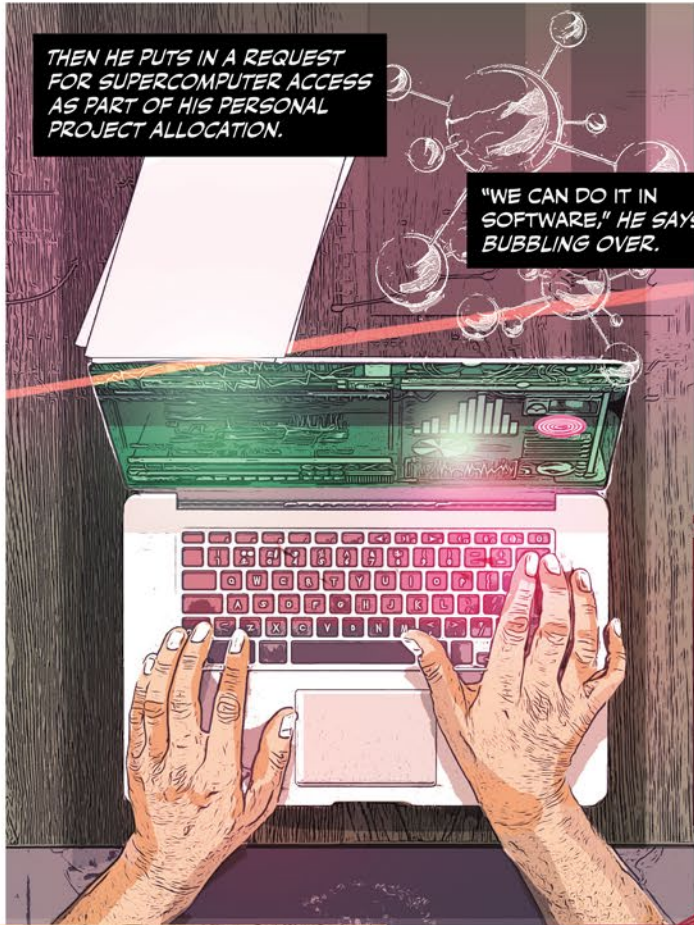


# TRY

TWO YEARS PASS.  
THEIR RELATIONSHIP IS DIFFERENT THIS TIME. MARIELLE FINDS SHE IS MORE THOUGHTFUL, MORE OPEN.



SHE EXPERIENCES THINGS MORE DEEPLY.



THEN HE PUTS IN A REQUEST FOR SUPERCOMPUTER ACCESS AS PART OF HIS PERSONAL PROJECT ALLOCATION.

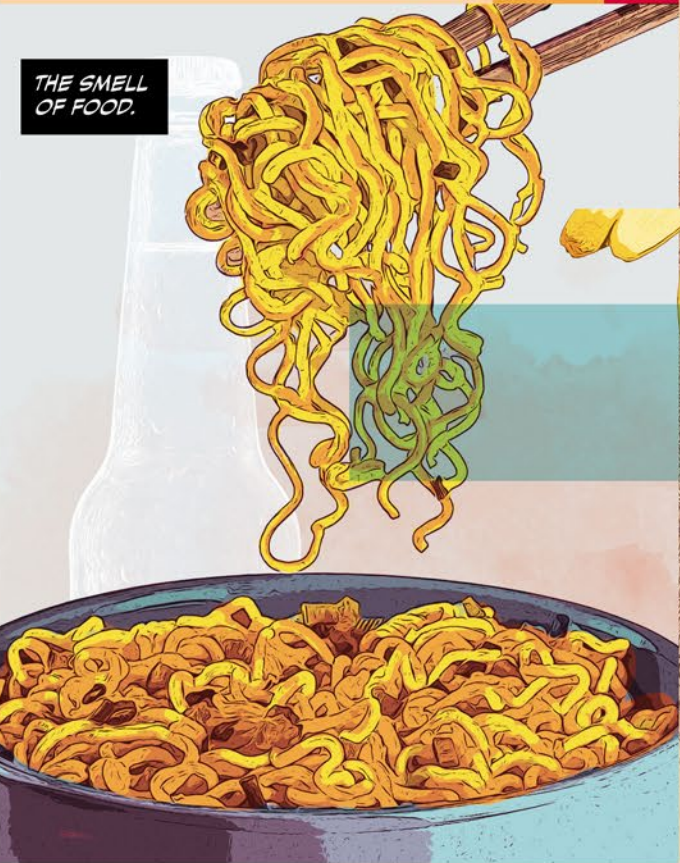
"WE CAN DO IT IN SOFTWARE," HE SAYS, BUBBLING OVER.

SHE FEELS LIKE SHE'S FALLING AGAIN.  
"HOW CAN YOU TEST IF WE'RE LIVING IN A SIMULATION USING SOFTWARE?"

MAYBE IT WILL BE A BLIND ALLEY. BUT HE HAS A BRILLIANT IDEA ABOUT USING NESTED SIMULATIONS TO PREDICT THE OPERATING CONSTRAINTS OF THE MACHINE THE UNIVERSE COULD BE RUNNING ON.



TOO BRILLIANT.



THE SMELL OF FOOD.

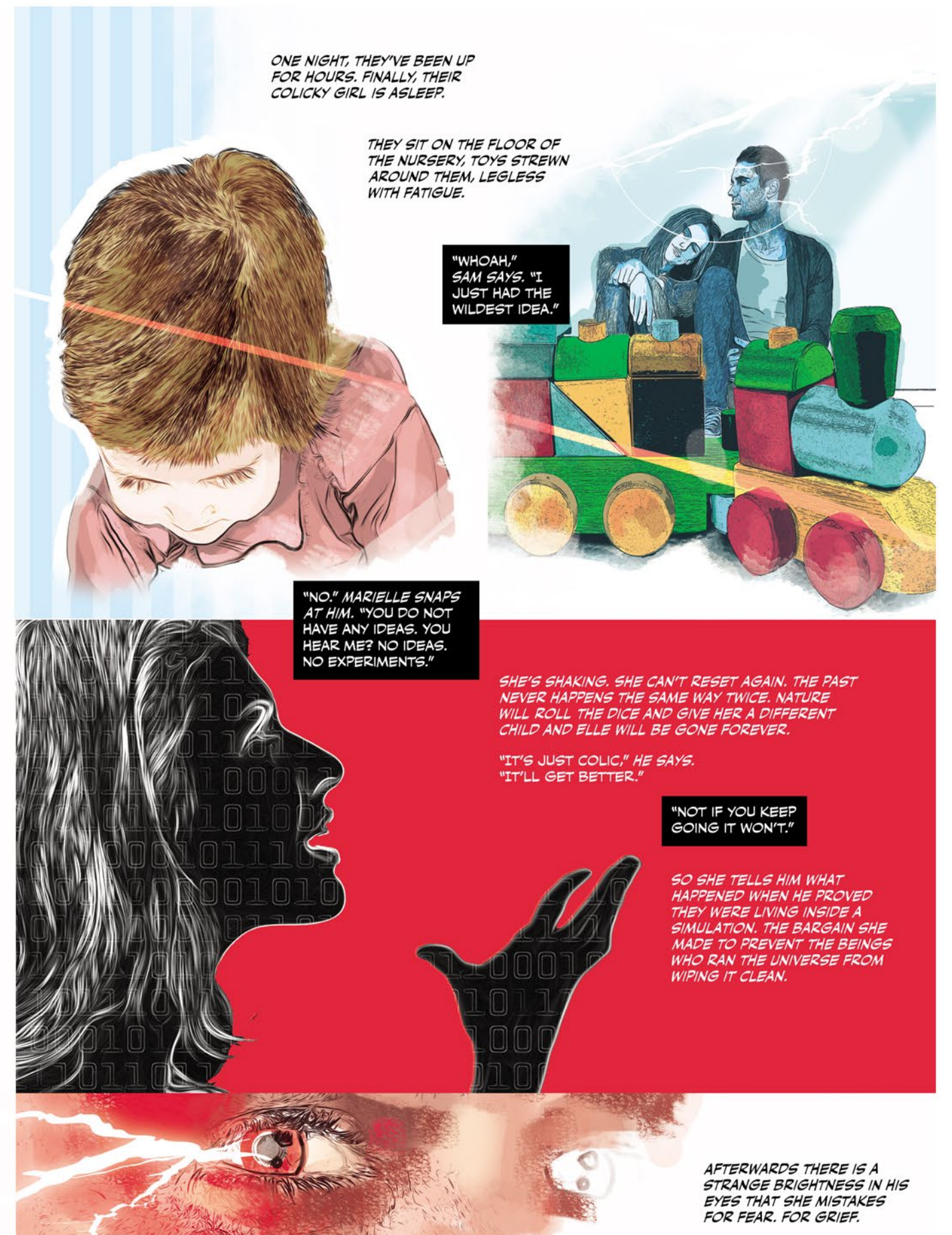


THE TASTE OF SALT ON SAM'S SKIN AFTER HE'S BEEN RUNNING.

SHE NUDGES HIM AWAY FROM INVESTIGATING THE GRANULAR STRUCTURE OF SPACE-TIME.











# TRY

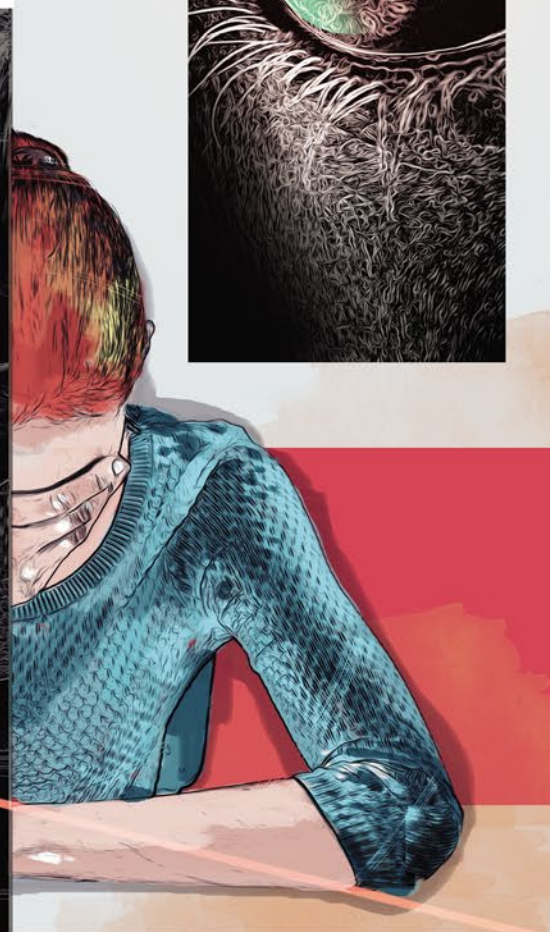
SEVEN YEARS LATER, ELLE IS AT SCHOOL. MARIELLE IS AT HOME, ILL. SHE USES SAM'S COMPUTER TO CATCH UP ON WORK AND AS SHE DOES HIS E-MAIL WINDOW POPS UP.

IT'S AN ACCEPTANCE FOR HIS PAPER ON THE SIMULATION HYPOTHESIS.

THE EDITOR OF THE JOURNAL IS EFFUSIVE. HE COMMENDS SAM FOR THE YEARS OF WORK HE'D PUT IN.

YEARS.

MARIELLE PUTS HER HEAD ON THE TABLE. SHE SOBS AND SOBS.



# THROW

SHE IS SUDDENLY IN A GREY ROOM.

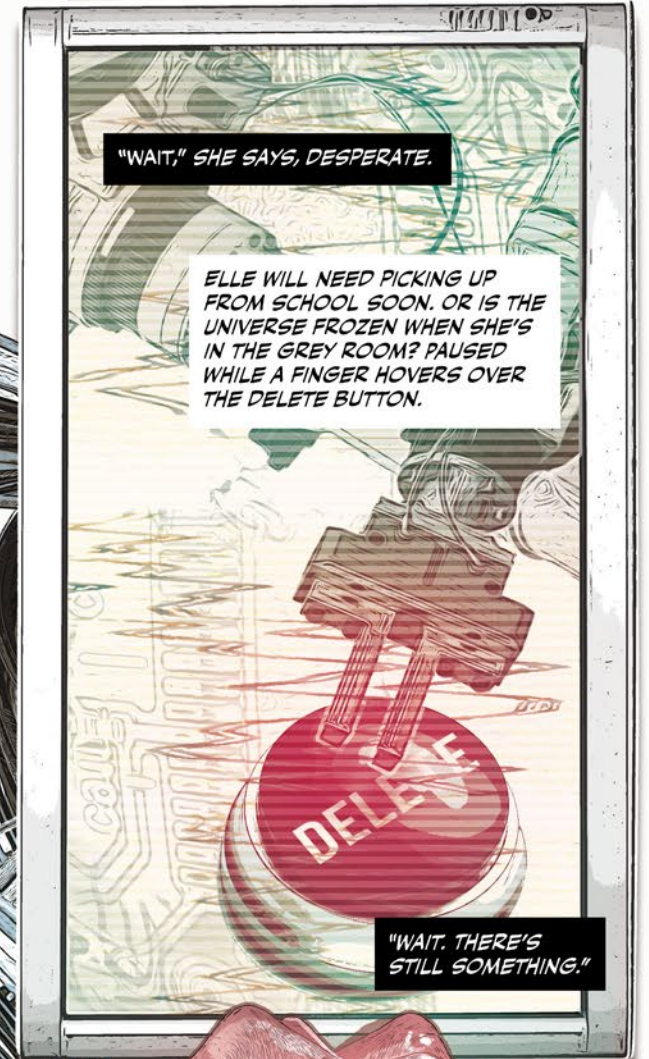
"I CAN DO IT - I CAN," SHE SAYS. "I MANAGED FOR 12 YEARS. DO YOU KNOW HOW MANY TIMES I RESET?"

"WAIT," SHE SAYS, DESPERATE.

ELLE WILL NEED PICKING UP FROM SCHOOL SOON. OR IS THE UNIVERSE FROZEN WHEN SHE'S IN THE GREY ROOM? PAUSED WHILE A FINGER HOVERS OVER THE DELETE BUTTON.

"WAIT. THERE'S STILL SOMETHING."

"TOO MANY TIMES." THE VOICE IS AS COLOURLESS AS THE ROOM. "YOU COULD NOT PREVENT THIS KNOWLEDGE FROM SPREADING AS YOU PROMISED. A WIPE IS REQUIRED."





# FINALLY

SHE RESETS TO  
MID-PREGNANCY,  
WHEN SHE AND  
SAM WERE HIKING.

AN AUTUMN SUNDAY  
FINDS THEM AT THE  
TOP OF GROUSE  
MOUNTAIN.

MARIELLE LAGS  
BEHIND. TELLS HIM  
IT'S THE WEIGHT  
OF THE BABY THAT  
SLOWS HER DOWN,  
RATHER THAN DREAD.

THEY WALK A  
NARROW PATH.

EVEN KNOWING WHAT  
SHE KNOWS, IT'S  
HARD TO BELIEVE  
EVERYTHING IS CODE.

ELLE, GROWING  
INSIDE HER.

THE SUN IN  
THE BLUE SKY.

HER HUSBAND.

SAM STANDS ON THE CLIFF  
EDGE ADMIRING THE VIEW.

SHE IS SO CLOSE  
TO HIM NOW.

SHE STEPS  
FORWARD...